

Copyright
by
Samuel Meir Factor
2023

The Dissertation Committee for Samuel Meir Factor
certifies that this is the approved version of the following dissertation:

**Kernel-Phase Interferometry for Detection of Close-in
Companions: Binary Demographics of Brown Dwarfs
from Birth to Maturity**

Committee:

Adam L. Kraus, Supervisor

Brendan P. Bowler

Neal J. Evans II

Michael J. Ireland

John H. Lacy

Stella S. R. Offner

**Kernel-Phase Interferometry for Detection of Close-in
Companions: Binary Demographics of Brown Dwarfs
from Birth to Maturity**

by

Samuel Meir Factor

DISSERTATION

Presented to the Faculty of the Graduate School of
The University of Texas at Austin
in Partial Fulfillment
of the Requirements
for the Degree of

DOCTOR OF PHILOSOPHY

THE UNIVERSITY OF TEXAS AT AUSTIN

August 2023

Acknowledgments

First, I would like to respectfully acknowledge that I live and work on indigenous land. I acknowledge the Alabama-Coushatta, Caddo, Carrizo/Comecrudo, Coahuiltecan, Comanche, Kickapoo, Lipan Apache, Tonkawa and Ysleta Del Sur Pueblo, and all the American Indian and Indigenous Peoples and communities who have been or have become a part of these lands and territories in Texas, here on Turtle Island, the ancestral name for what now is called North America.

I would like to thank my advisor for this work, Adam Kraus. This project started as an interesting topic he suggested for a mid-term/final project in his Planetary Astrophysics class and went on to become my dissertation. I am thankful for all of the mentorship, guidance, and feedback he has provided over the years. His breadth and depth of astronomy knowledge is inspiring. I would also like to thank my committee members, Drs. Brendan Bowler, Neal Evans, Michael Ireland, John Lacy, and Stella Offner, for their service. I would also like to thank the postdoc members of the binary stars research group—specifically Drs. Andrew Mann, Trent Dupuy, Will Best, Ben Toffelmire, and Aaron Rizzuto—and everyone who asked questions and gave suggestions at conferences.

I would not have gotten to this point without my previous research ad-

visors. First, Fred Ellis who gave me my first opportunity to conduct scientific research which resulted in three second author papers (Bender et al., 2013; Chitsazi et al., 2014; Lee et al., 2014). And second, A. Meredith Hughes, who guided me through my transition from physics to astrophysics. Her passion for teaching and research continue to inspire me to this day. The research I conducted under her mentorship and her radio astronomy course sparked my interest in a key aspect of my current research, interferometry, so much so that I got one of the fundamental equations tattooed on my forearm (See Figure 1.1).

Next, I would like to thank my graduate student colleagues, classmates, and friends at UT. One of the main reasons why I chose to come to UT Austin was the friendly and supportive graduate student community. Graduate school can be an extremely stressful experience and we all appreciate the support through both celebration and commiseration. Specifically I would like to thank my cohort Sinclaire Manning, Zach Vanderbosch, Sydney Sherman, and Jessica Luna; we suffered through some late night problem sets but were always joking and having fun on the side. I overlapped with many other amazing people in my time at UT including Briana Indahl (shout out to #EclipseCrew2017), Danny Krolkowski, Tyler Nelson, Catherine Manea, Melanie Rowland, Katie Chworowsky, and Quang Tran; we built friendships and memories that will last long after we leave Austin. Finally, to Emily Lubar, you were a shining light in the darkest parts of the pandemic and you continue to inspire me every single day.

I would not be in this world without my parents, Robert Factor and Kris Rasmussen. You encouraged and enabled me to pursue my dreams. From my very early aspirations to be a geologist/expedition doctor and helicopter pilot, you threw amazing themed birthday parties and got me into some great summer camps which sparked lifelong passions.

Finally, this work was funded by *HST* archival programs AR-14561 (Factor & Kraus, 2016) and AR-16612 (Factor & Kraus, 2021a) as well as a UT Austin Continuing Fellowship. This work has benefited from The Ultra-coolSheet, maintained by Will Best, Trent Dupuy, Michael Liu, Rob Siverd, and Zhoujian Zhang, and developed from compilations by Dupuy & Liu (2012), Dupuy & Kraus (2013), Liu et al. (2016), Best et al. (2018), and Best et al. (2021). This work has made use of data from the European Space Agency (ESA) mission *Gaia* (<https://www.cosmos.esa.int/gaia>), processed by the *Gaia* Data Processing and Analysis Consortium (DPAC, <https://www.cosmos.esa.int/web/gaia/dpac/consortium>). Funding for the DPAC has been provided by national institutions, in particular the institutions participating in the *Gaia* Multilateral Agreement.

Kernel-Phase Interferometry for Detection of Close-in Companions: Binary Demographics of Brown Dwarfs from Birth to Maturity

Publication No. _____

Samuel Meir Factor, Ph.D.
The University of Texas at Austin, 2023

Supervisor: Adam L. Kraus

Filling out the dearth of detections between direct imaging and radial velocity surveys will test theories of planet formation and (sub)stellar binarity across the full range of semi-major axes, connecting formation of close to wide separation gas giants and sub-stellar companions. Direct detection of close-in companions is notoriously difficult as classical techniques fail near the diffraction limit. In this dissertation, I present a new pipeline which searches for faint companions using kernel-phase interferometry (KPI), a technique utilizing interferometric analysis of the full unobscured telescope aperture. I demonstrate the pipeline, and the power of KPI, by performing two surveys and accompanying demographic analyses.

First, I search for companions in the entire *HST/NICMOS* F110W and F170M image archive of nearby brown dwarfs (BDs), demonstrating significant sensitivity to companions at half the diffraction limit. I discover no new

companions but recover and refine astrometry of 19 previous imaging companions and confirm two previous kernel-phase detections. I also present contrast curves to enable a population study and to demonstrate the strength of this technique at separations inaccessible to classical imaging techniques.

Second, after estimating physical properties of a subset of this sample, I use a Bayesian framework to compare these detections and detection limits to a model companion population. When correcting for Malmquist bias, I find a smaller population of companions with tighter separations than seen in previous studies. This is due to our use of KPI, which enables us to resolve the peak of the semimajor axis distribution with significant sensitivity to low-mass companions. I confirm the previously-seen trends of decreasing binary fraction with decreasing mass and a strong preference for tight and equal-mass systems in the field-age sub-stellar regime; only $\sim 1\%$ of systems are wider than 20 au or have a mass ratio $q < 0.6$.

Third, I present the results of a second KPI based survey of sub-stellar objects in Taurus and Upper Scorpius using archival HST/ACS. I present 6 new candidate detections at extremely tight separations, in addition to 4 previously known companions. This is the first application of KPI to visible-wavelength observations. I find an observed companion frequency of $F_{\text{obs}} = 0.24^{+0.10}_{-0.08}$ which is slightly higher than previous studies, consistent with our new detections.

Combining these two surveys and demographic analyses, I find a significant excess of young wide ($\rho > 10$ au) companions compared to the field. I also

find that the field population of wide companions is consistent with my population of systems formed in low density regions if it were to be diluted by *single* systems formed in high density regions. This is consistent with dynamical evolution preferentially dissolving systems born in high-density star-forming regions over those in low-density regions. I attribute the characteristics of the BD binary population to turbulent fragmentation setting the initial conditions followed by a brief period of dynamical evolution, removing the widest and lowest-mass companions, before the birth cluster dissolves.

Table of Contents

Acknowledgments	4
Abstract	7
List of Tables	15
List of Figures	16
Chapter 1. Introduction	26
1.1 Star and Companion Formation	27
1.1.1 Companion Formation Mechanisms	29
1.1.1.1 Direct collapse via fragmentation	29
1.1.1.2 Disk Instability	30
1.1.1.3 Core Accretion	31
1.1.2 Evolution from the Birth to Field Populations	31
1.2 Direct Imaging	33
1.2.1 Obstacles to Direct Imaging	33
1.2.2 Interferometry	36
1.2.3 Kernel-Phase Interferometry	41
1.2.3.1 Examples	44
1.2.4 Applications of Kernel-Phase Interferometry	48
1.3 Work Presented in this Dissertation	50
Chapter 2. NICMOS Kernel-Phase Interferometry I. Catalogue of Brown Dwarfs Observed in F110W and F170M	53
2.1 Chapter Abstract	53
2.2 Introduction	54
2.3 Observations	59
2.3.1 NICMOS Data	59

2.3.2	Target Sample	60
2.4	Methods	63
2.4.1	Kernel-phase Analysis	63
2.4.2	Kernel-Phase Pipeline	66
2.4.2.1	Aperture Characterization	67
2.4.2.2	Kernel-Phase calculation	68
2.4.2.3	Calibration	70
2.4.2.4	Model Fitting	74
2.4.3	Detection Limits	75
2.4.4	Bayesian Model Comparison	81
2.5	Results	82
2.5.1	Known Binaries	84
2.5.2	Marginal Detection	88
2.5.3	Spurious Detections	89
2.5.4	Notable Non-detections	94
2.5.5	Survey Detection Limits	98
2.6	Discussion	110
2.6.1	Binary Frequency	110
2.6.2	Implications for Dynamical Mass Measurements	112
2.6.3	Scramble and fit detection limits vs. Bayes factors	113
2.6.4	KPI In Context	115
2.7	Conclusions	116
2.8	Acknowledgments	118
Chapter 3.	NICMOS Kernel-Phase Interferometry II:	
	Demographics of Nearby Brown Dwarfs	119
3.1	Chapter Abstract	119
3.2	Introduction	120
3.3	Observations	124
3.3.1	NICMOS Data	124
3.4	Methods	126
3.4.1	Physical Properties of Binaries	126
3.4.2	Binary Population	130

3.5	Results: Binary Demographics	137
3.5.1	Demographics from an Uninformed Prior	138
3.5.2	Demographics from an Informed Prior	142
3.5.3	Mass-ratio Demographics	143
3.5.4	“Observed” Population Without Accounting for Malmquist Bias	149
3.6	Discussion	149
3.6.1	Demographics in the Context of Previous Surveys	149
3.6.2	Implications for Binary Formation	156
3.7	Summary	163
3.8	Acknowledgments	165
Chapter 4.	ACS/HRC Kernel-Phase Interferometry I. New Young Planetary-Mass Objects in Taurus and Upper Scorpius	167
4.1	Chapter Abstract	167
4.2	Introduction	168
4.3	Observations	170
4.3.1	Sample Selection	170
4.3.2	Observations	173
4.4	Methods	175
4.4.1	Aperture model	176
4.4.2	Image Preparation	177
4.4.3	Kernel-Phase Computation	179
4.4.4	Binary Modeling	180
4.4.5	Detection Limits	181
4.4.6	Physical Properties of Binaries	186
4.4.7	Binary Population	187
4.5	Results	190
4.5.1	Binary Detections	190
4.5.1.1	Known Binary Detections	192
4.5.1.2	Non-detection of a Candidate Binary	193
4.5.1.3	New Binary Detections	194

4.5.2	Detection Limits	196
4.5.3	Binary Demographics at a Young Age	197
4.6	Discussion	203
4.6.1	Demographics in the Context of Previous Surveys	203
4.6.2	Comparison to Orion and the Field Population	205
4.6.3	Implications for Binary Formation	208
4.7	Summary	211
4.8	Acknowledgments	213
Chapter 5.	Summary and Future Directions	214
5.1	Summary of Work Presented	214
5.2	Future Work	217
5.2.1	Finalize ACS KPI Analysis	217
5.2.2	Future directions of KPI	219
Appendices		221
Appendix A.	Figure Set corresponding to Figure 2.4: Corner plots, KP correlation Plots, and Images	222
Appendix B.	Figure Set corresponding to Figure 2.5: Detection Limits for Single Sources	241
Appendix C.	Figure Set corresponding to Figure 2.6: Detection Limits for Significant Detections (See Section 2.5.1)	283
Appendix D.	Figure Set corresponding to Figure 2.7: Detection Limits for Notable Non-Detections (See section 2.5.4)	293
Appendix E.	Figure Set corresponding to Figure 2.9: Detection Limits for Marginal and Spurious Detections (See Sections 2.5.2 and 2.5.3)	299
Appendix F.	Figure Set corresponding to Figure 3.2: Detection limits for different field ages	301

Appendix G. Figure Set corresponding to Figure 3.3: Corner plots for demographic fits for different ages	308
Appendix H. Figure Set corresponding to Figure 3.4: 2D population distributions and detections for different ages	315
Appendix I. Figure Set corresponding to Figure 3.6: Binary probability as a function of mass ratio for different ages	322
Appendix J. Figure Set corresponding to Figure 3.9: Mass-ratio power-law index injection results for different field ages	329
Appendix K. Figure Set corresponding to Figure 4.2: Corner plots, KP correlation Plots, and Images	336
Appendix L. Figure Set corresponding to Figure 4.3: Detection Limits for Significant Detections	355
Appendix M. Figure Set corresponding to Figure 4.4: Detection Limits for Single Sources	365
Bibliography	389

List of Tables

2.1	Observations	61
2.2	Target information	62
2.3	Binary astrometry & photometry	85
2.4	Individual 5σ Contrast Ratio Limits in F110W	102
2.5	Individual 5σ Contrast Ratio Limits in F170M	104
2.6	Individual 5σ Contrast Ratio Limits at Tight Separations . .	108
3.1	Observations	125
3.2	Absolute <i>HST</i> magnitude to LogL coefficients	129
3.3	Fit and Intermediary Binary Properties	131
3.4	Final Binary Properties	132
3.5	Binary Population Parameters	140
4.1	Upper-Scorpius and Taurus-Auriga Target Sample	174
4.2	Binary astrometry & photometry	184
4.3	Binary properties	188
4.4	Binary Population Parameters	200

List of Figures

1.1	The equation for a Fourier Transform	38
1.2	Example aperture geometries	45
2.1	<i>HST/NICMOS</i> Aperture model	68
2.2	The progression from image to kernel phase for a binary . . .	71
2.3	The progression from image to kernel phase for a BD with no companion	72
2.4	Binary fit posterior, kernel-phase correlation, and image	76
2.5	Detection limits for a non-detection	78
2.6	Detection limits for a significant detection	79
2.7	Detection limits for a noteable non-detection	80
2.8	Histogram of Bayes factors	83
2.9	Detection limit for the marginal detection of 2M 2028+0052 .	89
2.10	Binary fit posterior, kernel-phase correlation and image for 2M 2028 +0052	90
2.11	Binary fit posterior, kernel-phase correlation and image for 2M 0024 -0158	92
2.12	Images of 2M 0024-0158 showing bad pixels	93
2.13	Binary fit posterior, kernel-phase correlation and image for 2M 0205 -1159	95
2.14	Binary fit posterior, kernel-phase correlation and image for 2M 2204 -5646	96
2.15	Stacked detection limits in observed units	100
2.16	Difference in sensitivity between F110W and F170M	101
3.1	Empirical relations for converting 2MASS to <i>HST</i> photometry	130
3.2	Stacked detetction limits in physical units	133
3.3	Demographic model posterior distributions	139
3.4	Modeled and observed 2D population	144

3.5	Binary population as a function of projected separation	145
3.6	Binary population as a function of mass ratio	147
3.7	Mass-ratio power-law index as a function of age	148
3.8	Binary demographic parameters as a function of stellar mass .	155
3.9	Mass-ratio power-law index with an injected detection	157
4.1	<i>HST/ACS</i> aperture model	178
4.2	Binary fit posterior, kernel-phase correlation, and image for CTIO-USCo-55	182
4.3	Example detection limits for a significant detection	185
4.4	Example detection limits for a non-detection	185
4.5	Stacked survey detection limits in observed units	186
4.6	Stacked detection limits in physical units	191
4.7	Demographic model posterior distributions	199
4.8	Modeled and observed 2D population	201
4.9	Binary population as a function of projected separation	202
4.10	Binary population as a function of mass ratio	204
4.11	Demographic model posterior distributions of the field and young populations	209
A.1	Corner plot, KP correlation plots, and image for the fit to 2M 0004-4044 from program 10143.	222
A.2	Corner plot, KP correlation plots, and image for the fit to 2M 0025+4759 from program 10143.	223
A.3	Corner plot, KP correlation plots, and image for the fit to 2M 0147-4954 from program 10143.	224
A.4	Corner plot, KP correlation plots, and image for the fit to 2M 0423-0414 from program 9833.	225
A.5	Corner plot, KP correlation plots, and image for the fit to 2M 0423-0414 from program 10143.	226
A.6	Corner plot, KP correlation plots, and image for the fit to 2M 0429-3123 from program 10143.	227
A.7	Corner plot, KP correlation plots, and image for the fit to 2M 0700+3157 from program 10143.	228
A.8	Corner plot, KP correlation plots, and image for the fit to 2M 0850+1057 from program 9843.	229

A.9	Corner plot, KP correlation plots, and image for the fit to 2M 0926+5847 from program 9833.	230
A.10	Corner plot, KP correlation plots, and image for the fit to 2M 1021-0304 from program 9833.	231
A.11	Corner plot, KP correlation plots, and image for the fit to 2M 1534+1615 from program 11136.	232
A.12	Corner plot, KP correlation plots, and image for the fit to 2M 1553+1532 from program 9833.	233
A.13	Corner plot, KP correlation plots, and image for the fit to 2M 1728+3948 from program 9843.	234
A.14	Corner plot, KP correlation plots, and image for the fit to 2M 2052-1609 from program 11136.	235
A.15	Corner plot, KP correlation plots, and image for the fit to 2M 2052+0937 from program 10143.	236
A.16	Corner plot, KP correlation plots, and image for the fit to 2M 2252-1730 from program 10143.	237
A.17	Corner plot, KP correlation plots, and image for the fit to 2M 2252-1730 from program 11136.	238
A.18	Corner plot, KP correlation plots, and image for the fit to 2M 2255-5713 from program 10879.	239
A.19	Corner plot, KP correlation plots, and image for the fit to 2M 2351-2537 from program 10143.	240
B.1	Detection limits for 2M 0107+0041 from program 10143.	241
B.2	Detection limits for 2M 0123-4240 from program 10143.	242
B.3	Detection limits for 2M 0144-0716 from program 10143.	242
B.4	Detection limits for 2M 0151+1244 from program 9833.	243
B.5	Detection limits for 2M 0155+0950 from program 10143.	243
B.6	Detection limits for 2M 0207+0000 from program 9833.	244
B.7	Detection limits for 2M 0213+4444 from program 10143.	244
B.8	Detection limits for 2M 0228+1639 from program 10143.	245
B.9	Detection limits for 2M 0243-2453 from program 9833.	245
B.10	Detection limits for 2M 0251-0352 from program 10143.	246
B.11	Detection limits for 2M 0255-4700 from program 10143.	246
B.12	Detection limits for 2M 0257-3105 from program 10143.	247
B.13	Detection limits for 2M 0318-3421 from program 10143.	247

B.14 Detection limits for 2M 0348-6022 from program 9833.	248
B.15 Detection limits for 2M 0355+1133 from program 10143.	248
B.16 Detection limits for 2M 0415-0935 from program 9833.	249
B.17 Detection limits for 2M 0439-2353 from program 10143.	249
B.18 Detection limits for 2M 0443+0002 from program 10143.	250
B.19 Detection limits for 2M 0445-3048 from program 10143.	250
B.20 Detection limits for 2M 0500+0330 from program 10143.	251
B.21 Detection limits for 2M 0516-0445 from program 9833.	251
B.22 Detection limits for 2M 0523-1403 from program 10143.	252
B.23 Detection limits for 2M 0624-4521 from program 10143.	252
B.24 Detection limits for 2M 0624+2325 from program 9704.	253
B.25 Detection limits for 2M 0652+4710 from program 10143.	253
B.26 Detection limits for 2M 0727+1710 from program 9833.	254
B.27 Detection limits for 2M 0755+2212 from program 9833.	254
B.28 Detection limits for 2M 0825+2115 from program 10143.	255
B.29 Detection limits for 2M 0835-0819 from program 10143.	255
B.30 Detection limits for 2M 0837-0000 from program 9833.	256
B.31 Detection limits for 2M 0847-1532 from program 10143.	256
B.32 Detection limits for 2M 0859-1949 from program 10143.	257
B.33 Detection limits for 2M 0908+5031 from program 10143.	257
B.34 Detection limits for 2M 0911+7401 from program 10143.	258
B.35 Detection limits for 2M 0921-2104 from program 10143.	258
B.36 Detection limits for 2M 1022+5825 from program 10143.	259
B.37 Detection limits for 2M 1025+3212 from program 10143.	259
B.38 Detection limits for 2M 1043+2225 from program 10143.	260
B.39 Detection limits for 2M 1045-0149 from program 10143.	260
B.40 Detection limits for 2M 1048+0111 from program 10143.	261
B.41 Detection limits for 2M 1051+5613 from program 10143.	261
B.42 Detection limits for 2M 1058-1548 from program 10143.	262
B.43 Detection limits for 2M 1104+1959 from program 10143.	262
B.44 Detection limits for 2M 1108+6830 from program 10143.	263
B.45 Detection limits for 2M 1110+0116 from program 9833.	263

B.46 Detection limits for 2M 1155-3727 from program 10143.	264
B.47 Detection limits for 2M 1203+0015 from program 10143.	264
B.48 Detection limits for 2M 1213-0432 from program 10143.	265
B.49 Detection limits for 2M 1217-0311 from program 9833.	265
B.50 Detection limits for 2M 1221+0257 from program 10143.	266
B.51 Detection limits for 2M 1254-0122 from program 9833.	266
B.52 Detection limits for 2M 1300+1921 from program 10143.	267
B.53 Detection limits for 2M 1421+1827 from program 10143.	267
B.54 Detection limits for 2M 1425-3650 from program 10143.	268
B.55 Detection limits for 2M 1428+5923 from program 10143.	268
B.56 Detection limits for 2M 1439+1929 from program 10143.	269
B.57 Detection limits for 2M 1448+1031 from program 10143.	269
B.58 Detection limits for 2M 1503+2525 from program 9833.	270
B.59 Detection limits for 2M 1506+1321 from program 10143.	270
B.60 Detection limits for 2M 1507-1627 from program 10143.	271
B.61 Detection limits for 2M 1515+4847 from program 10143.	271
B.62 Detection limits for 2M 1552+2948 from program 10143.	272
B.63 Detection limits for 2M 1624+0029 from program 9833.	272
B.64 Detection limits for 2M 1658+7027 from program 10143.	273
B.65 Detection limits for 2M 1705-0516 from program 10143.	273
B.66 Detection limits for 2M 1721+3344 from program 10143.	274
B.67 Detection limits for 2M 1731+2721 from program 10143.	274
B.68 Detection limits for 2M 1750+1759 from program 9833.	275
B.69 Detection limits for 2M 1753-6559 from program 10143.	275
B.70 Detection limits for 2M 1807+5015 from program 10143.	276
B.71 Detection limits for 2M 2002-0521 from program 10143.	276
B.72 Detection limits for 2M 2036+1051 from program 10143.	277
B.73 Detection limits for 2M 2057-0252 from program 10143.	277
B.74 Detection limits for 2M 2104-1037 from program 10143.	278
B.75 Detection limits for 2M 2139+0220 from program 10143.	278
B.76 Detection limits for 2M 2148+4003 from program 10143.	279
B.77 Detection limits for 2M 2224-0158 from program 10143.	279

B.78	Detection limits for 2M 2228-4310 from program 9833.	280
B.79	Detection limits for 2M 2237+3922 from program 10143.	280
B.80	Detection limits for 2M 2249+3205 from program 10143.	281
B.81	Detection limits for 2M 2254+3123 from program 9833.	281
B.82	Detection limits for 2M 2325+4251 from program 10143.	282
B.83	Detection limits for 2M 2339+1352 from program 9833.	282
C.1	Detection limits for 2M 0004-4044 from program 10143.	283
C.2	Detection limits for 2M 0025+4759 from program 10143.	284
C.3	Detection limits for 2M 0147-4954 from program 10143.	284
C.4	Detection limits for 2M 0423-0414 from program 9833.	285
C.5	Detection limits for 2M 0423-0414 from program 11136.	285
C.6	Detection limits for 2M 0429-3123 from program 10143.	286
C.7	Detection limits for 2M 0700+3157 from program 10143.	286
C.8	Detection limits for 2M 0850+1057 from program 9843.	287
C.9	Detection limits for 2M 0926+5847 from program 9833.	287
C.10	Detection limits for 2M 1021-0304 from program 9833.	288
C.11	Detection limits for 2M 1534+1615 from program 11136.	288
C.12	Detection limits for 2M 1553+1532 from program 9833.	289
C.13	Detection limits for 2M 1728+3948 from program 9843.	289
C.14	Detection limits for 2M 2052-1609 from program 11136.	290
C.15	Detection limits for 2M 2152+0937 from program 10143.	290
C.16	Detection limits for 2M 2252-1730 from program 10143.	291
C.17	Detection limits for 2M 2252-1730 from program 11136.	291
C.18	Detection limits for 2M 2255-5713 from program 10879.	292
C.19	Detection limits for 2M 2351-2537 from program 10143.	292
D.1	Detection limits for 2M 0036+1821 from program 10143.	293
D.2	Detection limits for 2M 0045+1634 from program 10143.	294
D.3	Detection limits for 2M 0109+2949 from program 10879.	294
D.4	Detection limits for 2M 0314+1603 from program 10143.	295
D.5	Detection limits for 2M 0518-2828 from program 10247.	295
D.6	Detection limits for 2M 0528-2828 from program 11136.	296

D.7	Detection limits for 2M 0830+4828 from program 10879.	296
D.8	Detection limits for 2M 0915+0422 from program 10143.	297
D.9	Detection limits for 2M 1539-0520 from program 10143.	297
D.10	Detection limits for 2M 1707-0558 from program 10143.	298
D.11	Detection limits for 2M 1936-5502 from program 10143.	298
E.1	Detection limits for 2M 0024-0158 from program 10879.	299
E.2	Detection limits for 2M 0205-1159 from program 11136.	300
E.3	Detection limits for 2M 2204-5646 from program 11136.	300
F.1	Stacked detection limits in physical units for an age of 0.9 Gyr	302
F.2	Stacked detection limits in physical units for an age of 1.2 Gyr	303
F.3	Stacked detection limits in physical units for an age of 1.5 Gyr	304
F.4	Stacked detection limits in physical units for an age of 1.9 Gyr	305
F.5	Stacked detection limits in physical units for an age of 2.4 Gyr	306
F.6	Stacked detection limits in physical units for an age of 3.1 Gyr	307
G.1	Demographic model posterior distributions using an age of 0.9 Gyr	309
G.2	Demographic model posterior distributions using an age of 1.2 Gyr	310
G.3	Demographic model posterior distributions using an age of 1.5 Gyr	311
G.4	Demographic model posterior distributions using an age of 1.9 Gyr	312
G.5	Demographic model posterior distributions using an age of 2.4 Gyr	313
G.6	Demographic model posterior distributions using an age of 3.1 Gyr	314
H.1	Modeled and observed 2D population using an age of 0.9 Gyr	316
H.2	Modeled and observed 2D population using an age of 1.2 Gyr	317
H.3	Modeled and observed 2D population using an age of 1.5 Gyr	318
H.4	Modeled and observed 2D population using an age of 1.9 Gyr	319
H.5	Modeled and observed 2D population using an age of 2.4 Gyr	320
H.6	Modeled and observed 2D population using an age of 3.1 Gyr	321
I.1	Binary population as a function of q using an age of 0.9 Gyr .	323
I.2	Binary population as a function of q using an age of 1.2 Gyr .	324
I.3	Binary population as a function of q using an age of 1.5 Gyr .	325

I.4	Binary population as a function of q using an age of 1.9 Gyr	326
I.5	Binary population as a function of q using an age of 2.4 Gyr	327
I.6	Binary population as a function of q using an age of 3.1 Gyr	328
J.1	Mass-ratio power-law index with an injected detection using an age of 0.9 Gyr	330
J.2	Mass-ratio power-law index with an injected detection using an age of 1.2 Gyr	331
J.3	Mass-ratio power-law index with an injected detection using an age of 1.5 Gyr	332
J.4	Mass-ratio power-law index with an injected detection using an age of 1.9 Gyr	333
J.5	Mass-ratio power-law index with an injected detection using an age of 2.4 Gyr	334
J.6	Mass-ratio power-law index with an injected detection using an age of 3.1 Gyr	335
K.1	Binary fit posterior, kernel-phase correlation, and image of CTIO-USco-55 in F775W	337
K.2	Binary fit posterior, kernel-phase correlation, and image of CTIO-USco-55 in F850LP	338
K.3	Binary fit posterior, kernel-phase correlation, and image of CTIO-USco-66 in F555W	339
K.4	Binary fit posterior, kernel-phase correlation, and image of CTIO-USco-66 in F775W	340
K.5	Binary fit posterior, kernel-phase correlation, and image of CTIO-USco-66 in F850LP	341
K.6	Binary fit posterior, kernel-phase correlation, and image of CTIO-USco-130 in F850LP	342
K.7	Binary fit posterior, kernel-phase correlation, and image of CTIO-USco-131 in F775W	343
K.8	Binary fit posterior, kernel-phase correlation, and image of KPNO-Tau-1 in F775W	344
K.9	Binary fit posterior, kernel-phase correlation, and image of KPNO-Tau-4 in F850LP	345
K.10	Binary fit posterior, kernel-phase correlation, and image of KPNO-Tau-12 in F775W	346

K.11	Binary fit posterior, kernel-phase correlation, and image of KPNO-Tau-12 in F850LP	347
K.12	Binary fit posterior, kernel-phase correlation, and image of MHO-Tau-5 in F775W	348
K.13	Binary fit posterior, kernel-phase correlation, and image of MHO-Tau-8 in F555W	349
K.14	Binary fit posterior, kernel-phase correlation, and image of MHO-Tau-8 in F775W	350
K.15	Binary fit posterior, kernel-phase correlation, and image of MHO-Tau-8 in F850LP	351
K.16	Binary fit posterior, kernel-phase correlation, and image of V410-Xray-3 in F555W	352
K.17	Binary fit posterior, kernel-phase correlation, and image of V410-Xray-3 in F775W	353
K.18	Binary fit posterior, kernel-phase correlation, and image of V410-Xray-3 in F850LP	354
L.1	Detection limits for CTIO-USco-66	356
L.2	Detection limits for CTIO-USco-130	357
L.3	Detection limits for CTIO-USco-131	358
L.4	Detection limits for KPNO-Tau-1	359
L.5	Detection limits KPNO-Tau-4	360
L.6	Detection limits KPNO-Tau-12	361
L.7	Detection limits for MHO-Tau-5	362
L.8	Detection limits for MHO-Tau-8	363
L.9	Detection limits for V410-Xray-3	364
M.1	Detection limits for CTIO-USco-75	366
M.2	Detection limits for CTIO-USco-100	367
M.3	Detection limits for CTIO-USco-109	368
M.4	Detection limits for CTIO-USco-112	369
M.5	Detection limits for CTIO-USco-128	370
M.6	Detection limits for CTIO-USco-132	371
M.7	Detection limits for CTIO-USco-137	372
M.8	Detection limits for CFHT-Tau-1	373

M.9	Detection limits for CFHT-Tau-2	374
M.10	Detection limits for CFHT-Tau-3	375
M.11	Detection limits for CFHT-Tau-4	376
M.12	Detection limits for KPNO-Tau-2	377
M.13	Detection limits for KPNO-Tau-3	378
M.14	Detection limits for KPNO-Tau-5	379
M.15	Detection limits for KPNO-Tau-6	380
M.16	Detection limits for KPNO-Tau-7	381
M.17	Detection limits for KPNO-Tau-8	382
M.18	Detection limits for KPNO-Tau-9	383
M.19	Detection limits for KPNO-Tau-14	384
M.20	Detection limits for MHO-Tau-4	385
M.21	Detection limits for LH0419+15	386
M.22	Detection limits for V410-Anon-13	387
M.23	Detection limits for GM-Tau	388

Chapter 1

Introduction

Are we alone? This question is fundamental to humanity and drives us to explore the cosmos—searching for signs of life—and develop theories governing processes on the scale of star formation down to molecular biosignatures. My contribution to this question is toward the larger end of this scale: how do companions form around the smallest stars and how is this process different or similar between giant planets and (sub)stellar companions.

The most straightforward method for detecting companions to stars is to image them. The details of the direct imaging technique, which is not nearly as simple as the name would suggest, are outlined below in Section 1.2. Early direct-imaging surveys focused their efforts on young, nearby associations of stars, where planetary-mass companions would both be bright—due to their youth—and well separated from their host stars—due to their host’s proximity to the sun. The first planetary mass companion to be directly imaged was 2M1207 b, a $5.5 M_{\text{Jup}}$ companion to the $\sim 25 M_{\text{Jup}}$ brown dwarf (BD) 2MASSWJ 1207334-393254. Since then the number of directly imaged planetary mass companions ($\lesssim 30 M_{\text{Jup}}$) has grown to almost 70 objects¹.

¹NASA Exoplanet Archive as of 07/2023

The formation mechanisms of companions, from planetary mass to sub-stellar and stellar mass binary systems, is still under debate. Companion frequency, demographics, and orbital architecture can give us hints of the physics governing their formation, from rarely occurring giant planets (Bowler, 2016) to slightly more common sub-stellar companions (Reid et al., 2001; Close et al., 2002; Burgasser et al., 2003c, 2007; Allen, 2007; Fontanive et al., 2018; Factor & Kraus, 2023) to stellar companions which dominate the population (Duquennoy & Mayor, 1991; Raghavan et al., 2010; Duchêne & Kraus, 2013). How do planetary-mass and sub-stellar companions fit between the bottom-up planet formation and top-down binary-formation processes? Expanding both the number of observed companions and the available parameter space which can be searched will update our understanding of these objects and allow us to test our theories of their formation.

1.1 Star and Companion Formation

The canonical picture of star formation, while lacking in some of the detailed physics, describes the general process well (Shu, 1977; Shu et al., 1987). This process begins in large scale molecular clouds which, through ambipolar diffusion, gradually lose magnetic and turbulent support and become unstable. This collapse is defined by the Jeans length (λ_J) or mass (M_J) (Jeans, 1902) which is derived by balancing thermal pressure and gravitational collapse:

$$\lambda_J = \frac{c_s}{\sqrt{G\rho}} = \left(\frac{15k_B T}{4\pi G m_p \mu \rho} \right)^{1/2} \quad (1.1)$$

$$M_J = \frac{4\pi}{3} R_J^3 \rho, \quad (1.2)$$

where c_s is the sound speed, G is the gravitational constant, ρ is the gas density, k_B is the Boltzmann constant, T is the gas temperature, m_p is the mass of the proton, μ is the mean molecular weight, and R_J is half the Jeans length. In the early stages, the cloud collapses isothermally (Larson, 1969), with pressure $p \propto \rho^\eta$ and $\eta = 1$. As density increases, the Jeans mass *decreases* as long as $\eta < 4/3$, causing fragmentation. In this simple case, the typical mass of a core is set by opacity (i.e. how quickly it can radiate away potential gravitational energy as heat). The Jeans mass in a typical molecular cloud core is $M_J \approx 1 M_\odot$ (Larson, 1999), significantly higher than the sub-stellar boundary and hence it remains actively debated how the lowest-mass free-floating objects are formed.

As the cloud collapses, the gas becomes hot enough to fuse deuterium (and later hydrogen) and a protostar is born. Due to conservation of angular momentum, any small rotation at large scales results in large rotation in the core. This rotation, and damping of vertical motion, causes a disk to form around the protostar. As the protostar continues to accrete material from the surrounding envelope it drives a wind which opens a gap along the rotation axis of the star/disk system. As evolution progresses further, the disk is slowly accreted and photo-evaporated away leaving behind a star. This process takes a few Myr (Mamajek, 2009; Williams & Cieza, 2011).

1.1.1 Companion Formation Mechanisms

Many if not all of these processes are complicated by turbulence and magnetic fields, which introduce opportunities for fragmentation of the collapsing core or collapse within the circumstellar disk. These two mechanisms form the basis for how binary (sub)stellar systems are formed. A third mechanism, bottom-up core accretion, plays a role in the formation of less massive planetary companions. Finally, these systems are not born in isolation and can be unstable if they contain more than two large bodies. Thus, they also dynamically evolve with time.

1.1.1.1 Direct collapse via fragmentation

As a core collapses, turbulence and rotation can cause overdensities to fragment and collapse separately. Systems formed via this mechanism tend to be initially widely separated ($\gtrsim 100$ au) though not so wide that they are unbound (< 0.1 pc) (Offner et al., 2016; Guszejnov et al., 2017; Offner et al., 2023). On the lowest mass end, turbulence pushes the fragmentation below the typical $\sim 1 M_{\odot}$ Jeans mass, down to the opacity limit ($\sim 0.01 M_{\odot}$ or $\sim 10 M_{\text{Jup}}$; Boss, 1988; Bate et al., 2002) enabling the formation of substellar (BD) mass cores (Bate, 2012, 2014). Since fragmentation occurs early, while there is still a large reservoir of mass, subsequent accretion tends to bring binary pairs toward equal mass (Fisher, 2004). Turbulent fragmentation seems to be the dominant formation pathway for the lowest mass binaries (Offner et al., 2010).

Current hydrodynamical simulations like those cited above have yet to reach the ~ 1 au resolution needed to accurately simulate the tight separation BD-BD binary systems which dominate the field population. Even so, they have roughly reproduced the binary fraction and trends in mass ratio and separation of field age BDs (Kraus & Hillenbrand, 2012; Luhman, 2012; Offner et al., 2023). However, the formation mechanism behind the somewhat rare widely separated pairs (e.g. Radigan et al., 2009; Kraus et al., 2011; Faherty et al., 2020) is still unknown.

1.1.1.2 Disk Instability

Another location where material can become unstable is inside the disk which forms around a protostar. The general physics of collapse inside a disk is similar to that of core fragmentation except inside a rotating frame of reference. As mass continues to fall from the envelope onto the circumstellar disk, regions of the disk can become Toomre unstable ($1 > Q \equiv \frac{c_s \Omega}{\pi G \Sigma}$, Toomre, 1964). This tends to occur in the outer regions of massive and cool disks as such conditions favor collapse (lower orbital frequency, Ω , lower sound-speed, c_s , and higher surface density, Σ). Depending on the available mass, these clumps can go on to form stars, BDs, or giant planets (Tobin et al., 2016).

In the lowest mass regime, disks around forming BDs do not contain enough mass to form another BD (Burgasser et al., 2007). However, it is possible for BD-BD binaries to form as higher order multiples inside the disk around a more massive star and survive ejection (Stamatellos & Whitworth,

2009).

1.1.1.3 Core Accretion

The final mechanism for companion formation is bottom-up core accretion (Safronov, 1972). Binary BDs do not form via this mechanism, again as circum-sub-stellar disks do not contain enough mass, though planetary mass companions to stars may form this way. As μm -size dust grains settle in the mid-plain of a protoplanetary disk they can stick together to form pebbles, which grow into boulders, planetesimals, and rocky planets (Lambrechts & Johansen, 2012). This process encompasses a growth in scale of ~ 16 orders of magnitude and must overcome many hurdles such as rapid inward migration (Alibert et al., 2005) and the so called “meter barrier” (O’Brien & Greenberg, 2005). Once the core reaches a critical mass of $\sim 20 M_{\oplus}$ (Dodson-Robinson et al., 2008), runaway gas accretion can take place. Giant planet cores can more easily grow to this critical mass if they form outside the “snow line,” where the reservoir of solids is enhanced by ices such as water, CO_2 , and CO. The final composition of a giant planet is thus affected by its location within the disk (Öberg et al., 2011).

1.1.2 Evolution from the Birth to Field Populations

Once a companion—be it planetary mass or a (sub)stellar binary—has formed, its properties are not set in stone. Dynamical evolution, especially for inherently unstable high-order multiple systems, sculpts the companion

distribution from the birth population to the field population. BDs could also be formed via dynamical interactions through the decay of triple systems (Umbreit et al., 2005), or ejection of cores which did not have enough time to grow into more massive stars (Reipurth & Clarke, 2001).

For a binary, or hierarchical multiple, two outcomes are possible during a perturbing event. The orbit of a companion can either be boosted, potentially ejecting the companion, or contracted, hardening the system. In general, the former has been shown in simulations to be the dominant scenario. Wide, and therefore weakly bound, binaries tend to be destroyed with little to no hardening effect on tighter systems (Kroupa et al., 2001; Kroupa & Burkert, 2001; Parker & Goodwin, 2011).

There is a short window of time when these interactions could take place. Using the framework of Weinberg et al. (1987), Burgasser et al. (2003c) and Close et al. (2003) showed that only the widest ($\gtrsim 185$ au for BD mass) systems are significantly effected by interactions with other field stars, GMCs, and the galactic potential. Thus, any major sculpting of the population must take place *before* the birth cluster dissolves.

This effect has been seen at wide (> 20 au) separations by De Furio et al. (2022b), who note a significant excess of BD binaries in the young star-forming region of Orion in comparison to the field. The lifetime of a wide separation (100 au) BD-BD binary in a densely populated environment is $\sim 1 - 5$ Myr (De Furio et al., 2022b; Kroupa et al., 2003), much shorter than that of a stellar mass binary. This may explain why a number of wide BD

binary systems have been discovered in young star-forming regions, with no direct analogs in the field such as Oph 11 (Close et al., 2007), CTIO-USco-108 (Béjar et al., 2008), FU Tau (Luhman et al., 2009), 2MASS J0441+2301 (Todorov et al., 2010), and Oph 98. (Fontanive et al., 2020).

If dynamical interactions do play a significant role in the evolution of the low mass (sub)stellar binary population, the star-formation environment should have a significant effect on the resulting demographics. Detailed studies of closer in companions, such as those in Chapter 3 and 4, comparing binary demographics in the field and in young low-density star-forming regions have supported this conclusion. My work has increased the resolution of direct imaging, allowing studies of BD binarity near the peak of the separation distribution in the field and in nearby low-density star-forming regions. It is still difficult to image companions at similar physical separations in more distant high-density star-forming regions in order to compare the core, not just the tail, of the semimajor axis distribution.

1.2 Direct Imaging

1.2.1 Obstacles to Direct Imaging

In order to take an image of a planet or companion around another star, there are two obstacles which must be overcome: resolution and contrast. With respect to resolution, a few factors are at play. The first is the atmosphere blurring out images, what astronomers call “seeing”. Turbulence in the atmosphere (Kolmogorov, 1941a,b) causes pockets of hot/cold or low/high density

air which have slightly different indices of refraction. These pockets can be thought of as randomly aligned lenses which scramble the incoming light, or similarly tiny speed-bumps imposing random phase offsets which turn the incoming flat planar wave of light into a randomly corrugated surface.

There are two ways of dealing with atmospheric seeing. The first is to use high speed metrology and optics to measure and remove this distortion. This technique is called adaptive optics (Beckers, 1993; Hardy, 1998; Duchêne, 2008) and was actually adopted from technology originally developed for looking through the atmosphere in the opposite direction (i.e. spy satellites; Tyson, 2000). A wavefront sensor is used to measure phase offsets over the incoming wavefront (in the pupil plane) either by observing a point source nearby on sky to the science target (natural guide star, NGS) or by creating an artificial point source by shining a laser into the upper atmosphere (laser guide star, LGS). This phase information is then fed to a deformable mirror (e.g. Roberts & Neyman, 2002) which quickly and accurately imposes the opposite offset that the atmosphere imposed. The second, and more obvious way to deal with atmospheric seeing is to put the telescope above the atmosphere (i.e. in space). However, even with no atmospheric seeing, observations still encounter some blurring due to the wave nature of light.

There is a fundamental limit on the resolution of a telescope, imposed by diffraction. A single infinitesimally small point of light, when observed with a telescope (of finite size), will create an image with light spread out in an airy pattern (Airy, 1835) of angular size λ/D , where λ is the wavelength of light

being observed and D is the diameter of the telescope. This diffraction pattern is caused by path-length differences between rays of light which encounter disparate edges of the telescope (acting like a single or double slit; Young, 1804) and constructively or destructively interfere as a function of position on the detector.

The second major obstacle in direct imaging is contrast (Oppenheimer & Hinkley, 2009); companions can be much fainter than their host stars. The most common method for searching for faint companions is to place the target star behind an occulting mask called a coronagraph (Lyot, 1939; Sivaramakrishnan et al., 2001). This device effectively suppresses the starlight by $\gtrsim 99\%$, enabling the detection of faint companions at separations down to $\sim \text{few} \lambda/D$. More complex designs have since been developed which more effectively manipulate the light diffracted by or otherwise not blocked by the mask (Soummer et al., 2003; Soummer, 2005; Guyon et al., 2006).

No optical system is perfect so, even with effective starlight suppression, some amount of post-processing and analysis is needed to effectively characterize what light is coming from the star or imaged ghosts of the star due to residual wavefront errors—called speckles—and what might be a companion. Broadly speaking, these techniques are called point spread function (PSF) subtraction. One such technique, called angular differential imaging (ADI, Marois et al., 2006), relies on observing strategies which keep any speckles static and use the rotation of the sky to rotate any potential companions around by a predictable angle. Thus, anything that moves by the known amount of rota-

tion can be characterized as an astrophysical source, rather than a speckle. Another such tactic uses images of targets known (or at least suspected) to be single as references which can be used to perform reference star differential imaging (RDI). Complex reconstruction algorithms (e.g. LOCI) can then be used to combine this library and effectively subtract off the PSF (Lafrenière et al., 2007; Lafrenière et al., 2009).

All of these techniques treat the PSF as noise and remove it. If observations are taken in a diffraction-limited regime, the PSF contains valuable information about the source. Rather than discarding this information, an analysis could interpret it. The problem is that all of this information is hidden inside the diffraction pattern and in-order to access it we must enter the Fourier domain (*cue spooky music*). This is called interferometry.

1.2.2 Interferometry

Modern astronomical interferometry is most easily performed (and arguably understood) in the radio frequency domain, where the phase of the incoming wave of light can be directly measured and recorded (using heterodyne receivers). This type of data can be taken simultaneously by multiple telescopes at different locations and combined, or correlated, by a computer (in real time or long after the observations are complete) (Napier, 1995; Ho et al., 2004). The result is a direct measurement of the difference in phase of the incoming light between many pairs of discrete points. These pairs of telescopes (located at xy coordinates in the pupil plane, or a projection of it)

form a baseline and the vector connecting them defines a point in uv space (the xy plane scaled by wavelength).

The measurement made by correlating the signal from two telescopes is called a visibility, $V(u, v)$, and is a complex number giving the strength and phase offset (with respect to other baselines) of the interference at that specific point in uv space. In other words, each baseline samples the strength and phase of a single spatial frequency component (defined by its uv coordinate) of the observed scene. With enough of these measurements, the incoming wavefront can be inferred, which after an inverse-Fourier transform gives an image of the source ($I(\alpha, \beta) \xrightarrow{\mathcal{FT}} V(u, v)$, van Cittert, 1934; Thompson et al., 2017). Figure 1.1 shows the equation for a 1D Fourier transform converting a function of time (t , in seconds) to a function of frequency (ν , in Hz). In imaging, we convert the angular 2D sky brightness distribution I with coordinates α, β (in radians) to the visibility function V with coordinates u, v (in radians $^{-1}$, i.e. spatial/angular frequency).

In practice, this is a bit more complicated than just applying an inverse Fourier transform. Since the pupil response function, $\varepsilon(u, v)$, is discretely sampled, there is a significant amount of missing information and it is most likely not Nyquist sampled (Shannon, 1949). Thus, an algorithm must be used to fill in the gaps (e.g. CLEAN, Högbom, 1974). These algorithms not only fill in missing information but also attempt to remove the effects of the oddly shaped “PSF” (or dirty beam, $E(\alpha, \beta) = \mathcal{FT}^{-1}[\varepsilon(u, v)]$), created by the discrete baselines irregularly sampling the uv plane. In a sense, these two objectives are

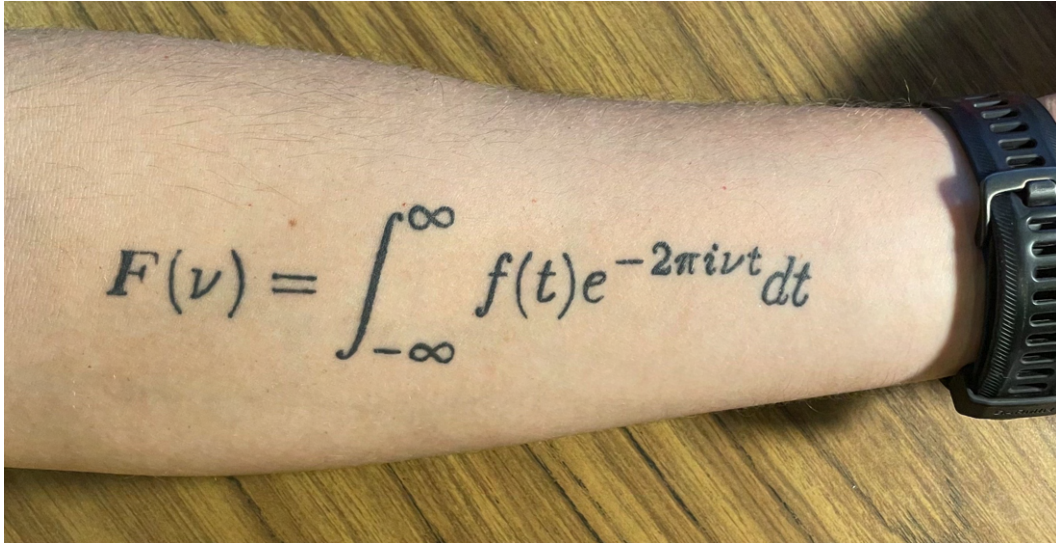


Figure 1.1: The equation for a Fourier transform tattooed on S. Factor’s forearm. $f(t)$ is the function, of time, being transformed into $F(\nu)$, a function of frequency.

the same thing, and these deconvolution algorithms are analogous to PSF subtraction algorithms discussed above. Combining light from many telescopes on long baselines has been used to image objects at scales inaccessible to single dish telescopes (e.g. asymmetrical structures in protoplanetary disks and accretion disks around super-massive black holes; Factor et al., 2017; Andrews et al., 2018; Event Horizon Telescope Collaboration et al., 2019).

In the shorter wavelength regime, CCDs or similar devices are used to detect light and thus, direct measurement of phase is impossible. Different beams of incoming light must be made to actively interfere *before* they are detected. Similar to radio interferometers, this can be done on large scales with discrete telescopes (e.g. Keck I and II, VLTI, and CHARA; Colavita et al.,

2004; Glindemann et al., 2000; ten Brummelaar et al., 2005). Light must be guided from the telescope into a beam combining facility and then into the instrument. These facilities, and their instruments, have produced spectacularly high resolution results from directly measuring the radii of stars (von Braun et al., 2011) to characterizing exoplanets through precise measurements of their orbits and spectra (GRAVITY Collaboration et al., 2020).

Interferometry can also be used on a single aperture telescope to recover information at (or even below) the diffraction limit. One surprising way to convert a single, large aperture, telescope into an interferometer is by intentionally misaligning segments of the primary mirror to create multiple images from different regions of the mirror (i.e. segment tilting, Monnier et al., 2009). Another much more common method is to place a non-redundant or sparse aperture mask (NRM/SAM), consisting of a sheet of opaque material with a number of precisely placed holes, in the pupil plane of the telescope. This technique is called aperture masking interferometry (AMI; Haniff et al., 1995; Tuthill et al., 2000), and effectively turns a single large mirror into a group of small mirrors. This type of observation was actually utilized long before modern astrophysics (Michelson, 1891; Michelson & Pease, 1921) and recently regained popularity (Tuthill, 2012).

In general, the image observed by a telescope is the convolution of the sky brightness distribution ($I(\alpha, \beta)$) with the PSF (or dirty beam discussed above, $E(\alpha, \beta)$) which, due to aberrations, is difficult to precisely characterize. In the configuration with a mask, light from each subaperture interferes with

the other subapertures creating an interferogram on the image plane, a highly precise though much more complicated PSF or beam. This image can then be Fourier transformed, giving the product of the visibility function ($V(u, v)$) and the pupil response function ($\varepsilon(u, v)$). No direct measurement of the phase of the incoming wavefront is measured in this case, the measured visibility only gives the difference in phase between subapertures.

As noted before, no optical system is perfect so again some post processing and analysis techniques are needed to achieve the highest resolution and sensitivity. One such technique is to use closure phases (Jennison, 1958) which self calibrate out instrumental phase offsets caused by aberrations (i.e. speckles). Recall that the phase of a given visibility is the difference between the phase “seen” at the two corresponding apertures. This phase is a combination of the intrinsic phase, due to the source brightness geometry, and any aberrations along the path the light took between the aperture and the detector. Each aperture contributes its own error term. Thus, summing the visibility phases measured in a triangle of baselines removes the phase errors caused by those baselines. Each of the three baselines contribute one positive and one negative phase error from each aperture and thus the error terms sum to zero. This is demonstrated in a few examples below (See Section 1.2.3.1).

Consequently, any residual phase in the closure-phase observable is caused by the incoming wavefront (i.e. the source geometry) rather than aberrations in the telescope. In other words, closure phases are phase-like observables which are independent of telescope aberrations (i.e. speckle noise).

Closure phases have been used to recover information at spatial scales inaccessible to classical PSF subtraction techniques (Kraus & Ireland, 2012; Sallum et al., 2015). However, one must keep in mind that since these are *phase*-like observables they are insensitive to symmetrical structures in the image (since the Fourier transform is Hermitian). This can be seen as a loss in sensitivity to equal brightness companions at extremely tight separations (See Section 2.5.5 and Figure 2.15).

While AMI is extremely powerful, in its ability to “resolve” structures at and below the λ/D diffraction limit, one large downside is the physical mask itself. Since the mask is sparse by nature it discards much ($\gtrsim 90\%$) of the incoming light, imposing a harsh flux limit on possible targets. If we instead observe without a mask, the continuous primary mirror is still an interferometer, although the “baselines” are now *highly* redundant. This is where kernel-phase interferometry shows its strength.

1.2.3 Kernel-Phase Interferometry

Kernel-phase interferometry, or more particularly the kernel-phase observable, is a generalization of the previously discussed closure phase used with aperture masking interferometry and other interferometric observing techniques (e.g. radio interferometry). Kernel-phase interferometry was first derived by Martinache (2010) and has since been applied to a variety of data-sets including observations from the *Hubble Space Telescope (HST)* and ground based telescopes using adaptive optics. A derivation of the technique can be

found in Section 2.4.1 and is included here in more detail.

Kernel-phase interferometry works by modeling the full telescope aperture as a grid of sub-apertures comprising a (highly redundant) interferometer. From this grid, a set of baselines (vectors in uv space) can be generated by pairing up apertures. At each of these points, a phase (or more generally, a complex visibility) can be sampled from the Fourier transform of the image. Kernel phases can then be constructed based on the geometry of the model aperture.

Each phase (Φ), measured at a point in uv space corresponding to a baseline, is made up of the true source phase (Φ_o) and a combination of random phase errors (ϕ) introduced by pupil path length differences from each of the apertures contributing to the baseline:

$$\Phi = \text{Arg} \left[\sum_{(i,j)} e^{i(\Phi_o + \phi_i - \phi_j)} \right], \quad (1.3)$$

where the pair (i, j) denotes the baselines contributing to the specific visibility. In words, the complex visibility is a superposition of vectors, and importantly phases do not strictly add. If we assume the error terms are small, we can use a Taylor series to approximate each complex phasor as a linear sum, $e^{i(\phi_i - \phi_j)} \approx 1 + i(\phi_i - \phi_j)$ allowing us to write the measured phase as a linear combination:

$$\Phi = \Phi_o + \frac{1}{r} \sum_{(i,j)} (\phi_i - \phi_j), \quad (1.4)$$

where r is the number of (i, j) pairs for a specific phase measurement (i.e. the number of redundant baselines contributing to the visibility). If we stack these

equations for each sampled point in uv space, we can write the vector of all measured phase information as:

$$\Phi = \Phi_0 + \mathbf{R}^{-1} \cdot \mathbf{A} \cdot \phi, \quad (1.5)$$

where the matrix \mathbf{R}^{-1} is a diagonal matrix with $1/r$ for each visibility, encoding the redundancies in the baselines. The matrix \mathbf{A} is a transfer matrix assembled from 1's and -1's in each row encoding the apertures contributing to each (redundant) baseline (any apertures not involved are 0 and apertures contributing multiple times to a single baseline are summed). For ϕ of length n (the number of sub-apertures), and Φ of length m (the number of unique baselines/visibilities), the shape of \mathbf{R} is $m \times m$ and \mathbf{A} is $m \times n$.

Since the goal is to derive a quantity which does not involve the phase error term, we then construct the kernel, \mathbf{K} , of \mathbf{A} such that $\mathbf{K} \cdot \mathbf{A} = \mathbf{0}$. The matrix \mathbf{K} can be calculated using singular value decomposition (SVD, Press et al., 2002). This algorithm gives

$$\mathbf{A} = \mathbf{U} \cdot \mathbf{W} \cdot \mathbf{V}^T, \quad (1.6)$$

where the matrix \mathbf{W} is a diagonal matrix of positive or zero “singular values.” The rows of \mathbf{K} are then the *columns* of \mathbf{U} corresponding to zero elements of \mathbf{W} . After multiplying equation 1.5 by \mathbf{R} and then \mathbf{K} we have

$$\mathbf{K} \cdot \mathbf{R} \cdot \Phi = \mathbf{K} \cdot \mathbf{R} \cdot \Phi_0. \quad (1.7)$$

This results in a set of phase-like observables ($\mathbf{K} \cdot \mathbf{R} \cdot \Phi$), called kernel phases, which are free of instrumental phase errors. Note that in some conventions

the \mathbf{R}^{-1} and \mathbf{A} matrices are combined (and thus the \mathbf{R} and \mathbf{K} matrices are as well) into a single transfer matrix.

1.2.3.1 Examples

The following are three simple examples, adopted from Martinache (2013a), illustrating the aperture geometry and associated matrices. In these cases, the aperture geometries are such that the matrices can be calculated by hand. For larger and more redundant grids the general procedure is the same though must be done on a computer.

The most simple (yet still non-trivial) non-redundant array is a triangle of apertures (top row of Figure 1.2). In this case, the three apertures correspond to three unique baselines (and three more using the opposite sign, though these do not give any additional information). The three measured phases are

$$\Phi^1 = \Phi_{\circ}^1 + (\phi_A - \phi_B) \quad (1.8)$$

$$\Phi^2 = \Phi_{\circ}^2 + (\phi_C - \phi_B) \quad (1.9)$$

$$\Phi^3 = \Phi_{\circ}^3 + (\phi_C - \phi_A). \quad (1.10)$$

Stacking these three equations gives $\Phi = \Phi_{\circ} + \mathbf{A} \cdot \phi$ with the matrix

$$\mathbf{A} = \begin{bmatrix} 1 & -1 & 0 \\ 0 & -1 & 1 \\ -1 & 0 & 1 \end{bmatrix}. \quad (1.11)$$

Since the baselines are unique, \mathbf{R} is the identity matrix and we can ignore it.

We could use the SVD to calculate the kernel of \mathbf{A} as outlined above but this

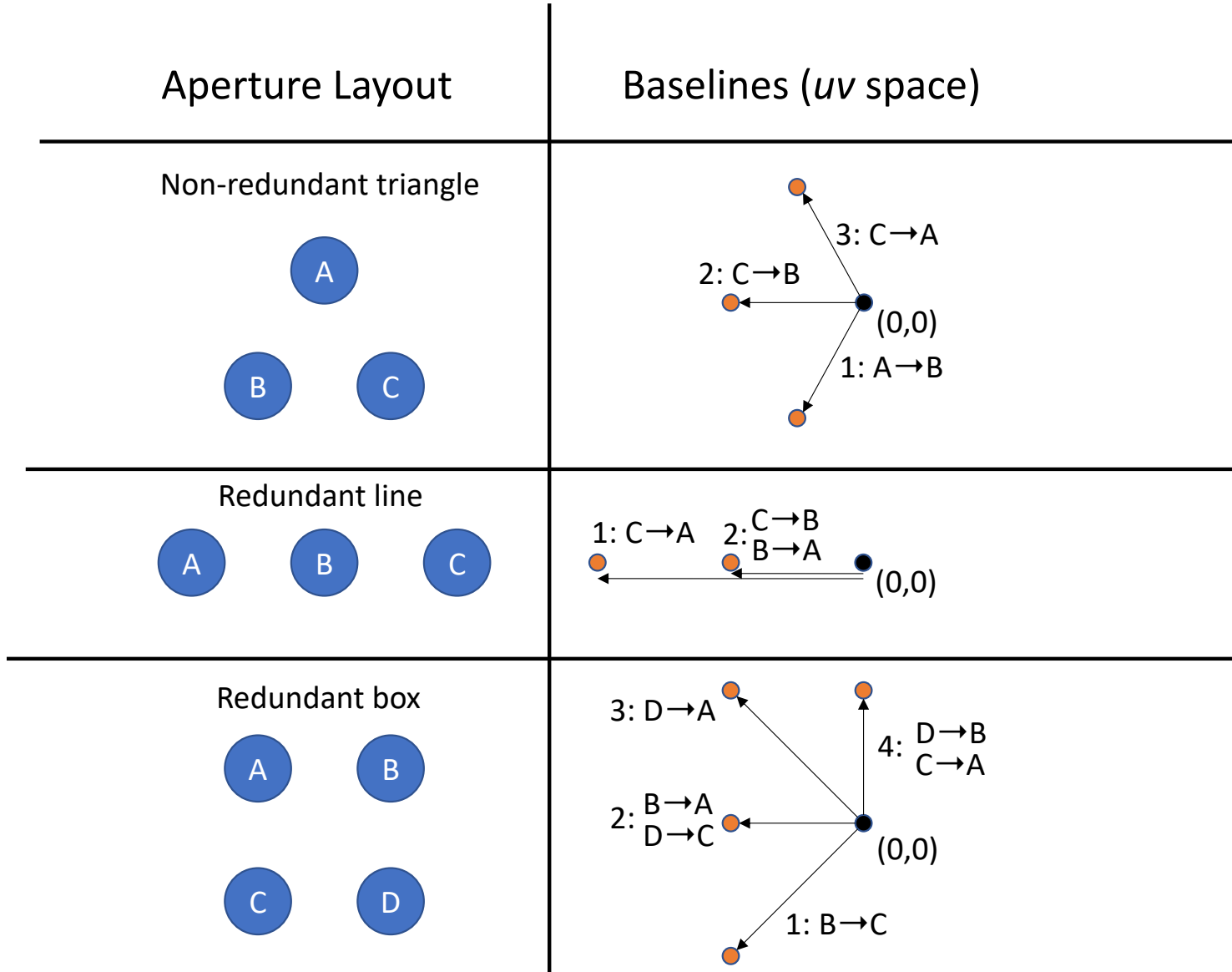


Figure 1.2: Three example aperture geometries (left) and the corresponding baselines (spatial frequencies) sampled in uv space (right). The right column corresponds to the $\varepsilon(u, v)$ pupil response function described above. Adapted from Martinache (2013a).

case is trivial:

$$\mathbf{K} = [1 \ -1 \ 1]. \quad (1.12)$$

In this case, there is one kernel phase which is actually almost a closure phase. If we use the baseline BC instead of CB (reversing the direction and inverting the sign of the second row of \mathbf{A}) the baselines connect to form a triangle of apertures. Each aperture contributes a positive and negative phase error term to the kernel phase since the three baselines go to and from each aperture exactly once, creating a loop. In this updated case $\mathbf{K} = [1 \ 1 \ 1]$, simply summing the sampled phases, thus forming a closure phase.

With a redundant setup, such as a line of three apertures (middle row of Figure 1.2), things get slightly more complicated. As before, we have three apertures but this time there are only two unique baselines, as the spacing between apertures is regular and one baseline is duplicated between two different pairs of apertures. Thus the measured phases (after applying the Taylor expansion) are

$$\Phi^1 = \Phi_{\circ}^1 + (\phi_C - \phi_A) \quad (1.13)$$

$$\begin{aligned} \Phi^2 &= \Phi_{\circ}^2 + \frac{1}{2} [(\phi_B - \phi_A) + (\phi_C - \phi_B)] \\ &= \Phi_{\circ}^2 + \frac{1}{2}(\phi_C - \phi_A) \end{aligned} \quad (1.14)$$

Again, we can stack these two equations, giving $\Phi = \Phi_{\circ} + \mathbf{R}^{-1}\mathbf{A} \cdot \phi$ with the matrices

$$\mathbf{R}^{-1} = \begin{bmatrix} 1 & 0 \\ 0 & 1/2 \end{bmatrix} \text{ and } \mathbf{A} = \begin{bmatrix} -1 & 0 & 1 \\ -1 & 0 & 1 \end{bmatrix}. \quad (1.15)$$

In words, while the two baselines sample different spatial frequencies (different uv coordinates), they contain the same (net) contributions from the apertures. Finally we can calculate the kernel of \mathbf{A} giving us a single kernel phase:

$$\mathbf{K} = [1 \ -1] . \quad (1.16)$$

Again in words, since the baselines contain the same apertures we can subtract the phases to remove the noise contributions, leaving behind the difference in source phase as our single self-calibrated observable.

The final example is slightly more complicated, a square of four apertures (bottom row of Figure 1.2). In this case, the four apertures correspond to four baselines, two of which are unique and two of which are redundant:

$$\Phi^1 = \Phi_{\circ}^1 + (\phi_B - \phi_C) \quad (1.17)$$

$$\Phi^2 = \Phi_{\circ}^2 + \frac{1}{2} [(\phi_B - \phi_A) + (\phi_D - \phi_C)] \quad (1.18)$$

$$\Phi^3 = \Phi_{\circ}^3 + (\phi_D - \phi_A) \quad (1.19)$$

$$\Phi^4 = \Phi_{\circ}^4 + \frac{1}{2} [(\phi_D - \phi_B) + (\phi_C - \phi_A)] . \quad (1.20)$$

Once again we can stack these four equations giving $\Phi = \Phi_{\circ} + \mathbf{R}^{-1} \mathbf{A} \cdot \phi$ with the matrices

$$\mathbf{R}^{-1} = \begin{bmatrix} 1 & 0 & 0 & 0 \\ 0 & 1/2 & 0 & 0 \\ 0 & 0 & 1 & 0 \\ 0 & 0 & 0 & 1/2 \end{bmatrix} \text{ and } \mathbf{A} = \begin{bmatrix} 0 & 1 & -1 & 0 \\ -1 & 1 & -1 & 1 \\ -1 & 0 & 0 & 1 \\ -1 & -1 & 1 & 1 \end{bmatrix} . \quad (1.21)$$

Finally we can calculate the kernel of \mathbf{A} giving us two kernel phases:

$$\mathbf{K} = \begin{bmatrix} 1 & -1 & 1 & 0 \\ 1 & 0 & -1 & 1 \end{bmatrix} . \quad (1.22)$$

In each of these three examples we have constructed matrices based on the specific geometries of the apertures. To apply this to data, we would sample the phases at each of the relevant locations in uv space, creating the vector Φ . To remove phase error terms (ϕ) we can multiply the measured phases by $\mathbf{K} \cdot \mathbf{R}$ (note that we have just constructed \mathbf{R}^{-1}), transforming our vector of phases into a (smaller) vector of kernel phases which are only dependant on the true source phase (Φ_0) as demonstrated in Equation 1.7.

1.2.4 Applications of Kernel-Phase Interferometry

The kernel-phase technique has been underutilized in surveys (relative to classical imaging techniques) since the original publication by Martinache (2010). Analysis by Pope et al. (2013) of *HST*/NICMOS camera 1 images of BDs from Reid et al. (2006, 2008a) proposed five new candidate companions (and four marginal detections) and recovered all previously known companions. I revisit this data-set, and extend it, in Chapter 2 of this work. Kammerer et al. (2019) detected five new and three known low-mass companions in archival imaging from VLT/NACO. They were limited by the available calibrators in the archival data-set. Wallace et al. (2020) surveyed 55 class I and II stars in Taurus using Keck/NIRC2. They used both RDI and KPI techniques to reach a contrast of ~ 6 mag (in L') at $0''.2$ though did not detect any new companions. Kammerer et al. (2021) used KPI on observations of the T Tauri triple system from VLT/VISIR-NEAR near the $\sim 9.7\ \mu\text{m}$ silicate feature to infer the geometry of the system's three components and circumstellar and

circumbinary disks.

There have however been a number of observational demonstrations and tests of the performance of KPI in specific circumstances as well as comparisons to NRM/SAM/AMI. Pope et al. (2016) compared the performance of KPI against classical PSF subtraction and NRM using Palomar/PHARO observations of the α Ophiuchi binary system. They found that KPI can reach comparable contrast limits to NRM more efficiently. They also emphasize the importance of calibration for ground based observations. Laugier et al. (2019) focused on recovering information from saturated *HST*/NICMOS camera 2 images of the Gl 494AB system and found that, for point sources, interpolation is good enough to reconstruct the lost information. Ceau et al. (2019) used detection tests to examine the theoretical limits of KPI used in conjunction with *JWST*/NIRISS. Sallum & Skemer (2019) used simulated Keck/NIRC2 and *JWST*/NIRCam and NIRISS data to compare the theoretical limits of NRM and KPI, finding that the two methods reach comparable sensitivity with KPI performing better at low SNR while NRM performs better on bright targets. Martinache et al. (2020) tested different aperture modeling prescriptions to show that a lower resolution model which incorporates a transmission factor (rather than a binary clear or opaque subaperture) was less affected by systematic errors and thus was sensitive to higher contrast companions. Laugier et al. (2020) demonstrated angular differential kernel-phase analysis of a binary star observed with Subaru/SCEXAO. Kammerer et al. (2023) demonstrated KPI on the NIRISS instrument on *JWST* and presented

a pipeline specifically for this analysis. They find that KPI and AMI perform similarly with comparable amounts of observing time, though KPI is superior to AMI for faint targets and at wide ($\gtrsim 325$ mas) separations. Most recently, Chaushev et al. (2023) demonstrated spectrally dispersed kernel-phase interferometry with SCExAO/CHARIS as well as a method to calibrate the data using spectral differential imaging.

Finally, a few theoretical extensions of the technique have been explored. These include Ireland (2013), who described calibration techniques and other bases which can be used to reduce systematic errors in kernel phases. Pope (2016) extended kernel phases to kernel amplitudes, and Pope et al. (2021) extended the analysis technique to coronagraphic data, utilizing automatic differentiation to calculate the relevant matrices for an obscured image.

In this work I present a new KPI analysis pipeline and apply it to two sets of observations from *HST*. I used it to search for companions around nearby field age BDs in observations from NICMOS and more distant young sub-stellar objects using ACS/HRC. I explored best practices for calibration in the archival NICMOS dataset and demonstrated the technique for the first time at optical wavelengths using ACS/HRC.

1.3 Work Presented in this Dissertation

This dissertation is broken up into three main bodies of work. In Chapter 2 I introduce a new kernel-phase interferometry pipeline. I then demonstrate it on the entire *HST*/NICMOS archive of observations of BDs observed

in F110W and F170M, a sample of 114 objects observed in 7 different programs. I refine astrometry and photometry of previously known companions and confirm two previous kernel-phase detections. I also present contrast curves, showing the pipeline is able to detect companions down to flux ratios of $\sim 10^2$ at separations down to half the diffraction limit. The binary fraction of this sample is consistent with previous surveys.

In Chapter 3 I present a demographic analysis of the previously discussed catalogue of field age BDs. I first estimate the physical properties of the sample using Gaia distances and a set of evolutionary models. I then use a Bayesian framework to combine our detections and sensitivity and infer a population defined by log-normal separation and power-law mass-ratio distributions. When correcting for Malmquist bias, I present a companion fraction of $F = 0.11^{+0.04}_{-0.03}$ and a separation distribution centered at $\rho = 2.2^{+1.2}_{-1.0}$ au. These values are smaller and tighter than seen in previous studies, due to my ability to resolve the peak of the semimajor axis distribution with significant sensitivity to low-mass companions. I confirm the previously-seen trends of decreasing binary fraction with decreasing mass and a strong preference for tight and equal-mass systems in the field-age sub-stellar regime. I attribute this to turbulent fragmentation setting the initial conditions followed by a brief period of dynamical evolution, removing the widest and lowest-mass companions, before the birth cluster dissolves.

In Chapter 4 I apply a modified version of the pipeline presented in Chapter 2 to the ACS/HRC camera on *HST*. This is the first time kernel-phase

interferometric analysis has been applied to this camera or at a wavelength below one micron. I analyse a sample of sub-stellar objects in the young star-forming regions of Taurus and Upper Scorpius. I present 6 new candidate detections at extremely tight separations in addition to 4 previously known companions. I then apply a similar analysis to that which was described in Chapter 3. I derive physical properties of the sample and model the population using a Bayesian framework. I find an observed companion frequency of $F_{\text{obs}} = 0.24^{+0.10}_{-0.08}$ which is slightly higher than previous studies due to our new detections. The demographics of our survey again confirm previously seen trends of a strong preference for equal-mass binaries and a decreasing companion frequency with decreasing mass. I compare the demographics of our sample of young objects in low-density star-forming regions to the field and find a significant excess. I find that the field population of wide ($\rho > 10$ au) companions is consistent with a population of wide systems formed only in low-density regions and diluted by single systems formed in high-density regions. This indicates that dynamical evolution removes wide-separation companions born in high-density regions, where the majority of stars form, before the cluster dissolves, while leaving the population born in low-density regions largely untouched.

Finally, in Chapter 5 I summarize the work I previously presented, connecting the common threads of the previous three chapters, and outline future work to be done in the field of high contrast imaging and low-mass binary formation.

Chapter 2

NICMOS Kernel-Phase Interferometry I. Catalogue of Brown Dwarfs Observed in F110W and F170M¹

2.1 Chapter Abstract

Filling out the dearth of detections between direct-imaging and radial-velocity surveys will test theories of planet formation and (sub)stellar binarity across the full range of semi-major axes, connecting formation of close to wide separation gas giants and substellar companions. Direct detection of close-in companions is notoriously difficult: coronagraphs and point spread function (PSF) subtraction techniques fail near the λ/D diffraction limit. We present a new faint companion detection pipeline called Argus which analyzes kernel phases, an interferometric observable analogous to closure phases from non-redundant aperture masking but utilizing the full unobscured telescope aperture. We demonstrate the pipeline, and the power of interferometry, by performing a companion search on the entire *HST*/NICMOS F110W and F170M image archive of 114 nearby brown dwarfs (observed in 7 different programs). Our pipeline is able to detect companions down to flux ratios of

¹Previously published in *The Astronomical Journal* as Factor & Kraus (2022a)

$\sim 10^2$ at half the classical diffraction limit. We discover no new companions but recover and refine astrometry of 19 previous imaging companions (two with multiple epochs) and confirm two previous kernel-phase detections. We discuss the limitations of this technique with respect to non-detections of previously confirmed or proposed companions. We present contrast curves to enable population studies to leverage non-detections and to demonstrate the strength of this technique at separations inaccessible to classical imaging techniques. The binary fraction of our sample ($\epsilon_b = 14.4^{+4.7\%}_{-3.0\%}$) is consistent with previous binary surveys, even with sensitivity to much tighter separation companions.

2.2 Introduction

The detection of companions to stars—both planets and stellar binaries—has traditionally relied on three methods: radial velocities (RVs), transits (i.e. eclipses), and direct imaging. Transits and RVs are both limited in their sensitivity to companions at large semimajor axes; transits are increasingly improbable for companions that are distant from their host star, and RV surveys must extend for at least one orbital period before a detection can be confirmed. In contrast, direct-imaging surveys are more sensitive to objects at larger distances from their host star, and hence they offer a singular view into outer solar systems and the peak of the binary semimajor-axis distribution. However, there is often a gap between these two regimes, inside the inner working angle of direct imaging and outside the regime where transits and RVs

can efficiently survey. Filling this gap would offer a crucial new view of both planet formation/evolution and stellar multiplicity.

Binary systems pose stringent tests for models of star and brown dwarf formation, as binaries are a common outcome. A successful formation theory should replicate the observed frequency, semimajor axis distribution, and mass function (e.g. Duchêne & Kraus, 2013) as well as the detailed orbital parameters (Dupuy & Liu, 2011), all as a function of system mass. The semimajor axis distribution can provide insight into the size/density evolution of the originating prestellar core, while the companion mass function results from the accretion history. However, it is unclear if the peak of the semimajor axis distribution of brown dwarf binaries has even been resolved (e.g. Burgasser et al., 2006b), particularly among populations of newly forming binaries with known formation environments (e.g. Kraus & Hillenbrand, 2012). Spectral synthesis might indicate that a significant number of binaries remain unresolved (Bardalez Gagliuffi et al., 2015), an assertion that could be tested with observations at higher spatial resolution.

While the use of coronagraphs and PSF subtraction techniques can improve detection limits, these techniques still do not achieve sufficient resolution. Imperfections in the optical path (and AO correction for ground based telescopes) introduce “speckles” which can be misinterpreted as companions. These speckles can be corrected based on temporal or chromatic behavior (i.e. ADI, SDI, and LOCI) at large angular separations, but those methods fail near λ/D . Interferometric analysis takes advantage of the wave nature of light and

can be used to produce a more stable and calibrated PSF, reject speckle noise, and detect companions with high contrast at or even below the diffraction limit. Rather than subtracting off the PSF, these techniques use the information contained in it to infer the geometry of the source. The discovery of the candidate newly forming giant planet LkCa15b by Kraus & Ireland (2012); Sallum et al. (2015) demonstrates the power of such techniques.

The most common interferometric analysis technique for single-aperture telescopes, non-redundant aperture masking interferometry (NRM or AMI; Tuthill et al., 2006; Tuthill, 2012), places a mask in the pupil plane, transforming a large single aperture into a sparse interferometer. Such a configuration produces an interferogram, or 2-D fringe pattern, which contains information about phase, in addition to intensity. Rather than simply looking for a companion in the image, an observable called a closure-phase is used to compare to a model image. Closure-phases are independent of the path length errors which cause speckles and thus contain true source phase information. NRM has been used for numerous applications in binary demographics and orbital analyses (Ireland et al., 2008; Kraus et al., 2008; Dupuy & Liu, 2017) and substellar/planetary companion discovery (Lloyd et al., 2006; Kraus & Ireland, 2012; Sallum et al., 2015).

A similar observable can be used with a full, rather than a masked, aperture. This technique models the full aperture as a grid of small apertures corresponding to a redundant set of baselines. Using simple linear algebra outlined below, Martinache (2010) derived an operator which, when applied to

the sampled phases, produces observables called kernel phases which are again independent of phase errors in each baseline. Diffraction limited observations are required, either from space or using ground based AO systems, as the phase errors *must* be small in order to properly account for the redundancies in the baselines.

While both methods are powerful tools for super-resolution imaging, NRM faces an observational limit. Since NRM uses a sparse mask, only $\sim 5\%$ of the light reaches the detector, imposing a flux limit on possible targets. Kernel-phase interferometry (KPI), on the other hand, utilizes the full telescope aperture. Thus it can achieve similar detection limits in a fraction of the time and can be applied to dimmer sources where NRM is not feasible. As no specialized mask is required, KPI can also be performed on archival data as long as the diffraction pattern is properly sampled. This allows the characterization of a companion's orbit using standard astrometric comparison of archival and current data.

This technique has been applied only a few times (relative to classical imaging techniques) since the original publication by Martinache (2010). Pope et al. (2016), Kammerer et al. (2019), Wallace et al. (2020), and Kammerer et al. (2021) all analyzed ground based AO imaging datasets (from Palomar/PHARO, VLT/NACO, Keck/NIRC2 and VLT/VISIR-NEAR, respectively) while Laugier et al. (2019) focused on recovering information from saturated *HST*/NICMOS camera 2 images. Analysis by Pope et al. (2013) of *HST*/NICMOS camera 1 images of brown dwarfs from Reid et al. (2006,

2008a) proposed five new candidate companions (and four marginal detections) and recovered all previously known companions. Clearly the technique is underutilized and merits further exploration.

This work analyzes the same two NICMOS data sets as Pope et al. (2013) as well as 5 more sets of archival observations. We introduce a new KPI pipeline named Argus² (Factor, 2022) with a careful treatment of phase errors, calibration, model comparison, and detection limits. We recover 19 observations of 17 previously known companions, including one of the new binaries found by Pope et al. (2013) (as well as one more which we marginally recover). We do not confirm any of their marginal detections. We present refined astrometry and photometry for the detected companions and discuss the resulting binary statistics. All sources which we do not recover can be explained by KPI’s insensitivity to wide companions or low SNR imaging.

This work is laid out as follows. Section 2.3 outlines the instrument and archival observations analyzed in this work. Section 2.4 details the kernel-phase technique and our new pipeline. Section 2.5 presents the results of our companion search with discussions of detections and non-detections. In section 2.6 we discuss the binary fraction of our sample, and put our KPI analysis in context. In Section 2.7 we summarize our conclusions.

²The open source python pipeline is available on GitHub: <https://github.com/smfactor/Argus>.

2.3 Observations

2.3.1 NICMOS Data

In this work we reanalyze archival *HST* observations using the Near Infrared Camera and Multi-Object Spectrometer (NICMOS). NICMOS was installed during servicing mission 2 and operated between 1997 and 1999 (Cycle 7 and 7N) when its solid nitrogen coolant ran out. It was restored to service during servicing mission 3B with a replacement cooling system and operated again from 2002 to 2008 (Cycle 11–16). All data sets analyzed in this work were taken during the second block.

NICMOS operates between 0.8 and $2.5\mu\text{m}$. This work uses the F110W and F170M filters corresponding to a diffraction limited resolution resolution (λ/D) of 95 mas and 147 mas, respectively. Thus the 43 mas pixels of NIC1 sample the PSF at 2.2 and 3.4 pixels per resolution element, respectively. The detector is 256×256 pixels for a field of view of $11'' \times 11''$. The X/Y pixel scale ratio for NIC1 is 1.0030 (~ 0.1 mas larger in the X direction). Since we only perform astrometry on the scale of a few pixels, we treat them as square.

NICMOS contains cold masks which block the thermal emission from the primary mirror edge and telescope spiders. This results in an effective primary mirror diameter of 2.388 m, secondary mirror occultation diameter of 0.8928 m, and a spider arm width of 0.1848 m (dimensions taken from TinyTim; Krist et al., 2011). Due to thermal stress on the NICMOS dewar, the cold masks are slightly shifted (Krist & Hook, 1997). Previous KPI analyses of *HST*/NICMOS data (e.g. Martinache, 2010; Pope et al., 2013) do not

implement this shift and we do not do as well. Calibration should remove most additional phase noise introduced by the imperfect model, though in the future we could use a gray aperture or characterize the aperture more accurately with a much higher resolution model (e.g. Martinache et al., 2020).

2.3.2 Target Sample

In this work we analyze the data sets listed in Table 2.1. These are all the high resolution (NIC1) brown dwarf imaging programs utilizing the F110W and F170M filters. These filters are the two most commonly used filters for imaging of brown dwarfs, roughly corresponding to the J and H bands. Observing set-ups differ between programs but generally consist of two or more dithered exposures in each filter.

Table 2.2 details the properties of the targets analyzed in this work. The sample covers spectral types from late M to T dwarfs at distances ranging from \sim 5–35 pc. Programs 9833, 10143, and 10879 were general imaging surveys of nearby brown dwarfs while programs 9843, 10247, and 11136 specifically targeted known binary systems. Program 9704 observed a PSF calibrator (spectral type M4V) in F170M to characterize the cold-mask shift and is included since it is a pristine and high SNR PSF. Program 11136 specifically prioritized wavelength coverage in a large number of filters over deep, high SNR, observations.

Table 2.1. Observations

Prog. ID	P.I.	Cycle	N_{obj}	Filters (in addition to F110W, F170M)	$N_{dithers}$	approx. epoch	Publication
9704	Schultz (2002)	11	1	F180M, F222M	0	12/2002	Roye et al. (2003)
9833	Burgasser (2003)	12	22	F090M, F110M, F145M, F170W	3-6	9/2003-7/2004	Burgasser et al. (2006b)
9843	Gizis (2003)	12	2	F090M, F145M, F170W	2	9-11/2003	Burgasser et al. (2011)
10143	Reid (2004)	13	56	F090M, F145M, F160W	2	9/2004-6/2006	Reid et al. (2006)
10247	Cruz (2004)	13	1	F090M, F145M, F160W	4	9/2004	Burgasser et al. (2006b)
10879	Reid (2006)	15	28	F090M, F108N, F110M, F113N, F145M, F160W	2	7/2006-5/2007	Reid et al. (2008a)
11136	Liu (2007)	16	7	F090M, F108N, F110M, F113N, F145M, F160W	3-7	5-8/2008	Dupuy et al. (2010)

Table 2.2. Target information

2MASSJ	SpT (ref.)	Parallax [mas] (ref.)	J [mag] (ref.)	H [mag] (ref.)	HST program
2MASS J00043484-4044058	L5+L5 (⁷)	82.1 ± 0.4(²)	13.109 ± 0.024(¹)	12.055 ± 0.026(¹)	10143
2MASS J00242463-0158201	M9.5V (³¹)	79.97 ± 0.22(²)	11.992 ± 0.035(¹)	11.084 ± 0.022(¹)	10879
2MASS J00250365+4759191	L4: (²⁰)	23.7 ± 1.1(⁴)	14.84 ± 0.04(¹)	13.667 ± 0.031(¹)	10143
2MASS J00361617+1821104	L3.5 (²⁸)	114.42 ± 0.21(²)	12.466 ± 0.027(¹)	11.588 ± 0.030(¹)	10143
2MASS J00452143+1634446	L2beta (²⁴)	65.02 ± 0.23(²)	13.059 ± 0.022(¹)	12.059 ± 0.035(¹)	10143
2MASS J01075242+0041563	L8 (³)	64 ± 5(⁴)	15.82 ± 0.06(¹)	14.51 ± 0.04(¹)	10143
2MASS J01092170+2949255	M9.5 (¹²)	62.78 ± 0.24(²)	12.912 ± 0.021(¹)	12.158 ± 0.024(¹)	10879
2MASS J01235905-4240073	L0.5 (²²)	38.78 ± 0.16(²)	13.153 ± 0.024(¹)	12.470 ± 0.023(¹)	10143
2MASS J01443536-0716142	L6.5 (³)	79.0 ± 0.6(²)	14.191 ± 0.026(¹)	13.008 ± 0.029(¹)	10143
2MASS J01473282-4954478	M8+L2 (⁷)	27.9 ± 0.4(²)	13.058 ± 0.027(¹)	12.366 ± 0.026(¹)	10143
2MASS J01514155+1244300	T0.5 (⁸)	46.7 ± 3.4(⁴)	16.57 ± 0.13(¹)	15.60 ± 0.11(¹)	9833
2MASS J01550354+0950003	L4 (¹⁴)	44.7 ± 0.7(²)	14.82 ± 0.04(¹)	13.763 ± 0.034(¹)	10143
2MASS J02052940-1159296	L7V (¹⁶)	50.6 ± 1.5(⁴)	14.587 ± 0.030(¹)	13.57 ± 0.04(¹)	11136
2MASS J02074284+0000564	T4.5 (²³)	35 ± 10(²)	16.730 ± 0.013(¹⁰)	16.81 ± 0.04(¹⁰)	9833
2MASS J02132880+4444453	L1.5 (¹¹)	51.7 ± 0.4(²)	13.494 ± 0.025(¹)	12.757 ± 0.024(¹)	10143
2MASS J02284243+1639329	M8.7V (⁶)	46.0 ± 0.4(²)	13.166 ± 0.026(¹)	12.325 ± 0.030(¹)	10879
2MASS J02431371-2453298	T6.0 (⁹)	94 ± 4(⁴)	15.38 ± 0.05(¹)	15.14 ± 0.11(¹)	9833
2MASS J02511490-0352459	L3 (¹¹)	90.6 ± 3.0(³⁶)	13.058 ± 0.027(¹)	12.254 ± 0.024(¹)	10879
2MASS J02550357-4700509	L9 (³)	205.33 ± 0.25(²)	13.246 ± 0.027(¹)	12.204 ± 0.024(¹)	10879
2MASS J02572581-3105523	L8.5 (³)	102.4 ± 0.6(²)	14.67 ± 0.04(¹)	13.520 ± 0.030(¹)	10143
2MASS J03140344+1603056	L0 (⁷)	73.43 ± 0.28(²)	12.526 ± 0.024(¹)	11.82 ± 0.04(¹)	10143
2MASS J03185403-3421292	L7 (³)	73 ± 8(⁴)	15.57 ± 0.05(¹)	14.35 ± 0.04(¹)	10879
2MASS J03480772-6022270	T7 (⁸)	120.1 ± 1.8(⁴⁵)	15.32 ± 0.05(¹)	15.56 ± 0.14(¹)	9833
2MASS J03552337+1133437	L5gamma (²⁴)	109.6 ± 0.7(²)	14.050 ± 0.024(¹)	12.530 ± 0.030(¹)	10143
2MASS J04151954-0935066	T8.0 (⁹)	174.3 ± 2.8(⁴)	15.69 ± 0.06(¹)	15.54 ± 0.11(¹)	9833
2MASS J04234858-0414035	L6.5+T2 (⁵)	67.9 ± 1.5(²)	14.465 ± 0.027(¹)	13.463 ± 0.035(¹)	9833,11136
2MASS J04291842-3123568	M7.5 (¹⁵)	59.38 ± 0.20(²)	10.874 ± 0.024(¹)	10.211 ± 0.024(¹)	10143
2MASS J04390101-2353083	L4.5 (³)	80.8 ± 0.5(²)	14.408 ± 0.029(¹)	13.409 ± 0.029(¹)	10143
2MASS J04433761+0002051	M9.0V (⁴⁰)	47.41 ± 0.19(²)	12.507 ± 0.026(¹)	11.804 ± 0.024(¹)	10879
2MASS J04455387-3048204	L2 (¹¹)	61.97 ± 0.18(²)	13.393 ± 0.026(¹)	12.580 ± 0.024(¹)	10143
2MASS J05002100+0330501	L4pec (¹⁴)	76.2 ± 0.4(²)	13.669 ± 0.024(¹)	12.683 ± 0.023(¹)	10143
2MASS J05160945-0445499	T5.5 (⁸)	44 ± 6(⁴)	15.98 ± 0.08(¹)	15.72 ± 0.17(¹)	9833
2MASS J05185959-2828372	L6+T4 (⁵)	48 ± 7(⁴)	15.98 ± 0.10(¹)	14.83 ± 0.07(¹)	10247,11136
2MASS J05233822-1430322	L2.5 (¹⁵)	78.36 ± 0.19(²)	13.084 ± 0.024(¹)	12.220 ± 0.022(¹)	10143
2MASS J06244132+2325585	M4V (³⁰)	117.74 ± 0.06(²)	8.662 ± 0.020(¹)	8.16 ± 0.06(¹)	9704
2MASS J06244595-4521548	L6.5 (³)	81.6 ± 0.5(²)	14.480 ± 0.029(¹)	13.335 ± 0.028(¹)	10143
2MASS J06523073+4710348	L3.5+L6.5 (³⁹)	109.7 ± 0.4(²)	13.511 ± 0.023(¹)	12.384 ± 0.024(¹)	10143
2MASS J07003664+3157266	L3+L6.5 (⁵)	88.28 ± 0.35(²)	12.923 ± 0.023(¹)	11.947 ± 0.016(¹)	10143
2MASS J07271824+1710012	T7.0 (⁹)	110.1 ± 2.3(⁴)	15.60 ± 0.06(¹)	15.76 ± 0.17(¹)	9833
2MASS J07554795+2212169	T5.2 (⁹)	58.9 ± 3.3(⁴⁶)	15.73 ± 0.06(¹)	15.67 ± 0.14(¹)	9833
2MASS J08251968+2115521	L7.5V (¹⁸)	92.2 ± 1.2(²)	15.100 ± 0.034(¹)	13.792 ± 0.032(¹)	10143
2MASS J08300825+4828482	L9.5 (³)	76.4 ± 3.4(⁴)	15.44 ± 0.05(¹)	14.34 ± 0.04(¹)	10879
2MASS J08354256-0819237	L6.5 (³)	138.61 ± 0.28(²)	13.169 ± 0.024(¹)	11.938 ± 0.024(¹)	10143
SDSS J083717.21-000018.0	T1 (⁸)	34 ± 13(⁴)	16.989 ± 0.018(¹⁰)	16.290 ± 0.018(¹⁰)	9833
2MASS J08472872-1532372	L1.5 (³)	56.92 ± 0.32(²)	13.513 ± 0.026(¹)	12.629 ± 0.027(¹)	10143
2MASS J08503593+1057156	L6.5+L8.5 (⁵)	31.4 ± 0.6(¹³)	16.47 ± 0.11(¹)	15.22 ± 0.09(¹)	9843
2MASS J08592547-1949268	L8 (³)	65 ± 6(⁴)	15.53 ± 0.05(¹)	14.44 ± 0.04(¹)	10879
2MASS J09083803+5032088	L8 (³)	95.8 ± 0.7(²)	14.549 ± 0.023(¹)	13.477 ± 0.030(¹)	10143
2MASS J09111297+7401081	L0 (¹¹)	40.08 ± 0.17(²)	12.921 ± 0.027(¹)	12.205 ± 0.030(¹)	10143
2MASS J09153413+0422045	L6 (³)	55.9 ± 1.1(¹⁹)	14.548 ± 0.030(¹)	13.531 ± 0.032(¹)	10143
2MASS J09211410-2104446	L1 (³)	79.31 ± 0.23(²)	12.779 ± 0.024(¹)	12.152 ± 0.022(¹)	10143
2MASS J09261537+5847212	T3.5+T5 (⁵)	43.7 ± 1.1(⁵)	15.90 ± 0.06(¹)	15.31 ± 0.09(¹)	9833
2MASS J10210969-0304197	T1+T4 (¹⁷)	33.7 ± 1.2(¹³)	16.25 ± 0.09(¹)	15.35 ± 0.10(¹)	9833
2MASS J10224821+5825453	L0.6V (⁶)	54.33 ± 0.31(²)	13.499 ± 0.026(¹)	12.640 ± 0.030(¹)	10879
2MASS J10255227+3212349	L9 (³)	37.3 ± 1.2(⁴¹)	16.89 ± 0.05(³⁷)	15.59 ± 0.17(¹)	10879
2MASS J10430758+2225236	L8.5 (³)	52.4 ± 2.9(⁴⁶)	15.97 ± 0.06(¹)	14.73 ± 0.04(¹)	10879
2MASS J10452400-0149576	L1 (²¹)	58.66 ± 0.24(²)	13.160 ± 0.024(¹)	12.352 ± 0.025(¹)	10143
2MASS J10484281+0111580	L1 (³)	66.46 ± 0.21(²)	12.924 ± 0.023(¹)	12.140 ± 0.022(¹)	10143
2MASS J10511900+5613086	L2 (⁷)	64.00 ± 0.19(²)	13.244 ± 0.026(¹)	12.420 ± 0.030(¹)	10143
2MASS J10584787-1548172	L3V (¹⁶)	54.6 ± 0.5(²)	14.155 ± 0.035(¹)	13.226 ± 0.025(¹)	10879
2MASS J11040127+1959217	L4 (³)	55.9 ± 0.4(²)	14.380 ± 0.026(¹)	13.476 ± 0.034(¹)	10143
2MASS J11083081+6830169	L1e (¹²)	61.35 ± 0.20(²)	13.120 ± 0.020(²⁵)	12.240 ± 0.020(²⁵)	10143
2MASS J11101001+0116130	T5.5 (²³)	52.1 ± 1.2(³²)	16.161 ± 0.008(¹⁰)	16.197 ± 0.021(¹⁰)	9833
2MASS J11553952-3727350	L2e (²¹)	84.57 ± 0.19(²)	12.811 ± 0.024(¹)	12.040 ± 0.026(¹)	10879
2MASS J12035812+0015500	L5.0V (⁶)	67.2 ± 0.6(²)	14.006 ± 0.026(¹)	13.056 ± 0.024(¹)	10879

While previous studies of these data sets have found tight companions, we analyzed all images with no prior knowledge other than a visual inspection for obvious secondary sources. KPI produces improved astrometric precision and searches for tighter and fainter companions around targets previously thought to be single. While Pope et al. (2013) previously analyzed the Reid et al. (2006, 2008a) observations using KPI, this work uses a new code-base with a detailed treatment of phase errors, calibration, model comparison, and detection limits in addition to analyzing data from 5 more *HST* programs. There are also a few more subtle differences in the analysis which are discussed further below.

2.4 Methods

2.4.1 Kernel-phase Analysis

The kernel-phase derivation was first presented by Martinache (2010) and is summarized here for clarity since the technique is still relatively obscure. KPI works by modeling the full telescope aperture as a grid of sub-apertures. From this grid, a set of baselines (vectors in *uv* space) can be generated by pairing apertures. Figure 2.1 shows our model of the *HST*/NICMOS aperture and the baselines it samples. Phases (or more generally, complex visibilities) are then sampled from the Fourier transform of the image at each of these points in *uv* space. Kernel phases can then be constructed based on the geometry of the model aperture using linear algebra outlined below.

Each measured phase (Φ) is made up of the true source phase (Φ_0) and

Table 2.2 (cont'd)

2MASSJ	SpT (ref.)	Parallax [mas] (ref.)	J [mag] (ref.)	H [mag] (ref.)	HST program
2MASS J12130336-0432437	L4.2V ⁽⁶⁾	59.5 ± 1.0 ⁽²⁾	14.68 ± 0.04 ⁽¹⁾	13.648 ± 0.025 ⁽¹⁾	10143
2MASS J12171110-0311131	T7.5 ⁽⁸⁾	90.8 ± 2.2 ⁽⁴⁾	15.86 ± 0.06 ⁽¹⁾	15.75 ± 0.12 ⁽¹⁾	9833
2MASS J12212770+0257198	L0.5 ⁽³⁾	53.95 ± 0.25 ⁽²⁾	13.169 ± 0.023 ⁽¹⁾	12.410 ± 0.025 ⁽¹⁾	10143
2MASS J12545393-0122474	T2e: ⁽³⁵⁾	74.2 ± 2.3 ⁽²⁾	14.891 ± 0.035 ⁽¹⁾	14.090 ± 0.025 ⁽¹⁾	9833
2MASS J13004255+1912354	L1.7V ⁽⁶⁾	71.68 ± 0.20 ⁽²⁾	12.717 ± 0.022 ⁽¹⁾	12.080 ± 0.023 ⁽¹⁾	10879
2MASS J14213145+1827407	M8.9V ⁽⁶⁾	52.67 ± 0.26 ⁽²⁾	13.231 ± 0.021 ⁽¹⁾	12.428 ± 0.021 ⁽¹⁾	10879
2MASS J14252798-3650229	L4 ⁽¹⁴⁾	84.52 ± 0.34 ⁽²⁾	13.747 ± 0.028 ⁽¹⁾	12.575 ± 0.022 ⁽¹⁾	10879
2MASS J14283132+5923354	L4.4V ⁽⁶⁾	45.4 ± 0.5 ⁽²⁾	14.78 ± 0.04 ⁽¹⁾	13.88 ± 0.04 ⁽¹⁾	10143
2MASS J14392836+1929149	L1V ⁽¹⁶⁾	69.6 ± 0.5 ⁽⁴⁾	12.759 ± 0.019 ⁽¹⁾	12.041 ± 0.019 ⁽¹⁾	10879
2MASS J14482563+1031590	L5.5 ⁽³⁾	71.3 ± 0.7 ⁽²⁾	14.556 ± 0.034 ⁽¹⁾	13.433 ± 0.033 ⁽¹⁾	10143
2MASS J15031961+2525196	T5.5 ⁽³⁴⁾	154.9 ± 1.1 ⁽²⁾	13.937 ± 0.024 ⁽¹⁾	13.856 ± 0.031 ⁽¹⁾	9833
2MASS J15065441+1321060	L3 ⁽¹²⁾	85.58 ± 0.29 ⁽²⁾	13.365 ± 0.023 ⁽¹⁾	12.380 ± 0.021 ⁽¹⁾	10879
2MASS J15074769-1627386	L5V ⁽¹⁸⁾	135.23 ± 0.33 ⁽²⁾	12.830 ± 0.027 ⁽¹⁾	11.895 ± 0.024 ⁽¹⁾	10143
2MASS J151500083+4847416	L6.5 ⁽¹⁵⁾	102.6 ± 0.6 ⁽¹⁹⁾	14.111 ± 0.029 ⁽¹⁾	13.099 ± 0.031 ⁽¹⁾	10879
2MASS J15341711+1615463	T1.5+T5.5 ⁽¹⁷⁾	24.9 ± 1.1 ⁽⁵⁾	16.75 ± 0.13 ⁽¹⁾	16.08 ± 0.16 ⁽¹⁾	11136
2MASS J15394189-0520428	L4.2V ⁽⁶⁾	58.8 ± 0.4 ⁽²⁾	13.922 ± 0.029 ⁽¹⁾	13.060 ± 0.026 ⁽¹⁾	10143
2MASS J15525906+2948485	Loe ⁽⁴²⁾	49.00 ± 0.20 ⁽²⁾	13.478 ± 0.026 ⁽¹⁾	12.606 ± 0.026 ⁽¹⁾	10143
2MASS J15530228+1532369	T6.5+T7.5 ⁽⁵⁾	75.1 ± 0.9 ⁽⁵⁾	15.82 ± 0.07 ⁽¹⁾	15.94 ± 0.16 ⁽¹⁾	9833
2MASS J16241436+0029158	T6V ⁽⁹⁾	90.9 ± 1.2 ⁽⁴⁾	15.49 ± 0.05 ⁽¹⁾	15.52 ± 0.10 ⁽¹⁾	9833
2MASS J16580380+7027015	L1(e) ⁽¹²⁾	54.12 ± 0.21 ⁽²⁾	13.288 ± 0.024 ⁽¹⁾	12.470 ± 0.032 ⁽¹⁾	10143
2MASS J17054834-0516462	L1 ⁽³⁾	52.67 ± 0.35 ⁽²⁾	13.309 ± 0.030 ⁽¹⁾	12.552 ± 0.024 ⁽¹⁾	10143
2MASS J17072343-0558249	M9+L3 ⁽⁷⁾	89.26 ± 2.2 ⁽⁴⁷⁾	12.052 ± 0.023 ⁽¹⁾	11.260 ± 0.027 ⁽¹⁾	10143
2MASS J17210390+3344160	L5.3:V ⁽⁶⁾	61.32 ± 0.20 ⁽²⁾	13.625 ± 0.023 ⁽¹⁾	12.952 ± 0.026 ⁽¹⁾	10879
2MASS J17281150+3948593	L5+L6.5 ⁽¹⁷⁾	36.4 ± 0.6 ⁽¹³⁾	15.99 ± 0.08 ⁽¹⁾	14.76 ± 0.07 ⁽¹⁾	9843
2MASS J17312974+2721233	L0 ⁽⁷⁾	83.74 ± 0.12 ⁽²⁾	12.094 ± 0.027 ⁽¹⁾	11.391 ± 0.030 ⁽¹⁾	10143
2MASS J17503293+1759042	T3.5 ⁽⁸⁾	36 ± 5 ⁽⁴⁾	16.34 ± 0.10 ⁽¹⁾	15.95 ± 0.13 ⁽¹⁾	9833
2MASS J17534518-6559559	L4 ⁽²⁶⁾	63.82 ± 0.32 ⁽²⁾	14.095 ± 0.028 ⁽¹⁾	13.108 ± 0.027 ⁽¹⁾	10143
2MASS J18071593+5015316	L1 ⁽³⁾	68.33 ± 0.13 ⁽²⁾	12.934 ± 0.024 ⁽¹⁾	12.127 ± 0.031 ⁽¹⁾	10143
2MASS J19360187-5502322	L4 ⁽²⁶⁾	45.0 ± 0.5 ⁽²⁾	14.49 ± 0.04 ⁽¹⁾	13.628 ± 0.035 ⁽¹⁾	10143
2MASS J20025073-0521524	L5.5 ⁽³⁾	56.7 ± 1.5 ⁽²⁾	15.32 ± 0.05 ⁽¹⁾	14.28 ± 0.05 ⁽¹⁾	10879
2MASS J20282035+0052265	L2.5 ⁽³⁾	35.2 ± 0.7 ⁽²⁾	14.298 ± 0.035 ⁽¹⁾	13.380 ± 0.030 ⁽¹⁾	10879
2MASS J20360316+1051295	L2 ⁽³⁾	42.4 ± 0.4 ⁽²⁾	13.950 ± 0.026 ⁽¹⁾	13.018 ± 0.022 ⁽¹⁾	10143
SDSS J205235.31-160929.8	L8.5+T1.5 ⁽⁵⁾	33.7 ± 0.7 ⁽¹³⁾	16.040 ± 0.030 ⁽⁴⁾	15.450 ± 0.030 ⁽⁴⁾	11136
2MASS J20575409-0252302	L1 ⁽³⁾	64.47 ± 0.24 ⁽²⁾	13.121 ± 0.024 ⁽¹⁾	12.268 ± 0.024 ⁽¹⁾	10143
2MASS J21041491-1037369	L2 ⁽³⁾	58.2 ± 0.4 ⁽²⁾	13.841 ± 0.029 ⁽¹⁾	12.975 ± 0.025 ⁽¹⁾	10143
2MASS J21392676+0220226	L8.5+T3.5 ⁽³⁸⁾	101.5 ± 2.0 ⁽²⁷⁾	15.26 ± 0.05 ⁽¹⁾	14.16 ± 0.05 ⁽¹⁾	10143
2MASS J21481633+4003594	L7 ⁽³⁾	123.3 ± 0.5 ⁽²⁾	14.147 ± 0.029 ⁽¹⁾	12.780 ± 0.030 ⁽¹⁾	10879
2MASS J21522609+0937575	L6+L6 ⁽⁷⁾	40.9 ± 6.9 ⁽⁴⁶⁾	15.190 ± 0.032 ⁽¹⁾	14.08 ± 0.04 ⁽¹⁾	10143
2MASS J22041052-5646577	T1V+T6V ⁽³³⁾	275.8 ± 0.7 ⁽²⁹⁾	11.908 ± 0.022 ⁽¹⁾	11.306 ± 0.024 ⁽¹⁾	11136
2MASS J22244381-0158521	L4.5V ⁽¹⁸⁾	86.6 ± 0.7 ⁽²⁾	14.073 ± 0.027 ⁽¹⁾	12.818 ± 0.026 ⁽¹⁾	10879
2MASS J22282889-4310262	T6.5 ⁽⁸⁾	92.1 ± 2.6 ⁽²⁷⁾	15.66 ± 0.07 ⁽¹⁾	15.36 ± 0.12 ⁽¹⁾	9833
2MASS J22373255+3922398	M9.5 ⁽¹¹⁾	47.61 ± 0.20 ⁽²⁾	13.343 ± 0.022 ⁽¹⁾	12.691 ± 0.021 ⁽¹⁾	10879
2MASS J22490917+3205489	L5 ⁽²⁰⁾	49.7 ± 3.2 ⁽⁴⁶⁾	15.48 ± 0.06 ⁽¹⁾	14.35 ± 0.05 ⁽¹⁾	10143
2MASS J22521073-1730134	L4.5+T3.5 ⁽⁵⁾	59.1 ± 0.8 ⁽²⁾	14.313 ± 0.029 ⁽¹⁾	13.360 ± 0.030 ⁽¹⁾	10143,11136
2MASS J22541892+3123498	T5.0 ⁽⁹⁾	72 ± 3 ⁽⁴⁸⁾	15.26 ± 0.05 ⁽¹⁾	15.02 ± 0.08 ⁽¹⁾	9833
2MASS J22551861-5713056	L6:+L8 ⁽⁷⁾	58.9 ± 0.6 ⁽²⁾	14.083 ± 0.030 ⁽¹⁾	13.189 ± 0.032 ⁽¹⁾	10879
2MASS J23254530+4251488	L8 ⁽¹¹⁾	67.6 ± 2.1 ⁽²⁾	15.49 ± 0.05 ⁽¹⁾	14.45 ± 0.05 ⁽¹⁾	10143
2MASS J23391025+1352284	T5.4 ⁽⁹⁾	62.7 ± 4.4 ⁽⁴⁶⁾	16.24 ± 0.11 ⁽¹⁾	15.82 ± 0.15 ⁽¹⁾	9833
2MASS J23515044-2537367	M9e ⁽²²⁾	49.1 ± 0.4 ⁽²⁾	12.471 ± 0.026 ⁽¹⁾	11.725 ± 0.022 ⁽¹⁾	10143

References. — Reference Key 1: Cutri et al. (2003), 2: Gaia Collaboration et al. (2018), 3: Faherty et al. (2012), 4: Schneider et al. (2014), 5: Skrzypek et al. (2016), 6: Dupuy & Liu (2012), 7: Bardalez Gagliuffi et al. (2015), 8: Schmidt et al. (2007), 9: Burgasser et al. (2002), 10: Gagné et al. (2015), 11: Dupuy & Liu (2017), 12: Reid et al. (2008b), 13: Faherty et al. (2009), 14: Marocco et al. (2013), 15: Kirkpatrick et al. (2000), 16: Gelino et al. (2014), 17: Smart et al. (2013), 18: Burgasser et al. (2003b), 19: Cruz et al. (2003), 20: Konopacky et al. (2010), 21: Burgasser et al. (2000), 22: Aller et al. (2016), 23: Lodieu et al. (2005), 24: Liu et al. (2006), 25: Burgasser et al. (2003a), 26: Leggett et al. (2001), 27: Tinney et al. (2014), 28: Reid et al. (2000), 29: Perryman et al. (1997), 30: Kirkpatrick et al. (1991), 31: Faherty et al. (2016), 32: Reid et al. (2006), 33: Burgasser et al. (2005), 34: Chiu et al. (2006), 35: Burgasser et al. (2006a), 36: Cardoso et al. (2015), 37: West et al. (2008), 38: Metchev et al. (2008), 39: Reylé et al. (2010), 40: Burgasser et al. (2010), 41: Deshpande et al. (2012), 42: Kirkpatrick et al. (2016), 43: Liu et al. (2016), 44: Marocco et al. (2015), 45: Kirkpatrick et al. (2019), 46: Best et al. (2020b), 47: Smart et al. (2018), 48: Manjavacas et al. (2013)

a combination of phase errors (ϕ) introduced by pupil path length differences from each of the apertures contributing to the baseline:

$$\Phi = \text{Arg} \left[\sum_{(j,k)} e^{i(\Phi_0 + \phi_j - \phi_k)} \right], \quad (2.1)$$

where the pair (j, k) denotes the baselines contributing to the specific visibility. The complex interferometric visibility is thus a superposition of vectors (i.e. the *phases* do not strictly add). If we assume these error terms are small, we can approximate each complex phasor as a linear sum, $e^{i(\phi_j - \phi_k)} \approx 1 + i(\phi_j - \phi_k)$, allowing us to write the measured phase as a linear combination:

$$\Phi \approx \Phi_0 + \frac{1}{r} \sum_{(j,k)} (\phi_j - \phi_k), \quad (2.2)$$

where r is the number of (j, k) pairs for that specific phase measurement (i.e. number of redundant baselines contributing to the visibility). If we stack these equations for each sampled point in uv space, we can write the vector of all measured phase information as

$$\Phi = \Phi_0 + \mathbf{R}^{-1} \cdot \mathbf{A} \cdot \phi, \quad (2.3)$$

where the matrix \mathbf{R}^{-1} is a diagonal matrix with $1/r$ for each visibility, encoding the redundancies in the baselines. The matrix \mathbf{A} is a transfer matrix assembled from 1's and -1's in each row encoding the apertures contributing to each (redundant) baseline (any apertures not involved are 0 and apertures contributing multiple times to a single baseline are summed). For ϕ of length n (the number of sub-apertures), and Φ of length m (the number of unique visibilities), the shape of \mathbf{R} is $m \times m$ and \mathbf{A} is $m \times n$.

Since our goal is to derive a quantity which does not involve the phase error term, we then construct the kernel, \mathbf{K} , of \mathbf{A} such that $\mathbf{K} \cdot \mathbf{A} = \mathbf{0}$. The matrix \mathbf{K} can be calculated using singular value decomposition (SVD, Press et al., 2002). This algorithm gives

$$\mathbf{A} = \mathbf{U} \cdot \mathbf{W} \cdot \mathbf{V}^T, \quad (2.4)$$

where the matrix \mathbf{W} is a diagonal matrix of positive or zero “singular values.” The rows of \mathbf{K} are then the *columns* of \mathbf{U} corresponding to zero elements of \mathbf{W} . After multiplying equation 2.3 by \mathbf{R} and then \mathbf{K} we have

$$\mathbf{K} \cdot \mathbf{R} \cdot \Phi = \mathbf{K} \cdot \mathbf{R} \cdot \Phi_0. \quad (2.5)$$

This results in a set of phase-like observables ($\mathbf{K} \cdot \mathbf{R} \cdot \Phi$), called kernel phases, which are free of instrumental phase errors.

2.4.2 Kernel-Phase Pipeline

The pipeline can be divided into four steps: aperture characterization, kernel-phase calculation, calibration, and model fitting. During aperture characterization we create a model interferometer that approximates the full aperture of the telescope, measure the associated baselines, and construct the transfer matrices. We then ingest the images and calculate the kernel phases. These kernel phases must then be calibrated to remove systematic errors. Once calibrated, we can then fit a single and binary model to the data and compare the results.

2.4.2.1 Aperture Characterization

First we must construct a set of subapertures that models the full aperture of the telescope. Dimensions of the primary mirror and its obstructions were taken from the TinyTim software package (Krist et al., 2011) and are outlined in section 2.3.1. The model used in this work, shown in the left panel of Figure 2.1, was chosen by balancing a few characteristics: the fraction of the total aperture covered by subapertures (F_{cov}), the length of the longest baseline (D_{max}), the phase coverage or number of kernel phases relative to number of phases sampled (N_{ker}/N_B), and the number of long baselines relative to the total number of baselines (N_{long}/N_B). In general, F_{cov} and D_{max} trend larger with smaller subaperture size while N_{ker}/N_B and N_{long}/N_B trend smaller. The total number of kernel phases must also be kept to a reasonable number to keep fitting fast and such that we do not try to extract more information than is contained in the image. The theoretical minimum spacing of apertures is set by the size of the image, or in our case the super-Gaussian windowing function (see Section 2.4.2.2). The field of view, and therefore the smallest spacial frequency sampled by the image, is $25\lambda/D$ and thus the minimum aperture spacing must be at least $D/25$ or 0.096 m. Our chosen spacing is $D/14.4$ or 0.166 m.

From the model of the aperture, the pipeline measures the baselines (right panel of Figure 2.1), constructs the \mathbf{A} matrix, and then calculates the kernel-phase transfer matrix \mathbf{K} . This step is only based on the telescope and sub-aperture geometry, and thus does not need to be repeated for each target.

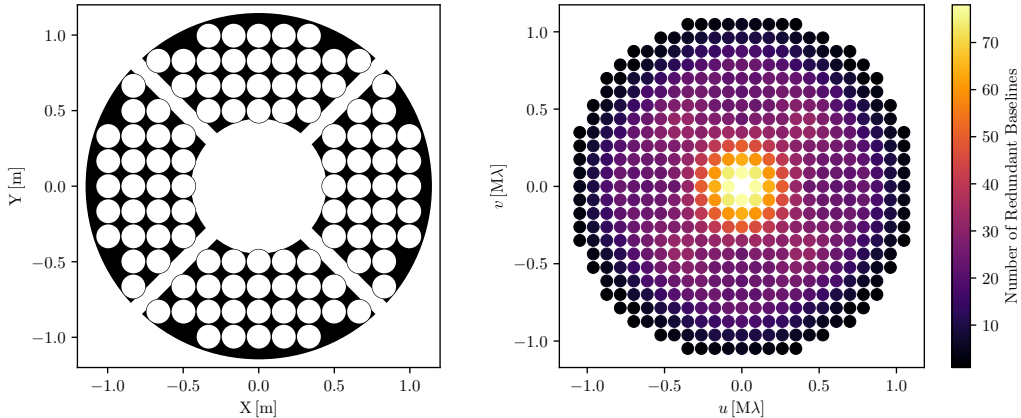


Figure 2.1: *Left:* *HST* aperture in black with simulated subapertures on top in white. *Right:* The corresponding baselines (at $1.7\mu\text{m}$), color coded by the number of distinct pairs of sub-apertures which contribute to the point. The 104 sub-apertures sample 258 spatial frequencies and generate 206 kernel phases.

2.4.2.2 Kernel-Phase calculation

The second step is to calculate kernel phases for each target. The pipeline reads in the images and interpolates over bad pixels. Bad pixels are identified from the data-quality flags associated with the individual images. Bad pixels are then iteratively replaced with the median of the 8 neighboring pixels. Other methods of dealing with bad pixels which avoid interpolation may be incorporated in future releases and are discussed further in Section 2.7. The pipeline then finds the flux centroid of the target ($x_{\text{cen}}, y_{\text{cen}}$) and windows the data with a super-Gaussian ($e^{-(r/\sigma)^4}$) of width $\sigma = 25\lambda/D$ (~ 2.4 and ~ 3.7 arc sec in F110W and F170M, respectively) to limit sensitivity to readout noise (as done in Kraus et al., 2008). The images are then Fourier

transformed using the basic `numpy` FFT routines. We then divided the complex visibilities by the position offset of the centroid: $e^{i(x_{\text{cen}}*u+y_{\text{cen}}*v)}$. Shifting in the Fourier domain avoids any pixel interpolation which may distort the phase information encoded in the image.

The phase at each point defined by the aperture model is then measured, along with the local dispersion. The errors associated with kernel phases are derived from the dispersion of the phases measured from the Fourier transform of the image. First, we define the scale on which the uv plane is sampled: $\Delta f = d/2\lambda$. This spatial frequency scale, Δf , is set by the grid spacing of the aperture model d (the diameter of the simulated sub-apertures), and the wavelength λ . This defines a circle of radius Δf around each point in the uv plane corresponding to all possible vectors from any point within the first sub aperture to any point within the second. The phase and associated error are then the mean and standard deviation of all points inside this circle given by the fast Fourier transform. These phases and associated errors are then propagated through the kernel-phase transfer matrix generated in the previous step to obtain the kernel phases and associated errors.

Sampling a number of phases around the baseline (rather than at a single point) appropriately captures the local dispersion of each phase, but not any systematic phase errors. Many previous applications of this analysis technique have introduced a global systematic error term, added in quadrature to the individual errors, to account for this and bring reduced χ^2 values of the best fit models closer to one. We fit this error term (iteratively, using

a basic python fitting routine, e.g. `scipy.optimize.curve_fit`; Virtanen et al., 2020) for each image since, for constant aberration, phase errors scale with λ and may vary over the detector.

Figure 2.2 shows intermediate steps for 2MASS J0147-4954 at this stage of the analysis: the bad pixel corrected and windowed image, the Fourier transform of the image (amplitude and phase) along with the modeled baselines, and the measured kernel phases. This target is marginally resolved at this wavelength, and a step function, characteristic of a binary, can clearly be seen in the Fourier-phase. The large dispersion of kernel phases in the upper right panel further indicates the presence of a companion. Figure 2.3 show the same plots but for 2MASS J1221+0257, a target with no companion. The flat phase and $\sim 100\times$ smaller kernel phases indicate that this target does not have a companion.

2.4.2.3 Calibration

The third step is calibration. The phase signal of a single centered point source should be zero everywhere, producing all zero kernel phases. However, path-length offsets in the telescope and instrument produce non-zero phases and kernel phases (as seen in Figure 2.3). If these offsets are stable, which they are for similar observing setups (and for inherently stable space based observatories), they can be calibrated out. Subtracting off the (non-zero) kernel phases of an observed point source sets the zero-point in the science target such that a single source would now have all zero kernel phases.

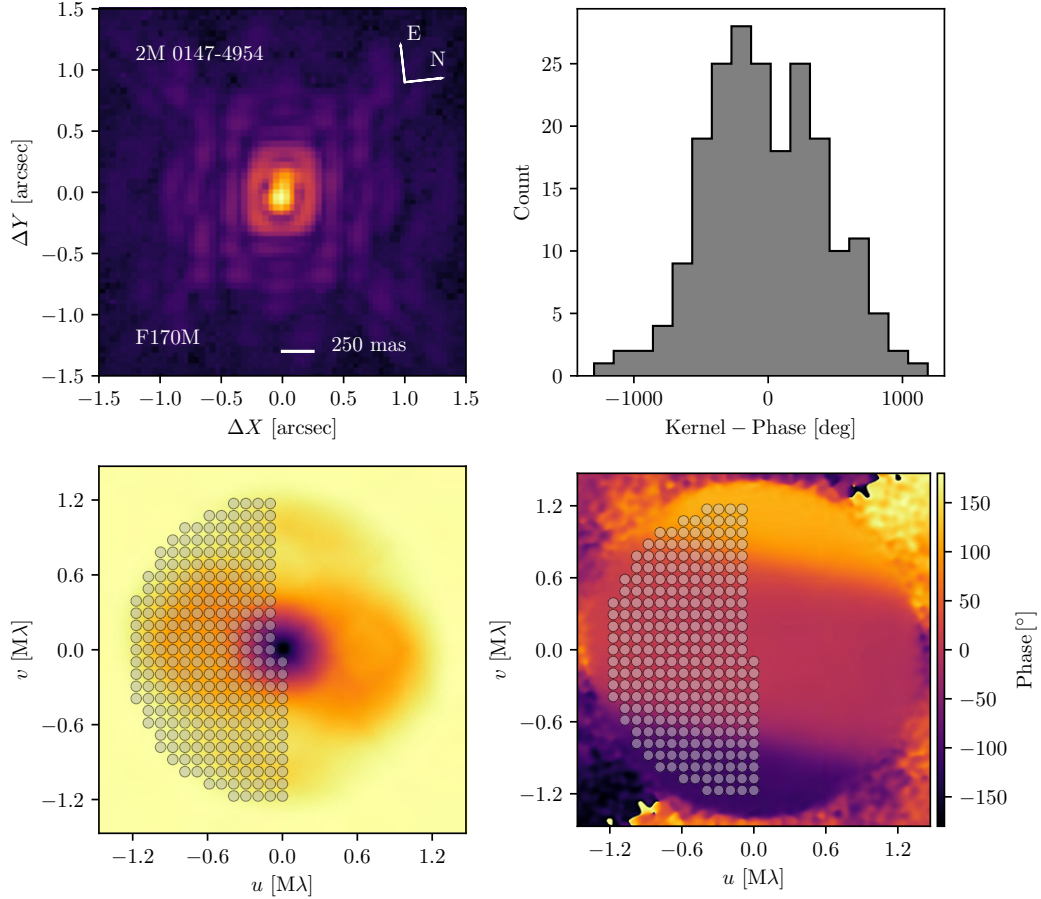


Figure 2.2: The progression from image to kernel phase for an observation of 2MASS J0147-4954, a brown dwarf with a companion at ~ 140 mas ($\sim 1\lambda/D$) and 2:1 contrast in F170M. *Top-left:* HST/NICMOS NIC1 image (fourth root scaling). *Bottom row:* Fourier amplitude (left), and Fourier phase (right). Gray circles show the spatial frequencies sampled by the model aperture shown in Figure 2.1. *Top-right* Histogram of measured kernel phases. A point source would have kernel phases of 0° (with some noise) which is clearly not the case.

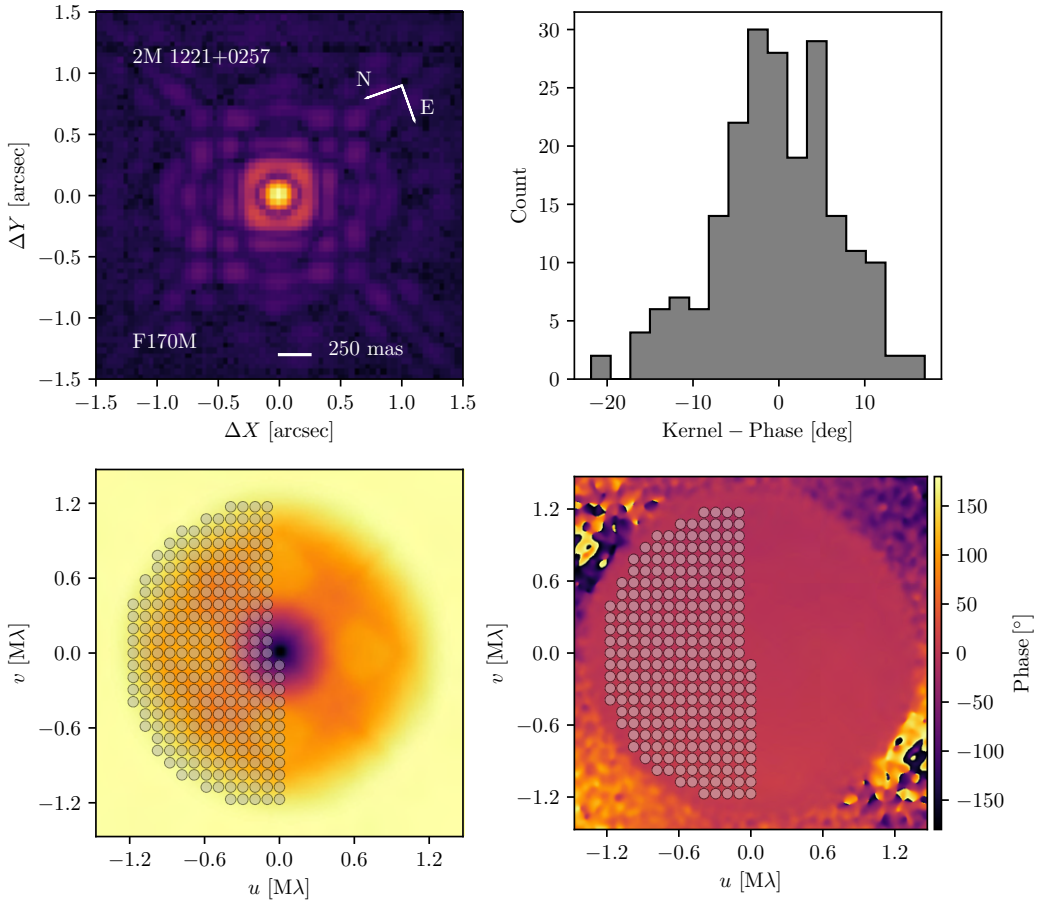


Figure 2.3: Similar to Figure 2.2 but for 2MASS J1221+0257, a brown dwarf with no companion. *Top-left:* *HST/NICMOS NIC1 image (fourth root scaling).* *Bottom row:* Fourier amplitude (left), and Fourier phase (right). Gray circles show the spatial frequencies sampled by the model aperture shown in Figure 2.1. *Top-right* Histogram of measured kernel phases. A point source would have kernel phases of 0° (with some noise) as is the case with this target.

Since no dedicated PSF calibrators were observed in these archival datasets, we use the science targets themselves as calibrators. To create kernel phases which can be used to calibrate science targets, a preliminary fit is run on each target to reject binaries and remove any small centroid offset error. As part of the data “onboarding” procedure, any images with visual signs of a companion are noted and rejected at this step. The best fit single point source model (x,y position offset) is then subtracted from the kernel phases of each point source to create calibrators. These are then used to calibrate science targets before fitting for binary parameters. Each science target is paired with 5 calibrators, balancing the increased confidence of a detection in multiple calibrators with the increased computation time of fitting multiple times. The results from these 5 independent fits are then used to characterize if a companion is present according to the metric discussed in Section 2.4.3.

We experimented with multiple calibrators chosen from the most singular sources (those which favored the single point source model over the double model the most), the closest on the detector, and a combination of the two metrics. We chose to use the calibrators located closest to the science target on the detector, as the detection limits (see Section 2.4.3) using those calibrators were significantly more sensitive. Targets which are co-located on the detector calibrate each other well since they accumulate similar phase offsets from passing through or reflecting off of the same region of optical elements within the telescope and instrument.

2.4.2.4 Model Fitting

The fourth and final step is to pass the calibrated kernel phases to a Bayesian inference algorithm which fits a single and a double point source model to the data. The free parameters of the model are a small position offset (to allow for sub-pixel refinement of the centroid) and binary separation, position angle, and contrast ratio. We have chosen to use a Gaussian prior on the centroid (centered at 0 with a standard deviation of 10 mas), log-uniform priors on separation and contrast, and a uniform prior on position angle (the code we use allows a “wrapped” prior which we turn on for position angle). The log-uniform prior is commonly used as an uninformative prior on scaling parameters like separation and contrast as it allows for a wide range of values with equal probability over each power of 10.

The fitting routine used in this work, PyMultiNest (Buchner et al., 2014), uses a nested sampling algorithm which samples the entire prior volume, probabilistically constricting that volume down to the best fit(s) (Feroz & Hobson, 2008; Feroz et al., 2009, 2019). Since it samples the entire (allowed) parameter space, it also allows the calculation of the Bayesian evidence which can then be used to calculate Bayes factors, comparing the single and double point source models (see Section 2.4.4).

Figure 2.4 shows the 1D and 2D posterior distributions along with the calibrated kernel phases generated from the data plotted against the best fit binary model for an binary system with a separation well below the diffraction limit, 2MASS J2351-2537. This test case, where the image does not clearly

show a companion but the kernel phases plainly indicate the presence of a binary, demonstrates the power of this interferometric analysis, detecting an unresolved binary with a contrast ratio of $\sim 2.5 : 1$ at $\sim 0.3\lambda/D$. Similar figures for all of our detected companions are shown in Appendix A.

2.4.3 Detection Limits

Detection limits were calculated in a similar manner to applications of NRM (Kraus et al., 2008, 2011). For each source-calibrator pair, the best fit single point-source model is subtracted from the calibrated kernel phases, leaving behind noise (assuming no companion is present). The indices of these kernel phases are then scrambled, creating a new realization of the noise with the same properties. A single point source is then added back in to the scrambled kernel phases at the position of the single point source originally subtracted to replicate the signal of the centroid offset.

We then fit for contrast on a 100x100 grid in separation–PA space. Posteriors from these fits are then combined, marginalizing over PA. Since the indices have been scrambled, these fits are to kernel phases containing no real companions and thus the posteriors indicate what regions of parameter space produce spurious detections due to noise.

The confidence levels are then drawn such that the $X\%$ confidence contour contains $100 - X\%$ of the posterior moving from least dense to most dense areas. This is done using a Kernel Density Estimate of the posterior as a function of separation and contrast. Example detection limits are shown in

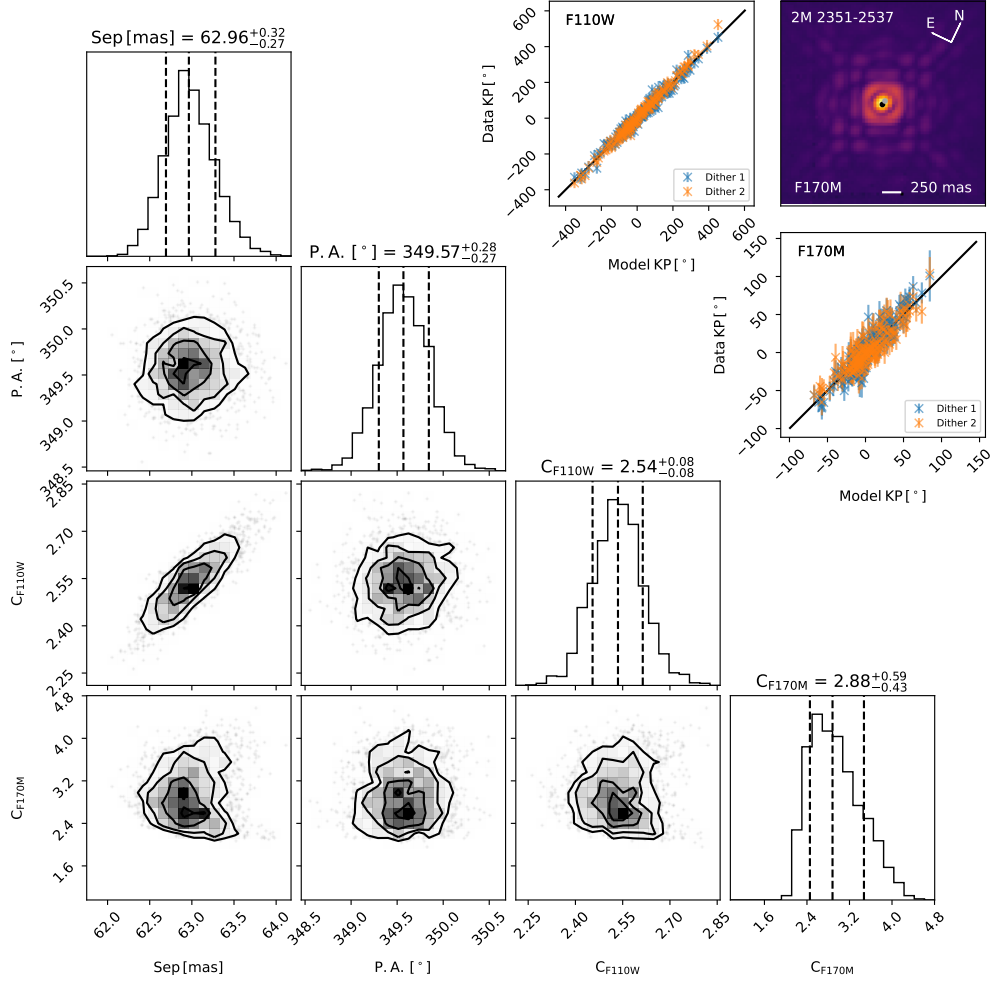


Figure 2.4: Results of fitting a double point source model to observations of 2MASS 2351-2537 (example image shown in the upper right corner with dots showing the position and contrast ratio of the two sources). *Lower Left:* Corner plot showing the posteriors of the four-parameter fit. Dashed lines indicate the median and $\pm 1\sigma$ values (16th, 50th, and 86th percentiles). *Top Right:* Data kernel phases plotted against the best-fit model kernel phases indicating a good fit. Detection limits for this fit show it is significant at the $> 5\sigma$ level and is consistent over multiple calibrators, while the Bayes-factors also indicate a preference for the binary model. Similar figures for each of our detections are shown in Appendix A while marginal and spurious detections are shown and discussed in Sections 2.5.2 and 2.5.3, respectively. The complete figure set (19 images) is available online at Factor & Kraus (2022b).

Figures 2.5, 2.6, and 2.7 for a target with no companion, a confident detection, and a notable non-detection, respectively. Corresponding figures for the rest of the sources are shown in Appendices B, C, and D, respectively with Marginal and Spurious detections shown in Appendix E.

We also run an injection/recovery grid to verify the NRM style scramble-and-fit detection limits, which is overlaid in those figures. This mainly serves as a check to confirm that the scramble-and-fit detection limits are correctly positioned with respect to the companions that the pipeline is able to recover.

A fit companion is considered a confident detection if it is detected at $> 5\sigma$ confidence in at least four of the five calibrators and the binary companion parameters are consistent between every pair of calibrators (with significant detections) in position and contrast within 5 and 1 times the 1σ error bars in the fits, respectively. These limits were selected in order to maximize the number of known companions we recover while minimizing the number of spurious detections. Decreasing the number of calibrators which a companion must be significantly detected in adds spurious detections, all of which are detections in only a single filter. Increasing the precision with which fits using different calibrators must be consistent with each other eliminates detections which we know are real from the literature. The fact that the positional error bars must be inflated while the contrast error bars do not suggests that the calibration uncertainty is much larger with respect to the statistical uncertainty in position than in contrast. Ceau et al. (2019) also discuss a hypothesis testing framework which we discuss further in Section 2.6.3.

2M 0144-0716 (Prog. ID: 10143)

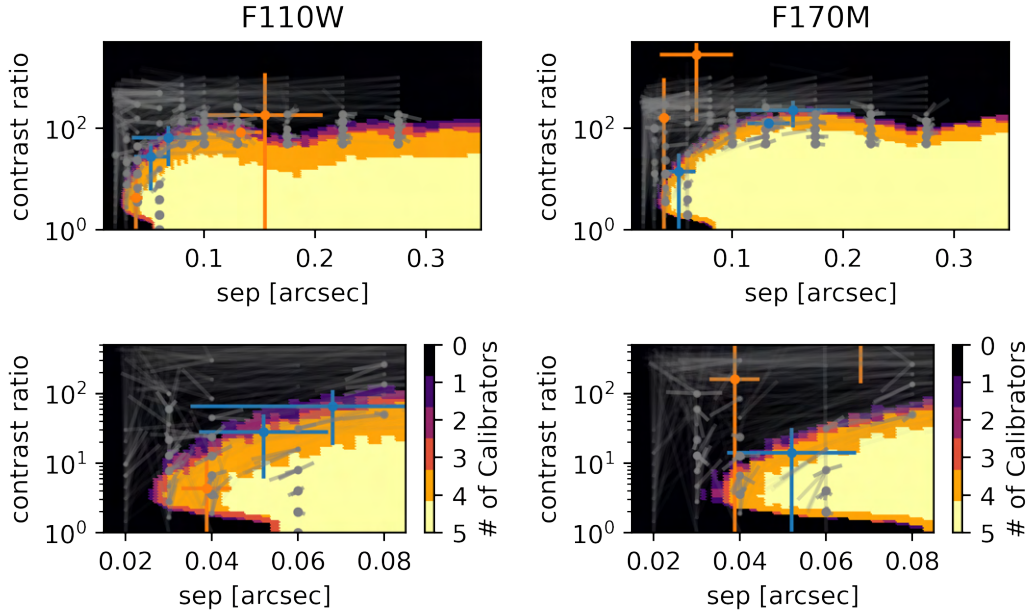


Figure 2.5: Example detection limits on a source with no companion detected. The color scale is the number of calibrators which would significantly ($> 5\sigma$) detect a companion as a function of separation and contrast ratio in the two filters (*left* and *right* columns). The *top row* shows the full range of separation, while the *bottom row* zooms in on the extremely close separation regime where there is a decrease in sensitivity to equal brightness companions (due to a decrease in asymmetry). Best fit companion parameters are plotted (with error bars) for the 5 calibrators in blue, if significantly detected, and in orange, if not significantly detected. In this case < 4 calibrators produce a significant detection and the parameters (including PA) are not consistent with each other so no companion is detected. Overlaid in gray are the results of an injection-recovery test. The injected source is indicated by a circle and is connected to the recovered parameters by a line. Symbol size and opacity is scaled by the proximity of the injected and recovered parameters. The complete figure set (83 images) is available online at Factor & Kraus (2022b) and in Appendix B.

2M 2351-2537 (Prog. ID: 10143)

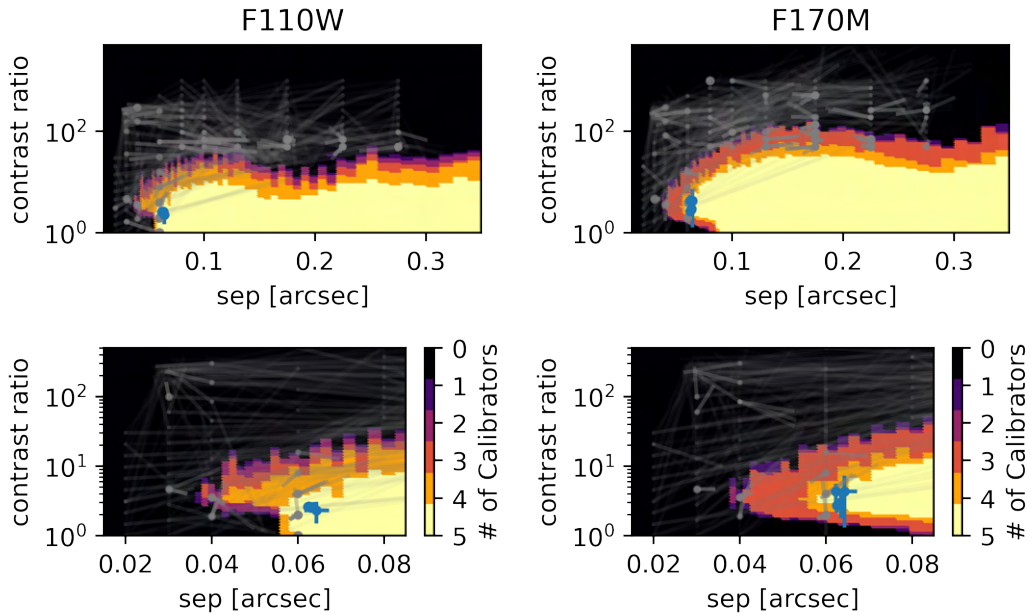


Figure 2.6: Similar to Figure 2.5 but for a significantly detected source. In this case all calibrators produce significant detections and the best fit parameters are consistent with each other. The complete figure set (19 images) is available online at Factor & Kraus (2022b) and in Appendix C.

2M 0314+1603 (Prog. ID: 10143)

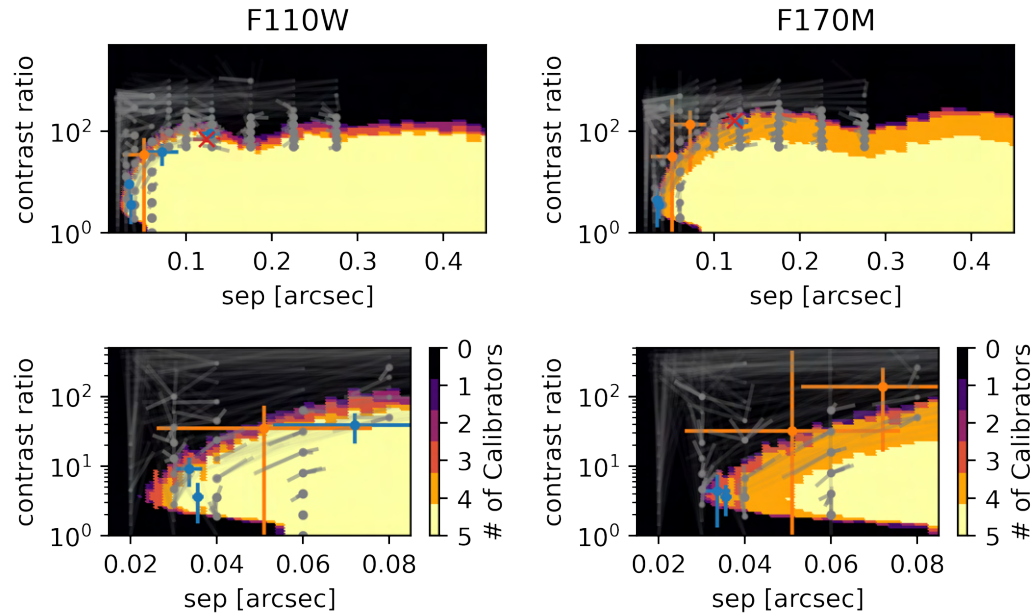


Figure 2.7: Similar to Figure 2.5 but for a notable non-detection. In this case 2M 0314+1603 was marginally detected by Pope et al. (2013). Their best fit parameters are indicated by the red X. One of our calibrators roughly recovers their values but they are not consistent between enough calibrators to consider this detection significant. The complete figure set (11 images) is available online at Factor & Kraus (2022b) and in Appendix D.

2.4.4 Bayesian Model Comparison

Since we are using PyMultiNest to fit our data, we also calculate the Bayesian evidence for the single and double point source models. This value can be used to compare the two models in a purely Bayesian manner, irrelevant of the best fit parameter values. Bayes's theorem (including the hypothesis along with the parameters) states

$$P(\theta|D, H) = \frac{P(D|\theta, H)P(\theta|H)}{P(D|H)}, \quad (2.6)$$

where θ is the model parameters, D is the data, H is the hypothesis (or specific model), $P(\theta|D, H)$ is the posterior, $P(D|\theta, H)$ is the likelihood, $P(\theta|H)$ is the prior, and $P(D|H)$ is the Bayesian evidence. The Bayesian evidence can be thought of as a normalization factor for the numerator, since the posterior distribution must integrate to 1. The Bayesian evidence is ignored by typical MCMC routines, since the integral (over all parameter values) is difficult to perform, and thus the equality is reduced to a proportionality. Since nested sampling algorithms (e.g. Buchner et al., 2014) sample the entire prior volume, they can calculate the Bayesian evidence. The ratio of the Bayesian evidence for two different models, called the Bayes factor, can then be used to compare two different models.

A histogram of Bayes factors (represented by the symbol K) for all of our targets is shown in Figure 2.8 color coded by our detection method described in Section 2.4.3. We distinguish between single targets, confident detections, confident detections in only one filter, a marginal detection, and

undetected targets with wide separation companions (which KPI is insensitive to).

Jeffreys (1961) set out guidelines for how to interpret K ranging from $K < 1$ supporting the single model to $K > 100$ indicating “decisive” evidence for a binary. This scale does not match well with our calculated values as all but one source strongly supports the binary model. While we do see a significant difference in K between binaries and single sources, the differentiating value is much larger than Jeffreys (1961) set out. This may be due to the large number of data-points we are fitting.

A few sources which we designated as binaries had small K values and a few which we designated as single had large K values. These sources are discussed further in Section 2.6.3 and are known shortcomings of the available datasets and KP analysis in general.

2.5 Results

We have detected companions in 21 observations corresponding to 19 binaries (two targets were observed twice) in our sample of 114 targets. We confirm one of the new kernel-phase detections presented in Pope et al. (2013), and marginally recover a second, but none of their other “confident” or “marginal” detections. Even with our increased sensitivity at extremely close separations, we do not detect any new companions. Astrometry and photometry for the companions is presented in Table 2.3. Posteriors, kernel-phase correlation plots, and postage stamp images for each target are shown in Figure 2.4 and

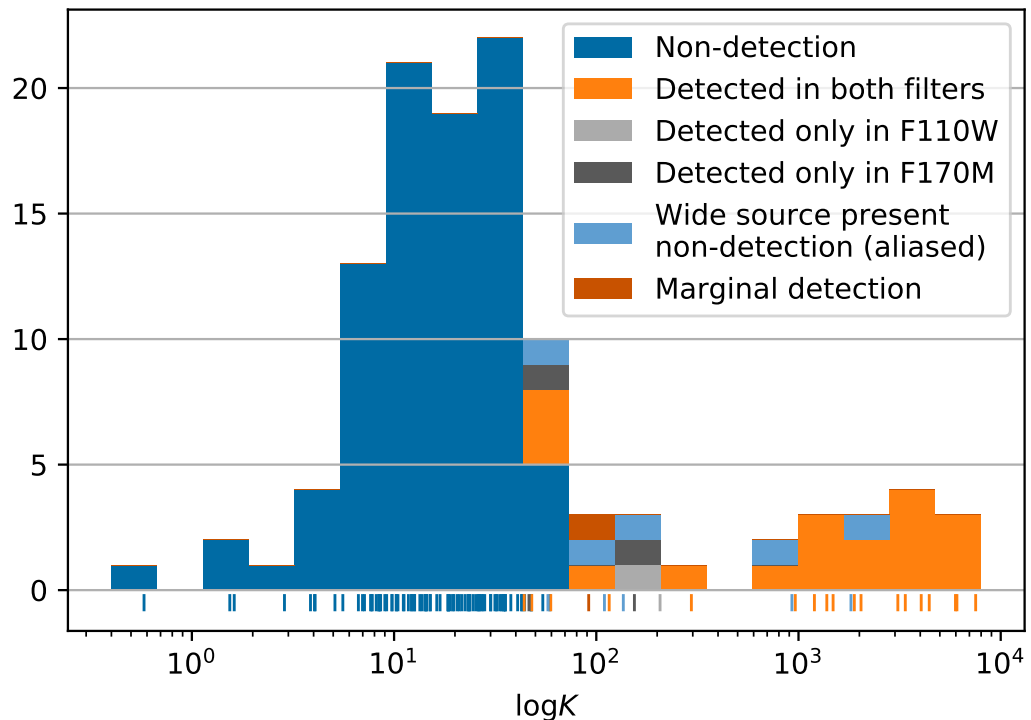


Figure 2.8: Histogram of Bayes factors (median value for the 5 calibrators) for the 117 observations in our sample, color coded by the assessment from our scramble and fit detection method. True (un-binned) positions are indicated with dashes under the histogram. Individual targets are discussed in Section 2.6.3.

the corresponding Figure Set. Our sample also includes 2 wide binaries which KPI is not sensitive to and thus we do not recover, as well as two observations of a suspected extremely tight binary which we do not recover a companion in (see Section 2.5.4).

2.5.1 Known Binaries

We find that 12 sources agree well with previously published astrometry and photometry. This includes **2M 2351-2537**, one of the new extremely tight (62.7 mas , $0.4\lambda/D$ in F110W and $0.66\lambda/D$ in F170M) binaries discovered using KPI by Pope et al. (2013). We discuss the remaining sources below, which have some discrepancy. No previously published astrometry and photometry could be found for the NICMOS imaging of **2M 1534+1615** from program 11136 (Liu, 2007) though our fits visually agree with the position of the companion in the images.

The companion to **2M 0004-4044** is not detected in the F170M filter. This target is a tight ($\sim 0.5\lambda/D$) equal brightness target which KPI is less sensitive to (since the system lacks asymmetry). The companion is however detected in the F110W filter where the diffraction limit is smaller. Pope et al. (2013) fit the full visibilities (rather than just the kernel phases) for this target to increase the sensitivity to the low-contrast companion. Our best fit parameters are slightly tighter and fainter than those of Pope et al. (2013), perpendicular to the contrast-separation degeneracy seen in tight-separation fits.

Table 2.3. Binary astrometry & photometry

Source	Sep. [mas]	$\sigma_{\text{sys,sep}}$ [mas]	PA [deg]	$\sigma_{\text{sys,PA}}$ [deg]	F110W contrast	$\sigma_{\text{sys,F110W}}$	F170M contrast	$\sigma_{\text{sys,F170M}}$
2M 0004-4044	83.2 ± 0.5	0.12	44.3 ± 0.6	0.4	1.126 ± 0.018	0.004	1.251 ± 0.023	0.0010
2M 0025+4739	334.5 ± 0.9	0.05	232.79 ± 0.13	0.005	1.353 ± 0.033	0.0030	2.022 ± 0.016	0.08
2M 0147-4954	138.8 ± 0.4	0.9	72.64 ± 0.14	0.20	2.345 ± 0.030	0.22	2.124 ± 0.010	0.007
2M 0423-0414 ¹	159.11 ± 0.24	0.15	19.77 ± 0.08	0.05	1.655 ± 0.011	0.015		
2M 0423-0414 ²	83.1 ± 0.7	0.8	183.1 ± 0.8	0.4	3.50 ± 0.23	0.010	2.06 ± 0.23	0.25
2M 0429-3123 ³	534 ± 4	0.17	285.2 ± 0.4	0.016	4.43 ± 0.12	0.28	2.77 ± 0.13	0.004
2M 0700+3157	179.4 ± 0.7	0.8	105.68 ± 0.18	0.23	2.93 ± 0.05	0.023	3.809 ± 0.033	0.06
2M 0850+1057	132.2 ± 0.7	0.4	128.11 ± 0.20	0.16	1.522 ± 0.018	0.005	2.423 ± 0.031	0.018
2M 0926+5847	67.22 ± 0.14	0.4	134.26 ± 0.28	0.5	1.104 ± 0.014	0.006	2.70 ± 0.28	0.06
2M 1021-0304	166.4 ± 0.5	1.4	244.83 ± 0.13	0.19	2.96 ± 0.35	0.09	2.516 ± 0.015	0.07
2M 1534+1615	114 ± 4	1.3	310.6 ± 1.6	0.6	1.363 ± 0.034	0.014	2.55 ± 0.27	0.07
2M 1553+1532	345.7 ± 0.7	0.7	189.69 ± 0.13	0.13	1.390 ± 0.018	0.011	1.408 ± 0.027	0.004
2M 1728+3948	157.75 ± 0.28	0.13	66.73 ± 0.10	0.05	4.4 ± 0.7	0.14	1.535 ± 0.007	0.0031
SDSS 2052-1609	102.1 ± 0.9	0.11	48.5 ± 1.1	0.6	1.157 ± 0.019	0.0007	1.126 ± 0.012	0.0005
2M 2152+0937	254.2 ± 0.6	0.034	94.31 ± 0.18	0.009	2.568 ± 0.028	0.027	3.21 ± 0.04	0.32
2M 2252-1730 ⁴	126.7 ± 0.7	0.9	353.96 ± 0.17	0.6	5.8 ± 0.7	0.14	3.3 ± 0.4	0.5
2M 2252-1730 ⁵	91.9 ± 1.9	2.0	172.9 ± 0.6	0.7	5.16 ± 0.14	0.19	4.53 ± 0.06	0.10
2M 2255-5713	178.3 ± 0.8	0.27	172.64 ± 0.22	0.24	2.58 ± 0.09	0.13	2.9 ± 0.9	0.7
2M 2351-2537	62.65 ± 0.34	0.5	348.74 ± 0.28	0.8				
Marginal (see section 2.5.2)								
2M 2028+0052	39.0 ± 3.3	4	118.3 ± 1.0	7	1.7 ± 3.2	3.5		
Spurious (see section 2.5.3)								
2M 0024-0158	202 ± 9	10	33.4 ± 1.3	1.8			1.21 ± 1.1	8
2M 0205-1159	106.0 ± 0.6	0.07	349.8 ± 1.0	0.32	1.75 ± 0.09	0.012	1.122 ± 0.023	0.008
2M 2204-5646	127.9 ± 2.3	0.34	310.7 ± 2.1	1.8	3.02 ± 0.28	0.14	5.2 ± 0.4	0.4

Note. — 1: Observations from program 9833 (7/2004) 2: Observations from program 11136 (8/2008) 3: 2M 0429-3123 is just wider separation than the grid used for detection limits but fitted parameters agree with literature values (see discussion of this source in Section 2.5.1). 4: Observations from program 10143 (6/2005) 5: Observations from program 11136 (5/2008)

2M 0025+4759 is slightly wider than the best fit parameters from Pope et al. (2013). Our contrast in F110W is consistent but our F170M contrast ($C_{\text{F170M}} = 1.25 \pm 0.02$) is slightly higher than both Pope et al. (2013) ($C_{\text{F170M}} = 1.03 \pm 0.04$) and Reid et al. (2006) ($C_{\text{F170M}} = 1.11$). Pope et al. (2013) also fit the visibilities of this roughly equal brightness source rather than the kernel phases since they knew it was a low-contrast companion.

2M 0423-0414 was observed by both Burgasser et al. (2006b) and Liu (2007). We detect the companion in F170M in both epochs but in F110W in only one epoch. The companion is much tighter in the second epoch and the observations are much lower SNR so it is not surprising that we do not detect it in the shorter wavelength filter. Our astrometry and photometry is consistent with that presented by Dupuy & Liu (2017) though we do pick up some separation-contrast degeneracy in the later, close-separation epoch (our separation is slightly tighter and contrast slightly higher). Dupuy & Liu (2017) also derived a dynamical mass for this system from its orbital motion in these and other *HST*/ACS observations.

2M 0429-3123 is just wider than the upper edge of our detection limit grid but the best fit parameters are consistent between calibrators and agree with literature values. We thus consider this a significant detection. Our best fit separation (534 ± 4 mas) splits the difference in separation between Reid et al. (2006) (550 mas) and Pope et al. (2013) (525.2 ± 1.2 mas) while our contrast is consistent.

2M 0926+5847 is consistent with Burgasser et al. (2006b) with the

exception of F170M (they report $C_{\text{F170M}} = 1.4 \pm 0.4$ while we report $C_{\text{F170M}} = 2.70 \pm 0.28$). Our F170M contrast value is more consistent with Dupuy & Liu (2017, $C_{\text{F170}} = 2.2 \pm 0.2$), though still slightly higher contrast. KPI is much more precise than PSF fitting at the separation of this companion (67.22 ± 0.14 mas) and our contrast values are consistent with the color/spectral type relations of T dwarfs (Leggett et al., 2002).

SDSS 2052-1609 was observed at low SNR in program 11136 (Liu, 2007). Our separation and position angle agree with Dupuy & Liu (2017) with higher precision though our best fit F110W contrast ($C_{\text{F110W}} = 4.4 \pm 0.7$) is significantly higher than theirs ($C_{\text{F110W}} = 1.2 \pm 0.4$). Our high contrast F110W fit does not seem consistent with the images even though this target should be easily recovered by KPI. It is possible that the super-Gaussian window we used to exclude noise far away from the target is too wide ($\sigma = 25\lambda/D$) for these low SNR observations where the wings of the PSF are not present. Orbital motion is seen between this and other observations and was fit by Dupuy & Liu (2017).

2M 2252-1730 was observed by Reid et al. (2006) and later by Liu (2007). Our best fit parameters are consistent with the Reid et al. (2006) and Pope et al. (2013) epoch while we pick up some separation-contrast degeneracy in the later Liu (2007) epoch. Our values (sep = 91.9 ± 1.9 mas, $C_{\text{F110W}} = 5.8 \pm 0.7$) are slightly wider and significantly higher contrast than those presented by Dupuy & Liu (2017) (sep = 87 ± 3 mas, $C_{\text{F110W}} = 1.9 \pm 0.7$). As with **SDSS 2052-1609**, our high contrast F110W fit is likely caused by too wide

of a super-Gaussian window. Orbital motion is seen between the two epochs and was fit by Dupuy & Liu (2017).

2.5.2 Marginal Detection

2M 2028+0052 is not detected in F170M and just barely fails to pass our confidence test in F110W. While four of five calibrators produce fits which are well grouped, one pair of calibrators is inconsistent with each other in position at 5.16σ (just above our 5σ cutoff) and another pair is inconsistent with each other in contrast at 1.07σ (just above our 1σ cutoff). This target also has a slightly elevated Bayes Factor with respect to sources we categorize as single. We thus present this as a marginal detection. Adding more calibrators and a more careful treatment of bad pixels, thus reducing the noise, will help to refine this determination. It also has an elevated RUWE (1.418; Gaia Collaboration, 2020), even when fitting for the astrometric color (Lindegren et al., 2021), suggesting the presence of a companion. Dahn et al. (2017) also notes elevated and periodic ($\lesssim 2$ years) residuals in their parallax solution.

Our best fit parameters are consistent with those of Pope et al. (2013), when considering the intercalibrator systematic error-bars. Our best fit parameters are heavily weighted toward a single higher precision fit, while the fits using the other calibrators are much lower precision (as can be seen in the detection limit plot shown in Figure 2.9. Figure 2.10 shows the corner plot for the high precision fit. There appears to be a small bump in the posterior at a lower contrast in F170M which may be consistent with the Pope et al. (2013)

2M 2028+0052 (Prog. ID: 10879)

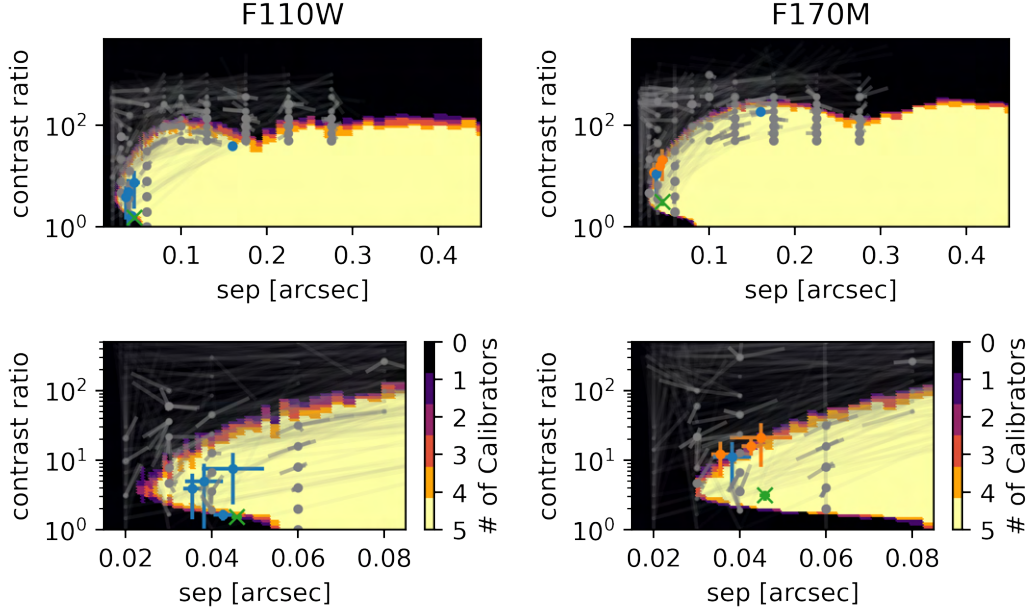


Figure 2.9: Similar to Figure 2.5 but for the marginal detection of 2M 2028+0052. The best fit parameters from Pope et al. (2013) are indicated by the green X. The full figure set (4 images) is available online at Factor & Kraus (2022b) and in Appendix E.

contrast.

2.5.3 Spurious Detections

We detect a high contrast “companion” around **2M 0024-0158** in F170M but with no detection in F110W. Figure 2.11 shows the corner plot, kernel-phase correlation plots, and a representative image for this target. Visual inspection of the images and associated data-quality frames demonstrates that this detection is spurious. The position of the detection almost exactly

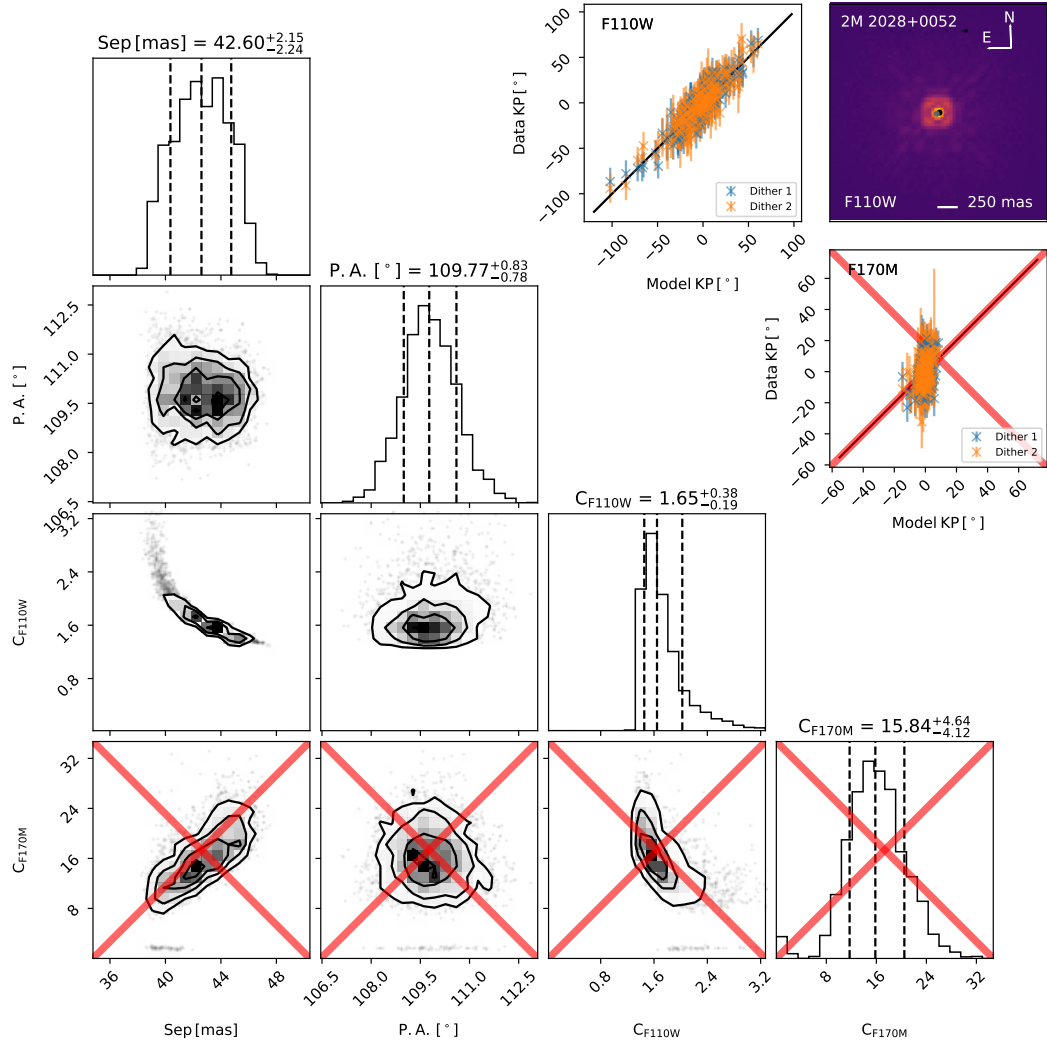


Figure 2.10: Similar to Figure 2.4 but for the marginal detection of 2MASS 2028+0052. Red X's indicate no detection in F170M.

lines up with bad pixels which were coincidentally located at the same position, relative to the target, in both dither positions. Our bad-pixel correction technique (replacing the pixel with the median of the 8 surrounding pixels) injected a brighter than expected pixel in the F170M images, since it fell in the first dark airy ring. This pixel was then interpreted as a companion. In the F110W images the bad pixel fell in the first bright airy ring and did not inject the signal of a companion. This can be seen in Figure 2.12. We present this case as a cautionary tale to show how image-plane based bad-pixel rejection routines can inject signals in the Fourier plane. In the future, bad-pixel rejection techniques in the Fourier plane should be used as described by Ireland (2013) and implemented in Kammerer et al. (2019).

A simple visual inspection of the fits to **2M 0205-1159** and **2M 2204-5646**, shown in Figures 2.13 and 2.14, shows a clear discrepancy between the visually obvious companion and the best fit parameters. Both of these targets were observed in program 11136 which observed using a large number of filters, sacrificing SNR for more wavelength coverage. Therefore, while the core of the PSFs are clear, little to none of the wings of the diffraction pattern is recovered. While we present our best fit parameters for completeness of the survey, we will give these sources a more careful treatment in a future letter. In addition, **2M 0205-1159** is a previously known triple system (Bouy et al., 2005). The position and contrast of our best fit companion is likely a combination of the B and C components. Fitting this system with a triple point source model will be done in a future letter as the addition of a third source adds nontrivial

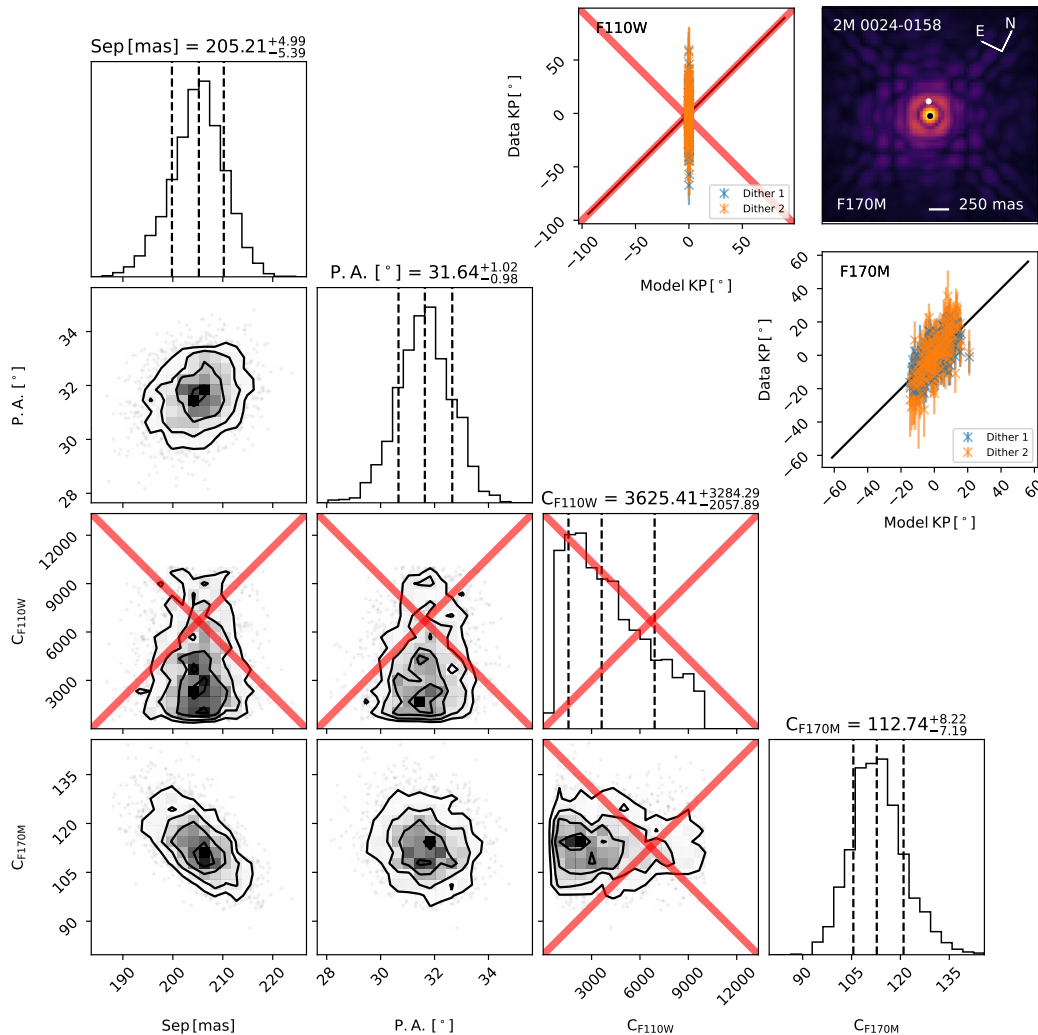


Figure 2.11: Similar to Figure 2.4 but for 2MASS 0024-0158. Large red X's over the 1- and 2D histograms indicate no detection in the F110W filter. This fit locked onto the signal produced by a bad pixel.

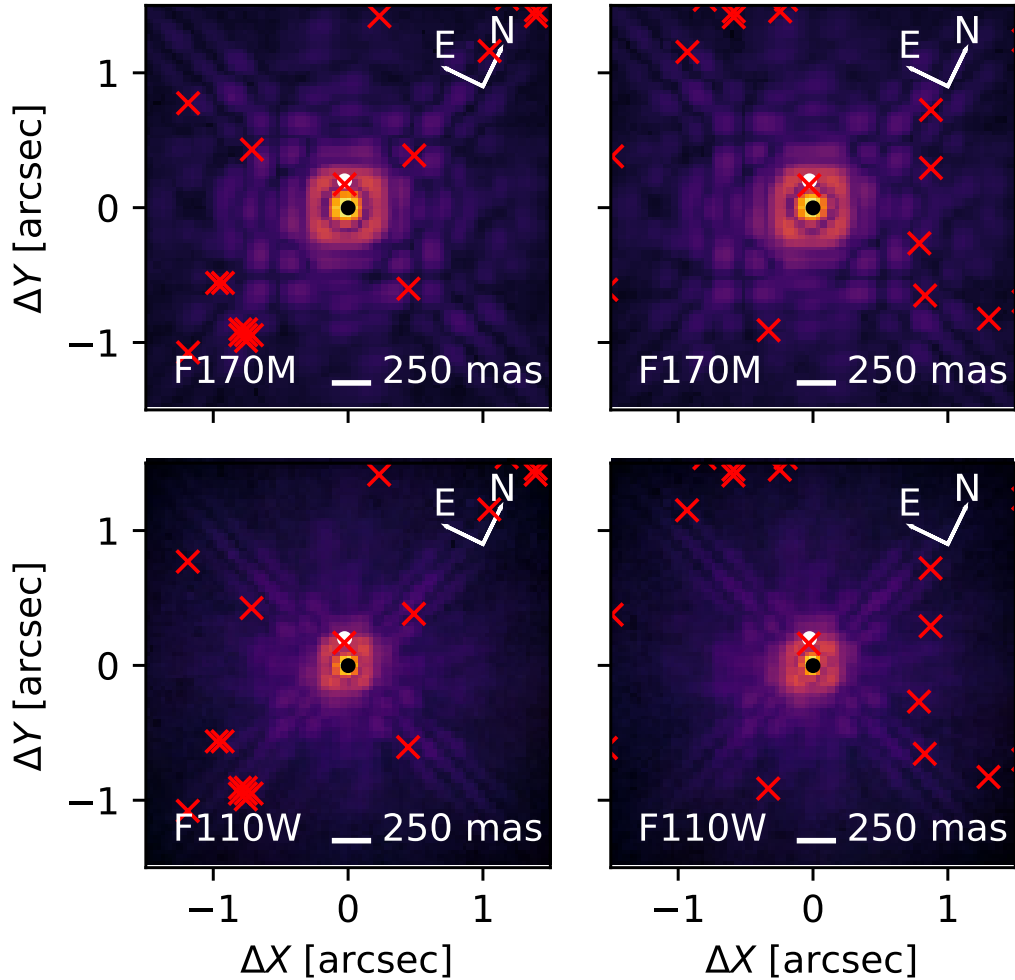


Figure 2.12: Both filter and dither position images of 2M 0024-0158. The location of the primary is indicated by a black circle and the location of the best fit “companion” is shown by a white circle. The locations of bad pixels are indicated with red X’s. Note that in both dither positions there is a bad pixel at almost exactly the same location relative to the target and that in F170M the bad pixel is located in the first dark ring while in F110W it is located in the first bright ring. Our bad-pixel rejection imperfectly replaced the bad pixel on the dark ring and yielded a spurious faint detection in F170M.

degeneracies in the model.

2.5.4 Notable Non-detections

We do not significantly detect any of the marginal detections presented in Pope et al. (2013) and only detect two of their five confident detections (**2M 2351-2537** significantly and **2M 2028+0052** marginally, discussed above). While some of our best fit parameters with a *single* calibrator are consistent with their results and that single fit may be significant (e.g. **2M 0314+1603** and **2M 1936-5502**), they are not consistent between multiple calibrators (see Figure 2.7 and the relevant figure in Appendix D) and we therefore do not classify them as detections. This demonstrates the strength of and need for a robust calibration strategy. Due to the extreme separation of these proposed companions, a ground-truth validation of these companions is difficult though not impossible. Possible techniques include LGSQO on a large ground based telescope or astrometry (e.g. future work of Gaia Collaboration et al., 2021; Dahn et al., 2017). While binary fits are still not part of Gaia data releases, RUWE can be used as a proxy for the presence of a companion (Lindegren et al., 2018; Belokurov et al., 2020; Lindegren et al., 2021, Kraus et al. in prep.). All of the marginal and confident detections (with the exception of the two sources we recover) have RUWE of ~ 1 (Gaia Collaboration, 2020). If these companions are real we would expect them to have an elevated RUWE like **2M 2351-2537** (RUWE = 5.417), though equal brightness companions have less of an astrometric signal and faint targets have inherently more noise.

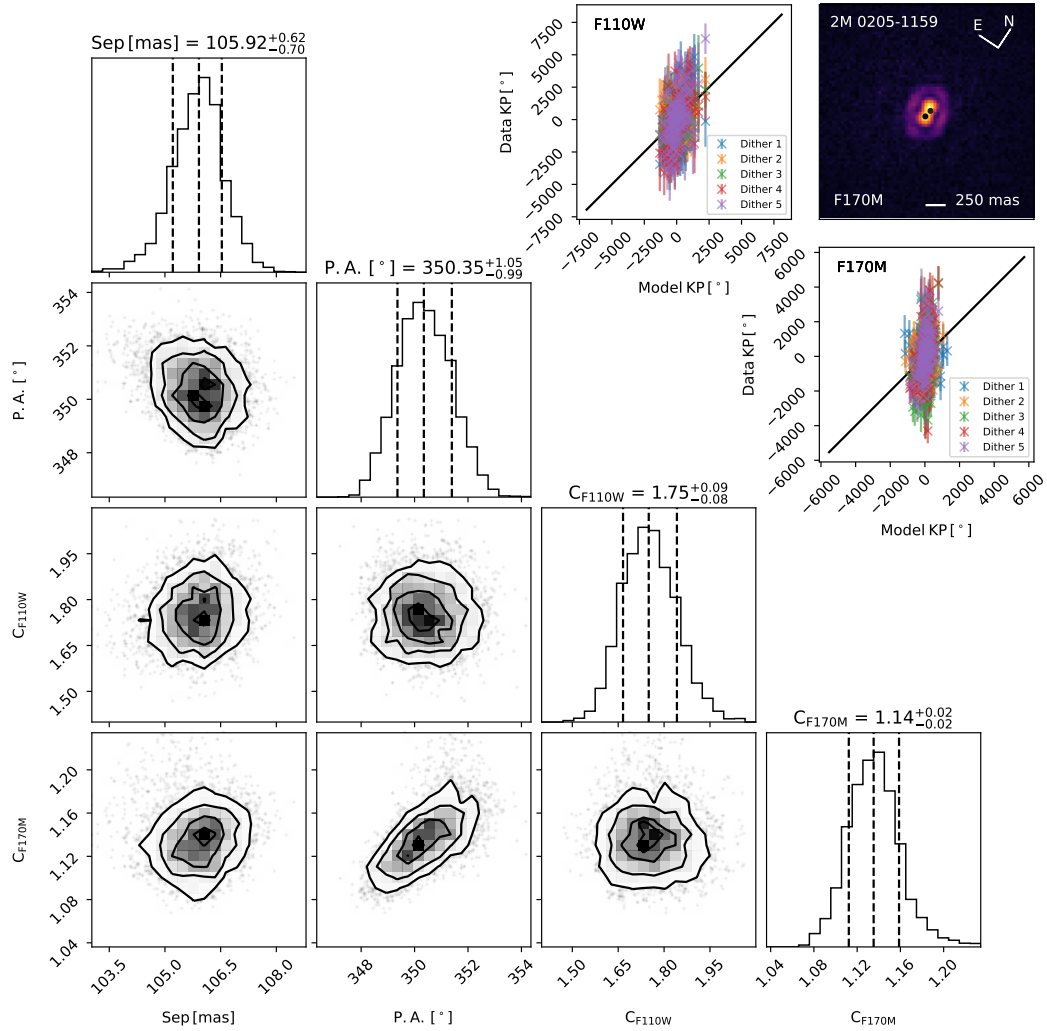


Figure 2.13: Similar to Figure 2.4 but for the spurious fit to 2MASS 0205-1159. This source is a triple system and thus is not well fit with a binary model.

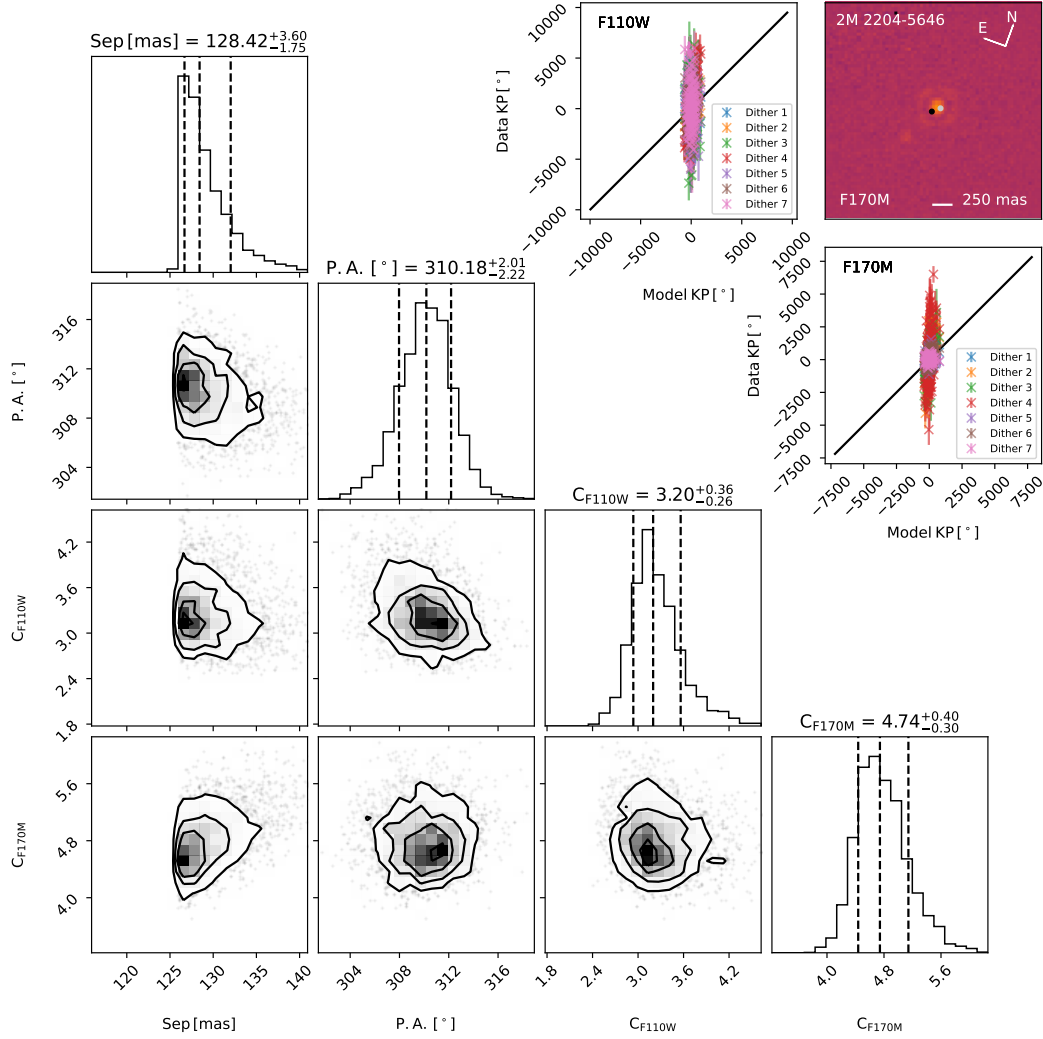


Figure 2.14: Similar to Figure 2.4 but for 2MASS 2204-5646. Our binary model did not recover the true values of the wide companion in this low SNR observation.

It is also difficult for our implementation of KPI to recover wide companions at separations greater than ~ 0.6 arcsec accurately. These companions suffer from aliasing in the Fourier plane as sampled by our aperture model and do not require high resolution where KPI excels. Since these companions are generally noticeable under visual inspection, one could tune the prior to isolate the true signal from aliases but it would be more straightforward to use classical PSF fitting techniques.

2M 0915+0422 is a wide separation companion (738.6 ± 0.15 mas Pope et al., 2013) and thus our pipeline is strongly affected by aliasing in the Fourier plane. Our fits do not recover the literature values for this companion. We do detect a significant companion but at an alias of the known companion.

2M 1707-0558 is also a wide separation companion (1009.5 ± 1 mas; Pope et al., 2013) and again our pipeline is strongly affected by aliasing in the Fourier plane. We do recover the companion in two of five calibrators but the aliasing is strongly affecting our best fit parameters so we do not present them here. Our best fit separation is slightly wider than both Reid et al. (2006) and Pope et al. (2013) though our contrasts are more consistent with Reid et al. (2006).

2M 1705+0516 and **2M 1731+2721** both have wide objects in the images that, based on color and follow up observations (Dupuy, private communication), appear to be background sources.

We do not detect a companion to **2M 0518-2828** in either of the two

epochs (programs 10247 and 11136). Cruz et al. (2004) published the near infrared spectrum of this object which had features of both an L and T dwarf, suggesting that it was an unresolved binary. Burgasser et al. (2006b) then published *HST*/NICMOS images of this target and found that the PSF was “slightly elongated”, more so in the shorter wavelength filters. The elongation is extremely small in F110W and absent in F170M so our non-detection is not unexpected. Burgasser et al. (2006b) measured a separation of 51 ± 12 mas and a contrast of $C_{\text{F110W}} = 2.1 \pm 1.0$ (0.8 ± 0.5 mag) and $C_{\text{F170M}} = 2.3 \pm 1.3$ (0.9 ± 0.6 mag). The separation is what is limiting us in this case as, for context, it is roughly 10 mas tighter than **2M 2351-2537** at slightly lower contrast. If KPI can be done in F090M (larger pixel scale relative to λ/D and larger aberrations relative to λ) a detection may be possible.

2.5.5 Survey Detection Limits

A superposition of all detection limits is shown in Figure 2.15. Detection limits for each target are shown in Figures 2.5, 2.6, and 2.7 and the corresponding Appendices, and are summarized in Tables 2.4–2.6 at a set of separations. In the best cases, significant detections of companions can be achieved up to a contrast of $\sim 100 : 1$ and down to a separation of $\sim 0''.1$. Below $\sim 0''.1$ the contrast limit drops steeply and becomes bimodal, with KPI becoming insensitive to equal-brightness companions at extremely tight separations due to the loss of asymmetry. A full treatment of the covariance matrix could increase the contrast limits at large separations due to the consideration

of photon noise (Ireland, 2013).

Comparing the difference in sensitivity between the two filters, as shown in Figure 2.16, reveals some clear takeaways. At close separation the shorter wavelength F110W filter is more sensitive since the diffraction limit is smaller. At wider separations, observations in the longer wavelength F170M filter are more sensitive since optical aberrations are smaller with respect to the wavelength of light. These two filters also work in harmony by canceling out the dips in sensitivity as the brightness of the airy pattern fluctuates. A detection in two filters is also helpful to discern between real detections and spurious detections (such as for **2M 0024-00158**, caused by a bad pixel).

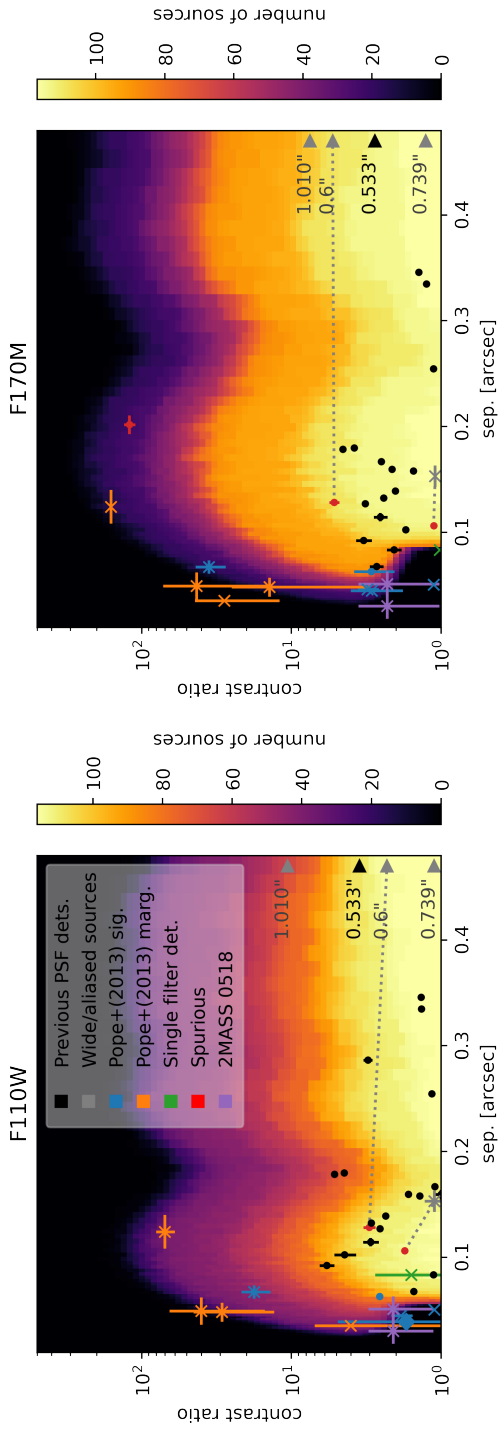


Figure 2.15: Stacked 5σ detection limits as a function of separation for all sources in the survey. Filled circles indicate the positions of detected companions, the diamond is our one marginal detection, and X's indicate literature values for non-detections. Points are color coded by type of detection and are outlined in the legend. Black symbols indicate companions previously found by PSF fitting. Blue and orange symbols indicate the “significant” and “marginal” detections from Pope et al. (2013), respectively. Green X's indicate the literature contrast values of the two sources (one in each filter) which we only detected in one filter. Red points indicate the positions of “spurious” detections (see Section 2.5.3) with dotted lines to gray X's indicating the literature values. Purple symbols indicate the position of 2MASS 0518-2828 (see Section 2.5.4). Two sources were extremely wide and were not recovered due to strong aliasing and are shown by gray arrows, at a separation given by the labeled text. The survey detection limits in both filters, in units of number of sources, are available as the Data behind the Figure online at Factor & Kraus (2022b).

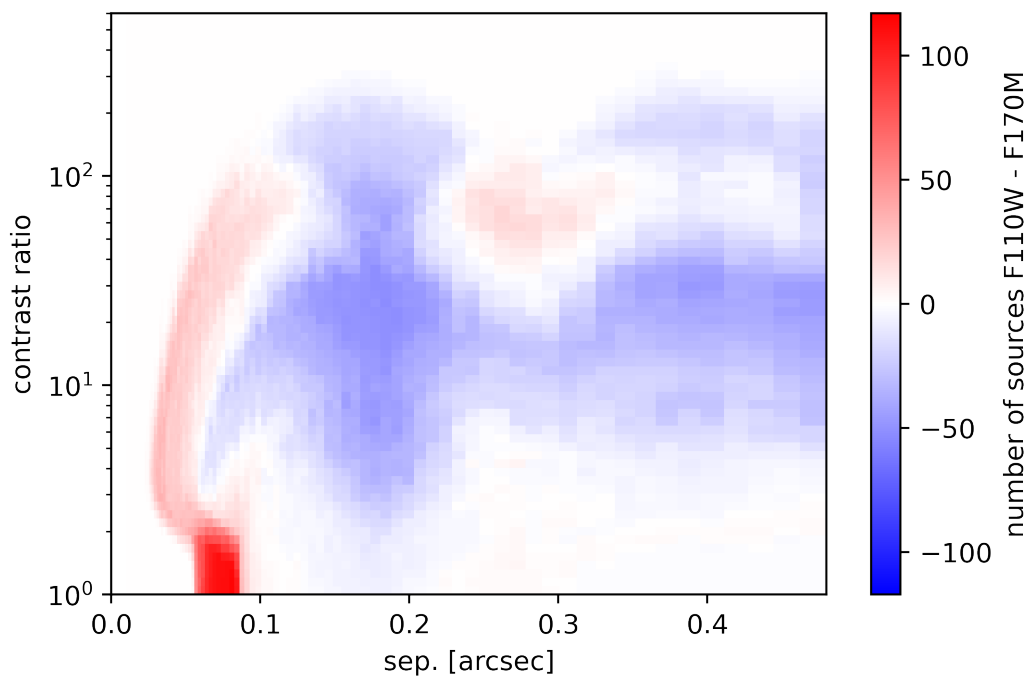


Figure 2.16: The difference in sensitivity between F110W and F170M (given in number of observations our analysis was sensitive to out of a total of 117) as a function of separation and contrast. F110W is more sensitive at close separations where the diffraction limit dominates, while F170M is more sensitive globally since aberrations are smaller with respect to the longer wavelength.

Table 2.4. Individual 5σ Contrast Ratio Limits in F110W

Source	Contrast Limit in F110W at Sep. [mas]						
	55–65	75–85	90–110	160–200	250–300	350–400	450–500
2M 0004-4044	2.3 ± 0.6, 2.1 ± 0.5	3.35 ± 0.26	4.43 ± 0.30	2.42 ± 0.24	3.7 ± 0.7	4.6 ± 0.8	3.9 ± 0.5
2M 0024-0158	63 ± 7	115 ± 5	138 ± 6	66 ± 4	126 ± 5	138 ± 12	100 ± 5
2M 0025+4759		1.5 ± 0.4	1.59 ± 0.13		1.52 ± 0.16	2.01 ± 0.21	2.8 ± 0.5
2M 0036+1821	34.5 ± 3.2	65.8 ± 2.8	79.2 ± 3.1	41.3 ± 1.7	75.7 ± 3.5	87.0 ± 3.3	55 ± 5
2M 0045+1634	55 ± 6	95 ± 4	115 ± 9	62.9 ± 2.9	110 ± 9	126 ± 5	83 ± 4
2M 0107+0041	32.8 ± 3.4	60 ± 5	72 ± 7	37.6 ± 2.4	72 ± 7	72.2 ± 3.0	50 ± 9
2M 0109+2949	55 ± 10	95 ± 11	115 ± 8	63 ± 10	105 ± 4	121 ± 9	80 ± 7
2M 0123-4240	6.1 ± 1.7	12.3 ± 1.4	17.9 ± 2.4	9.3 ± 2.2	13.5 ± 1.9	16.3 ± 1.6	13.6 ± 1.3
2M 0144-0716	43 ± 5	72 ± 11	87 ± 9	48 ± 4	76 ± 6	100 ± 7	60 ± 11
2M 0147-4954	4.5 ± 0.8, 1.4 ± 0.5	7.7 ± 0.4	9.3 ± 0.9	3.9 ± 0.6	9.8 ± 1.5	8.9 ± 0.7	6.74 ± 0.31
2M 0151+1244	38 ± 5	59.9 ± 2.8	79 ± 10	39 ± 4	72 ± 6	95 ± 4	60 ± 11
2M 0155+0950	4.04 ± 0.27, 1.4 ± 0.4	13.5 ± 2.7	11.2 ± 0.8	5.9 ± 1.7	11.9 ± 2.4	12.9 ± 1.0	7.40 ± 0.34
2M 0205-1159	1.0 ± 0	2.8 ± 0.4	4.0 ± 0.4	2.01 ± 0.24	3.5 ± 0.4	4.23 ± 0.31	4.65 ± 0.22
2M 0207+0000	7.1 ± 1.6, 1.00 ± 0.20	13.5 ± 2.9	19.6 ± 1.9	10.7 ± 1.2	16.3 ± 1.8	19.6 ± 0.8	15.6 ± 0.7
2M 0213+4444	79 ± 7	138 ± 11	183 ± 22	91 ± 9	183 ± 13	192 ± 9	111 ± 15
2M 0228+1639	25 ± 4	45.3 ± 3.5	54.6 ± 2.1	27.2 ± 3.2	52.2 ± 2.4	57.3 ± 2.7	36.0 ± 1.7
2M 0243-2453	13.6 ± 2.6	26 ± 9	26 ± 4	18 ± 4	24.8 ± 3.1	29 ± 4	19.7 ± 1.8
2M 0251-0352	2.8 ± 0.6, 1.0 ± 0.6	9.3 ± 1.9	7.7 ± 0.5	3.9 ± 1.3	8.2 ± 1.7	8.5 ± 0.6	5.4 ± 0.5
2M 0255-4700	73 ± 12	105 ± 10	152 ± 11	76 ± 8	121 ± 15	167 ± 6	105 ± 10
2M 0257-3105	34.3 ± 3.3	60 ± 9	72.2 ± 3.1	36.0 ± 2.4	60 ± 8	72.2 ± 3.0	52.2 ± 2.4
2M 0314+1603	41 ± 4	72 ± 11	95 ± 4	50 ± 6	83 ± 7	105 ± 4	72 ± 14
2M 0318-3421	24.8 ± 3.3	41.3 ± 1.7	55 ± 4	26.0 ± 2.4	46 ± 6	57 ± 4	36.0 ± 1.7
2M 0348-6022	46 ± 7	87 ± 7	95 ± 8	49.8 ± 2.1	91 ± 7	110 ± 8	76 ± 11
2M 0355+1133	16.3 ± 1.8	28 ± 4	34 ± 5	21 ± 4	31.3 ± 3.4	36 ± 4	26 ± 5
2M 0415-0935	6.4 ± 2.2, 1.00 ± 0.32	13.5 ± 2.1	21.5 ± 2.3	11.2 ± 2.4	15.6 ± 2.3	17.9 ± 1.7	15.7 ± 2.2
2M 0423-0414	3.1 ± 0.7, 1.00 ± 0.15	5.9 ± 0.6	8.5 ± 1.0	4.2 ± 0.5	7.1 ± 0.5	7.4 ± 0.9	6.74 ± 0.31
2M 0423-0414	3.05 ± 0.34, 1.0 ± 0.6	5.9 ± 1.0	7.7 ± 0.8	3.05 ± 0.34	6.43 ± 0.25	7.4 ± 0.6	4.9 ± 0.8
2M 0429-3123				1.39 ± 0.14	1.10 ± 0.10	1.52 ± 0.16	2.10 ± 0.09
2M 0439-2353	55 ± 5	95 ± 14	126 ± 12	59.9 ± 2.8	121 ± 13	145 ± 11	95 ± 18
2M 0443+0002	66 ± 6	105 ± 8	152 ± 13	69 ± 8	132 ± 11	152 ± 21	105 ± 20
2M 0445-3048	4.6 ± 2.0, 1.00 ± 0.26	9.3 ± 2.2	13.5 ± 1.3	6.1 ± 0.9	11.2 ± 0.7	12.9 ± 1.0	8.9 ± 0.4
2M 0500+0330	45 ± 6	79 ± 6	79 ± 14	48 ± 7	96 ± 14	105 ± 20	60 ± 11
2M 0518-2828	6.7 ± 1.0, 1.00 ± 0.20	12.3 ± 1.4	14.8 ± 1.2	8.5 ± 0.5	14.8 ± 0.6	17.9 ± 1.9	10.7 ± 0.5
2M 0518-2828	5.1 ± 1.1, 1.00 ± 0.32	10.2 ± 1.5	12.3 ± 0.9	6.1 ± 0.5	11.8 ± 0.9	14.2 ± 1.0	9.8 ± 0.5
2M 0523-1403	57 ± 4	95 ± 4	138 ± 14	63 ± 8	121 ± 6	100 ± 13	91 ± 4
2M 0624-4521	52 ± 5	87 ± 11	95 ± 7	48 ± 6	83 ± 15	100 ± 10	83 ± 4
2M 0652+4710	9.8 ± 0.7, 1.00 ± 0.04	17.9 ± 0.8	26.0 ± 2.2	11.2 ± 1.1	22.6 ± 3.3	27.2 ± 2.0	17.9 ± 3.3
2M 0700+3157	13.6 ± 3.0	17.9 ± 2.7	26 ± 4	11.8 ± 1.4	23.6 ± 3.1	27 ± 5	17.9 ± 3.3
2M 0727+1710	8.9 ± 1.2, 1.00 ± 0.09	16.3 ± 0.7	19.6 ± 1.3	9.8 ± 0.7	17.9 ± 1.9	19.6 ± 0.8	12.9 ± 0.6
2M 0755+2212	55 ± 6	95 ± 7	105 ± 16	60 ± 6	105 ± 4	121 ± 16	95 ± 18
2M 0825+2115	14.2 ± 2.1	24 ± 4	26 ± 4	18 ± 4	24.8 ± 2.6	26 ± 4	20 ± 4
2M 0830+4828	48 ± 11	72 ± 5	105 ± 9	50 ± 6	96 ± 9	115 ± 16	57.3 ± 2.7
2M 0835-0819	50 ± 8	72.2 ± 3.3	95 ± 10	50 ± 5	87 ± 11	115 ± 11	75.7 ± 3.5
2M 0847-1532	45 ± 9	87 ± 13	105 ± 6	55 ± 9	100 ± 5	115 ± 13	75.7 ± 3.5
2M 0850+1057	3.68 ± 0.33, 1.4 ± 0.4	10.2 ± 2.2	13.5 ± 1.1	4.9 ± 0.7	10.7 ± 1.1	11.8 ± 1.5	8.5 ± 0.8
2M 0859-1949	45.3 ± 3.0	87 ± 4	105 ± 9	52.2 ± 3.5	105 ± 7	115 ± 11	73 ± 7
2M 0908+5032	49.8 ± 3.3	72 ± 13	87 ± 10	48 ± 6	95 ± 4	100 ± 7	69.0 ± 3.2
2M 0911+7401	49.8 ± 2.1	95 ± 4	126 ± 11	63 ± 6	115 ± 16	132 ± 6	83 ± 4
2M 0915+0422		1.00 ± 0.15	1.59 ± 0.31	1.10 ± 0.08	1.67 ± 0.17	2.42 ± 0.20	3.1 ± 0.5
2M 0921-2104	47.6 ± 2.2	79 ± 12	105 ± 12	52 ± 7	95 ± 13	100 ± 10	76 ± 11
2M 0926+5847	6.1 ± 1.4, 1.00 ± 0.32	18 ± 4	19.6 ± 1.4	9.8 ± 1.4	19.6 ± 2.1	21 ± 4	12.4 ± 1.1
2M 1021-0304		3.05 ± 0.29	3.7 ± 0.4	1.45 ± 0.34	2.32 ± 0.22	3.4 ± 0.4	3.20 ± 0.15
2M 1022+5825	63 ± 5	95 ± 9	126 ± 14	69 ± 8	121 ± 6	138 ± 5	95 ± 18
2M 1025+3212	20 ± 4	31 ± 7	45.3 ± 3.1	20.6 ± 2.1	38 ± 5	45 ± 6	32 ± 6
2M 1043+2225	36 ± 6	59.9 ± 2.8	79 ± 8	38 ± 5	76 ± 8	83 ± 9	55 ± 10
2M 1045-0149	33 ± 4	55 ± 8	72 ± 5	34 ± 4	66 ± 6	79 ± 5	43.3 ± 2.0
2M 1048+0111	11.8 ± 2.1	20 ± 4	24 ± 4	15.6 ± 3.4	21.5 ± 3.4	24 ± 5	18.8 ± 0.9
2M 1051+5613	43 ± 5	72 ± 5	95 ± 10	52 ± 9	95 ± 13	105 ± 7	75.7 ± 3.5
2M 1058-1548	76 ± 11	152 ± 12	183 ± 18	87 ± 16	183 ± 18	183 ± 18	126 ± 24
2M 1104+1959	26 ± 4	60 ± 7	66 ± 4	34 ± 4	63 ± 7	76 ± 6	47.6 ± 2.2
2M 1108+6830	52 ± 7	95 ± 4	126 ± 7	66 ± 9	115 ± 16	132 ± 10	91 ± 4
2M 1110+0116	34 ± 5	65.8 ± 2.8	87 ± 4	45 ± 4	76 ± 13	91 ± 7	55 ± 5
2M 1155-3727	55 ± 4	87 ± 11	115 ± 14	60 ± 9	110 ± 11	121 ± 6	91 ± 4
2M 1203+0015	69 ± 7	115 ± 5	138 ± 7	79 ± 9	138 ± 13	152 ± 6	105 ± 10
2M 1213-0432	48 ± 8	79 ± 12	95 ± 15	55 ± 10	100 ± 5	110 ± 15	70 ± 10

Table 2.4 (cont'd)

Source	55–65	75–85	Contrast Limit in F110W at Sep. [mas]				
			90–110	160–200	250–300	350–400	450–500
2M 1217-0311	53 ± 8	79 ± 4	105 ± 12	57 ± 7	110 ± 5	115 ± 12	80 ± 7
2M 1221+0257	83 ± 9	138 ± 6	167 ± 7	91 ± 8	159 ± 13	183 ± 18	126 ± 24
2M 1254-0122	6.1 ± 2.0, 1.00 ± 0.32	12.3 ± 2.9	19.6 ± 2.1	10.3 ± 2.3	14.2 ± 1.8	17.1 ± 1.8	13.6 ± 1.3
2M 1300+1912	48 ± 7	79 ± 8	105 ± 11	52 ± 10	105 ± 9	100 ± 10	73 ± 7
2M 1421+1827	62.9 ± 2.9	105 ± 4	138 ± 10	65.8 ± 3.0	121 ± 15	138 ± 6	95 ± 18
2M 1425-3650	92 ± 15	138 ± 13	183 ± 8	83 ± 12	159 ± 13	192 ± 14	115 ± 22
2M 1428+5923	52 ± 4	87 ± 4	115 ± 14	55 ± 5	97 ± 20	115 ± 4	75.7 ± 3.5
2M 1439+1929	73 ± 9	138 ± 15	167 ± 20	80 ± 11	159 ± 12	175 ± 18	105 ± 20
2M 1448+1031	60 ± 8	105 ± 13	126 ± 4	66 ± 4	121 ± 10	126 ± 5	100 ± 5
2M 1503+2525	6.5 ± 2.0, 1.00 ± 0.32	14.8 ± 2.7	19.6 ± 2.5	10.7 ± 1.8	14.2 ± 2.5	17.9 ± 1.2	14.2 ± 0.7
2M 1503+2525	16.3 ± 1.7	19.6 ± 2.4	34 ± 5	14 ± 4	24.8 ± 3.1	26 ± 4	19.7 ± 1.8
2M 1506+1321	49.8 ± 3.3	87 ± 8	115 ± 10	52 ± 6	101 ± 16	115 ± 5	80 ± 7
2M 1507-1627	9.8 ± 1.0	12.3 ± 1.9	19.6 ± 0.9	11.2 ± 0.5	21.5 ± 1.6	20.6 ± 1.7	14.9 ± 1.4
2M 1515+4847	39 ± 5	72 ± 8	87 ± 10	50 ± 8	83 ± 12	95 ± 7	57.3 ± 2.7
2M 1534+1615	3.05 ± 0.29	4.43 ± 0.30	2.10 ± 0.35	3.9 ± 0.4	5.3 ± 0.6	5.10 ± 0.24	
2M 1539-0520	7.1 ± 1.1, 1.00 ± 0.32	13.5 ± 2.0	16.3 ± 2.2	8.1 ± 0.9	16.3 ± 1.6	18.8 ± 2.5	12.4 ± 1.1
2M 1552+2948	22.8 ± 3.2	41 ± 5	49.8 ± 2.2	23.6 ± 3.1	48 ± 8	60 ± 6	39.5 ± 1.8
2M 1553+1532	1.60 ± 0.15	1.59 ± 0.27	1.10 ± 0.30	1.60 ± 0.20	2.21 ± 0.10	2.8 ± 0.5	
2M 1624+0029	36 ± 6	72 ± 7	95 ± 10	52 ± 8	80 ± 12	100 ± 13	73 ± 7
2M 1658+7027	60 ± 10	105 ± 4	115 ± 9	66 ± 10	121 ± 9	126 ± 8	91 ± 4
2M 1705-0516	2.78 ± 0.34, 2.1 ± 0.6	5.3 ± 1.0	5.9 ± 1.0	2.4 ± 0.4	5.6 ± 0.5	5.6 ± 0.6	4.23 ± 0.20
2M 1707-0558	1.7 ± 0.5	2.31 ± 0.29	1.20 ± 0.16	2.31 ± 0.22	3.05 ± 0.12	3.51 ± 0.16	
2M 1721+3344	57 ± 6	105 ± 12	115 ± 5	63 ± 6	115 ± 10	126 ± 8	87 ± 17
2M 1728+3948	3.7 ± 0.6, 1.6 ± 0.6	5.9 ± 0.4	7.1 ± 0.9	2.8 ± 0.5	6.4 ± 0.4	7.7 ± 1.4	4.23 ± 0.20
2M 1731+2721	52 ± 7	95 ± 9	126 ± 9	69 ± 13	126 ± 5	132 ± 6	87 ± 8
2M 1750+1759	6.5 ± 1.9, 1.00 ± 0.26	13.5 ± 1.3	19.6 ± 1.8	9.3 ± 1.5	14.2 ± 1.8	17.9 ± 1.7	13.5 ± 2.4
2M 1753-6559	76 ± 8	105 ± 8	138 ± 17	76 ± 8	121 ± 15	167 ± 16	101 ± 14
2M 1807+5015	60 ± 7	95 ± 7	115 ± 9	69 ± 12	115 ± 4	115 ± 16	87 ± 8
2M 1936-5502	39 ± 6	59.9 ± 2.8	72 ± 9	39 ± 8	80 ± 11	83 ± 4	57.3 ± 2.7
2M 2002-0521	60 ± 10	105 ± 8	115 ± 10	60 ± 7	115 ± 12	138 ± 10	83 ± 4
2M 2028+0052	50 ± 6	87 ± 10	105 ± 7	52 ± 7	91 ± 7	100 ± 5	62.9 ± 2.9
2M 2036+1051	43 ± 5	79 ± 10	105 ± 7	52 ± 7	100 ± 13	105 ± 4	66 ± 12
2M 2057-0252	9.8 ± 0.5	19.6 ± 2.9	26.0 ± 1.8	12.3 ± 1.4	23.6 ± 3.1	27.2 ± 2.0	17.9 ± 3.3
2M 2104-1037	24.8 ± 3.3	37.6 ± 2.9	55 ± 5	28 ± 4	46 ± 6	55 ± 5	34.5 ± 3.2
2M 2139+0220	38 ± 4	72 ± 10	87 ± 8	38 ± 6	87.0 ± 3.3	95 ± 17	69.0 ± 3.2
2M 2148+4003	7.1 ± 0.9, 1.0 ± 0.4	13.5 ± 2.0	16.3 ± 2.2	7.7 ± 0.8	16.3 ± 1.1	18.8 ± 2.5	11.8 ± 0.5
2M 2152+0937	1.59 ± 0.34	2.54 ± 0.25	1.00 ± 0.23	2.01 ± 0.16	2.78 ± 0.11	3.4 ± 0.6	
2M 2204-5646	2.31 ± 0.35	3.4 ± 0.5	1.59 ± 0.32	3.35 ± 0.25	3.7 ± 0.7	3.4 ± 0.6	
2M 2224-0158	36 ± 4	59.9 ± 2.5	72 ± 6	37.6 ± 3.1	69 ± 5	79 ± 11	52.2 ± 2.4
2M 2228-4310	50 ± 11	79 ± 16	115 ± 10	60 ± 8	100 ± 10	115 ± 5	80 ± 7
2M 2237+3922	79.2 ± 3.0	138 ± 11	167 ± 6	87 ± 6	145 ± 15	183 ± 7	132 ± 6
2M 2249+3205	18.8 ± 2.7	37.6 ± 3.0	45 ± 4	21.5 ± 1.8	41 ± 4	45 ± 6	32.8 ± 1.5
2M 2252-1730	3.86 ± 0.18, 1.7 ± 0.7	7.1 ± 0.5	8.5 ± 1.2	4.4 ± 0.7	8.5 ± 0.8	9.8 ± 1.3	7.1 ± 1.2
2M 2252-1730	3.37 ± 0.31	5.86 ± 0.25	7.74 ± 0.34	3.7 ± 0.5	6.7 ± 0.7	7.7 ± 0.5	6.5 ± 0.6
2M 2254+3123	39 ± 5	72 ± 6	95 ± 5	49.8 ± 3.2	91 ± 10	95 ± 6	66 ± 6
2M 2255-5713	14.2 ± 2.9	21.5 ± 2.6	31.3 ± 2.1	15.6 ± 1.5	28.5 ± 3.1	31 ± 4	22 ± 4
2M 2325+4251	38 ± 7	65.8 ± 3.0	95 ± 7	45 ± 5	83 ± 4	100 ± 5	66 ± 12
2M 2339+1352	55 ± 7	87 ± 4	115 ± 12	60 ± 8	115 ± 8	126 ± 12	87 ± 8
2M 2351-2537	8.6 ± 1.6	17.9 ± 1.4	17.9 ± 2.4	8.1 ± 1.9	16.3 ± 1.1	18.8 ± 1.5	12.3 ± 2.2
SDSS 0837-0000	8.5 ± 1.9, 1.0 ± 0	16 ± 4	19.6 ± 3.2	10.7 ± 1.6	18.8 ± 3.0	18.8 ± 2.0	10.7 ± 0.5
SDSS 2052-1609	3.35 ± 0.15	4.43 ± 0.21	2.54 ± 0.21	4.6 ± 0.4	5.34 ± 0.35	5.10 ± 0.24	

Note. — Median 5 σ contrast (within the stated separation range) in 4 of 5 calibrators. No entry indicates no significant detection at that separation is possible. Two entries (at tight separations) is caused by a reduction in sensitivity to equal brightness targets and indicates a significant detection is possible *between* the two values. The diffraction limit (λ/D) is roughly 95 and 147 mas in F110W and F170M, respectively.

Table 2.5. Individual 5σ Contrast Ratio Limits in F170M

Source	Contrast Limit in F170M at Sep. [mas]						
	55–65	75–85	90–110	160–200	250–300	350–400	450–500
2M 0004-4044	6.3 ± 2.6, 2.01 ± 0.21	16.3 ± 2.5, 1.32 ± 0.15	28 ± 5	60 ± 5	26.1 ± 3.0	54.6 ± 2.1	55 ± 10
2M 0024-0158	33 ± 7, 1.59 ± 0.20	66 ± 8, 1.20 ± 0.10	95 ± 13	201 ± 34	105 ± 14	201 ± 22	167 ± 32
2M 0025+4739			1.9 ± 0.5	3.7 ± 0.6	1.39 ± 0.11	3.9 ± 0.4	2.92 ± 0.14
2M 0036+1821	16 ± 4, 1.83 ± 0.09	31 ± 4, 1.45 ± 0.06	60 ± 9	95 ± 6	48 ± 8	105 ± 4	87 ± 17
2M 0045+1634	20.6 ± 1.5, 1.83 ± 0.09	45 ± 7, 1.45 ± 0.16	79 ± 14	126 ± 6	63 ± 5	138 ± 5	115 ± 11
2M 0107+0041	17.1 ± 1.8, 1.75 ± 0.07	38 ± 4, 1.45 ± 0.17	66 ± 7	115 ± 5	54.6 ± 2.3	115 ± 8	100 ± 5
2M 0109+2949	33 ± 7, 1.59 ± 0.10	66 ± 8, 1.20 ± 0.13	138 ± 9	211 ± 33	110 ± 11	231 ± 11	220 ± 40
2M 0123-4240	9.3 ± 1.0, 2.01 ± 0.09	23.6 ± 2.7, 1.59 ± 0.07	38 ± 8	69 ± 5	33 ± 4	72 ± 10	60 ± 11
2M 0144-0716	26 ± 4, 1.59 ± 0.20	55 ± 4, 1.20 ± 0.13	105 ± 15	175 ± 16	83 ± 6	183 ± 7	145 ± 7
2M 0147-4954	18 ± 4, 1.59 ± 0.06	41 ± 5, 1.20 ± 0.10	66 ± 7	126 ± 18	4.2 ± 0.8	8.5 ± 2.5	10.4 ± 1.9
2M 0151+1244					57 ± 7	126 ± 12	115 ± 11
2M 0155+0950						24.8 ± 1.2	22.6 ± 1.1
2M 0205-1159						5.6 ± 0.4	5.3 ± 0.9
2M 0207+0000	7.5 ± 1.6, 2.01 ± 0.16	17.9 ± 0.7, 1.59 ± 0.07	31 ± 4	52 ± 5	24.8 ± 2.0	54.6 ± 2.3	52.2 ± 2.4
2M 0213+4444	50 ± 7, 1.59 ± 0.20	115 ± 9, 1.20 ± 0.10	201 ± 29	351 ± 12	167 ± 6	368 ± 27	336 ± 16
2M 0228+1639	7.4 ± 0.6, 2.10 ± 0.08	17.9 ± 1.4, 1.59 ± 0.07	28 ± 6	54.6 ± 2.5	26 ± 4	57 ± 4	50 ± 9
2M 0243-2453	7.7 ± 1.2, 2.10 ± 0.08	20 ± 4, 1.59 ± 0.07	34 ± 4	55 ± 4	23.6 ± 1.7	57 ± 6	47.6 ± 2.2
2M 0251-0352	4.9 ± 0.4, 2.10 ± 0.26	12.3 ± 1.4, 1.59 ± 0.18	21.5 ± 3.3	39.5 ± 3.5	17.9 ± 1.7	41.3 ± 1.6	35 ± 6
2M 0255-4700	14.9 ± 3.3, 1.75 ± 0.07	38 ± 4, 1.32 ± 0.15	60 ± 4	110 ± 5	54.6 ± 2.1	110 ± 5	100 ± 5
2M 0257-3105	23 ± 4, 1.75 ± 0.21	49.8 ± 2.3, 1.45 ± 0.21	87 ± 11	152 ± 14	72.2 ± 3.0	152 ± 15	132 ± 6
2M 0314+1603	34 ± 4, 1.59 ± 0.06	66 ± 10, 1.32 ± 0.15	105 ± 16	183 ± 14	100 ± 7	201 ± 13	167 ± 32
2M 0318-3421	21.5 ± 3.4, 1.75 ± 0.21	45 ± 4, 1.32 ± 0.13	79 ± 5	126 ± 15	63 ± 5	145 ± 15	126 ± 24
2M 0348-6022	20.6 ± 3.3, 1.59 ± 0.07	50 ± 6, 1.20 ± 0.13	72 ± 10	138 ± 7	63 ± 5	139 ± 20	132 ± 6
2M 0355+1133	8.5 ± 1.3, 2.01 ± 0.09	19.6 ± 2.3, 1.45 ± 0.07	34.3 ± 3.1	60 ± 7	29.9 ± 1.4	60 ± 7	57.3 ± 2.7
2M 0415-0935	5.6 ± 1.5, 2.21 ± 0.32	13.5 ± 0.6, 1.59 ± 0.07	24 ± 5	45.3 ± 1.6	22.6 ± 2.4	47.6 ± 3.5	43.3 ± 2.0
2M 0423-0414	4.23 ± 0.20, 2.42 ± 0.11	12.3 ± 2.8, 1.59 ± 0.12	18 ± 4	37.6 ± 3.1	15.6 ± 1.3	34 ± 5	29.9 ± 1.4
2M 0429-3123			3.4 ± 0.7, 1.0 ± 0.4	6.7 ± 1.4	3.5 ± 0.6	7.4 ± 0.8	7.7 ± 1.4
2M 0439-2353				1.75 ± 0.09	1.10 ± 0.10	1.83 ± 0.14	2.21 ± 0.10
2M 0443+0002				292 ± 22	138 ± 13	306 ± 14	280 ± 40
2M 0445-3048				266 ± 17	126 ± 17	279 ± 21	240 ± 50
2M 0500+0330				91 ± 6	34.3 ± 1.4	91 ± 14	83 ± 4
2M 0518-2828				242 ± 20	105 ± 10	231 ± 19	254 ± 12
				28 ± 4	54.6 ± 3.5	26.0 ± 1.7	50 ± 9

Table 2.5 (cont'd)

Source	55–65	75–85	Contrast Limit in F170M at Sep. [mas]	250–300				350–400				450–500			
				90–110	160–200	250–300	350–400	250–300	350–400	250–300	350–400	250–300	350–400	250–300	350–400
2M 0518-2828	5.1 ± 1.5, 2.21 ± 0.32	14.8 ± 1.8, 1.59 ± 0.12	28 ± 5	54.6 ± 1.8	26.0 ± 2.7	54.6 ± 2.1	44 ± 6								
2M 0523-1403	36 ± 5, 1.59 ± 0.06	72 ± 13, 1.20 ± 0.13	126 ± 18	231 ± 15	105 ± 12	221 ± 9	231 ± 11								
2M 0624+2325	7.4 ± 1.4, 2.21 ± 0.16	17.9 ± 2.6, 1.59 ± 0.12	24 ± 4	50 ± 7	24.8 ± 1.2	45 ± 6	41 ± 8								
2M 0624+4521	31 ± 7, 1.59 ± 0.06	72 ± 5, 1.32 ± 0.15	95 ± 15	201 ± 7	87 ± 9	192 ± 9	183 ± 35								
2M 0632+4710	13.6 ± 2.0, 1.75 ± 0.07	31.3 ± 3.0, 1.45 ± 0.06	55 ± 8	95 ± 6	50 ± 5	100 ± 5	91 ± 4								
2M 0700+3157		2.92 ± 0.14, 2.23 ± 0.31	5.9 ± 2.1	14.2 ± 2.3	5.9 ± 1.5	12.9 ± 1.3	9.8 ± 0.5								
2M 0727+1710		3.1 ± 0.7, 2.1 ± 0.5	34 ± 5	66 ± 6	34.3 ± 2.3	66 ± 8	62.9 ± 2.9								
2M 0755+2212	9.8 ± 2.1, 1.83 ± 0.15	23.6 ± 1.8, 1.45 ± 0.11	31 ± 5	60 ± 4	27 ± 6	59.9 ± 2.3	50 ± 9								
2M 0825+2115	7.1 ± 0.8, 2.10 ± 0.08	17.9 ± 2.0, 1.59 ± 0.07	115 ± 22	183 ± 22	100 ± 7	221 ± 8	194 ± 27								
2M 0830+4828	33 ± 6, 1.67 ± 0.08	66 ± 6, 1.20 ± 0.18	105 ± 13	192 ± 18	87 ± 6	183 ± 16	183 ± 35								
2M 0835+0819	27.2 ± 2.8, 1.59 ± 0.20	72 ± 6, 1.32 ± 0.15	55 ± 12	175 ± 13	83 ± 7	202 ± 34	175 ± 8								
2M 0847-1532	27.2 ± 2.8, 1.59 ± 0.07	55 ± 12, 1.45 ± 0.12	3.6 ± 0.8, 2.42 ± 0.11	5.3 ± 1.1	10.2 ± 0.4	4.1 ± 0.5	11.2 ± 0.7	11.8 ± 0.5							
2M 0850+1057			66 ± 11	115 ± 5	60 ± 4	132 ± 14	110 ± 5								
2M 0859-1949	18.8 ± 2.5, 1.75 ± 0.07	37.6 ± 3.0, 1.32 ± 0.15	28 ± 4	45.3 ± 3.5	24.8 ± 1.2	49.8 ± 3.3	47.6 ± 2.2								
2M 0908+5032	6.7 ± 1.2, 2.01 ± 0.25	14.8 ± 1.1, 1.45 ± 0.06	87 ± 4, 1.20 ± 0.10	138 ± 18	254 ± 17	121 ± 10	266 ± 10	243 ± 23							
2M 0911+7401	43 ± 6, 1.59 ± 0.06				1.92 ± 0.18		1.75 ± 0.07	2.03 ± 0.28							
2M 0915+0422															
2M 0921-2104	23.6 ± 2.5, 1.67 ± 0.08	50 ± 4, 1.32 ± 0.19	87 ± 13	152 ± 14	69 ± 6	167 ± 12	121 ± 6								
2M 0926+5847	7.4 ± 1.4, 1.83 ± 0.15	17.9 ± 2.7, 1.20 ± 0.12	34 ± 4	55 ± 7	24.8 ± 1.2	53 ± 7	55 ± 10								
2M 1021-0304		2.5 ± 0.6, 2.1 ± 0.5	4.9 ± 0.8	8.9 ± 2.4	4.1 ± 0.6	10.2 ± 0.8	10.2 ± 1.8								
2M 1022+5825	22.6 ± 2.4, 1.67 ± 0.08	45 ± 6, 1.32 ± 0.11	79 ± 10	138 ± 14	66 ± 6	159 ± 12	145 ± 7								
2M 1025+3212	12.3 ± 2.3, 1.92 ± 0.08	24 ± 7, 1.45 ± 0.11	45 ± 6	79 ± 6	37.6 ± 2.5	79.2 ± 3.3	75.7 ± 3.5								
2M 1043+2225	27 ± 4, 1.67 ± 0.08	66 ± 7, 1.32 ± 0.15	105 ± 16	183 ± 10	83 ± 7	192 ± 14	153 ± 14								
2M 1045-0149	23.6 ± 3.2, 1.75 ± 0.12	45.3 ± 3.5, 1.45 ± 0.06	66 ± 12	138 ± 7	72.2 ± 2.8	145 ± 11	126 ± 24								
2M 1048+0111	18.0 ± 2.6, 1.52 ± 0.07	50 ± 7, 1.10 ± 0.08	66 ± 12	138 ± 14	57 ± 5	138 ± 5	133 ± 19								
2M 1051+5613	20.6 ± 2.1, 1.75 ± 0.21	45 ± 4, 1.32 ± 0.06	72 ± 9	121 ± 6	62.9 ± 2.9	126 ± 9	115 ± 11								
2M 1058-1548	48 ± 6, 1.67 ± 0.08	105 ± 12, 1.32 ± 0.15	167 ± 22	292 ± 27	138 ± 15	306 ± 32	279 ± 13								
2M 1104+1959	14.2 ± 2.4, 1.67 ± 0.08	34.3 ± 1.6, 1.20 ± 0.06	55 ± 11	95.5 ± 3.2	45 ± 5	100 ± 10	92 ± 13								
2M 1108+6830	12.3 ± 1.2, 1.75 ± 0.21	23.6 ± 2.9, 1.45 ± 0.12	50 ± 8	79 ± 4	39.5 ± 2.9	87 ± 4	75.7 ± 3.5								
2M 1110+0116	5.1 ± 1.6, 2.1 ± 0.5	13.5 ± 1.3, 1.45 ± 0.11	28 ± 4	45 ± 5	21.5 ± 2.1	45.3 ± 1.7	45 ± 9								
2M 1155-3727	31 ± 6, 1.59 ± 0.06	66 ± 8, 1.10 ± 0.08	105 ± 13	211 ± 21	105 ± 12	192 ± 14	192 ± 9								
2M 1203+0015	16.4 ± 2.0, 1.67 ± 0.08	34.3 ± 2.6, 1.32 ± 0.11	60 ± 10	105 ± 7	52 ± 4	110 ± 11	100 ± 5								
2M 1213-0432	7.8 ± 2.0, 1.8 ± 0.4	16.3 ± 2.0, 1.20 ± 0.09	28.5 ± 2.4	55 ± 4	27.2 ± 2.2	57 ± 4	57.3 ± 2.7								

Table 2.5 (cont'd)

Source	55–65	75–85	Contrast Limit in F170M at Sep. [mas]				
			90–110	160–200	250–300	350–400	450–500
2M 1217-0311	5.9 ± 1.4, 1.92 ± 0.15	16.3 ± 1.9, 1.45 ± 0.06	26 ± 4	50 ± 4	23.6 ± 0.9	50 ± 7	48 ± 7
2M 1221+0257	55 ± 10, 1.59 ± 0.06	11.5 ± 5, 1.10 ± 0.08	201 ± 17	351 ± 12	175 ± 8	368 ± 27	336 ± 16
2M 1254-0122	8.9 ± 1.3, 1.83 ± 0.09	21.5 ± 3.2, 1.45 ± 0.17	38 ± 5	66 ± 5	31.3 ± 2.8	66 ± 4	62.9 ± 2.9
2M 1300+1912	31 ± 5, 1.59 ± 0.07	66 ± 12, 1.32 ± 0.15	105 ± 18	192 ± 23	96 ± 9	183 ± 12	184 ± 17
2M 1421+1827	39.5 ± 2.9, 1.67 ± 0.08	87 ± 14, 1.32 ± 0.10	138 ± 10	266 ± 17	126 ± 12	254 ± 12	240 ± 50
2M 1425-3650	60 ± 9, 1.59 ± 0.06	11.5 ± 9, 1.20 ± 0.13	201 ± 14	351 ± 12	183 ± 7	368 ± 27	320 ± 60
2M 1428+5923	30 ± 6, 1.67 ± 0.08	79 ± 9, 1.20 ± 0.09	105 ± 12	221 ± 21	100 ± 15	211 ± 10	200 ± 40
2M 1439+1929	42 ± 9, 1.59 ± 0.07	79 ± 8, 1.32 ± 0.15	138 ± 10	254 ± 23	126 ± 8	266 ± 18	243 ± 23
2M 1448+1031	17.1 ± 2.5, 1.59 ± 0.07	37.6 ± 2.9, 1.32 ± 0.15	66 ± 5	110 ± 10	55 ± 4	115 ± 8	105 ± 20
2M 1503+2525	10.2 ± 1.4, 1.75 ± 0.07	21.5 ± 2.6, 1.45 ± 0.06	38 ± 6	66 ± 4	29 ± 5	72 ± 5	63 ± 9
2M 1503+2525	13.6 ± 1.9, 1.83 ± 0.14	28.5 ± 2.2, 1.32 ± 0.10	50 ± 6	87 ± 6	39.5 ± 1.8	83 ± 9	73 ± 7
2M 1506+1321	39 ± 6, 1.75 ± 0.07	87 ± 12, 1.32 ± 0.10	138 ± 16	266 ± 21	121 ± 13	243 ± 23	240 ± 50
2M 1507-1627	13.5 ± 2.1, 1.67 ± 0.08	28 ± 4, 1.32 ± 0.11	55 ± 10	100 ± 9	47.6 ± 3.5	96 ± 11	100 ± 5
2M 1515+4847	20.6 ± 3.5, 1.67 ± 0.08	45 ± 5, 1.32 ± 0.19	79 ± 7	138 ± 22	63 ± 5	139 ± 13	132 ± 6
2M 1534+1615			4.9 ± 0.6	9.3 ± 0.6	4.0 ± 0.5	9.3 ± 0.4	8.9 ± 0.4
2M 1539-0520	7.4 ± 1.3, 2.10 ± 0.09	17.9 ± 2.6, 1.59 ± 0.07	31.3 ± 2.8	57 ± 6	26.0 ± 1.1	55 ± 6	52.2 ± 2.4
2M 1552-2948	5.9 ± 0.7, 2.10 ± 0.16	12.3 ± 1.5, 1.59 ± 0.07	23.6 ± 2.5	43.3 ± 3.1	20.6 ± 2.1	45.3 ± 1.7	41 ± 8
2M 1553+1532			2.03 ± 0.28	4.2 ± 0.5	1.45 ± 0.31	4.9 ± 0.7	4.65 ± 0.22
2M 1624+0029	5.9 ± 0.9, 2.10 ± 0.14	13.5 ± 0.6, 1.45 ± 0.11	28 ± 5	49.8 ± 2.1	21.5 ± 2.3	45.3 ± 1.9	50 ± 5
2M 1638+7027	55 ± 5, 1.59 ± 0.20	105 ± 16, 1.32 ± 0.15	201 ± 19	351 ± 15	167 ± 23	336 ± 27	321 ± 30
2M 1705-0516	10.7 ± 2.1, 1.92 ± 0.08	26.0 ± 2.1, 1.45 ± 0.07	45 ± 5	79.2 ± 3.3	38 ± 5	79 ± 6	69.0 ± 3.2
2M 1707-0558			1.83 ± 0.22	1.05 ± 0.05	1.83 ± 0.09	1.83 ± 0.09	2.11 ± 0.20
2M 1721+3344	33 ± 4, 1.67 ± 0.08	79 ± 6, 1.20 ± 0.09	115 ± 20	221 ± 17	100 ± 8	211 ± 10	202 ± 19
2M 1728+3948			2.1 ± 0.4	4.4 ± 0.9	1.68 ± 0.32	4.6 ± 0.7	3.37 ± 0.31
2M 1731+2721	48 ± 9, 1.52 ± 0.07	11.5 ± 5, 1.10 ± 0.08	201 ± 21	320 ± 13	145 ± 7	351 ± 26	306 ± 14
2M 1750+1759	7.4 ± 0.5, 1.92 ± 0.08	16.3 ± 1.6, 1.59 ± 0.07	31 ± 7	54.6 ± 2.9	24.8 ± 3.1	63 ± 10	56 ± 10
2M 1753-6559	38 ± 8, 1.59 ± 0.07	87 ± 7, 1.20 ± 0.13	138 ± 23	242 ± 16	110 ± 11	242 ± 10	220 ± 40
2M 1807+5015	44 ± 8, 1.59 ± 0.20	95 ± 7, 1.32 ± 0.11	167 ± 29	266 ± 35	139 ± 17	306 ± 32	280 ± 40
2M 1936-5502	22.8 ± 3.2, 1.75 ± 0.07	50 ± 6, 1.32 ± 0.06	79 ± 12	152 ± 10	73 ± 8	152 ± 10	127 ± 12
2M 2002-0521	34 ± 4, 1.75 ± 0.07	79 ± 6, 1.45 ± 0.17	115 ± 15	221 ± 14	105 ± 14	221 ± 8	200 ± 40
2M 2028+0052	43 ± 5, 1.59 ± 0.20	87 ± 10, 1.32 ± 0.15	138 ± 16	242 ± 16	126 ± 5	242 ± 21	240 ± 50
2M 2036+1051	41 ± 4, 1.59 ± 0.20	87 ± 10, 1.10 ± 0.13	138 ± 10	242 ± 27	126 ± 5	254 ± 19	240 ± 50
2M 2057-0252	11.8 ± 1.7, 1.92 ± 0.13	24 ± 4, 1.59 ± 0.07	50 ± 8	91 ± 6	43.3 ± 2.0	91 ± 7	91 ± 4

Table 2.5 (cont'd)

Source	55–65	75–85	Contrast Limit in F170M at Sep. [mas]				
			90–110	160–200	250–300	350–400	450–500
2M 2104-1037	14.2 ± 3.4, 1.83 ± 0.15	34 ± 4, 1.45 ± 0.07	54.6 ± 3.2	105 ± 9	45 ± 4	105 ± 14	83 ± 4
2M 2139+0220	9.9 ± 2.0, 2.01 ± 0.15	23.6 ± 2.9, 1.45 ± 0.11	38 ± 6	72 ± 5	34.3 ± 1.4	73 ± 7	69.0 ± 3.2
2M 2148+4003	7.1 ± 1.7, 2.10 ± 0.15	19.6 ± 2.3, 1.45 ± 0.11	31.3 ± 3.5	55 ± 5	28.5 ± 2.1	63 ± 5	53 ± 7
2M 2152+0937			2.1 ± 0.4	3.7 ± 0.6	1.5 ± 0.5	4.4 ± 0.8	3.86 ± 0.18
2M 2204-5646			4.9 ± 0.8	10.2 ± 0.8	5.1 ± 0.9	11.2 ± 2.3	9.8 ± 0.5
2M 2224-0158	30 ± 5, 1.59 ± 0.07	60 ± 6, 1.32 ± 0.11	95 ± 10	167 ± 18	79 ± 12	159 ± 7	159 ± 7
2M 2228-4310	6.5 ± 1.5, 2.21 ± 0.32	16.3 ± 0.7, 1.59 ± 0.07	28 ± 4	49.8 ± 1.8	24.8 ± 1.8	47.6 ± 2.2	50 ± 9
2M 2237+3922	57 ± 6, 1.59 ± 0.06	115 ± 9, 1.20 ± 0.13	183 ± 28	351 ± 15	167 ± 23	368 ± 27	320 ± 60
2M 2249+3205	15.6 ± 2.5, 1.75 ± 0.07	34.3 ± 2.7, 1.45 ± 0.06	55 ± 7	87 ± 8	45.3 ± 3.0	91 ± 7	91 ± 4
2M 2252-1730			4.4 ± 0.8, 2.31 ± 0.26	7.7 ± 2.2	12.3 ± 2.3	7.4 ± 0.8	14.2 ± 2.5
2M 2252-1730	4.9 ± 1.2, 2.3 ± 0.6	11.2 ± 2.4, 1.45 ± 0.30	18 ± 4	34.3 ± 1.8	14.2 ± 0.7	33 ± 4	29.9 ± 1.4
2M 2254+3123	5.6 ± 1.5, 2.21 ± 0.29	14.8 ± 1.4, 1.45 ± 0.06	28 ± 6	52 ± 4	22.6 ± 1.8	50 ± 5	50 ± 5
2M 2255-5713			3.7 ± 0.6, 2.01 ± 0.09	7.7 ± 2.8	17.1 ± 2.8	7.1 ± 2.1	16.4 ± 1.9
2M 2325+4251	5.3 ± 0.8, 2.31 ± 0.18	12.3 ± 0.6, 1.45 ± 0.14	21.5 ± 2.9	37.6 ± 3.5	18.8 ± 1.5	43.3 ± 2.0	36.0 ± 1.7
2M 2339+1352	7.9 ± 1.7, 2.21 ± 0.10	17.9 ± 0.8, 1.75 ± 0.07	31.3 ± 3.3	54.6 ± 3.5	27.2 ± 2.0	60 ± 6	48 ± 7
2M 2351-2537	6.4 ± 1.6, 2.01 ± 0.15	14.8 ± 2.6, 1.45 ± 0.11	26 ± 6	55 ± 5	26.1 ± 3.0	52 ± 4	52.2 ± 2.4
SDSS 0837-0000	11.2 ± 1.5, 1.92 ± 0.07	26 ± 5, 1.45 ± 0.11	41 ± 9	83 ± 7	38 ± 4	87 ± 6	83 ± 4
SDSS 2052-1609			4.0 ± 0.7, 2.42 ± 0.11	7.1 ± 0.9	12.9 ± 1.5	5.1 ± 0.4	13.6 ± 1.6
							10.7 ± 0.5

Note. — Median 5σ contrast (within the stated separation range) in 4 of 5 calibrators. No entry indicates no significant detection at that separation is possible. Two entries (at tight separations) is caused by a reduction in sensitivity to equal brightness targets and indicates a significant detection is possible *between* the two values. The diffraction limit (λ/D) is roughly 95 and 147 mas in F110W and F170M, respectively.

Table 2.6. Individual 5σ Contrast Ratio Limits at Tight Separations

Source	F110W Limit at Sep. [mas]		F170M Limit at Sep. [mas]	
	15–25	25–35	35–45	25–35
2M 0024-0158	4.4 ± 1.1, 3.1 ± 0.7	8 ± 4, 2.1 ± 0.4	24 ± 6, 1.67 ± 0.08	5.9 ± 1.4, 2.5 ± 0.6
2M 0036+1821	4.0 ± 1.0, 3.7 ± 0.9	5.3 ± 2.2, 2.54 ± 0.27	12 ± 4, 1.92 ± 0.08	8.9 ± 2.3, 2.10 ± 0.30
2M 0045+1634	6.4 ± 1.0, 3.7 ± 0.9	9 ± 4, 2.1 ± 0.4	20.6 ± 3.5, 1.75 ± 0.09	4.4 ± 0.4, 2.92 ± 0.14
2M 0107+0041	7.7 ± 3.2, 2.31 ± 0.28	6.4 ± 1.0, 2.31 ± 0.19	12.3 ± 3.2, 2.01 ± 0.14	5.9 ± 1.0, 2.54 ± 0.11
2M 0109+2949	20 ± 6, 1.67 ± 0.08	20 ± 6, 1.67 ± 0.08	4.9 ± 1.2, 2.9 ± 0.4	5.9 ± 0.9, 2.54 ± 0.12
2M 0123-4240	3.7 ± 0.9, 2.5 ± 0.6	7.7 ± 1.8, 2.1 ± 0.4	14 ± 4, 1.75 ± 0.11	9.9 ± 3.2, 2.21 ± 0.18
2M 0144-0716	6.2 ± 1.8, 2.42 ± 0.25	13.5 ± 3.4, 1.83 ± 0.09	7.1 ± 1.8, 2.10 ± 0.12	7.1 ± 1.2, 2.21 ± 0.10
2M 0151+1244	4.4 ± 0.5, 2.54 ± 0.19	14 ± 5, 1.92 ± 0.19	2.8 ± 0.7, 2.5 ± 0.6	18 ± 4, 1.92 ± 0.09
2M 0207+0000	2M 0213+4444	31 ± 7, 1.59 ± 0.06	31 ± 7, 1.59 ± 0.06	8.5 ± 3.2, 2.3 ± 0.4
2M 0228+1639	9.3 ± 2.8, 2.10 ± 0.16	4.0 ± 1.6, 2.31 ± 0.21	4.0 ± 1.6, 2.31 ± 0.21	4.65 ± 0.22, 2.5 ± 0.4
2M 0243-2453	10.2 ± 3.1, 2.10 ± 0.22	24 ± 4, 1.67 ± 0.08	10.7 ± 2.9, 1.92 ± 0.10	6.4 ± 1.0, 2.31 ± 0.22
2M 0255-4700	5.3 ± 0.9, 2.31 ± 0.35	7.7 ± 2.2, 2.31 ± 0.21	16 ± 4, 1.75 ± 0.09	7.7 ± 3.4, 2.1 ± 0.4
2M 0257-3105	3.7 ± 0.9, 3.1 ± 0.7	3.7 ± 0.9, 3.1 ± 0.7	8.5 ± 2.7, 2.01 ± 0.24	5.9 ± 0.9, 2.31 ± 0.11
2M 0314+1603	9.3 ± 1.5, 2.10 ± 0.09	9.3 ± 1.5, 2.10 ± 0.09	16 ± 4, 1.75 ± 0.07	6.4 ± 0.9, 2.54 ± 0.23
2M 0318-3421	5.9 ± 1.9, 2.21 ± 0.23	4.23 ± 0.20, 2.8 ± 0.5	18 ± 5, 12.3 ± 3.1	14 ± 5, 1.92 ± 0.12
2M 0348-6022	9.3 ± 3.4, 2.01 ± 0.31	23 ± 4, 1.59 ± 0.07	25 ± 6, 1.75 ± 0.07	13.6 ± 2.6, 1.92 ± 0.18
2M 0355+1133	6.4 ± 2.7, 2.54 ± 0.35	6.4 ± 2.7, 2.54 ± 0.35	20 ± 5, 1.75 ± 0.09	11.8 ± 3.1, 2.01 ± 0.22
2M 0415-0935	9.3 ± 4, 2.10 ± 0.20	21 ± 4, 1.67 ± 0.08	4.6 ± 1.0, 2.79 ± 0.35	10.7 ± 2.0, 2.10 ± 0.09
2M 0423-0414	8.5 ± 2.3, 2.1 ± 0.4	18 ± 4, 1.67 ± 0.12	4.43 ± 0.19, 3.05 ± 0.13	10.2 ± 1.9, 2.10 ± 0.20
2M 0439-2353	9.3 ± 0.8, 3.1 ± 0.7	4.1 ± 0.8, 2.32 ± 0.22	4.0 ± 0.6, 2.54 ± 0.11	4.9 ± 0.9, 2.8 ± 0.5
2M 0443+0002	7.7 ± 2.0, 2.3 ± 0.4	3.4 ± 0.8, 2.5 ± 0.6	20.6 ± 3.4, 1.75 ± 0.11	
2M 0500+0330	6.4 ± 4, 2.10 ± 0.29	4.4 ± 1.6, 2.54 ± 0.29	4.4 ± 0.9, 2.78 ± 0.31	
2M 0523-1403	8.5 ± 2.3, 2.1 ± 0.4	16 ± 4, 1.75 ± 0.09	4.6 ± 1.0, 2.79 ± 0.35	
2M 0624-4521	7.7 ± 2.0, 2.3 ± 0.4	16 ± 4, 1.75 ± 0.09	4.43 ± 0.19, 3.05 ± 0.13	
2M 0652+4710	8 ± 4, 2.10 ± 0.27	16 ± 4, 1.75 ± 0.09	5.9 ± 1.4, 2.5 ± 0.6	
2M 0700+3157	7.7 ± 2.2, 2.31 ± 0.24	16 ± 4, 1.83 ± 0.12	9.3 ± 1.6, 2.21 ± 0.15	
2M 0727+1710	7.8 ± 3.0, 2.01 ± 0.27	16 ± 5, 1.59 ± 0.10	8.5 ± 2.1, 2.10 ± 0.14	
2M 0755+2212				8.1 ± 1.7, 2.10 ± 0.23
2M 0825+2115				
2M 0830+4828				
2M 0835-0819				
2M 0847-1532				

Table 2.6 (cont'd)

Source	15–25	F110W Limit at Sep. [mas]		F170M Limit at Sep. [mas]	
		25–35	35–45	25–35	35–45
2M 0859-1949		7.7 ± 2.2, 2.10 ± 0.24	16.3 ± 3.4, 1.75 ± 0.06	5.9 ± 1.4, 2.54 ± 0.19	
2M 0908+5032		8.2 ± 2.1, 2.01 ± 0.24	16 ± 4, 1.67 ± 0.08	12.3 ± 3.1, 2.01 ± 0.14	
2M 0911+7401		8.5 ± 3.2, 2.10 ± 0.21	23 ± 4, 1.75 ± 0.11	7.7 ± 1.9, 2.10 ± 0.32	
2M 0921-2104		6 ± 4, 2.31 ± 0.26	18 ± 5, 1.75 ± 0.11	6.4 ± 1.5, 2.31 ± 0.18	
2M 1022+5825		10.3 ± 2.5, 2.10 ± 0.20	24 ± 7, 1.67 ± 0.12	3.7 ± 0.9, 3.1 ± 0.7	
2M 1025+3212			6.7 ± 1.5, 2.10 ± 0.29	8.9 ± 2.1, 2.21 ± 0.27	
2M 1043+2225		6.5 ± 1.1, 2.21 ± 0.18	14 ± 5, 1.83 ± 0.13	6.5 ± 1.7, 2.42 ± 0.35	
2M 1045-0149		4.9 ± 0.7, 2.54 ± 0.18	11 ± 4, 1.92 ± 0.25	5.6 ± 1.8, 2.4 ± 0.4	
2M 1048+0111			4.4 ± 1.9, 2.54 ± 0.25	5.9 ± 1.5, 2.54 ± 0.28	
2M 1051+5613		7.8 ± 3.1, 2.3 ± 0.4	17 ± 5, 1.75 ± 0.08	15 ± 4, 2.10 ± 0.13	
2M 1058-1548	4.4 ± 1.7, 3.05 ± 0.35	12 ± 5, 2.10 ± 0.24	34 ± 8, 1.59 ± 0.07	7.7 ± 2.2, 2.54 ± 0.21	5.1 ± 0.7, 2.55 ± 0.24
2M 1104+1959		5.3 ± 0.7, 2.21 ± 0.10	11 ± 4, 1.75 ± 0.13		
2M 1108+6830		8 ± 4, 2.10 ± 0.27	22 ± 5, 1.67 ± 0.08		
2M 1110+0116		5.3 ± 2.1, 2.54 ± 0.34	13.5 ± 2.5, 2.01 ± 0.09		
2M 1155-3727	3.7 ± 0.9, 3.4 ± 0.8	9.3 ± 2.3, 2.10 ± 0.33	19 ± 5, 1.75 ± 0.07	9.8 ± 1.9, 2.10 ± 0.13	
2M 1203+0015	4.4 ± 1.1, 3.1 ± 0.7	11 ± 4, 2.10 ± 0.15	26 ± 7, 1.67 ± 0.08	4.4 ± 0.5, 2.78 ± 0.21	
2M 1213-0432		8.5 ± 2.3, 2.1 ± 0.4	18.8 ± 2.8, 1.75 ± 0.07		
2M 1217-0311		8 ± 4, 2.3 ± 0.4	21.5 ± 2.5, 1.75 ± 0.08		
2M 1221+0257	5.9 ± 0.9, 2.54 ± 0.12	14 ± 4, 1.92 ± 0.15	29 ± 8, 1.75 ± 0.07	7.7 ± 2.4, 2.45 ± 0.4	19 ± 4, 1.92 ± 0.07
2M 1254-0122			4.1 ± 0.4, 2.92 ± 0.14		
2M 1300+1912		9.3 ± 2.8, 2.1 ± 0.4	18 ± 6, 1.75 ± 0.11	5.3 ± 1.3, 2.8 ± 0.7	8.1 ± 1.2, 2.31 ± 0.19
2M 1421+1827		10.2 ± 3.2, 2.10 ± 0.26	22 ± 4, 1.75 ± 0.07	5.3 ± 1.0, 2.78 ± 0.21	13 ± 4, 2.10 ± 0.14
2M 1425-3650	5.9 ± 1.9, 2.78 ± 0.22	14 ± 5, 1.92 ± 0.31	34 ± 7, 1.67 ± 0.08	8.5 ± 2.4, 2.31 ± 0.16	21 ± 5, 1.92 ± 0.18
2M 1428+5923		7.7 ± 2.7, 2.10 ± 0.20	19 ± 5, 1.67 ± 0.08	5.3 ± 1.3, 2.8 ± 0.7	9.9 ± 3.5, 2.10 ± 0.30
2M 1439+1929	5.4 ± 1.0, 2.66 ± 0.12	12 ± 5, 1.92 ± 0.22	27 ± 6, 1.59 ± 0.10	5.9 ± 1.4, 2.66 ± 0.28	13 ± 4, 2.01 ± 0.14
2M 1448+1031		10.2 ± 3.4, 2.10 ± 0.29	25 ± 6, 1.75 ± 0.07		
2M 1503+2525			3.69 ± 0.34, 2.92 ± 0.14		
2M 1503+2525			4.0 ± 1.2, 1.92 ± 0.26		
2M 1506+1321		8.5 ± 2.0, 1.92 ± 0.17	17 ± 4, 1.75 ± 0.07	5.4 ± 0.5, 2.66 ± 0.12	14 ± 4, 2.10 ± 0.13
2M 1507-1627			4.4 ± 1.1, 2.3 ± 0.6		
2M 1515+4847		5.9 ± 2.0, 2.31 ± 0.30	14 ± 5, 1.75 ± 0.11	6.4 ± 2.1, 2.54 ± 0.27	
2M 1552+2948		4.0 ± 1.0, 2.25 ± 0.6	8.9 ± 2.4, 2.01 ± 0.33		
2M 1624+0029		9.3 ± 2.3, 2.10 ± 0.35	16.4 ± 3.2, 1.75 ± 0.08		

2.6 Discussion

2.6.1 Binary Frequency

While we present astrometry and photometry for all detections, we must restrict our analysis of binary populations to targets in programs 9833 (Burgasser et al., 2006b), 10143 (Reid et al., 2006), and 10879 (Reid et al., 2008a) and we must exclude programs specifically targeting binaries (9843, 10247, 11136). This removes any bias in our sample toward binarity and enables a study of binary demographics. This brings the total number of objects in our sample down to 106 (from 114). The number of binary systems in our statistical sample drops to 15 (from 21) when also accounting for the 2 wide companions which KPI is not sensitive to.

To compare our binary fraction with Reid et al. (2008a) and Pope et al. (2013) we restrict our sample to 20 pc. This is much more straightforward than in the previous studies due to recent parallax surveys (e.g. Gaia Collaboration et al., 2018, 2021; Best et al., 2020b). Our total number of sources then drops to 83, including 10 binaries while excluding 5. If we include **2M 0036+1821** and **2M 0355+1133**, which we do not detect companions around but were observed to have companions by Bernat et al. (2010), this number rises to 12/83. Estimating the uncertainty using binomial statistics (Burgasser et al., 2003c) gives a binary fraction of $\epsilon_b = 14.4_{-3.0}^{+4.7}\%$. This binary fraction is slightly lower than the number presented in Pope et al. (2013) ($\epsilon_b = 17.2_{-3.7}^{+5.7}\%$) though they are consistent within the quoted errors.

The typical mass of a brown dwarf is significantly lower than the Jeans

Table 2.6 (cont'd)

Source	15–25	F110W Limit at Sep. [mas]		F170M Limit at Sep. [mas]	
		25–35	35–45	25–35	35–45
2M 1658+7027		9.3 ± 3.0, 2.10 ± 0.35	22 ± 6, 1.75 ± 0.07	7.4 ± 1.5, 2.54 ± 0.16	16 ± 4, 2.01 ± 0.14
2M 1721+3344		10.4 ± 3.4, 2.10 ± 0.25	21 ± 4, 1.75 ± 0.06	5.1 ± 1.0, 2.7 ± 0.5	10 ± 4, 2.21 ± 0.18
2M 1731+2721		12 ± 4, 2.10 ± 0.25	24 ± 5, 1.67 ± 0.08	7.1 ± 0.6, 2.31 ± 0.11	16 ± 4, 1.92 ± 0.06
2M 1753-6559	5.60 ± 0.26, 2.5 ± 0.4	11.2 ± 3.4, 2.10 ± 0.14	26 ± 7, 1.75 ± 0.07	5.86 ± 0.27, 2.54 ± 0.24	11.8 ± 2.5, 2.10 ± 0.09
2M 1807+5015		10.2 ± 2.4, 2.10 ± 0.21	21 ± 5, 1.75 ± 0.09	6.1 ± 1.5, 2.66 ± 0.18	15.6 ± 2.4, 1.92 ± 0.07
2M 1936-5502		5.9 ± 1.3, 2.31 ± 0.31	12.9 ± 1.9, 1.92 ± 0.12		6.5 ± 1.5, 2.42 ± 0.18
2M 2002-0521	5.3 ± 1.3, 2.5 ± 0.6	8.5 ± 3.4, 2.10 ± 0.30	21 ± 7, 1.75 ± 0.06	5.10 ± 0.24, 2.79 ± 0.26	10.2 ± 2.8, 2.21 ± 0.20
2M 2028+0052		8.3 ± 2.9, 2.2 ± 0.4	18 ± 4, 1.75 ± 0.09	6.1 ± 0.6, 2.54 ± 0.17	11.2 ± 2.5, 2.10 ± 0.13
2M 2036+1051		6.9 ± 3.4, 2.4 ± 0.6	16.3 ± 3.4, 1.75 ± 0.07	5.9 ± 1.2, 2.25 ± 0.5	11.9 ± 3.3, 2.01 ± 0.14
2M 2057-0252			4.3 ± 1.0, 2.32 ± 0.22		4.9 ± 1.2, 2.5 ± 0.6
2M 2104-1037		3.7 ± 0.9, 2.5 ± 0.6	8.2 ± 2.3, 1.9 ± 0.4		4.9 ± 0.6, 2.78 ± 0.11
2M 2139+0220		8.2 ± 1.9, 2.10 ± 0.23	11.8 ± 3.1, 1.75 ± 0.11		
2M 2224+0158		7.4 ± 1.2, 2.31 ± 0.10	12.9 ± 2.1, 1.83 ± 0.09		
2M 2228-4310		10.2 ± 2.4, 2.10 ± 0.22	17.1 ± 3.2, 1.92 ± 0.08		
2M 2237+3922	7.1 ± 1.0, 2.31 ± 0.11	14 ± 4, 1.92 ± 0.18	31 ± 7, 1.52 ± 0.11	7.1 ± 2.3, 2.54 ± 0.31	18 ± 4, 1.92 ± 0.12
2M 2249+3205		4.4 ± 1.1, 2.8 ± 0.7	5.1 ± 1.7, 2.42 ± 0.19		5.3 ± 1.3, 2.5 ± 0.6
2M 2254+3123		7.1 ± 1.8, 2.10 ± 0.14	16.3 ± 2.1, 1.75 ± 0.09		
2M 2255-5713			5.3 ± 1.1, 2.31 ± 0.35		
2M 2325+4251		6.1 ± 1.2, 2.31 ± 0.28	15 ± 4, 1.75 ± 0.09		
2M 2339+1352		10.2 ± 3.0, 2.10 ± 0.28	21 ± 4, 1.75 ± 0.11		
2M 2351-2537			4.3 ± 0.6, 2.92 ± 0.14		
SDSS 0837-0000			3.4 ± 0.8, 2.8 ± 0.7		

Note. — Median 5σ contrast (within the stated separation range) in 4 of 5 calibrators. No entry indicates no significant detection at that separation is possible. Two entries (at tight separations) is caused by a reduction in sensitivity to equal brightness targets and indicates a significant detection is possible between the two values. The diffraction limit (λ/D) is roughly 95 and 147 mas in F110W and F170M, respectively.

mass of a collapsing protostellar cloud. Thus two theories for the formation mechanism of brown dwarfs have been proposed: gravoturbulent collapse and embryo ejection (Basu, 2012). Since embryo ejection is an energetic event, the binary fraction it produces is small: $< 5 - 8\%$ (Bate et al., 2002; Bate, 2012). Our significantly higher binary fraction, and that of Pope et al. (2013) and other observational studies (e.g. Reid et al., 2006, 2008a), supports the conclusion that embryo ejection plays a minimal role in brown dwarf formation. A more detailed demographic analysis of the full unbiased sample (not distance limited but still excluding programs targeting binaries) will be presented in a future work using a Bayesian population analysis similar to Allen (2007). The semimajor-axis and mass-ratio distributions will be important to quantify in establishing the companion frequency, especially since all of these quantities are covariant when considering typical detection limits.

2.6.2 Implications for Dynamical Mass Measurements

Our sample includes three targets which were observed twice. We detect companions around two of these sources and see orbital motion between the two epochs. Our astrometry for these two sources and six other sources with only one epoch is consistent with Dupuy & Liu (2017) though our fits are much higher precision. Two other sources are listed in Table 3 of Dupuy & Liu (2017) which have *HST*/NICMOS imaging, though in filters other than F110W and F170M. These sources, along with others with relevant imaging in other filters will be analyzed in a future letter. Since no specific observing

set up is required for KPI (unlike NRM observations), KPI is a particularly powerful tool for resolving binary orbits since it allows precovery of relative astrometry and photometry from archival observations of known binaries even when the binary was undetected or had much larger uncertainties when studied with image-plane analysis techniques.

2.6.3 Scramble and fit detection limits vs. Bayes factors

One caveat of our scramble and fit method of measuring detection limits is that it does not recover the deepest possible contrast limit when the target has a strong binary signal. When the kernel phases are scrambled to generate a new realization of the noise, we want no signal to be present, so we subtract off the best fit model. In this survey where we treated all sources the same, we simply subtracted the best fit single point source model to remove any small position offset. When a binary is present, subtracting off only a signal source leaves signal behind, raising the measured noise threshold. To properly characterize the sensitivity around a non-single source, the proper model (with the correct parameter values) must be subtracted. This is particularly difficult when triple sources are possible (e.g. **2M 0205-1159**). For this source, our fitting routine failed to produce the companion fit that appears to match under visual inspection (because it is a triple) though it was characterized as significant. On the other hand, Bayes Factors are agnostic of the best fit parameters as they consider the entire volume of parameter space. They are however difficult to interpret if there are unmodeled systematics. For example,

a few wide binaries which are aliased (and thus difficult to recover with KPI) are not considered significant detections by our scramble-and-fit method but do show high Bayes factors, indicating that a binary model is preferred even if our best fit parameters are clearly incorrect.

As seen in Figure 2.8, there are a few sources with high Bayes factors which did not pass our criteria for a detection and *visa versa*. The three sources with the highest Bayes factors (which suggest binarity), but for which we do not find a successful KPI fit, are **2M 0429-3123**, **2M 1707-0558**, and **2M 0915+0422** (in order by descending Bayes factor). These are all wide binaries that are aliased by our aperture model and KPI struggles to accurately recover. We do characterize **2M 0429-3123** as a binary as its best fit parameters match with literature values while the companion was just outside our grid for detection limits. On the other hand our fits to **2M 1707-0558**, and **2M 0915+0422** both picked up on aliases and failed to recover the visually obvious companion. Similarly **2M 1705-0516** and **2M 1731+2721** both have high Bayes factors and a wide (aliased) secondary source in the images that is a background source. A more careful treatment of the Bayesian prior could encourage the fits to converge on the non-aliased signal, though it is clear from the Bayes factor that these sources prefer the binary model over the single one. Since Bayes factors are independent of best fit parameters, they allow us to infer the presence of a companion even if our best fit parameters are clearly aliased and thus incorrect.

Our marginal detection of **2M 2028+0052** is also supported by its

elevated Bayes factor with respect to other single sources. This source is discussed further in Section 2.5.2.

Conversely the companions which we characterized as detections which had the lowest Bayes factors include **2M 0205-1159** and **2M 2204-5646**, two of our “spurious” detections (one is a low SNR wide binary and the other is a triple). Detections with relatively low SNR observations, including **2M 1534+1615**, **SDSS 2052-1609**, and **2M 2252-1730**, also had low Bayes factors. In fact, all of these targets were observed in program 11136, which traded exposure time in the main filters for wider wavelength coverage in more filters. This indicates that high SNR observations, which significantly recover the wings of the PSF, are key to confident and accurate KPI detections.

We have also examined a modified version of the likelihood ratio test discussed in Ceau et al. (2019). Instead of the null hypothesis being all 0 kernel phases we have replaced it with our single source model, allowing for a small centroid offset. This test gives similar results to the Bayes Factors though with slightly more overlap between significant detections and non-detections.

2.6.4 KPI In Context

Since our detection significance is determined on a source-specific basis, our survey wide stacked detection limit is as close as we can come to a pipeline-specific contrast curve similar to Figure 2 and 3 of Pope et al. (2013) (calculated using an injection-recovery grid with a noise term representative of the sample as a whole). We also use a 5σ (99.99994%) detection threshold and separate

out the two filters while Pope et al. (2013) presents only a single 99.9% contrast curve. With the aforementioned caveats, the detection limits of our two KPI surveys are fairly similar. Both show a cutoff to equal-brightness companions at around 55 mas (in F110W for our survey, our cut-off in F170M is closer to 80 mas) with slightly higher contrast detections possible down to roughly 30 mas. Our high-contrast limits at wider separations are more difficult to compare given the difference in confidence threshold but appear qualitatively similar, with high confidence detections up to contrast values of roughly 100:1.

Comparing our KPI contrast limits to imaging surveys (e.g. Reid et al., 2006, 2008a) shows the power of KPI at close separations. Imaging sensitivity significantly drops at separations below $\sim 0''.5$ while ours is flat down to less than $\sim 0''.1$. At wide separations KPI suffers from aliasing in the Fourier plane and is ineffective at detecting sources without prior knowledge. In this wide separation domain PSF fitting performs well and KPI is not necessary. Sallum & Skemer (2019) showed, using simulated *JWST* observations that NRM/AMI outperforms KPI at separations below the diffraction limit by 0.5–1 mag while KPI is comparable to or better than NRM/AMI outside the diffraction limit.

2.7 Conclusions

We have presented a new pipeline named Argus for super-resolution detection of companions using KPI. The pipeline generates, calibrates, and fits kernel phases from high resolution images. The pipeline uses a scramble and fit method (similar to previous NRM pipelines) to determine the detection

significance, though it can also use Bayes factors to determine if the source is non-singular. Our multi-calibrator method for determining if a detection is real is much more strict than previous KPI pipelines, though it finds roughly similar contrast limits. The pipeline is open source and is available on GitHub (see Footnote 2).

We have demonstrated the pipeline on the entire *HST*/NICMOS F110W and F170M image archive of nearby brown dwarfs (observed in 7 different programs). We recover 19 known companions (including two targets with two epochs) from our sample of 114 targets. We confirm one of the four new companions discovered by Pope et al. (2013) and marginally recovered a second, but we recover none of their marginal detections. We conclude that robust calibration with multiple well-matched calibrators is critical for determining the validity of a candidate companion, especially in the super-resolution regime where no spatially distinct PSF is present.

We report a binary fraction of $\epsilon_b = 14.4_{-3.0}^{+4.7}\%$, consistent with previous studies. We will perform a more detailed population level analysis of the catalogue presented here in a future paper. This work will simultaneously characterize the binary fraction, semimajor axis distribution, and mass-ratio distributions using a Bayesian framework similar to Allen (2007) to better understand how these low mass objects form. Future upgrades to the pipeline could include more robust bad pixel rejection techniques (Ireland, 2013) and triple point source models. It also should be straightforward to make the code easily adaptable to other space based cameras amenable to KPI such as the

high resolution channel of *HST*/ACS and the imaging instruments aboard *JWST*.

2.8 Acknowledgments

We thank Trent Dupuy, Will Best, and Michael Ireland for useful discussions about this work, and many others who have offered their thoughts at conferences. We also thank the anonymous referee for their helpful feedback which improved the manuscript. This work was funded by *HST* program AR-14561. This work has benefited from The UltracoolSheet, maintained by Will Best, Trent Dupuy, Michael Liu, Rob Siverd, and Zhoujian Zhang, and developed from compilations by Dupuy & Liu (2012), Dupuy & Kraus (2013), Liu et al. (2016), Best et al. (2018), and Best et al. (2021). This work has made use of data from the European Space Agency (ESA) mission *Gaia* (<https://www.cosmos.esa.int/gaia>), processed by the *Gaia* Data Processing and Analysis Consortium (DPAC, <https://www.cosmos.esa.int/web/gaia/dpac/consortium>). Funding for the DPAC has been provided by national institutions, in particular the institutions participating in the *Gaia* Multilateral Agreement.

Chapter 3

NICMOS Kernel-Phase Interferometry II: Demographics of Nearby Brown Dwarfs¹

3.1 Chapter Abstract

Star formation theories have struggled to reproduce binary brown dwarf population demographics (frequency, separation, mass ratio). Kernel-phase interferometry is sensitive to companions at separations inaccessible to classical imaging, enabling tests of formation at new physical scales below the hydrogen burning limit. We analyze the detections and sensitivity limits from our previous kernel-phase analysis of archival *HST*/NICMOS surveys of field brown dwarfs. After estimating physical properties of the 105 late M to T dwarfs using Gaia distances and evolutionary models, we use a Bayesian framework to compare these results to a model companion population defined by log-normal separation and power-law mass-ratio distributions. When correcting for Malmquist bias, we find a companion fraction of $F = 0.11_{-0.03}^{+0.04}$ and a separation distribution centered at $\rho = 2.2_{-1.0}^{+1.2}$ au, smaller and tighter than seen in previous studies. We also find a mass-ratio power-law index which strongly favors equal-mass systems: $\gamma = 4.0_{-1.5}^{+1.7} - 11_{-3}^{+4}$ depending on the assumed age

¹Previously published in *The Astronomical Journal* as Factor & Kraus (2023)

of the field population (0.9–3.1 Gyr). We attribute the change in values to our use of kernel-phase interferometry which enables us to resolve the peak of the semimajor axis distribution with significant sensitivity to low-mass companions. We confirm the previously-seen trends of decreasing binary fraction with decreasing mass and a strong preference for tight and equal-mass systems in the field-age sub-stellar regime; only $0.9_{-0.6}^{+1.1}\%$ of systems are wider than 20 au and $< 1.0_{-0.6}^{+1.4}\%$ of systems have a mass ratio $q < 0.6$. We attribute this to turbulent fragmentation setting the initial conditions followed by a brief period of dynamical evolution, removing the widest and lowest-mass companions, before the birth cluster dissolves.

3.2 Introduction

Star formation, and more specifically binary (or multiple) formation, is a foundational process in astrophysics, contributing to stellar populations and the stellar content of galaxies, interacting binaries and the transients they produce, as well as planet formation and habitability. A successful theory should replicate trends in not only the single star IMF, but also companion mass-ratio and separation distributions as well as frequency as a function of host mass, age, and other fundamental parameters (Duchêne & Kraus, 2013). Over the past two decades thousands of brown dwarfs (BDs) have been discovered (Best et al., 2020a), spurring detailed studies of our local neighborhood (Kirkpatrick et al., 2019; Best et al., 2021) including binary brown dwarfs (Burgasser et al., 2007) and dynamical masses (Dupuy & Liu, 2017), and enabling studies of

demographic trends below the hydrogen burning limit, challenging formation theories at new scales (Luhman, 2012; Offner et al., 2023).

While no comprehensive theory for multiple star (or BD) formation currently exists, many processes likely play a role, including core fragmentation, disk fragmentation, and dynamical interaction/evolution. Since BDs are significantly below the Jeans mass of a typical core ($\sim 1 M_{\odot}$), some more complicated physics beyond classical collapse must be having an effect. Turbulent fragmentation provides a clear formation pathway for lower mass objects and high-order multiple systems (Bate et al., 2002; Bonnell et al., 2008; Bate, 2009, 2012; Offner et al., 2010; Guszejnov et al., 2017). Disk fragmentation likely plays a minimal roll in forming a BD in the disk around another BD since the mass budget is too low (Burgasser et al., 2007), though it is possible for BD-BD binaries to form as a higher order multiple inside the disk around a more massive star and survive ejection (Stamatellos & Whitworth, 2009).

High-order systems tend to be dynamically unstable, especially when considering the larger star forming surroundings. They evolve on relatively short timescales, ejecting some objects and binding the remnants into tight binary systems (Reipurth & Clarke, 2001). Current state of the art simulations are approaching the spatial scales needed to model brown dwarf binaries and their circumsubstellar disks. Sink particles are seeded and accretion takes place on scales of 0.5–5 au (Bate et al., 2003; Bate, 2009, 2012) or even larger (Offner et al., 2009; Grudić et al., 2022), on the same scales as (or larger than) a typical brown dwarf binary, while disks are only resolved down to scales of

1–10 au. Historically, a softened Newtonian potential has also been used close to sink particles, enhancing binary disruption. Even so, recent simulations have roughly reproduced the observed BD binary fraction and trends in mass ratio and separation seen in the field population (Luhman, 2012; Offner et al., 2023), though still struggle to form the somewhat rare widely separated pairs (Radigan et al., 2009; Kraus et al., 2011; Faherty et al., 2020).

Previous demographic surveys have found a BD binary population heavily skewed toward equal mass ratios, and modeled the population with a power-law with index $\gamma \sim 2 - 5$ (Reid et al., 2006; Burgasser et al., 2007; Allen, 2007, surveys which were sensitive to mass ratios of $q \gtrsim 0.2$). Fontanive et al. (2018) studied later spectral type objects (T5–Y0) and found a slightly stronger mass-ratio power-law index of $\gamma \sim 6$ (with sensitivity down to $q \gtrsim 0.4$). Direct imaging surveys and searches for co-moving sources in astrometric surveys have constrained the overall BD binary fraction to $\sim 20\%$ (Reid et al., 2001; Close et al., 2002; Burgasser et al., 2003c; Bouy et al., 2003; Close et al., 2003; Gizis et al., 2003; Reid et al., 2006; Allen, 2007; Burgasser et al., 2007; Aberasturi et al., 2014) with few companions on wide orbits with semimajor axes $\gtrsim 20$ au. Surveys using the radial velocity technique, though limited to the brightest targets, have searched for extremely tight companions and similarly found a much lower frequency for companions on orbits with semimajor axes $\lesssim 1$ au of $2.5_{-1.6}^{+8.6}\%$ (Blake et al., 2010) (see also Basri & Reiners, 2006; Joergens, 2008; Hsu et al., 2021). The semimajor axis distribution has been modeled as log-normal, centered around ~ 6 au with a width of $0.2 - 0.3$ dex

(Reid et al., 2006; Burgasser et al., 2007; Allen, 2007). The Fontanive et al. (2018) study of later spectral type objects found a roughly similar semimajor axis distribution with a lower overall companion frequency of $8 \pm 6\%$ (and $2 \pm 2\%$ for tight companions with separations < 1 au). In contrast, stellar-mass binaries show a much flatter mass-ratio distribution ($\gamma \sim -2$ to ~ 1 for A0–M4 primaries), a higher companion fraction ($\sim 70\%$ to $\sim 35\%$), and a broader semimajor axis distribution centered at wider separations (~ 390 to ~ 10 au) (De Rosa et al., 2014; Kraus & Hillenbrand, 2012; Winters et al., 2019, see further discussion in Section 3.6.1 and Figure 3.8). Yet there is still some uncertainty in the mean of the separation distribution of BD binaries as RV surveys have not run long enough to detect the most common companions and the mean separation appears to be roughly at the inner working angle of direct imaging surveys, which can not yet resolve the closest companions.

In this work, we take advantage of interferometric analysis to push our inner working angle to tighter separations than previously accessible via classical imaging techniques/analysis and work to resolve the peak of the underlying semimajor-axis distribution. We perform a demographic analysis on the catalogue of BD binaries presented in Factor & Kraus (2022a), built by applying a new kernel-phase interferometry pipeline to the entire *HST*/NICMOS imaging archive of nearby brown dwarfs in F110W and F170M (observed in 7 programs, 3 of which are analyzed in this work and are outlined in Section 3.3). That work built on previous analysis by searching for companions at tighter separations than was possible with classical PSF subtraction and

revisiting candidate companions proposed in a previous kernel-phase analysis (Pope et al., 2013). While no new companions were discovered around these well studied targets, we did confirm one candidate companion and marginally recover a second, both proposed by Pope et al. (2013), and did not recover other candidates. We also measured detection limits for each target, important for the survey analysis done in this work. In this work, we derive physical parameters from the observed parameters using the method described in Section 3.4.1 and model the demographic parameters as described in Section 3.4.2. We then compare our results (Section 3.5) to previous surveys and theories of binary formation (Section 3.6).

3.3 Observations

3.3.1 NICMOS Data

We adopt our sample from the catalogue presented in Paper 1 of this series (Factor & Kraus, 2022a). That work analyzed archival *HST* observations of field brown dwarfs using the Near Infrared Camera and Multi-Object Spectrometer (NICMOS). Camera 1 of NICMOS has a 256×256 pixel detector, with a pixel scale of 43 mas, for a field of view of $11'' \times 11''$. Our previous KPI analysis had an outer working angle of $0''.5$ due to strong aliasing in the Fourier domain caused by wide separation companions. In this work we supplement our sensitivity to wide companions based on the sensitivity of classical imaging surveys, further described in Section 3.4.2.

A detailed description of the datasets is presented in Factor & Kraus

Table 3.1. Observations

Prog. ID	P.I.	Cycle	N_{obj}	N_{dith}	approx. epoch	Publication
9833	Burgasser (2003)	12	22	3–6	9/2003–7/2004	Burgasser et al. (2006b)
10143	Reid (2004)	13	56	2	9/2004–6/2006	Reid et al. (2006)
10879	Reid (2006)	15	28	2	7/2006–5/2007	Reid et al. (2008a)

Note. — Program 9833 observed in F090M in addition to F110W and F170M

(2022a) but to briefly summarize, that work analyzed data from 7 programs observing brown dwarfs in F110W and F170M (roughly corresponding to J and H bands). For this work we narrow that sample down to three programs—9833, 10143, and 10879—which conducted an unbiased search for binaries instead of targeting known pairs. Details of those programs are presented in Table 3.1.

Table 2 in Factor & Kraus (2022a) details the properties of the targets analyzed in that work, a subset of which are analyzed here. This sample covers 105 targets (including 15 binaries) with spectral types of late M ($\sim 10\%$), L ($\sim 70\%$), and T ($\sim 20\%$) dwarfs (roughly 95–30 M_{Jup} depending on the assumed age of the field population) at distances ranging from ~ 5 –35 pc. Analysis of the full sample, presented in Factor & Kraus (2022a), applied a new KPI pipeline (Factor, 2022) to these observations using a novel multi-calibrator approach.

Table 4–6 and Figure Sets 5–8 in Factor & Kraus (2022a) present the detection limits for each target analyzed in this work. The method used to de-

rive these limits is described in detail in Section 3.3 of Factor & Kraus (2022a) but to briefly summarize, we scramble the indices of the model subtracted kernel phases (i.e. randomly reorder the residual phase noise) in order to generate a new instance of the intrinsic noise. We then fit the noise on a grid of PA and separation to see what spurious companions are mimicked by noise. In the best cases, significant detections of companions can be achieved up to a contrast of $\sim 100 : 1$ down to a separation of $\sim 0''.1$ and significantly closer at lower contrast.

Table 3.3 presents the observational properties of the relevant binary systems while Table 3.4 presents the physical properties derived using the methods described below. A companion is considered a significant detection if it is significantly ($> 5\sigma$ confidence) detected in at least 4 calibrators and fitted parameters are consistent with each other within 1σ in contrast and 5σ in position. Our sample does not include the marginal detection (2M 2028+0052) but does include the two wide separation companions (2M 0915+0422 and 2M 1707-0558) which were aliased in our earlier KPI analysis but are easily seen in the images. We adopt astrometry and photometry from Pope et al. (2013).

3.4 Methods

3.4.1 Physical Properties of Binaries

To perform a demographic analysis of detections and detection limits for binary companions we must first convert observed quantities (angular separation and contrast) into physical quantities (projected separation and mass

ratio). Distances derived from Gaia eDR3 parallaxes were used (Bailer-Jones et al., 2021; Gaia Collaboration et al., 2021) when available and other literature sources when not (e.g. Best et al., 2020b, and others). For details, see the citations in Table 2 of Factor & Kraus (2022a, note that the Gaia parallaxes in that table are from DR2).

Converting angular separation to projected separation is as simple as multiplying by the distance to the target. Converting contrast into mass is not as trivial. Since brown dwarf spectral types are not a reliable mass metric, we choose to convert from absolute magnitude to bolometric luminosity using an empirical relation and finally to mass using a model dependent isochrone.

To compute this relation, we use unresolved photometry in the NICMOS F110W and F170M filters when available (and 2MASS J and H otherwise) and convert these photometric measurements to absolute magnitudes using the distances from above. If 2MASS photometry was used, we infer the corresponding NICMOS magnitudes using an empirical relation built using synthetic photometry of the sample of brown dwarfs compiled in Filippazzo et al. (2015). They gathered near- and mid-infrared spectra and photometry for field age and young (which we excluded) targets of spectral type M6–T9. Using geometric parallaxes, they derive bolometric luminosities for these targets and bolometric corrections for J band photometry though, since we use *HST* bands, we derive our own relation based on their work.

Near infrared spectra for the empirical sample were downloaded from the BDNYC database (Filippazzo et al., 2016; Rodriguez, 2016). Synthetic

photometry was then performed using PySynthphot (STScI Development Team, 2013) in the relevant *HST* and 2MASS filters. We then fit a broken (for *H*) linear function to derive *HST*–2MASS color as a function of absolute 2MASS magnitude. This relation is shown in the left panel of Figure 3.1 and the coefficients are given by Equations 3.1 and 3.2.

$$F110W - J = 0.052 \pm 0.002 \times J - 0.07 \pm 0.02 \quad (3.1)$$

$$F170M - H = \begin{cases} -0.003 \pm 0.003 \times H - 0.04 \pm 0.04 & H < 13.30 \pm 0.05 \\ 0.263 \pm 0.006 \times H - 3.58 \pm 0.09 & H > 13.30 \pm 0.05 \end{cases} \quad (3.2)$$

We then split the unresolved (now absolute) *HST* band photometry into its constituent parts for a given contrast and convert these component magnitudes into bolometric luminosities using a second empirical relation also built on the Filippazzo et al. (2015) sample. Again, we fit a piecewise linear relation (this time mediated by a 5th degree sigmoid), to the bolometric luminosities as a function of absolute *HST* magnitude. This relation is shown in the right panel of Figure 3.1 and the coefficients are given by Equation 3.3 and Table 3.2.

$$\begin{aligned} \log L &= (a_1 * M_{\text{HST}} + b_1) \left(1 - \frac{1}{1 + e^{-5(M_{\text{HST}} - M_0)}} \right) \\ &+ (a_2 * M_{\text{HST}} - b_2) \left(\frac{1}{1 + e^{-5(M_{\text{HST}} - M_0)}} \right) \end{aligned} \quad (3.3)$$

Table 3.2. Absolute *HST* magnitude to LogL coefficients

Filter	M_0	a_1	a_2	b_1	b_2
F110W	16.076 ± 0.016	-0.3403 ± 0.0015	-0.263 ± 0.007	0.623 ± 0.019	-1.04 ± 0.11
F170M	13.16 ± 0.13	-0.402 ± 0.003	-0.2756 ± 0.0018	0.83 ± 0.03	-0.82 ± 0.03

From bolometric luminosity, the conversion to mass is done using an isochrone from the ATMO2020 models (Phillips et al., 2020). We derived masses using all relevant ages (0.9, 1.2, 1.5, 2.4, and 3.1 Gyr) available from the ATMO2020 models and ran our fits for each assumed field age (see Section 3.6.1 for a more in depth discussion of the choice of field age with respect to the work of Aganze et al., 2022). We chose the ATMO2020 models due to its wide range of mass, especially at the low end, at field age ($0.075 M_{\odot}$ down to $0.002 M_{\odot}$ or $\sim 79 - 2M_{\text{Jup}}$). Even though we do not detect companions at such low masses, our sensitivity does reach those masses. The median mass of our sample is $\sim 65 - 75 M_{\text{Jup}}$ (depending on the assumed field age) so a small amount of extrapolation is needed to extend the grid to the highest mass primaries in our sample.

Fitted separations and contrasts (both from Factor & Kraus, 2022a), and observed and intermediary derived properties of detected binaries are given in Table 3.3. Projected separations and masses (and mass ratios) are given in Table 3.4 and plotted on top of the stacked sensitivity of the Factor & Kraus (2022a) analysis in Figure 3.2 for a given assumed field age (see Appendix F and Factor & Kraus, 2022c, for other assumed ages). As noted in Reid et al.

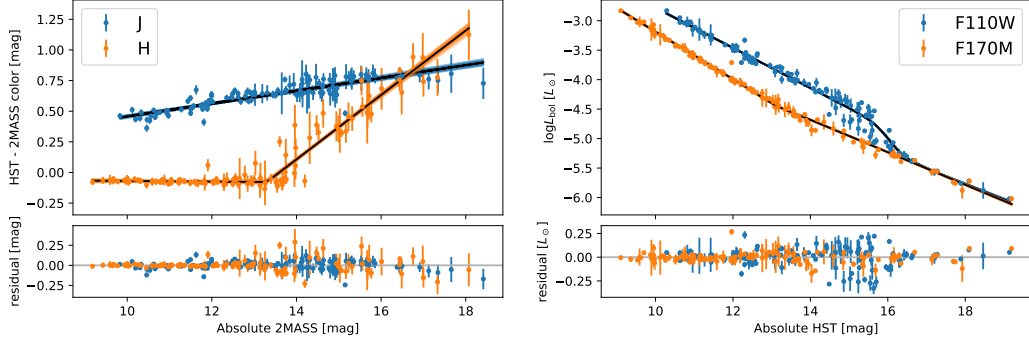


Figure 3.1: Empirical relations for converting 2MASS photometry to the corresponding *HST*-2MASS colors (left) and NICMOS photometry to bolometric luminosity (right) built using synthetic photometry of the sample of brown dwarfs in Filippazzo et al. (2015, points and error bars). Equations for the *HST*-2MASS colors are given in Equations 3.1 and 3.2 and the equation for *HST* absolute magnitude to $\log L$ is given in Equation 3.3 and coefficients in Table 3.2. Black lines are drawn using the median parameters while colored lines are 100 samples drawn from the posterior distributions.

(2006), due to the similar slopes of the isochrones in L_{bol} -Mass space, a higher q is inferred when using an older age.

3.4.2 Binary Population

We apply a similar Bayesian modeling approach to Kraus et al. (2011) and Kraus & Hillenbrand (2012) (adapted from Allen, 2007) to infer the underlying binary population from our sample of observations. This technique is particularly suited to the relatively small number of detections at close separations since there is no need to throw out data to create a volume limited sample or correct for regions of incompleteness. However, we must still account for Malmquist bias in our magnitude limited sample.

Table 3.3. Fit and Intermediary Binary Properties

Source	distance [pc]	ρ [mas]	m_{F110W} [mag]	m_{F170M} [mag]	c_{F110W}	c_{F170M}	$\log L_A$ [L_\odot]	$\log L_B$ [L_\odot]
2M 0004-4044	12.13 ± 0.06 ¹	83.2 ± 0.5	13.80 ± 0.05	12.10 ± 0.05	1.126 ± 0.018	nan ± nan	-4.161 ± 0.018	-4.205 ± 0.018
2M 0025+4759	54.0 ± 0.4 ²	334.5 ± 0.9	15.56 ± 0.05	13.55 ± 0.05	1.353 ± 0.033	1.251 ± 0.023	-3.533 ± 0.014	-3.637 ± 0.014
2M 0147-4954	34.7 ± 0.4 ¹	138.8 ± 0.4	13.27 ± 0.05	13.08 ± 0.05	2.345 ± 0.030	2.022 ± 0.016	-3.562 ± 0.015	-3.281 ± 0.015
2M 0423-0414	14.28 ± 0.19 ¹	159.11 ± 0.24	15.28 ± 0.05	13.62 ± 0.05	1.655 ± 0.011	2.124 ± 0.011	-4.466 ± 0.017	-4.683 ± 0.016
2M 0429-3123	17.00 ± 0.05 ¹	534 ± 4	11.23 ± 0.05	10.17 ± 0.05	3.50 ± 0.23	2.77 ± 0.13	-2.919 ± 0.014	-3.375 ± 0.018
2M 0700+3157	11.23 ± 0.05 ¹	179.4 ± 0.7	13.17 ± 0.05	11.27 ± 0.05	4.43 ± 0.12	3.809 ± 0.033	-3.779 ± 0.013	-4.343 ± 0.015
2M 0915+0422	17.7 ± 0.3 ¹	738.60 ± 0.15	15.30 ± 0.05	13.57 ± 0.05	1.11686 ± 0.00020	1.08643 ± 0.00020	-4.380 ± 0.017	-4.418 ± 0.017
2M 0926+5847	23.0 ± 0.5 ³	67.22 ± 0.14	16.57 ± 0.05	15.64 ± 0.05	1.522 ± 0.018	2.70 ± 0.28	-4.685 ± 0.018	-4.971 ± 0.026
2M 1021-0304	29.7 ± 1.3 ³	166.4 ± 0.5	17.09 ± 0.05	15.88 ± 0.05	1.104 ± 0.015	2.516 ± 0.015	-4.639 ± 0.021	-4.856 ± 0.022
2M 1853+1532	13.32 ± 0.16 ⁴	345.7 ± 0.7	16.55 ± 0.04	16.43 ± 0.04	1.363 ± 0.034	1.408 ± 0.027	-5.341 ± 0.011	-5.451 ± 0.010
2M 1707-0558	11.95 ± 0.03 ¹	1009.5 ± 1.0	12.59 ± 0.05	11.25 ± 0.05	5.15 ± 0.15	3.34 ± 0.20	-3.629 ± 0.014	-4.206 ± 0.017
2M 2152+0937	24 ± 4 ⁵	254.2 ± 0.6	16.02 ± 0.05	14.02 ± 0.05	1.157 ± 0.019	1.126 ± 0.012	-4.36 ± 0.10	-4.41 ± 0.10
2M 2252-1730	16.53 ± 0.16 ¹	126.7 ± 0.7	15.10 ± 0.05	13.46 ± 0.05	2.568 ± 0.028	3.21 ± 0.04 ₄	-4.246 ± 0.016	-4.637 ± 0.013
2M 2255-5713	17.97 ± 0.16 ¹	178.3 ± 0.8	14.694 ± 0.030 ^a	13.115 ± 0.032 ^a	5.16 ± 0.14	4.53 ± 0.06	-4.057 ± 0.010	-4.646 ± 0.010
2M 2351-2537	20.34 ± 0.19 ¹	62.65 ± 0.34	12.90 ± 0.05	11.84 ± 0.05	2.58 ± 0.09	2.9 ± 0.9	-3.376 ± 0.017	-3.720 ± 0.020

HST band photometry derived from 2MASS photometry.

References. — 1: Bailer-Jones et al. (2021), 2: Gaia Collaboration et al. (2018), 3: Dupuy & Liu (2012), 4: Dupuy & Liu (2017), 5: Best et al. (2020b)

Table 3.4. Final Binary Properties

Source	ρ [au]	$q_{1,2}$	$M_{A,1,2}$ [$M_{J_{\text{up}}}$]	$M_{B,1,2}$ [$M_{J_{\text{up}}}$]	$q_{3,1}$	$M_{A,3,1}$ [$M_{J_{\text{up}}}$]	$M_{B,3,1}$ [$M_{J_{\text{up}}}$]
2M 0004-4044	1.013 ± 0.008	0.977 ± 0.013	66.2 ± 0.6	64.7 ± 0.6	0.992 ± 0.004	75.87 ± 0.24	75.28 ± 0.25
2M 0025+4759	18.06 ± 0.14	0.966 ± 0.006	84.1 ± 0.4	81.3 ± 0.4	0.9839 ± 0.0030	83.94 ± 0.18	82.59 ± 0.18
2M 0147-4954	4.98 ± 0.07	0.907 ± 0.006	91.9 ± 0.4	83.3 ± 0.4	0.9542 ± 0.0031	87.57 ± 0.20	83.56 ± 0.20
2M 0423-0414	2.34 ± 0.05	0.852 ± 0.016	54.6 ± 0.7	46.5 ± 0.6	0.930 ± 0.007	71.18 ± 0.32	66.2 ± 0.4
2M 0429-3123	8.99 ± 0.07	0.876 ± 0.006	101.0 ± 0.4	88.5 ± 0.5	0.9359 ± 0.0031	91.86 ± 0.18	85.98 ± 0.23
2M 0700+3157	2.032 ± 0.11	0.771 ± 0.009	77.4 ± 0.4	59.6 ± 0.6	0.9076 ± 0.0034	80.76 ± 0.17	73.29 ± 0.23
2M 0915+0422	13.48 ± 0.27	0.974 ± 0.016	58.1 ± 0.7	56.6 ± 0.7	0.991 ± 0.006	72.69 ± 0.28	72.06 ± 0.30
2M 0926+5847	1.54 ± 0.04	0.813 ± 0.020	46.4 ± 0.7	37.7 ± 0.7	0.857 ± 0.015	66.12 ± 0.4	56.7 ± 0.9
2M 1021-0304	4.94 ± 0.18	0.844 ± 0.016	48.0 ± 0.7	40.5 ± 0.5	0.907 ± 0.014	67.3 ± 0.5	61.0 ± 0.8
2M 1553+1532	4.60 ± 0.06	0.914 ± 0.011	27.72 ± 0.26	25.35 ± 0.20	0.918 ± 0.010	43.83 ± 0.34	40.24 ± 0.31
2M 1707-0558	11.88 ± 0.06	0.793 ± 0.008	81.5 ± 0.4	64.6 ± 0.6	0.9101 ± 0.0034	82.70 ± 0.18	75.26 ± 0.23
2M 2152+0937	6.2 ± 1.1	0.97 ± 0.09	59 ± 4	57 ± 4	0.989 ± 0.032	73.1 ± 1.6	72.2 ± 1.7
2M 2252-1730	2.143 ± 0.32	0.760 ± 0.009	63.2 ± 0.5	48.1 ± 0.4	0.901 ± 0.005	74.71 ± 0.22	67.32 ± 0.32
2M 2255-5713	3.030 ± 0.33	0.687 ± 0.005	69.56 ± 0.30	47.77 ± 0.32	0.8694 ± 0.0035	77.19 ± 0.12	67.11 ± 0.24
2M 2351-2537	1.275 ± 0.014	0.893 ± 0.008	88.4 ± 0.5	79.0 ± 0.6	0.948 ± 0.004	85.96 ± 0.22	81.52 ± 0.26

Note. — 1,2 and 3,1 refer to the assumed age of the field population when converting magnitude or bolometric luminosity to mass. Masses and mass ratios calculated using other ages considered in this work are given in the online table.

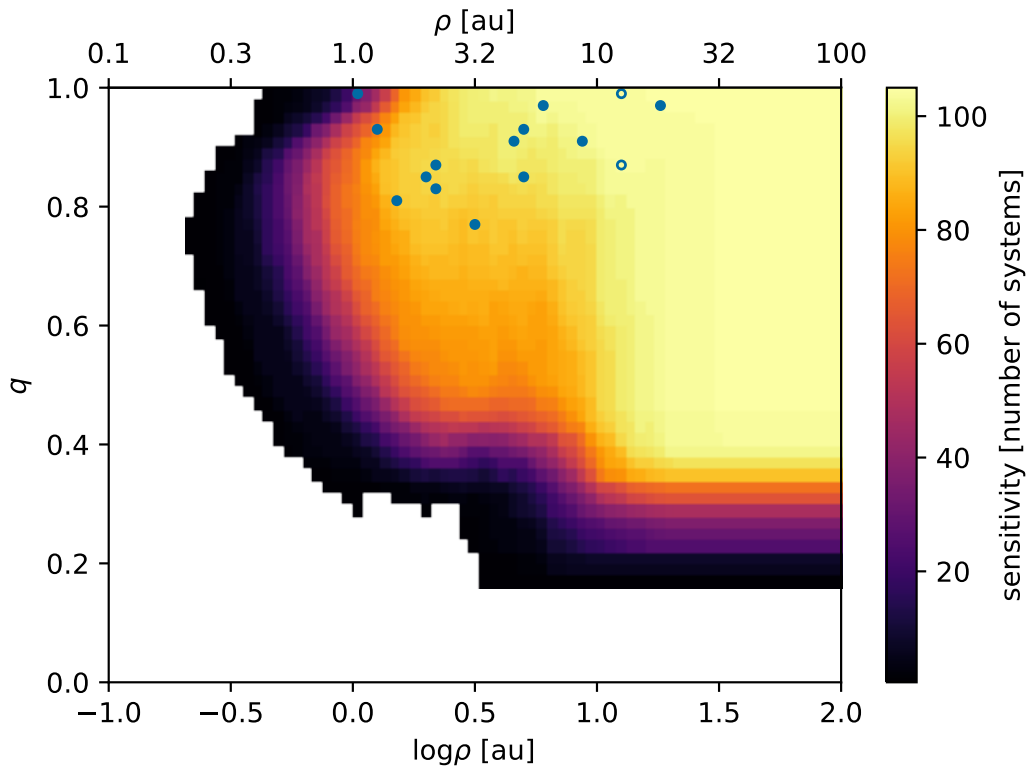


Figure 3.2: Stacked detection limits, in units of number of systems, as a function of projected separation, ρ , in au and mass ratio, q , using a field age of 1.9 Gyr (similar to Figure 15 of Factor & Kraus, 2022a, though now in physical units rather than observational units). Filled circles show detected companions and open circles indicate the two wide separation companions not detected in Factor & Kraus (2022a) but included in our sample using astrometry and photometry from Pope et al. (2013) (see Section 3.3.1). We set a conservative detection limit at separations $> 0''.5$ (where our KPI pipeline is not sensitive) of $\Delta m = 6.5$ from Reid et al. (2006). Corresponding plots for other field ages are available in Appendix F and at Factor & Kraus (2022c).

The binary population is characterized by a companion frequency F , a power-law mass-ratio distribution with exponent γ , and a log-normal projected-separation distribution with mean $\overline{\log(\rho)}$ and standard deviation $\sigma_{\log(\rho)}$. As in Kraus et al. (2011), we choose to model the separation distribution in terms of the observed projected separation (ρ) rather than the underlying semimajor axis (a)². The binary population model is then used in our likelihood function by comparing it to the observations over a grid $(\Delta \log(\rho), \Delta q)$ in parameter space. The expected companion frequency in a bin is given by the probability R according to:

$$R(\log(\rho), q | F, \gamma, \overline{\log(\rho)}, \sigma_{\log(\rho)}) \Delta \log \rho \Delta q = \\ \frac{\gamma + 1}{\sqrt{2\pi} \sigma_{\log(\rho)}} F q^\gamma \exp\left(-\frac{(\log(\rho) - \overline{\log(\rho)})^2}{2\sigma_{\log(\rho)}^2}\right) \Delta \log \rho \Delta q \quad (3.4)$$

Before this companion frequency is used in the likelihood function, we must first include Malmquist bias (Malmquist, 1922) in order to compare it to our magnitude limited sample. In previous studies this bias correction was applied to the detection limits by artificially increasing the sensitivity to binaries since they should be over represented in the underlying sample. However, this method does not account for unresolved binaries which are treated as single sources. Instead, we build Malmquist bias into our population model by

²This avoids making an assumption about the eccentricity distribution which may change with future observations. Converting ρ to a can be done using a simple conversion factor calculated using montecarlo simulations of projected orbits. For very low-mass binaries $a/\rho = 1.16^{+0.81}_{-0.31}$, for no discovery bias, or as low as $a/\rho = 0.85^{+0.11}_{-0.14}$, for a survey with an inner working angle comparable to a (Dupuy & Liu, 2011).

increasing the number of binaries, as a function of contrast, that we should expect to observe (though not necessarily resolve). Since our model is a function of mass ratio $q = M_B/M_A$ and Malmquist bias is a function of total brightness or contrast $C = F_A/F_B$, we must first convert q to C . We chose the contrast in F110W (C_{F110W}) since it closely resembles the 2MASS- J filter used to select the sample. Since we already convert C to q , as described above, the inverse is numerically trivial. We calculate the Malmquist correction using the same method as Burgasser et al. (2003c) and Allen (2007),

$$V_{\text{max}}/V_{\text{flux}} = \left(1 + \frac{1}{C_{\text{F110W}}}\right)^{3/2}, \quad (3.5)$$

for each source then average to apply a single correction to the model. We ran the fit with and without the Malmquist correction in order to both determine the underlying and unbiased population and compare our results to previous analysis of “observed” populations.

The Bayesian likelihood in a given bin $(\log(\rho), q)$ with N_{det} companions detected and N_{sen} targets which were sensitive to such a companion is then the Binomial likelihood:

$$P(N_{\text{det}}, N_{\text{sen}} | F, \gamma, \overline{\log(\rho)}, \sigma_{\log(\rho)}) \propto R^{N_{\text{det}}} \times (1 - R)^{(N_{\text{sen}} - N_{\text{det}})}. \quad (3.6)$$

The grid is derived from the overall survey detections and sensitivity and is shown in Figure 3.2 along with the binary systems. The full grid spans $\log(\rho) = -4$ to 3 in 175 bins and $q = 0$ to 1 in 50 bins. Since our calculated limits only extend to 0.5 arcsec we adopt a 100% detection threshold of $\Delta m =$

6.5 magnitudes for all separations $> 0''.5$. This is a conservative estimate of the sensitivity of the Reid et al. (2006) analysis. The $\log(\rho)$ axis of our grid is much larger than the region occupied by our detections (our detections span a range of ~ 75 bins) to give our detection limits (where we are sensitive but did not detect any companions) and informed prior (see Section 3.5.2) leverage over the model parameters.

This likelihood function is then passed to a fitting routine, in our case `emcee` (Foreman-Mackey et al., 2013) which implemented the affine invariant sampler described in Goodman & Weare (2010). We ran the fit using 64 “walkers” for 10000 steps (discarding the first 1000 for “burn-in”), exceeding 50 autocorrelation times for all four parameters while only running for a few minutes.

We first ran the fit with uninformed (wide and flat) priors on all four parameters ($F = 0$ to 2.5 , $\gamma = -1$ to 20 , $\overline{\log(\rho)} = -4$ to 3 , and $\sigma_{\log(\rho)} = 0$ to 4). This produced an interesting binary distribution, though one that is inconsistent with previous RV studies. Thus, we ran our fits a second time with an informed prior (though technically implemented as a penalized likelihood), restricting the tight (< 1 au) binary fraction to $2.5^{+8.6}_{-1.6}\%$ (Blake et al., 2010). This was implemented by summing up R (Equation 3.4) for all projected separation bins < 1 au (resulting in the tight companion fraction) and penalizing the likelihood based on the difference between this sum and the measurement of Blake et al. (2010). This resulted in a much more tightly constrained posterior on the population distribution parameters. Blake et al. (2010) estimated

a 94% completeness for targets with $0.01 < a < 1$ au while our completeness is $\sim 50\%$ at 1 au and drops to $\sim 0\%$ by 0.3 au. While the measurement by Blake et al. (2010) assumed a much flatter mass-ratio distribution ($\gamma = 1.8$ from Allen, 2007), they claim their sensitivity (and thus their measurement of binary fraction) is relatively insensitive to the distribution. We apply this prior to the underlying companion distribution, marginalizing over q , so their choice of γ will have little effect on our results.

3.5 Results: Binary Demographics

Previous studies of brown dwarf demographics using a similar model (log-normal projected-separation and power-law mass-ratio distributions) have found a population heavily skewed toward equal mass ($\gamma \sim 2 - 5$) with a semimajor axis distribution centered around ~ 6 au and a total companion frequency of $\sim 20\%$ (Reid et al., 2006; Burgasser et al., 2007; Allen, 2007). Fontanive et al. (2018) studied later spectral type objects (T5–Y0) and found a roughly similar semimajor axis distribution with a lower companion frequency of $8 \pm 6\%$ and a slightly stronger mass-ratio power-law index of $\gamma \sim 6$. Radial velocity studies searching for tight companions (separation < 1 au) have found a much lower companion frequency of $2.5^{+8.6}_{-1.6}\%$ (Blake et al., 2010) and $2 \pm 2\%$ for late type objects (Fontanive et al., 2018). Initially we ran our demographic fits using a wide and uninformed prior. Since our detections run up against our inner working angle, these fits yielded a companion distribution with an extremely high binary fraction at tight separations, inconsistent with previous

studies. We therefore incorporated an informed prior, restricting the amount of tight binaries, and found a population much more consistent with previous studies. Since the age and mass of a brown dwarf are degenerate (for a given absolute magnitude) we also ran all of our fits with a set of assumed field ages. This only affected the mass-ratio power-law index and had no effect on the total companion frequency or semimajor axis parameters. We ran our fits with and without the Malmquist bias correction in order to study both the underlying unbiased population and the “observed” binary population, to compare with previous studies. Incorporating Malmquist bias reduced both the companion frequency, F , and mass-ratio power-law index, γ , while having no effect on the separation distribution parameters, $\overline{\log(\rho)}$ and $\sigma_{\log(\rho)}$. F decreases because binaries are over-represented in the observed sample, while γ decreases since equal-brightness (i.e. high q) systems are more over-represented than those with fainter (i.e. lower q) companions.

3.5.1 Demographics from an Uninformed Prior

Posterior distributions using an uninformed prior are shown as a corner plot in blue in Figure 3.3 for an assumed field age of 1.9 Gyr (see Appendix G and Factor & Kraus, 2022c, for other ages). Median and central 68% credible intervals for the model hyper-parameters are given in Table 3.5. Since age only affects the derived mass and has no bearing on separation, the only parameter affected by the assumed field age is γ and it is discussed below.

The uninformed prior resulted in a posterior distribution on companion

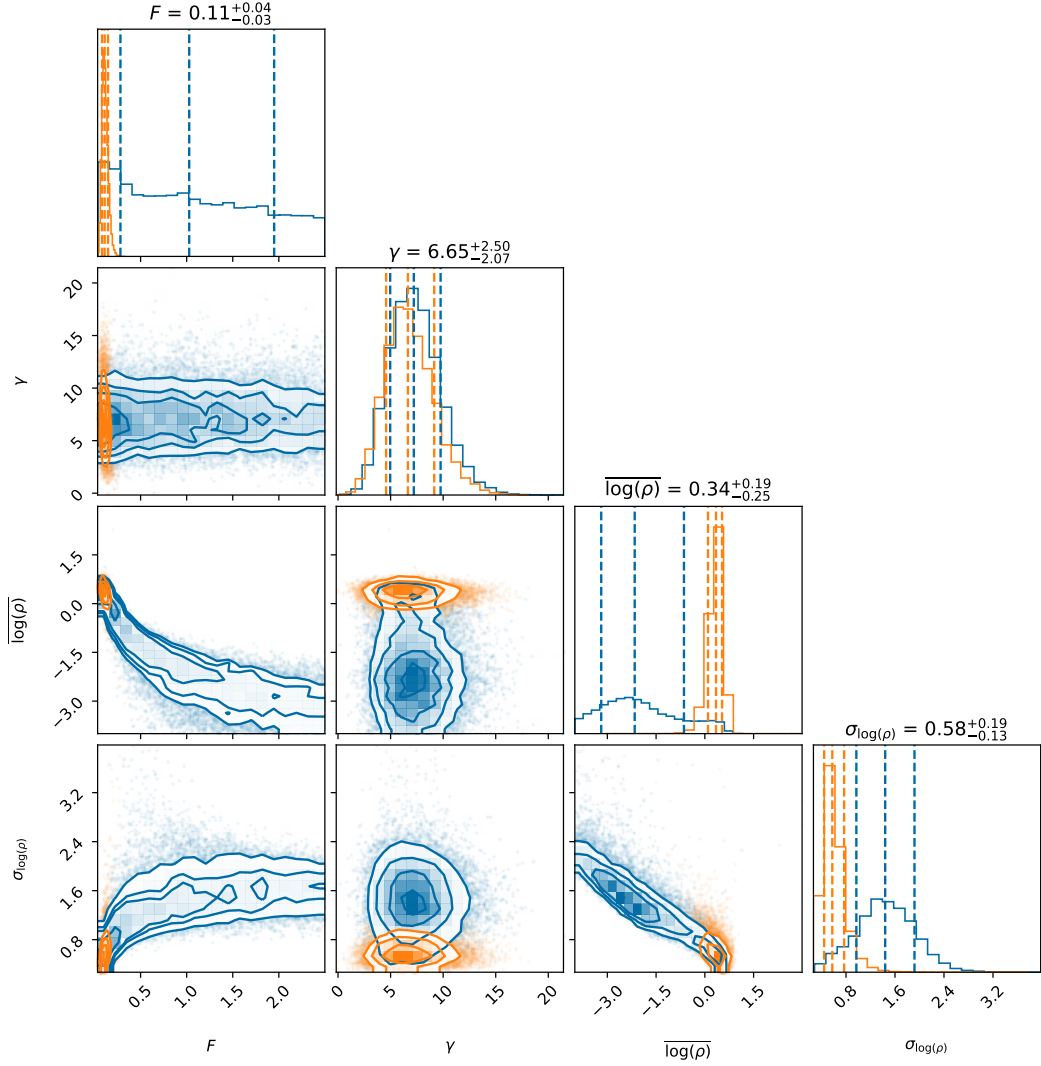


Figure 3.3: Corner plot showing the 1- and 2D posteriors of our demographic fit using a field age of 1.9 Gyr. Blue contours show the results using a uniform uninformed prior while orange contours show the results restricting the tight (< 1 au) binary fraction to $2.5^{+8.6\%}_{-1.6\%}$ (Blake et al., 2010). Dashed lines indicate the median and $\pm 1\sigma$ (16th, 50th, and 84th percentile) values (given in Table 3.5). The parameter values listed above each plot correspond to the fits using the informed prior. Corresponding plots for other field ages are shown in Appendix G and online at Factor & Kraus (2022c). Data behind the figure is available for the MCMC chains shown in this figure and those for other ages at Factor & Kraus (2022d).

Table 3.5. Binary Population Parameters

Isochrone	γ	F	$\overline{\log(\rho)}$	$\sigma_{\log(\rho)}$
Informed Prior, Underlying Population				
3.1 Gyr	11^{+4}_{-3}	$0.11^{+0.04}_{-0.03}$	$0.34^{+0.18}_{-0.25}$	$0.58^{+0.20}_{-0.13}$
2.4 Gyr	9 ± 3	$0.11^{+0.04}_{-0.03}$	$0.34^{+0.19}_{-0.25}$	$0.58^{+0.19}_{-0.13}$
1.9 Gyr	7^{+3}_{-2}	$0.11^{+0.04}_{-0.03}$	$0.34^{+0.19}_{-0.25}$	$0.58^{+0.19}_{-0.13}$
1.5 Gyr	$5.5^{+2.1}_{-1.8}$	$0.11^{+0.04}_{-0.03}$	$0.34^{+0.19}_{-0.25}$	$0.58^{+0.20}_{-0.13}$
1.2 Gyr	$4.6^{+1.8}_{-1.6}$	$0.11^{+0.04}_{-0.03}$	$0.34^{+0.19}_{-0.24}$	$0.57^{+0.20}_{-0.13}$
0.9 Gyr	$4.0^{+1.7}_{-1.5}$	$0.11^{+0.04}_{-0.03}$	$0.34^{+0.19}_{-0.25}$	$0.58^{+0.19}_{-0.13}$
Informed Prior, Observed Population ^a				
3.1 Gyr	14 ± 4	$0.22^{+0.07}_{-0.06}$	$0.35^{+0.18}_{-0.25}$	$0.58^{+0.20}_{-0.13}$
2.4 Gyr	11 ± 3	$0.22^{+0.07}_{-0.06}$	$0.33^{+0.19}_{-0.26}$	$0.58^{+0.20}_{-0.13}$
1.9 Gyr	9^{+3}_{-2}	$0.22^{+0.07}_{-0.05}$	$0.35^{+0.18}_{-0.25}$	$0.57^{+0.20}_{-0.13}$
1.5 Gyr	7 ± 2	$0.22^{+0.07}_{-0.05}$	$0.35^{+0.18}_{-0.25}$	$0.57^{+0.20}_{-0.13}$
1.2 Gyr	$6.2^{+2.0}_{-1.7}$	$0.22^{+0.07}_{-0.06}$	$0.35^{+0.19}_{-0.25}$	$0.57^{+0.20}_{-0.13}$
0.9 Gyr	$5.5^{+1.8}_{-1.6}$	$0.22^{+0.07}_{-0.06}$	$0.34^{+0.19}_{-0.25}$	$0.57^{+0.20}_{-0.13}$
Uninformed Prior, Underlying Population				
3.1 Gyr	12^{+4}_{-3}	$1.0^{+0.9b}_{-0.8}$	$-2.2^{+1.5c}_{-1.0}$	1.5 ± 0.5
2.4 Gyr	10 ± 3	$1.1^{+0.9b}_{-0.8}$	$-2.2^{+1.5c}_{-1.0}$	1.5 ± 0.5
1.9 Gyr	7^{+3}_{-2}	$1.0^{+0.9b}_{-0.8}$	$-2.2^{+1.5c}_{-1.0}$	1.4 ± 0.5
1.5 Gyr	$5.9^{+2.2}_{-1.9}$	$1.0^{+0.9b}_{-0.8}$	$-2.1^{+1.5c}_{-1.1}$	1.4 ± 0.5
1.2 Gyr	$4.9^{+1.9}_{-1.6}$	$1.0^{+0.9b}_{-0.8}$	$-2.2^{+1.5c}_{-1.0}$	1.4 ± 0.5
0.9 Gyr	$4.3^{+1.8}_{-1.5}$	$1.0^{+0.9b}_{-0.8}$	$-2.1^{+1.5c}_{-1.0}$	1.4 ± 0.5

Note. — Values presented here are median and central 68% credible intervals.

^aThe “observed” population parameters were fit without correcting for Malmquist bias.

^bThe median and central 68% confidence intervals are not good metrics as the posterior on F with the uninformed prior is relatively flat over the span of the allowed parameters with a weak peak near the same value as with the informed prior (see Figure 3.3).

^cThe posterior on $\overline{\log(\rho)}$ with the uninformed prior has a weak secondary peak near the same value as with the informed prior (see Figure 3.3).

frequency which is peaked at small F with a long tail extending to extremely high companion fraction. Companion frequency is also degenerate with a broad (large $\sigma_{\log(\rho)}$) separation distribution centered at $\rho \sim 0.006$ au. While there is a weak peak at $F \sim 0.1$ and $\overline{\log(\rho)} \sim 0.3$ (likely corresponding to the true underlying distribution, see Section 3.5.2) it is overwhelmed by a distribution containing a large number of undetectable companions inside the inner working angle of our survey. In order for a survey to rule out unresolved companions the inner working angle must fall well inside the peak of the separation distribution. If this is the case, a decrease in detections can then be attributed to the population rather than a cutoff in sensitivity. Since our survey includes detections that run up against the inner working angle (~ 1 au), we cannot rule out a significant population of unresolved companions. Thus, a companion distribution centered at $\overline{\log(\rho)} = -2.2$ or $\bar{\rho} = 0.006$ au (well within our inner working angle) must also be wide ($\sigma_{\log(\rho)} = 1.4$) and requires an extremely high companion fraction to reproduce the observations since our observed companions are located in the upper wing of the distribution.

We note a strong degeneracy between F and both separation parameters: $\overline{\log(\rho)}$ and $\sigma_{\log(\rho)}$. This was also seen in previous studies (e.g. Allen, 2007; Kraus et al., 2011). This degeneracy can be explained since a companion distribution centered at a tighter separation ($\overline{\log(\rho)}$) needs both a higher companion fraction (F) and a wider distribution ($\sigma_{\log(\rho)}$) to reproduce the observed companions which are now further out in the wing of the distribution. This also explains the strong degeneracy between $\overline{\log(\rho)}$ and $\sigma_{\log(\rho)}$. Allen (2007) also

noted a degeneracy between F and $\overline{\log(\rho)}$ attributed to their inability to rule out a population of tight, unresolved, binaries. With a sufficiently large sample the curvature in the wing of the distribution can be used to break this degeneracy (assuming the underlying distribution is truly log-normal) but we are nowhere close to having enough detections for this to be possible.

3.5.2 Demographics from an Informed Prior

While the demographics derived using the uninformed prior are consistent with our observations they are not consistent with previous studies of brown dwarf binarity at separations inside our inner working angle. Blake et al. (2010) used six years of near-infrared RV measurements of 50 late-M and L dwarfs from Keck/NIRSPEC to infer the tight (< 1 au) binary fraction to be $2.5^{+8.6}_{-1.6}\%$. This binary fraction is significantly lower than the $140 \pm 100\%$ (essentially every system is a binary or triple) our posterior parameters would predict if marginalized over the same range in separation and inflated to simulate an observed sample (accounting for Malmquist bias). Thus, we ran a second set of fits restricting the tight binary fraction to be consistent with that of Blake et al. (2010) (as discussed at the end of Section 3.4.2). The distribution produced while considering the Blake et al. (2010) information is much more consistent with previous studies. The tight (< 1 au) binary fraction of our posterior binary BD population (again, corrected for Malmquist bias) is $6^{+6}_{-4}\%$, slightly higher than though well within the 1σ error bars of Blake et al. (2010). To the best of our knowledge, this is the first time an RV

prior has been incorporated in a direct imaging BD demographics survey to account for unresolved companions. The use of this prior is further discussed in Section 3.6. The posteriors produced by this fit are shown in orange in Figure 3.3 and median values and central 68% credible intervals for the model hyper-parameters are given in Table 3.5. The full 2D binary population is shown in the left panel of Figure 3.4 beside the observed population (correcting for Malmquist bias and sensitivity) and our raw sensitivity along with our detections.

The observed and inferred binary probability density as a function of projected separation (marginalized over mass ratio q) is shown in Figure 3.5. Histogram error-bars are drawn according to Burgasser et al. (2003c) and agree well with the “observed” distribution drawn by correcting the companion distribution (calculated using the median-fit hyper parameters) for Malmquist bias and applying the survey sensitivity. The increase in observed binaries above the underlying distribution is due to Malmquist bias while the drop in observed binaries at close separations (< 1 au) is due to a steep drop in sensitivity. Also shown is the information from Blake et al. (2010) used to constrain the unresolved population ($2.5_{-1.6}^{+8.6}\%$ spread out evenly over $\log(\rho) = -2$ to 0).

3.5.3 Mass-ratio Demographics

Since the mass of a brown dwarf depends on the assumed age, we re-ran the demographic fit with multiple assumed field ages. The information

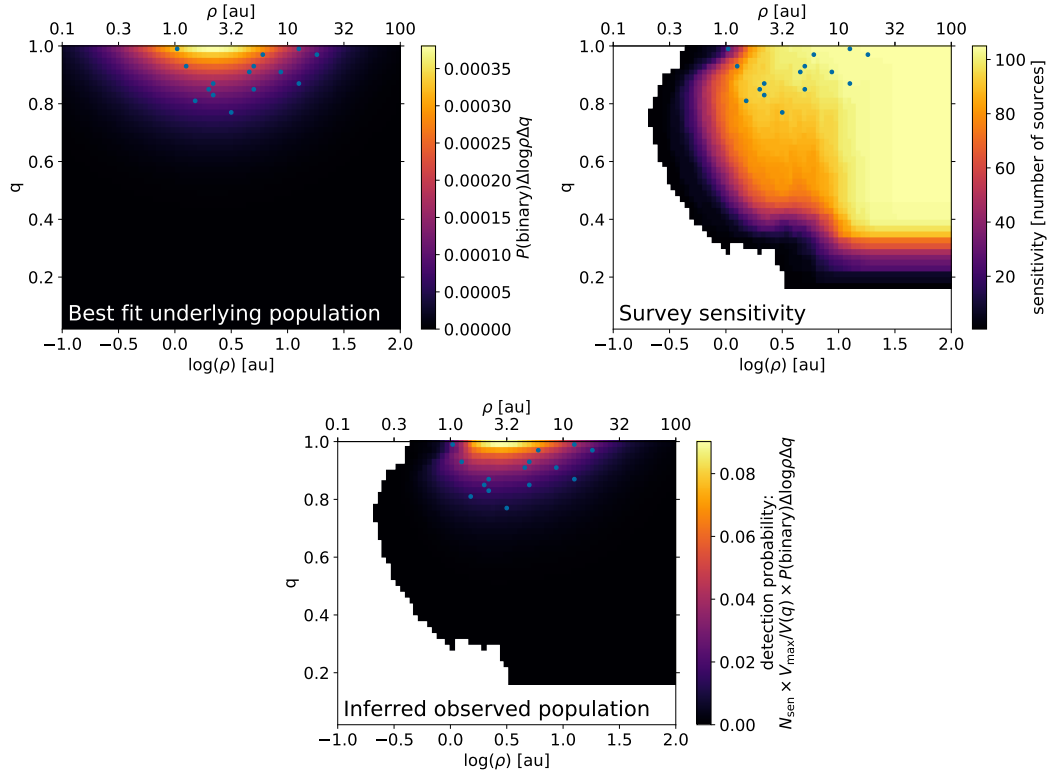


Figure 3.4: The progression from underlying population and survey sensitivity to observed population. Blue points indicate detected companions. *Top left*: Underlying companion population produced from the median values of our informed prior fit. *Top right*: Survey sensitivity in units of number of targets. *Bottom center*: Observed population (i.e. the inferred probability that we should detect a companion in a given bin), calculated by correcting the underlying population for Malmquist bias (as a function of mass ratio) and applying our survey sensitivity. Mass ratios were calculated assuming a field age of 1.9 Gyr. Similar figures for other assumed field ages are shown in Appendix H and online at Factor & Kraus (2022c).

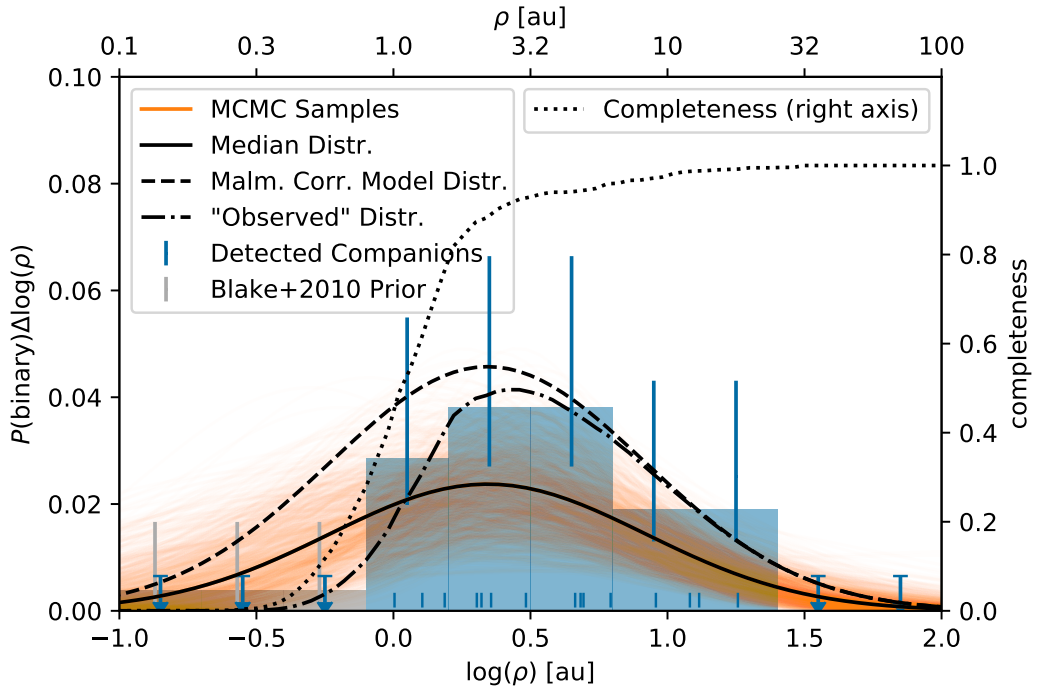


Figure 3.5: Binary population as a function of projected separation. The blue histogram shows the detected companion separations and error bars calculated using Burgasser et al. (2003c) with dashes below showing the un-binned values. Grey bars and error bars correspond to the Blake et al. (2010) measurement of tight separation binaries ($2.5^{+8.6\%}_{-1.6\%}$ spread out evenly over $\log(\rho) = -2$ to 0). Orange curves are 1000 companion probability densities drawn from the posterior distributions using the informed prior while the solid black curve is drawn using the median parameters ($F = 0.11^{+0.04}_{-0.03}$, $\log(\rho) = 0.34^{+0.19}_{-0.25}$, $\sigma_{\log(\rho)} = 0.58^{+0.20}_{-0.13}$, i.e the top left panel of Figure 3.4 marginalized over q). The black dashed line shows the Malmquist corrected distribution (see Section 3.4.2) and the dash-dotted line shows the “observed” distribution (bottom center panel of Figure 3.4), calculated by multiplying the Malmquist corrected binary-population distribution by our sensitivity (shown in Figure 3.2 or the top right panel of Figure 3.4). The black dotted line is the completeness fraction (right vertical axis), the ratio between the black dashed and dash-dotted lines or equivalently the marginalized and normalized sensitivity.

incorporated in the informed prior only affects the tight-binary fraction and has no information about mass ratio, thus the posteriors on γ are essentially the same when using the informed or uninformed prior. Similarly, as age only affects the derived mass (or mass ratio q), other model parameters do not significantly change as a function of age.

Figure 3.6 shows the binary fraction as a function of mass ratio for an assumed field age of 1.9 Gyr (see Appendix I and online at Factor & Kraus, 2022c, for other ages). Once again, the “observed” distribution (median posterior distribution corrected for Malmquist bias times sensitivity) matches well with the histogram of detected companions. As opposed to the separation distribution (shown in Figure 3.5), our sensitivity is relatively constant well beyond the region of parameter space inhabited by our detections so no additional information is needed to prevent the fit from producing distributions with a large population of faint undetectable companions.

As stated above, we ran our demographic fit for a variety of field ages ranging from 0.9–3.1 Gyr. Since age only affects the mass (or mass ratio) of a companion and not the separation, the only demographic parameter that changes with age is γ (and it is not affected by the choice of prior on the amount of tight separation binaries). Figure 3.7 shows the posterior distributions on γ as a function of the assumed field age. Median values and central 68% credible intervals are given in Table 3.5 and range from $\gamma = 4.0_{-1.5}^{+1.7}$ to $\gamma = 11_{-3}^{+4}$ assuming an age of 0.9 or 3.1 Gyr, respectively.

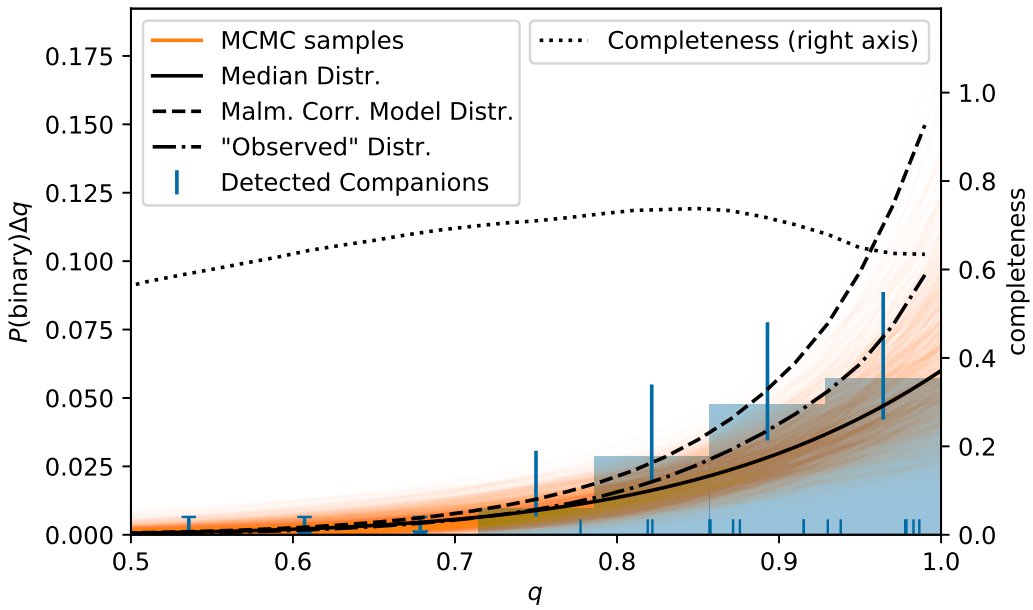


Figure 3.6: Similar to Figure 3.5 but as a function of mass ratio. Mass ratios are derived using a 1.9 Gyr assumed field age and a median power-law index of $\gamma = 7^{+3}_{-2}$ and overall companion frequency of $F = 0.11^{+0.04}_{-0.03}$. Similar figures for other assumed field ages are shown in Appendix I and are available online at Factor & Kraus (2022c).

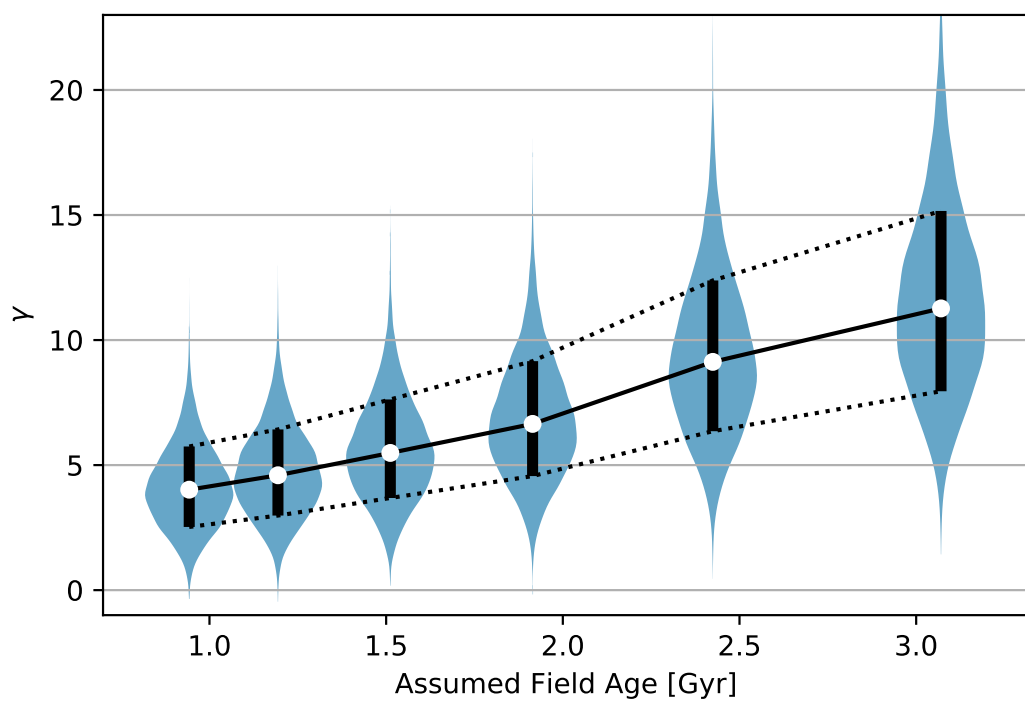


Figure 3.7: Posteriors of the mass-function power-law index γ as a function of assumed field age. White points and black vertical lines correspond to median and $\pm 1\sigma$ values.

3.5.4 “Observed” Population Without Accounting for Malmquist Bias

In order to compare our results to literature studies which report parameters of the *observed* population we run our fits a final time without accounting for Malmquist bias. The results of these fits are presented in Table 3.5. The separation distribution hyper parameters are essentially identical since Malmquist bias corrects for the number of binaries (resolved or unresolved) as a function of contrast (or mass ratio q) which are included in a magnitude limited sample (due to their increased brightness). Accordingly F is much larger when Malmquist bias is not accounted for as companions are naturally over-represented in the observed sample. The mass-ratio power-law index, γ , is roughly 1σ larger when Malmquist bias is not accounted for as equal brightness (high q) companions are more over-represented than faint (low q) companions.

3.6 Discussion

3.6.1 Demographics in the Context of Previous Surveys

Our BD binary demographic parameters are largely consistent with the previous literature values. We compare our values with three studies of early type BDs and one of late type BDs: the original study on a subset of our data set (Reid et al., 2006), a meta-analysis of BD binary studies (Allen, 2007), a review of BD binarity (Burgasser et al., 2007), and a study of late T and Y dwarfs of even lower mass than included in our sample (Fontanive et al.,

2018). Using our sample of 15 detected binaries in 105 targets ($\epsilon_b = 14_{-3}^{+4}\%$, with error bars from binomial statistics following Burgasser et al., 2003c) and fitting for the full population as described in Section 3.5, we infer an underlying companion frequency of $F = 0.11_{-0.03}^{+0.04}$. “Observing” this population by multiplying the full 2D companion distribution by our detection limits and applying a Malmquist bias correction gives a predicted number of observed companions of 15_{-3}^{+4} and an observed companion frequency of $14_{-3}^{+4}\%$, both consistent with our observed value. Fitting the “observed” population gives a companion frequency of $F = 0.22_{-0.06}^{+0.07}$ (from the fits ran without accounting for Malmquist bias), consistent with the values of the three studies of L dwarfs ($0.24_{-0.02}^{+0.06}$, 0.20 ± 0.04 , and $0.22_{-0.04}^{+0.08}$, respectively) to well within 1σ , while our unbiased (Malmquist bias corrected) underlying companion frequency is $2-3\sigma$ lower than these values. Since Reid et al. (2006) does not account for Malmquist bias this is not surprising. On the other hand Allen (2007) and Burgasser et al. (2007), who uses the same method, both account for Malmquist bias in their sensitivity window function but arrive at a similar companion frequency, $F \sim 0.22$, to that of Reid et al. (2006). Fontanive et al. (2018) reports a binary fraction of $F = 0.08 \pm 0.06$, continuing the trend of decreasing binary fraction with decreasing primary mass.

Our mean separation ($\overline{\log(\rho)} = 0.34_{-0.25}^{+0.19}$ or $\bar{\rho} = 2.2_{-1.0}^{+1.2}$ au) is tighter than the values from the above L dwarf studies ($\overline{\log(\rho)} = 0.8_{-0.12}^{+0.06}$, $0.86_{-0.12}^{+0.06}$, and $0.86_{-0.18}^{+0.06}$, respectively, or $\bar{\rho} \sim 6 - 7$ au) by $\sim 2\sigma$, while our separation standard-deviation ($\sigma_{\log(\rho)} = 0.58_{-0.13}^{+0.2}$) is larger than the above studies

$(\sigma_{\log(\rho)} = 0.28 \pm 0.4$, 0.28 ± 0.04 , and $0.24^{+0.08}_{-0.06}$, respectively) by $0.7 - 2.2\sigma$. While our mean separation is consistent (at $\sim 0.3\sigma$) with the value reported in Fontanive et al. (2018, $\overline{\log(\rho)} = 2.9^{+0.8}_{-1.4}$), their $\sigma_{\log(\rho)} = 0.21^{+0.14}_{-0.08}$ is again smaller by 1.9σ . Since our KPI technique has a much smaller inner working angle and our analysis includes one new tight companion (2M 2351-2537, discovered by Pope et al. (2013) and confirmed by Factor & Kraus (2022a)), it is not surprising that our separation distribution has moved in. Our separation distribution must then also be wider to stay consistent with the widely separated companions. The information in our “informed prior” (from the RV survey by Blake et al., 2010) keeps the mean from moving even closer in. Also worth noting is the fact that we used distances measured from geometric parallaxes (Bailer-Jones et al., 2021; Gaia Collaboration et al., 2021) to convert observed separations (in arcsec) to projected separations (in au) rather than spectroscopic parallaxes used the studies discussed above (except for Fontanive et al., 2018, who used a combination of the two methods). Geometric parallaxes are more accurate and precise than spectroscopic parallaxes. The Malmquist correction had no effect on these parameters.

Most previous BD demographic studies used restricted priors to avoid the tight separation/high companion frequency solution that we found using an uninformed prior in Section 3.5.1. Of the four previously discussed studies, Fontanive et al. (2018) is the only one which explicitly lists the bounds of their prior. They use a flat prior that is relatively narrow around the expected value, effectively eliminating the tight median separation solutions. While using a

flat prior with a limited range is effective at rejecting unreasonable solutions, the bounds can be arbitrary. If a wide flat prior produces unphysical results (such as a population with $a \sim R_{\text{BD}}$) a more robust strategy is to establish where the data or likelihood function is lacking leverage and use a physically- or observationally-motivated informed prior (or a modified likelihood function as technically done in this work). Burgasser et al. (2007) does not use a prior informed by the RV surveys they discuss, though they do note that their posterior distributions have “non-negligible dispersions, as parameters spaces outside the observational window function (e.g. very tight binaries) add considerable uncertainty”. This likely refers to the solutions we saw in our uninformed prior runs and is tentatively seen in the tails of their posterior distributions. Allen (2007) noted a degeneracy between F and $\overline{\log(\rho)}$ which they attribute to resolution limits. We also see this strong degeneracy when using the uninformed prior (and less so when restricting the number of tight companions).

Since BD mass is degenerate with age for a given flux or luminosity, we ran our fits for a wide range of plausible field ages. Aganze et al. (2022) recently analyzed a sample of ultracool dwarfs out of the galactic plane and modeled the scale-heights, vertical velocity dispersion, and ages. They found disk population ages of $3.6^{+0.8}_{-1.0}$ Gyr for late M dwarfs, $2.1^{+0.9}_{-0.5}$ Gyr for L dwarfs, and $2.4^{+2.4}_{-0.8}$ Gyr for T dwarfs, with an additional 1–2 Gyr systematic uncertainty. With almost 70% of our sample being L dwarfs ($\sim 20\%$ T dwarfs and $\sim 10\%$ late M dwarfs) our average field age should be on the lower end of

those values, though with such large systematics, the entire range of field ages we used (0.9–3.1 Gyr) are consistent with their measurements.

Our results show a significantly steeper mass-ratio power law index, γ , than previous studies (depending on the assumed field age). We recover values between $\gamma = 4.0_{-1.5}^{+1.7}$ and $\gamma = 11_{-3}^{+4}$ for assumed field ages of 0.9 and 3.1 Gyr, respectively. Of the three L dwarf studies discussed above, Allen (2007) reports the most shallow index: $\gamma = 1.8_{-0.6}^{+0.4}$. They claim their value is softened by the large number of late M dwarfs included in their sample so it is not surprising that our values are larger by $1.4 - 2.8\sigma$. Reid et al. (2006), who analyzed a subset of the late M and L dwarfs in this sample, reported $\gamma = 3.6 \pm 1$ which is consistent within 1σ with our values up to an age of 1.5 Gyr and 2.3σ lower than our largest value. Burgasser et al. (2007) report a slightly steeper value, $\gamma = 4.8_{-1.6}^{+1.4}$, which is consistent within 1σ with our values up to an age of 1.9 Gyr and 1.8σ lower than our largest value. Fontanive et al. (2018) report the steepest value of $\gamma = 6_{-3}^{+4}$, consistent within 1σ with all of our values.

The source of the discrepancy in γ values is likely due to our survey's greater sensitivity to lower mass companions near the peak of the separation distribution. Thus, the lack of high contrast/low mass detections can be interpreted as a dearth of such companions rather than a deficiency in sensitivity. Another source of this discrepancy is the difference in how we and previous studies derived our masses/mass ratios from observed fluxes/flux-ratios. Reid et al. (2006) used 0.5, 1, and 5 Gyr isochrones from Burrows et al. (1997) and

Chabrier et al. (2000), while Allen (2007) used a distribution of ages from Burrows et al. (2001), and the review by Burgasser et al. (2007) used the original authors' methods, including the references listed above and dynamical masses. Fontanive et al. (2018) used a distribution of ages and the Baraffe et al. (2003) models. We used a more modern set of models (Phillips et al., 2020) which extend to extremely low masses.

Figure 3.8 shows our best fit parameters in the context of the four BD binarity surveys discussed above and representative values for stellar binaries. Our values follow the general trends as a function of primary mass with discrepancies discussed above. Our study continues to confirm three trends previously noted with BD binarity: a low ($\sim 10\%$) binary fraction, a preference for tight pairs (small $\overline{\log(\rho)}$), and a preference for equal-mass pairs (large γ). With our increased sensitivity to close-in companions, it appears that the trend in separation could be steeper than previous studies proposed. We also confirm the dearth of wide separation companions seen in previous studies; our posterior binary BD populations have a wide (> 20 au) observed (corrected for Malmquist bias) companion fraction of $0.9_{-0.6}^{+1.1}\%$. We therefore conclude that extremely wide pairs (e.g. Luhman, 2004; Chauvin et al., 2004; Faherty et al., 2020) are formed via a different process than most BD binaries or, as is more likely the case, dynamical evolution plays a significant role in BD binary formation as these wide systems tend to also be young.

Because the mass-ratio distribution is so extreme and the sample size is not huge, it is worthwhile to test the robustness of our results to an additional

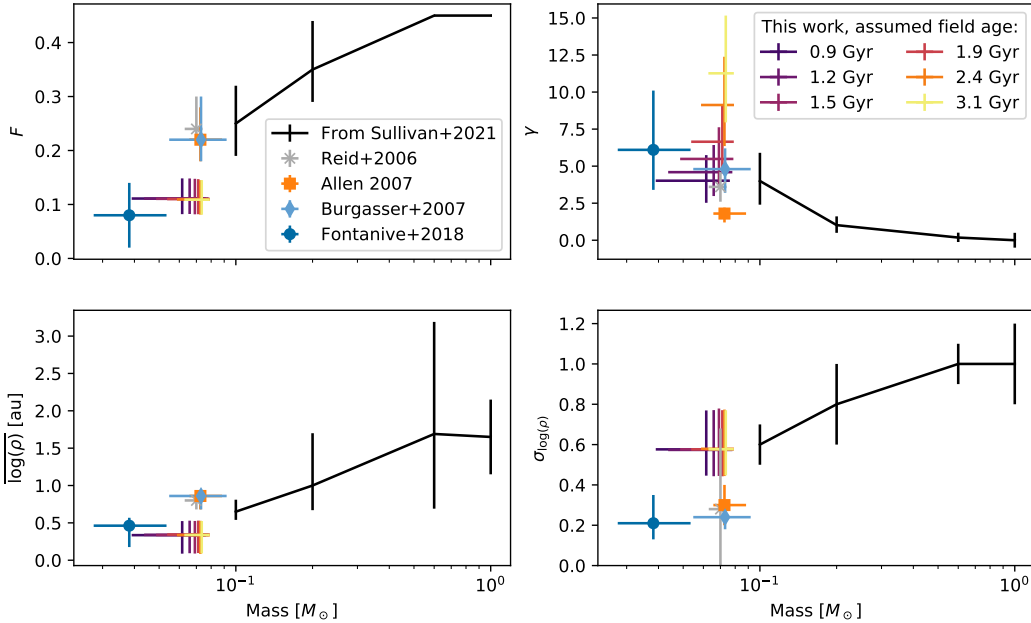


Figure 3.8: Binary demographic parameters as a function of stellar mass. Black points are taken from Table 1 of Sullivan & Kraus (2021), who compiled parameters from a variety of sources (De Rosa et al., 2014; Raghavan et al., 2010; Kraus & Hillenbrand, 2012; Winters et al., 2019; Tokovinin & Briceño, 2020). The dark blue circle corresponds to the work of Fontanive et al. (2018) (for T5–Y0), the grey X is from Reid et al. (2006), the orange square is from Allen (2007), and the light blue diamond is from Burgasser et al. (2007). Fits from this work are shown on a color scale from purple to yellow for different assumed field ages. Assumed age mainly affects the derived masses of the sources and γ , the mass-ratio power-law index, while having little to no effect on the three other parameters. Mass error-bars show the central 68% interval. We use projected separation, ρ , and semimajor axis, a , interchangeably as the conversion between the two values is ~ 1 (Dupuy & Liu, 2011).

detection. Figure 3.9 shows the results of refitting our demographic parameters with an additional (synthetic) companion injected at a range of q values (holding separation constant at the median separation). As expected, the inferred γ would change only slightly with an additional companion discovered with $q \gtrsim 0.6$. While discovering a statistically usable companion (discovered in a broad survey rather than a survey targeting suspected binaries) with a mass ratio less than $q = 0.6$ would be rare given the inferred population, it would be extremely significant (e.g. 2MASS 1207b, Chauvin et al., 2004) and would change the population parameters significantly. Even assuming our shallowest mass-ratio distribution (a field age of 0.9 Gyr), our posterior binary BD populations have a low mass ratio ($q < 0.6$) companion frequency of $1.0_{-0.6}^{+1.4}\%$ (and even lower for older ages). Similarly to wide companions, we therefore conclude that low-mass companions like 2MASS 1207b are not drawn from the same distribution as most BD binary pairs in the field, again suggesting evolution since 2MASS 1207b is young.

3.6.2 Implications for Binary Formation

Current state of the art large-scale simulations still do not have the resolution necessary to produce and evolve a statistically significant population of binary BD systems. Bate (2012) calculates a multiplicity fraction of 0.27 ± 0.15 for primaries in the mass range $0.07 - 0.10 M_\odot$ though the uncertainty is large due to small number statistics. Using the slightly wider mass range of $0.03 - 0.20 M_\odot$ they calculate a multiplicity fraction of 0.20 ± 0.05 , slightly

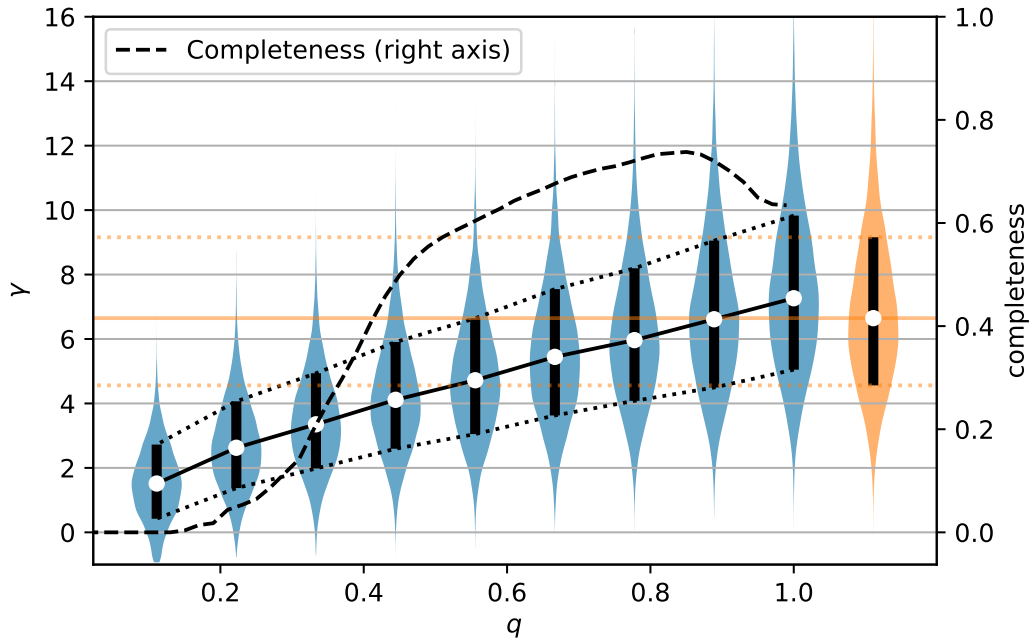


Figure 3.9: Posteriors of the mass-ratio power-law index, γ , as a function of the mass ratio, q , of an injected additional binary detection assuming a field age of 1.9 Gyr. The additional detection was injected at the median of the previously derived separation distribution (2.2 au) so as to have the least possible effect on other parameters. The orange distribution is with no injected detection. White points and black vertical lines correspond to the median and $\pm 1\sigma$ (central 68%) values. The black dashed line (right vertical axis) shows the completeness of our survey as a function of q . Similar figures for other assumed field ages are shown in Appendix J and are available online at Factor & Kraus (2022c).

larger than our value by 1.5σ . While Bate (2012) only produced three binary systems with primary masses less than $0.1M_\odot$, these three systems have a clear bias toward equal masses ($q = 0.61, 0.94$, and 0.98) though only one system had stopped accreting. Guszejnov et al. (2017) also finds a strong preference for equal mass companions for primaries of mass $\sim 0.1M_\odot$. Fitting the data presented in Figure 5 of Guszejnov et al. (2017) we measure a power-law index of $\gamma \sim 4.0 - 4.4$ for their two models. This is consistent at $\sim 1\sigma$ with our four smallest (youngest) values and similar to the γ value measured by Burgasser et al. (2007).

On the other hand, the separation distribution of the three binary BD systems from Bate (2012) seems to be heavily influenced by the resolution of the simulation. The semimajor axis of these systems are 10.6, 26.1, and 36.4 au, two of which are in the rare population of systems with $a > 20$ au. Only the 10.6 au system has stopped accreting though, so the other two systems may tighten their orbits with more time. This was also seen in the simulations of Bate (2009), that BD binaries evolve with time, and observationally by Close et al. (2007) and Burgasser et al. (2007), that young wide binaries are disrupted by dynamical interactions in the formation environment. De Furio et al. (2022b) studied binary BDs in the Orion Nebula Cluster (ONC) and also found a wide companion fraction significantly above that of the field population, hinting at the importance of dynamical interactions. The simulations presented in Bate (2009) did produce a large number of BD binaries, though again the separation distribution is likely affected by the resolution of the

simulation. This distribution had a median separation of 10 au, significantly wider the mean of our separation distribution at $2.2_{-1.0}^{+1.2}$ au. This simulation also uses an older equation of state and no radiative feedback. Guszejnov et al. (2017) does not discuss the semimajor axis distribution for their BD binaries.

Another possible formation pathway for BD binaries is the decay of triple systems (Reipurth & Clarke, 2001). Umbreit et al. (2005) ran an analytical simulation of BD formation integrating the accretion and dynamical evolution of initially triple BD systems. They very accurately reproduce the semimajor axis distribution, with no systems wider than 20 au and a peak at $a \sim 3$ au, within 1σ of our mean separation and significantly smaller than values from previous studies. Fitting a log-normal distribution to the data shown in Figure 8 of Umbreit et al. (2005) we measure a $\sigma_{\log(a)} \sim 0.2$ dex, more consistent with previous studies than with our value. Umbreit et al. (2005) do not discuss the mass-ratio distribution or companion frequency of their simulations so it is hard to compare our results in more detail. Reipurth & Mikkola (2015) also conducted a numerical simulation of disintegrating triples which roughly reproduced the observed semimajor axis distribution and strong preference for equal mass companions. However, their simulations produced a significantly higher binary fraction than observed in the field, which they attribute to ignoring the breakup of higher-order multiples. If brown dwarfs form primarily through dynamical interactions such as ejection they should have higher velocities and a larger spatial distribution than stars, which is not seen in young star forming regions (Luhman, 2012). This will be interesting

to revisit in the Gaia era with higher precision astrometry.

Close et al. (2003) created a toy model and noted a simple scaling between the mean separation and mass of binaries in the BD and stellar mass regime (i.e. $a_{\odot, \text{BD}} \sim 0.13a_{\odot, \text{TTau}}$ and $M_{\text{BD}} \sim 0.13M_{\text{TTau}}$). They argue that this scale factor is set by fragmentation. However, they noted that while mean separation does scale with mass, the width of the distribution does not. Scaling the entire stellar mass separation distribution down to BD mass would produce an extremely large number of wide binaries ($\sim 26\%$ of systems with $a > 40$ au) which is inconsistent with the observed population. What they do not take into account is the binding energy of these systems. Scaling both the mass and separation does not conserve binding energy since there is a mass squared term. Since the binding energy also decreases with mass, the widest systems would be more likely to be disrupted, thus narrowing the semimajor axis distribution. Assuming binding energy dominates the survival of wide binary systems, scaling the above $\sim 26\%$ of systems in “wide” orbits using binding energy rather than just separation would produce the same fraction of systems wider than ~ 5 au. Our posterior distribution produces a companion fraction of $3 \pm 1\%$ for systems wider than 5 au, which is $28^{+11}_{-9}\%$ of systems (from a total companion fraction of $0.11^{+0.04}_{-0.03}$), consistent with this toy model. This also explains the decrease in companion frequency from the stellar mass to BD regime since dynamical interactions tend to disrupt weakly bound systems, rather than hardening them (Kroupa et al., 2001; Kroupa & Burkert, 2001; Parker & Goodwin, 2011).

This also helps to explain the preference for equal mass companions in BD binary systems. Stellar mass binaries have a much flatter companion mass distribution, scaling both masses down would maintain this. Since low mass companions have lower binding energy, a low q BD binary is bound more weakly than a similarly scaled stellar mass system, and would be more easily removed thus biasing the mass-ratio distribution toward $q = 1$. If this is the case tight binaries should have a flatter mass-ratio distribution than wider binaries. This test requires more detections than we have in our survey and would likely need to consider spectral binaries and directly imaged systems together.

A process where dynamical interactions play a role naturally implies evolution in the BD binary population. As discussed above, Burgasser et al. (2007) noted that younger BD binary systems have significantly wider separation and flatter mass-ratio distributions, suggesting that wide and low mass companions are initially present from fragmentation but are then removed by field age. Targeted surveys have discovered a number of young benchmark BD binary systems with no direct analogs in the field: Oph 11 (Close et al., 2007), USco CTIO-108 (Béjar et al., 2008), FU Tau (Luhman et al., 2009), 2MASS J0441+2301 (Todorov et al., 2010), Oph 98 (Fontanive et al., 2020). De Furio et al. (2022b) also found a wide (> 20 au) companion fraction in the young ONC that is significantly higher than the field.

If dynamical processing does play a significant role in BD binary formation the star-formation environment should have a significant effect on the re-

sulting binary demographics. Many star-forming environments are even denser than the ONC (Lada & Lada, 2003) and would therefore process binary systems more heavily than the ONC. It is possible that much of the field sample came from those environments and would consequently have fewer wide systems. While observing binaries in denser regions than the ONC is difficult due to their distance, looking at the other end of the scale—in the sparsest regions (e.g. Taurus)—is attainable with current archival datasets (e.g. Kraus et al., 2005; Kraus et al., 2006) and is a prime candidate for reanalysis using higher resolution techniques such as KPI. Currently, tight binaries ($\lesssim 10$ au) can only be detected in the field and are not resolvable at the distances of young clusters. Thus, caution must be taken when comparing populations at tight separations as any comparison in this regime is based on extrapolation. For example, using precise PSF template fitting De Furio et al. (2022a) achieved sensitivity down to λ/D or ~ 10 au at the distance of the ONC and found that a log-normal and power-law separation distribution fit the observed binary M dwarf population equally well. KPI (on the aforementioned observations of nearby star forming regions or on future JWST datasets) could reach separations previously inaccessible to classical imaging techniques and enable longitudinal (i.e. age based) demographic studies at separations approaching the mean of the semimajor axis distribution.

We thus find it likely that turbulent fragmentation provides the initial conditions for binary BD formation while dynamical evolution modifies the population, dissolving low-mass, wide, and potentially high order multiple

systems. This leaves behind a population of tight and equal mass companions as seen in our and other studies. As shown by Burgasser et al. (2003c), using the framework of Weinberg et al. (1987), only the widest ($\gtrsim 185$ au for BD mass, Close et al., 2003) systems are significantly effected by interactions with other field stars, GMCs, and the galactic potential, so this truncation must take place relatively quickly, before the birth cluster dissolves. De Furio et al. (2022b) used the same framework to calculate the lifetime of a wide separation (100 au) BD-BD binary in the ONC to be ~ 5 Myr ($\sim 4 - 20 \times$ shorter than stellar mass binaries) while Kroupa et al. (2003) showed the lifetime of wide (> 20 au) VLM binaries in a similar environment to be ~ 1 Myr, both demonstrating the importance of early-time dynamical interactions while the system can still interact with cluster members rather than field stars. Assuming that $\sim 10\%$ of BD objects form in low mass clusters (and are thus less disrupted), Close et al. (2007) predict that $\sim 0.6 \pm 0.3\%$ of field BD binaries will be wide ($a > 100$ au) which is consistent with their measurement of $f_{\text{BD}_{\text{wide} \& \text{old}}} \sim 0.3 \pm 0.1\%$. The question is still open as to why BD binaries seem to be more tightly bound than solar type binaries as noted by Close et al. (2003) and Burgasser et al. (2007).

3.7 Summary

In this work, we have derived physical properties of the the KPI companion detections and limits from Factor & Kraus (2022a) and fit them with a binary population model. We apply Bayesian modeling techniques adapted

from Allen (2007), Kraus et al. (2011), and Kraus & Hillenbrand (2012), using a Binomial likelihood function to compare our detections to the model distribution. Since we directly consider the detection limits of each observation, this method allows us (and the authors of previous studies) to use all of the observations in a data-set rather than building a volume limited sample and throwing out precious detections. However, we must still account for the Malmquist bias included in our magnitude limited sample which we implement by inflating the number of binaries in our population model according to their contrast ratio. We fit the demographic parameters to our observations using `emcee` (Foreman-Mackey et al., 2013) using wide and flat priors and find more information is required to obtain physically possible results. We thus incorporate limits on the unresolved tight-binary population from Blake et al. (2010) and recover values roughly consistent with previous studies though differing in some interesting ways.

While the overall companion frequency of our underlying population is smaller than previous studies ($F = 0.11_{-0.03}^{+0.04}$), the companion frequency of the observed population (without inflating our model to account for Malmquist bias, $F = 0.22_{-0.06}^{+0.07}$) is consistent with previous studies. Our separation distribution is closer ($\bar{\rho} = 2.2_{-1.0}^{+1.2}$ au) and more broad ($\sigma_{\log(\rho)} = 0.58_{-0.13}^{+0.20}$ dex) than previous studies, likely due to the higher resolution of our detection method (KPI) and our incorporation of wide priors with a limit on the unresolved population. Our mass-ratio power-law index ($\gamma = 4.0_{-1.5}^{+1.7}$ to 11_{-3}^{+4} depending on the assumed field age of 0.9 to 3.1 Gyr, respectively) is stronger than previous

studies. We attribute this to our different derivation of mass from observed flux and our greater sensitivity to, and non detection of, lower mass (higher contrast) companions.

We confirm the trends seen in observational studies over the past two decades of decreasing binary fraction with decreasing mass and a strong preference for tight equal-mass systems in the sub-stellar regime. We attribute this to turbulent fragmentation setting the initial conditions followed by a relatively brief period of dynamical evolution, pruning off the widest and lowest mass companions, before the birth cluster dissolves. Unfortunately, large-scale simulations of star formation are still lacking the resolution to produce a large number of binary BDs and thus lack the statistical weight to examine these processes in great detail. We encourage those working on these simulations to keep pushing to higher resolution since these results will provide valuable metrics to compare with observations.

3.8 Acknowledgments

We thank Trent Dupuy and Will Best for useful discussions about this work, and many others who have offered their thoughts at conferences. We also thank the anonymous referee for their helpful feedback which improved the manuscript. This work was funded by *HST* program AR-14561. This work has benefited from The UltracoolSheet (at <http://bit.ly/UltracoolSheet>, Best et al., 2020a), maintained by Will Best, Trent Dupuy, Michael Liu, Rob Siverd, and Zhoujian Zhang, and developed from compilations by Dupuy &

Liu (2012), Dupuy & Kraus (2013), Liu et al. (2016), Best et al. (2018), and Best et al. (2021). This work has made use of data from the European Space Agency (ESA) mission *Gaia* (<https://www.cosmos.esa.int/gaia>), processed by the *Gaia* Data Processing and Analysis Consortium (DPAC, <https://www.cosmos.esa.int/web/gaia/dpac/consortium>). Funding for the DPAC has been provided by national institutions, in particular the institutions participating in the *Gaia* Multilateral Agreement.

Chapter 4

ACS/HRC Kernel-Phase Interferometry I. New Young Planetary-Mass Objects in Taurus and Upper Scorpius

4.1 Chapter Abstract

We present the results of a binary survey and demographic analysis based on archival *HST*/ACS imaging of substellar objects in Taurus and Upper Scorpius. We have analyzed the images using kernel-phase interferometry, and present 6 new candidate detections at extremely tight separations in addition to 4 previously known companions. We derived physical properties of our sample and performed a demographic analysis of our detections and sensitivity using a Bayesian framework. We find an observed companion frequency, using our 2D detection limits, of $F_{\text{obs}} = 0.24^{+0.10}_{-0.08}$ which is slightly higher than previous studies, consistent with our new detections. We also report a companion frequency of systems wider than 5 au, our survey’s 90% completeness limit, of $F_{\rho > 5 \text{ au}} = 0.17^{+0.07}_{-0.06}$. The demographics of our survey confirm previously seen trends of a strong preference for equal mass binaries (strong mass-ratio power-law index $\gamma = 12^{+5}_{-4}$) and a decreasing companion frequency with decreasing mass. The significant excess of young companions compared to the field indicates that dynamical evolution is an important process. We find that the field

population of wide companions is consistent with a population of wide systems formed only in low density regions and diluted by single systems formed in high density regions.

4.2 Introduction

Binary systems are a common outcome of star formation, and thus a comprehensive theory should reproduce their frequency as well as orbital architectures and mass-ratio distribution (e.g. Duchêne & Kraus, 2013; Offner et al., 2023). Companions form via turbulent fragmentation of a collapsing core (on wide orbits; Bate et al., 2002; Bonnell et al., 2008; Bate, 2009; Offner et al., 2010; Bate, 2012; Guszejnov et al., 2017) or accretion disk fragmentation (at close separations; Stamatellos & Whitworth, 2009) and evolve via dynamical interactions with other bodies (Reipurth & Clarke, 2001). At the low mass end of the initial mass function (IMF), previous observational studies have found a decreasing companion fraction with decreasing mass and a strong preference for tight and equal-mass systems in the substellar mass regime (Factor & Kraus, 2023), also seen in simulations (Bate, 2014). By establishing binary demographics in different environments (high- and low-density star-forming regions) and at different times (still in the birth cluster and at field age), the influence of these distinct processes can be traced toward the ultimate production of the observed population of the Milky Way.

Multiplicity studies of field brown dwarfs and planetary-mass companions (Close et al., 2003; Gizis et al., 2003; Reid et al., 2008a; Allen, 2007)

benefit from the proximity of objects, allowing surveys to probe the inner architecture of systems, but suffer from ambiguous masses since precise ages are difficult to measure and the masses and ages are degenerate (Factor & Kraus, 2022a, 2023). In the field, any specific imprints of early evolution or environmental influences from the birth cluster are washed out as populations mix. However, rare objects (e.g. Radigan et al., 2009; Faherty et al., 2020) are easier to find since the overall population is much larger in number.

Since ages in clusters are much more accurate than in the field, accurate studies of companion mass are possible in these regions (Kraus et al., 2005; Kraus et al., 2006; Kraus & Hillenbrand, 2012; De Furio et al., 2019, 2022b). In addition, lower mass companions are brighter at young ages making planetary mass companions much more accessible for a given contrast limit. Comparisons between binary demographics in the field and in young star-forming regions have hinted that some evolution does occur, finding statistically more wide companions in young regions (Close et al., 2007; Burgasser et al., 2007; Kraus et al., 2011; De Furio et al., 2022b). In addition, comparison between different star-forming regions can illustrate the role stellar density or total mass of the birth cluster plays in the early lives of these systems.

Until recently, studies of substellar multiplicity in young star-forming regions have only been able to resolve wide companions ($\gtrsim 10$ au), sampling only the tail of the separation distribution and leaving the dominant population (i.e. tight binaries) unknown. Interferometry-based analysis techniques, such as non-redundant aperture masking interferometry (NRM or AMI; Kraus

& Ireland, 2012; Sallum et al., 2015; Rizzuto et al., 2016), and advanced point spread function (PSF) fitting techniques (De Furio et al., 2019, 2022b,a) are now opening the space at and below λ/D . Our previous analysis of field brown dwarfs applied an interferometric analysis technique called kernel-phase interferometry (KPI; Martinache, 2010) to archival *HST*/NICMOS imaging (Factor & Kraus, 2022a). KPI is applicable to any suitably high resolution imaging data and can detect companions down to $\sim 0.5\lambda/D$ at high contrasts of $\sim 100 : 1$. In the field, we achieved significant sensitivity to companions at sub-au scales. While optical aberrations will be larger with respect to the observed wavelength, Kernel-phase analysis can also be applied at optical wavelengths for critically-sampled cameras like ACS/HRC, though it has not yet been demonstrated.

In this work we apply KPI (see Section 4.4) to archival *HST*/ACS imaging of the nearby star-forming regions of Taurus-Auriga and Upper Scorpius (see Section 4.3). We present our astrometry and photometry and detection limits (Section 4.5), achieving sensitivity at scales of a few au, and perform a demographic analysis of the population (Section 4.6).

4.3 Observations

4.3.1 Sample Selection

In this work we reanalyze observations of very low mass objects (VL-MOs) in two nearby star-forming regions: Upper Scorpius (USco) and Taurus-Auriga. These two regions are among the nearest star-forming regions, with

only moderate extinction, and thus were among the first places where samples of young brown dwarfs (BDs) were identified. The observations were originally proposed by White (2003) and analyzed, using PSF fitting, in Kraus et al. (2005) and Kraus et al. (2006).

The sample contains 34 VLMOs which were drawn from previous surveys of the regions. The targets in USco were selected from a survey for low-mass members by Ardila et al. (2000). Twelve of the 15 candidate members with spectral types of M5.5 or later were observed in this program. USco 132 and USco 137 have since been determined to be field dwarfs (Muzerolle et al., 2003; Luhman et al., 2018) and thus while we include them in our companion search, we omit them from our demographic analysis.

The VLMOs in Taurus were selected from Briceño et al. (1998); Ardila et al. (2000); Martín et al. (2001); Luhman et al. (2003). All 18 confirmed Taurus members with spectral types later than M5.5 were observed. Four additional targets were also included (V410-Xray-3, V410-Anon-13, GM Tau, and LH 0419+15) based on their likely Taurus membership and spectral type. At the time the observations were proposed (January 2003) this was a complete list of known Taurus members with spectral types later than M5.5. Similar to the two targets discussed above, more recent membership studies of Taurus have determined that LH 0419+15 is not a member (Kraus et al., 2017; Krokowski et al., 2021). While we include it in our image analysis we exclude it from the demographic analysis.

In both regions, membership was originally confirmed spectroscopically

via the detection of lithium absorption, excess H α emission, or low surface gravity, all of which are indicators of youth. More recent studies have confirmed membership using similar spectroscopic techniques in conjunction with highly accurate distance and proper motion measurements from Gaia (Gaia Collaboration et al., 2018, 2021). Targets included in this analysis are listed in Table 4.1 along with their Gaia DR3 ID, RA/Dec from Gaia DR3, unresolved photometry presented in Kraus et al. (2005) and Kraus et al. (2006) (V , i' , and z' magnitudes calculated from the observed F555W, F775W, and F850LP magnitudes, respectively), and the adopted spectral types from Luhman et al. (2017, 2018); Luhman (2022, 2023). We also include Gaia renormalized unit weight error (RUWE).

RUWE can be used as a proxy for the presence of a companion (Lindgren et al., 2018; Belokurov et al., 2020; Wood et al., 2021, Kraus et al. in prep.). Previous studies of field age objects have used a cutoff value of 1.2 to signal the presence of a companion though young stars tend to have a higher RUWE overall so this value is uncertain, especially for young objects (Fitton et al., 2022). The resolved binaries (though not wide enough to be resolved in Gaia) USco-55 and USco-66 both have significantly elevated RUWEs (2.88 and 2.1, respectively). The third companion presented in Kraus et al. (2005), USco-109, was not detected by Kraus & Hillenbrand (2012) and does not have an elevated RUWE (1.10). V410 Xray-3 was resolved by Kraus & Hillenbrand (2012) and also has an elevated RUWE of 1.53. The second companion presented in Kraus et al. (2006), MHO-Tau-8, was not detected by Kraus &

Hillenbrand (2012) but does have a slightly elevated RUWE of 1.35. Other targets in this sample which have slightly elevated RUWE but have not been resolved previously are CFHT-Tau-1 (1.29), CFHT-Tau-2 (1.24), CFHT-Tau-3 (1.31), and KPNO-Tau-14 (1.25). Only one target, KPNO-Tau-12, does not have a RUWE, likely because it is too faint for an astrometric solution ($G = 21.088$, Gaia Collaboration, 2020).

4.3.2 Observations

The images were acquired using the High Resolution Channel of the Advanced Camera for Surveys (ACS/HRC) on the *Hubble Space Telescope* (*HST*). Observations were made using the filters F555W (V), F775W (i'), and F850LP (z') and taken between 07/2003 and 02/2004. Total integration times ranged from 200 to 510 seconds. The camera has a field of view of $29'' \times 25''$ and a pixel size of 28×25 mas. While the pixels are physically square, ACS/HRC is located far off axis causing large distortion in the 1024×1024 detector. This will be discussed in detail in Section 4.4. The λ/D diffraction limit at each of the observed wavelengths is ~ 46 , 66, and 79 mas, respectively or ~ 1.7 , 2.4, and 2.9 pixels. Importantly, the shortest wavelength filter is not Nyquist sampled.

Reduced images were downloaded from the MAST archive. The flat-fielded but undrizzled images were used in this analysis to avoid any smearing of the diffraction pattern caused by the drizzling algorithm. One downside of this is that cosmic ray hits and other bad pixels are present in the images. For

Table 4.1. Upper-Scorpius and Taurus-Auriga Target Sample

Name	Gaia DR3 ID	RA	dec	V (F555W)	i' (F775W)	z' (F850LP)	Sr-T (ref.) ^b	RUWE
USco-53 ^a	6243124436675563904	16 02 45.75	-23 04 50.97	18.07 ± 0.02	15.29 ± 0.04	14.20 ± 0.06	M5.5 (1.8)	2.878
USco-66 ^a	62463263624389449728	16 01 49.55	-23 51 08.27	18.18 ± 0.015	15.577 ± 0.014	14.596 ± 0.007	M5 (8)	2.014
USco-67	6237173192548569600	15 59 25.92	-23 05 08.25	18.47 ± 0.002	15.52 ± 0.001	14.32 ± 0.001	M5.75 (8)	1.085
USco-75	62437088906793775744	16 00 30.23	-23 34 45.62	18.71 ± 0.002	15.80 ± 0.001	14.61 ± 0.001	M5.5 (8)	1.102
USco-100	6243676322792317952	16 02 04.31	-20 50 42.58	19.09 ± 0.002	15.99 ± 0.001	14.73 ± 0.001	M5.75 (8)	1.116
USco-109 ^a	6243132751731497728	16 01 19.15	-23 06 39.45	19.84 ± 0.03	16.75 ± 0.04	15.52 ± 0.016	M5.5 (8)	1.100
USco-112	624667567831565824	16 00 26.70	-20 56 31.62	18.04 ± 0.001 ^c	16.15 ± 0.001	15.17 ± 0.001	M5.25 (8)	1.020
USco-128	6247077943051415680	15 59 11.35	-23 38 00.36	21.29 ± 0.007	17.79 ± 0.002	16.34 ± 0.002	M6.5 (8)	1.050
USco-130	624714366769257472	15 59 43.66	-20 14 39.68	21.39 ± 0.008	17.80 ± 0.002	16.30 ± 0.002	M6.5 (8)	1.123
USco-131	6243186456003514752	16 00 19.44	-22 56 28.90	21.98 ± 0.011	18.22 ± 0.002	16.67 ± 0.002	M7 (8)	1.020
USco-132	6247185523394594816	15 59 37.77	-22 54 13.84	22.11 ± 0.013	18.31 ± 0.002	16.59 ± 0.002	M7. (1.8)	1.167
USco-137	62370312481683334336	15 56 47.99	-23 47 42.53	22.92 ± 0.023	19.27 ± 0.004	17.75 ± 0.003	M7 (1.8)	1.068
CFHT-Tau-1	1452937045877650988	04 15 28	+22 30 30.76	23.427 ± 0.026	18.612 ± 0.003	16.612 ± 0.002	M6 (9)	1.295
CFHT-Tau-2	145220066117853696	04 36 10.38	+22 59 56.00	22.520 ± 0.014	18.112 ± 0.002	16.307 ± 0.002	M7.5 (3)	1.242
CFHT-Tau-3	145217379737969992	04 36 38.93	+22 58 11.85	21.654 ± 0.009	17.970 ± 0.002	16.119 ± 0.001	M7.75 (3)	1.001
CFHT-Tau-4	145200156688543104	04 39 47.48	+26 01 40.69	21.556 ± 0.008	16.920 ± 0.001	14.951 ± 0.001	M7 (3)	1.307
KPNO-Tau-1	163165738856771200	04 15 14.72	+28 00 09.38	24.063 ± 0.044	19.572 ± 0.004	17.596 ± 0.003	M8.5 (3)	1.089
KPNO-Tau-2	1644953232918666624	04 18 51.15	+28 14 33.30	21.376 ± 0.007	17.670 ± 0.002	16.074 ± 0.001	M7.5 (3)	0.985
KPNO-Tau-3	15128387045877650988	04 26 24.39	+26 24 13.72	20.239 ± 0.004	16.959 ± 0.001	15.484 ± 0.001	M6 (3)	1.203
KPNO-Tau-4	1512650029547593936	04 27 28.00	+26 12 05.09	24.722 ± 0.071	20.072 ± 0.006	17.897 ± 0.004	M9.5 (3)	1.135
KPNO-Tau-5	151327159721125888	04 29 45.67	+26 30 46.56	19.690 ± 0.004	16.226 ± 0.001	14.706 ± 0.001	M7.5 (3)	1.133
KPNO-Tau-6	151296579553731456	04 30 07.25	+26 08 20.71	22.292 ± 0.012	19.097 ± 0.003	17.301 ± 0.003	M8.5 (3)	1.055
KPNO-Tau-7	151102790628500288	04 30 57.20	+26 26 39.55	22.068 ± 0.011	18.358 ± 0.002	16.661 ± 0.002	M8.25 (3)	1.095
KPNO-Tau-8	145133763615830784	04 35 41.84	+22 34 31.59	19.261 ± 0.003	16.147 ± 0.001	14.863 ± 0.001	M5.75 (3)	0.963
KPNO-Tau-9	145299339585095424	04 35 51.43	+22 49 11.85	24.918 ± 0.084	20.035 ± 0.006	18.056 ± 0.004	M8.5 (3)	1.199
KPNO-Tau-12	164487734085106800	04 19 01.28	+28 02 04.14	23.228 ± 0.023	20.781 ± 0.009	18.998 ± 0.006	M9 (6)	1.249
KPNO-Tau-14	351130591477573632	04 33 07.81	+26 16 06.56	20.735 ± 0.007	16.297 ± 0.001	14.502 ± 0.001	M6 (6)	1.249
MHO-Tau-4	331429923867740176	04 31 24.06	+18 00 21.46	18.678 ± 0.002	15.246 ± 0.001	13.732 ± 0.001	M7 (10)	1.048
MHO-Tau-5	3314309890186259712	04 32 16.07	+18 12 46.38	17.595 ± 0.001	14.489 ± 0.001	13.114 ± 0.001	M6 (3)	1.125
MHO-Tau-8	3314780133963632000	04 33 01.97	+24 26 00.07	17.951 ± 0.002	14.453 ± 0.001	12.976 ± 0.001	M6 (3)	1.353
LH 0419+15	33119838305743428224	04 22 30.76	+15 26 31.01	21.835 ± 0.010	18.028 ± 0.002	16.488 ± 0.002	M6.5 (7)	1.139
V410 X-ray-3	164513022853486160	04 18 07.97	+28 26 03.67	18.319 ± 0.002	15.046 ± 0.001	13.629 ± 0.001	M6.25 (2,4,5,9,10)	1.540
V410 Anon-13	1645192763285752	04 18 17.11	+28 28 41.93	22.175 ± 0.012	17.782 ± 0.002	15.732 ± 0.001	M5.75 (3)	1.123
GM Tau	148449845165337600	04 38 21.34	+26 09 13.78	17.577 ± 0.001	15.169 ± 0.001	13.908 ± 0.001	M5 (4,7)	1.080

Note. — Photometry reported in Kraus et al. (2005) for USco targets and Kraus et al. (2006) for Tauris, converted from *HST* F555W, F775W, and F850LP filter magnitudes to V , i' , and z' . Uncertainties are statistical; systematic uncertainties due to aperture corrections and conversion to standard systems are ~ 0.03 magnitudes.

References. — 1: Ardila et al. (2000), 2: Briceño et al. (1998), 3: Briceño et al. (2002), 4: Herczeg & Hillenbrand (2014), 5:Luhman et al. (1998), 6: Luhman et al. (2003), 7:Luhman et al. (2017), 8: Luhman et al. (2018), 9: Strom & Strom (1994), 10: White & Basri (2003)

^aUnresolved photometry was calculated by combining component magnitudes.

^bSpectral types are the adopted types from Luhman et al. (2017, 2018); Luhman (2022, 2023) with individual citations referenced.

^cThe V magnitude for U Sco-112 is anomalously bright. (See Kraus et al., 2005, Footnote 2)

the exposure times used in these observations $\lesssim 1.5\%$ of pixels are affected by cosmic ray hits or charge diffusion from hits in neighboring pixels (Hathi et al., 2023, Section 4.3.5). We experimented with two methods for removing these and other bad pixels which are discussed further in Section 4.4.

We also must be mindful of other artifacts present in the HRC detector such as a halo and two spikes (parallel to the x axis) in the redder filters caused by photons passing through the detector and scattering off of the mounting substrate. Images of these artifacts can be found in section 5.6.5 of the ACS Instrument Handbook (Hathi et al., 2023). Further discussion of the halo can be found in Gilliland & Riess (2003, for ACS/WFC) and with respect to photometry in Sirianni et al. (2005) and Bohlin (2016). These artifacts should calibrate out as they are consistent between science target and calibrator.

4.4 Methods

Kernel-phase interferometry, first described by Martinache (2010), uses a set of self calibrating observables similar to closure phases used in non-redundant aperture masking interferometry (NRM or AMI). The phases measured by an interfemometer (redundant or non-redundant) can be written as a linear combination of the inherent phase due to source geometry and error terms contributed by each aperture. Assuming small phase errors (diffraction limited imaging or high Strehl), these terms can be removed using a linear combination of self-calibrating baselines, leaving behind the true source phase.

This framework can be summarized by the following two equations.

The first describes the relationship between the vector of measured phases, Φ , the vector of true source phases, Φ_0 , and the vector of phase errors contributed by each aperture, ϕ :

$$\Phi = \Phi_0 + \mathbf{R}^{-1} \cdot \mathbf{A} \cdot \phi, \quad (4.1)$$

where \mathbf{R} is a matrix encoding the redundancy of each baseline and \mathbf{A} is a matrix encoding the relationship between the apertures and the baselines. In the case of a non-redundant aperture mask the \mathbf{R} matrix is the identity matrix while in the unobscured (i.e. redundant) case it weights baselines based on their redundancy.

The error terms can be removed by multiplying by \mathbf{K} , the kernel of \mathbf{A} , such that $\mathbf{K} \cdot \mathbf{A} = \mathbf{0}$. This matrix can be calculated using singular value decomposition. The error independent kernel phases can then be calculated from the measured phases by

$$\mathbf{K} \cdot \mathbf{R} \cdot \Phi = \mathbf{K} \cdot \mathbf{R} \cdot \Phi_0. \quad (4.2)$$

The analysis pipeline used in this work is similar to that described in Factor & Kraus (2022a) though differs slightly in some crucial aspects.

4.4.1 Aperture model

We first build a model of the *HST*/ACS aperture using XAOSIM, which includes the mirror pads that were ignored in our previous work. We then use XARA (Martinache, 2010, 2013b; Martinache et al., 2020) to create the relevant matrices from this model. We chose to use XARA for this step, rather

than our previous Argus code (Factor, 2022), since it is more widely used by the community and it already implemented the DFT used in the following step, which is required when dealing with the distorted images produced by ACS/HRC. Based on tests that we ran using a set of simple aperture geometries, Argus and XARA produce the same matrices. We also now use the gray aperture model described in Martinache et al. (2020), which is not implemented in Argus. A grey aperture model includes the covering fraction of the subaperture as a “transmission” factor. This enables a higher fidelity model, reducing the impact of systematic errors, without drastically increasing the resolution of the model which increases computation time.

We chose an aperture model with a spacing of 12 cm, resulting in 315 apertures and 622 distinct baselines producing 308 kernel phases. This aperture spacing imposes a limit on the maximum separation before aliasing occurs of $0.^{\circ}48$, well beyond the range where classical PSF fitting techniques work as well or better than KPI. Our aperture model and resulting sampled baselines are shown in Figure 4.1.

4.4.2 Image Preparation

The next step in the pipeline is preparing the images before we calculate kernel phases. Since ACS/HRC is 25° off axis, there are large distortions in the images, causing the physically square detector to project a roughly parallelogram shape on the sky. To account for the geometric distortion of the images, we adopt the distortion solution from the TinyTim package (Krist

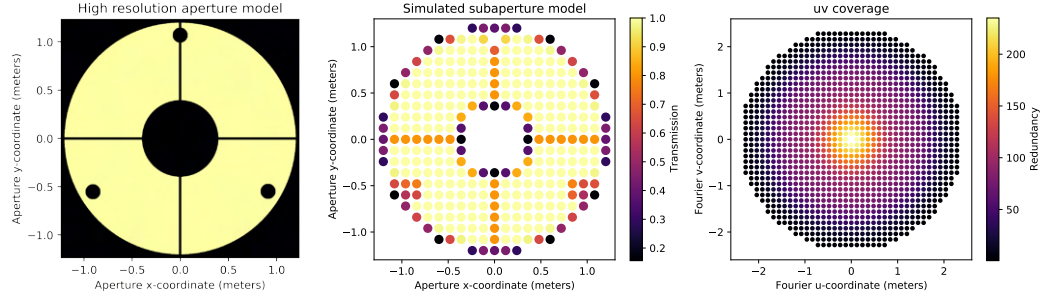


Figure 4.1: Left: high resolution model of the *HST* pupil (including the secondary obscuration, spider arms, and mirror pads) as seen by ACS/HRC. Center: Simulated subapertures colored by their transparency. Right: *uv* coverage (i.e. the baselines corresponding to the simulated interferometer in the center panel.) colored by their redundancy.

et al., 2011) which uses a 3rd degree polynomial to map X–Y pixel location to the V2–V3 axis of the telescope field of view. Higher order features are captured in the distortion solution presented in Anderson & King (2004), and should be considered in future analysis, though the polynomial solution is good to 0.1 pixels. They also note that the ACS/HRC PSF does not change shape appreciably with location on the CCD or with time. This makes calibration more accurate.

We calculate the flux centroid (using the distortion corrected pixel locations) and offset the V2–V3 coordinate values to the location of the target and window the data using a super-Gaussian with $\sigma = 25\lambda/D$ to reduce the sensitivity to readout noise (as done in Kraus et al., 2008).

As in our previous analysis we interpolate over bad pixels using the median of the surrounding valid pixel values. Bad pixels (including hot, cold, cosmic rays, etc.) were identified using the data quality flags present in the

reduced image fits files. Since we now use a DFT it is possible to use any image shape, even one with “holes” in it. We therefore also experimented with leaving out bad pixels from the DFT, rather than potentially injecting signal into a location which had bad data (See Section 4.3 of Factor & Kraus, 2022a). We found that interpolating over bad pixels gave deeper sensitivity than removing them before applying the Fourier transform. It is possible that the reverse may be true depending on the location of a bad pixel that is particularly close to the target. We will explore this further with respect to *JWST* imaging (Factor & Kraus, 2021b).

4.4.3 Kernel-Phase Computation

To calculate the interferometric visibilities, or more specifically the Fourier phases, we must calculate a Fourier transform. In our previous analysis of *HST*/NICMOS data we utilized a fast Fourier transform (FFT) which requires regularly sampled data. Due to the previously discussed distortions, ACS/HRC images are not sampled on a rectilinear grid (when projected on the sky). Instead we have modified XARA, which already implemented a DFT matrix, to allow the user to supply the sky-coordinate grid rather than assuming that the grid is rectilinear. We use this modified version of XARA to calculate phases from the images and kernel phases using the previously described matrices derived from the aperture model.

4.4.4 Binary Modeling

We model the extracted kernel phases using the single and double point source models implemented in Argus and fit using PyMultiNest (Buchner et al., 2014). These model prescriptions differ from those included in XARA in that they are centered on the flux centroid, rather than the primary source. We believe this is the more physical choice for unresolved targets.

We first fit all sources, except the 5 reported as binaries in previous studies, with a single point source model (a simple position offset) to account for any inaccuracies in the image based flux centroid used to calculate the initial kernel phases. We then recalculate the kernel phases using these updated centroids and these sources become the pool for calibrators used in our final round of fitting.

Calibrators are chosen similarly to Factor & Kraus (2022a) in that we choose the calibrator targets located closest to the science target on the detector. Since the proper motions of these targets were known to much higher precision than the field brown dwarfs we previously analyzed the centering was much more consistent. In future work it may be better to choose the brightest targets as calibrators since all of the science targets are located in the same region of the detector/focal plane.

We then fit this science/calibrator target pair with a single and double point source model and compare the results. Corner plots, showing the posterior distributions of the binary parameters, for the detections determined to

be significant are shown in Figure 4.2 and Appendix K along with a representative image of the target, in the specific filter, and a plot correlating the model and data kernel phases.

We experimented with fitting using the kernel-phase covariance matrix but could not get it to produce accurate results for the known binaries. This is likely due to the relatively small number of images (i.e independent measurements of each kernel phase).

4.4.5 Detection Limits

We calculated detection limits using the same method described in Factor & Kraus (2022a) which we briefly summarize here. We first subtract the best fit single point source model from the science kernel phases, leaving behind only noise (assuming no companion is also present). Before proceeding we scramble the indices of the kernel phases, creating a new instance of the noise with the same statistical properties. We then fit the contrast of a (nonexistent) companion on a fixed grid over separation and PA. This reveals the distribution of companion signals mimicked by noise. The confidence is then calculated using a KDE. For example, the 99% confidence contour is drawn such that 99% of all fits in this grid are outside this contour, moving from the lowest density area outward. This allows us to properly recover the turn-down in sensitivity at extremely tight separations where sensitivity is lost to similar brightness companions (due to loss of asymmetry).

Due to the amount of computation required to run an entire detection

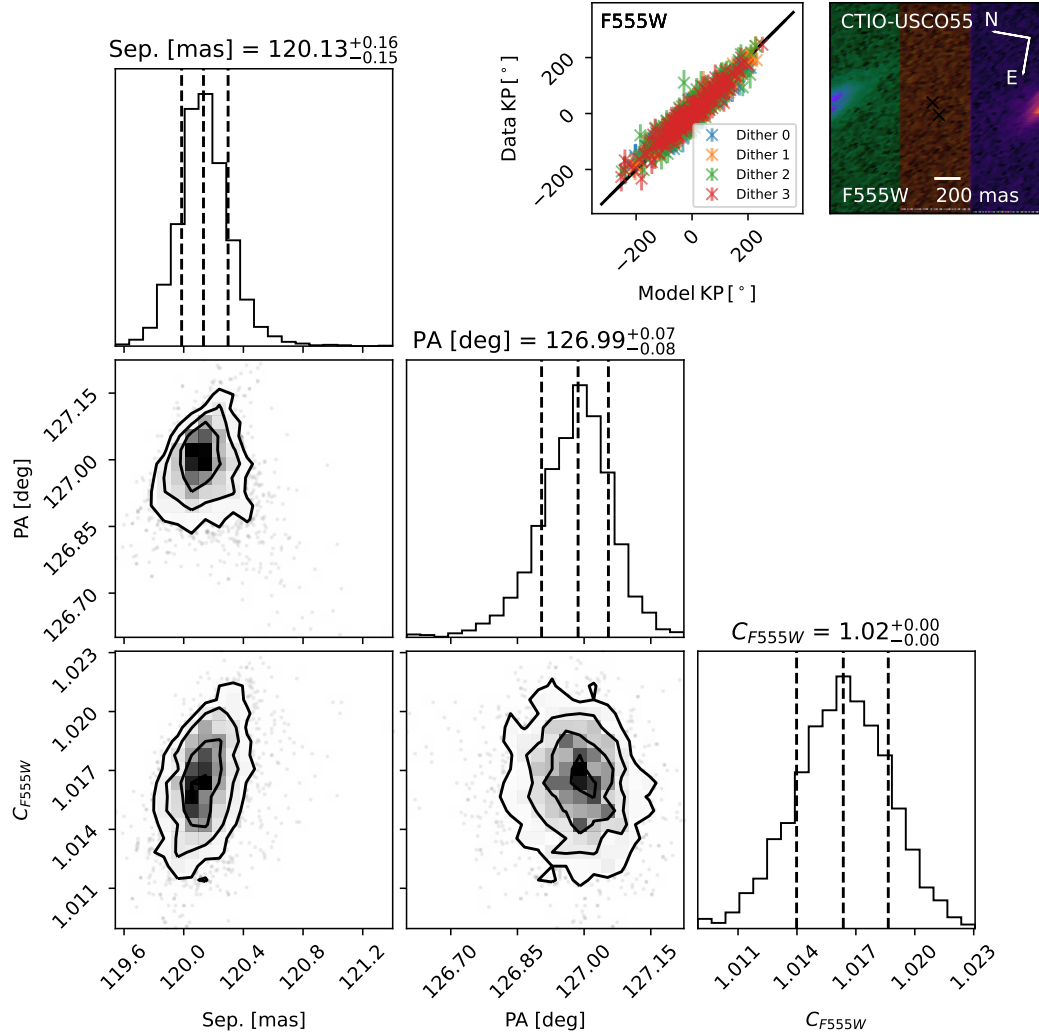


Figure 4.2: Results of fitting a double point source to observations of CTIO-USco55 in F555W (example image shown in the upper right corner with X's showing the position and contrast ratio of the two sources). Lower Left: Corner plot showing the posterior distributions of the binary fit. Dashed lines indicate the median and $\pm 1\sigma$ values. (16th, 50th, and 86th percentiles). Top Center: Data kernel phases plotted against the best-fit model kernel phases indicating a good fit. Similar plots for other detections are shown in Appendix K.

limit grid, only 5 sources are complete at this time. For each of these targets we stacked the 5σ confidence areas. In order to be considered a significant detection a proposed companion would need to be detected in three of five calibrators. We then paired each science target up with the detection limit grid closest in flux and assessed each of the five science target-calibrator pairs according to the previously discussed metric.

We now have 5 fits to the same science target, now assessed to be individually significant or not. We then combined these fits and determined a detection to be significant if it is detected significantly in four of five calibrators and the fit parameters are consistent with each other within $3 \times \sigma$ in contrast and $10 \times \sigma$ in position. This is consistent with our previous work on NICMOS data (Factor & Kraus, 2022a) in that positional parameters show more inter-calibrator variance than contrast. Since we fit each filter separately, if a single filter is determined to be significant then we also report parameters in other filters if they are close but do not pass the previously discussed metric (e.g. 4 significant detections consistent within $5 \times \sigma$ in contrast and $15 \times \sigma$ in position). Best fit astrometry and photometry for significant detections are presented in Table 4.2. The detection limits used to score each individual fit, along with the best fit parameters (colored by their significance), are shown in Figures 4.3 and 4.4 and Appendix L and M. Stacked survey detection limits and detections are shown in Figure 4.5.

Table 4.2. Binary astrometry & photometry

Source	Sep. [mas]	$\sigma_{\text{sys,sep}}$ [mas]	PA [deg]	$\sigma_{\text{sys,PA}}$ [deg]	Filter	Contrast	$\sigma_{\text{sys,C}}$
USco-55	119.76 ± 0.08	0.25	125.53 ± 0.04	0.8	F555W	1.0013 ± 0.0004	0.007
USco-55	120.259 ± 0.018	0.4	127.316 ± 0.012	0.13	F775W	1.2995 ± 0.0010	0.004
USco-55	120.946 ± 0.031	0.4	127.420 ± 0.020	0.032	F850LP	1.3394 ± 0.0018	0.006
USco-66	67.50 ± 0.14	0.8	32.99 ± 0.10	0.30	F555W	1.059 ± 0.006	0.015
USco-66	64.441 ± 0.007	0.0021	40.453 ± 0.019	0.0014	F775W	1.00078 ± 0.00029	0.000032
USco-66	64.57 ± 0.06	0.13	29.53 ± 0.06	0.19	F850LP	1.00006 ± 0.00007	0.00015
MHO-TAU8	36.05 ± 0.15	3.1	277.43 ± 0.28	7	F555W	1.494 ± 0.016	0.130
MHO-TAU8	36.71 ± 0.10	0.8	281.24 ± 0.35	2.3	F775W	1.442 ± 0.015	0.06
MHO-TAU8 ^a	34.63 ± 0.20	1.3	285.0 ± 0.5	3.1	F775W	1.62 ± 0.04	0.6
MHO-TAU8 ^b	34.1 ± 1.7	1.4	286.5 ± 1.1	8	F850LP	1.60 ± 0.35	0.8
V410-XRAY3 ^b	33.9 ± 0.9	4	333.4 ± 1.2	7	F555W	1.71 ± 0.12	1.4
V410-XRAY3	36.33 ± 0.29	1.7	338.53 ± 0.15	1.9	F775W	3.90 ± 0.22	0.9
V410-XRAY3	36.7 ± 0.8	4	346.0 ± 0.9	5	F850LP	3.0 ± 1.0	3.5
New Candidate Companions							
USco-130	45.14 ± 0.09	0.4	324.7 ± 0.8	1.1	F850LP	1.048 ± 0.007	0.0034
USco-131	36.68 ± 0.26	6	174.2 ± 0.9	5	F775W	1.146 ± 0.026	1.2
KPNO-TAU1	28.1 ± 1.7	1.4	134.7 ± 1.3	4	F775W	1.6 ± 0.4	1.4
KPNO-TAU4	45.80 ± 0.30	21	145.5 ± 1.0	24	F850LP	1.106 ± 0.016	5
KPNO-TAU12	39.75 ± 0.18	0.5	244.6 ± 0.6	6	F775W	1.163 ± 0.017	0.08
KPNO-TAU12 ^c	42.7 ± 2.1	0.5	263.3 ± 3.0	3.5	F850LP	1.5 ± 1.1	0.14
MHO-TAU5	39.69 ± 0.25	0.28	145.0 ± 1.1	1.7	F775W	1.32 ± 0.04	0.09

^aFit to only the two short exposures in F775W

^bOnly three significant science-target calibrator pairs were significant though the position matches a significant detection in another filter.

^cOnly two significant science-target calibrator pairs were significant though the position matches a significant detection in another filter.

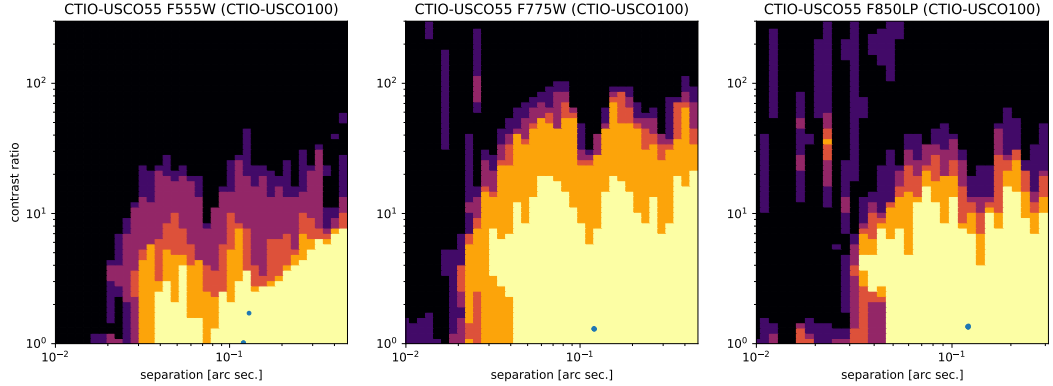


Figure 4.3: Example detection limits on CTIO-USCo-55, a source with a significant detection. The science target is indicated in the title of each panel along with the detection limit grid in parentheses. The color scale is the number of calibrators (0 to 5 and black to yellow) which would significantly ($> 5\sigma$) detect a companion as a function of separation and contrast ratio in the three filters (three columns). Best fit companion parameters are plotted (with error bars) for the 5 calibrators in blue, if significantly detected, and in orange, if not significantly detected. Similar plots for other significant detections are shown in Appendix L.

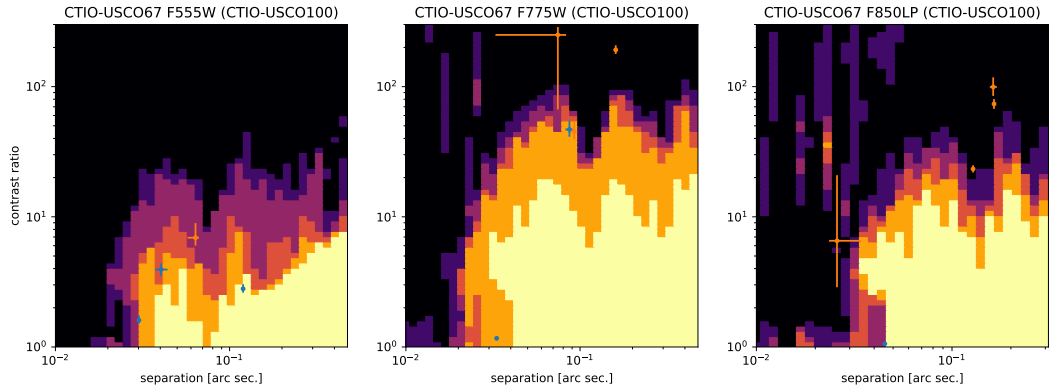


Figure 4.4: Similar to Figure 4.3 but for CTIO-USCo-67, a non significant detection. In this case any fit which was significant was not consistent with the other detections and the target as a whole was determined to be a non-detection. Similar plots for other non-significant detections are shown in Appendix M.

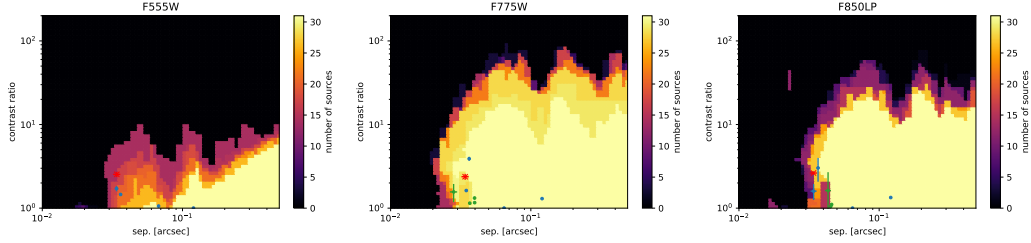


Figure 4.5: Stacked 5σ detection limits as a function of separation for all sources in the survey in the three filters. Blue circles indicate the positions of previously known detected companions and green circles indicate the positions of new detections. The red x indicates the non-detection of CTIO-USSco-109 with photometry and astrometry from Kraus et al. (2005).

4.4.6 Physical Properties of Binaries

To perform a demographic analysis of detections and detection limits for binary companions we must first convert observed quantities (angular separation and contrast) into physical quantities (projected separation and mass ratio). Distances derived from Gaia eDR3 parallaxes were used (Bailer-Jones et al., 2021; Gaia Collaboration et al., 2021). A single target—KPNO-Tau-12—was too faint to have a parallax in Gaia DR3, or any other survey, so we used the mean and standard deviation of all Taurus members in our sample. In future work it may be possible to tie this source to a specific subgroup from Krolikowski et al. (2021) and assign a more accurate distance.

Converting angular separation to projected separation is as simple as multiplying by the distance to the target. Converting contrast into mass is not as trivial. Since brown dwarf spectral types are not a reliable mass metric, we choose to convert from absolute magnitude to mass using a model dependent

isochrone. We split the unresolved (now absolute) photometry into its constituent parts for a given contrast and convert these component magnitudes into mass using the dusty models from Chabrier et al. (2000); Baraffe et al. (2002). These models give absolute magnitude in i band. We convert the observed F775W magnitudes to this filter using the relation presented in Kraus et al. (2006): $m_{775} - m_{i'} = +0.07 \pm 0.03$. We use the 10 Myr isochrone for USco members (Sullivan & Kraus, 2021) and interpolate between the 1 and 5 Myr grids to derive a 3 Myr isochrone for Taurus members (Krolikowski et al., 2021). It may be possible to tie individual members to subgroups of each region, each with its own age, though this will not greatly affect the results and thus we leave it to future work. Physical properties of the detections are presented in Table 4.3 (observed properties were presented in Table 4.2).

4.4.7 Binary Population

We apply the same Bayesian modeling approach used in our previous work (Factor & Kraus, 2023), similar to that of Kraus et al. (2011) and Kraus & Hillenbrand (2012) (adapted from Allen, 2007), to infer the underlying binary population from our sample of observations. This technique is particularly suited to the small number of detections at close separations since there is no need to throw out data to create a volume limited sample or correct for regions of incompleteness.

The binary population is characterized by a companion frequency F , a power-law mass-ratio distribution with exponent γ , and a log-normal projected

Table 4.3. Binary properties

Source	Distance [pc]	$M_{\text{ir}} \text{ (F775W)}$	C_{F775}	Proj. sep. [au]	Mass ratio q	$M_A \text{ [} M_{\text{Jup}} \text{]}$	$M_B \text{ [} M_{\text{Jup}} \text{]}$
CTIO-USC055	102.1 ± 1.9	10.25 ± 0.06	1.2995 ± 0.0010	12.28 ± 0.23	0.87 ± 0.05	32.1 ± 1.8	27.9 ± 0.7
CTIO-USC066	145.0 ± 2.6	9.77 ± 0.04	1.00078 ± 0.00029	9.35 ± 0.17	1.00 ± 0.04	45.0 ± 1.2	44.9 ± 1.2
CTIO-USC0131	146 ± 8	12.39 ± 0.12	1.146 ± 0.026	5.37 ± 0.30	0.975 ± 0.029	16.93 ± 0.35	16.50 ± 0.35
KPNO-TAU1	131 ± 11	13.99 ± 0.18	1.6 ± 0.4	3.7 ± 0.4	0.92 ± 0.06	8.2 ± 0.5	7.59 ± 0.31
KPNO-TAU12	144 ± 18 ^a	14.99 ± 0.27	1.163 ± 0.017	5.7 ± 0.7	0.98 ± 0.05	6.90 ± 0.26	6.75 ± 0.25
MHO-TAU5	146.9 ± 1.1	8.653 ± 0.016	1.32 ± 0.04	5.83 ± 0.06	0.959 ± 0.004	27.86 ± 0.08	26.72 ± 0.09
MHO-TAU8	127.6 ± 1.3	8.924 ± 0.021	1.62 ± 0.04	4.42 ± 0.05	0.927 ± 0.005	27.18 ± 0.09	25.20 ± 0.10
V410-XRAY3	123.8 ± 1.5	9.583 ± 0.026	3.90 ± 0.22	4.50 ± 0.06	0.783 ± 0.009	25.73 ± 0.11	20.15 ± 0.20

^a Distance adopted from the mean and standard deviation of all Taurus members included in this sample.

separation (ρ) distribution with mean $\overline{\log(\rho)}$ and standard deviation $\sigma_{\log(\rho)}$. As in Factor & Kraus (2023) and Kraus et al. (2011), we choose to model the separation distribution in terms of the observed projected separation (ρ) rather than the underlying semimajor axis (a)¹. The binary population model is then used in our likelihood function by comparing it to the observations over a grid $(\Delta \log(\rho), \Delta q)$ in parameter space. The expected companion frequency in a bin is given by the probability R according to:

$$R(\log(\rho), q | F, \gamma, \overline{\log(\rho)}, \sigma_{\log(\rho)}) \Delta \log(\rho) \Delta q = \frac{\gamma + 1}{\sqrt{2\pi} \sigma_{\log(\rho)}} F q^\gamma \exp\left(-\frac{(\log(\rho) - \overline{\log(\rho)})^2}{2\sigma_{\log(\rho)}^2}\right) \Delta \log \rho \Delta q \quad (4.3)$$

The Bayesian likelihood in a given bin $(\log(\rho), q)$ with N_{det} companions detected and N_{sen} targets which were sensitive to such a companion is then the Binomial likelihood:

$$P(N_{\text{det}}, N_{\text{sen}} | F, \gamma, \overline{\log(\rho)}, \sigma_{\log(\rho)}) \propto R^{N_{\text{det}}} \times (1 - R)^{(N_{\text{sen}} - N_{\text{det}})}. \quad (4.4)$$

The grid is derived from the overall survey detections and sensitivity and is shown in Figure 4.6 along with the binary systems. The full grid spans $\log(\rho) = -4$ to 3 in 175 bins and $q = 0$ to 1 in 50 bins. Since our calculated limits only extend to 0.5 arcsec we adopt a 100% detection threshold of $\Delta m = 6.5$ magnitudes for all separations > 0.5 arcsec. This is a conservative estimate

¹This avoids making an assumption about the eccentricity distribution which may change with future observations. Converting ρ to a can be done using a simple conversion factor calculated using montecarlo simulations of projected orbits. For very low-mass binaries $a/\rho = 1.16_{-0.31}^{+0.81}$, for no discovery bias, or as low as $a/\rho = 0.85_{-0.14}^{+0.11}$, for a survey with an inner working angle comparable to a (Dupuy & Liu, 2011).

of the sensitivity of the Kraus et al. (2005); Kraus et al. (2006) analysis. The $\log(\rho)$ axis of our grid is much larger than the region occupied by our detections (our detections span a range of ~ 75 bins) to give our detection limits (where we are sensitive but did not detect any companions) leverage over the model parameters.

This likelihood function is then passed to a fitting routine, in our case `emcee` (Foreman-Mackey et al., 2013), which implemented the affine invariant sampler described in Goodman & Weare (2010). We ran the fit using 64 “walkers” for 10,000 steps (discarding the first 1,000 for “burn-in”), exceeding 50 autocorrelation times for all four parameters while only running for a few minutes.

We ran the fit with uninformed (wide and flat) priors on all four parameters ($F = 0$ to 2.5 , $\gamma = -1$ to 20 , $\overline{\log(\rho)} = -4$ to 3 , and $\sigma_{\log(\rho)} = 0$ to 4). This produced an interesting binary distribution, though one that is inconsistent with the theorized population. We discuss this further in Section 4.5.3.

4.5 Results

4.5.1 Binary Detections

We have detected companions around 10 targets in our sample of 34 sources. We confirm and refine astrometry of 4 previously known targets, two of which are well resolved in *HST*/ACS and two of which are well below the diffraction limit. We do not recover a companion around one previously reported binary (CTIO-USco-109). With our increased sensitivity tocompan-

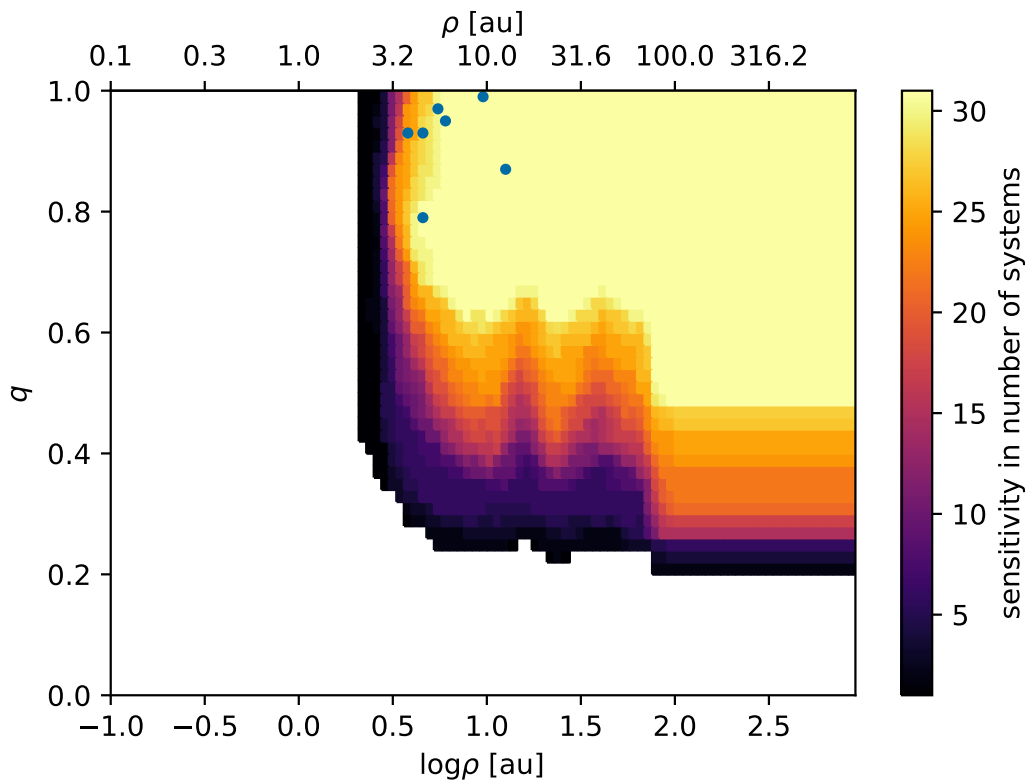


Figure 4.6: Stacked detection limits, in units of number of systems, as a function of projected separation, ρ , in au and mass ratio, q , using an age of 3 Myr for Taurus and 10 Myr for USco (similar to Figure 4.5, though now in physical units rather than observational units). Circles show detected companions. We set a conservative detection limit at separations $> 0''.5$ (where our KPI pipeline is not sensitive) of $\Delta i' = 6.5$ from Kraus et al. (2005); Kraus et al. (2006).

ions below the diffraction limit, we report 6 new candidate tight separation companions. Astrometry and photometry for the companions are presented in Table 4.2. Posteriors, kernel-phase correlation plots, and postage stamp images for each target are shown in Figure 4.2 and Appendix K.

4.5.1.1 Known Binary Detections

The four targets in our sample which were known to be binaries all generally agree with previously published astrometry and photometry. CTIO-USco-55 is an almost equal brightness (in F555W, though slightly higher contrast in F775W and F850LP) binary and thus it is not surprising that our PA is 180° degrees off from that of Kraus et al. (2005), though it agrees with that of Kraus & Hillenbrand (2012) based on AO imaging at K band. Our F555W contrast is significantly lower (closer to equal brightness) than that of Kraus et al. (2005). CTIO-USco-66 is almost equal brightness in all three filters (where PSF fitting gave slightly higher contrast than KPI in F775W and F850LP) and has a slightly tighter separation than the PSF fitting based astrometry. Comparison with photometry from Kraus & Hillenbrand (2012) appears to show significant orbital motion between JD-2452862.6 and JD-2453772 (08/11/2023 and 02/07/2006) in both separation ($+ \sim 10$ mas) and PA ($+ \sim 8^\circ$). Our derived mass ratios for both of these sources are consistent with Kraus et al. (2005) though our projected separations are both slightly tighter due to more accurate Gaia based distances.

The two known binaries in this sample of Taurus, MHO-Tau-8 and

V410-Xray-3 reported by Kraus et al. (2006), were well below the diffraction limit and thus our KPI method should be significantly more accurate. Kraus et al. (2006) reported them both to be at a separation of 44 (± 8 and ± 2 mas, respectively) while we report them to be at a slightly tighter separation of ~ 35 mas. Our PA agrees with Kraus et al. (2006) for MHO-Tau-8, though is significantly different for V410-Xray-3. Our PA agrees with that of Kraus & Hillenbrand (2012), so this appears to be an error in Kraus et al. (2006). We believe this error was likely caused by an incorrectly calculated arctan, as our PAs are roughly consistent when reflected over the x-axis. We report both targets as lower contrast than Kraus et al. (2006), though a wider separation and higher contrast is along the separation-contrast degeneracy seen below the diffraction limit (e.g. see Figures K.16–K.18). As stated above, our KPI analysis should be much more accurate for unresolved targets. Our derived mass ratios for these two sources are slightly lower though V410-Xray-3 is still our most extreme q system.

4.5.1.2 Non-detection of a Candidate Binary

Using our current (i.e. preliminary) detection limit metrics, we do not significantly detect a companion to CTIO-USco-109. This target was reported to have a 34 ± 2 mas companion at a PA of 302 ± 3 degrees at a contrast of 2.5 ± 0.2 , 2.4 ± 0.2 , and 2.63 ± 0.8 by Kraus et al. (2005) though it was not detected by Kraus & Hillenbrand (2012) due to poor AO correction. As seen in Figure M.3, we do see a grouping of fits near this separation and approximate

contrast, though offset by $\sim 90^\circ$ in PA (which could due be another arctan error, see previous discussion of V410-Xray-3). As our detection limit grid is unfinished at this time (see Section 4.4.5), this may become a significant or marginal detection using our final metric as this candidate is right on the edge of our inner working angle.

4.5.1.3 New Binary Detections

We present 6 new candidate companions using our current (i.e. preliminary) detection limit grid and metric. Three targets are detected only in F775W (CTIO-USco-131, KPNO-Tau1, and MHO-Tau-5) and two are detected only in F850LP (CTIO-USco-130 and KPNO-Tau-4) while one target (KPNO-Tau-12) is detected in F775W and marginally in F850LP (two tightly grouped target-calibrator pairs consistent with the astrometry in F775W). All of these targets are well below the diffraction limit and range from 28–45 mas in separation.

CTIO-USco-130 has four target-calibrator pairs which are grouped extremely tightly indicating a strong detection in F850LP. A companion at this separation (45 mas) should be detectable in F775W though the source is much fainter in F775W than in F850LP. KPNO-Tau-4 is similar to CTIO-USco-130 in that it has a tight grouping of three target-calibrator pairs (with two further away with large error bars) in F580LP but no similar grouping, and thus no detection, in F775W. The tightness of this grouping is indicative of a good detection, though this may change with the full detection limit grid.

Conversely, CTIO-USco-131 has four target-calibrator pairs grouped much more loosely in F775W and no detection in F850LP. While this source passes our current metric for a detection, it is marginal. KPNO-Tau-1 is similar to CTIO-USco-131 with a grouping of four target-calibrator pairs near the inner working angle of F775W with no detection in F850LP. Again, while this source passes our current metric for a detection, it is marginal. If this detection is confirmed with the final detection limit grid, this would be an interesting detection of a 3.7 ± 0.4 au projected separation binary with a mass ratio of $q = 0.92 \pm 0.06$ and component masses of $M_A = 8.2 \pm 0.5 M_{\text{Jup}}$ and $M_B = 7.6 \pm 0.3 M_{\text{Jup}}$.

MHO-Tau-5 has a tight grouping of all five target-calibrator pairs showing a confident detection in F775W. At this contrast and separation (Sep.= 39.7 ± 0.3 mas and $C_{\text{F775W}} = 1.32 \pm 0.04$), and using the currently available detection limit grids, a detection in F850LP is not feasible. MHO-Tau-5 is one of the brightest sources in this sample. While the *HST* data is not flagged as saturated it was close to the limit so Kraus et al. (2006) decided to only fit the shorter of the two exposure lengths used in the program. We fit both separately and only saw the signal in the long exposure fits. KPI has been demonstrated on saturated data (Laugier et al., 2019) though this does not appear to be required as no pixels are flagged as saturated. This new tight separation (Proj. Sep.= 5.83 ± 0.06 au) binary has a mass ratio of $q = 0.959 \pm 0.004$ with component masses of $M_A = 27.86 \pm 0.08 M_{\text{Jup}}$ and $M_B = 26.72 \pm 0.09 M_{\text{Jup}}$.

Finally, KPNO-Tau-12 shows a tight grouping of all five target-calibrator pairs in F775W and two in F850LP near the same position. This is the faintest target in our sample and thus the images are low signal to noise. Additionally, there is a cosmic ray hit near the science target in one of the four images in F775W. Thus, for this detection to be considered real, we must rerun the fits excluding the anomalous image, though the co-located marginal detection in F850LP lends some evidence to the detection being real. If this target continues to be significant with the full detection limit grid and excluding the anomalous image, this would be the second lowest mass BD binary currently known: $q = 0.98$ with component masses of $M_A = 6.90 \pm 0.26 M_{\text{Jup}}$ and $M_B = 6.75 \pm 0.25 M_{\text{Jup}}$ at a projected separation of 5.7 ± 0.7 au. The lowest mass system is 2MASS 1119-1137, a $3.7^{+1.2}_{-0.9} M_{\text{Jup}}$ with a 3.6 au projected separation (Best et al., 2017). The mass was calculated using hot start models and, based on an 82% probability of membership in TWA, a 10 Myr age. This source is a much higher confidence member of a group, though Taurus is also more distant. The faintness of this target makes followup difficult, though not impossible.

4.5.2 Detection Limits

The stacked survey detection limits and detections shown in Figure 4.5 illustrate the strengths and weaknesses of the KPI technique when applied to ACS/HRC. Unsurprisingly, the sensitivity in F555W is by far the worst. The objects observed in this program are very red and thus the SNR is low in this

filter. Additionally, the ~ 25 mas pixel size is at the Nyquist sampling limit for that wavelength. F775W appears to be the most sensitive and has a good trade-off between increased signal but not too much loss of resolution with a longer/redder wavelength. F850LP shows good sensitivity overall though is less sensitive than F775W at tight separations, due to the larger diffraction pattern, and overall at high contrast likely due to the detector artifacts seen in the reddest filters (previously discussed in Section 4.3.2). We will present detection limits for each target, summarizing the plots in table form, when the final detection limit grids are complete.

4.5.3 Binary Demographics at a Young Age

As discussed in Section 4.3.1, three of the 34 targets observed in this program have since been deemed to be non-members of Taurus or USco. Thus, our demographics sample consists of the 31 remaining sources. The eight binaries included in our demographic analysis are those with significant detections in F775W, and whose properties are listed in Table 4.3. Figure 4.7 shows the 1- and 2D posteriors of our demographic model, with a summary of the median and 68% credible intervals for each of the hyper-parameters given in Table 4.4. We also report the observed companion fraction, F_{obs} , calculated by applying our survey detection limits to the modeled distribution, as well as the wide companion fraction made with a few different separation cuts (relevant to other studies discussed below). The full 2D binary population is shown in the left panel of Figure 4.8 beside our raw sensitivity and the observed population

(correcting for sensitivity) along with our detections.

Since our closest separation detections are located at the inner working angle of our survey, we are unable to constrain the unresolved companion distribution. In other words, we are unable to attribute a decrease in the number of observed tight separation companions to a turn-down in the underlying population or a decrease in sensitivity. We encountered a similar issue when modeling the demographics of field age BDs in Factor & Kraus (2023). In our previous work, we placed a prior on the unresolved population based on an RV survey (Blake et al., 2010). Unfortunately, a comparable survey, specifically in the mass and age range of our sample, does not exist. Thus the posterior parameter distribution is dominated by a large and unconstrained companion fraction (F) with a median separation ($\overline{\log(\rho)}$) below the inner working angle of our survey. The observed companion frequency (F_{obs}), and those with separation cuts ($F_{\rho>X_{\text{au}}}$), are more relevant and illustrative parameters than the overall companion fraction (F).

The observed and inferred binary probability density as a function of projected separation (marginalized over mass ratio q) is shown in Figure 4.9. Histogram error-bars are drawn according to Burgasser et al. (2003c) and agree well with the “observed” distribution drawn by applying the survey sensitivity to the companion distribution. The effect of an unconstrained population of unresolved companions can clearly be seen as a steep rise in the inferred population at separations below our sensitivity limit.

Unlike in our previous work on field age brown dwarfs, the age of our

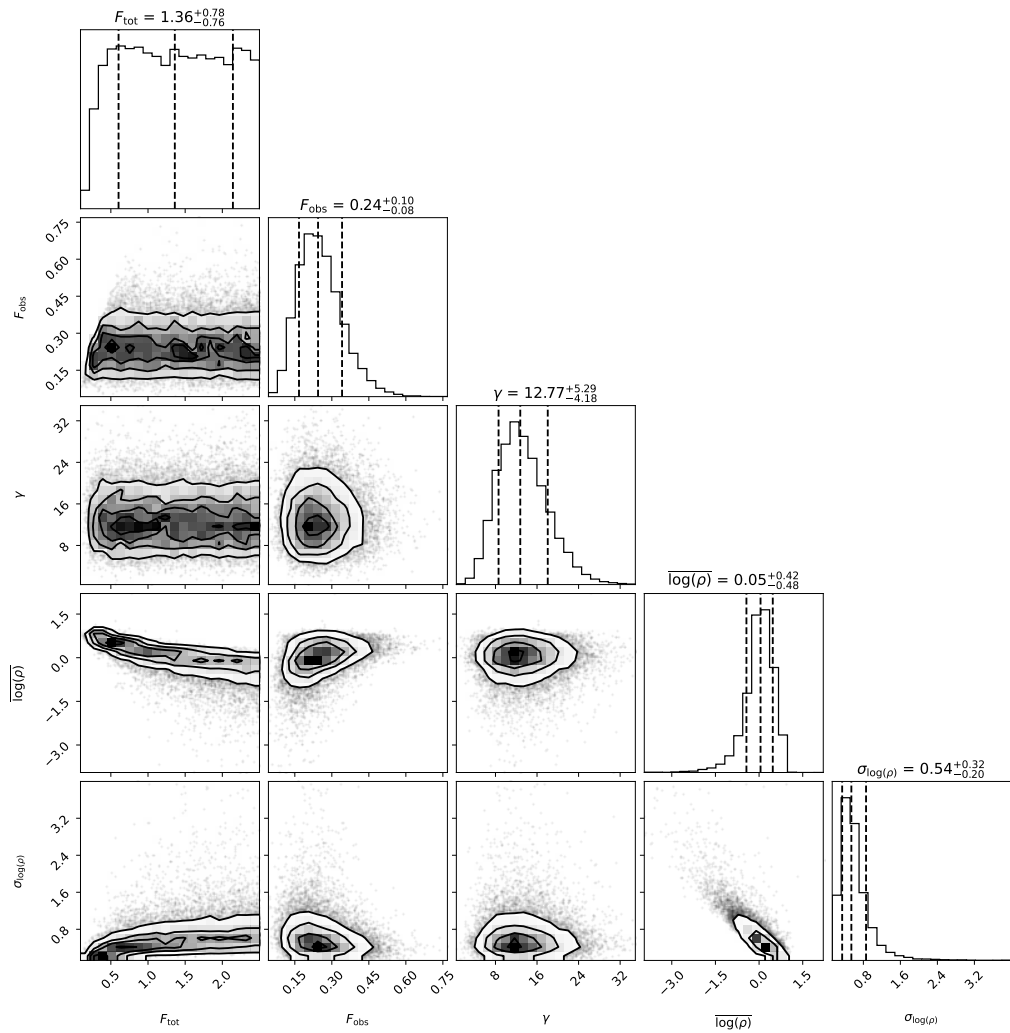


Figure 4.7: Corner plot showing the 1- and 2D posteriors of our demographic fit. Dashed lines indicate the median and $\pm 1\sigma$ (16th, 50th, and 84th percentile) values (given in Table 4.4).

Table 4.4. Binary Population Parameters

Fit Parameters		Measured Statistics	
Parameter	Value	Parameter	Value
$F_{\text{tot}}^{\text{a}}$	1.4 ± 0.8	$F_{\text{obs}}^{\text{b}}$	$0.24^{+0.10}_{-0.08}$
γ	12^{+5}_{-4}	$F_{\rho>4\text{au}}$	$0.20^{+0.08}_{-0.06}$
$\overline{\log(\rho)}$	$0.1^{+0.4}_{-0.5}$	$F_{\rho>5\text{au}}^{\text{c}}$	$0.17^{+0.07}_{-0.06}$
$\sigma_{\log(\rho)}$	$0.5^{+0.3}_{-0.2}$	$F_{\rho>10\text{au}}$	$0.05^{+0.05}_{-0.03}$

Note. — Values presented here are median and central 68% credible intervals.

^aThe median and central 68% confidence intervals are not good metrics as the posterior on F is relatively flat over the span of the allowed parameters (see Figure 4.7).

^bCalculated by applying our 2D sensitivity limits to the posterior distribution and marginalizing.

^cOur survey is 90% complete at this separation.

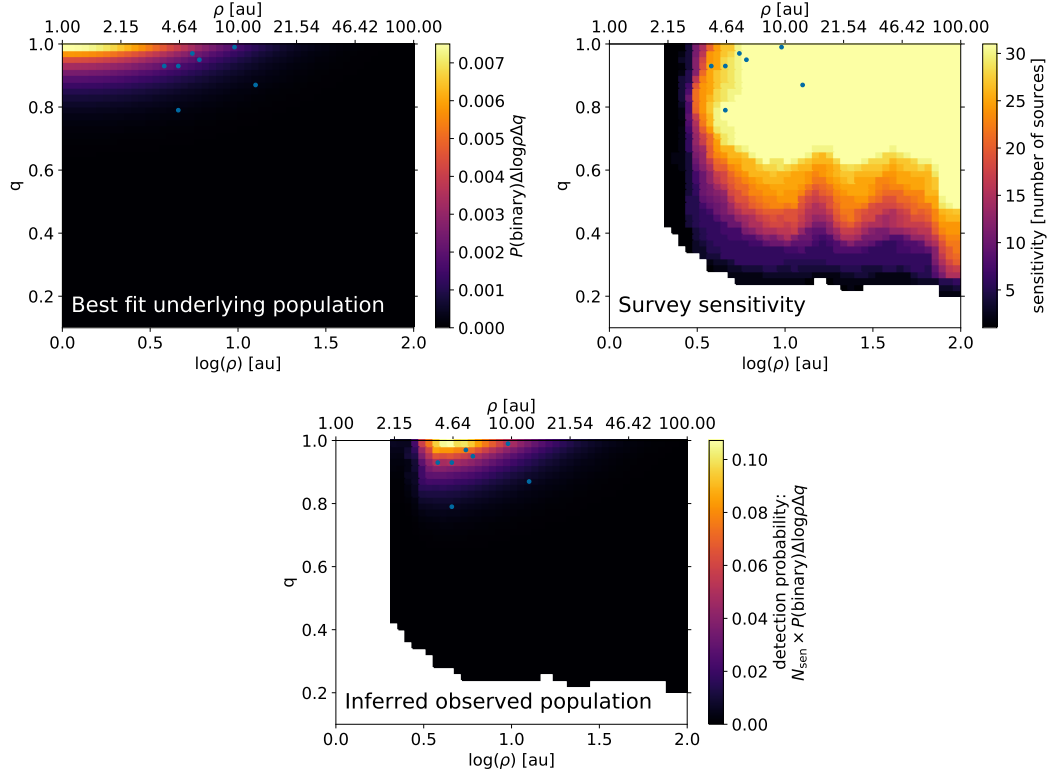


Figure 4.8: The progression from underlying population and survey sensitivity to observed population. Blue points indicate detected companions. *Top left:* Underlying companion population produced from the median values of our fit. *Top right:* Survey sensitivity in units of number of targets. *Bottom center:* Observed population (i.e. the inferred probability that we should detect a companion in a given bin), calculated by applying our survey sensitivity to the population.

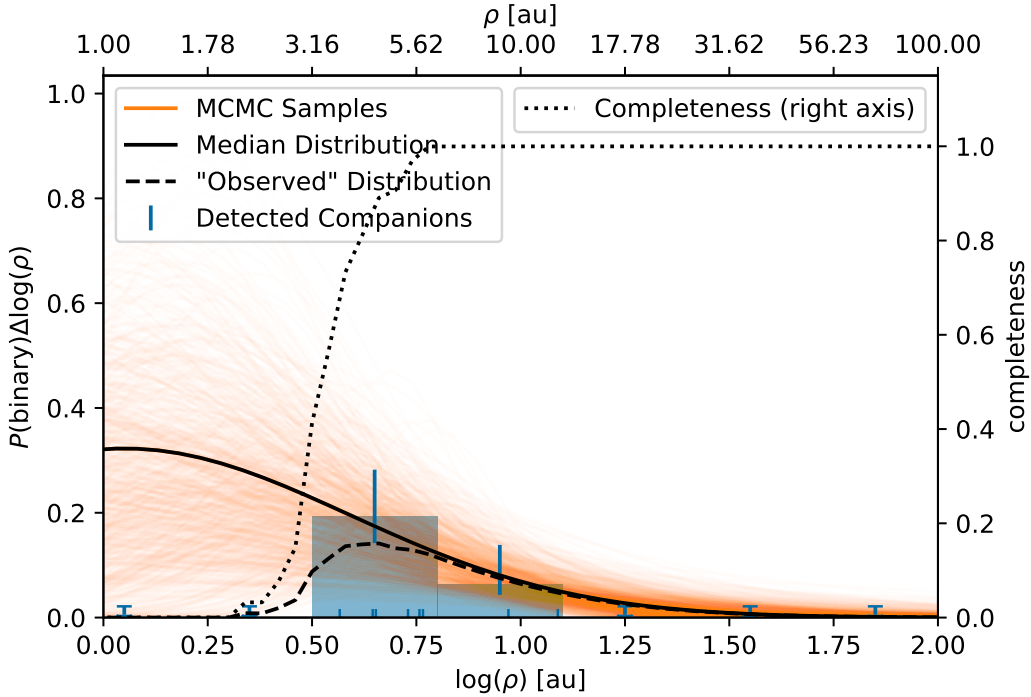


Figure 4.9: Binary population as a function of projected separation. The blue histogram shows the detected companion separations and error bars calculated using Burgasser et al. (2003c) with dashes below showing the un-binned values. Orange curves are 1000 companion probability densities drawn from the posterior distributions using the informed prior while the solid black curve is drawn using the median parameters ($F = 1.4 \pm 0.8$, $\log(\rho) = 0.1^{+0.4}_{-0.5}$, $\sigma_{\log(\rho)} = 0.5^{+0.03}_{-0.02}$, i.e the top left panel of Figure 4.8 marginalized over q). The dashed line shows the “observed” distribution (bottom center panel of Figure 4.8), calculated by multiplying the underlying binary-population distribution by our sensitivity (shown in Figure 4.6 or the top right panel of Figure 4.8). The black dotted line is the completeness fraction (right vertical axis), the ratio between the black solid and dashed lines or equivalently the marginalized and normalized sensitivity.

sample(s) is well known. Thus we ran our population model for a single set of masses/mass ratios. Figure 4.10 shows the binary fraction as a function of mass ratio (for $\rho > 3$ au). Once again, the “observed” distribution (median posterior distribution times sensitivity) matches well with the histogram of detected companions. As opposed to the separation distribution (shown in Figure 4.9), our sensitivity is relatively constant well beyond the region of parameter space inhabited by our detections so no additional information is needed to prevent the fit from producing distributions with a large population of faint undetectable companions. In this case, a slight decrease in sensitivity to equal mass (and thus equal brightness) companions is apparent, characteristic of the KPI technique due to a loss of asymmetry.

4.6 Discussion

4.6.1 Demographics in the Context of Previous Surveys

Unsurprisingly, as we detected new tight-separation companions, our measured companion frequency is higher than that of previous analyses of these observations. Kraus et al. (2005) reports a binary fraction of $F = 0.25^{+0.16}_{-0.09}$ for USco (3 of 12 targets) while Kraus et al. (2006) reports a binary fraction of $F = 0.09^{+0.10}_{-0.03}$ for Taurus (2 of 22 targets) and a combined frequency of $F = 0.15^{+0.08}_{-0.04}$, all for $a \gtrsim 4$ au. Our observed companion frequency, calculated by applying our sensitivity limits to the median modeled population, is $F_{\text{obs}} = 0.24^{+0.10}_{-0.08}$ while restricting to (projected) separations greater than 4 au, to compare with the above values, we measure $F_{\rho>4\text{au}} = 0.20^{+0.08}_{-0.06}$. Our value is

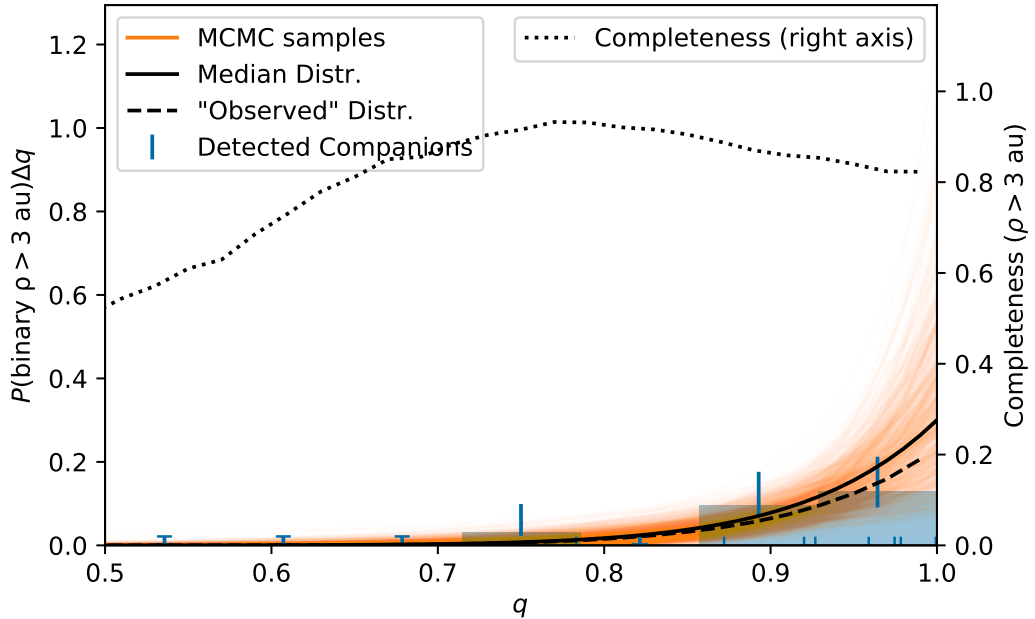


Figure 4.10: Similar to Figure 4.9 but as a function of mass ratio. Mass ratios are derived median power-law index of $\gamma = 12^{+5}_{-4}$ and overall companion frequency of $F_{\rho>3\text{au}} = 0.28^{+0.12}_{-0.09}$.

slightly but not significantly higher than their combined frequency.

Comparing our results to the lowest mass bin of Kraus & Hillenbrand (2012), which is just above the mass of the targets in this survey, shows a similarly large F which is degenerate with $\overline{\log(\rho)}$ and trends higher with tighter median separation. Our $\sigma_{\log(\rho)}$ is consistent with their value while our median separation is slightly tighter, which is to be expected given our analysis method, though with large error-bars. Our sample does not include any wide (> 20 au) binaries, which Kraus & Hillenbrand (2012) note to appear to be more likely to be high mass ratio ($q < 0.5$). When limiting their sample to close ($\rho < 20$ au) binaries they find a power-law index of $\gamma = 4.0^{+1.9}_{-1.6}$ which continues the trend of stronger power-law index with decreasing mass. Our mass-ratio power-law index is even higher, $\gamma = 12.4^{+5}_{-4}$, strengthening the previously discussed trend.

4.6.2 Comparison to Orion and the Field Population

While the physics of binary formation is likely to be more-or-less universal, environment can still play a role in the evolution of binary systems. Mass of the birth cluster, and more specifically the resulting stellar density, would have a significant affect on the amount of dynamical processing and the number of systems which survive until field age. In the following section, we compare the binary demographics of low density star-forming regions of Taurus and USco, presented in this work, to that of the young high density region of Orion, presented in De Furio et al. (2022b,a), and the field age BD

population, presented in Factor & Kraus (2023).

As previously stated, our sample does not include any wide separation binaries (our widest system is USco-55 at $\rho = 12.3 \pm 0.2$ au). Thus, comparing our work to the surveys of Orion by De Furio et al. (2022b,a) should not be leaned on too heavily. De Furio et al. (2022b) report a sub-stellar ($0.012 - 0.1 M_{\odot}$) binary frequency of $F = 0.12^{+0.06}_{-0.032}$ for systems with mass ratio $q > 0.5$ and projected separation $20 < \rho < 200$ au. In a higher mass bin ($0.08 - 0.7 M_{\odot}$) De Furio et al. (2022a) were able to access slightly tighter separations of down to 10 au over all mass ratios and reported a similar companion frequency of $F = 0.13^{+0.05}_{-0.03}$. Applying similar cuts to a marginalization of our model population gives companion frequencies of $F_{q>0.5,\rho>20\text{au}} = 0.011^{+0.027}_{-0.009}$ and $F_{\rho>10\text{au}} = 0.05^{+0.05}_{-0.03}$, respectively. It is worth emphasizing that our values are based on an observed sample with one or no detections in the specified regime and a population model heavily skewed toward unresolved ($\rho < 3$ au) systems. With a larger sample, and one not so tightly focused on close-separation companions, more insight could be gained on the potentially different populations of wide companions.

Luckily, a more complete sample of wide systems exists for young clusters and the field, to which De Furio et al. (2022b) and De Furio et al. (2022a) compare their sample. De Furio et al. (2022b) find that their sample of Orion has a significant excess of wide (23-200 au) sub-stellar binaries compared to that of the Galactic field ($F_{\rho>23\text{au},\text{field}} = 0.09 \pm 0.006$ Reid et al., 2006) ($p = 0.02$). Comparing to the Factor & Kraus (2023) population of field BDs

would have yielded a more significant discrepancy as our 5 au wide companion fraction was only $3 \pm 1\%$. While they do find an excess when comparing the ONC to young populations in Taurus (2 of 60 targets: $F = 0.033^{+0.041}_{-0.011}$) (Kraus et al., 2006; Konopacky et al., 2007; Kraus & Hillenbrand, 2012; Todorov et al., 2014), Chamaeleon I (0 of 24 targets $F = 0.03^{+0.04}_{-0.02}$) (Luhman, 2004), and USco (1 of 40 targets $F = 0.04^{+0.04}_{-0.02}$) (Biller et al., 2011; Kraus & Hillenbrand, 2012) they do not find this excess to be significant ($p \sim 0.05$ or roughly 2σ). In a higher mass range ($0.08 - 0.7 M_{\odot}$), De Furio et al. (2022a) were able to access tighter separations and found a 1.5σ higher companion frequency compared to the field population of Reggiani & Meyer ($F = 0.244^{+0.076}_{-0.053}$, 2013); Susemiekhl & Meyer ($F = 0.244^{+0.076}_{-0.053}$, 2022), while a probability of 0.0002 the ONC is consistent with the Taurus population of Kraus et al. (2011, 12 of 34 targets $F = 0.36 \pm 0.08$).

While we are not able to meaningfully compare our population to the ONC, a more useful comparison is between our population of young objects and the analysis of the field population in Factor & Kraus (2023), which also used the KPI detection method. Figure 4.11 shows the posterior distributions of the young population from this work and the field age population from Factor & Kraus (2023, assuming a field age of 2.4 Gyr to calculate system masses). We choose to show $F_{\rho>5\text{au}}$ as this work is $\gtrsim 90\%$ complete at that separation. The young regions of Taurus and USco (orange) clearly displays an excess of moderate to wide separation ($\rho > 5$ au) companions when compared to the field (blue) at 2.1σ significance. Our mass-ratio power-law index is

consistent with, though slightly higher than, the assumed 2.4 Gyr old field population, though this discrepancy increases with younger assumed field ages. The separation distribution parameters are both consistent though $\overline{\log(\rho)}$ is better constrained in the field population due to our ability to constrain the unresolved population (Blake et al., 2010).

4.6.3 Implications for Binary Formation

Our demographic survey continues to confirm previously seen trends (in observations and simulations, outlined in Offner et al., 2023) of decreasing multiplicity fraction with decreasing mass and a strong preference for equal mass systems. Combining this survey and previous surveys of similar regions, more dense regions, and the field can provide a more holistic view of sub-stellar multiplicity formation. Summarizing the comparisons made above, our analysis of young sub-stellar objects ($0.008 - 0.07 M_{\odot}$) in the low density environments of Taurus and USco shows a significant excess of companions over moderate separations ($\rho > 5$ au) compared to the old field population. The companion frequency of very wide sub-stellar companions ($20 < \rho < 200$ au) in the high-density star-forming region of Orion is also significantly higher than the field though only moderately higher than the young low-density star-forming regions of Taurus, Cha I, and USco De Furio et al. (2022b). In the slightly higher mass range of $0.08 - 0.7 M_{\odot}$ De Furio et al. (2022a) find a wide ($\rho > 10$ au) companion frequency in the ONC consistent with the field and with fewer companions than Taurus.

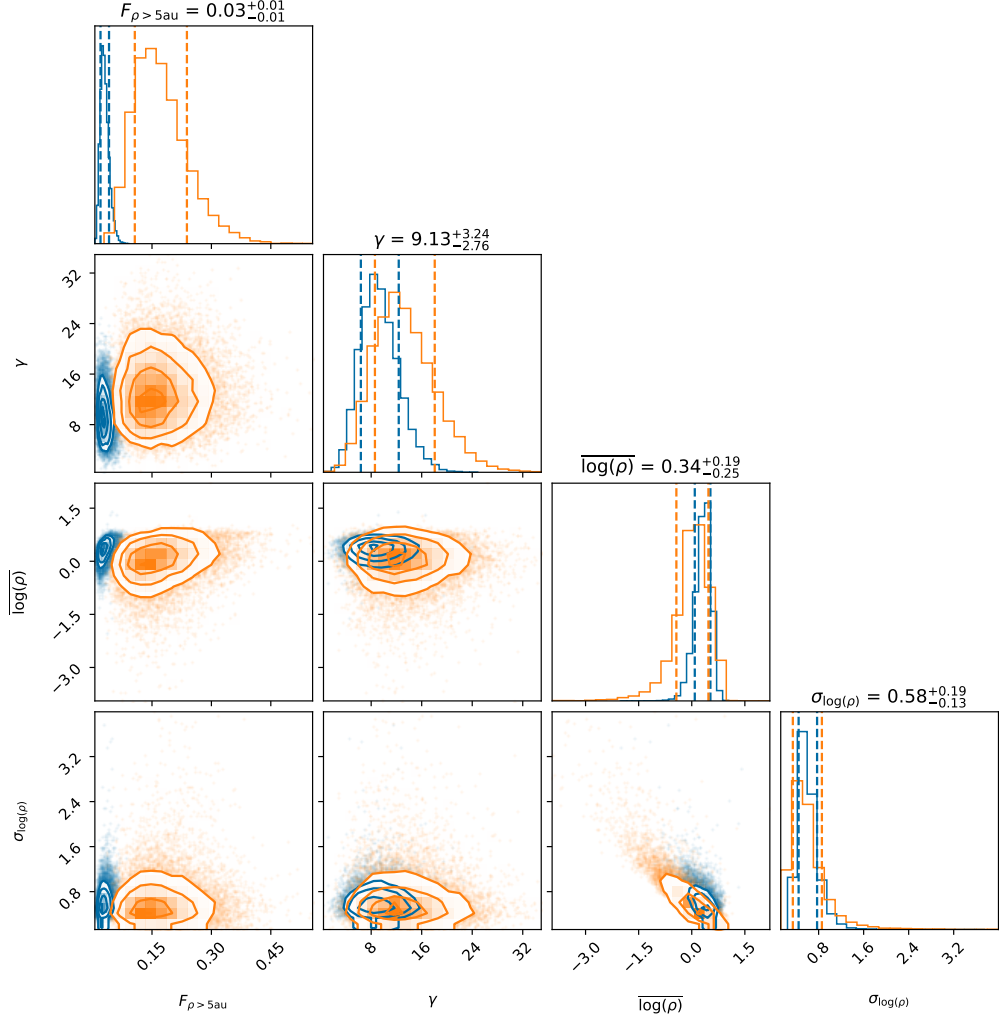


Figure 4.11: Similar to Figure 4.7 but comparing the young (orange, this work) and field age (blue, from Factor & Kraus, 2023, assuming a field age of 2.4 Gyr) demographic parameters. We choose to compare $F_{\rho > 5\text{au}}$ where this survey is 90% complete. Dashed lines indicate the central 68% confidence interval. Titles of the figure correspond to the median and $\pm 1\sigma$ (16th, 50th, and 84th percentiles) values for the field age population. Similar values for the young population are as follows and are given in Table 4.4: $F_{\rho > 5\text{au}} = 0.17^{+0.07}_{-0.06}$, $\gamma = 12^{+5}_{-4}$, $\log(\rho) = 0.1^{+0.4}_{-0.5}$, and $\sigma_{\log(\rho)} = 0.5^{+0.3}_{-0.2}$.

These comparisons are all consistent with the previous conclusions of Factor & Kraus (2023) and De Furio et al. (2022b), that wide sub-stellar companions form with higher frequency than seen in the field, but dissolve through dynamical interaction *before the birth cluster dissolves*. Since most field stars were born in massive clusters (such as the ONC, Lada & Lada, 2003), the discrepancy between the field and ONC wide companion population implies some dynamical evolution must occur. The dynamical interaction must take place within the cluster as any potential interaction in the field is not likely to dissolve the system (Weinberg et al., 1987; Burgasser et al., 2003c; Close et al., 2007). Dynamical interactions would have a stronger effect inside more dense clusters, such as the ONC, than in more diffuse clusters such as Taurus. These interactions have been previously shown to preferentially remove companions rather than compacting or hardening their orbits (Kroupa et al., 2001; Kroupa & Burkert, 2001; Parker & Goodwin, 2011)

If we assume the most extreme case, that all wide ($\rho > 10$ au) companions in the field were born in diffuse clusters (or similarly that all wide companions born in dense regions are removed by the time the birth cluster dissolves), we can calculate the expected wide companion frequency based on our young sample and compare it to the observed field frequency as done in Close et al. (2007) for BDs and Patience et al. (2002) for stellar binaries. The wide companion frequency of our sample is $F_{\rho>10\text{au}} = 0.05^{+0.05}_{-0.03}$. When diluted by 90% to account for the fraction of stars formed in massive clusters (Lada & Lada, 2003) this produces a predicted wide companion frequency in the

field of $F_{\rho>10\text{au}} = 0.005^{+0.005}_{-0.003}$. This matches (within 1σ) the wide companion frequency predicted by Factor & Kraus (2023), $F_{\rho>10\text{au}} = 0.013^{+0.009}_{-0.006}$. The predicted value is marginally less than the field value, which might indicate that rarely some wide systems which are born in dense regions survive until field age or that the 90:10% ratio is slightly off. It is also likely that the 10 au cutoff we used is in fact a more soft transition. Extremely wide separation systems may be present in high density regions like Orion (e.g. two $\rho > 100$ au systems in De Furio et al., 2022b) but can only survive to the field if born in low density regions like Taurus (SCH0359 J0359+2009, FU Tau and others, Martinez & Kraus, 2019; Luhman et al., 2009) (Close et al., 2007). It is also possible that these extremely wide systems are actually unresolved hierarchical multiples (rather than simple binaries) which would increase their system mass, making them more tightly bound than previously thought (e.g. Law et al., 2010; Chomez et al., 2023).

4.7 Summary

In this work we have reanalyzed archival *HST*/ACS imaging of substellar objects in Taurus and Upper Scorpius. We have applied a unique interferometric post-processing analysis technique called kernel-phase interferometry (Martinache, 2010) which is sensitive to faint companions below the diffraction limit. We have used this technique to refine astrometry and photometry of known companions and search for new companions at separations previously inaccessible using classical PSF fitting. We detect 4 previously

known companions in all three filters and do not detect one previous candidate (CTIO-USco-109). We present 6 new candidate detections, one of which is in both F775W and F850LP.

We derived physical properties of our sample using Gaia DR3 parallaxes (Bailer-Jones et al., 2021; Gaia Collaboration et al., 2021) and DUSTY isochrones (Chabrier et al., 2000; Baraffe et al., 2002). We then performed a demographic analysis of our detections and sensitivity using a Bayesian framework. We find that our population model is dominated by a high frequency of unresolved companions. We thus report our inferred companion frequency with a cut on separation. Our observed companion frequency (using our 2D detection limits) is $F_{\text{obs}} = 0.24^{+0.10}_{-0.08}$ which is slightly higher than previous studies, consistent with our new detections. Our survey is 90% complete at a separation of 5 au and we infer a companion frequency for systems wider than this separation of $F_{\rho>5\text{au}} = 0.17^{+0.07}_{-0.06}$. The demographics of our survey confirm previously seen trends of a strong preference for equal mass binaries (strong mass-ratio power-law index $\gamma = 12^{+5}_{-4}$) and a decreasing companion frequency with decreasing mass.

Comparing our results to studies of Orion and the field sheds light on substellar multiplicity formation at newly uncovered separations. We find a significant excess of young companions in low density star forming regions down to our 90% completeness limit of $\rho = 5$ au. Wide ($\rho > 10$ au) substellar binaries are significantly more common in young regions than in the field, indicating that dynamical processing is an important process. We find

that the field population of wide companions is consistent with a population of wide systems formed only in low density regions and diluted by single systems formed in high density regions.

4.8 Acknowledgments

We thank Will Best for useful discussions about this work, and many others who have offered their thoughts at conferences. This work was funded by *HST* program AR-16612. This work has made use of data from the European Space Agency (ESA) mission *Gaia* (<https://www.cosmos.esa.int/gaia>), processed by the *Gaia* Data Processing and Analysis Consortium (DPAC, <https://www.cosmos.esa.int/web/gaia/dpac/consortium>). Funding for the DPAC has been provided by national institutions, in particular the institutions participating in the *Gaia* Multilateral Agreement.

Chapter 5

Summary and Future Directions

5.1 Summary of Work Presented

In my dissertation, I presented work applying kernel-phase interferometry to two archival datasets, searching for new sub-stellar companions and analyzing the demographics of the observed populations. In Chapter 2, I presented a catalogue of field age brown dwarf binaries based on the entire *HST*/NICMOS archive of observations of BDs in F110W and F170M. I introduced a new kernel-phase interferometry pipeline and demonstrated it on the previously mentioned well studied dataset. I refined astrometry and photometry of previously known companions and confirmed two previous kernel-phase detections. I also presented contrast curves, calculated in a robust method previously only used with NRM observations, showing the pipeline was able to detect companions down to flux ratios of $\sim 10^2$ at separations down to half the diffraction limit. I found that the binary fraction of this sample is consistent with previous surveys.

In Chapter 3, I presented a demographic analysis of the previously discussed catalogue. I first estimated the physical properties of the sample using Gaia DR3 distances and evolutionary models assuming a range of possible field

ages. I then used a Bayesian framework which combined my detections and sensitivity to infer an underlying binary population. The companion population model I used was defined by log-normal separation and power-law mass-ratio distributions. After correcting the sample for Malmquist bias, by inflating the number of predicted companions as a function of companion brightness, I found a companion fraction of $F = 0.11^{+0.04}_{-0.03}$ and a separation distribution centered at $\rho = 2.2^{+1.2}_{-1.0}$ au. These values were smaller and tighter than seen in previous studies, due to the high resolution of KPI enabling me to resolve the peak of the semimajor axis distribution with significant sensitivity to low-mass companions.

I confirmed the previously-seen trends of decreasing binary fraction with decreasing mass and a strong preference for tight and equal-mass systems in the field-age sub-stellar regime. For example, $\sim 1\%$ of binary BDs are at wide separations (> 20 au) or extreme mass ratios ($q < 0.6$) according to the inferred population. I attribute this to turbulent fragmentation setting the initial conditions, followed by a brief period of dynamical evolution, removing the widest and lowest-mass companions, before the birth cluster dissolves. This dynamical evolution must take place in the cluster as any interactions with field stars, GMCs or the galactic potential would not be strong enough to remove companions. Since large scale simulations still do not have the resolution required to simulate the formation of substellar objects and their circumsubstellar/binary disks, there is a bit of a mystery as to the detailed formation physics.

In Chapter 4 I applied a modified version of the pipeline presented in Chapter 2 to the ACS/HRC camera on *HST*, demonstrating kernel-phase interferometry for the first time on this camera at a wavelength shorter than $1 \mu\text{m}$. I analyzed a sample of sub-stellar objects in the young star-forming regions of Taurus and Upper Scorpius. Using a preliminary grid of detection limits, I presented 6 new candidate detections at extremely tight separations in addition to the 4 previously known companions. One of these candidates would be the second lowest mass binary currently known, if it survives a more detailed analysis (described below in Section 5.2).

I then analyzed the binary population of this new sample of young sub-stellar binaries. I derived physical properties of the sample and modeled the population using the same Bayesian framework as was described in Chapter 3. I found an observed companion frequency of $F_{\text{obs}} = 0.24^{+0.10}_{-0.08}$ which was slightly higher than previous studies due to our new detections. The demographics of our survey again confirmed previously seen trends of a strong preference for equal-mass binaries and a decreasing companion frequency with decreasing mass. Previous studies have also shown a significant excess of wide ($\rho > 20 \text{ au}$) companions in high-density star-forming regions compared to the field so I compared the demographics of our sample of objects in low-density star-forming regions to the field and also found a significant excess. I found that the field population of wide ($\rho > 10 \text{ au}$) companions is consistent with a population of wide systems formed only in low density regions and diluted by single systems formed in high density regions. This indicates that dynamical

evolution removes wide separation companions born in high-density regions, where the majority of stars form, before the cluster dissolves while leaving the population born in low-density regions largely untouched.

5.2 Future Work

5.2.1 Finalize ACS KPI Analysis

As I noted in Section 4.4.5, I used preliminary detection limits to determine if potential companions were significantly detected or not. While this may seem like an obvious first next step, I believe we can actually achieve better results by returning to the kernel-phase calculation stage with a narrower window for low SNR observations, and to the binary fitting stage with a more nuanced calibration strategy. As seen in Chapter 2, fits to low SNR observations of clear binaries gave incorrect parameters, possibly due to the large amount of noise and small signal propagated through the Fourier transform. A narrower super-Gaussian window will increase the SNR of the visibilities. On the calibration side, the proper-motions of the targets in these observations were known to much higher precision than the field objects observed with NICMOS. Thus, the targets are all well centered on the detector and the metric presented in Chapter 2 for choosing calibrators is less important for this sample. Thus it would be good to explore other calibration strategies such as simply choosing the brightest targets. One potential down side of this is that a target may bright due to the presence of a companion. This problem is easily mitigated by using more calibrators and excluding those which are

later determined to have companions.

A careful examination of the candidate detection around KPNO-Tau-12 is also warranted. As I noted in Section 4.5.1.3, one image in F775W has a cosmic ray hit near the target which we will need to exclude from the fits to be certain it does not inject a companion signal as seen in the case of 2MASS 0024-0158 (see Section 2.5.3). If this detection is finally determined to be significant it will be an exciting, though difficult, candidate to follow up on with further high resolution imaging.

Another target which warrants a more careful examination is CTIO-USco-109. The current (preliminary) detection limits do not show a significant detection, though there is a slight grouping of fits hinting at a possible signal. It is possible, with the improvements discussed above, that a significant detection could emerge. Follow-up imaging from Keck/NERC2 in 2021 (Kraus & Rizzuto, private communication) shows that the companion is real and has moved to a wider separation in the past 18 years, though it may be closer to equal brightness than previously reported, making it a tricky target for KPI.

A small change in the number of detected companions will not affect the demographic analysis or its conclusions about the formation of binary BDs. However, with a larger sample, combining other surveys of young objects, it may be possible to model the population as a mixture between tightly-separated and similar mass *binary* companions (similar to the model we used) and extreme mass-ratio *planetary-mass* companions (modeled as a power-law in mass instead of mass ratio). This would enable the study of this intriguing

region of parameter space where binary formation crosses over with planet formation. This work also motivates further theoretical exploration of these objects as current simulations do not resolve the spatial and mass scales on which BD binaries form.

5.2.2 Future directions of KPI

As I hope I have shown in this dissertation, KPI is an extremely powerful tool for detecting companions—stellar, sub-stellar, or planetary mass—at separations previously thought to be inaccessible. However, there is nuance to the application of KPI which merits further exploration. I have secured funding through a Cycle 1 *JWST* archival proposal (AR-2509; Factor & Kraus, 2021b) to modify my existing KPI pipeline for use with *HST*'s successor. This project will use existing PSF calibration images, acquired through other programs, to explore what observing and calibration strategies produce the highest sensitivity.

In a more general sense, KPI remains a black box of confusion to an outside user. Its continued application will bring the technique in front of more members of the community who are not experts in interferometry. As *JWST/NIRISS* has an AMI mode this is already taking place. A review of current interferometric analysis techniques and pipelines would be extremely useful to the community and was recently in the works as part of a masking hackathon.

Furthermore, as I discussed in Section 1.2.4, several theoretical exten-

sions to KPI have been proposed in addition to narrow demonstrations of the technique in niche situations. Incorporating these extensions and specific use cases into a widely applicable and modular open source pipeline would allow new users to familiarize themselves with the basics of the technique without having to learn a new software package when they want to go further.

Since KPI analysis does not require a specific observing setup (as opposed to AMI) it can be performed on any imaging dataset taken on a camera and at a wavelength which the PSF is well sampled. I have demonstrated this strength in the two surveys I have performed in this dissertation. Continued application of KPI, to archival programs and through programs specifically designed for KPI, will further open the discovery space of sub-stellar and planetary-mass companions. With a larger population of detections and sensitivity to a wider region of parameter space we can continue to test formation models at new and interesting scales. In the coming years, with *JWST* already delivering data and the next generation of ground-based 30 m class telescopes coming online in the more distant future, the potential applications of KPI will be vast. Applying KPI to current *JWST* programs surveying young star-forming regions is the natural next step for this work, extending the search for sub-stellar companions.

Appendices

Appendix A

Figure Set corresponding to Figure 2.4: Corner plots, KP correlation Plots, and Images

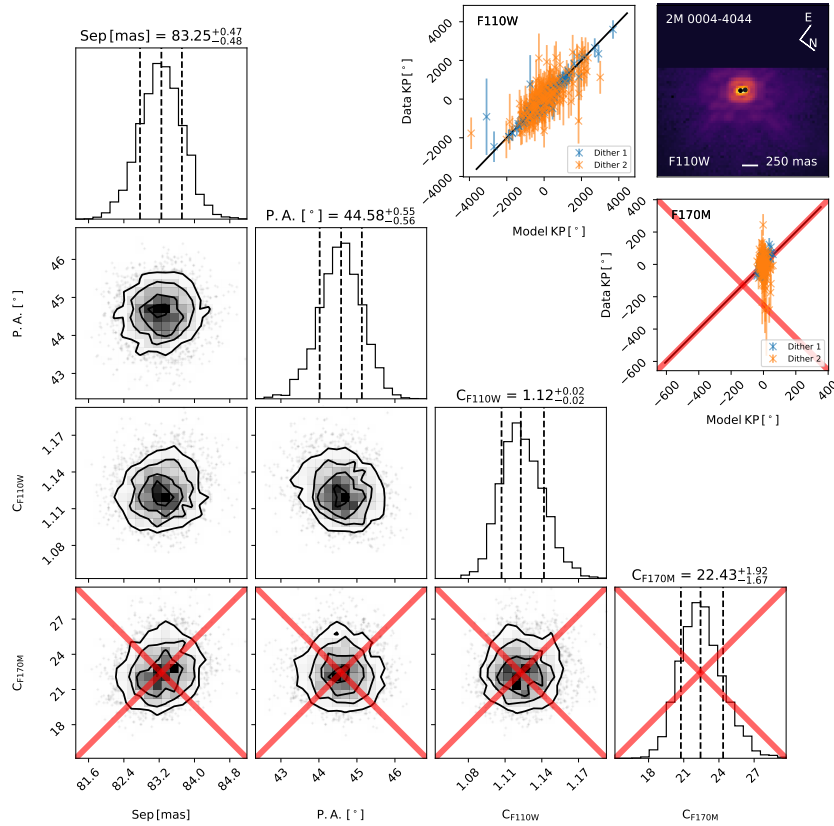


Figure A.1: Corner plot, KP correlation plots, and image for the fit to 2M 0004-4044 from program 10143.

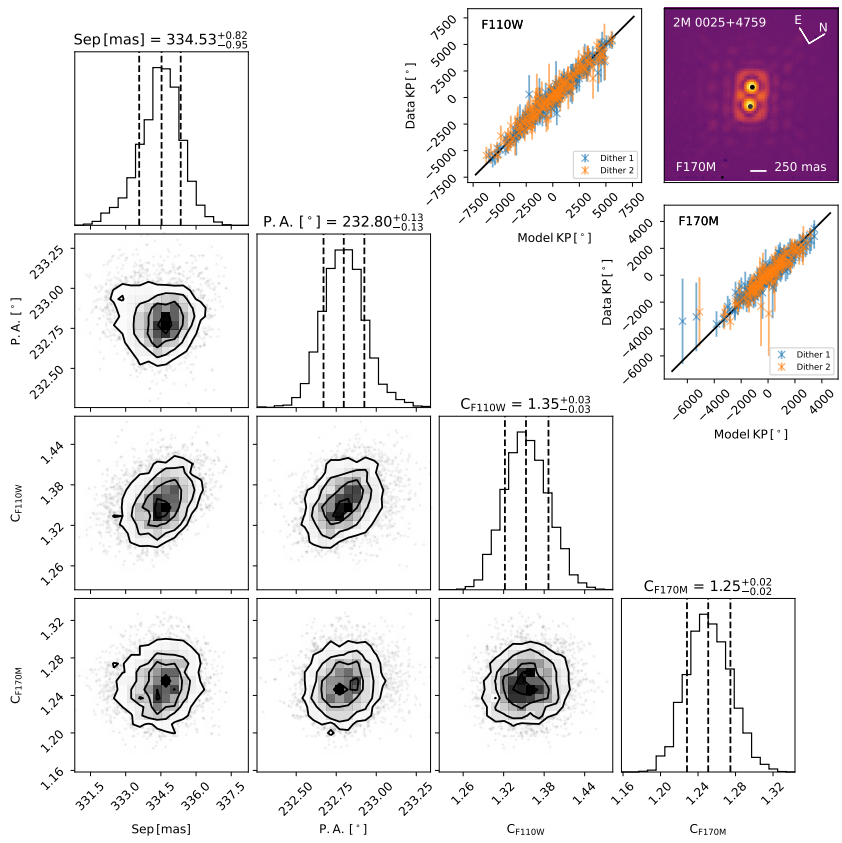


Figure A.2: Corner plot, KP correlation plots, and image for the fit to 2M 0025+4759 from program 10143.

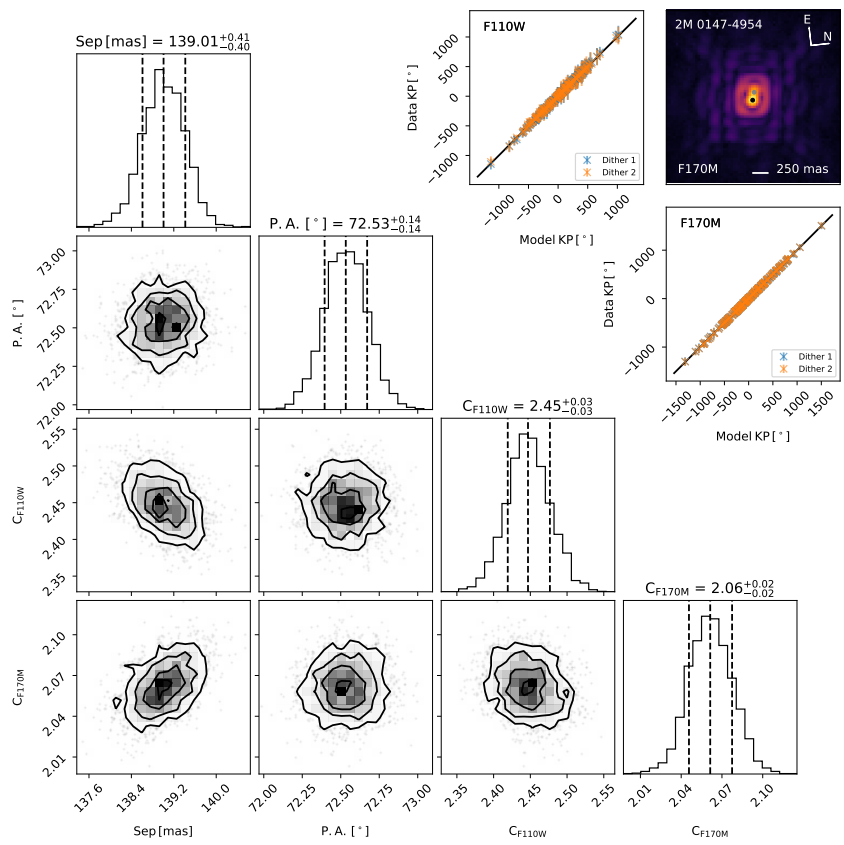


Figure A.3: Corner plot, KP correlation plots, and image for the fit to 2M 0147-4954 from program 10143.

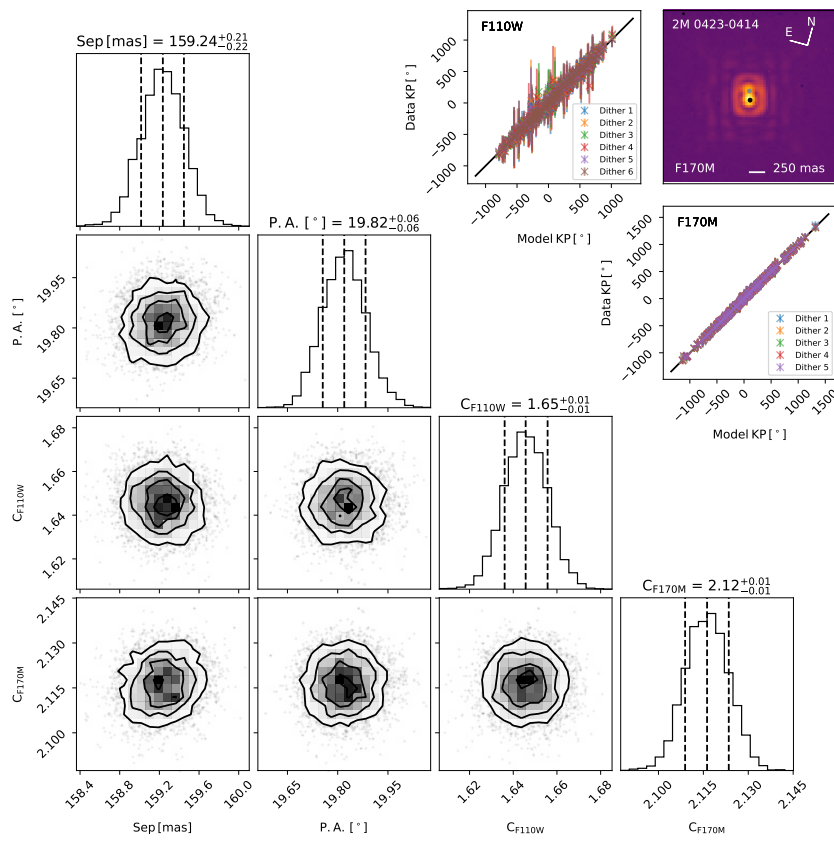


Figure A.4: Corner plot, KP correlation plots, and image for the fit to 2M 0423-0414 from program 9833.

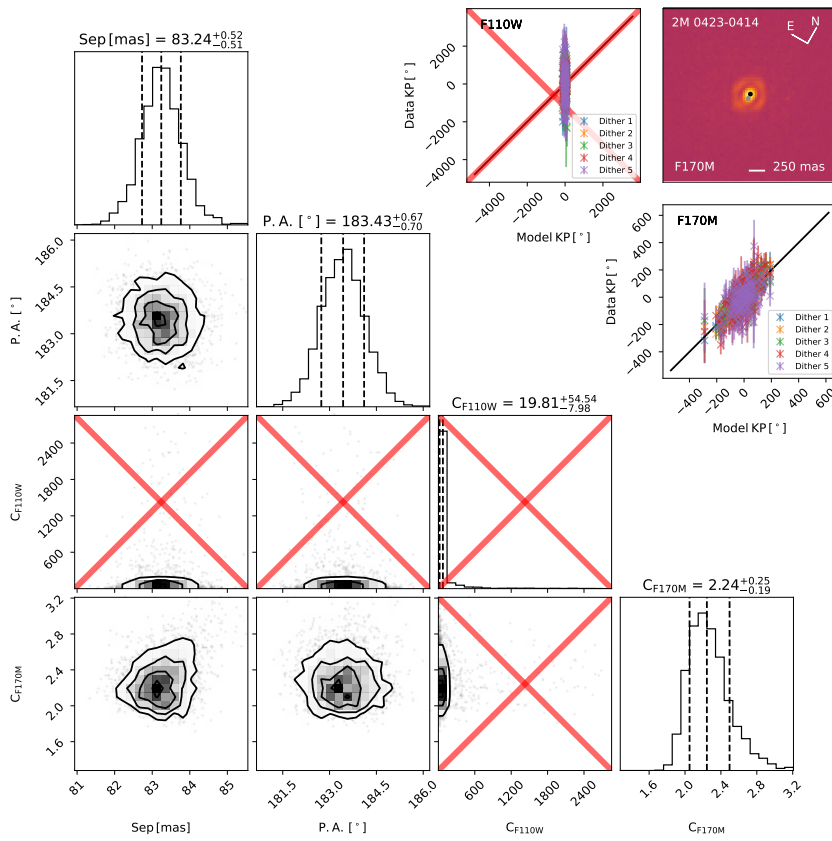


Figure A.5: Corner plot, KP correlation plots, and image for the fit to 2M 0423-0414 from program 10143.

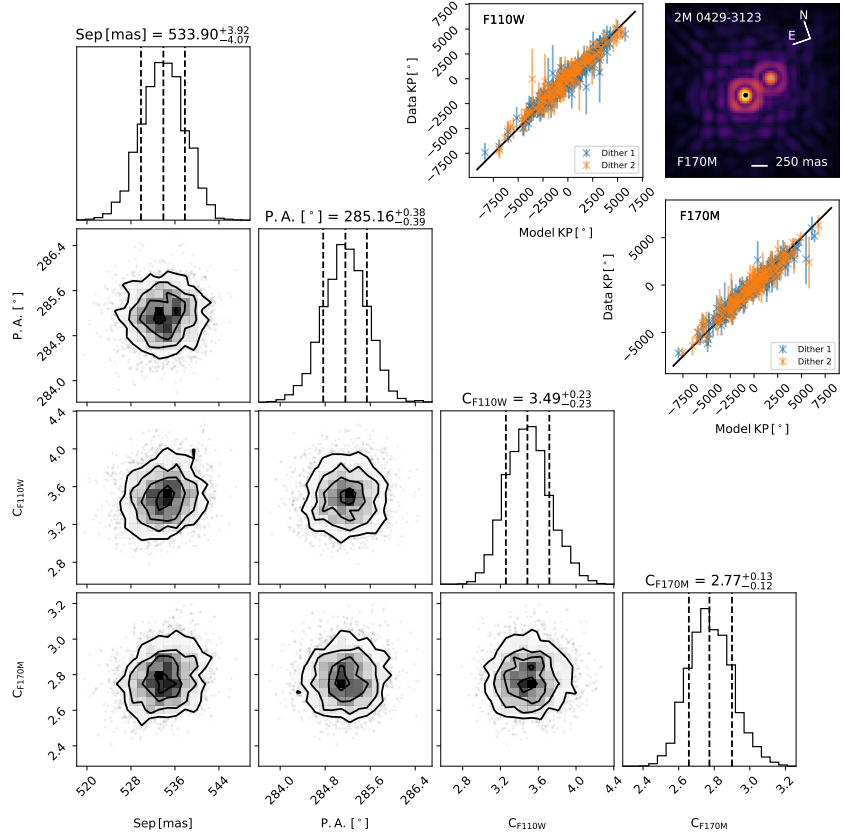


Figure A.6: Corner plot, KP correlation plots, and image for the fit to 2M 0429-3123 from program 10143.

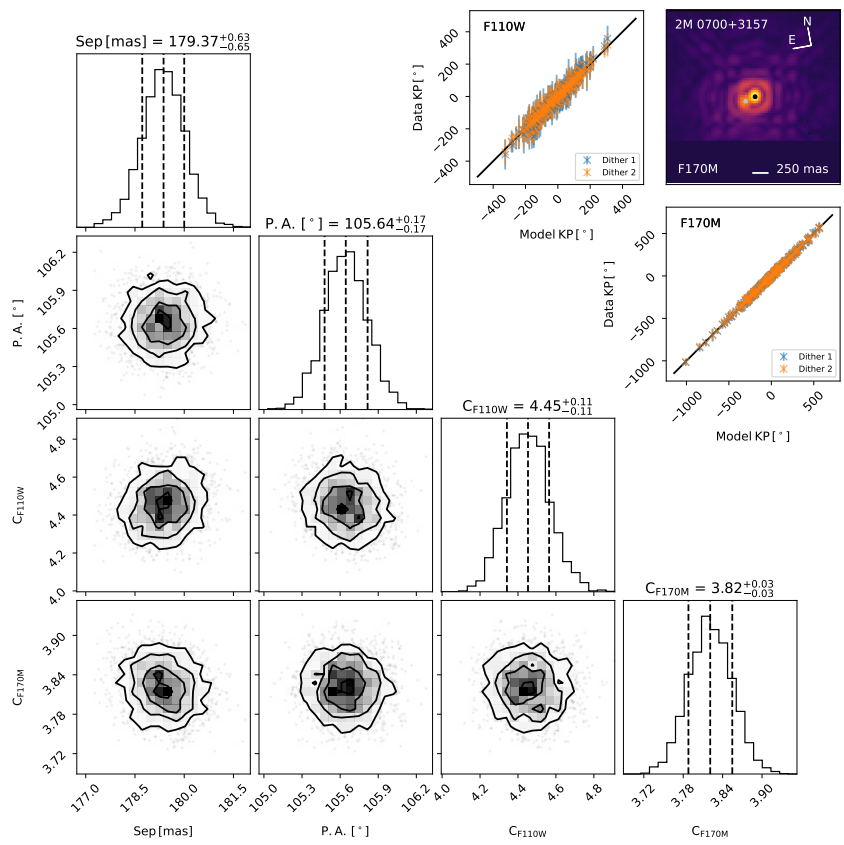


Figure A.7: Corner plot, KP correlation plots, and image for the fit to 2M 0700+3157 from program 10143.

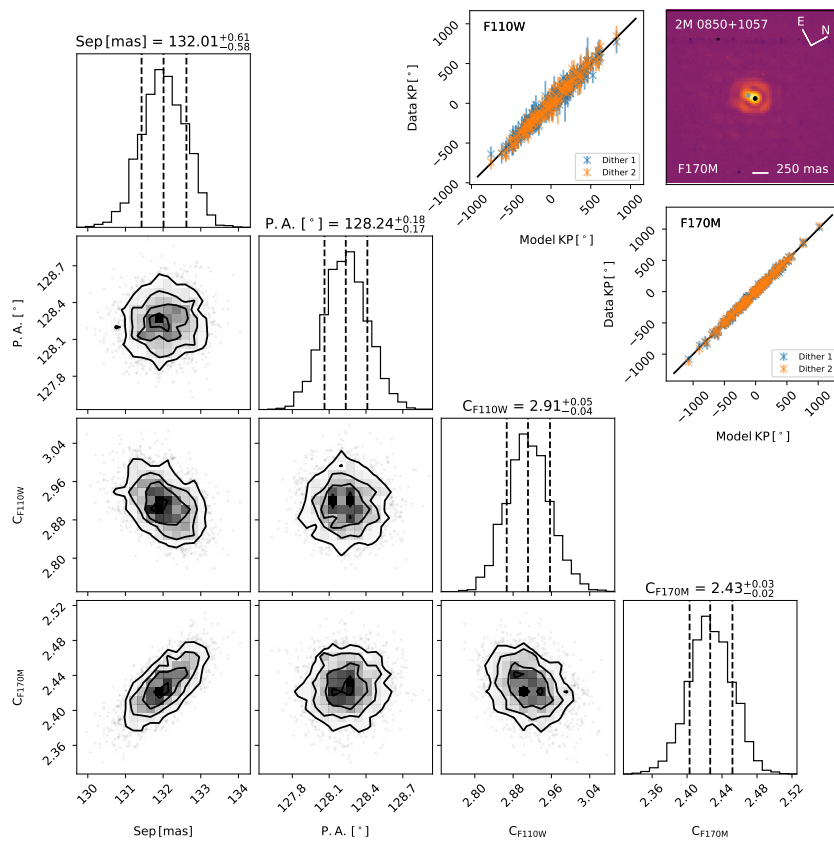


Figure A.8: Corner plot, KP correlation plots, and image for the fit to 2M 0850+1057 from program 9843.

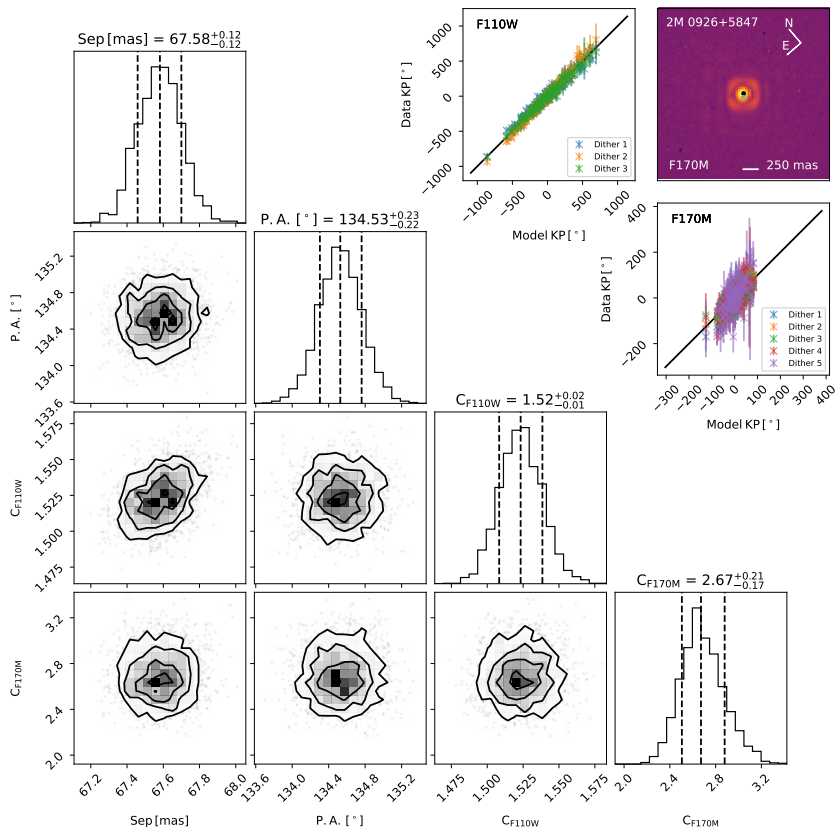


Figure A.9: Corner plot, KP correlation plots, and image for the fit to 2M 0926+5847 from program 9833.

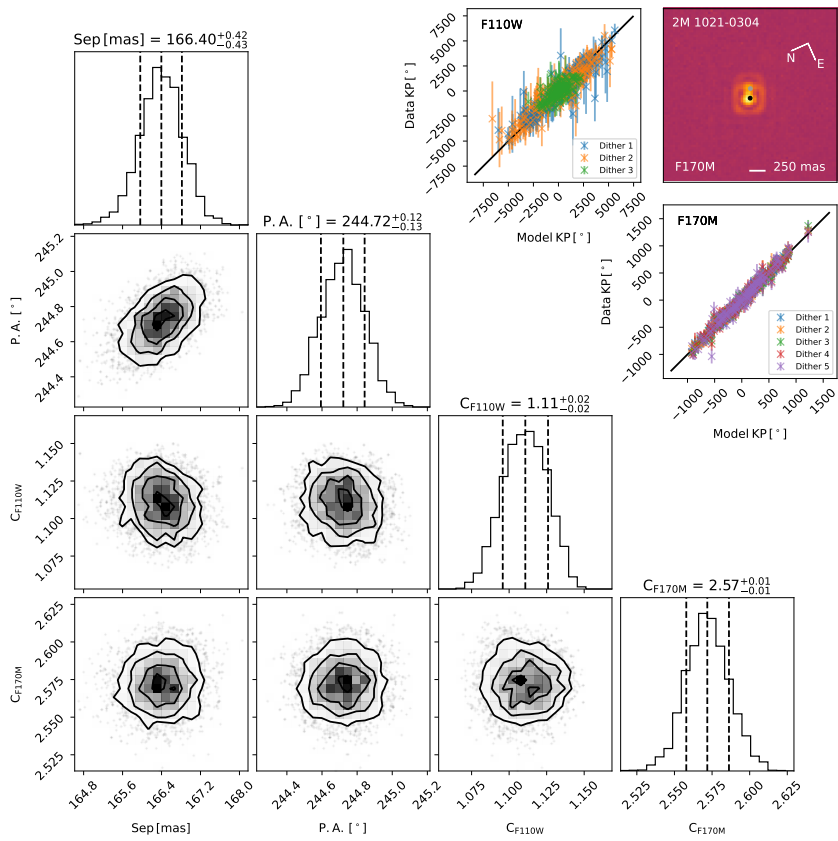


Figure A.10: Corner plot, KP correlation plots, and image for the fit to 2M 1021-0304 from program 9833.

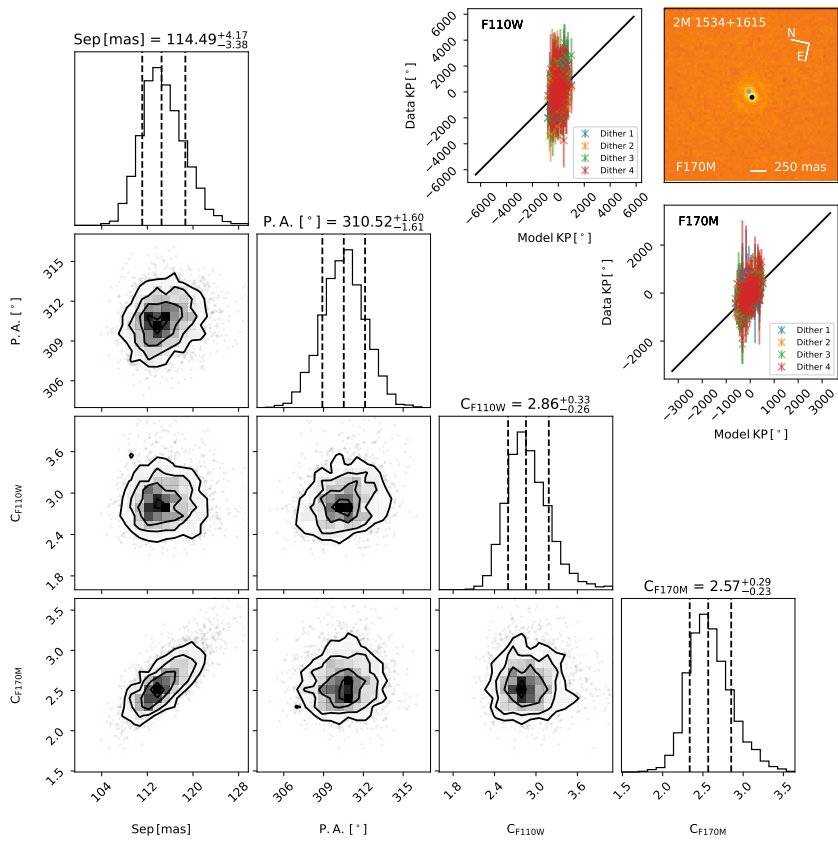


Figure A.11: Corner plot, KP correlation plots, and image for the fit to 2M 1534+1615 from program 11136.

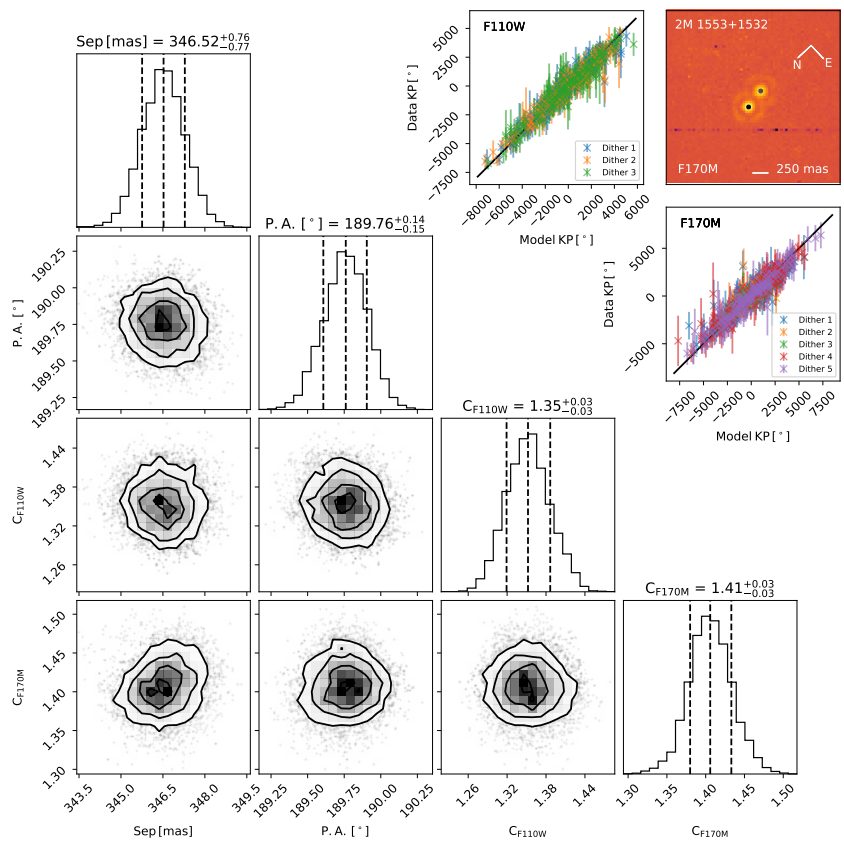


Figure A.12: Corner plot, KP correlation plots, and image for the fit to 2M 1553+1532 from program 9833.

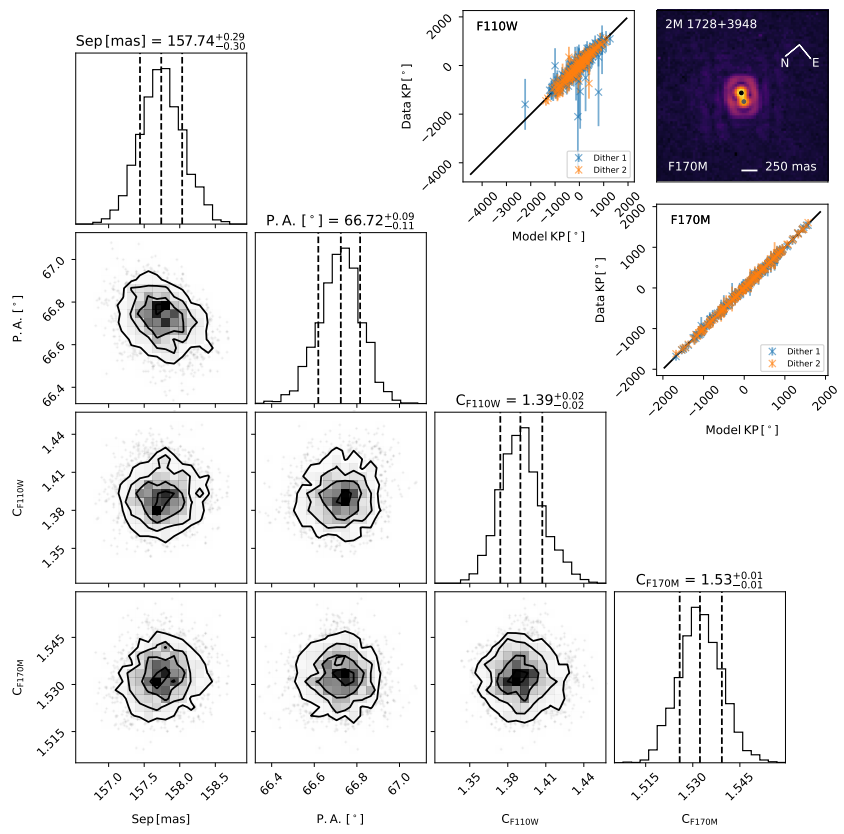


Figure A.13: Corner plot, KP correlation plots, and image for the fit to 2M 1728+3948 from program 9843.

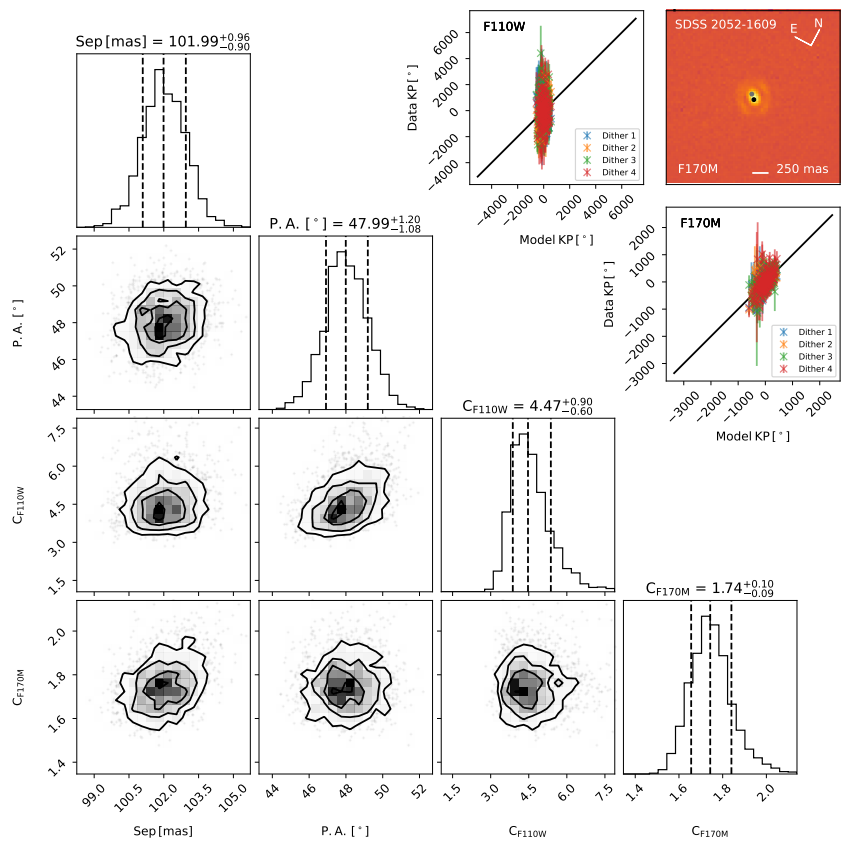


Figure A.14: Corner plot, KP correlation plots, and image for the fit to 2M 2052-1609 from program 11136.

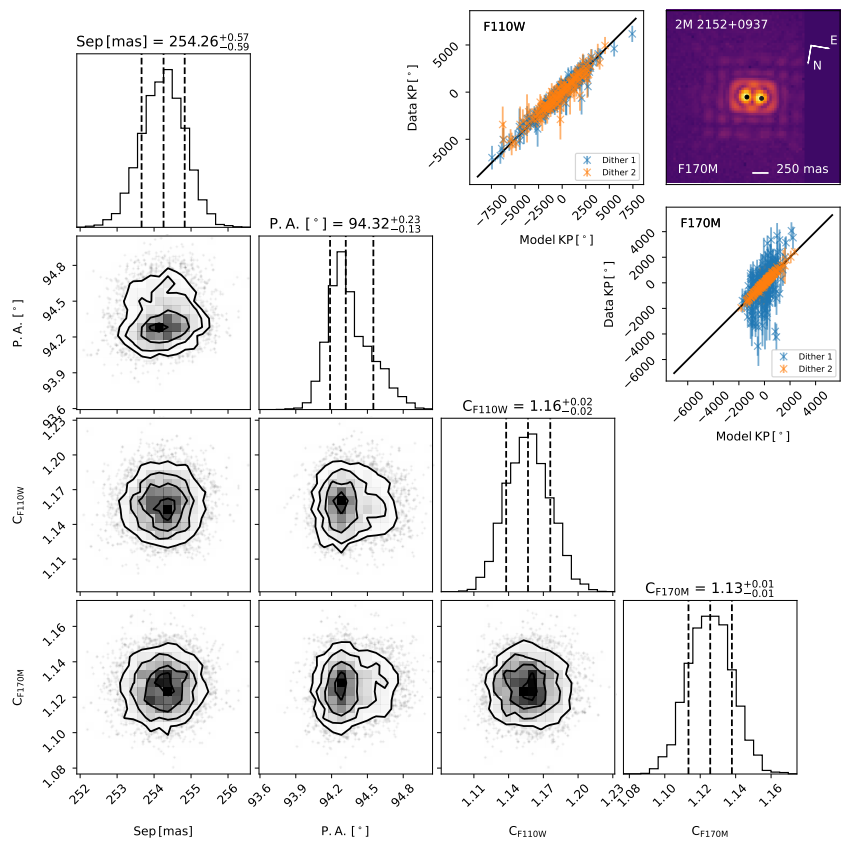


Figure A.15: Corner plot, KP correlation plots, and image for the fit to 2M 2152+0937 from program 10143.

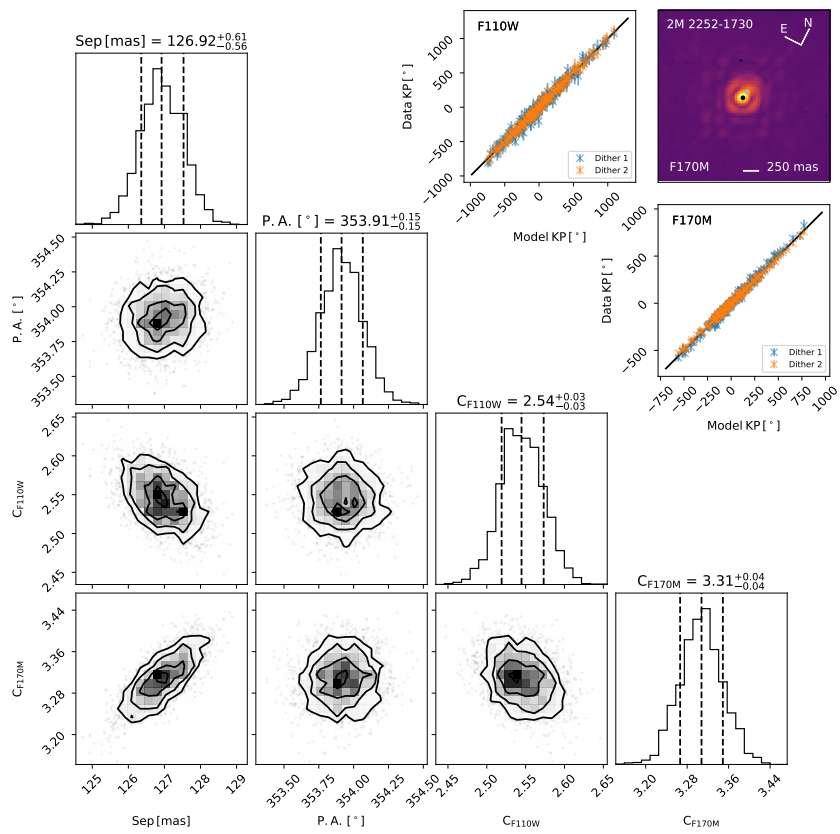


Figure A.16: Corner plot, KP correlation plots, and image for the fit to 2M 2252-1730 from program 10143.

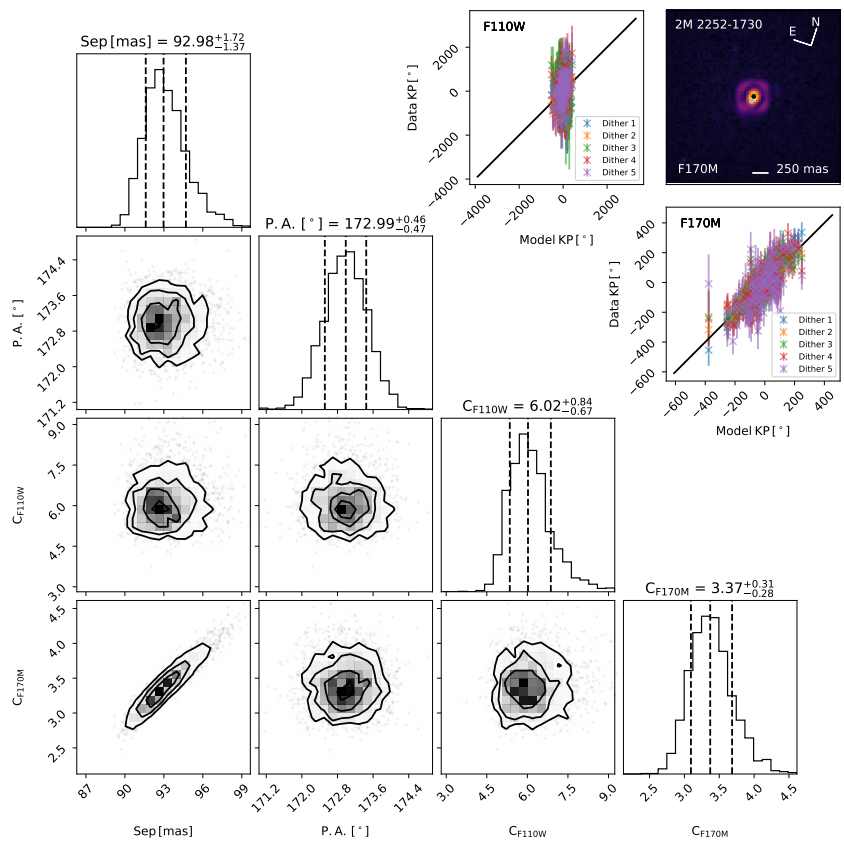


Figure A.17: Corner plot, KP correlation plots, and image for the fit to 2M 2252-1730 from program 11136.

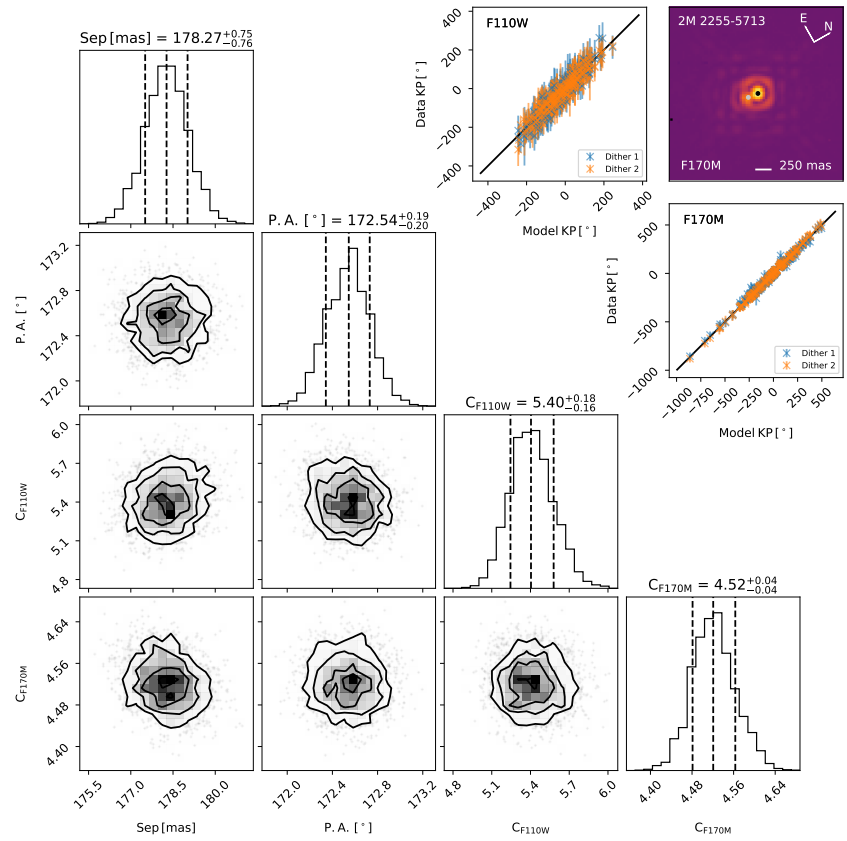


Figure A.18: Corner plot, KP correlation plots, and image for the fit to 2M 2255-5713 from program 10879.

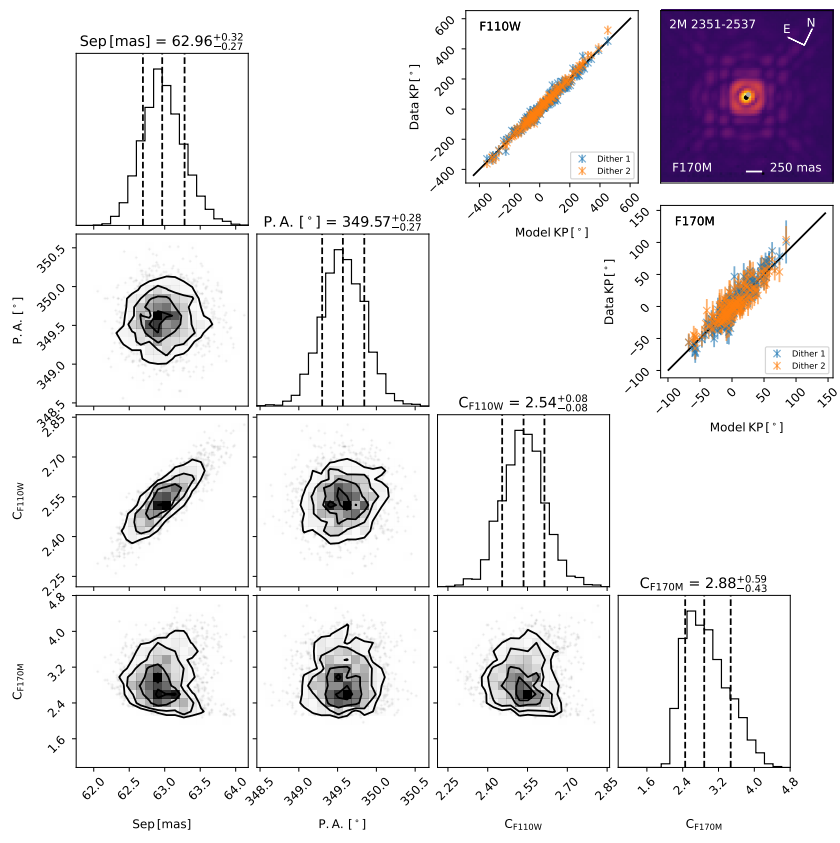


Figure A.19: Corner plot, KP correlation plots, and image for the fit to 2M 2351-2537 from program 10143.

Appendix B

Figure Set corresponding to Figure 2.5: Detection Limits for Single Sources

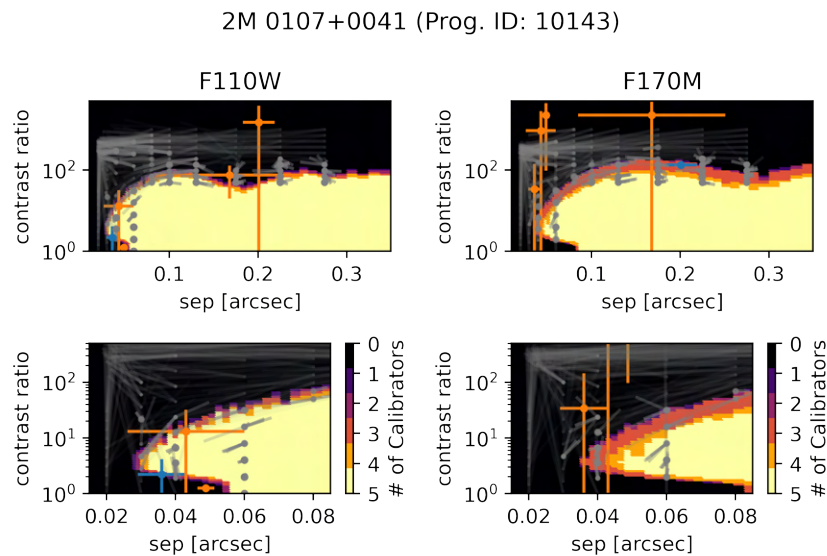


Figure B.1: Detection limits for 2M 0107+0041 from program 10143.

2M 0123-4240 (Prog. ID: 10143)

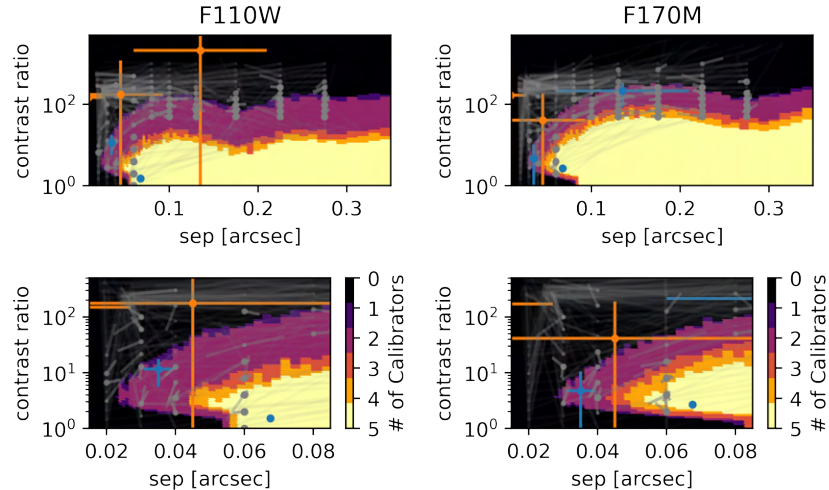


Figure B.2: Detection limits for 2M 0123-4240 from program 10143.

2M 0144-0716 (Prog. ID: 10143)

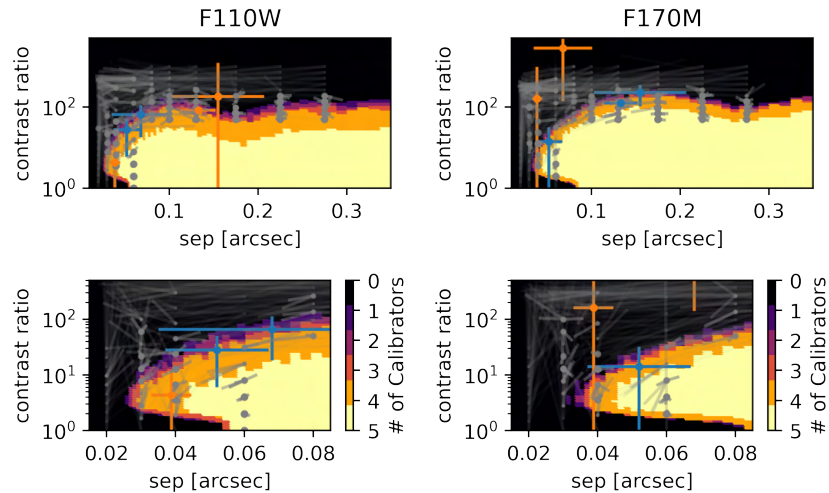


Figure B.3: Detection limits for 2M 0144-0716 from program 10143.

2M 0151+1244 (Prog. ID: 9833)

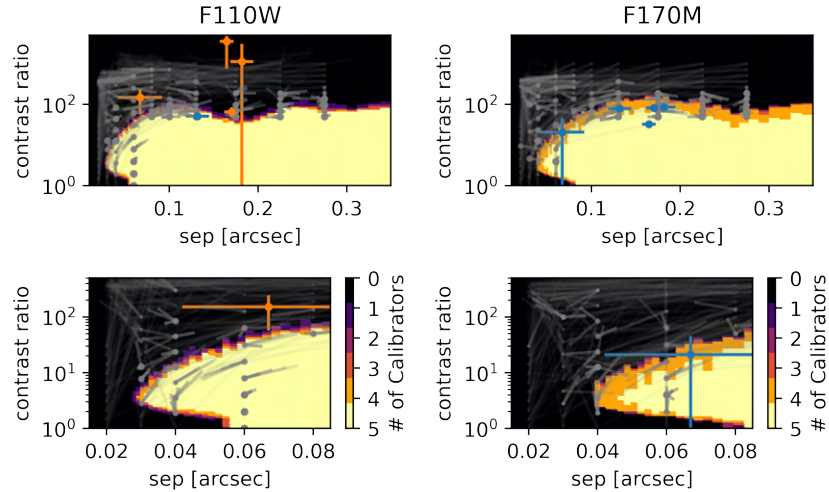


Figure B.4: Detection limits for 2M 0151+1244 from program 9833.

2M 0155+0950 (Prog. ID: 10143)

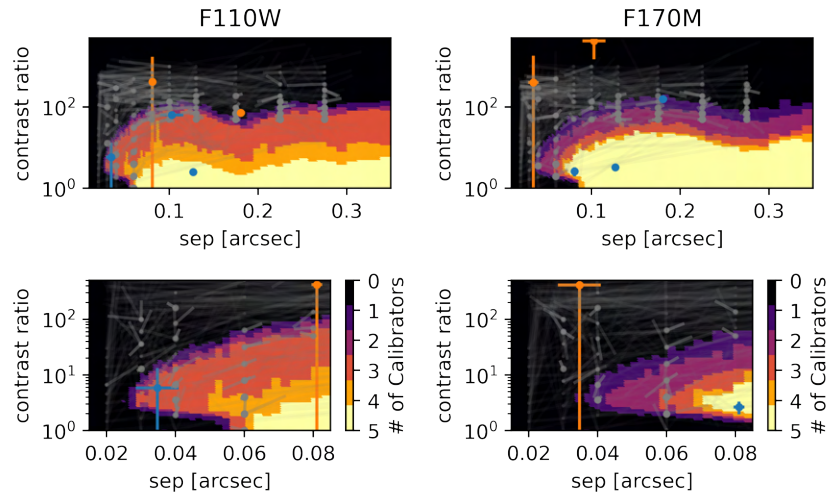


Figure B.5: Detection limits for 2M 0155+0950 from program 10143.

2M 0207+0000 (Prog. ID: 9833)

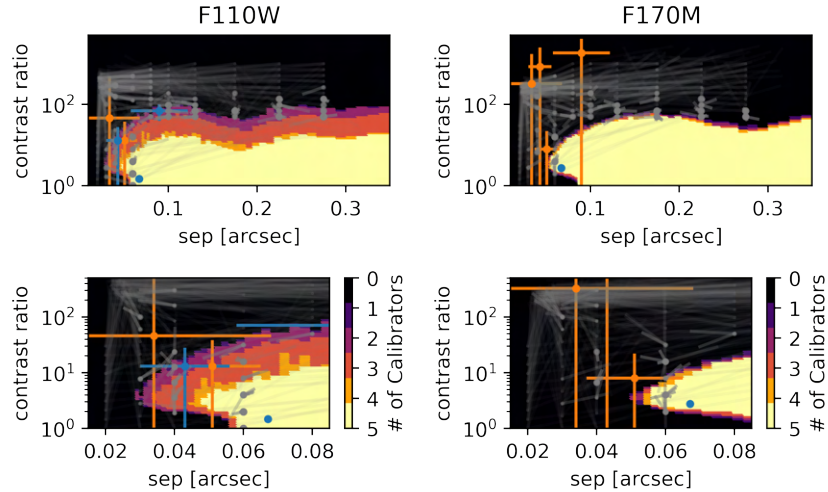


Figure B.6: Detection limits for 2M 0207+0000 from program 9833.

2M 0213+4444 (Prog. ID: 10143)

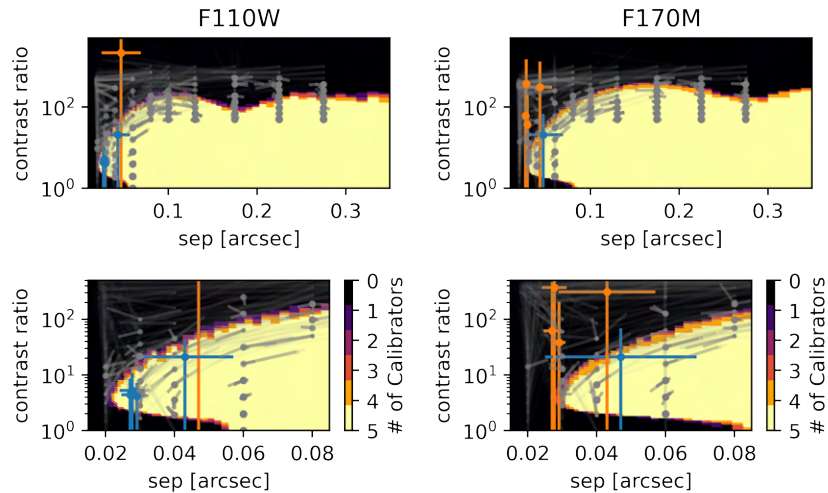


Figure B.7: Detection limits for 2M 0213+4444 from program 10143.

2M 0228+1639 (Prog. ID: 10879)

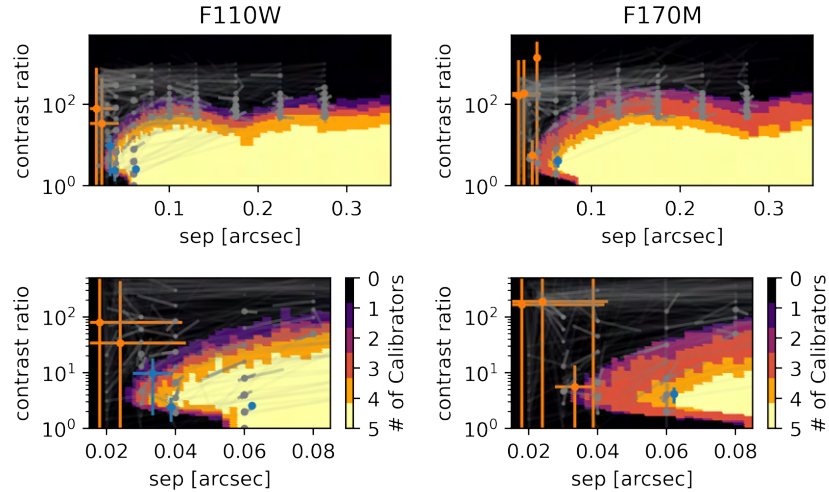


Figure B.8: Detection limits for 2M 0228+1639 from program 10143.

2M 0243-2453 (Prog. ID: 9833)

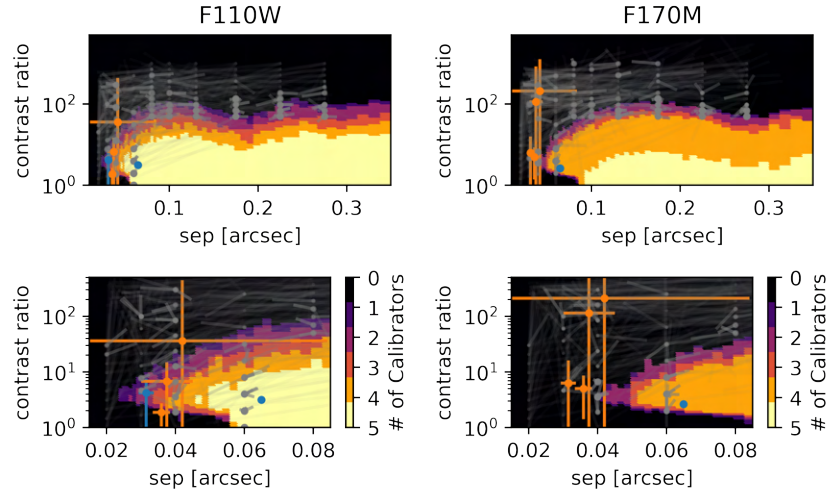


Figure B.9: Detection limits for 2M 0243-2453 from program 9833.

2M 0251-0352 (Prog. ID: 10879)

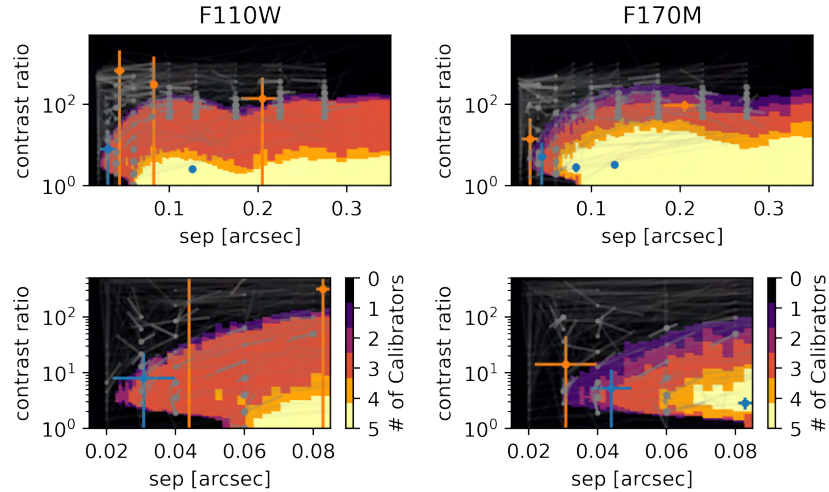


Figure B.10: Detection limits for 2M 0251-0352 from program 10143.

2M 0255-4700 (Prog. ID: 10879)

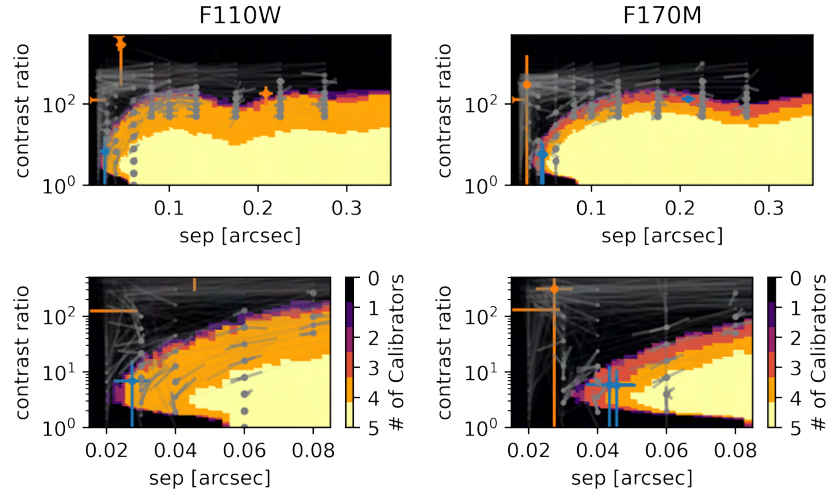


Figure B.11: Detection limits for 2M 0255-4700 from program 10143.

2M 0257-3105 (Prog. ID: 10143)

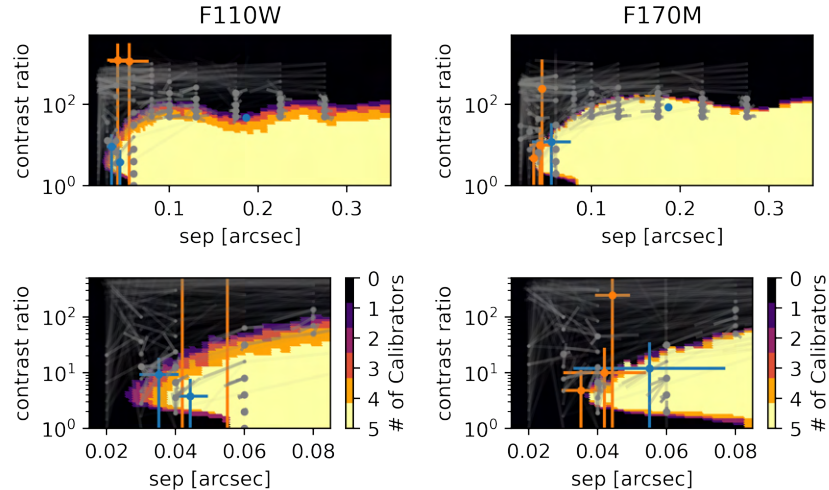


Figure B.12: Detection limits for 2M 0257-3105 from program 10143.

2M 0318-3421 (Prog. ID: 10879)

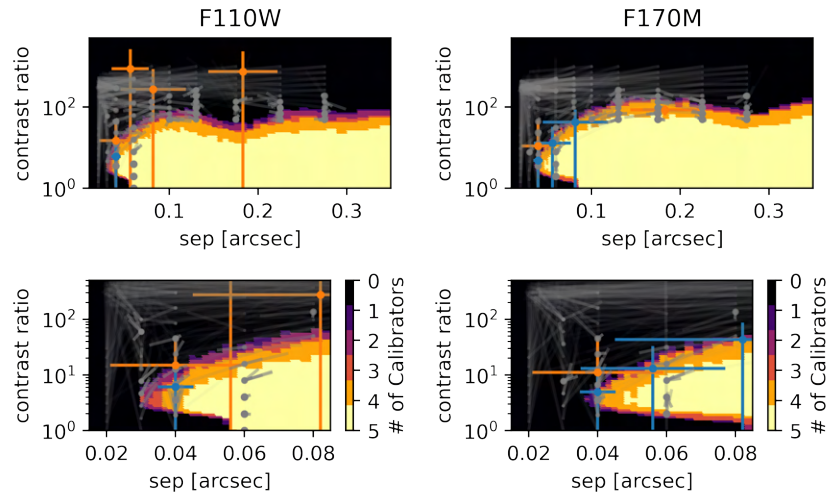


Figure B.13: Detection limits for 2M 0318-3421 from program 10143.

2M 0348-6022 (Prog. ID: 9833)

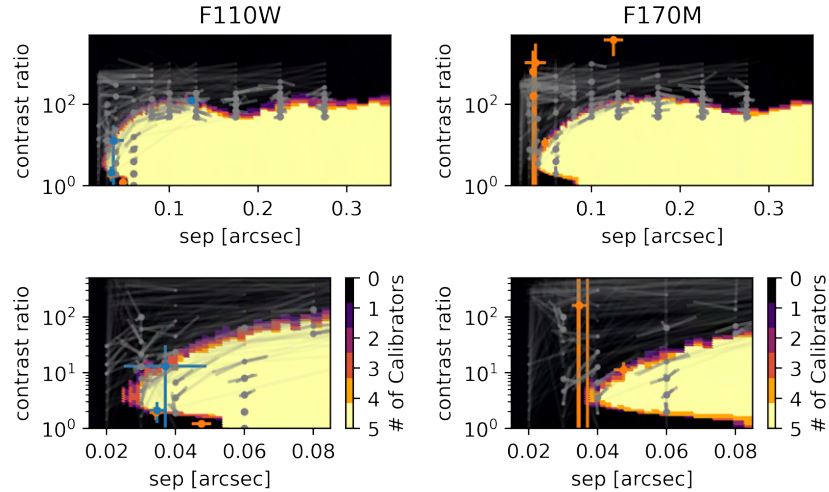


Figure B.14: Detection limits for 2M 0348-6022 from program 9833.

2M 0355+1133 (Prog. ID: 10143)

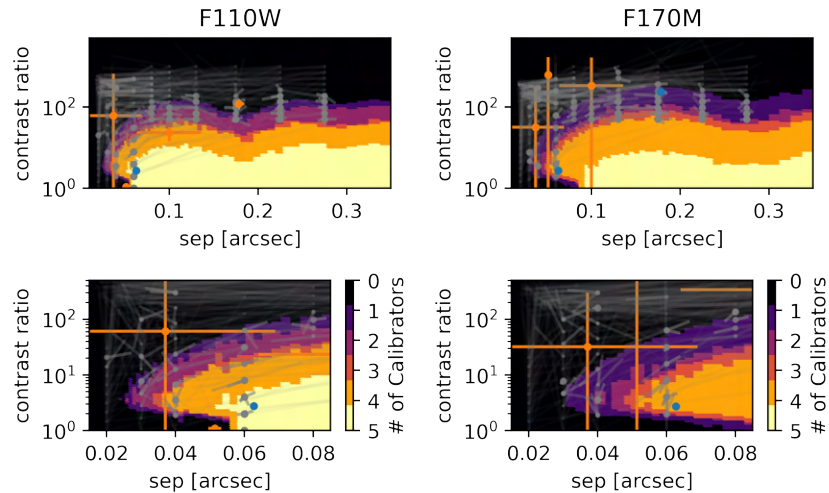


Figure B.15: Detection limits for 2M 0355+1133 from program 10143.

2M 0415-0935 (Prog. ID: 9833)

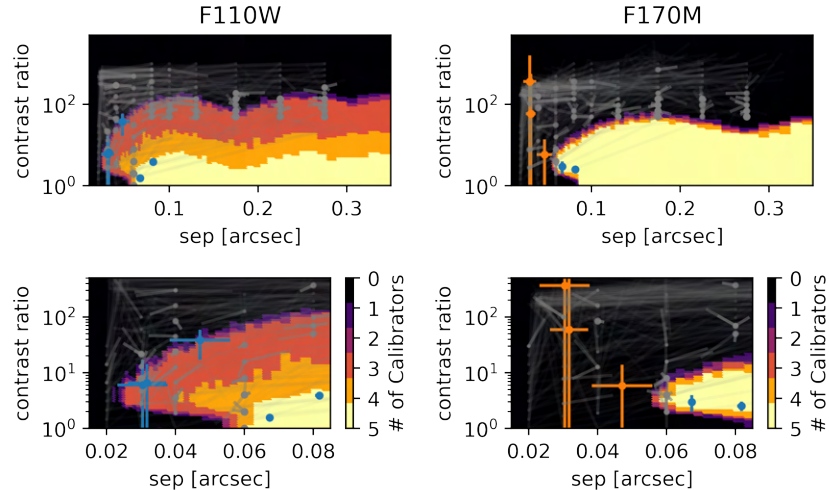


Figure B.16: Detection limits for 2M 0415-0935 from program 9833.

2M 0439-2353 (Prog. ID: 10143)

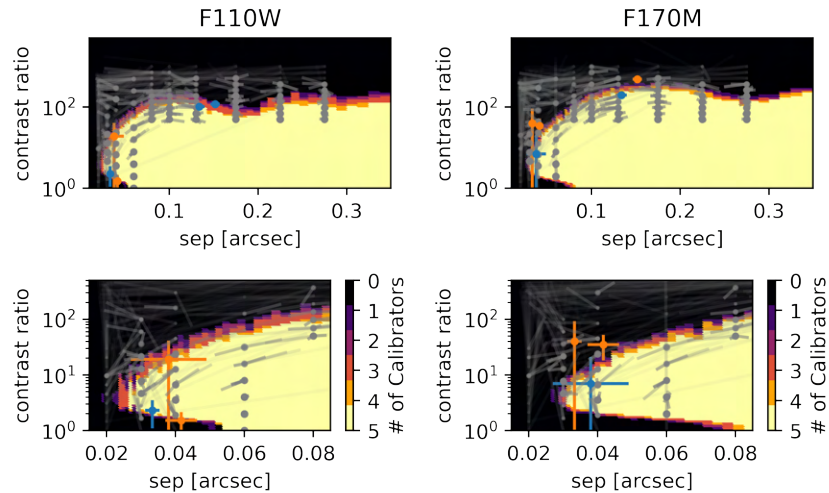


Figure B.17: Detection limits for 2M 0439-2353 from program 10143.

2M 0443+0002 (Prog. ID: 10879)

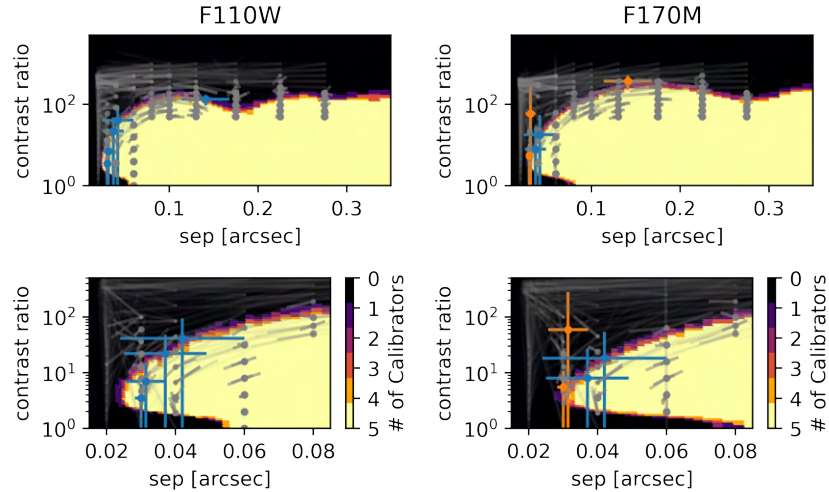


Figure B.18: Detection limits for 2M 0443+0002 from program 10143.

2M 0445-3048 (Prog. ID: 10143)

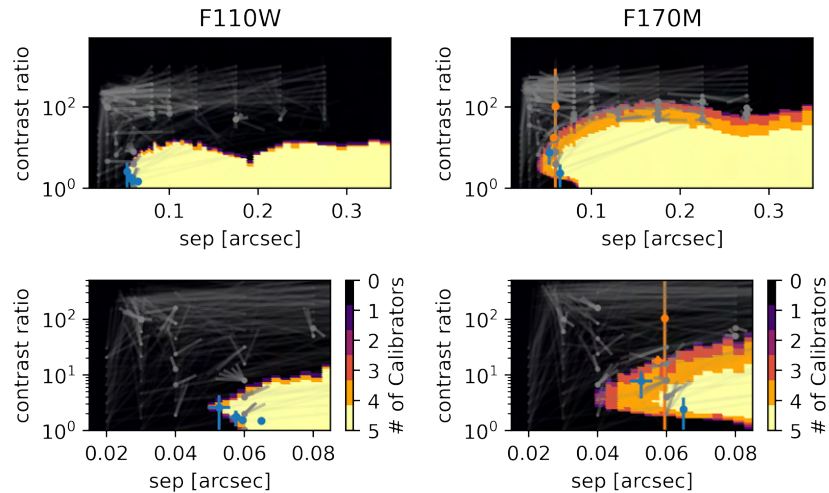


Figure B.19: Detection limits for 2M 0445-3048 from program 10143.

2M 0500+0330 (Prog. ID: 10143)

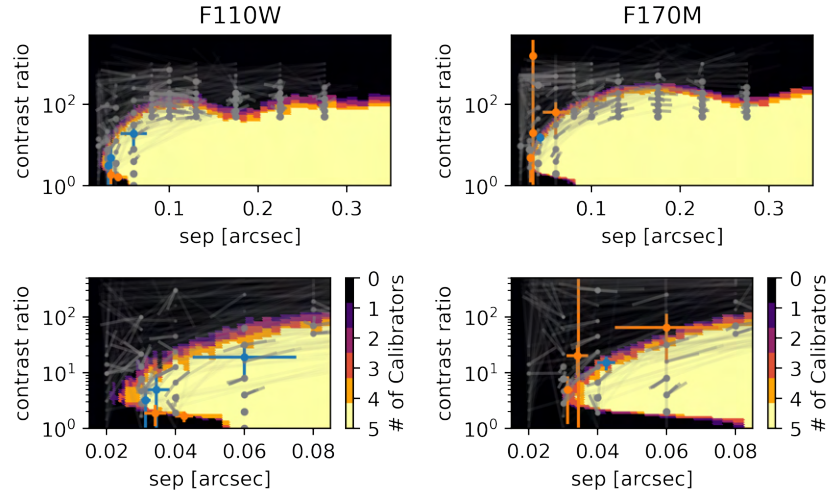


Figure B.20: Detection limits for 2M 0500+0330 from program 10143.

2M 0516-0445 (Prog. ID: 9833)

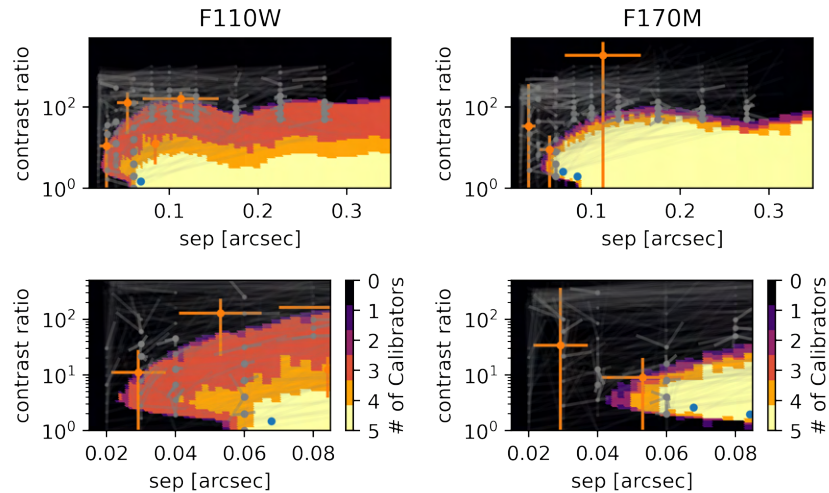


Figure B.21: Detection limits for 2M 0516-0445 from program 9833.

2M 0523-1403 (Prog. ID: 10143)

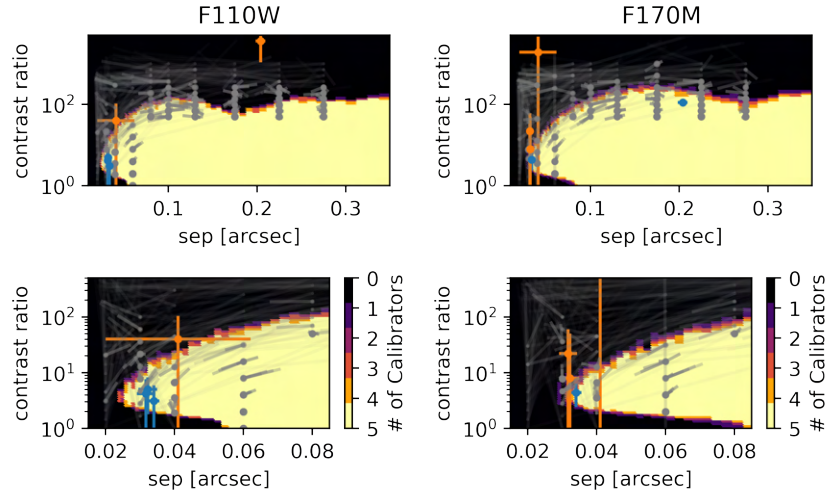


Figure B.22: Detection limits for 2M 0523-1403 from program 10143.

2M 0624-4521 (Prog. ID: 10143)

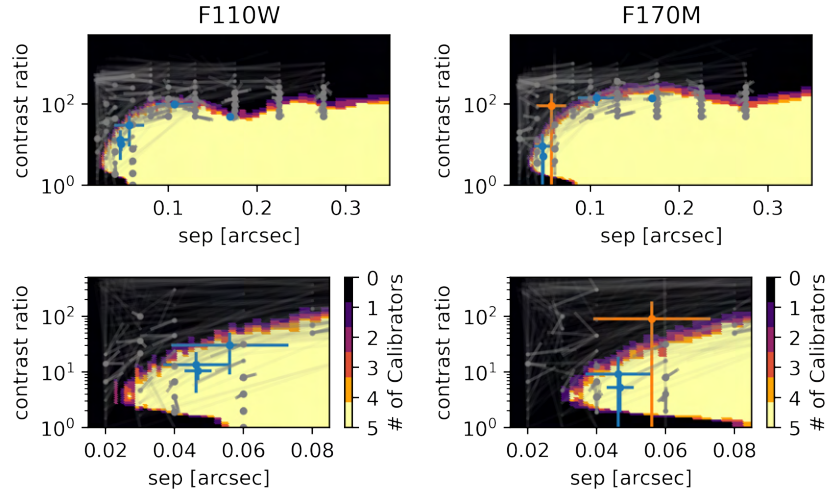


Figure B.23: Detection limits for 2M 0624-4521 from program 10143.

2M 0624+2325 (Prog. ID: 9704)

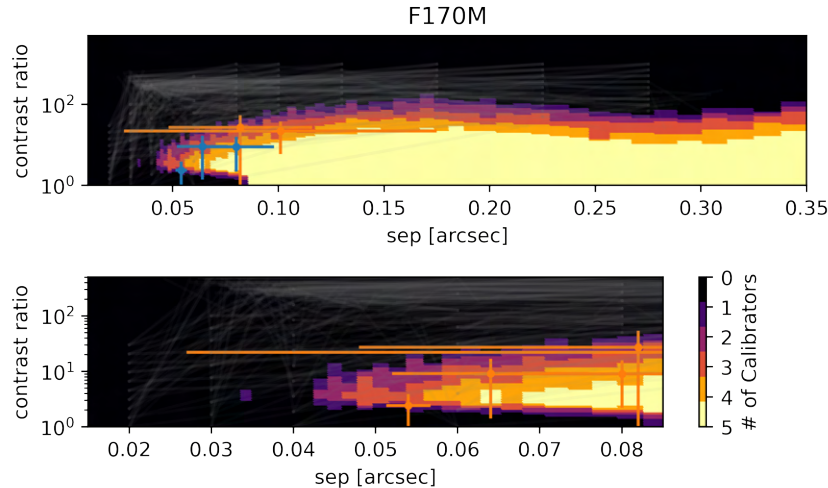


Figure B.24: Detection limits for 2M 0624+2325 from program 9704.

2M 0652+4710 (Prog. ID: 10143)

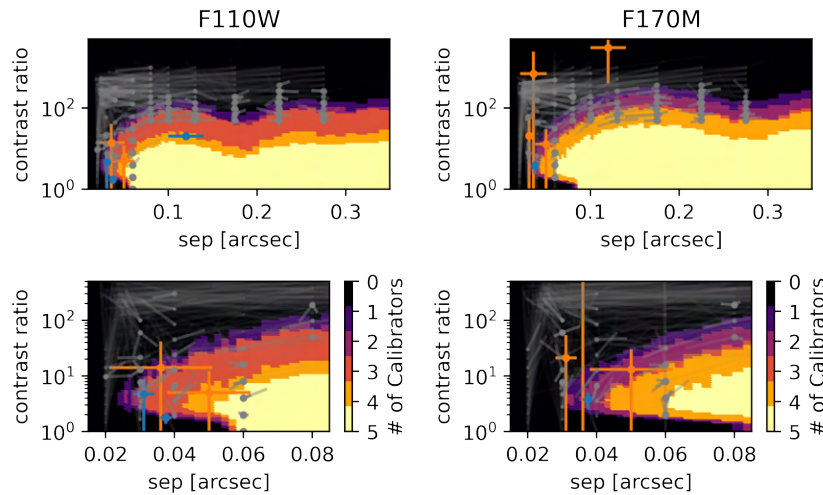


Figure B.25: Detection limits for 2M 0652+4710 from program 10143.

2M 0727+1710 (Prog. ID: 9833)

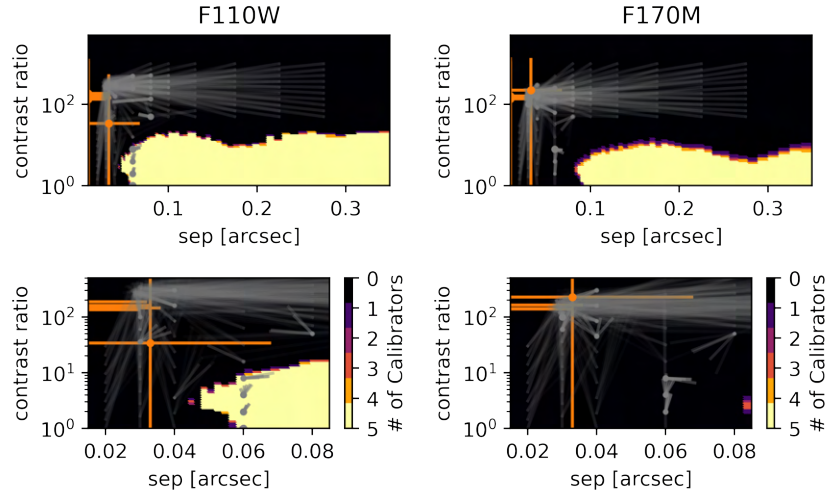


Figure B.26: Detection limits for 2M 0727+1710 from program 9833.

2M 0755+2212 (Prog. ID: 9833)

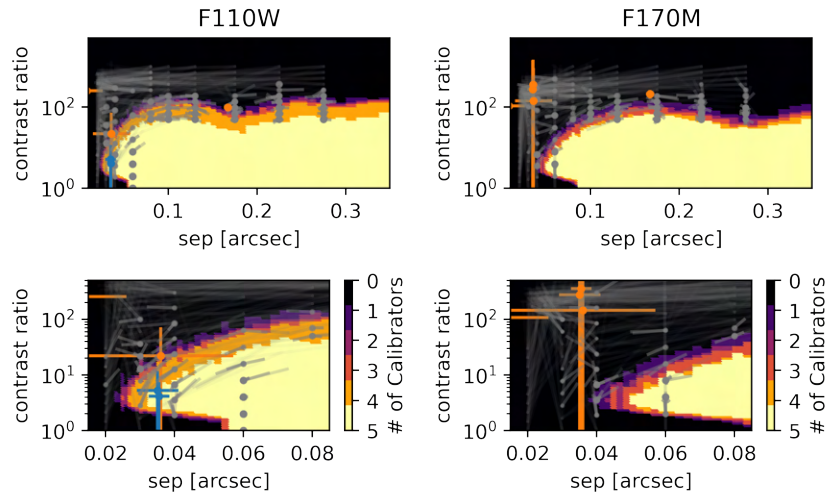


Figure B.27: Detection limits for 2M 0755+2212 from program 9833.

2M 0825+2115 (Prog. ID: 10143)

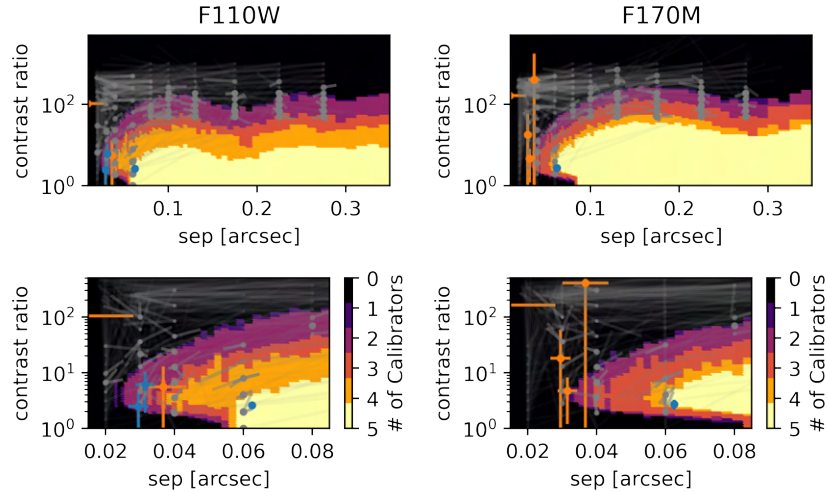


Figure B.28: Detection limits for 2M 0825+2115 from program 10143.

2M 0835-0819 (Prog. ID: 10143)

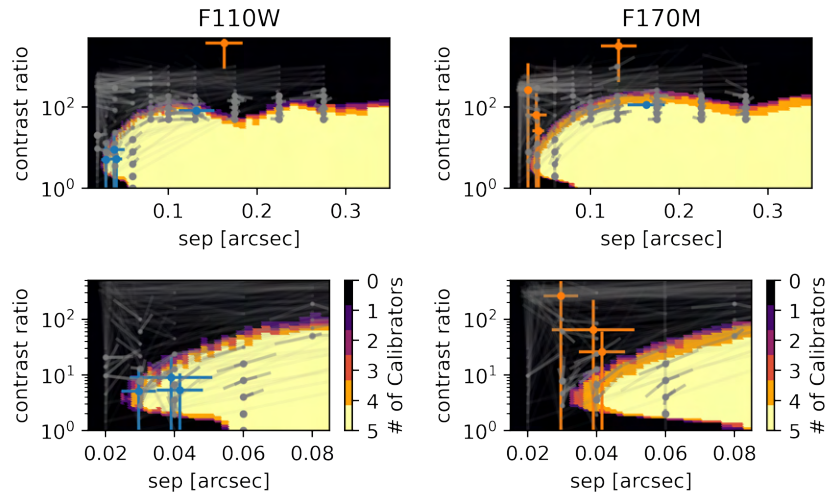


Figure B.29: Detection limits for 2M 0835-0819 from program 10143.

SDSS 0837-0000 (Prog. ID: 9833)

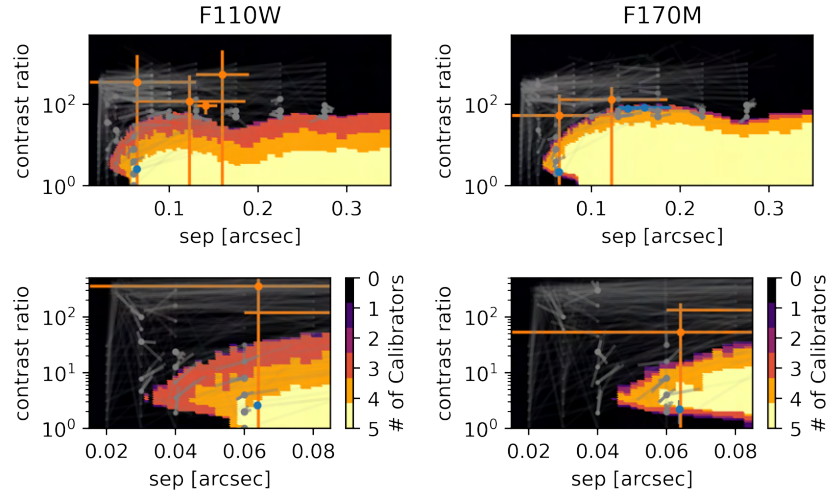


Figure B.30: Detection limits for 2M 0837-0000 from program 9833.

2M 0847-1532 (Prog. ID: 10143)

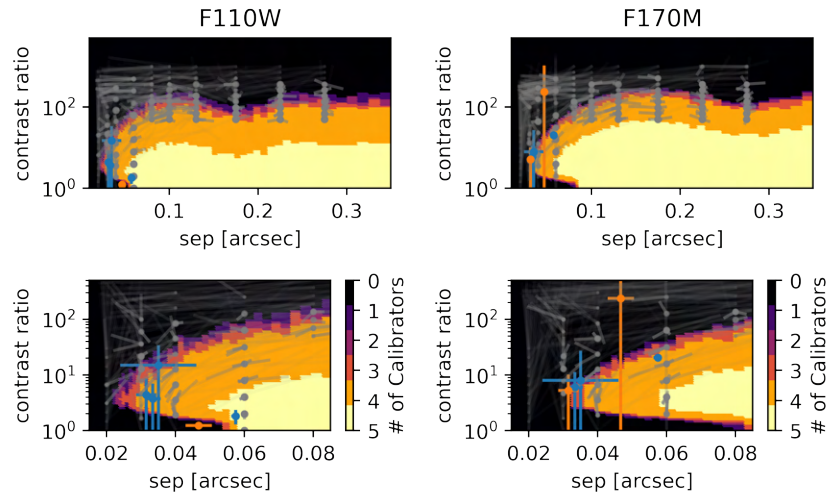


Figure B.31: Detection limits for 2M 0847-1532 from program 10143.

2M 0859-1949 (Prog. ID: 10879)

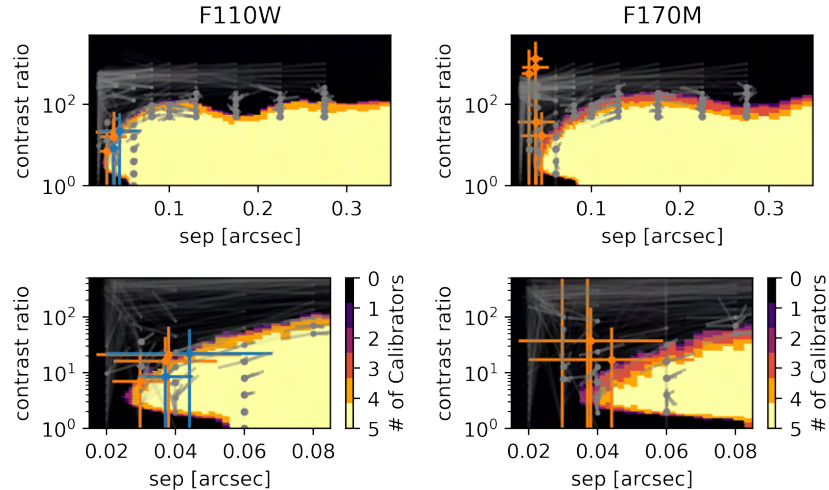


Figure B.32: Detection limits for 2M 0859-1949 from program 10143.

2M 0908+5032 (Prog. ID: 10143)

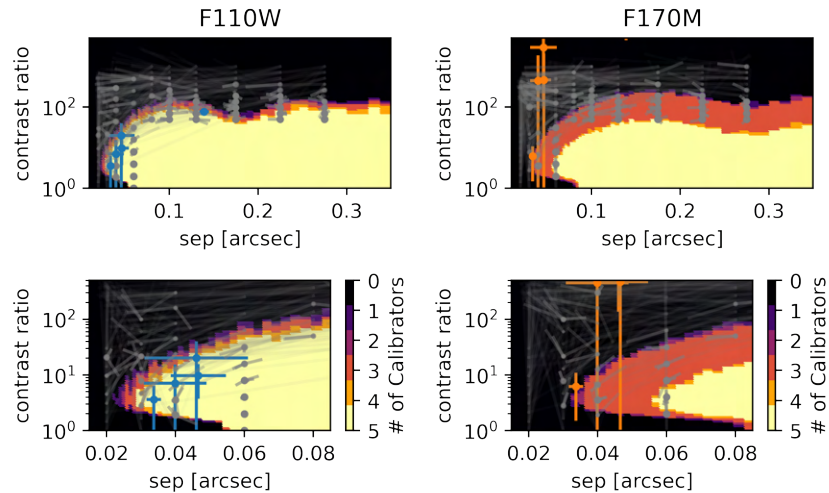


Figure B.33: Detection limits for 2M 0908+5031 from program 10143.

2M 0911+7401 (Prog. ID: 10143)

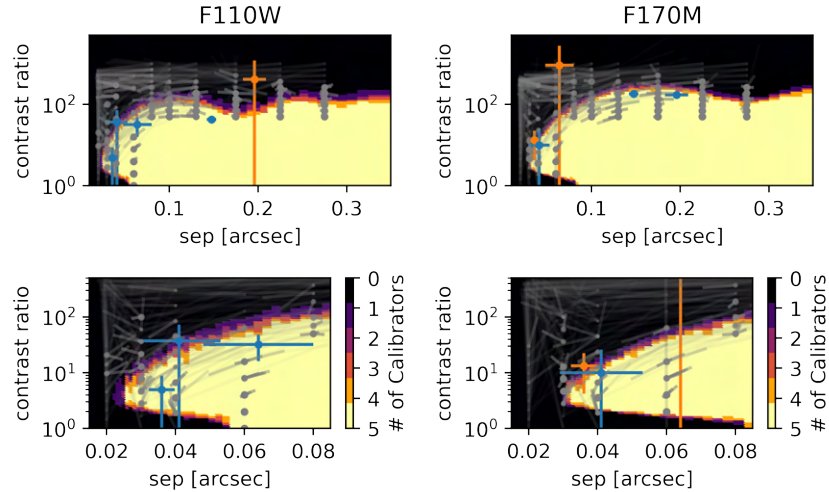


Figure B.34: Detection limits for 2M 0911+7401 from program 10143.

2M 0921-2104 (Prog. ID: 10143)

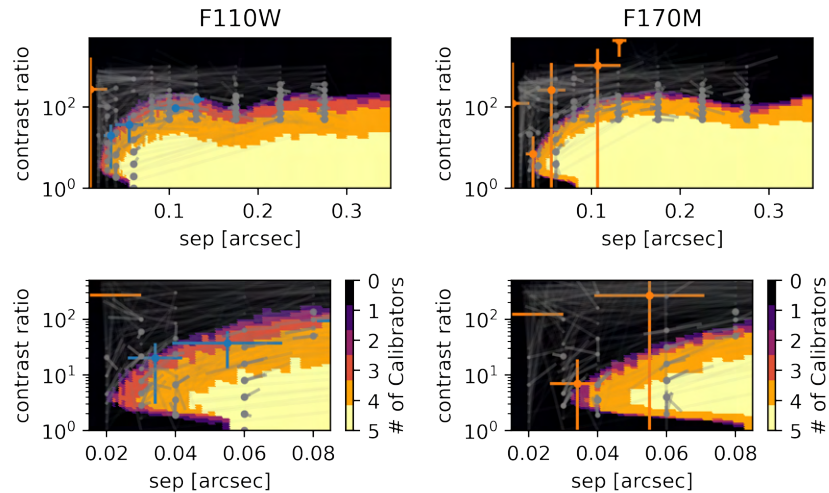


Figure B.35: Detection limits for 2M 0921-2104 from program 10143.

2M 1022+5825 (Prog. ID: 10879)

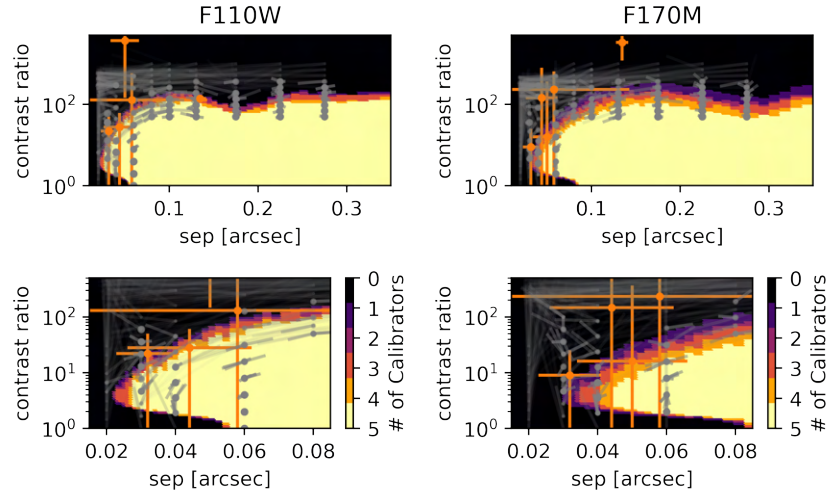


Figure B.36: Detection limits for 2M 1022+5825 from program 10143.

2M 1025+3212 (Prog. ID: 10879)

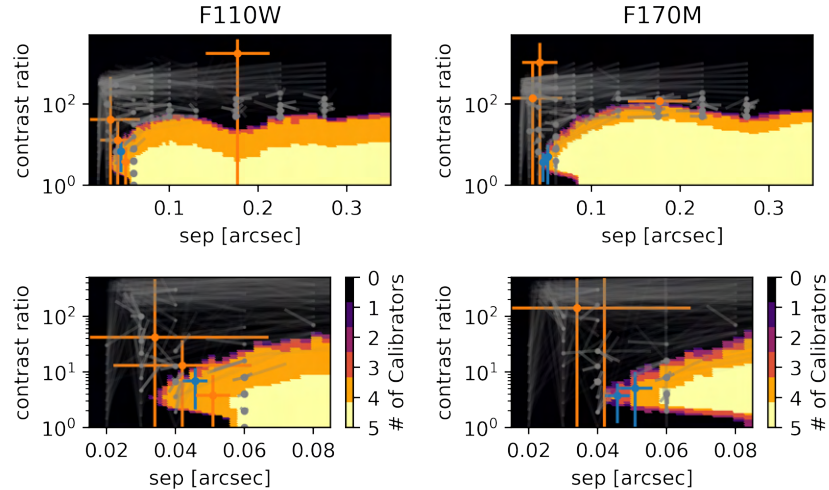


Figure B.37: Detection limits for 2M 1025+3212 from program 10143.

2M 1043+2225 (Prog. ID: 10879)

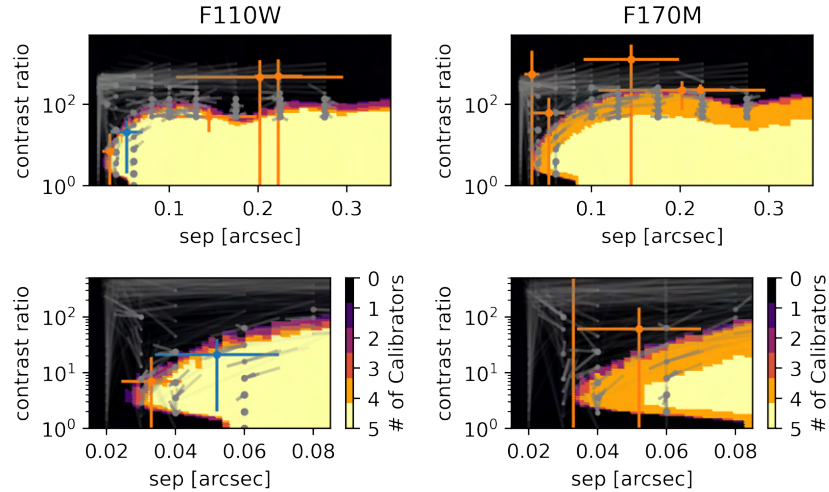


Figure B.38: Detection limits for 2M 1043+2225 from program 10143.

2M 1045-0149 (Prog. ID: 10143)

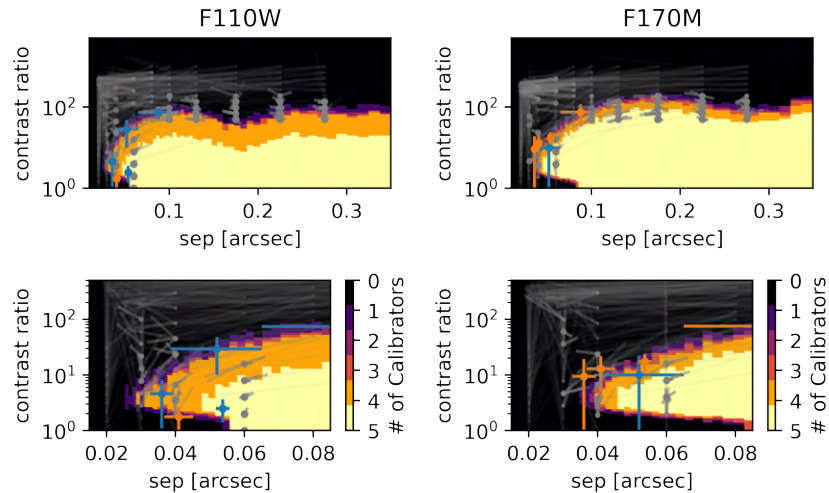


Figure B.39: Detection limits for 2M 1045-0149 from program 10143.

2M 1048+0111 (Prog. ID: 10143)

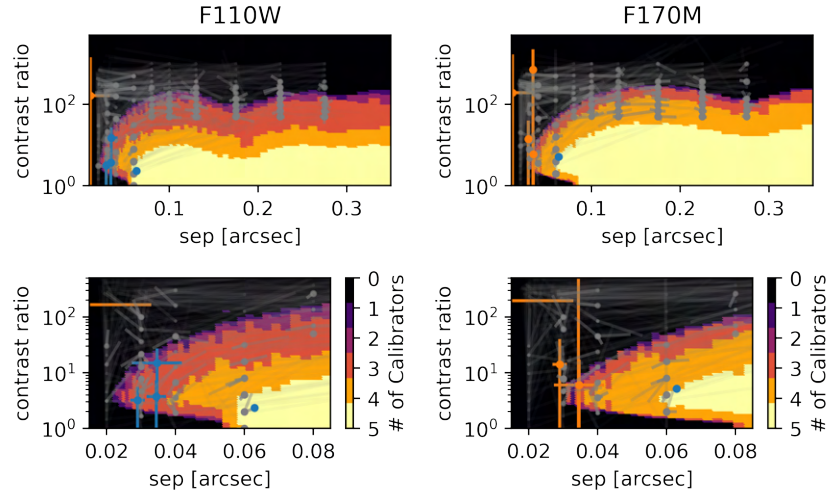


Figure B.40: Detection limits for 2M 1048+0111 from program 10143.

2M 1051+5613 (Prog. ID: 10143)

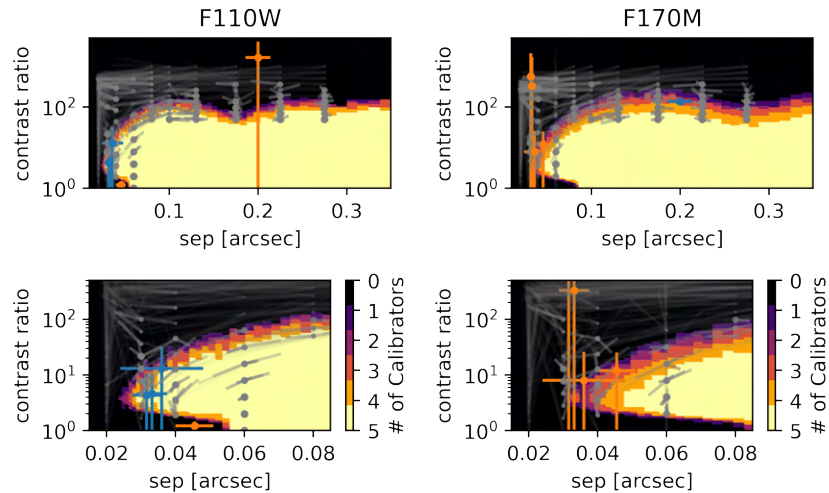


Figure B.41: Detection limits for 2M 1051+5613 from program 10143.

2M 1058-1548 (Prog. ID: 10879)

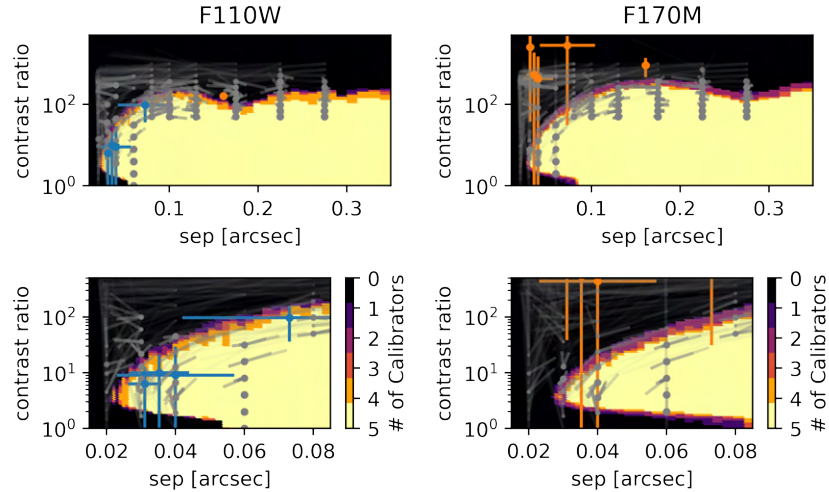


Figure B.42: Detection limits for 2M 1058-1548 from program 10143.

2M 1104+1959 (Prog. ID: 10143)

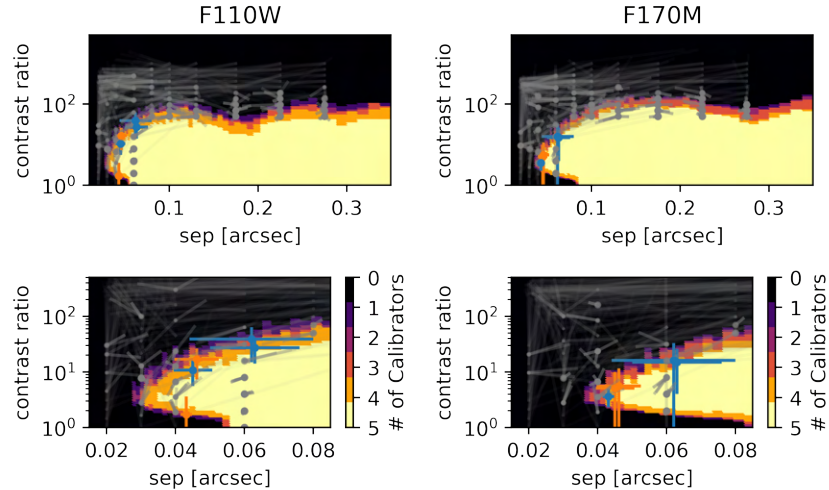


Figure B.43: Detection limits for 2M 1104+1959 from program 10143.

2M 1108+6830 (Prog. ID: 10143)

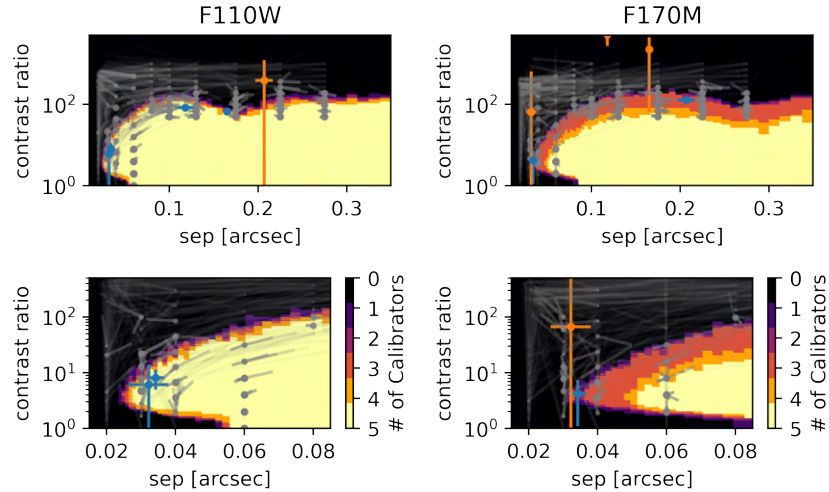


Figure B.44: Detection limits for 2M 1108+6830 from program 10143.

2M 1110+0116 (Prog. ID: 9833)

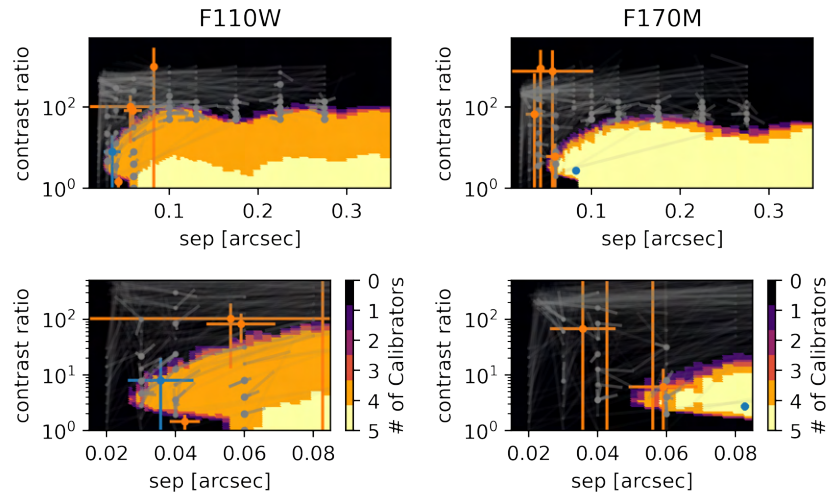


Figure B.45: Detection limits for 2M 1110+0116 from program 9833.

2M 1155-3727 (Prog. ID: 10879)

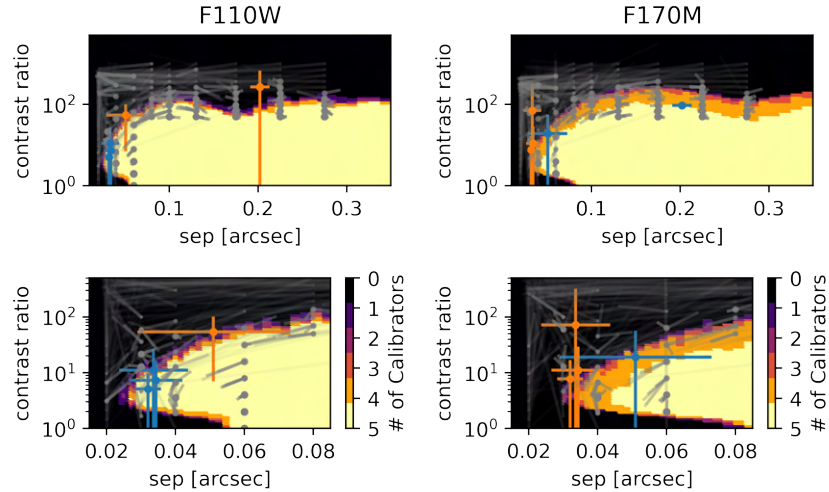


Figure B.46: Detection limits for 2M 1155-3727 from program 10143.

2M 1203+0015 (Prog. ID: 10879)

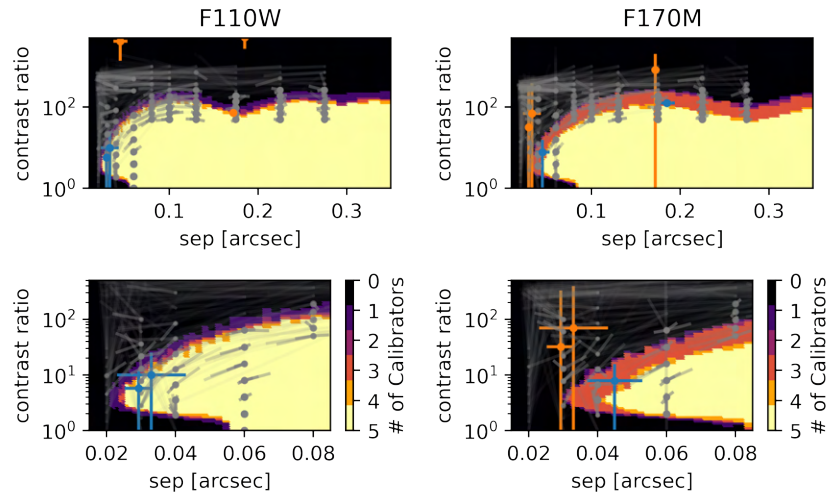


Figure B.47: Detection limits for 2M 1203+0015 from program 10143.

2M 1213-0432 (Prog. ID: 10143)

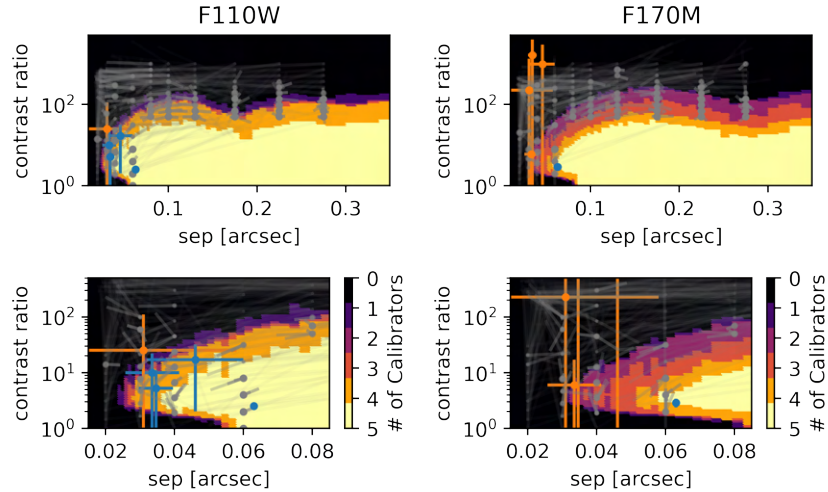


Figure B.48: Detection limits for 2M 1213-0432 from program 10143.

2M 1217-0311 (Prog. ID: 9833)

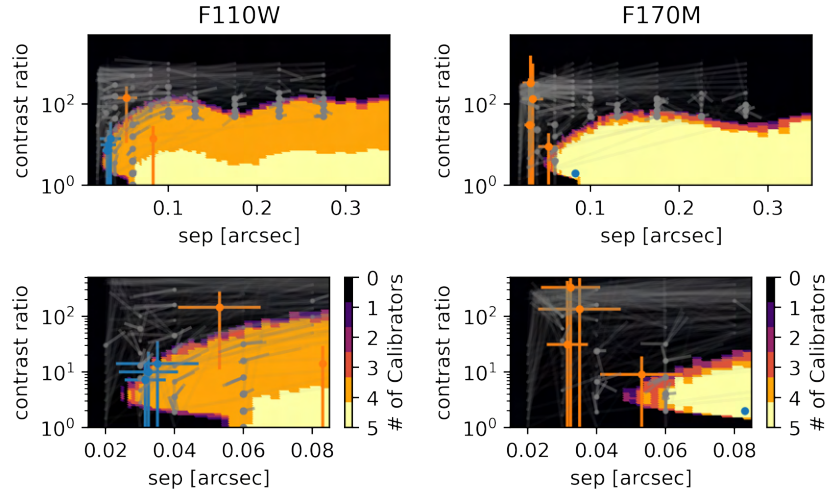


Figure B.49: Detection limits for 2M 1217-0311 from program 9833.

2M 1221+0257 (Prog. ID: 10143)

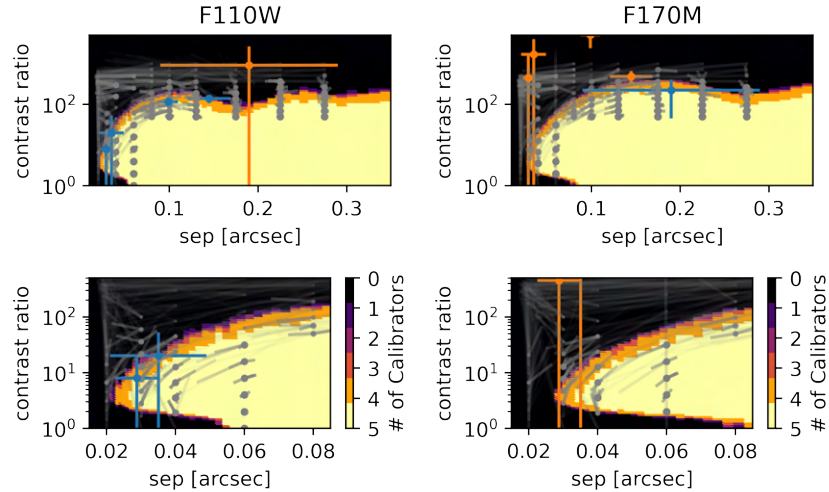


Figure B.50: Detection limits for 2M 1221+0257 from program 10143.

2M 1254-0122 (Prog. ID: 9833)

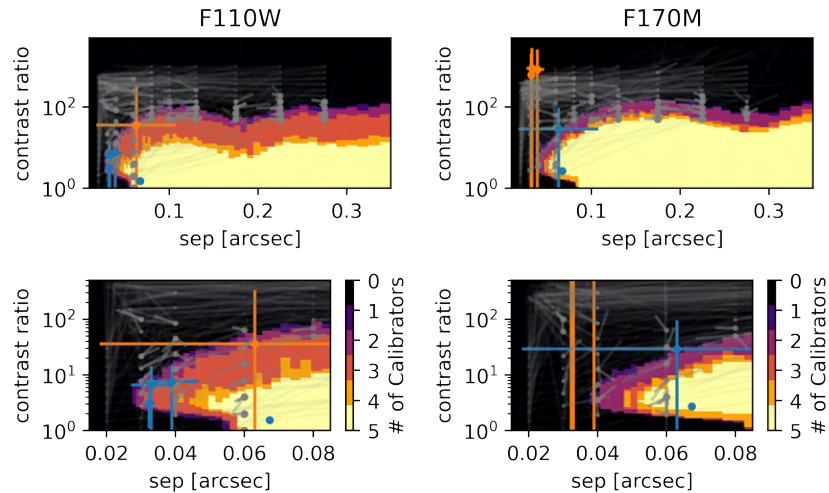


Figure B.51: Detection limits for 2M 1254-0122 from program 9833.

2M 1300+1912 (Prog. ID: 10879)

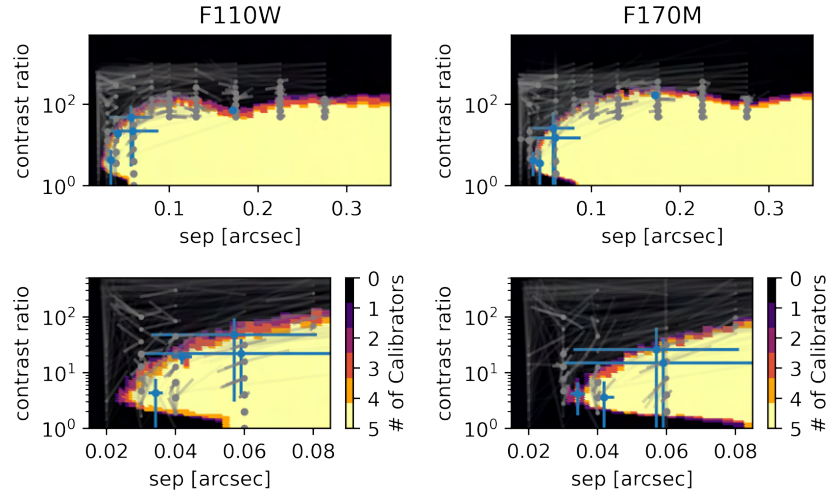


Figure B.52: Detection limits for 2M 1300+1921 from program 10143.

2M 1421+1827 (Prog. ID: 10879)

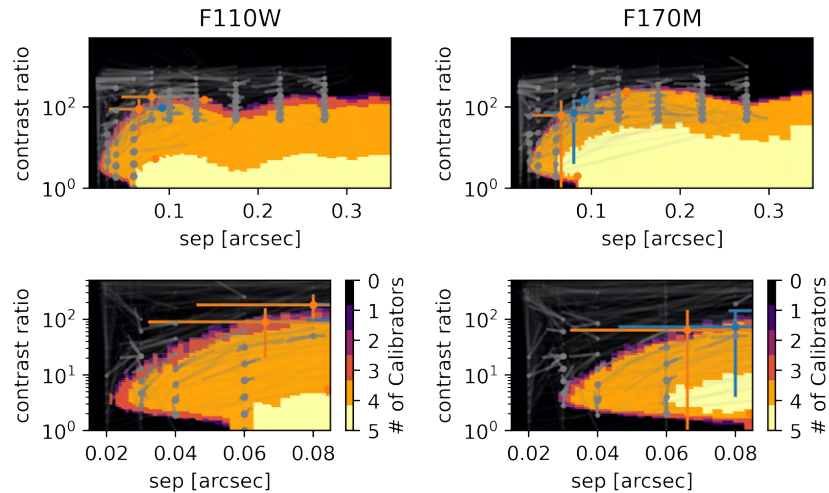


Figure B.53: Detection limits for 2M 1421+1827 from program 10143.

2M 1425-3650 (Prog. ID: 10879)

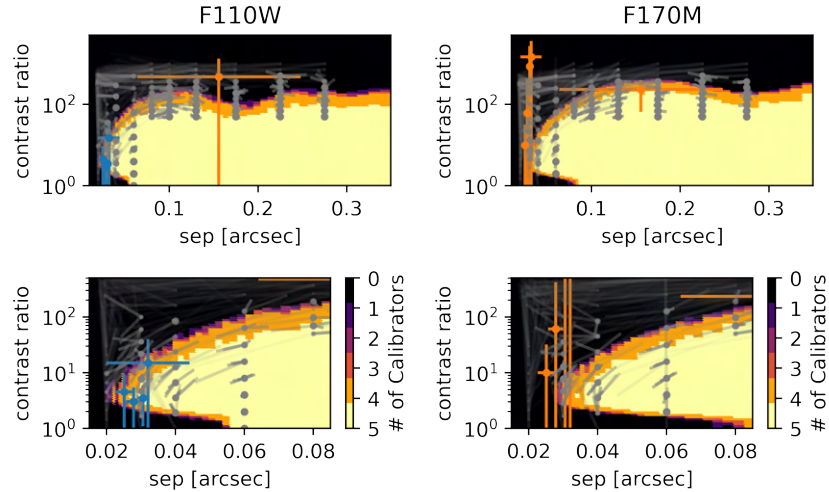


Figure B.54: Detection limits for 2M 1425-3650 from program 10143.

2M 1428+5923 (Prog. ID: 10143)

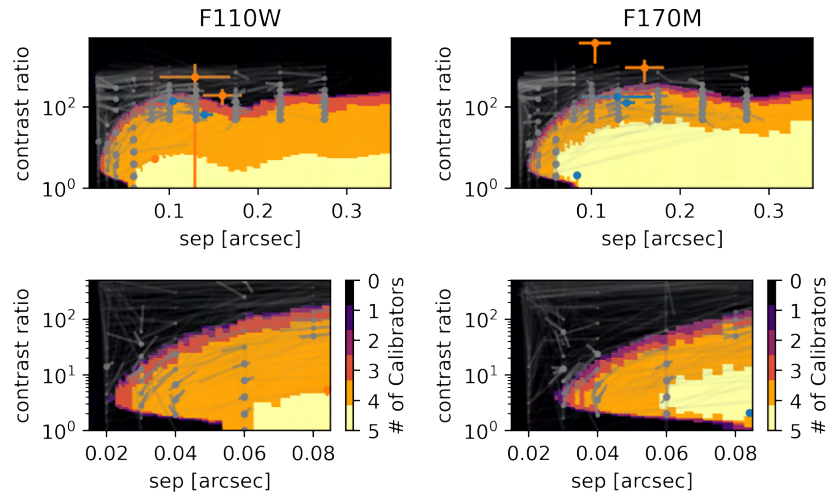


Figure B.55: Detection limits for 2M 1428+5923 from program 10143.

2M 1439+1929 (Prog. ID: 10879)

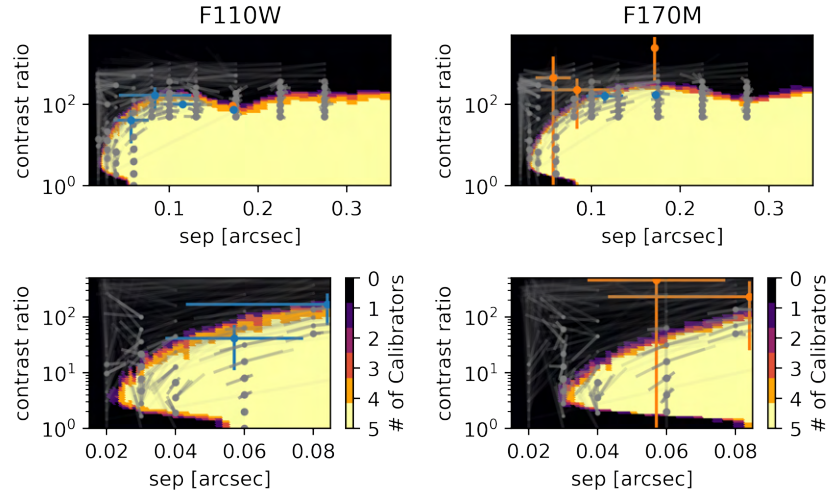


Figure B.56: Detection limits for 2M 1439+1929 from program 10143.

2M 1448+1031 (Prog. ID: 10143)

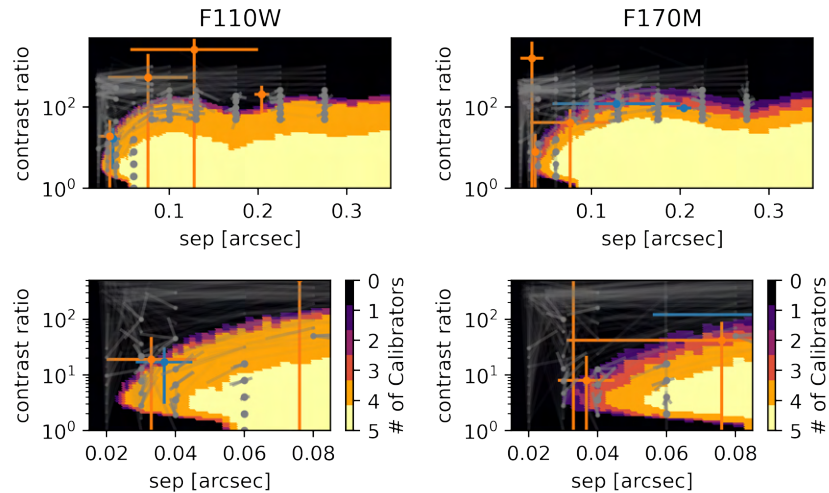


Figure B.57: Detection limits for 2M 1448+1031 from program 10143.

2M 1503+2525 (Prog. ID: 9833)

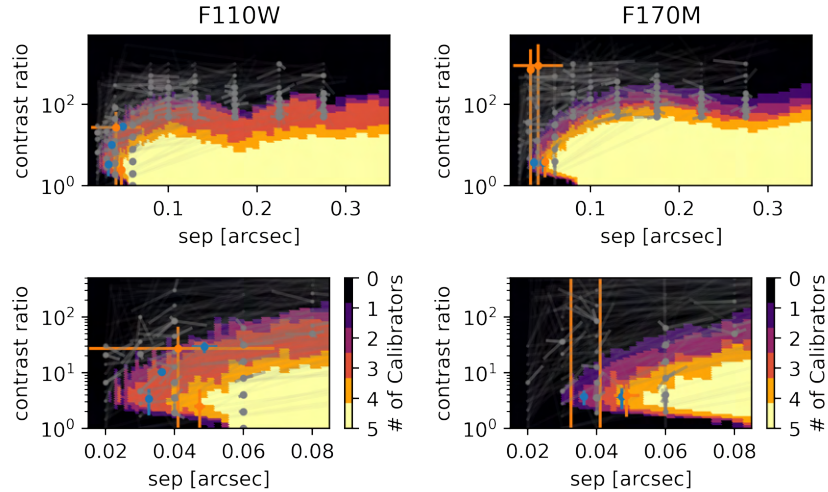


Figure B.58: Detection limits for 2M 1503+2525 from program 9833.

2M 1506+1321 (Prog. ID: 10879)

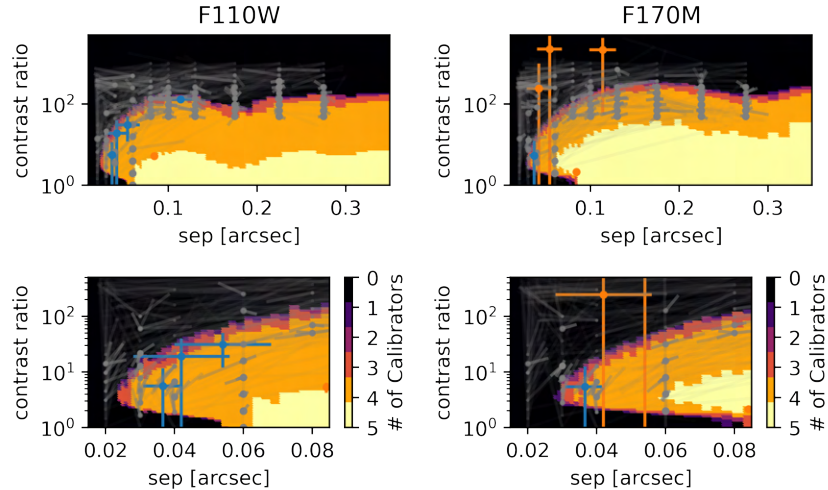


Figure B.59: Detection limits for 2M 1506+1321 from program 10143.

2M 1507-1627 (Prog. ID: 10143)

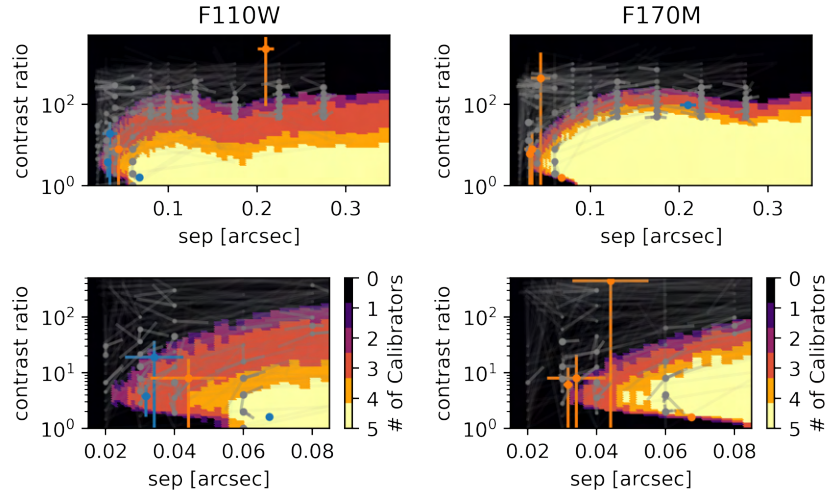


Figure B.60: Detection limits for 2M 1507-1627 from program 10143.

2M 1515+4847 (Prog. ID: 10879)

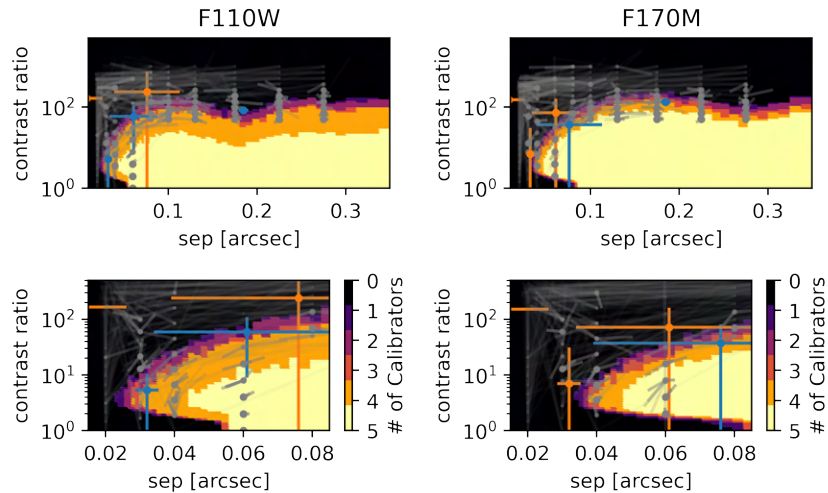


Figure B.61: Detection limits for 2M 1515+4847 from program 10143.

2M 1552+2948 (Prog. ID: 10143)

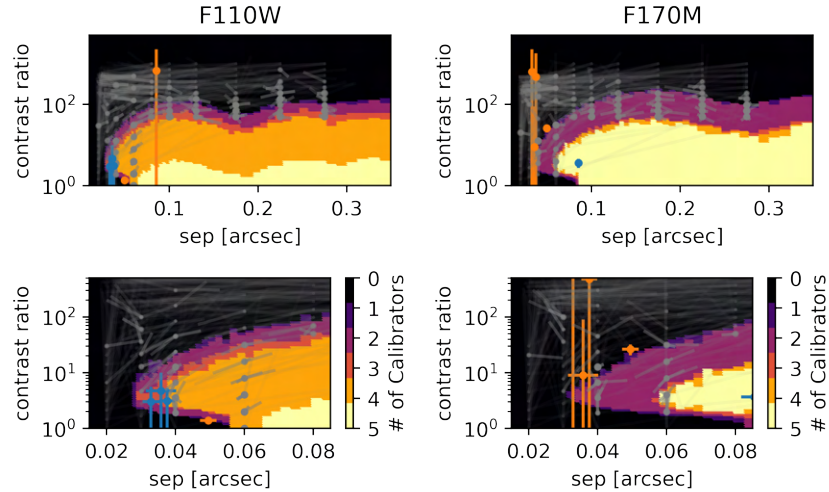


Figure B.62: Detection limits for 2M 1552+2948 from program 10143.

2M 1624+0029 (Prog. ID: 9833)

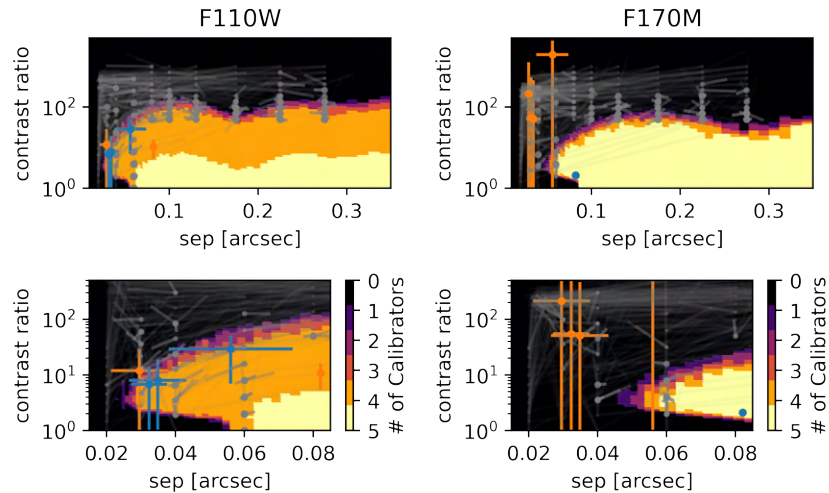


Figure B.63: Detection limits for 2M 1624+0029 from program 9833.

2M 1658+7027 (Prog. ID: 10143)

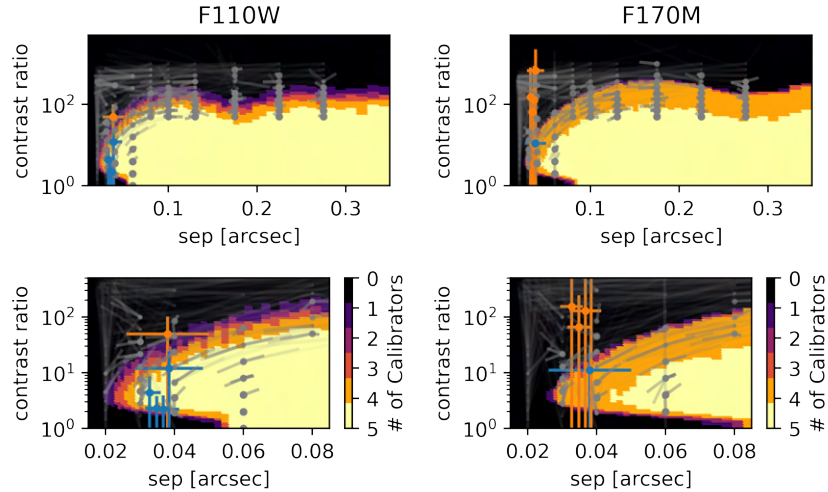


Figure B.64: Detection limits for 2M 1658+7027 from program 10143.

2M 1705-0516 (Prog. ID: 10143)

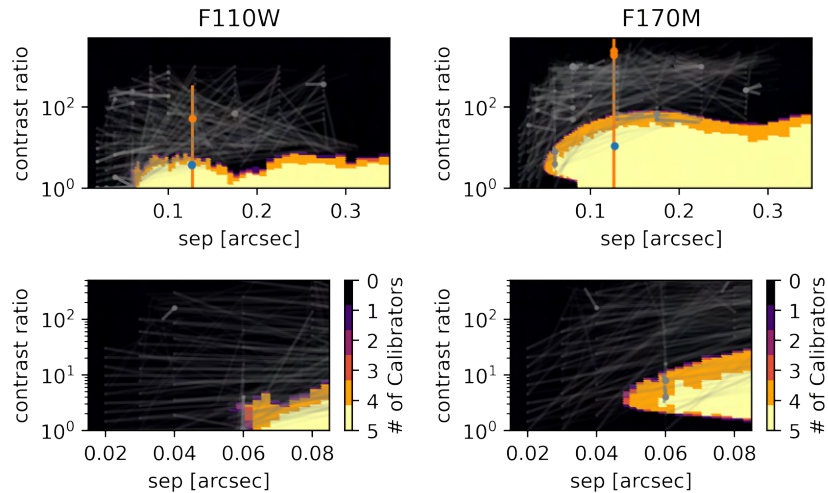


Figure B.65: Detection limits for 2M 1705-0516 from program 10143.

2M 1721+3344 (Prog. ID: 10879)

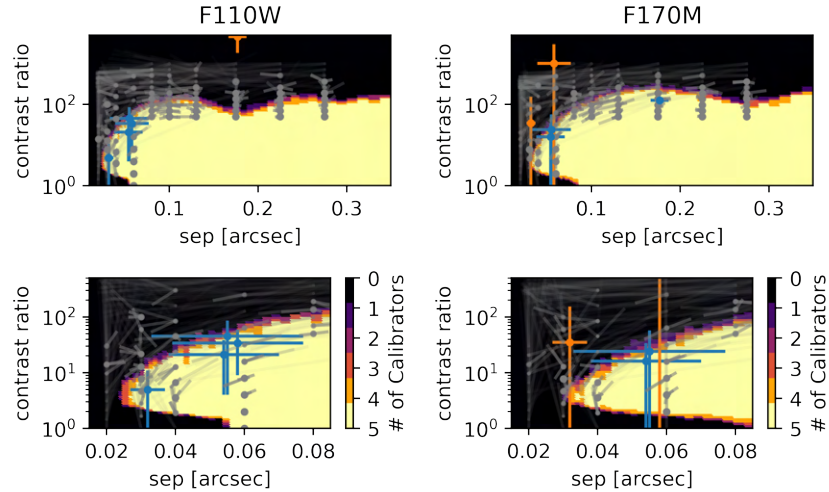


Figure B.66: Detection limits for 2M 1721+3344 from program 10143.

2M 1731+2721 (Prog. ID: 10143)

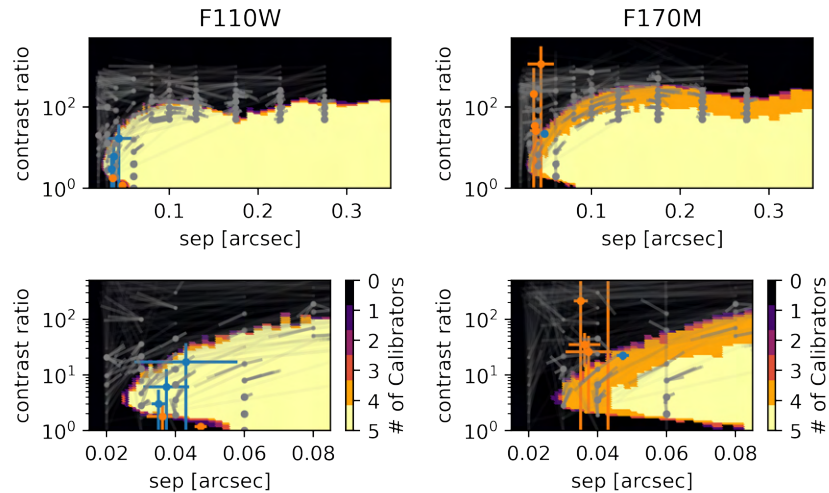


Figure B.67: Detection limits for 2M 1731+2721 from program 10143.

2M 1750+1759 (Prog. ID: 9833)

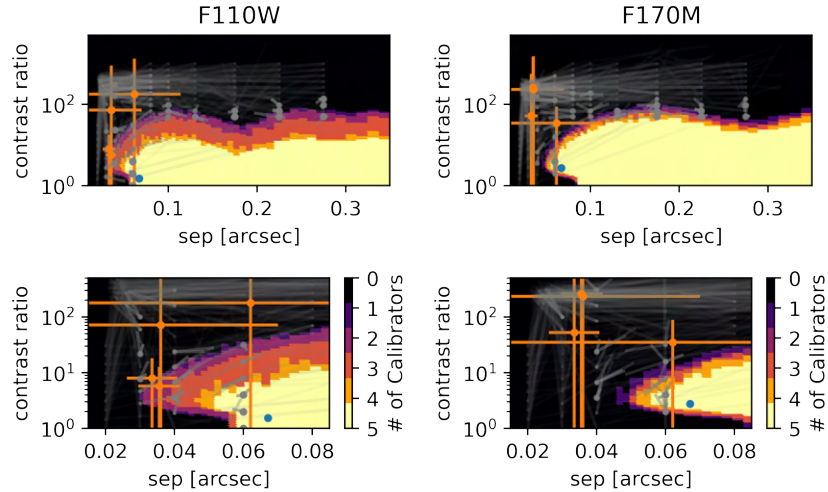


Figure B.68: Detection limits for 2M 1750+1759 from program 9833.

2M 1753-6559 (Prog. ID: 10143)

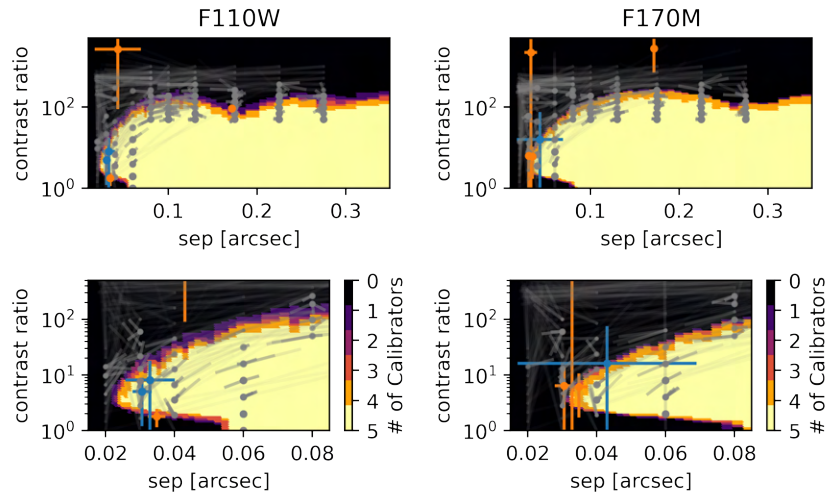


Figure B.69: Detection limits for 2M 1753-6559 from program 10143.

2M 1807+5015 (Prog. ID: 10143)

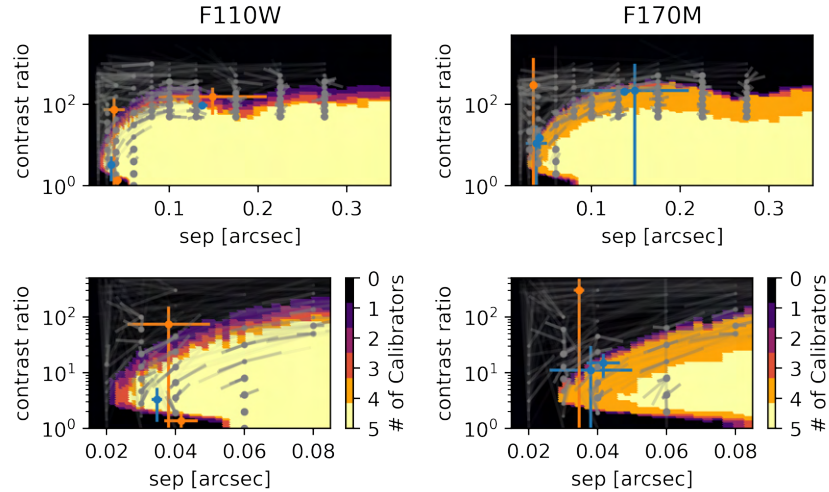


Figure B.70: Detection limits for 2M 1807+5015 from program 10143.

2M 2002-0521 (Prog. ID: 10879)

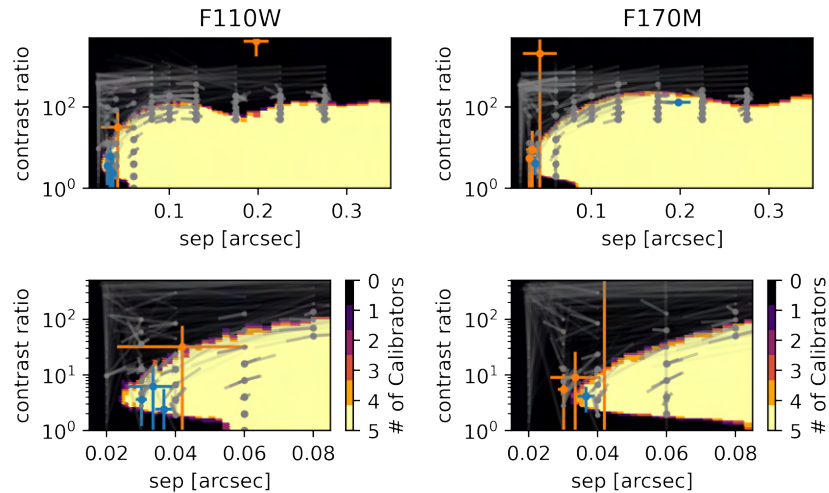


Figure B.71: Detection limits for 2M 2002-0521 from program 10143.

2M 2036+1051 (Prog. ID: 10143)

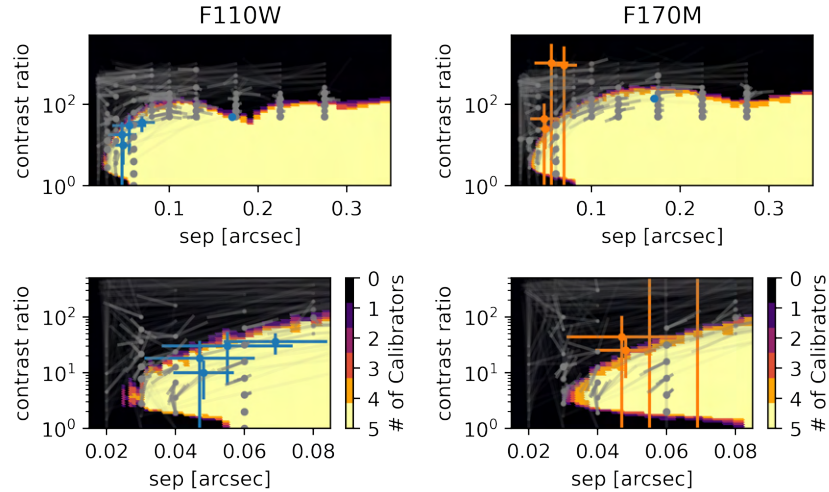


Figure B.72: Detection limits for 2M 2036+1051 from program 10143.

2M 2057-0252 (Prog. ID: 10143)

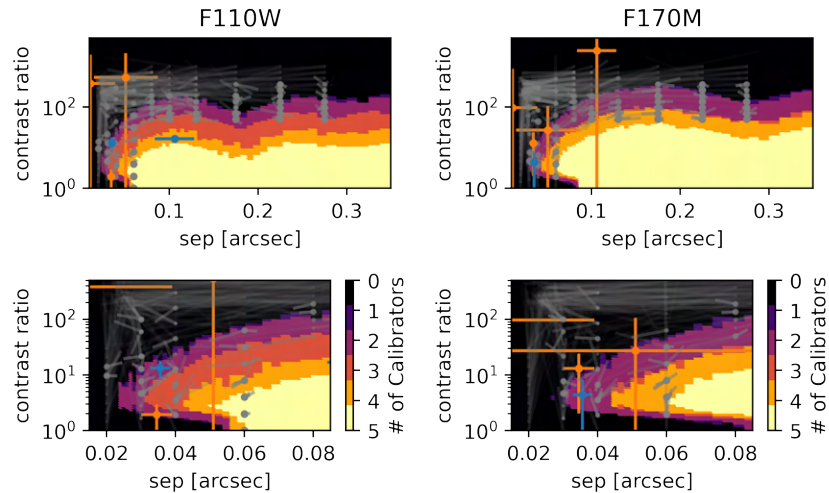


Figure B.73: Detection limits for 2M 2057-0252 from program 10143.

2M 2104-1037 (Prog. ID: 10143)

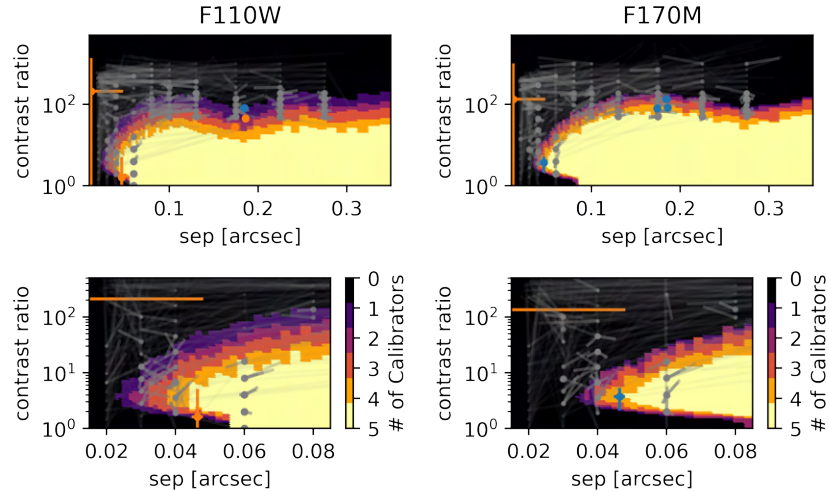


Figure B.74: Detection limits for 2M 2104-1037 from program 10143.

2M 2139+0220 (Prog. ID: 10143)

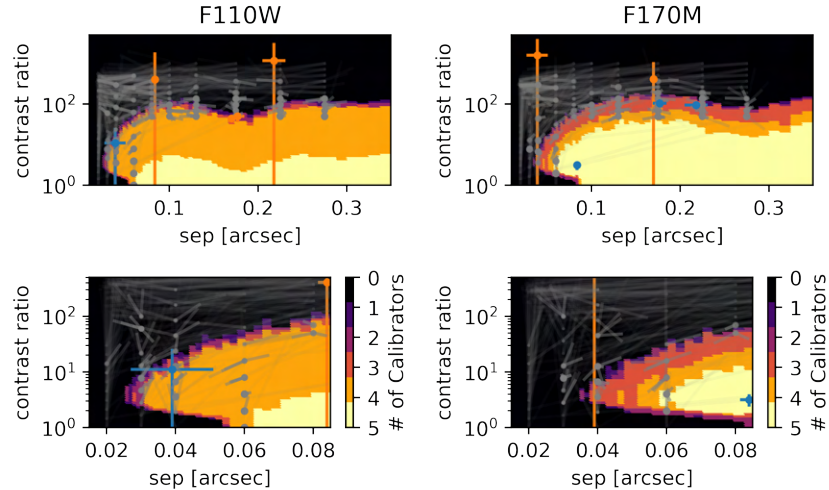


Figure B.75: Detection limits for 2M 2139+0220 from program 10143.

2M 2148+4003 (Prog. ID: 10879)

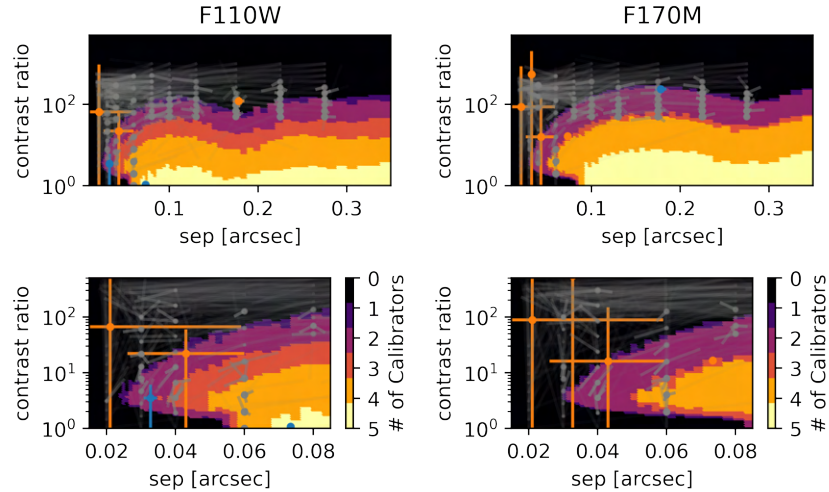


Figure B.76: Detection limits for 2M 2148+4003 from program 10143.

2M 2224-0158 (Prog. ID: 10879)

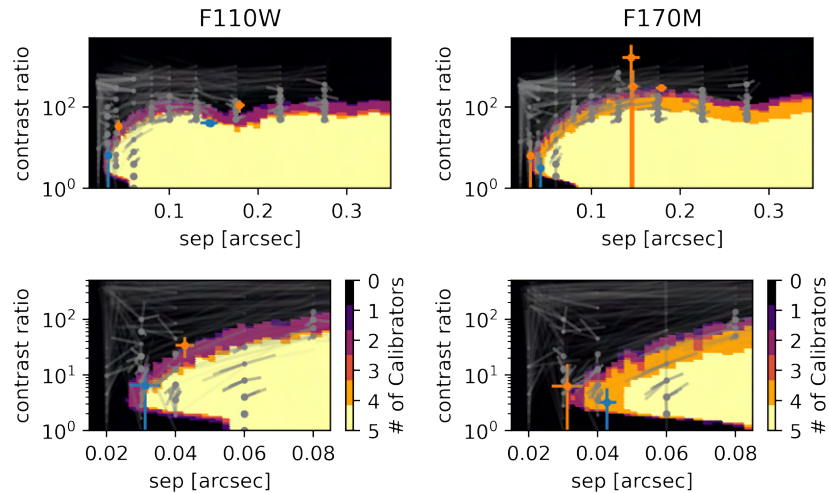


Figure B.77: Detection limits for 2M 2224-0158 from program 10143.

2M 2228-4310 (Prog. ID: 9833)

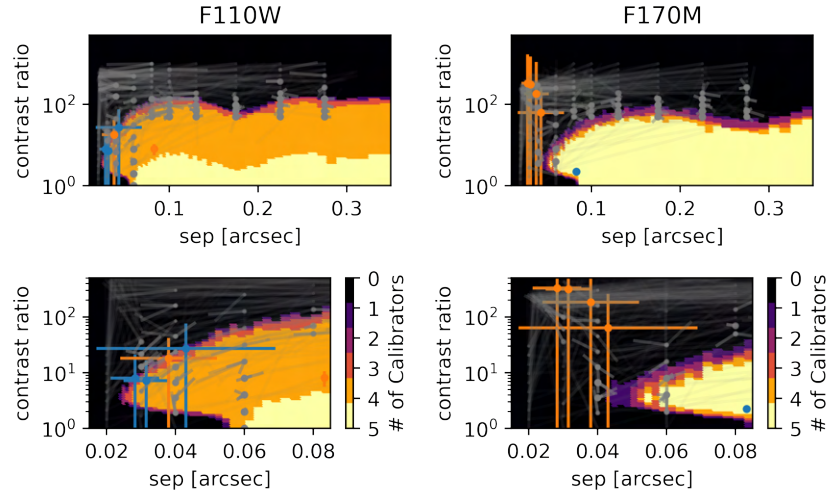


Figure B.78: Detection limits for 2M 2228-4310 from program 9833.

2M 2237+3922 (Prog. ID: 10879)

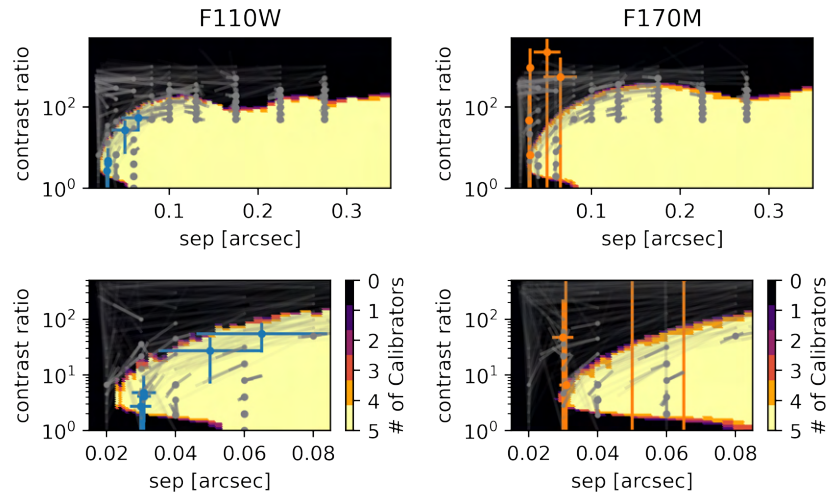


Figure B.79: Detection limits for 2M 2237+3922 from program 10143.

2M 2249+3205 (Prog. ID: 10143)

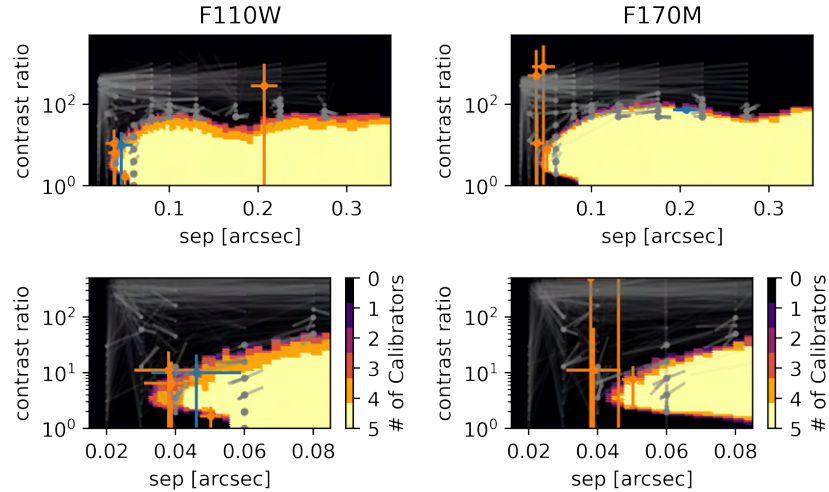


Figure B.80: Detection limits for 2M 2249+3205 from program 10143.

2M 2254+3123 (Prog. ID: 9833)

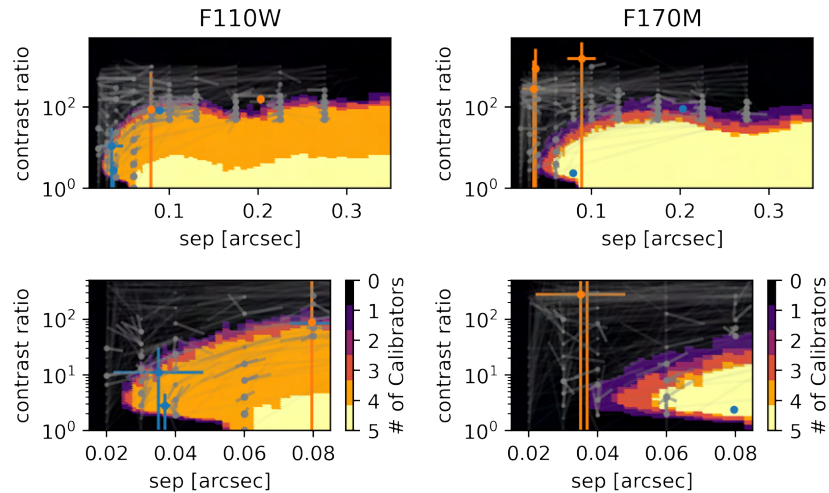


Figure B.81: Detection limits for 2M 2254+3123 from program 9833.

2M 2325+4251 (Prog. ID: 10143)

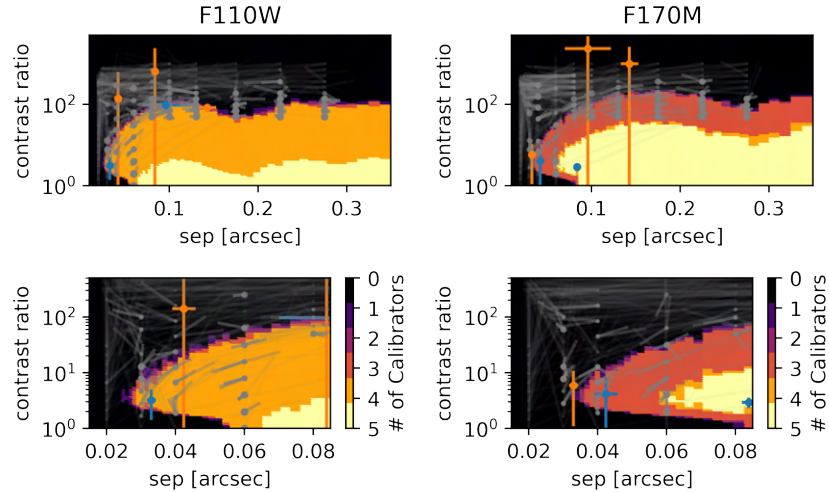


Figure B.82: Detection limits for 2M 2325+4251 from program 10143.

2M 2339+1352 (Prog. ID: 9833)

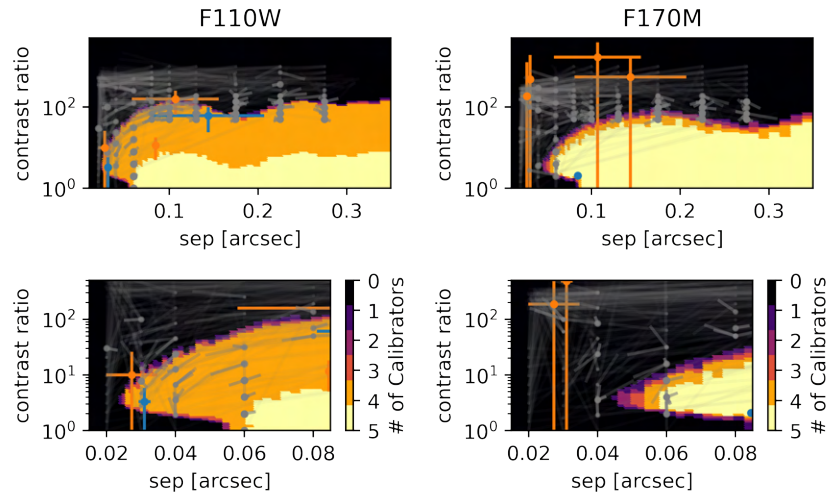


Figure B.83: Detection limits for 2M 2339+1352 from program 9833.

Appendix C

Figure Set corresponding to Figure 2.6: Detection Limits for Significant Detections (See Section 2.5.1)

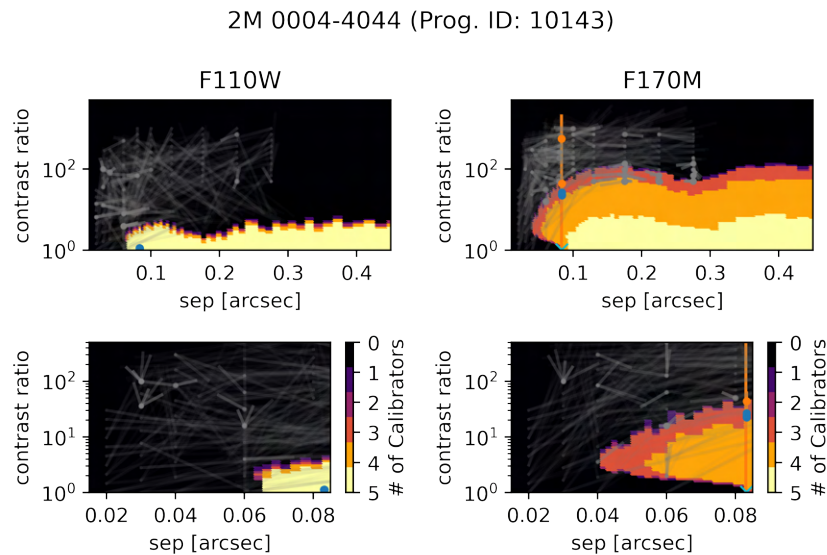


Figure C.1: Detection limits for 2M 0004-4044 from program 10143.

2M 0025+4759 (Prog. ID: 10143)

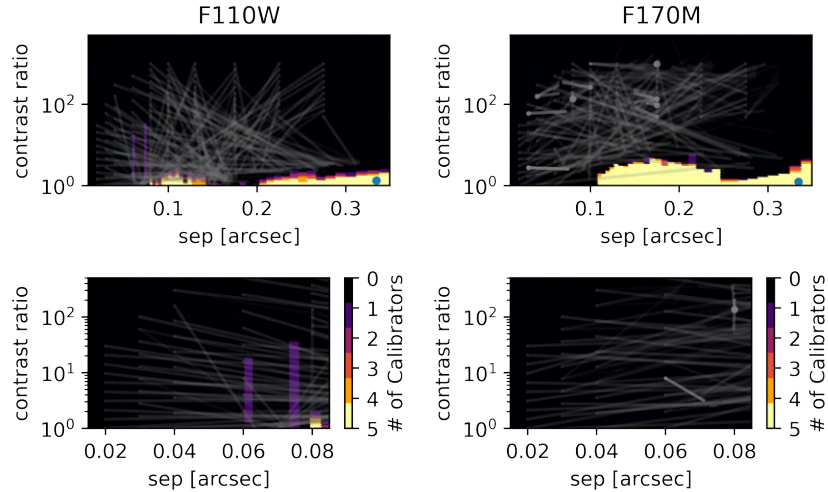


Figure C.2: Detection limits for 2M 0025+4759 from program 10143.

2M 0147-4954 (Prog. ID: 10143)

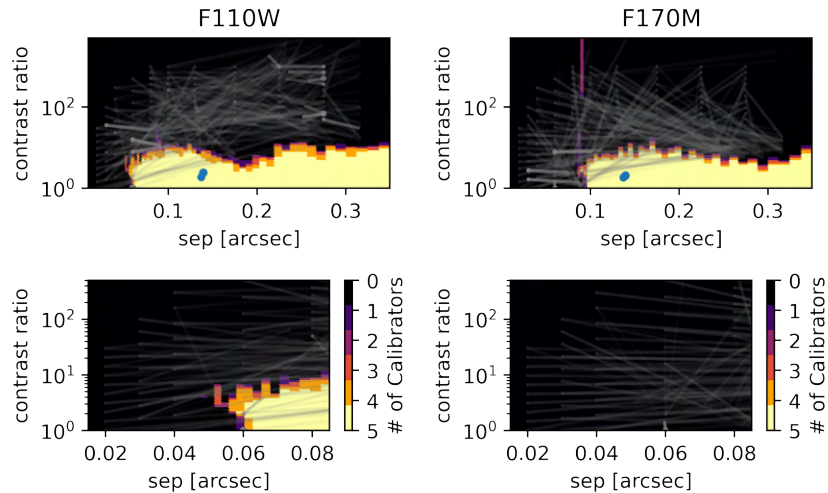


Figure C.3: Detection limits for 2M 0147-4954 from program 10143.

2M 0423-0414 (Prog. ID: 9833)

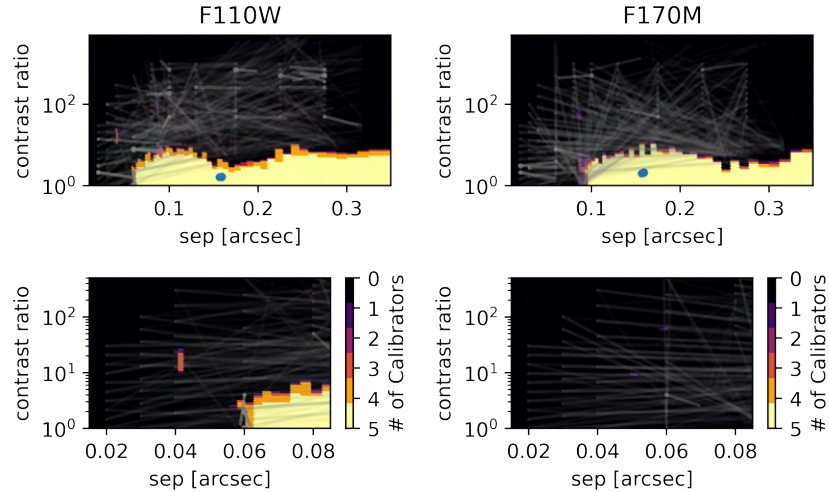


Figure C.4: Detection limits for 2M 0423-0414 from program 9833.

2M 0423-0414 (Prog. ID: 11136)

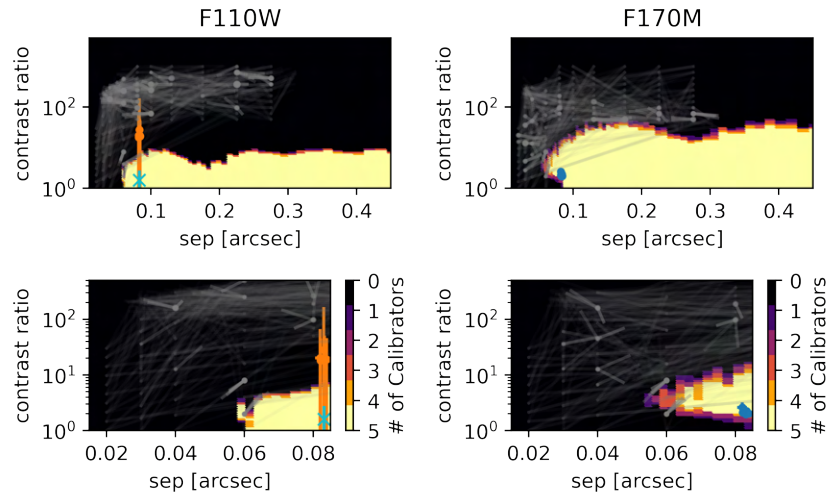


Figure C.5: Detection limits for 2M 0423-0414 from program 11136.

2M 0429-3123 (Prog. ID: 10143)

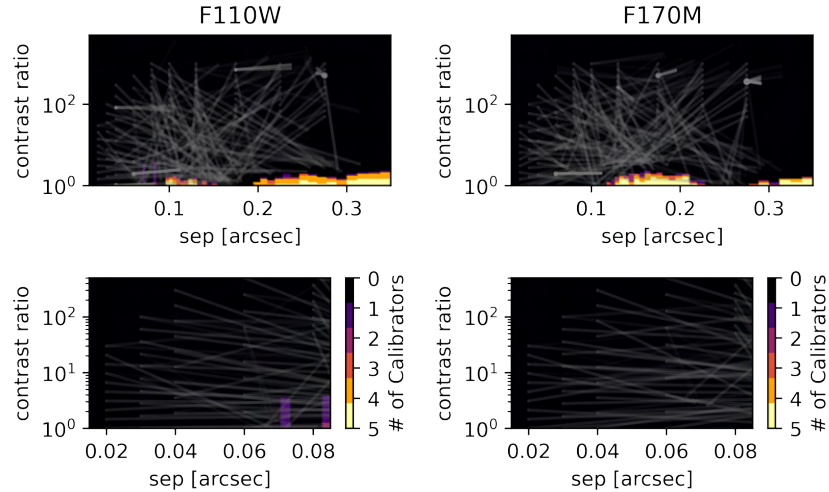


Figure C.6: Detection limits for 2M 0429-3123 from program 10143.

2M 0700+3157 (Prog. ID: 10143)

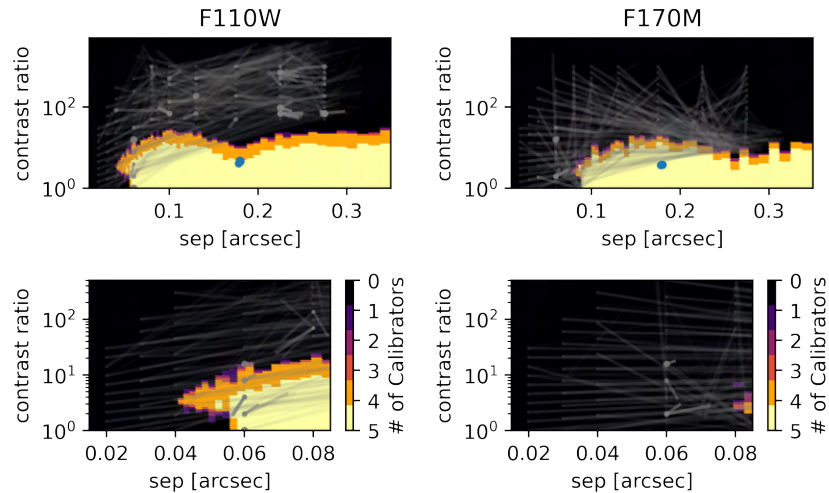


Figure C.7: Detection limits for 2M 0700+3157 from program 10143.

2M 0850+1057 (Prog. ID: 9843)

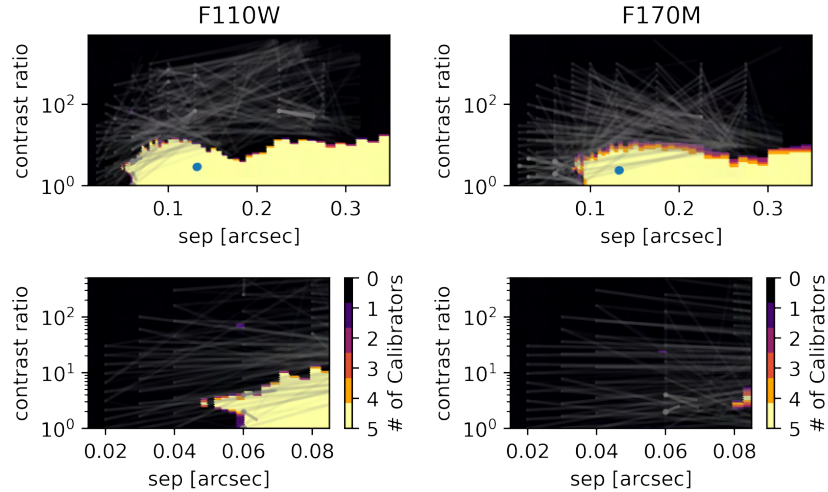


Figure C.8: Detection limits for 2M 0850+1057 from program 9843.

2M 0926+5847 (Prog. ID: 9833)

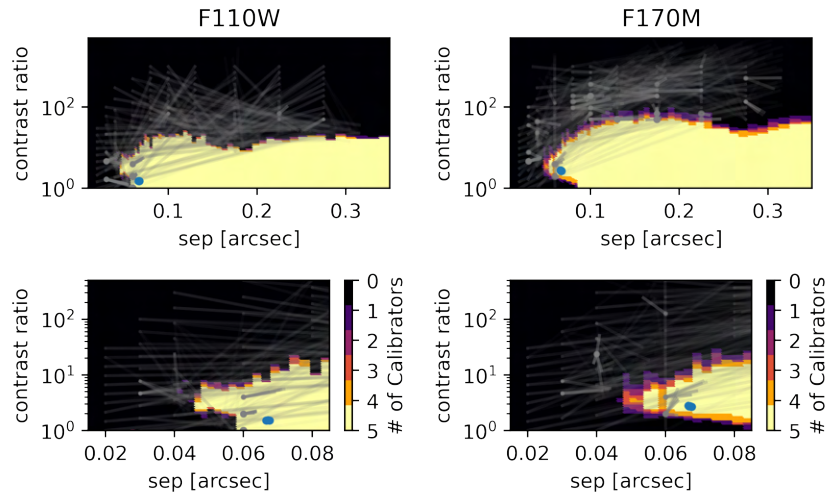


Figure C.9: Detection limits for 2M 0926+5847 from program 9833.

2M 1021-0304 (Prog. ID: 9833)

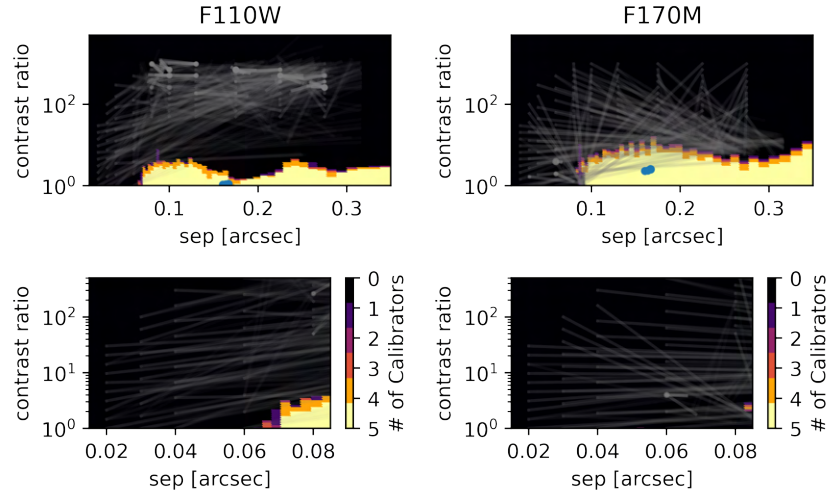


Figure C.10: Detection limits for 2M 1021-0304 from program 9833.

2M 1534+1615 (Prog. ID: 11136)

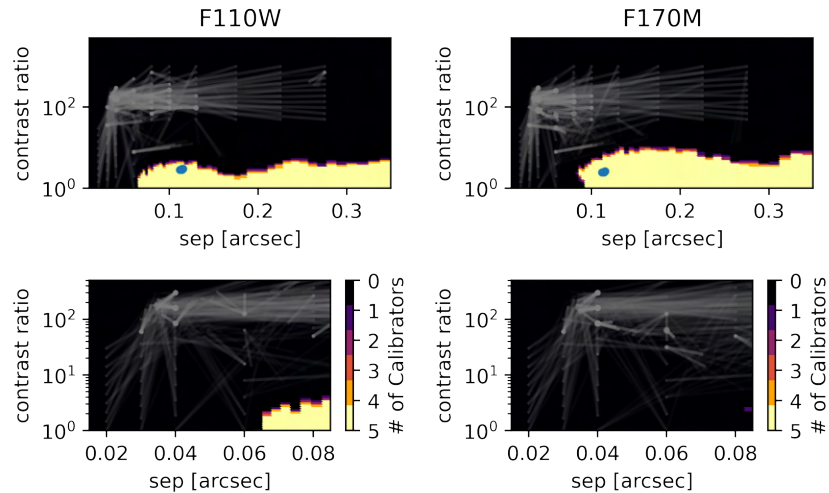


Figure C.11: Detection limits for 2M 1534+1615 from program 11136.

2M 1553+1532 (Prog. ID: 9833)

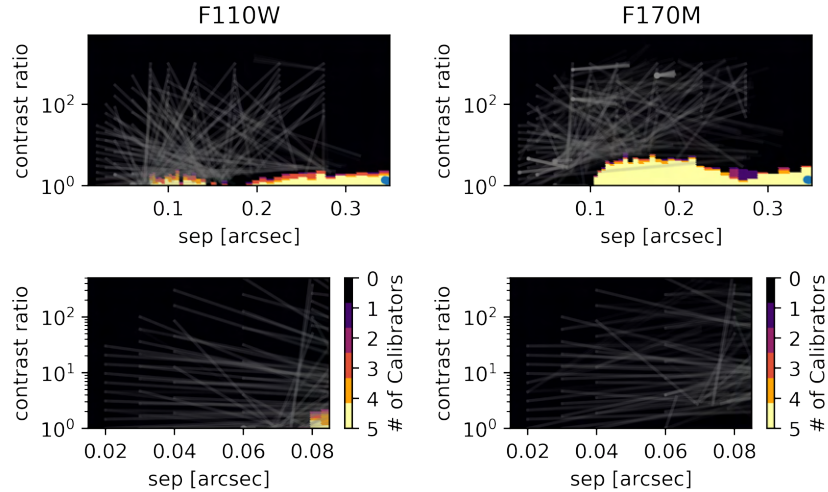


Figure C.12: Detection limits for 2M 1553+1532 from program 9833.

2M 1728+3948 (Prog. ID: 9843)

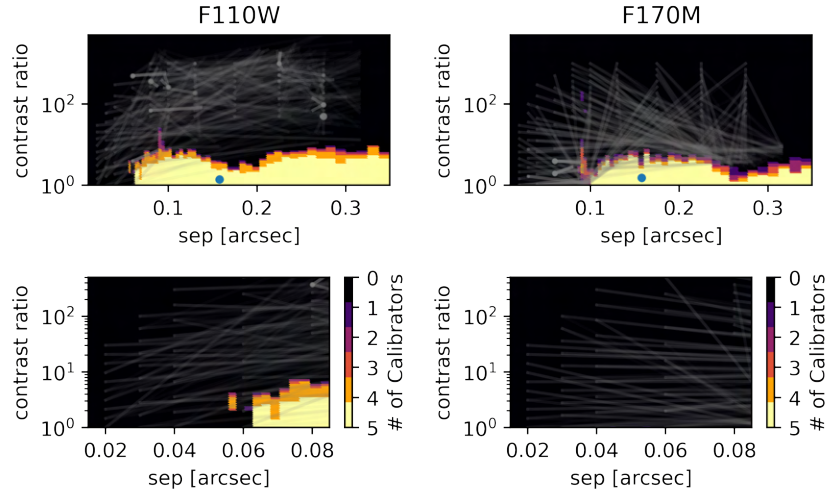


Figure C.13: Detection limits for 2M 1728+3948 from program 9843.

SDSS 2052-1609 (Prog. ID: 11136)

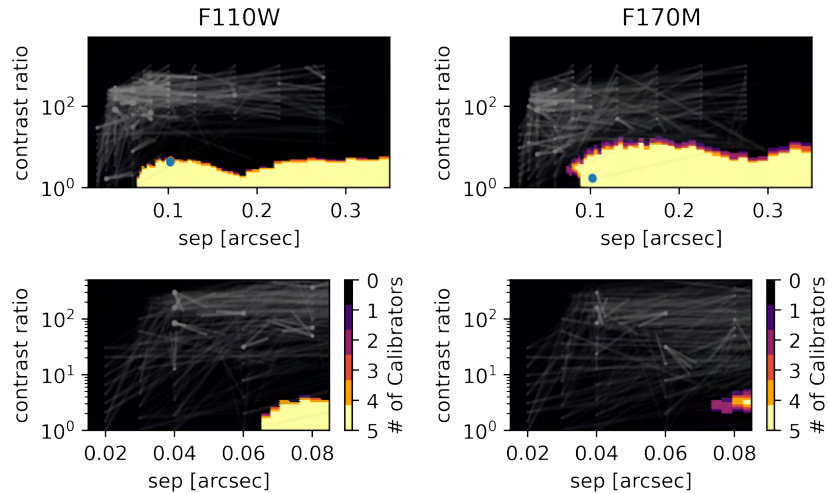


Figure C.14: Detection limits for 2M 2052-1609 from program 11136.

2M 2152+0937 (Prog. ID: 10143)

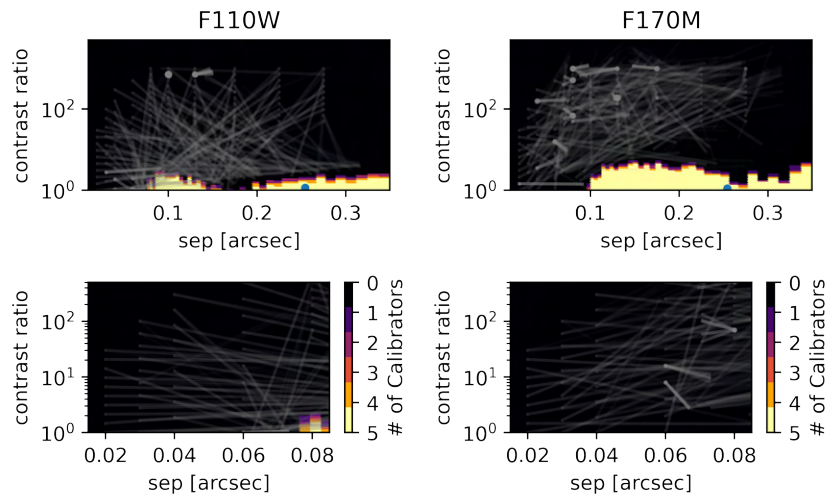


Figure C.15: Detection limits for 2M 2152+0937 from program 10143.

2M 2252-1730 (Prog. ID: 10143)

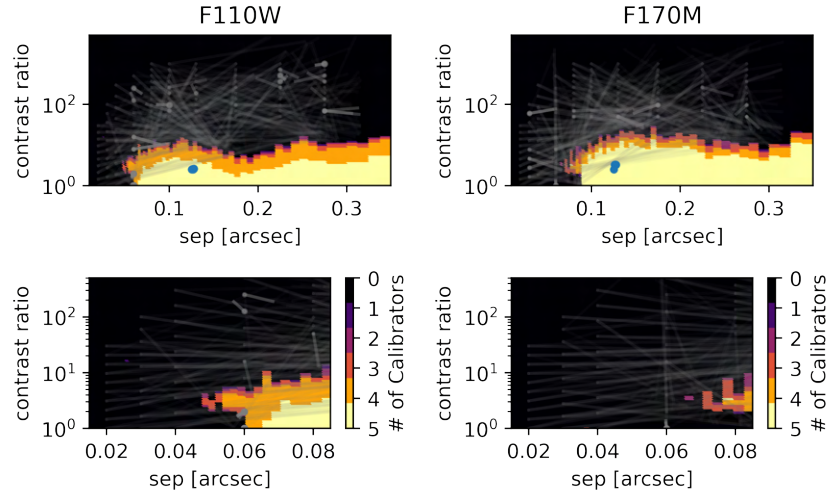


Figure C.16: Detection limits for 2M 2252-1730 from program 10143.

2M 2252-1730 (Prog. ID: 11136)

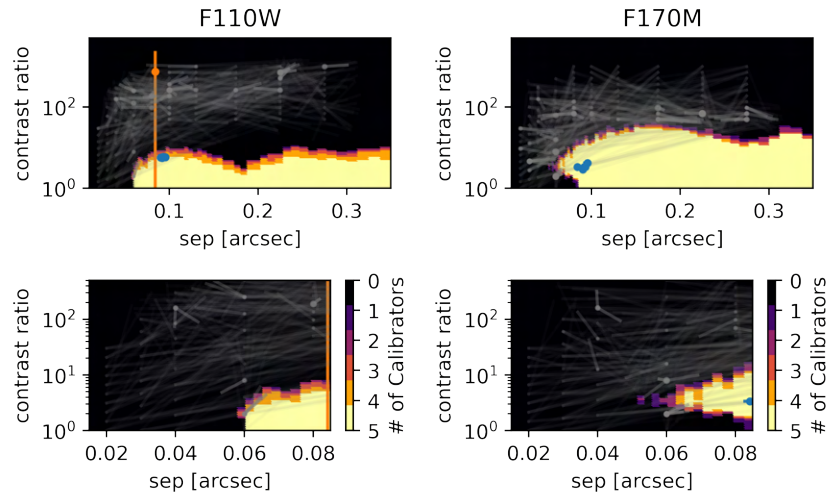


Figure C.17: Detection limits for 2M 2252-1730 from program 11136.

2M 2255-5713 (Prog. ID: 10879)

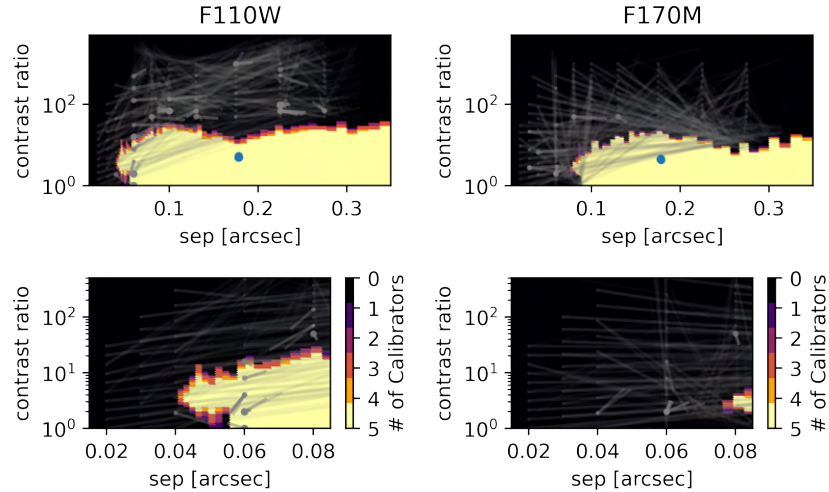


Figure C.18: Detection limits for 2M 2255-5713 from program 10879.

2M 2351-2537 (Prog. ID: 10143)

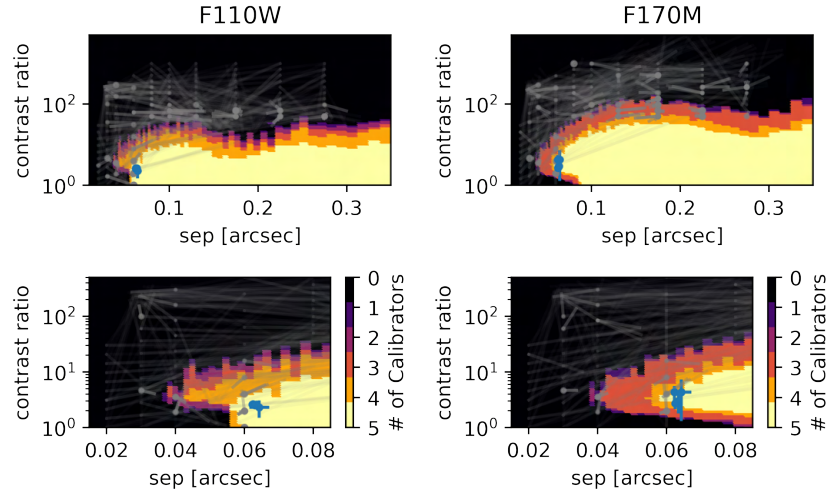


Figure C.19: Detection limits for 2M 2351-2537 from program 10143.

Appendix D

Figure Set corresponding to Figure 2.7: Detection Limits for Notable Non-Detections (See section 2.5.4)

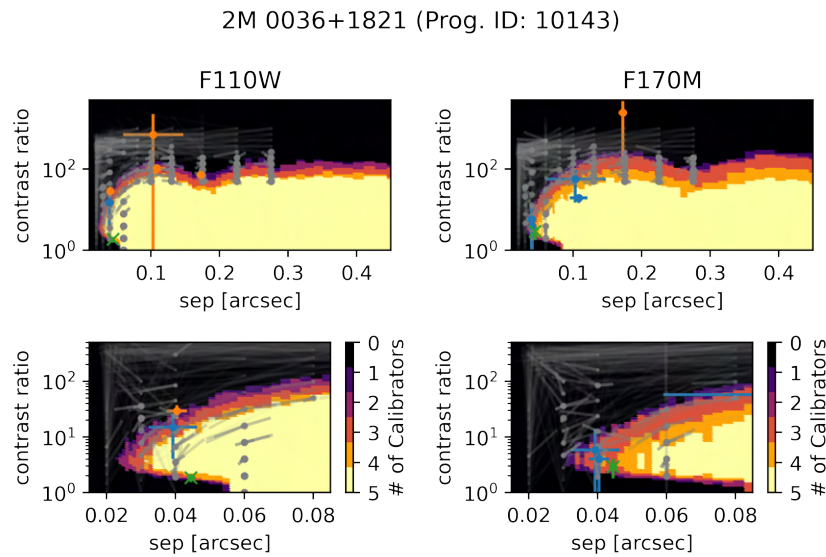


Figure D.1: Detection limits for 2M 0036+1821 from program 10143.

2M 0045+1634 (Prog. ID: 10143)

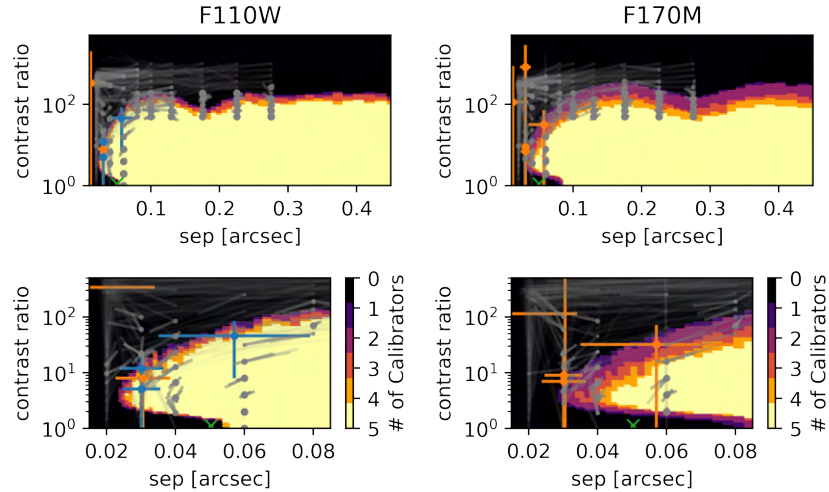


Figure D.2: Detection limits for 2M 0045+1634 from program 10143.

2M 0109+2949 (Prog. ID: 10879)

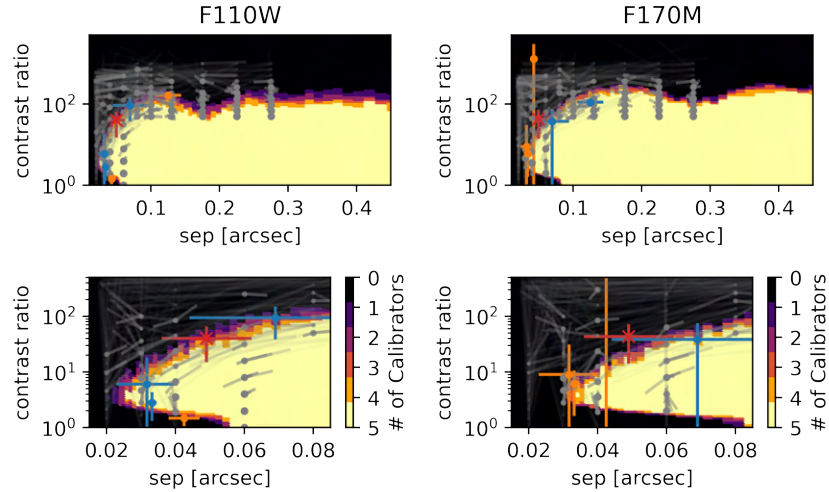


Figure D.3: Detection limits for 2M 0109+2949 from program 10879.

2M 0314+1603 (Prog. ID: 10143)

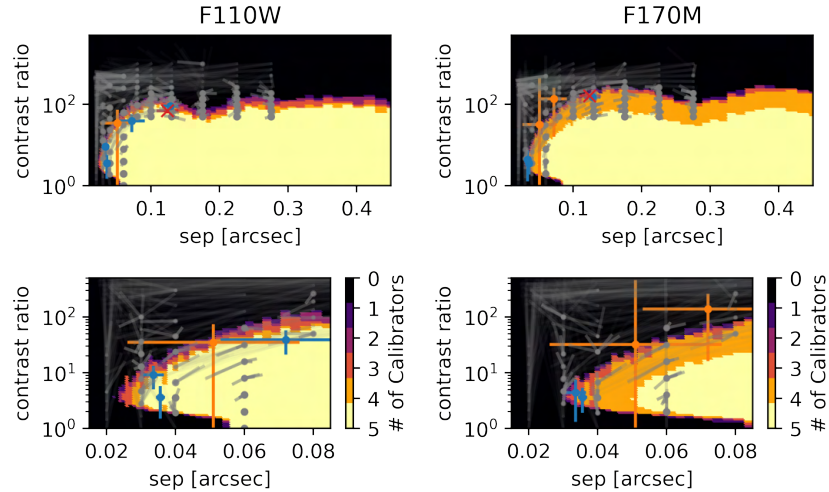


Figure D.4: Detection limits for 2M 0314+1603 from program 10143.

2M 0518-2828 (Prog. ID: 10247)

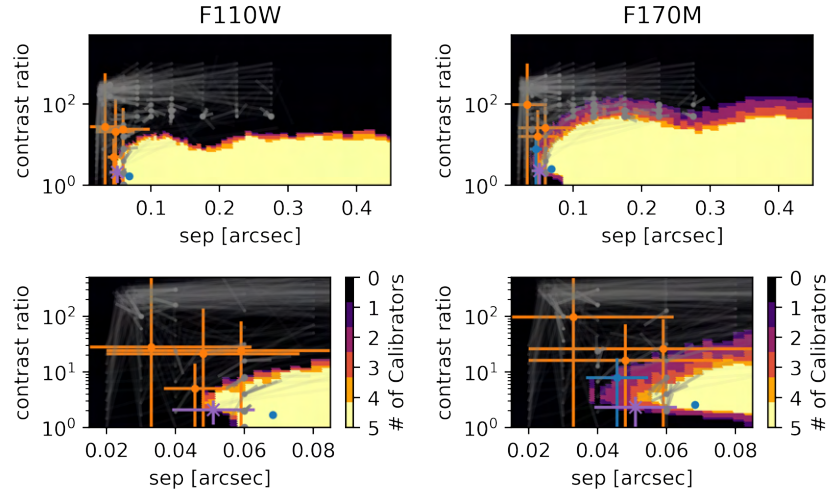


Figure D.5: Detection limits for 2M 0518-2828 from program 10247.

2M 0518-2828 (Prog. ID: 11136)

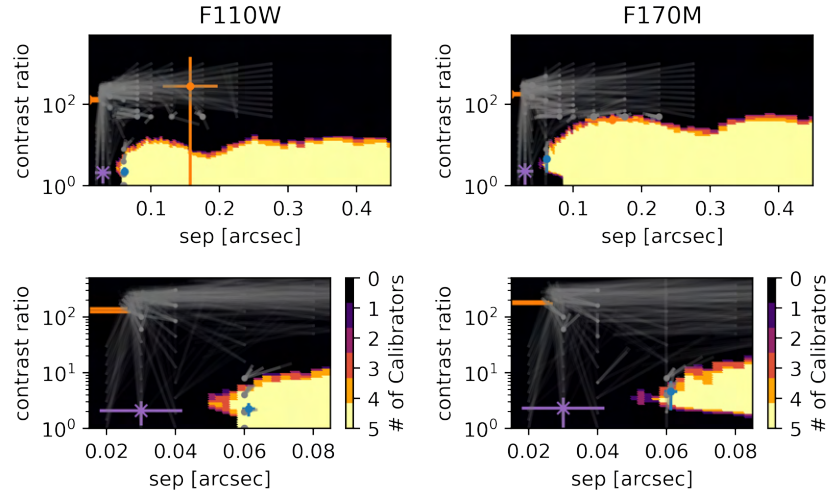


Figure D.6: Detection limits for 2M 0528-2828 from program 11136.

2M 0830+4828 (Prog. ID: 10879)

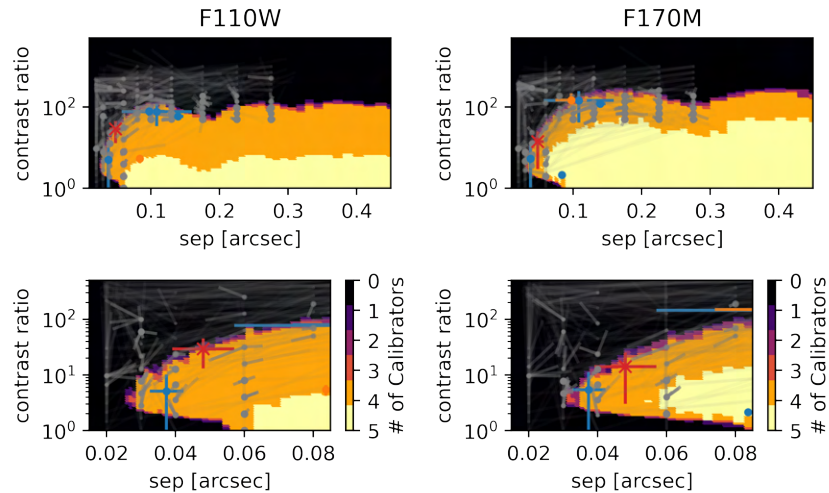


Figure D.7: Detection limits for 2M 0830+4828 from program 10879.

2M 0915+0422 (Prog. ID: 10143)

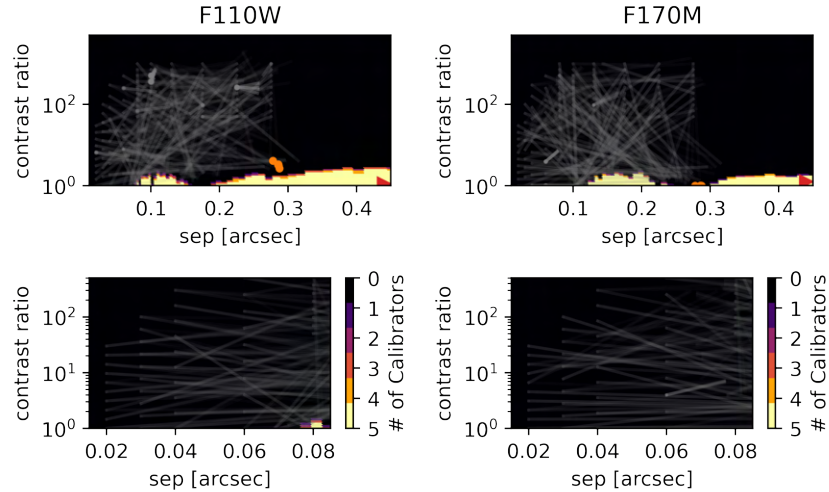


Figure D.8: Detection limits for 2M 0915+0422 from program 10143.

2M 1539-0520 (Prog. ID: 10143)

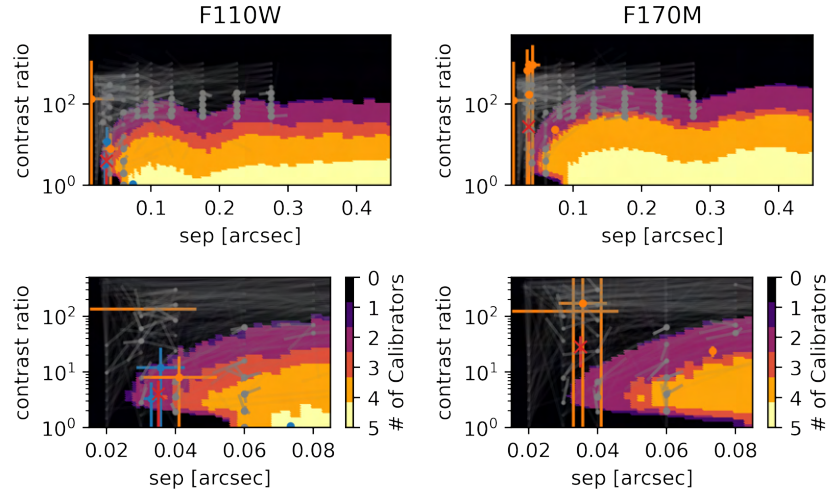


Figure D.9: Detection limits for 2M 1539-0520 from program 10143.

2M 1707-0558 (Prog. ID: 10143)

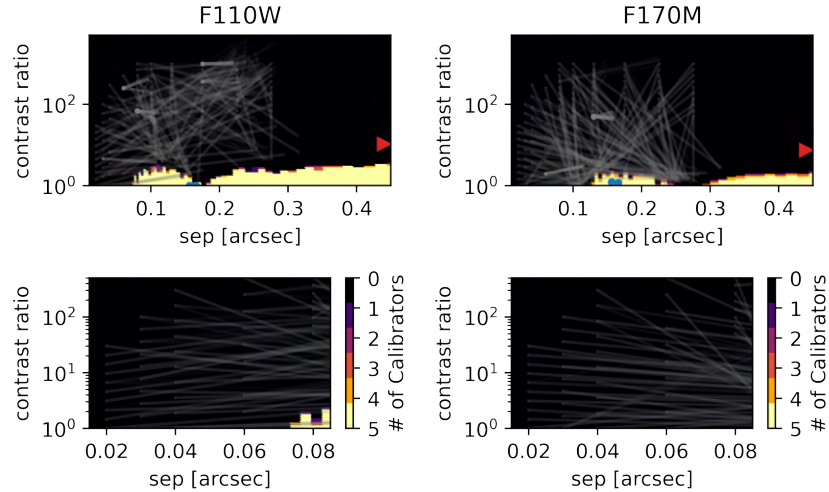


Figure D.10: Detection limits for 2M 1707-0558 from program 10143.

2M 1936-5502 (Prog. ID: 10143)

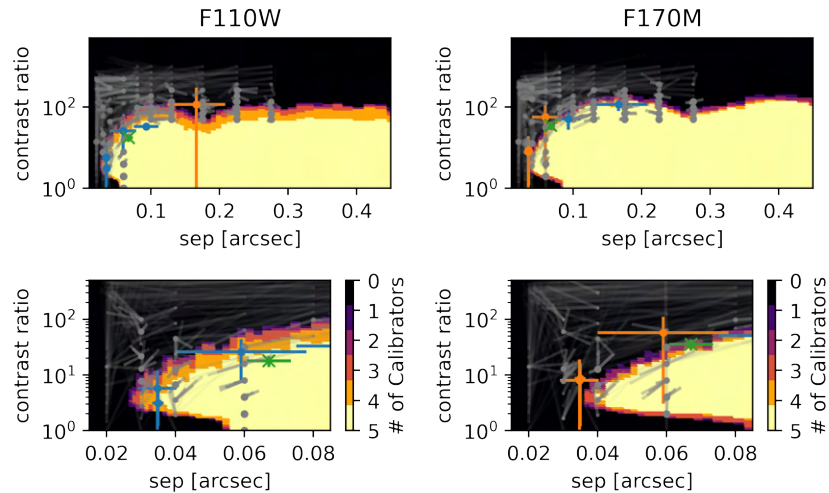


Figure D.11: Detection limits for 2M 1936-5502 from program 10143.

Appendix E

**Figure Set corresponding to Figure 2.9:
Detection Limits for Marginal and Spurious
Detections (See Sections 2.5.2 and 2.5.3)**

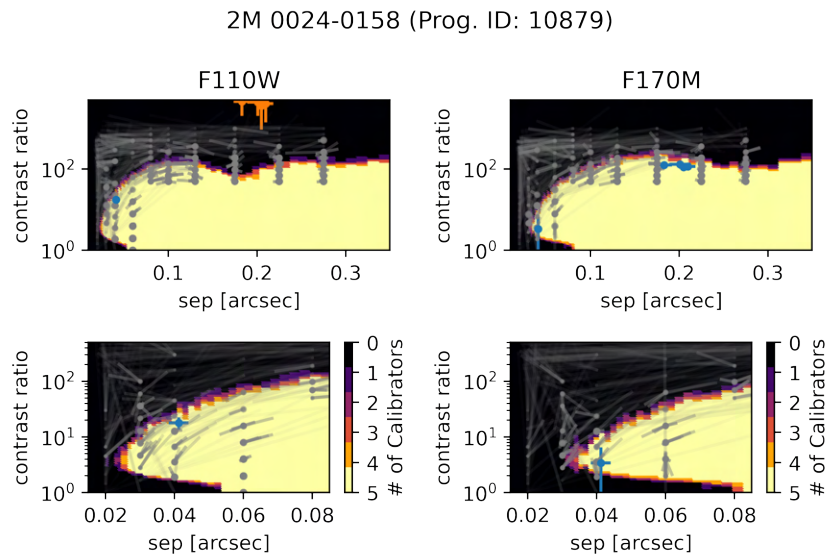


Figure E.1: Detection limits for 2M 0024-0158 from program 10879.

2M 0205-1159 (Prog. ID: 11136)

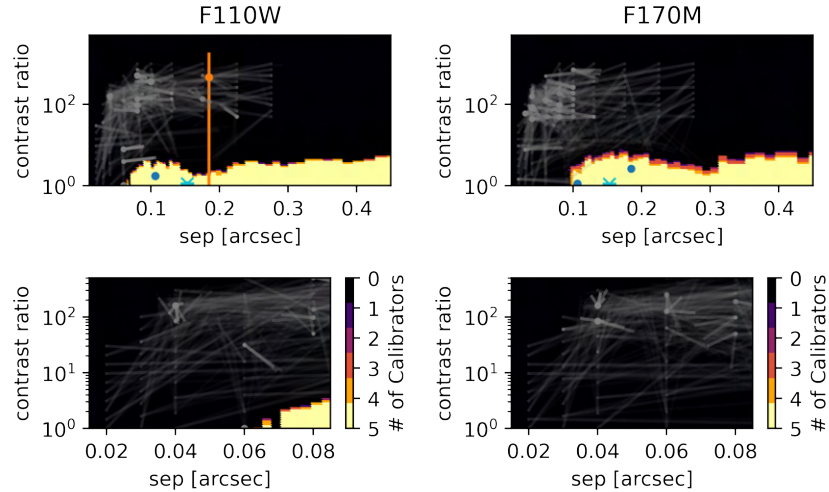


Figure E.2: Detection limits for 2M 0205-1159 from program 11136.

2M 2204-5646 (Prog. ID: 11136)

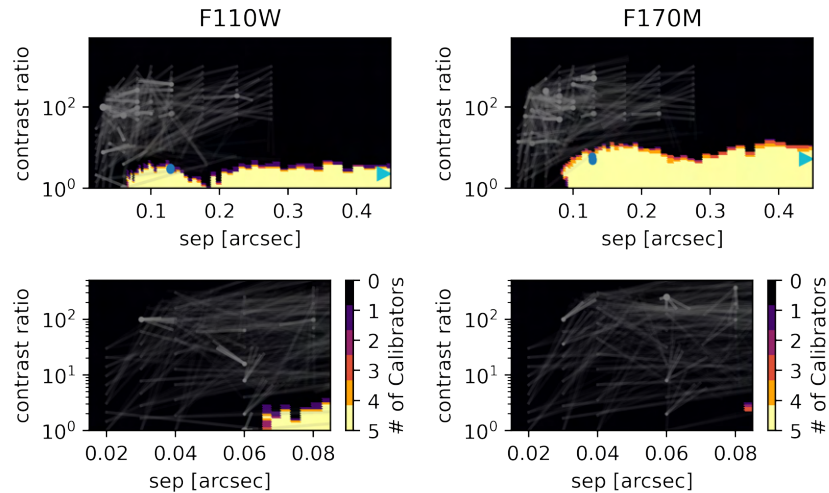


Figure E.3: Detection limits for 2M 2204-5646 from program 11136.

Appendix F

**Figure Set corresponding to Figure 3.2:
Detection limits for different field ages**

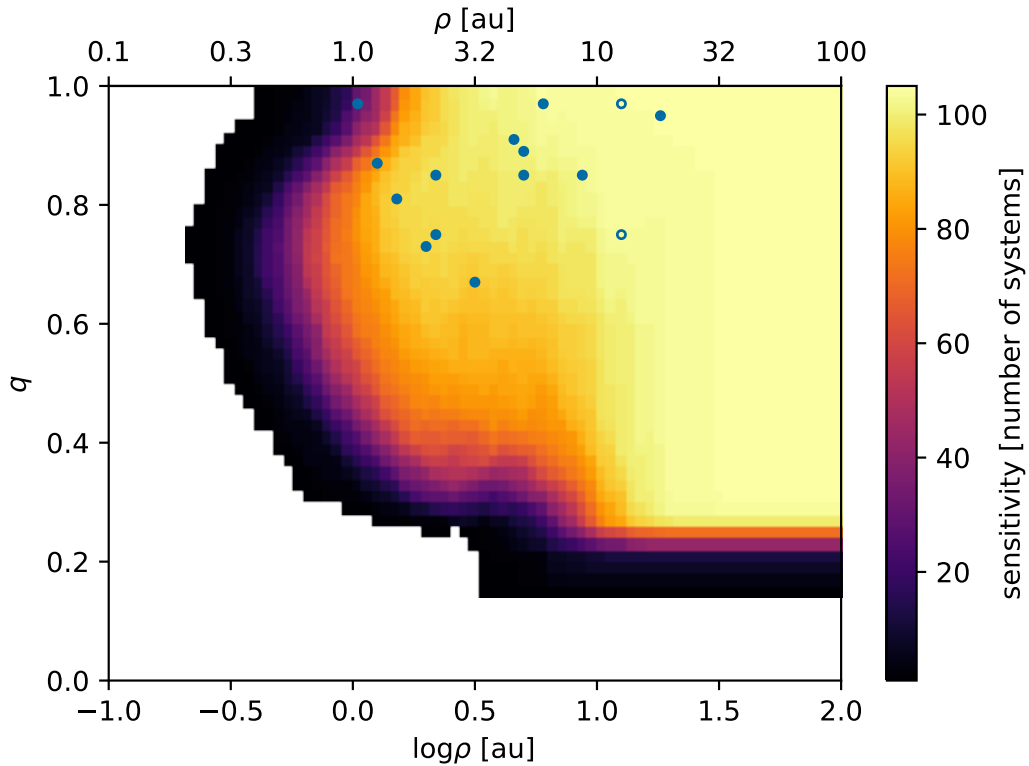


Figure F.1: Stacked detection limits, in units of number of systems, as a function of projected separation, ρ , in au and mass-ratio, q , using a field age of 0.9 Gyr (similar to Figure 15 of Factor & Kraus, 2022a, though now in physical units rather than observational units). Filled circles show detected companions and open circles indicate the two wide separation companions not detected in Factor & Kraus (2022a) but included in our sample using astrometry and photometry from Pope et al. (2013) (see Section 3.3.1). We set a conservative detection limit at separations $> 0\farcm5$ (where our KPI pipeline is not sensitive) of $\Delta m = 6.5$ from Reid et al. (2006).

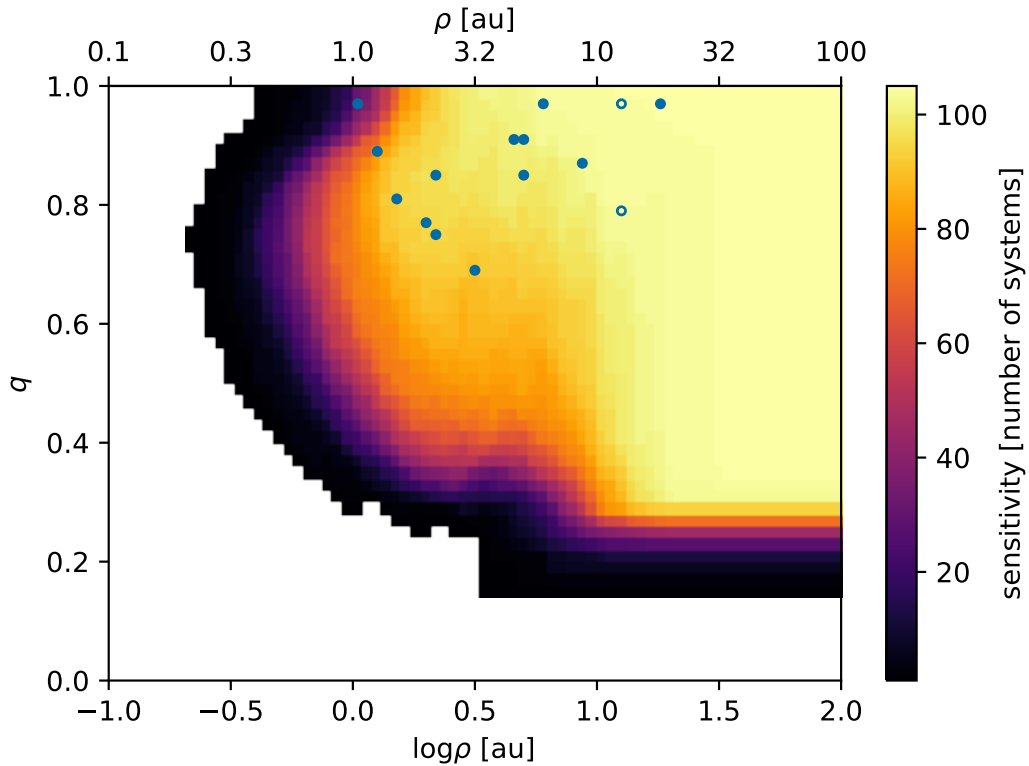


Figure F.2: Stacked detection limits, in units of number of systems, as a function of projected separation, ρ , in au and mass-ratio, q , using a field age of 1.2 Gyr (similar to Figure 15 of Factor & Kraus, 2022a, though now in physical units rather than observational units). Filled circles show detected companions and open circles indicate the two wide separation companions not detected in Factor & Kraus (2022a) but included in our sample using astrometry and photometry from Pope et al. (2013) (see Section 3.3.1). We set a conservative detection limit at separations $> 0''.5$ (where our KPI pipeline is not sensitive) of $\Delta m = 6.5$ from Reid et al. (2006).

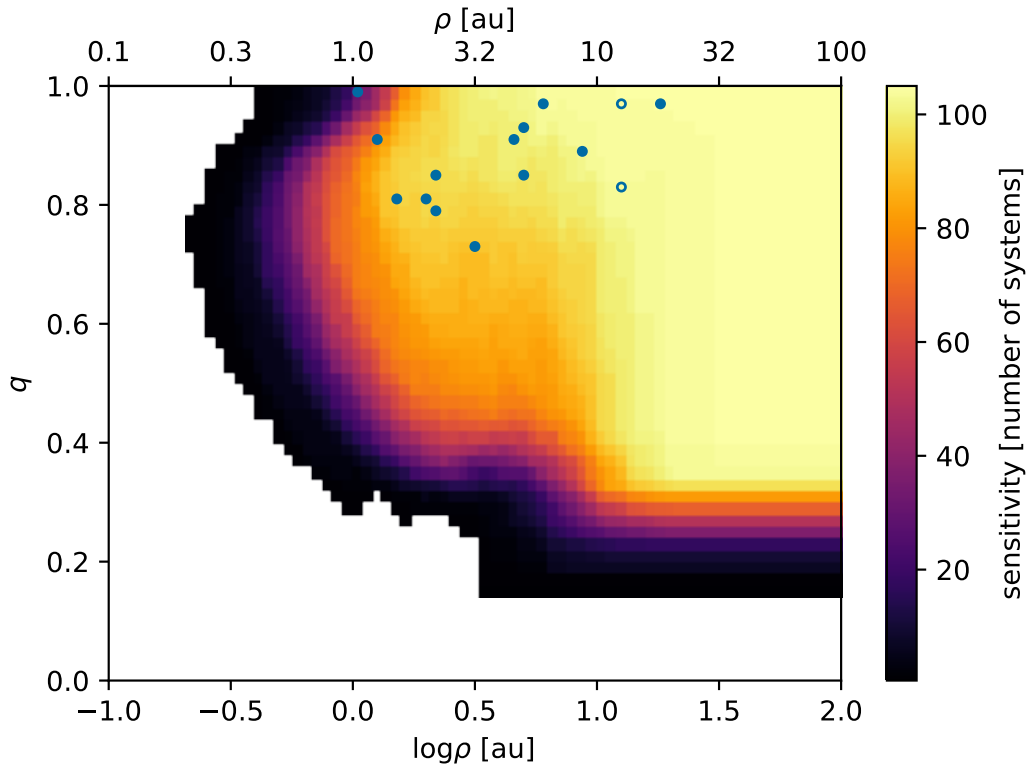


Figure F.3: Stacked detection limits, in units of number of systems, as a function of projected separation, ρ , in au and mass-ratio, q , using a field age of 1.5 Gyr (similar to Figure 15 of Factor & Kraus, 2022a, though now in physical units rather than observational units). Filled circles show detected companions and open circles indicate the two wide separation companions not detected in Factor & Kraus (2022a) but included in our sample using astrometry and photometry from Pope et al. (2013) (see Section 3.3.1). We set a conservative detection limit at separations $> 0''.5$ (where our KPI pipeline is not sensitive) of $\Delta m = 6.5$ from Reid et al. (2006).

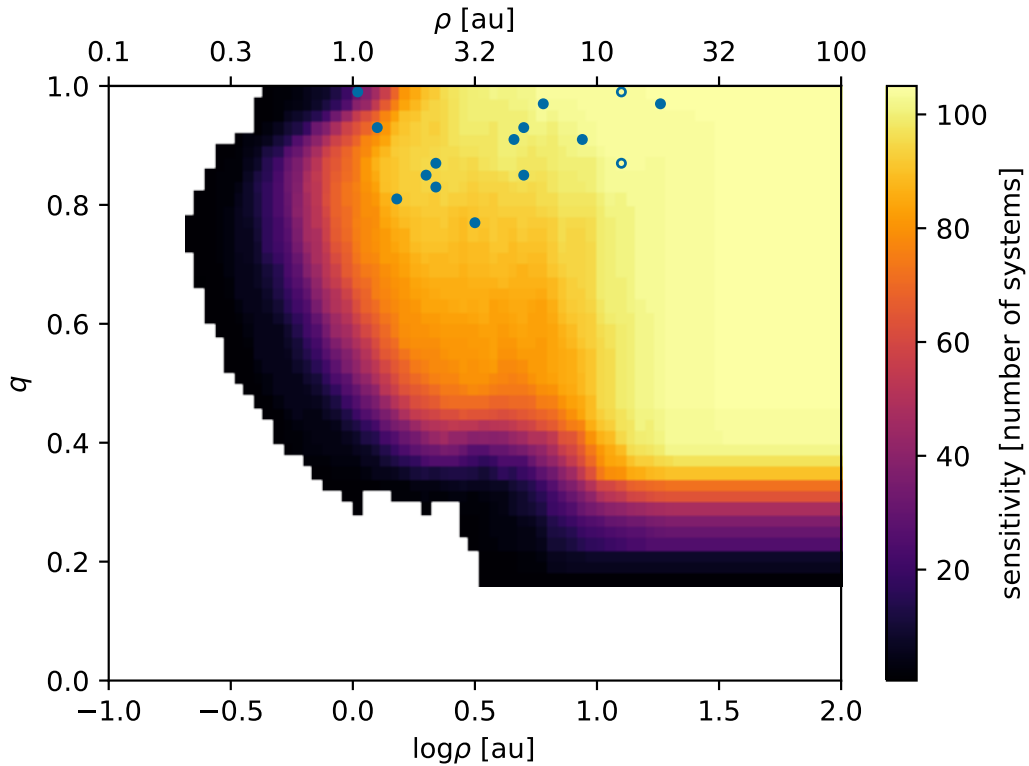


Figure F.4: Stacked detection limits, in units of number of systems, as a function of projected separation, ρ , in au and mass-ratio, q , using a field age of 1.9 Gyr (similar to Figure 15 of Factor & Kraus, 2022a, though now in physical units rather than observational units). Filled circles show detected companions and open circles indicate the two wide separation companions not detected in Factor & Kraus (2022a) but included in our sample using astrometry and photometry from Pope et al. (2013) (see Section 3.3.1). We set a conservative detection limit at separations $> 0''.5$ (where our KPI pipeline is not sensitive) of $\Delta m = 6.5$ from Reid et al. (2006).

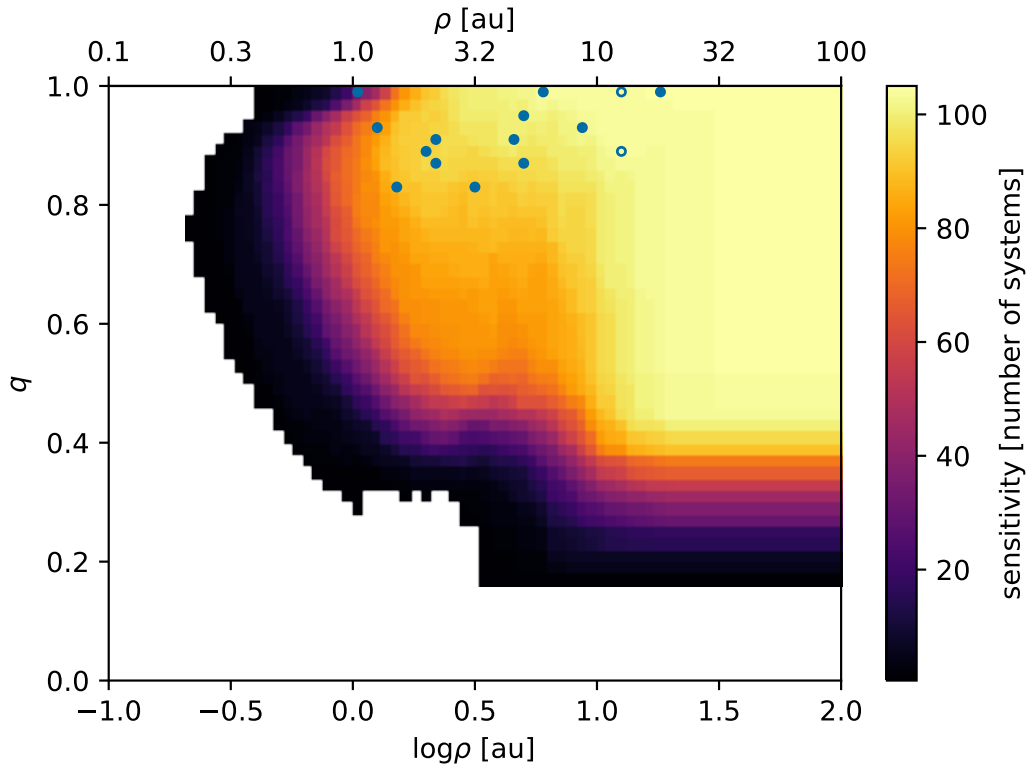


Figure F.5: Stacked detection limits, in units of number of systems, as a function of projected separation, ρ , in au and mass-ratio, q , using a field age of 2.4 Gyr (similar to Figure 15 of Factor & Kraus, 2022a, though now in physical units rather than observational units). Filled circles show detected companions and open circles indicate the two wide separation companions not detected in Factor & Kraus (2022a) but included in our sample using astrometry and photometry from Pope et al. (2013) (see Section 3.3.1). We set a conservative detection limit at separations $> 0''.5$ (where our KPI pipeline is not sensitive) of $\Delta m = 6.5$ from Reid et al. (2006).

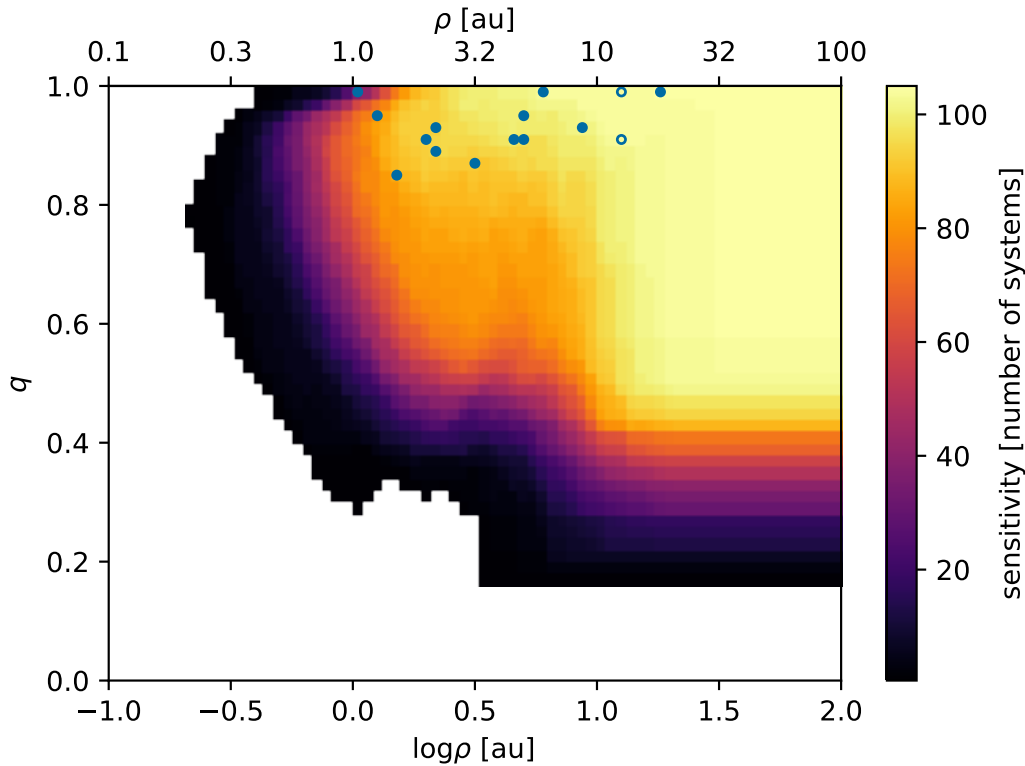


Figure F.6: Stacked detection limits, in units of number of systems, as a function of projected separation, ρ , in au and mass-ratio, q , using a field age of 3.1 Gyr (similar to Figure 15 of Factor & Kraus, 2022a, though now in physical units rather than observational units). Filled circles show detected companions and open circles indicate the two wide separation companions not detected in Factor & Kraus (2022a) but included in our sample using astrometry and photometry from Pope et al. (2013) (see Section 3.3.1). We set a conservative detection limit at separations $> 0''.5$ (where our KPI pipeline is not sensitive) of $\Delta m = 6.5$ from Reid et al. (2006).

Appendix G

**Figure Set corresponding to Figure 3.3:
Corner plots for demographic fits for different
ages**

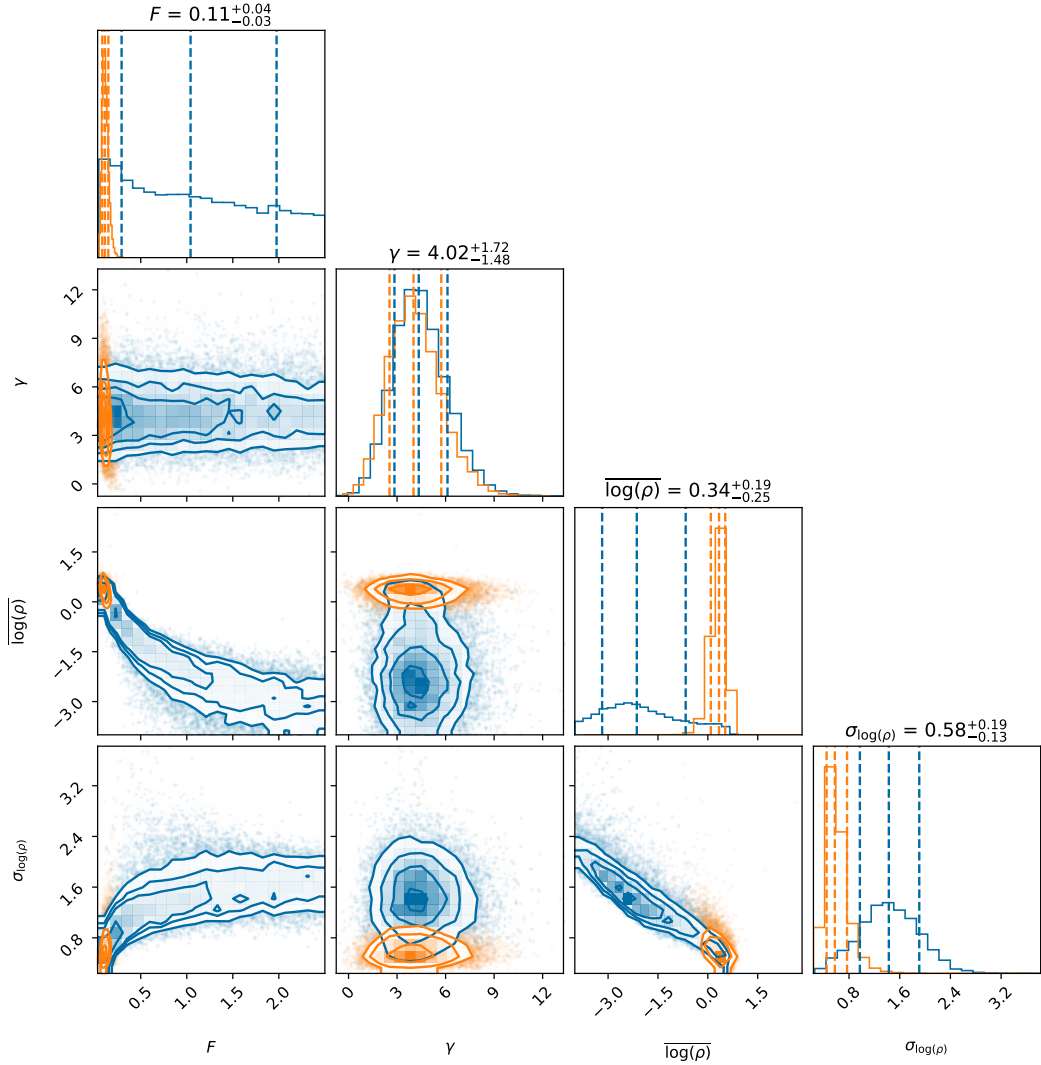


Figure G.1: Corner plot showing the 1- and 2D posteriors of our demographic fit using a field age of 0.9 Gyr. Blue contours show the results using a uniform uninformed prior while orange contours show the results restricting the tight (< 1 au) binary fraction to $2.5^{+8.6\%}_{-1.6\%}$ (Blake et al., 2010). Dashed lines indicate the median and $\pm 1\sigma$ (16th, 50th, and 84th percentile) values (given in Table 3.5). The parameter values listed above each plot correspond to the fits using the informed prior. Data behind the figure is available for the MCMC chains shown in this figure at Factor & Kraus (2022d).

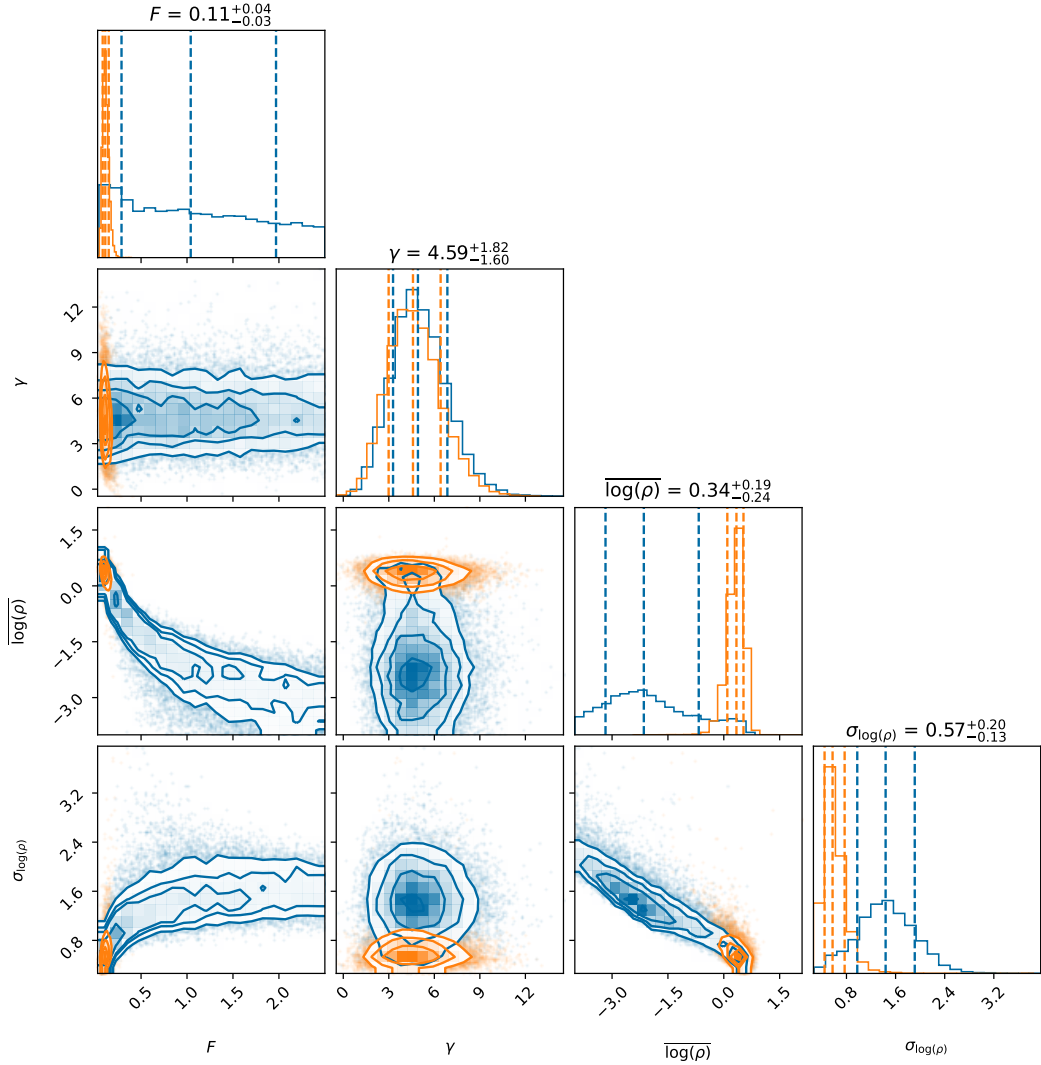


Figure G.2: Corner plot showing the 1- and 2D posteriors of our demographic fit using a field age of 1.2 Gyr. Blue contours show the results using a uniform uninformed prior while orange contours show the results restricting the tight (< 1 au) binary fraction to $2.5^{+8.6\%}_{-1.6\%}$ (Blake et al., 2010). Dashed lines indicate the median and $\pm 1\sigma$ (16th, 50th, and 84th percentile) values (given in Table 3.5). The parameter values listed above each plot correspond to the fits using the informed prior. Data behind the figure is available for the MCMC chains shown in this figure at Factor & Kraus (2022d).

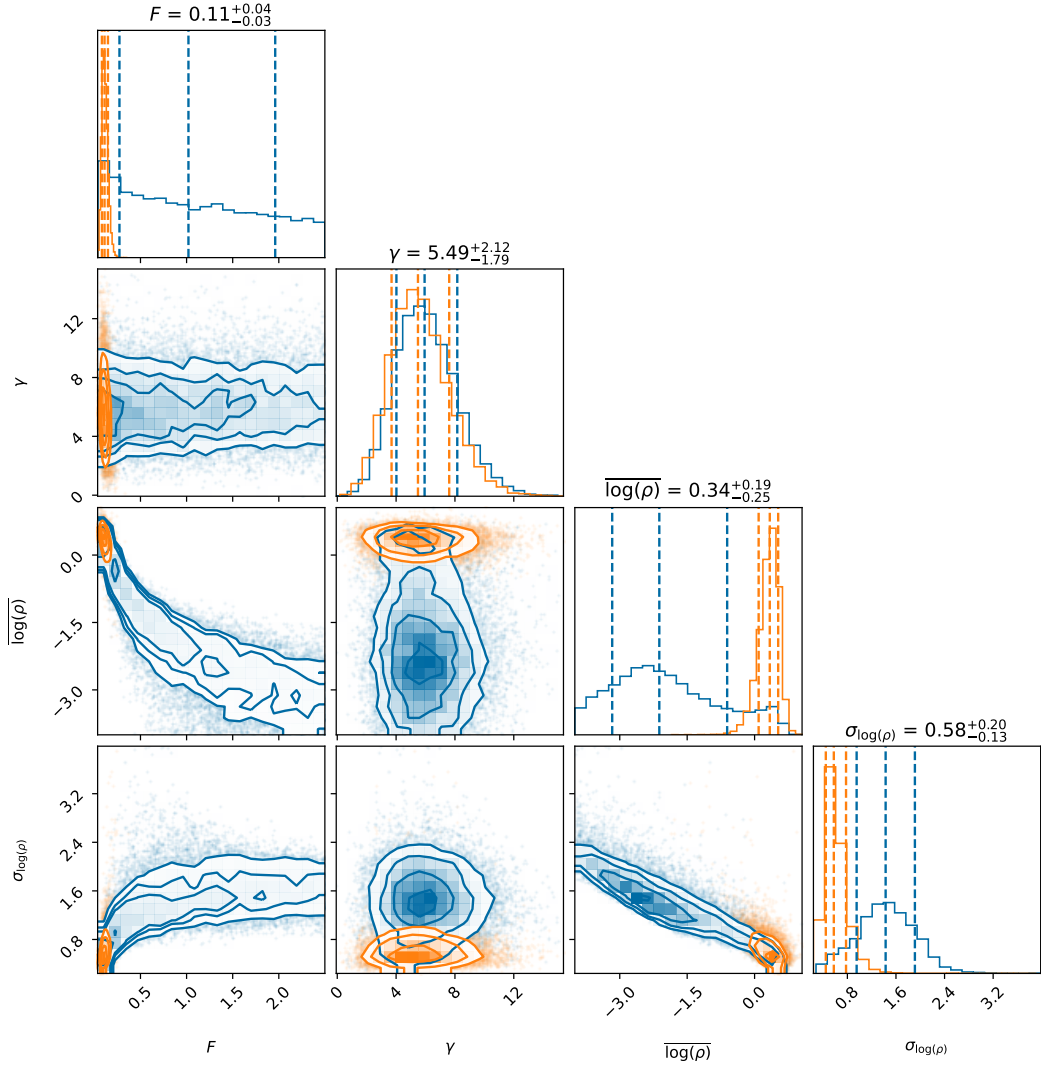


Figure G.3: Corner plot showing the 1- and 2D posteriors of our demographic fit using a field age of 1.5 Gyr. Blue contours show the results using a uniform uninformed prior while orange contours show the results restricting the tight (< 1 au) binary fraction to $2.5^{+8.6\%}_{-1.6\%}$ (Blake et al., 2010). Dashed lines indicate the median and $\pm 1\sigma$ (16th, 50th, and 84th percentile) values (given in Table 3.5). The parameter values listed above each plot correspond to the fits using the informed prior. Data behind the figure is available for the MCMC chains shown in this figure at Factor & Kraus (2022d).

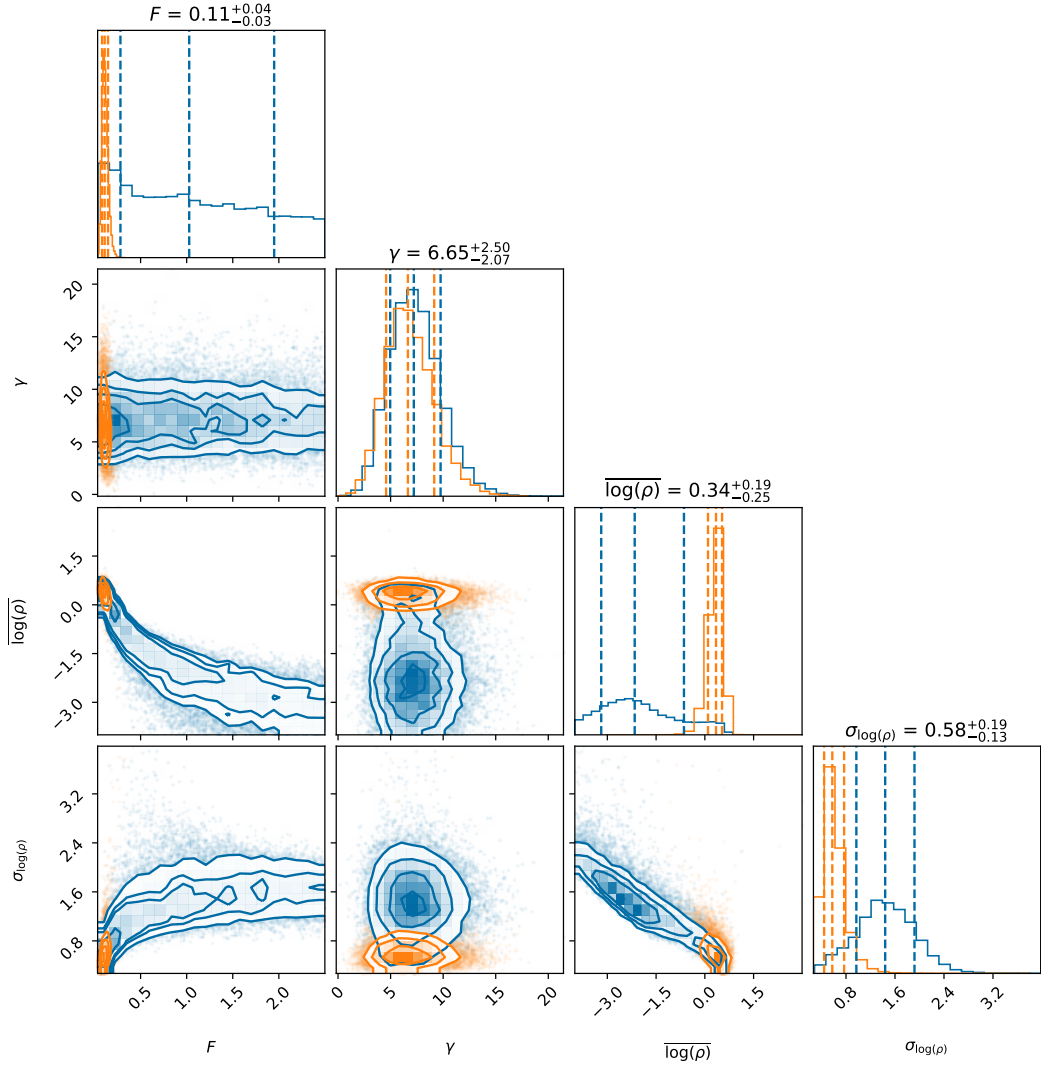


Figure G.4: Corner plot showing the 1- and 2D posteriors of our demographic fit using a field age of 1.9 Gyr. Blue contours show the results using a uniform uninformed prior while orange contours show the results restricting the tight (< 1 au) binary fraction to $2.5^{+8.6\%}_{-1.6\%}$ (Blake et al., 2010). Dashed lines indicate the median and $\pm 1\sigma$ (16th, 50th, and 84th percentile) values (given in Table 3.5). The parameter values listed above each plot correspond to the fits using the informed prior. Data behind the figure is available for the MCMC chains shown in this figure at Factor & Kraus (2022d).

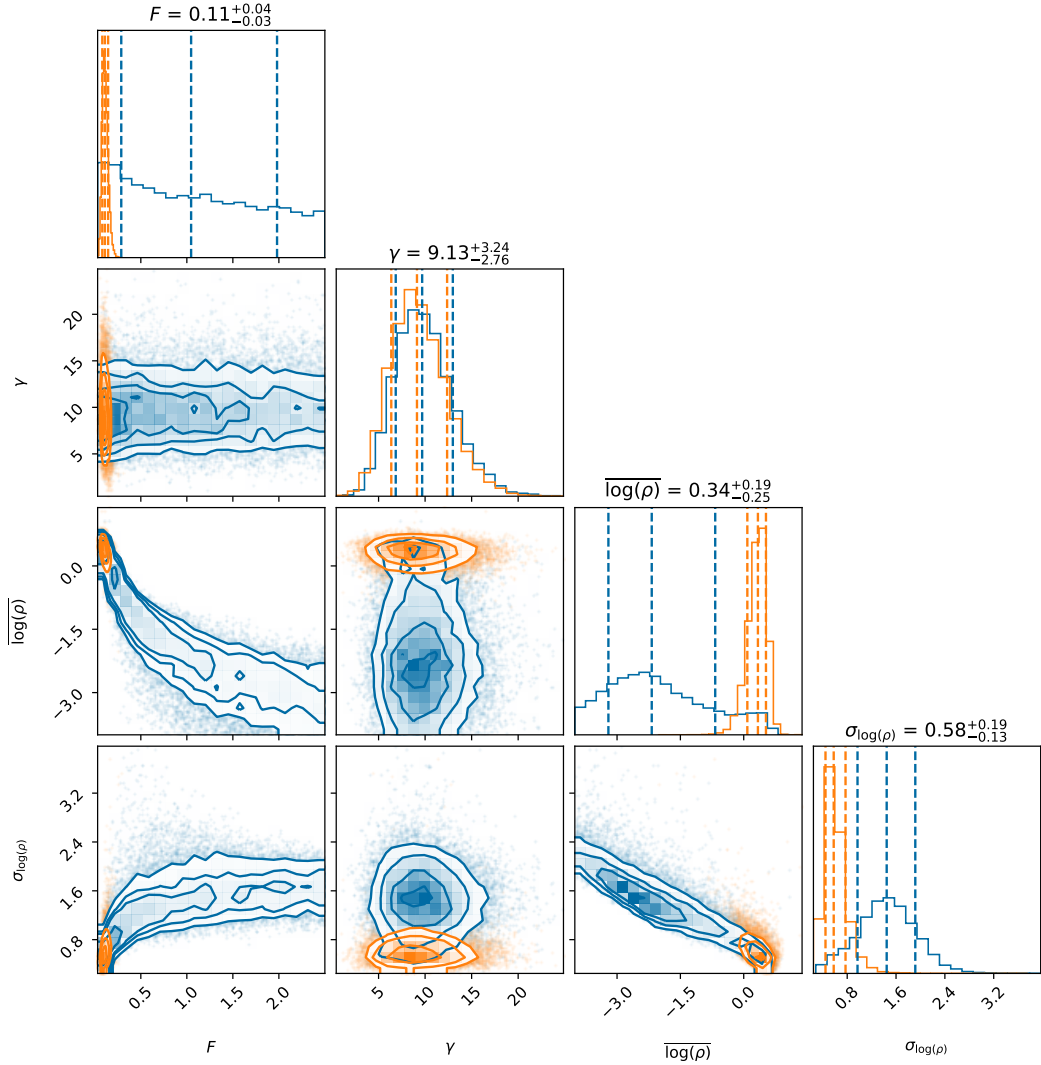


Figure G.5: Corner plot showing the 1- and 2D posteriors of our demographic fit using a field age of 2.4 Gyr. Blue contours show the results using a uniform uninformed prior while orange contours show the results restricting the tight (< 1 au) binary fraction to $2.5^{+8.6\%}_{-1.6\%}$ (Blake et al., 2010). Dashed lines indicate the median and $\pm 1\sigma$ (16th, 50th, and 84th percentile) values (given in Table 3.5). The parameter values listed above each plot correspond to the fits using the informed prior. Data behind the figure is available for the MCMC chains shown in this figure at Factor & Kraus (2022d).

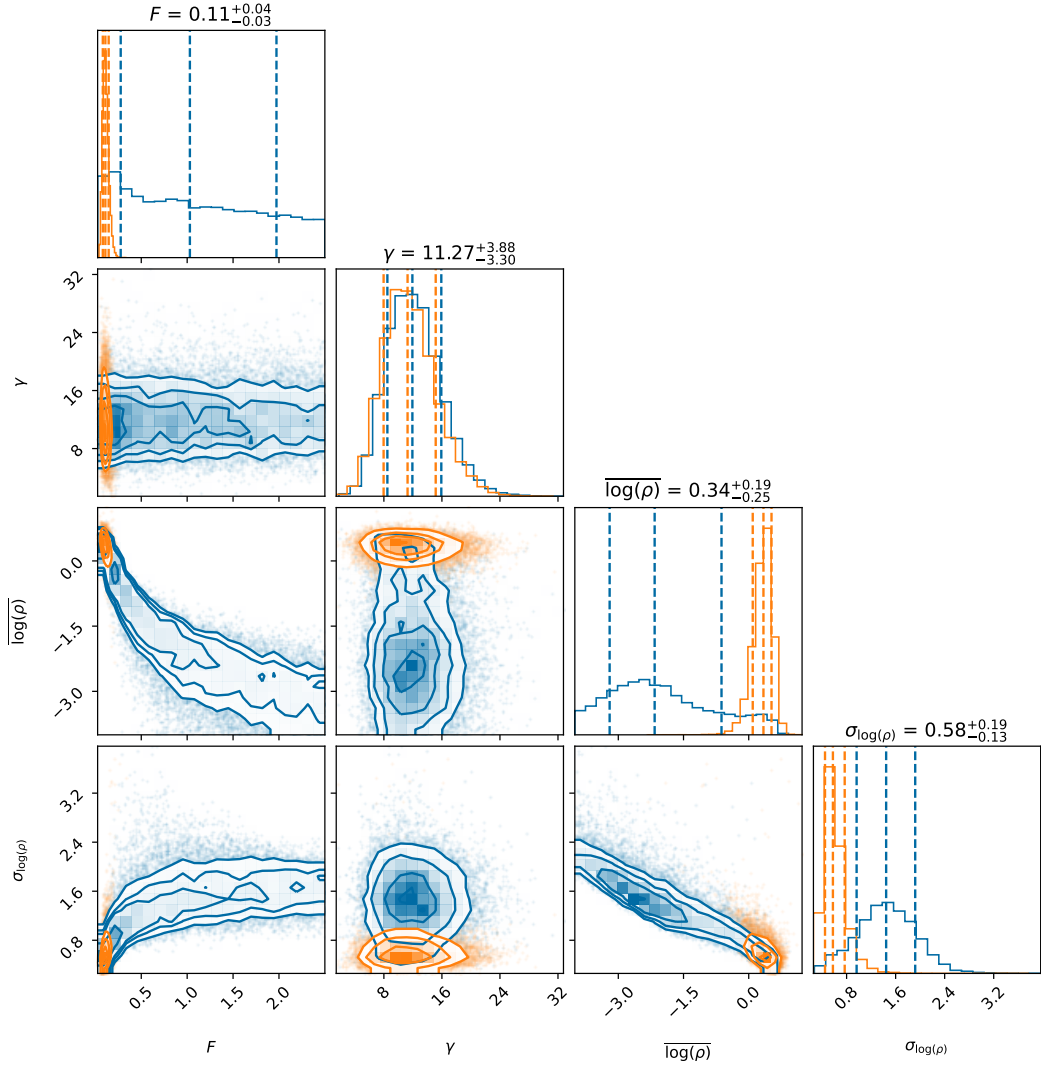


Figure G.6: Corner plot showing the 1- and 2D posteriors of our demographic fit using a field age of 3.1 Gyr. Blue contours show the results using a uniform uninformed prior while orange contours show the results restricting the tight (< 1 au) binary fraction to $2.5^{+8.6\%}_{-1.6\%}$ (Blake et al., 2010). Dashed lines indicate the median and $\pm 1\sigma$ (16th, 50th, and 84th percentile) values (given in Table 3.5). The parameter values listed above each plot correspond to the fits using the informed prior. Data behind the figure is available for the MCMC chains shown in this figure at Factor & Kraus (2022d).

Appendix H

Figure Set corresponding to Figure 3.4: 2D population distributions and detections for different ages

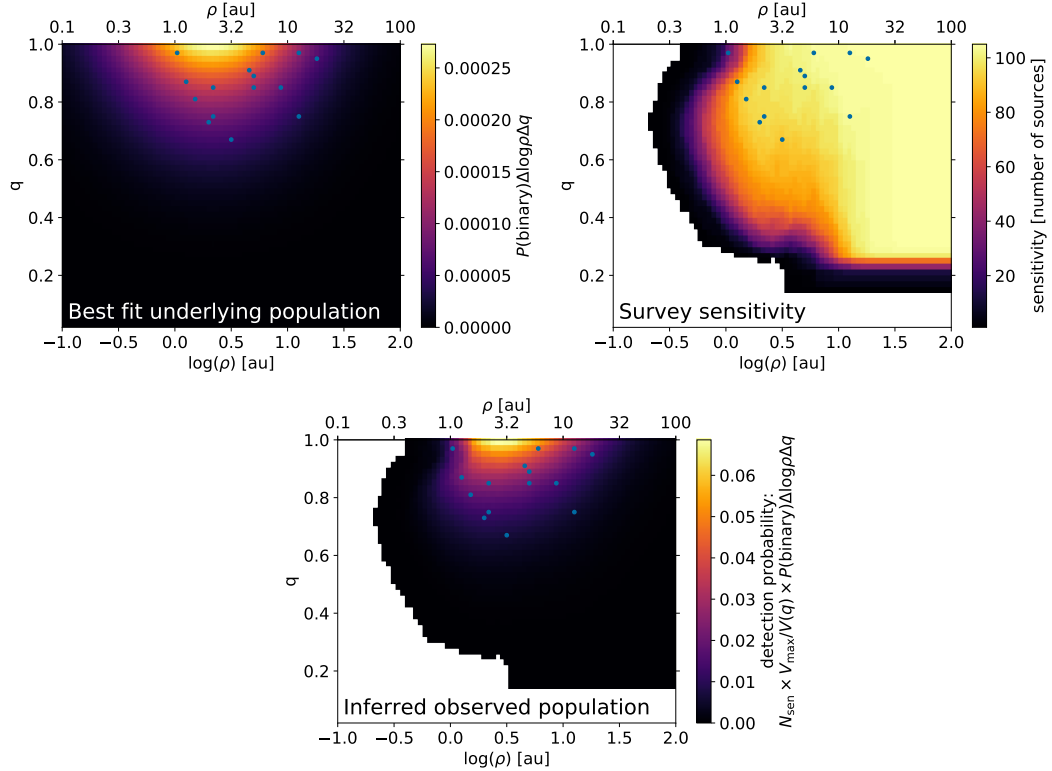


Figure H.1: The progression from underlying population and survey sensitivity to observed population. Blue points indicate detected companions. *Top left:* Underlying companion population produced from the median values of our informed prior fit. *Top right:* Survey sensitivity in units of number of targets. *Bottom center:* Observed population (i.e. the inferred probability that we should detect a companion in a given bin), calculated by correcting the underlying population for Malmquist bias (as a function of mass-ratio) and applying our survey sensitivity. Mass ratios were calculated assuming a field age of 0.9 Gyr.

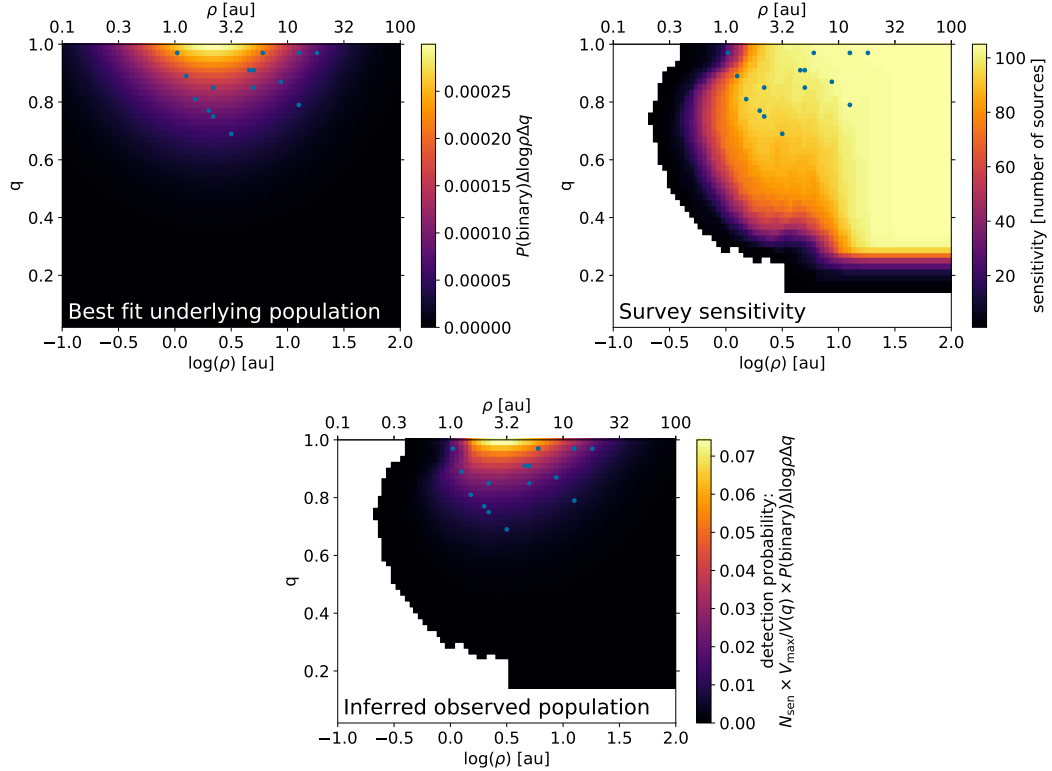


Figure H.2: The progression from underlying population and survey sensitivity to observed population. Blue points indicate detected companions. *Top left*: Underlying companion population produced from the median values of our informed prior fit. *Top right*: Survey sensitivity in units of number of targets. *Bottom center*: Observed population (i.e. the inferred probability that we should detect a companion in a given bin), calculated by correcting the underlying population for Malmquist bias (as a function of mass-ratio) and applying our survey sensitivity. Mass ratios were calculated assuming a field age of 1.2 Gyr.

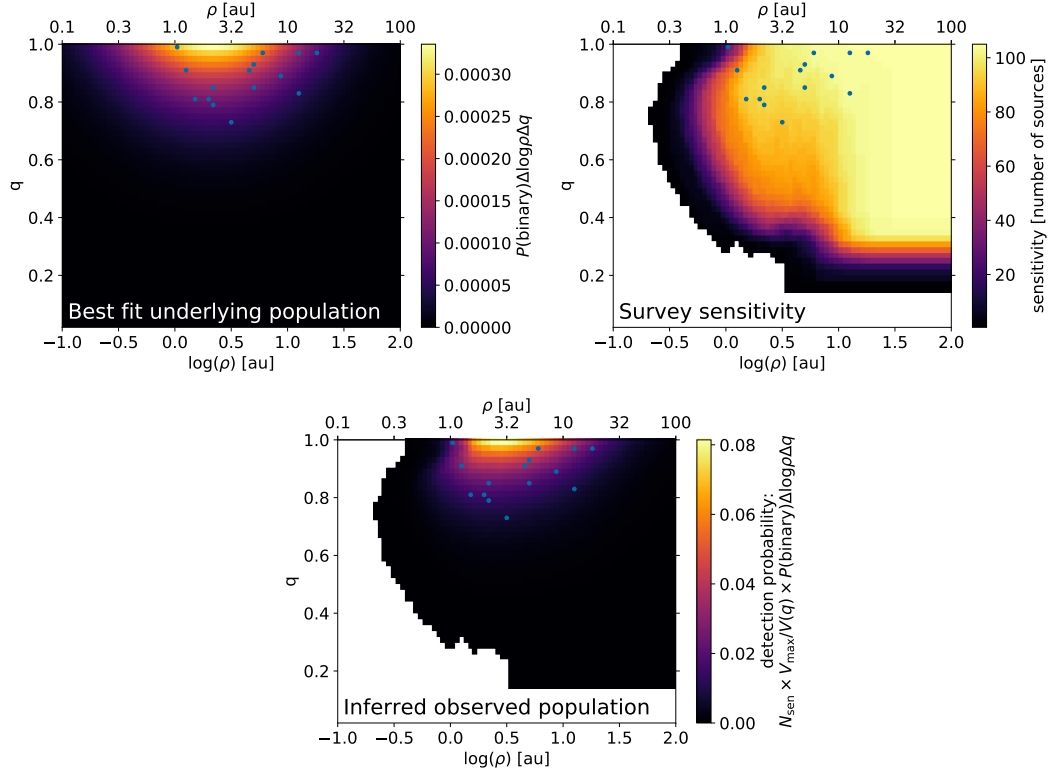


Figure H.3: The progression from underlying population and survey sensitivity to observed population. Blue points indicate detected companions. *Top left:* Underlying companion population produced from the median values of our informed prior fit. *Top right:* Survey sensitivity in units of number of targets. *Bottom center:* Observed population (i.e. the inferred probability that we should detect a companion in a given bin), calculated by correcting the underlying population for Malmquist bias (as a function of mass-ratio) and applying our survey sensitivity. Mass ratios were calculated assuming a field age of 1.5 Gyr.

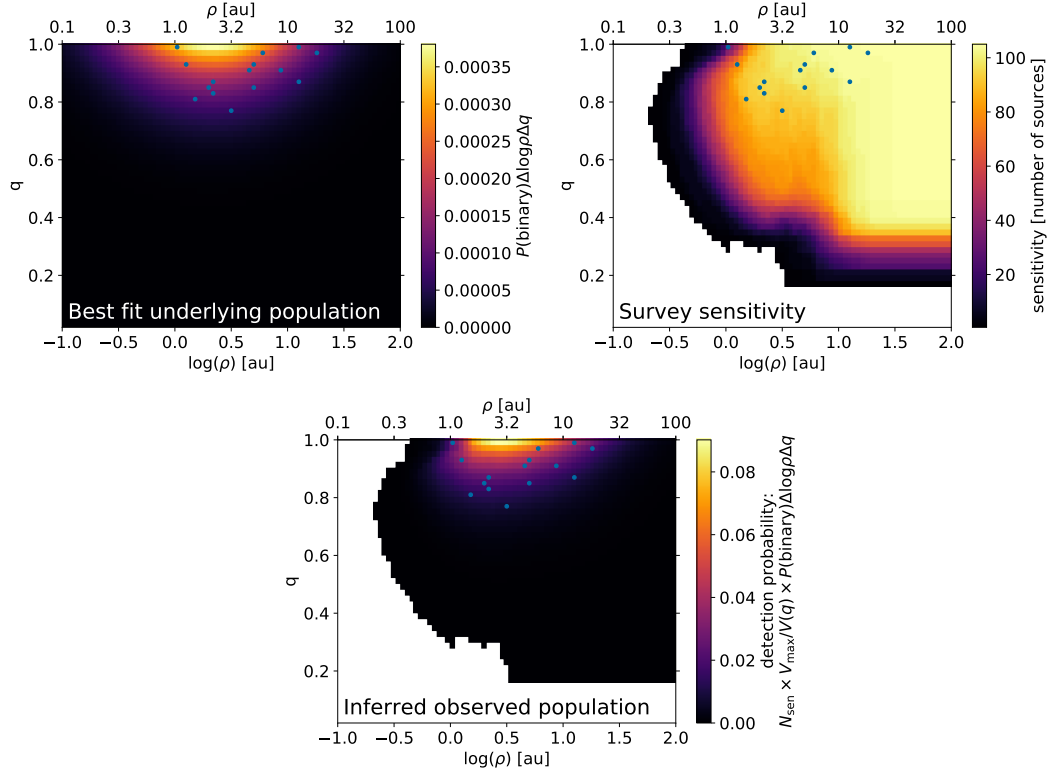


Figure H.4: The progression from underlying population and survey sensitivity to observed population. Blue points indicate detected companions. *Top left:* Underlying companion population produced from the median values of our informed prior fit. *Top right:* Survey sensitivity in units of number of targets. *Bottom center:* Observed population (i.e. the inferred probability that we should detect a companion in a given bin), calculated by correcting the underlying population for Malmquist bias (as a function of mass-ratio) and applying our survey sensitivity. Mass ratios were calculated assuming a field age of 1.9 Gyr.

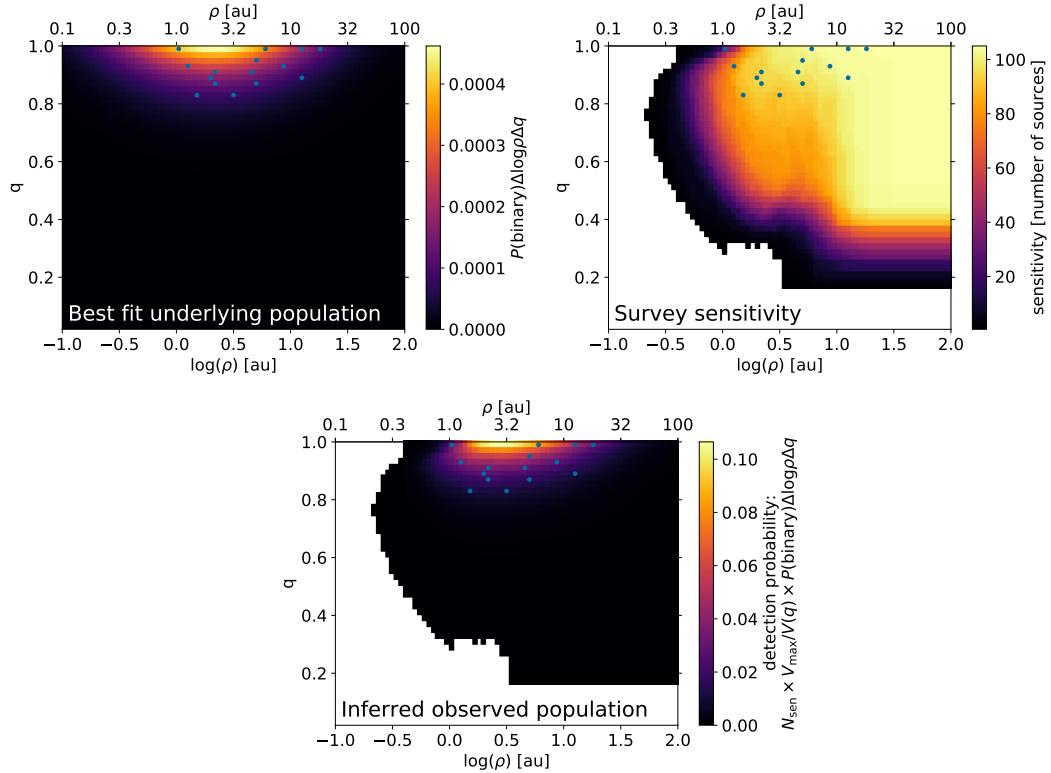


Figure H.5: The progression from underlying population and survey sensitivity to observed population. Blue points indicate detected companions. *Top left:* Underlying companion population produced from the median values of our informed prior fit. *Top right:* Survey sensitivity in units of number of targets. *Bottom center:* Observed population (i.e. the inferred probability that we should detect a companion in a given bin), calculated by correcting the underlying population for Malmquist bias (as a function of mass-ratio) and applying our survey sensitivity. Mass ratios were calculated assuming a field age of 2.4 Gyr.

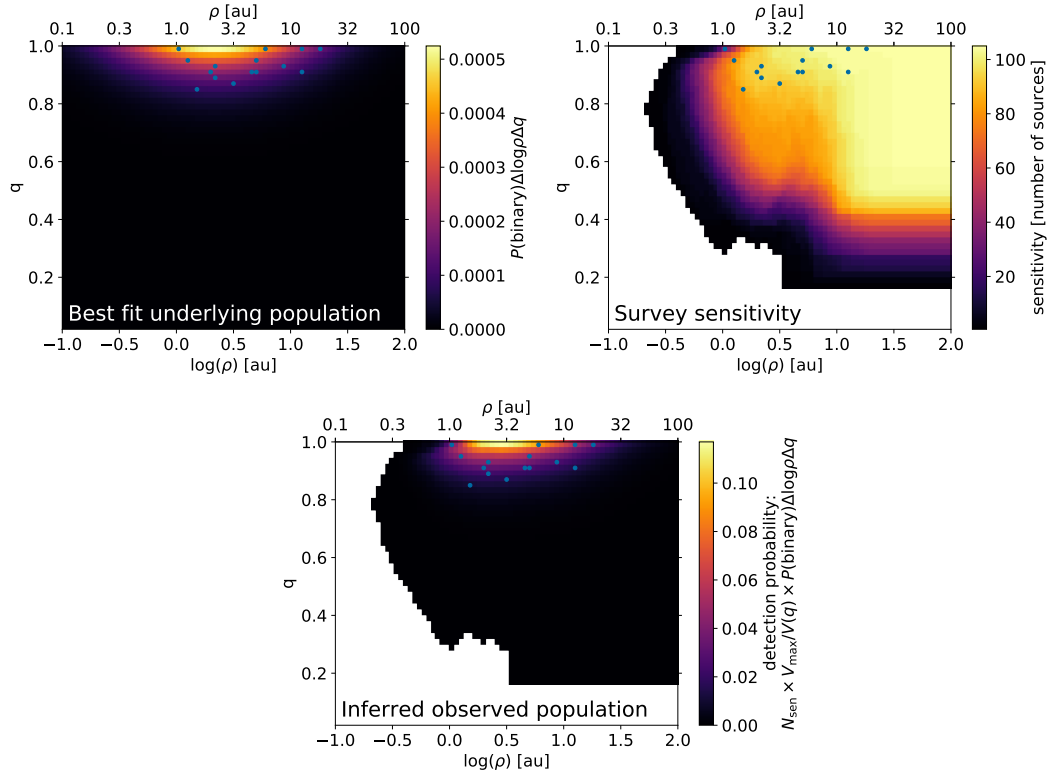


Figure H.6: The progression from underlying population and survey sensitivity to observed population. Blue points indicate detected companions. *Top left:* Underlying companion population produced from the median values of our informed prior fit. *Top right:* Survey sensitivity in units of number of targets. *Bottom center:* Observed population (i.e. the inferred probability that we should detect a companion in a given bin), calculated by correcting the underlying population for Malmquist bias (as a function of mass-ratio) and applying our survey sensitivity. Mass ratios were calculated assuming a field age of 3.1 Gyr.

Appendix I

**Figure Set corresponding to Figure 3.6:
Binary probability as a function of mass ratio
for different ages**

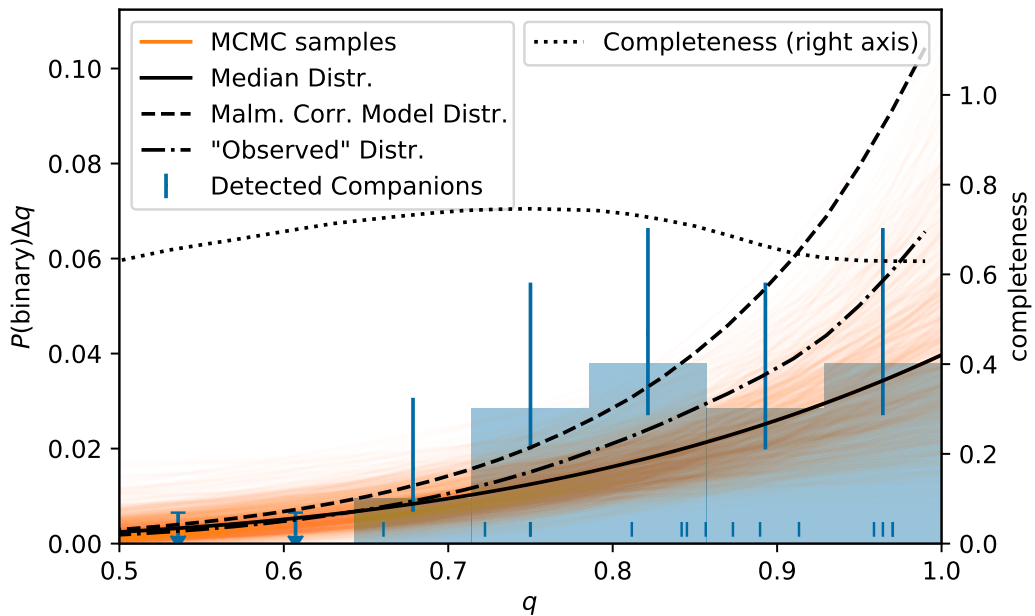


Figure I.1: Binary population as a function of mass-ratio q assuming a field age of 0.9 Gyr. Observed companions are shown in blue. Orange distributions are drawn from our posterior while the solid black line is drawn using the median parameters. Dashed line is the Malmquist corrected median distribution and the dash-dotted line is the “observed” distribution, calculated by multiplying the Malmquist corrected distribution by our sensitivity. The dotted line shows the completeness fraction (right vertical axis).

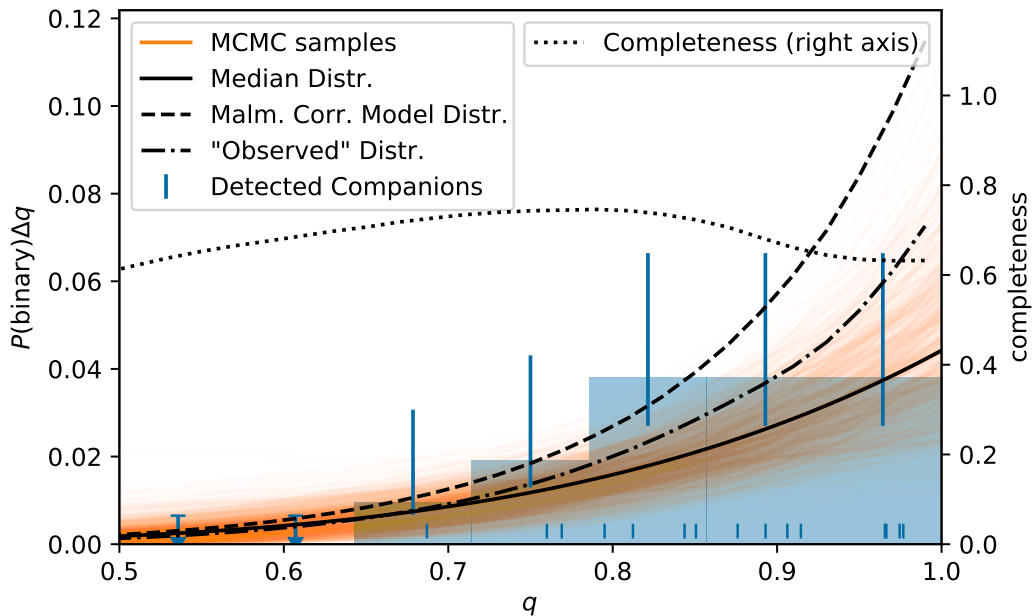


Figure I.2: Binary population as a function of mass-ratio q assuming a field age of 1.2 Gyr. Observed companions are shown in blue. Orange distributions are drawn from our posterior while the solid black line is drawn using the median parameters. Dashed line is the Malmquist corrected median distribution and the dash-dotted line is the “observed” distribution, calculated by multiplying the Malmquist corrected distribution by our sensitivity. The dotted line shows the completeness fraction (right vertical axis).

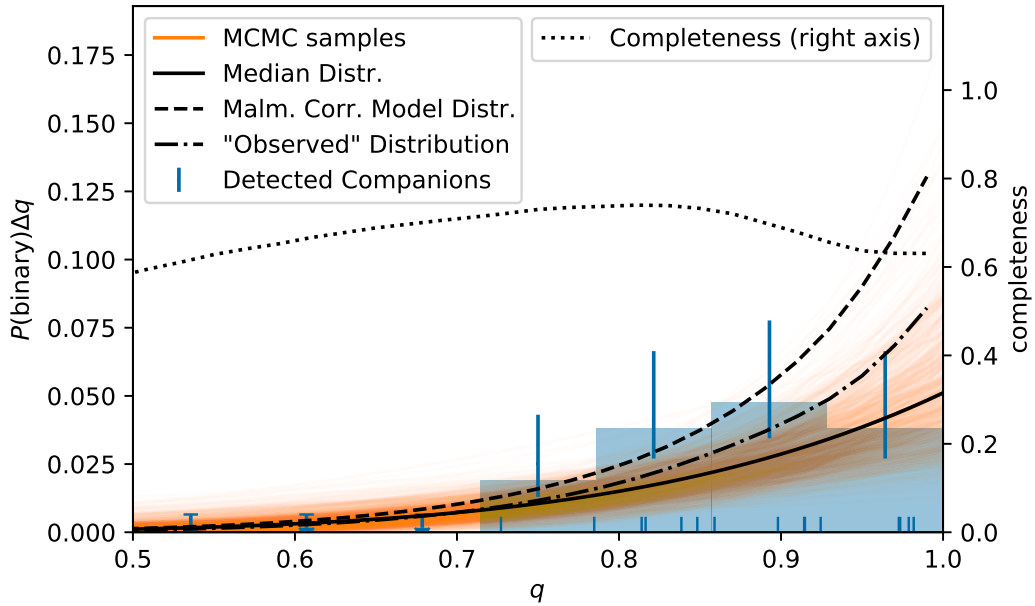


Figure I.3: Binary population as a function of mass-ratio q assuming a field age of 1.5 Gyr. Observed companions are shown in blue. Orange distributions are drawn from our posterior while the solid black line is drawn using the median parameters. Dashed line is the Malmquist corrected median distribution and the dash-dotted line is the “observed” distribution, calculated by multiplying the Malmquist corrected distribution by our sensitivity. The dotted line shows the completeness fraction (right vertical axis).

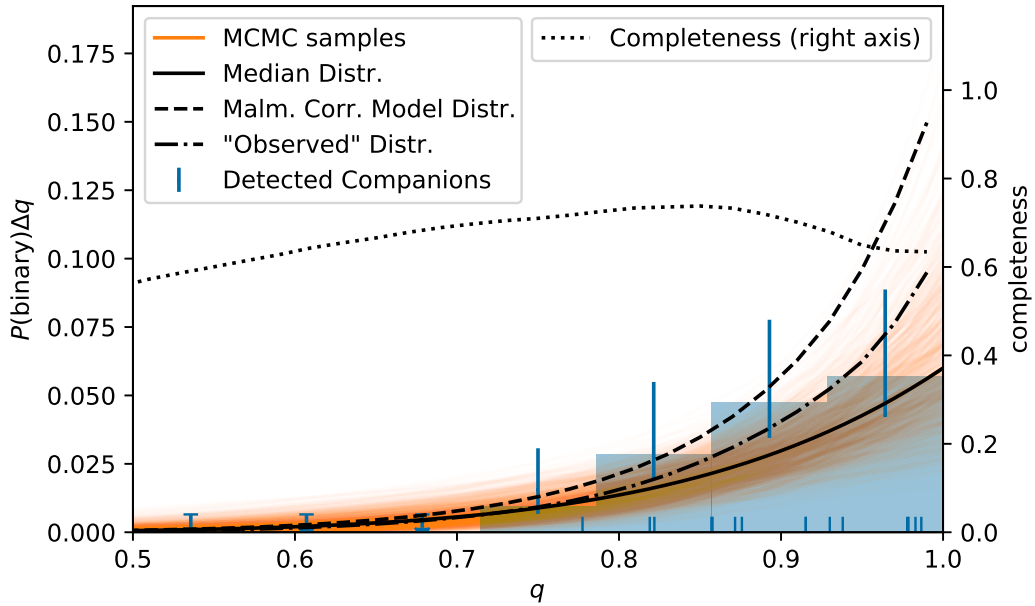


Figure I.4: Binary population as a function of mass-ratio q assuming a field age of 1.9 Gyr. Observed companions are shown in blue. Orange distributions are drawn from our posterior while the solid black line is drawn using the median parameters. Dashed line is the Malmquist corrected median distribution and the dash-dotted line is the “observed” distribution, calculated by multiplying the Malmquist corrected distribution by our sensitivity. The dotted line shows the completeness fraction (right vertical axis).

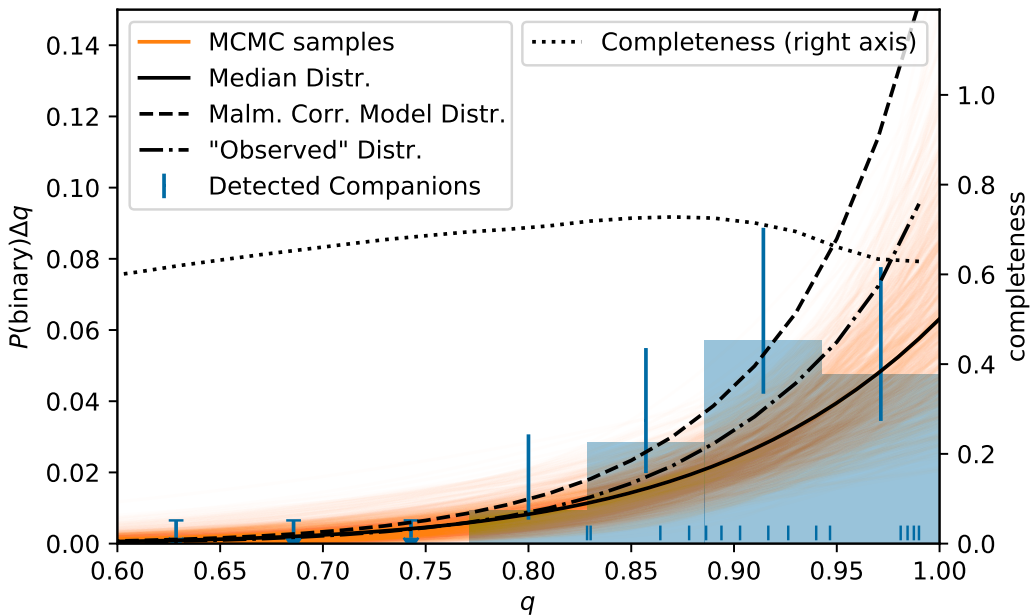


Figure I.5: Binary population as a function of mass-ratio q assuming a field age of 2.4 Gyr. Observed companions are shown in blue. Orange distributions are drawn from our posterior while the solid black line is drawn using the median parameters. Dashed line is the Malmquist corrected median distribution and the dash-dotted line is the “observed” distribution, calculated by multiplying the Malmquist corrected distribution by our sensitivity. The dotted line shows the completeness fraction (right vertical axis).

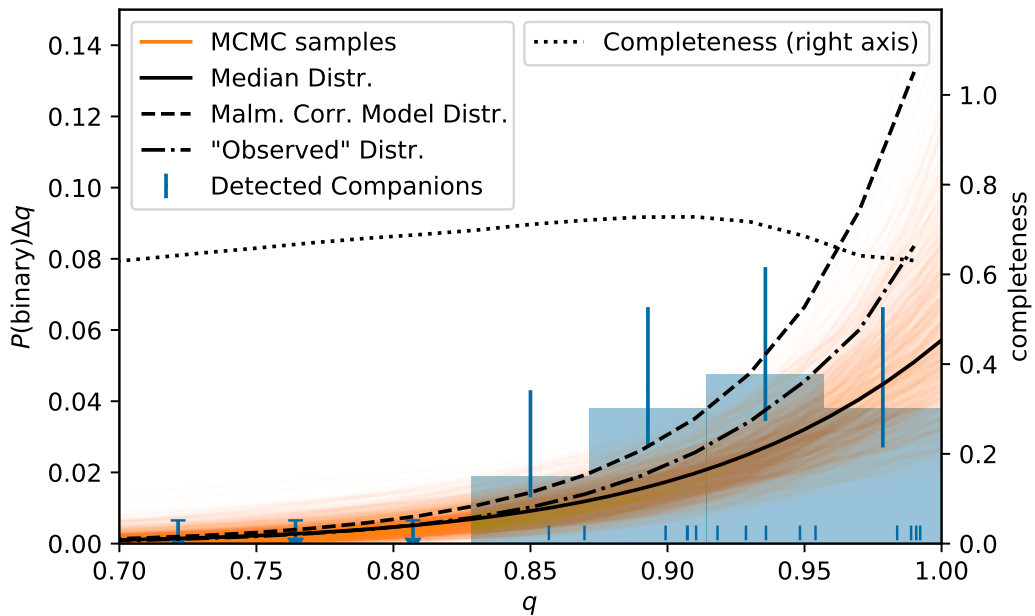


Figure I.6: Binary population as a function of mass ratio q assuming a field age of 3.1 Gyr. Observed companions are shown in blue. Orange distributions are drawn from our posterior while the solid black line is drawn using the median parameters. Dashed line is the Malmquist corrected median distribution and the dash-dotted line is the “observed” distribution, calculated by multiplying the Malmquist corrected distribution by our sensitivity. The dotted line shows the completeness fraction (right vertical axis).

Appendix J

**Figure Set corresponding to Figure 3.9:
Mass-ratio power-law index injection results
for different field ages**

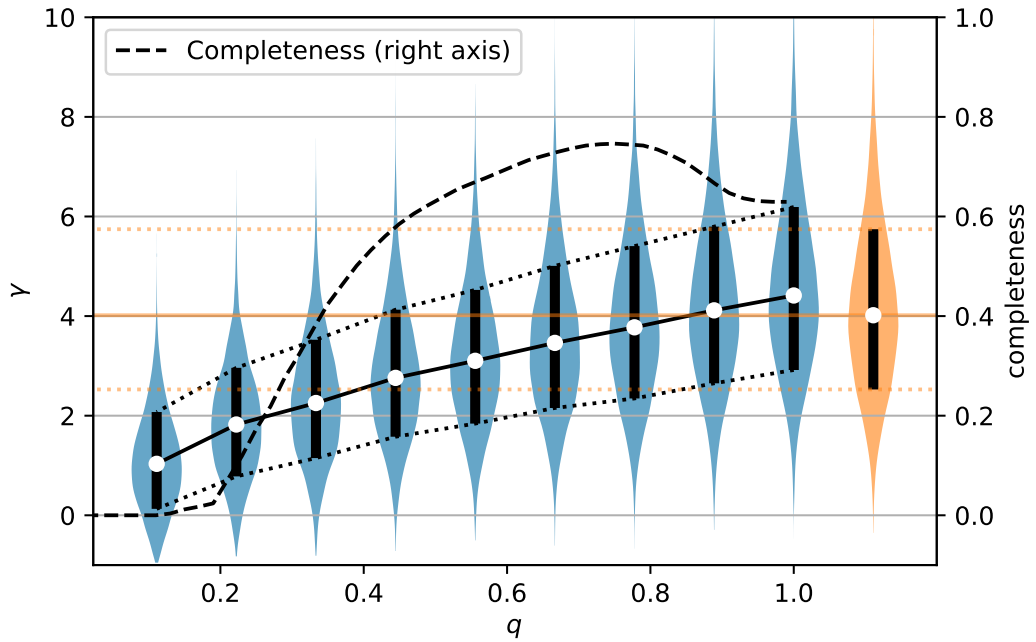


Figure J.1: Posteriors of the mass-ratio power-law index, γ , as a function of the mass-ratio, q , of an injected additional binary detection assuming a field age of 0.9 Gyr. The additional detection was injected at the median of the previously derived separation distribution (2.2 au) so as to have the least possible effect on other parameters. The orange distribution is with no injected detection. White points and black vertical lines correspond to the median and $\pm 1\sigma$ (central 68%) values. The black dashed line (right vertical axis) shows the completeness of our survey as a function of q .

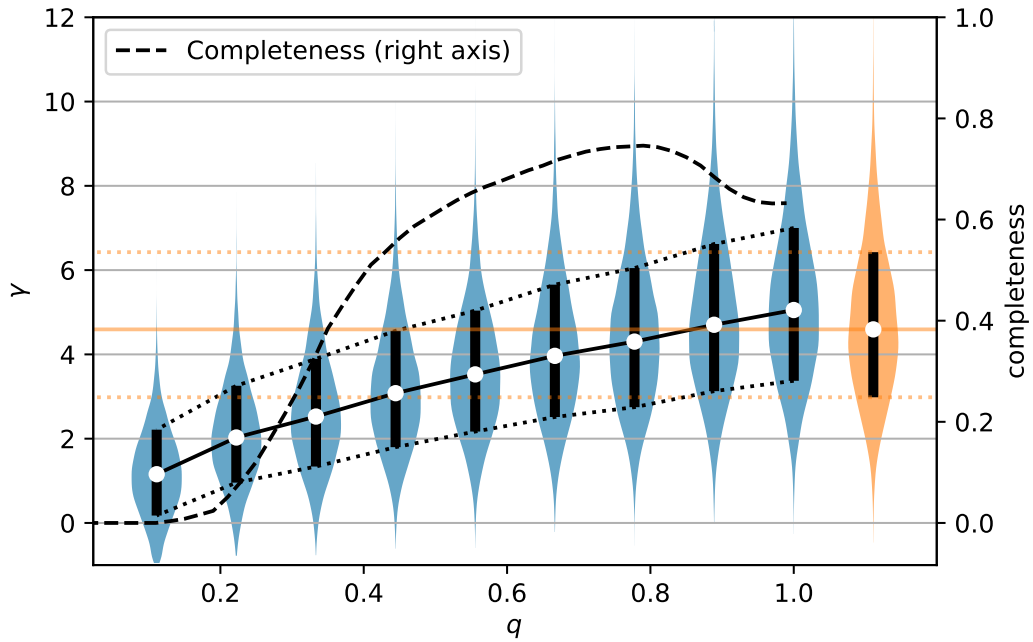


Figure J.2: Posteriors of the mass-ratio power-law index, γ , as a function of the mass-ratio, q , of an injected additional binary detection assuming a field age of 1.2 Gyr. The additional detection was injected at the median of the previously derived separation distribution (2.2 au) so as to have the least possible effect on other parameters. The orange distribution is with no injected detection. White points and black vertical lines correspond to the median and $\pm 1\sigma$ (central 68%) values. The black dashed line (right vertical axis) shows the completeness of our survey as a function of q .

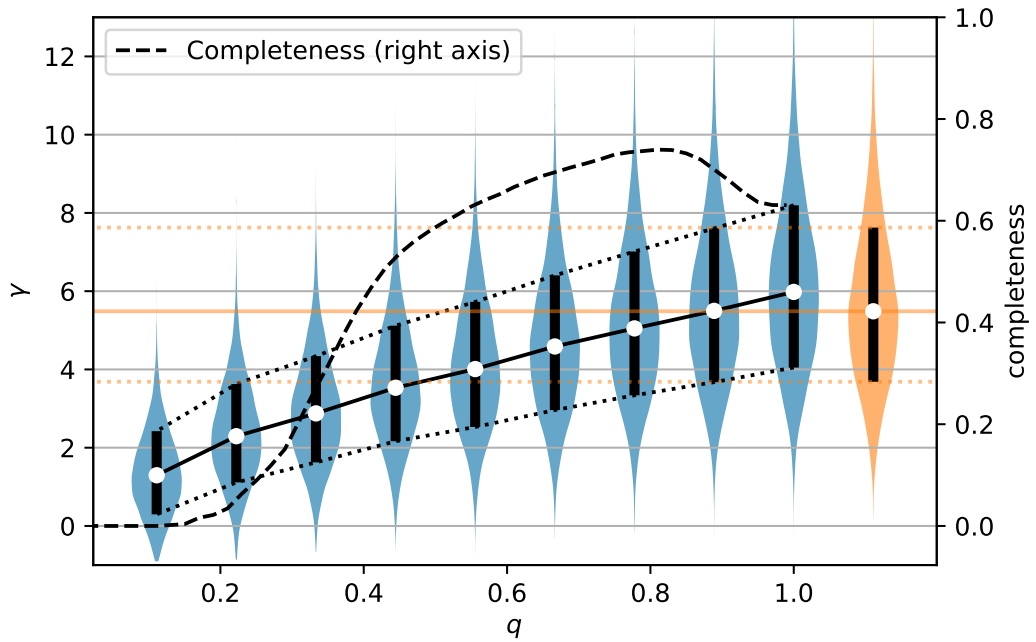


Figure J.3: Posteriors of the mass-ratio power-law index, γ , as a function of the mass-ratio, q , of an injected additional binary detection assuming a field age of 1.5 Gyr. The additional detection was injected at the median of the previously derived separation distribution (2.2 au) so as to have the least possible effect on other parameters. The orange distribution is with no injected detection. White points and black vertical lines correspond to the median and $\pm 1\sigma$ (central 68%) values. The black dashed line (right vertical axis) shows the completeness of our survey as a function of q .

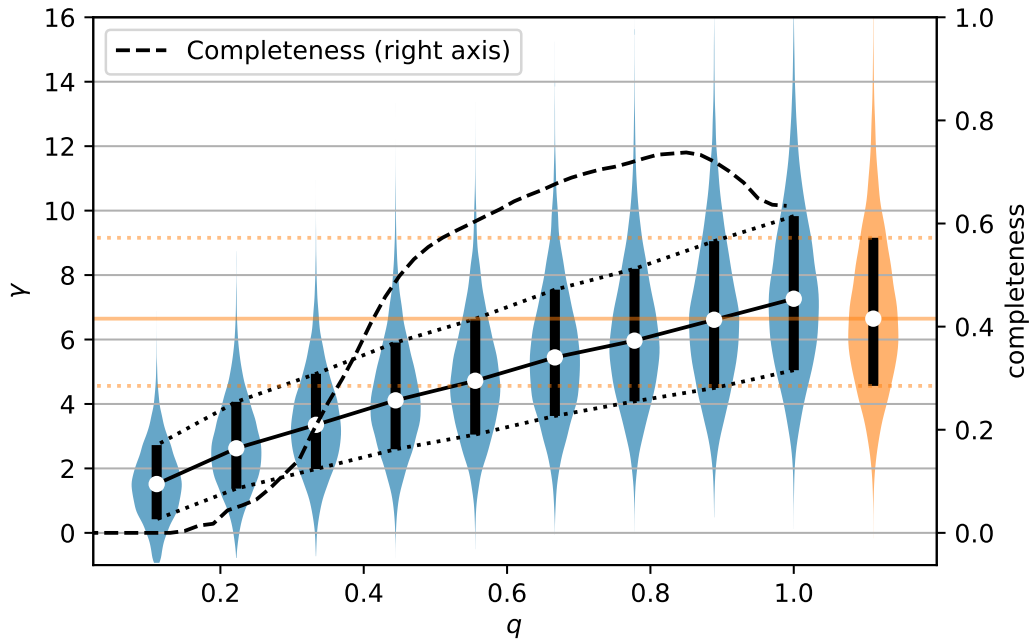


Figure J.4: Posteriors of the mass-ratio power-law index, γ , as a function of the mass-ratio, q , of an injected additional binary detection assuming a field age of 1.9 Gyr. The additional detection was injected at the median of the previously derived separation distribution (2.2 au) so as to have the least possible effect on other parameters. The orange distribution is with no injected detection. White points and black vertical lines correspond to the median and $\pm 1\sigma$ (central 68%) values. The black dashed line (right vertical axis) shows the completeness of our survey as a function of q .

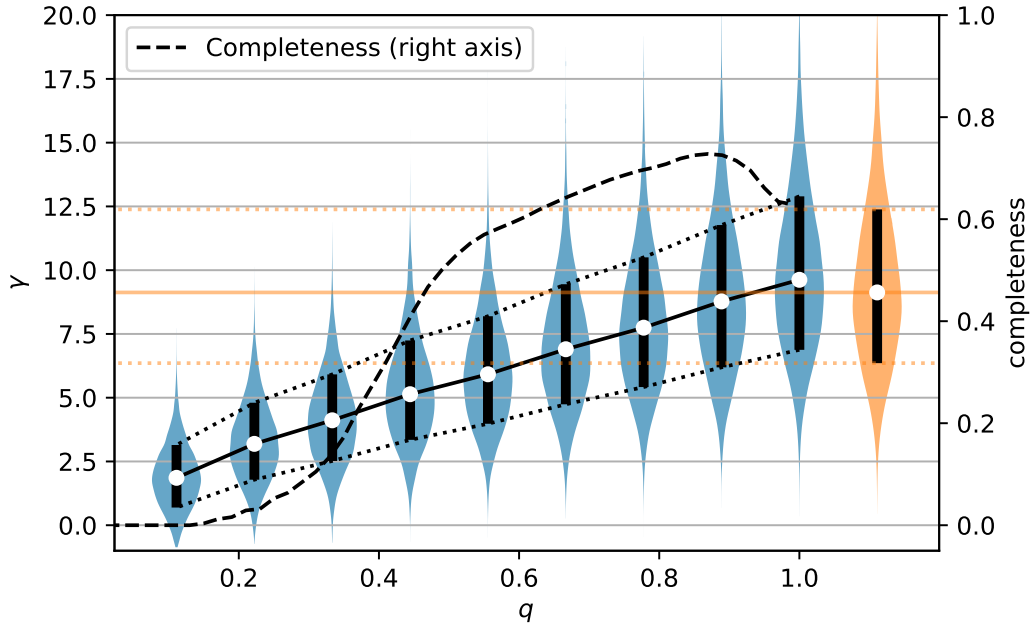


Figure J.5: Posteriors of the mass-ratio power-law index, γ , as a function of the mass-ratio, q , of an injected additional binary detection assuming a field age of 2.4 Gyr. The additional detection was injected at the median of the previously derived separation distribution (2.2 au) so as to have the least possible effect on other parameters. The orange distribution is with no injected detection. White points and black vertical lines correspond to the median and $\pm 1\sigma$ (central 68%) values. The black dashed line (right vertical axis) shows the completeness of our survey as a function of q .

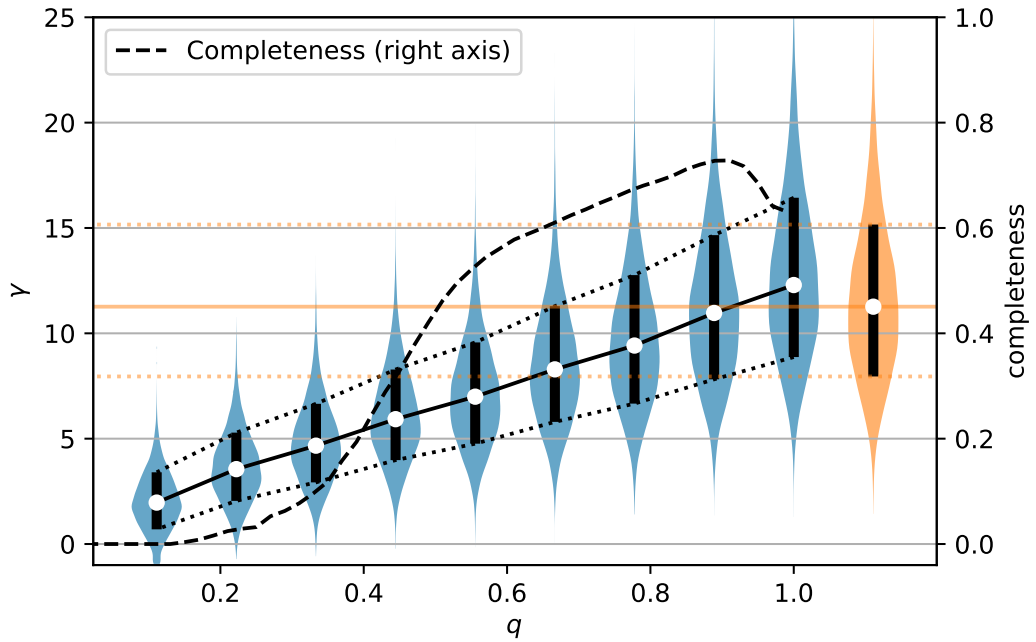


Figure J.6: Posteriors of the mass-ratio power-law index, γ , as a function of the mass-ratio, q , of an injected additional binary detection assuming a field age of 3.1 Gyr. The additional detection was injected at the median of the previously derived separation distribution (2.2 au) so as to have the least possible effect on other parameters. The orange distribution is with no injected detection. White points and black vertical lines correspond to the median and $\pm 1\sigma$ (central 68%) values. The black dashed line (right vertical axis) shows the completeness of our survey as a function of q .

Appendix K

**Figure Set corresponding to Figure 4.2:
Corner plots, KP correlation Plots, and
Images**

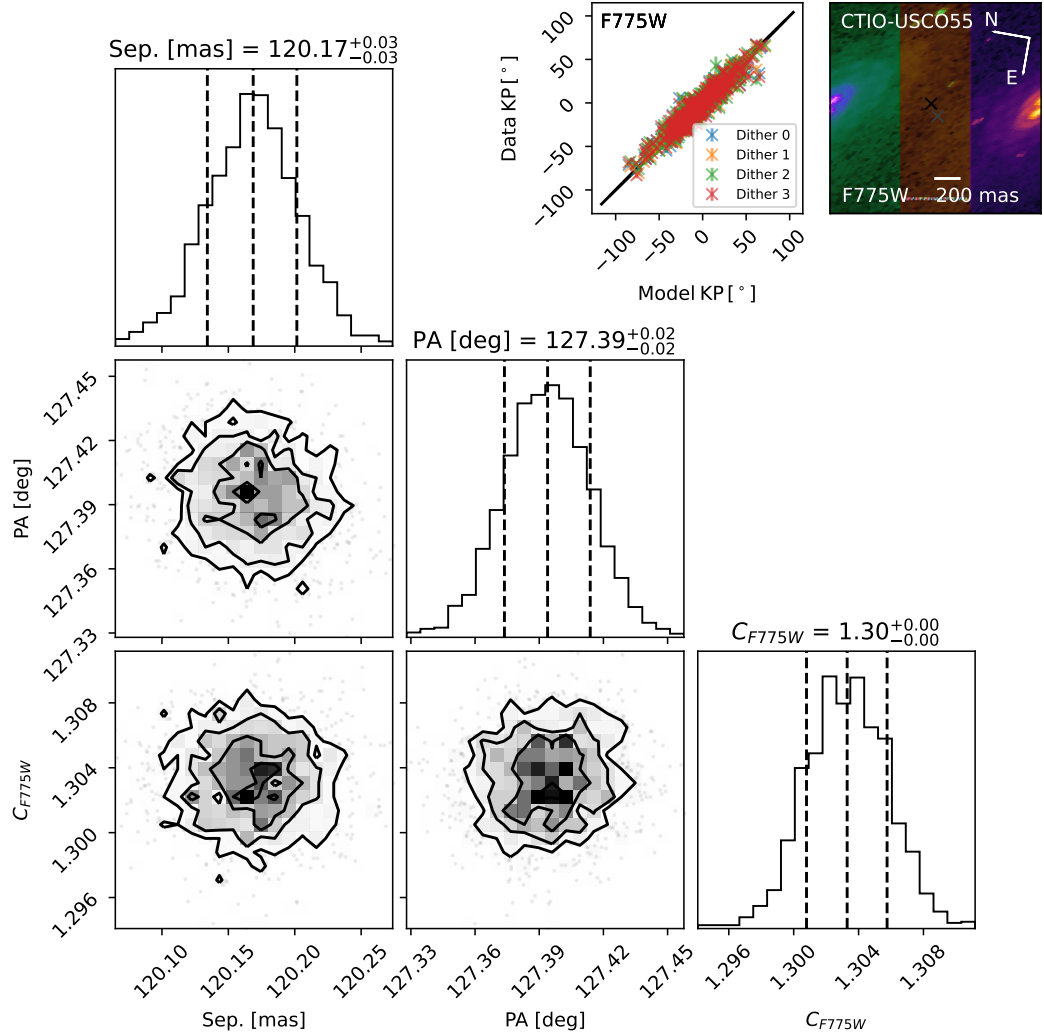


Figure K.1: Results of fitting a double point source to observations of CTIO-USco-55 in F775W (example image shown in the upper right corner with X's showing the position and contrast ratio of the two sources). Lower Left: Corner plot showing the posterior distributions of the binary fit. Dashed lines indicate the median and $\pm 1\sigma$ values. (16th, 50th, and 86th percentiles). Top Center: Data kernel phases plotted against the best-fit model kernel phases indicating a good fit.

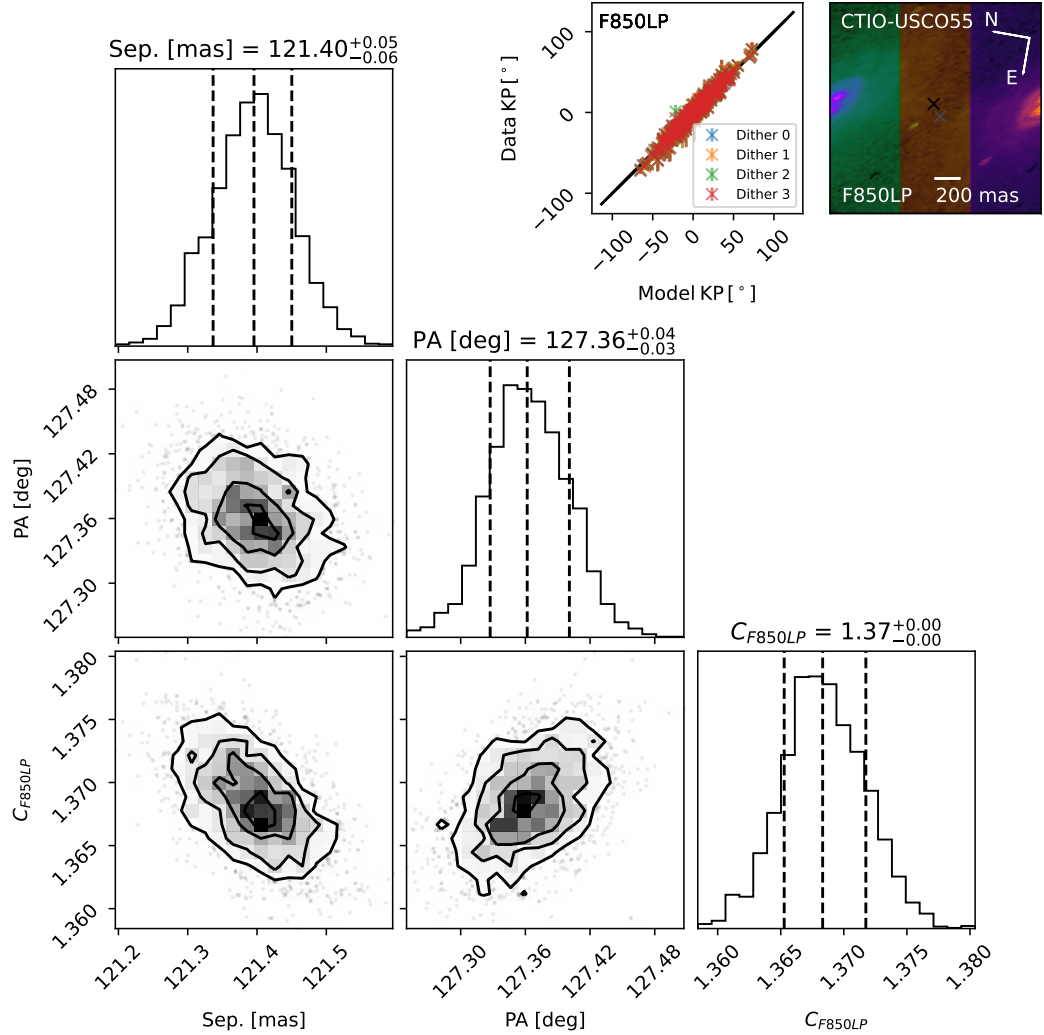


Figure K.2: Results of fitting a double point source to observations of CTIO-USco-55 in F850LP (example image shown in the upper right corner with X's showing the position and contrast ratio of the two sources). Lower Left: Corner plot showing the posterior distributions of the binary fit. Dashed lines indicate the median and $\pm 1\sigma$ values. (16th, 50th, and 86th percentiles). Top Center: Data kernel phases plotted against the best-fit model kernel phases indicating a good fit.

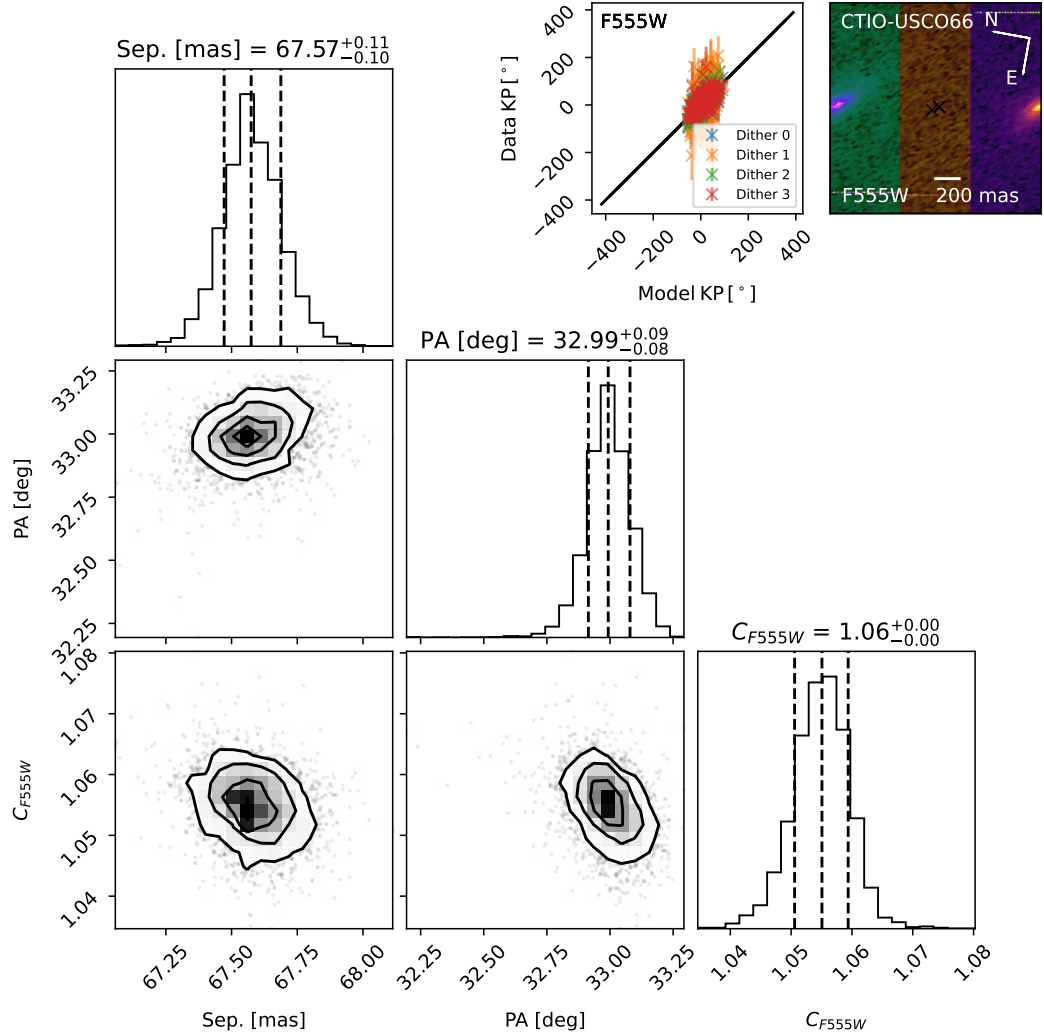


Figure K.3: Results of fitting a double point source to observations of CTIO-USco-66 in F555W (example image shown in the upper right corner with X's showing the position and contrast ratio of the two sources). Lower Left: Corner plot showing the posterior distributions of the binary fit. Dashed lines indicate the median and $\pm 1\sigma$ values. (16th, 50th, and 86th percentiles). Top Center: Data kernel phases plotted against the best-fit model kernel phases indicating a good fit.

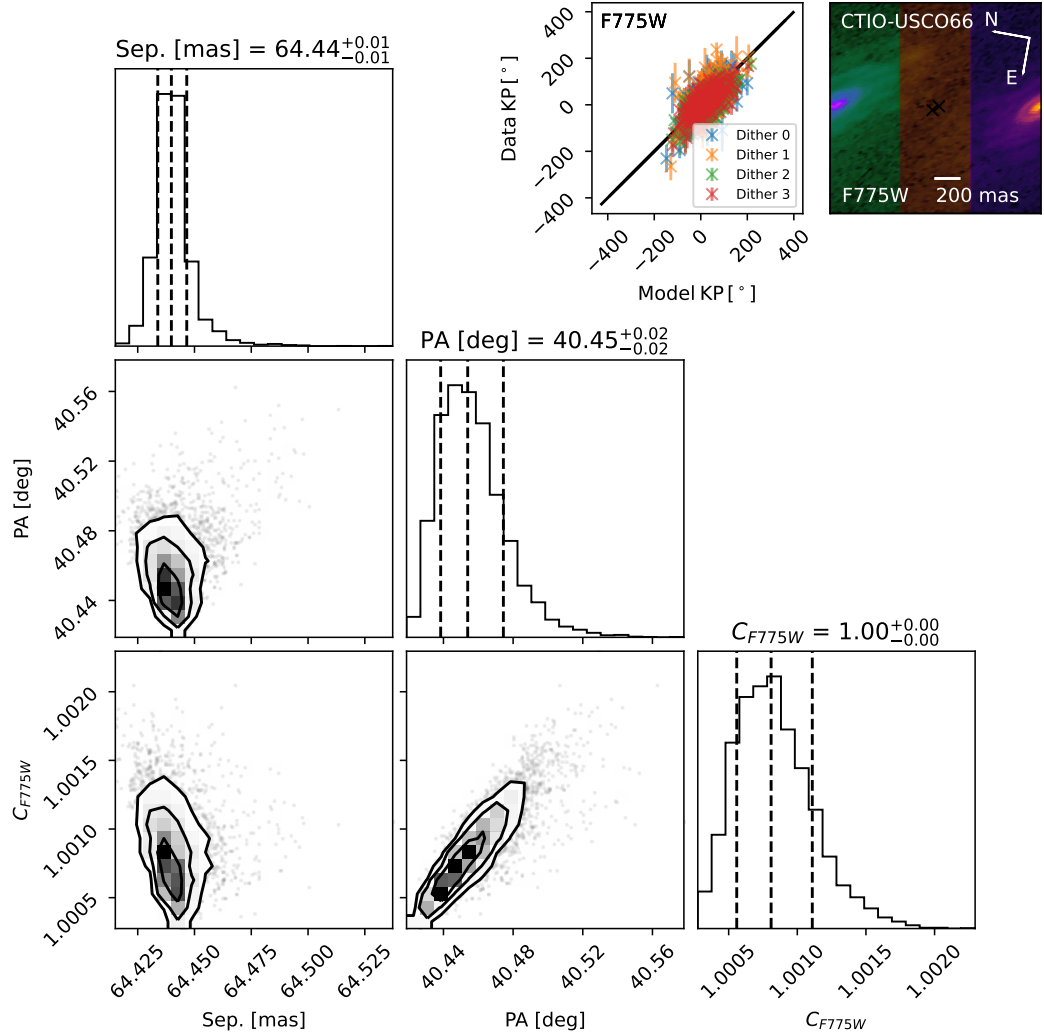


Figure K.4: Results of fitting a double point source to observations of CTIO-USCO-66 in F775W (example image shown in the upper right corner with X's showing the position and contrast ratio of the two sources). Lower Left: Corner plot showing the posterior distributions of the binary fit. Dashed lines indicate the median and $\pm 1\sigma$ values. (16th, 50th, and 86th percentiles). Top Center: Data kernel phases plotted against the best-fit model kernel phases indicating a good fit.

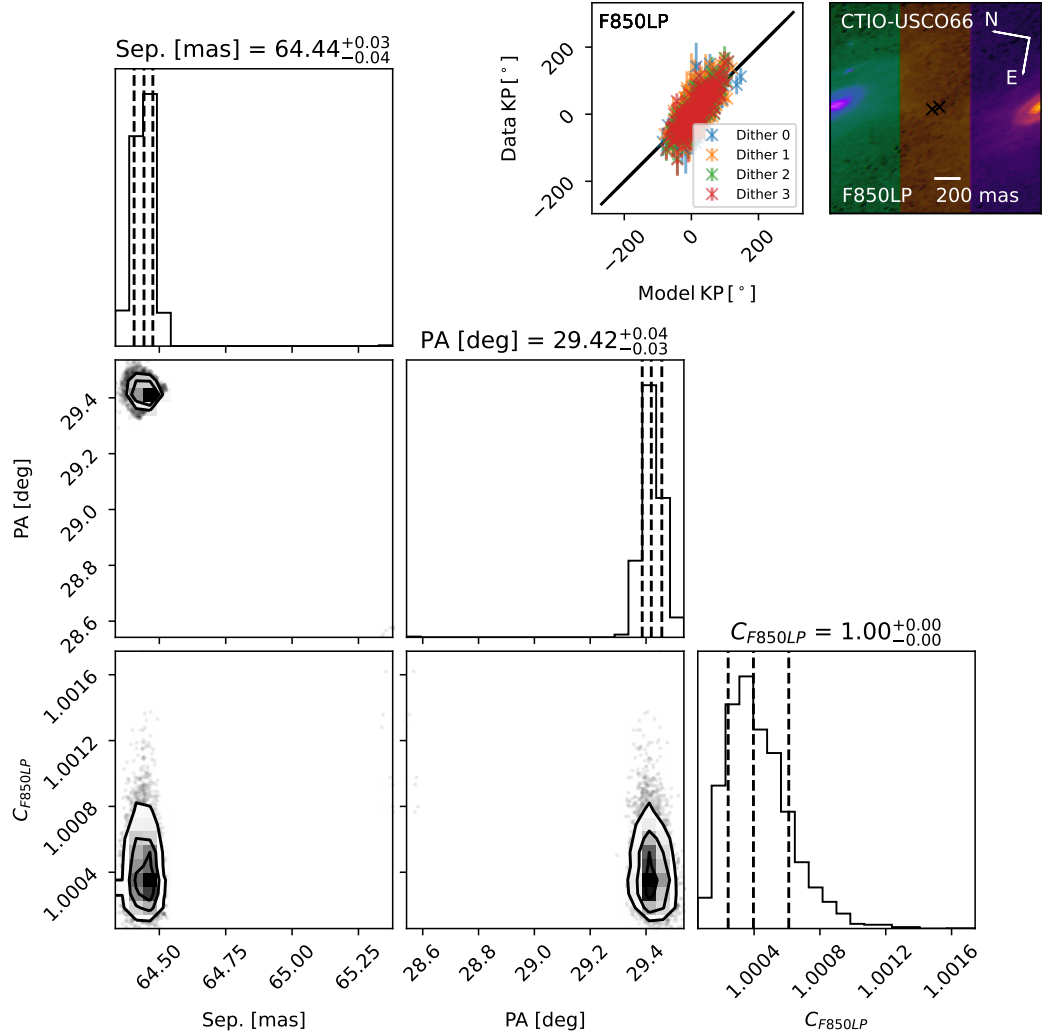


Figure K.5: Results of fitting a double point source to observations of CTIO-USCO-66 in F850LP (example image shown in the upper right corner with X's showing the position and contrast ratio of the two sources). Lower Left: Corner plot showing the posterior distributions of the binary fit. Dashed lines indicate the median and $\pm 1\sigma$ values. (16th, 50th, and 86th percentiles). Top Center: Data kernel phases plotted against the best-fit model kernel phases indicating a good fit.

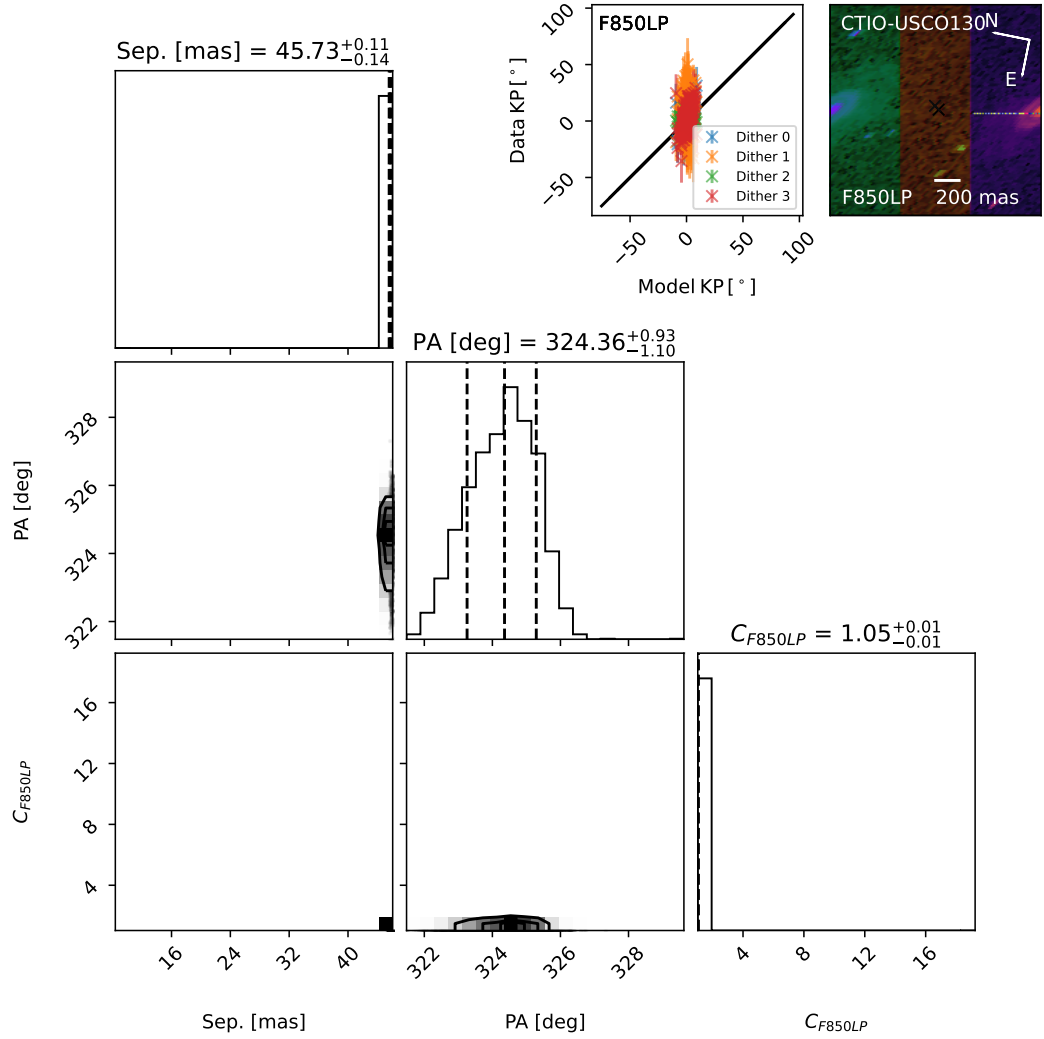


Figure K.6: Results of fitting a double point source to observations of CTIO-USco-130 in F850LP (example image shown in the upper right corner with X's showing the position and contrast ratio of the two sources). Lower Left: Corner plot showing the posterior distributions of the binary fit. Dashed lines indicate the median and $\pm 1\sigma$ values. (16th, 50th, and 86th percentiles). Top Center: Data kernel phases plotted against the best-fit model kernel phases indicating a good fit.

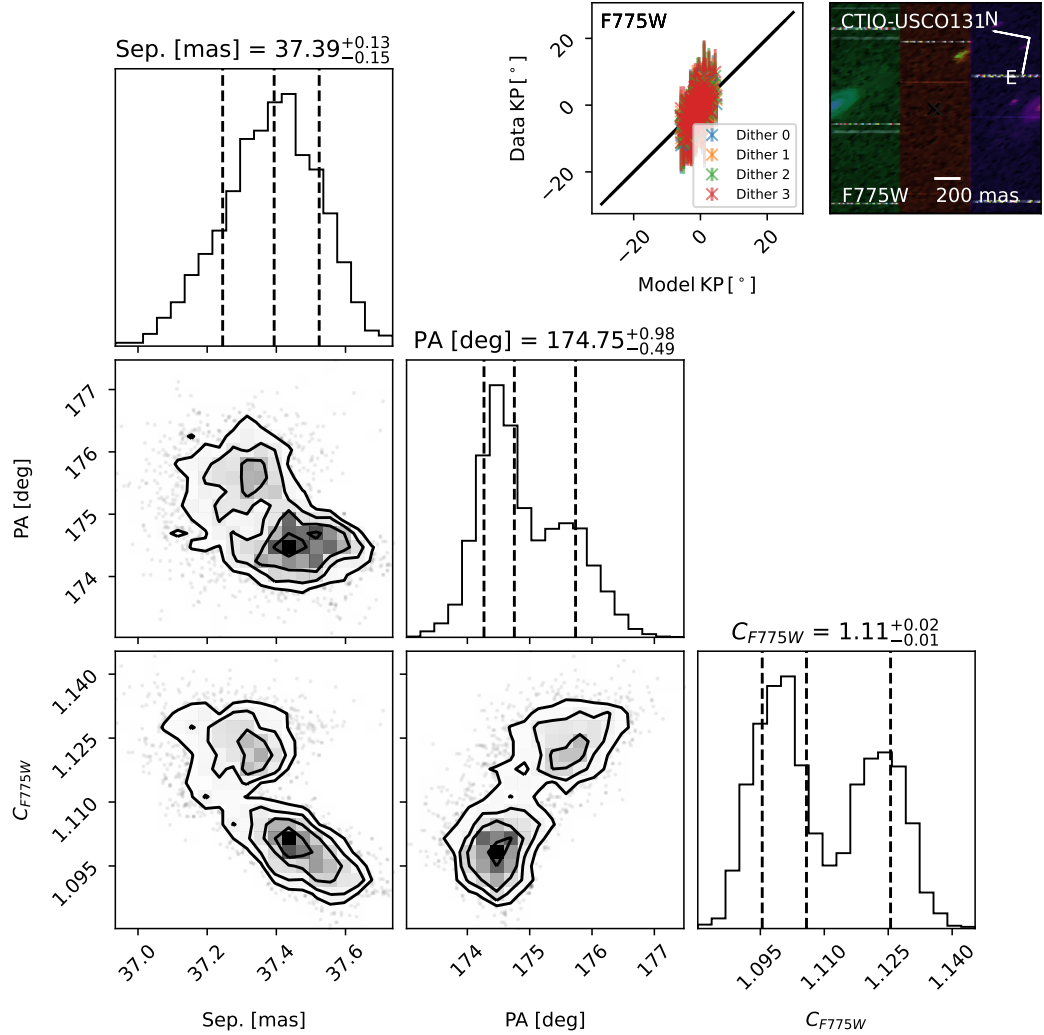


Figure K.7: Results of fitting a double point source to observations of CTIO-USco-131 in F775W (example image shown in the upper right corner with X's showing the position and contrast ratio of the two sources). Lower Left: Corner plot showing the posterior distributions of the binary fit. Dashed lines indicate the median and $\pm 1\sigma$ values. (16th, 50th, and 86th percentiles). Top Center: Data kernel phases plotted against the best-fit model kernel phases indicating a good fit.

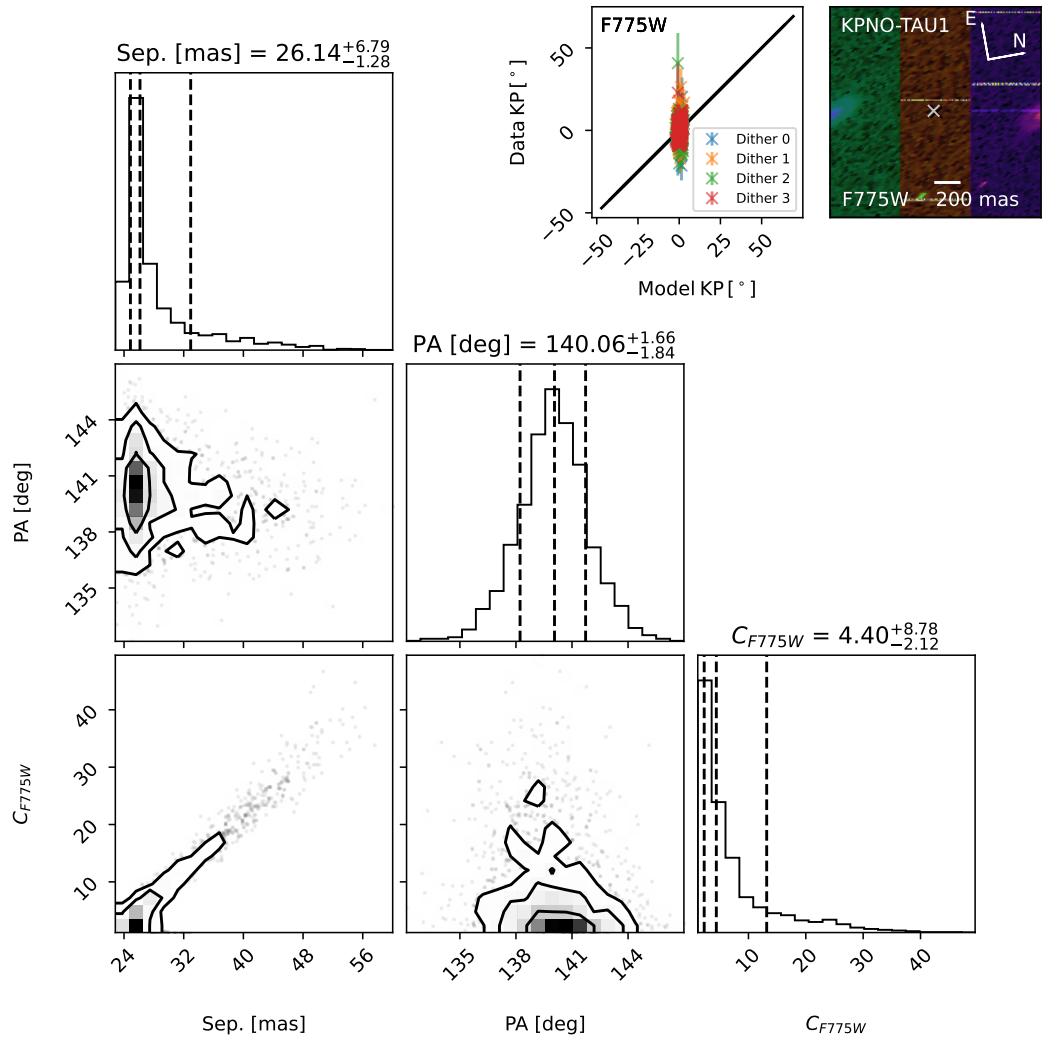


Figure K.8: Results of fitting a double point source to observations of KPNO-Tau-1 in F775W (example image shown in the upper right corner with X's showing the position and contrast ratio of the two sources). Lower Left: Corner plot showing the posterior distributions of the binary fit. Dashed lines indicate the median and $\pm 1\sigma$ values. (16th, 50th, and 86th percentiles). Top Center: Data kernel phases plotted against the best-fit model kernel phases indicating a good fit.

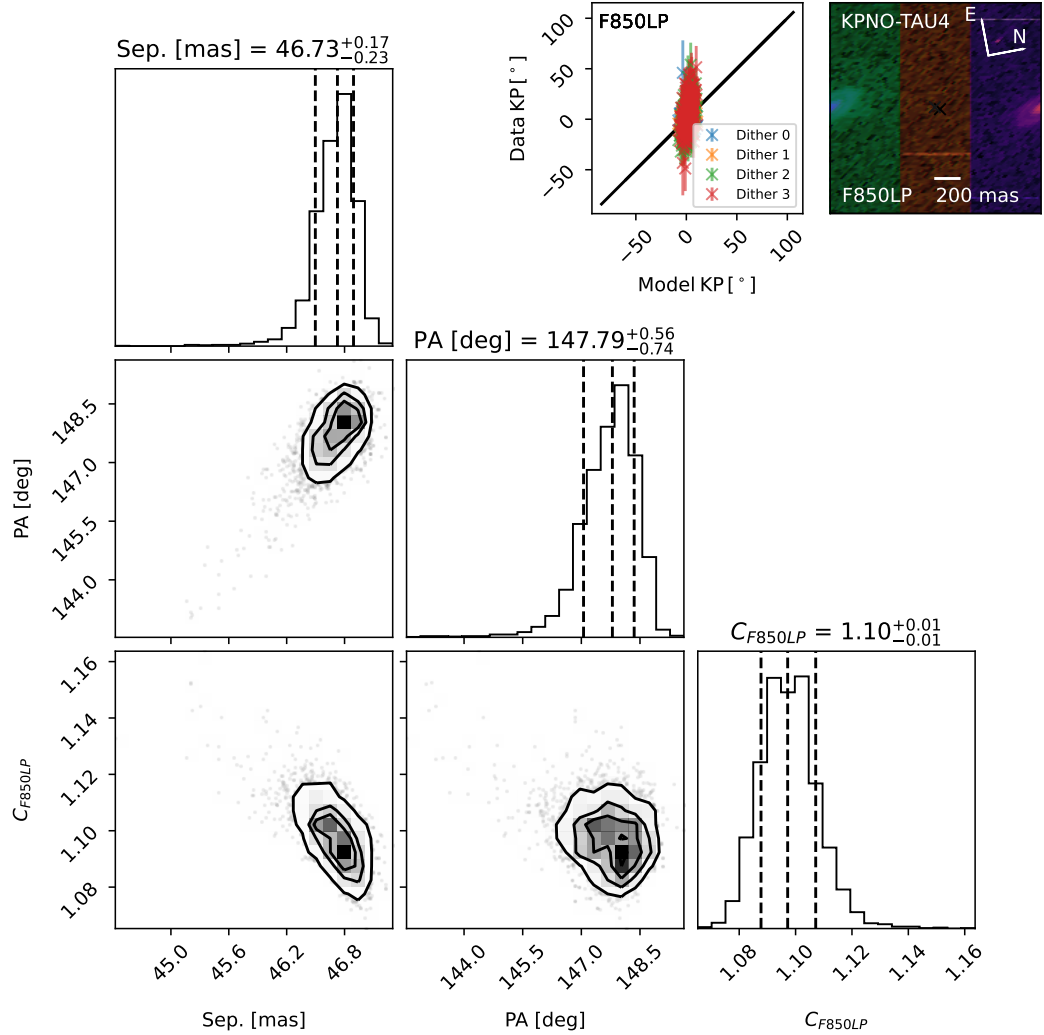


Figure K.9: Results of fitting a double point source to observations of KPNO-Tau-4 in F850LP (example image shown in the upper right corner with X's showing the position and contrast ratio of the two sources). Lower Left: Corner plot showing the posterior distributions of the binary fit. Dashed lines indicate the median and $\pm 1\sigma$ values. (16th, 50th, and 86th percentiles). Top Center: Data kernel phases plotted against the best-fit model kernel phases indicating a good fit.

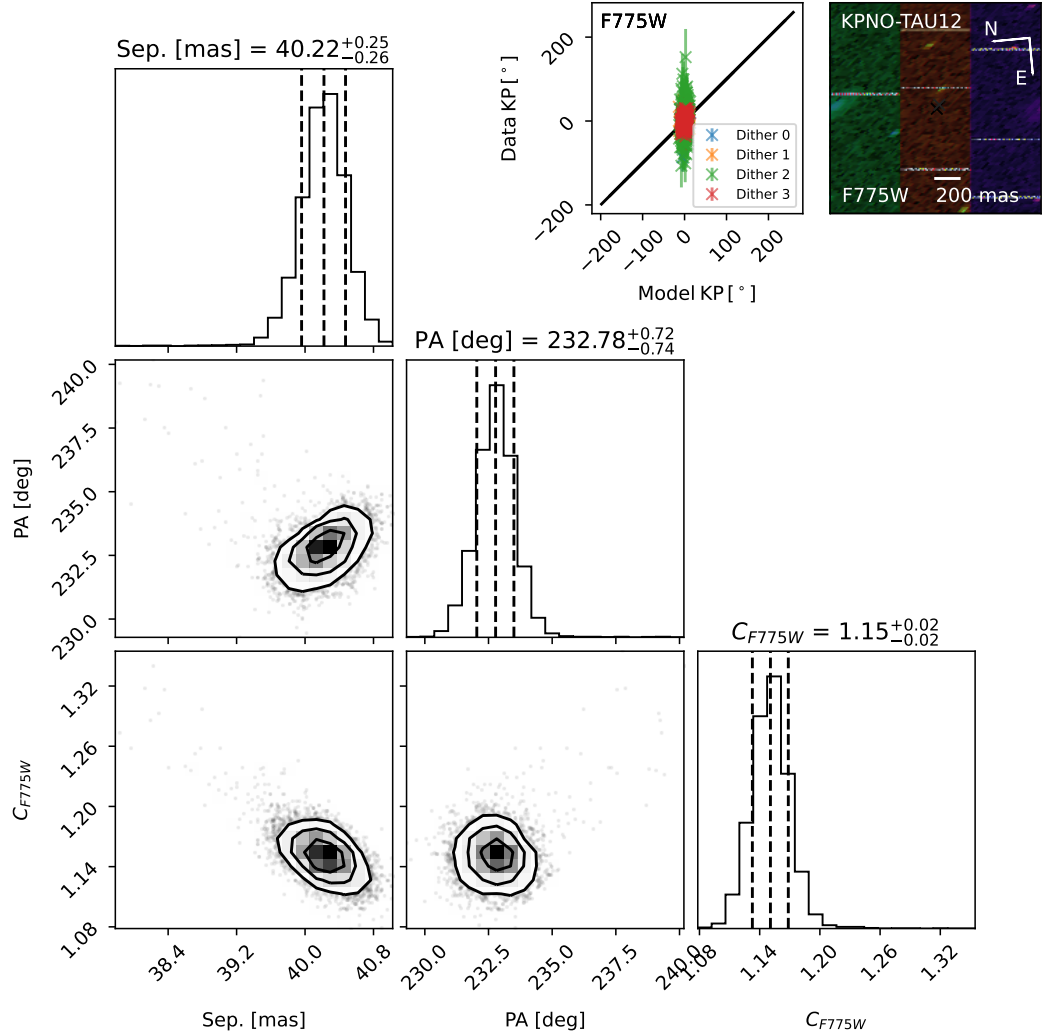


Figure K.10: Results of fitting a double point source to observations of KPNO-Tau-12 in F775W (example image shown in the upper right corner with X's showing the position and contrast ratio of the two sources). Lower Left: Corner plot showing the posterior distributions of the binary fit. Dashed lines indicate the median and $\pm 1\sigma$ values. (16th, 50th, and 86th percentiles). Top Center: Data kernel phases plotted against the best-fit model kernel phases indicating a good fit.

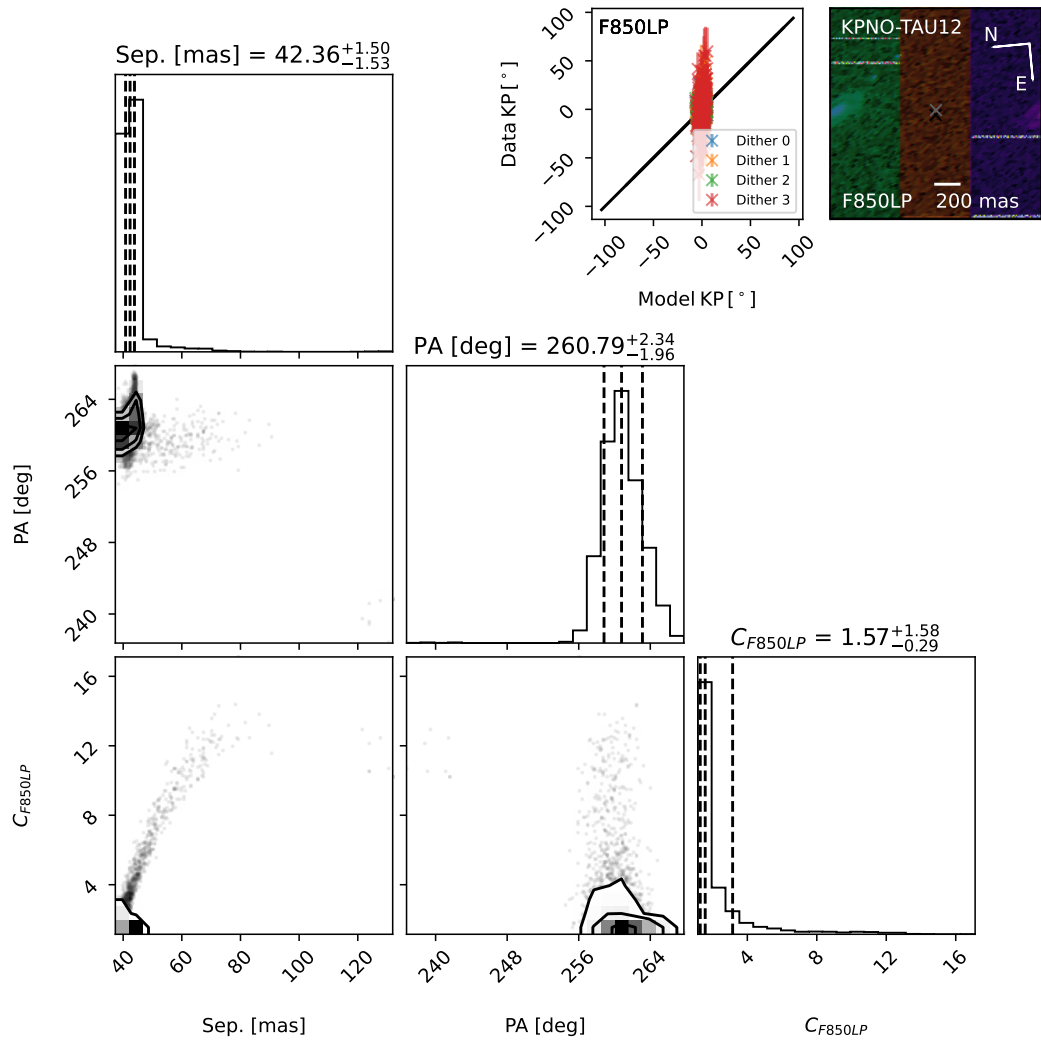


Figure K.11: Results of fitting a double point source to observations of KPNO-Tau-12 in F850LP (example image shown in the upper right corner with X's showing the position and contrast ratio of the two sources). Lower Left: Corner plot showing the posterior distributions of the binary fit. Dashed lines indicate the median and $\pm 1\sigma$ values. (16th, 50th, and 86th percentiles). Top Center: Data kernel phases plotted against the best-fit model kernel phases indicating a good fit.

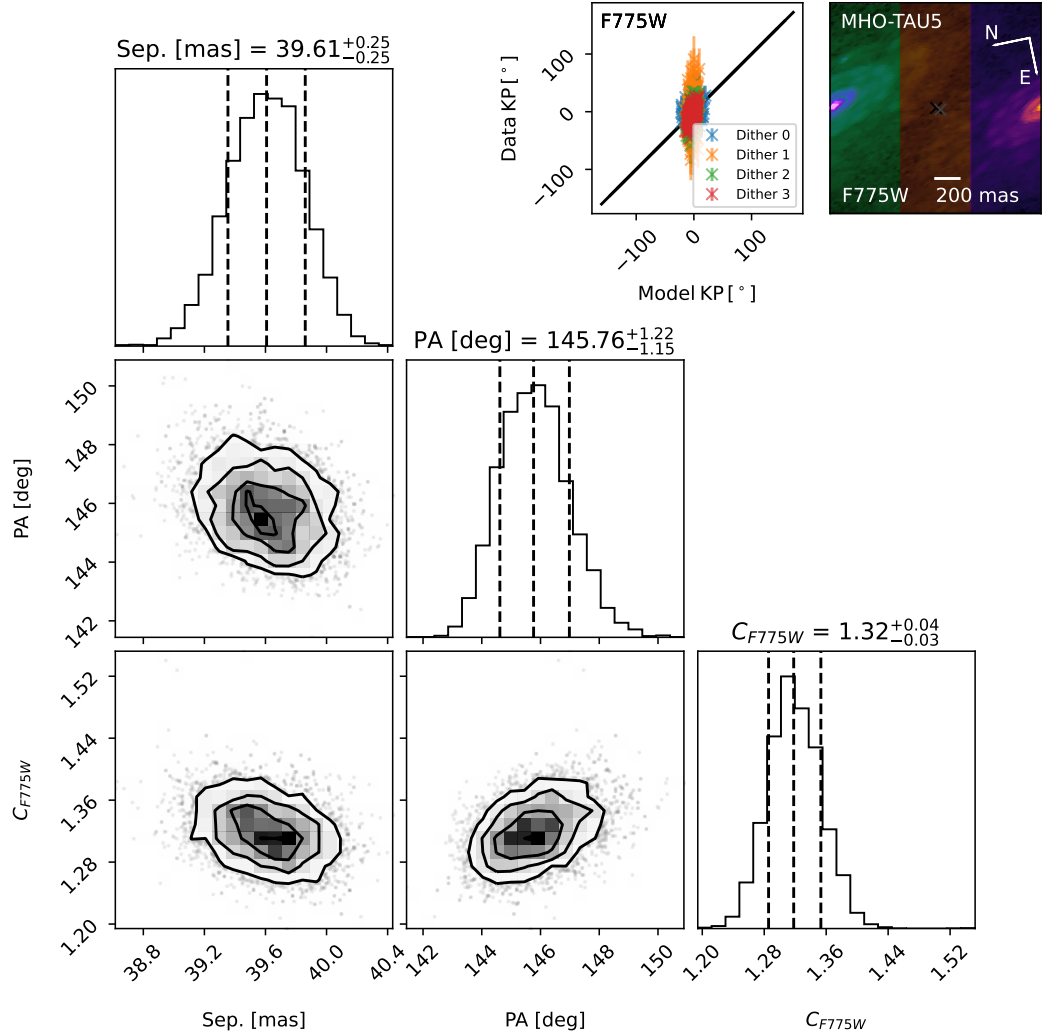


Figure K.12: Results of fitting a double point source to observations of MHO-Tau-5 in F775W (example image shown in the upper right corner with X's showing the position and contrast ratio of the two sources). Lower Left: Corner plot showing the posterior distributions of the binary fit. Dashed lines indicate the median and $\pm 1\sigma$ values. (16th, 50th, and 86th percentiles). Top Center: Data kernel phases plotted against the best-fit model kernel phases indicating a good fit.

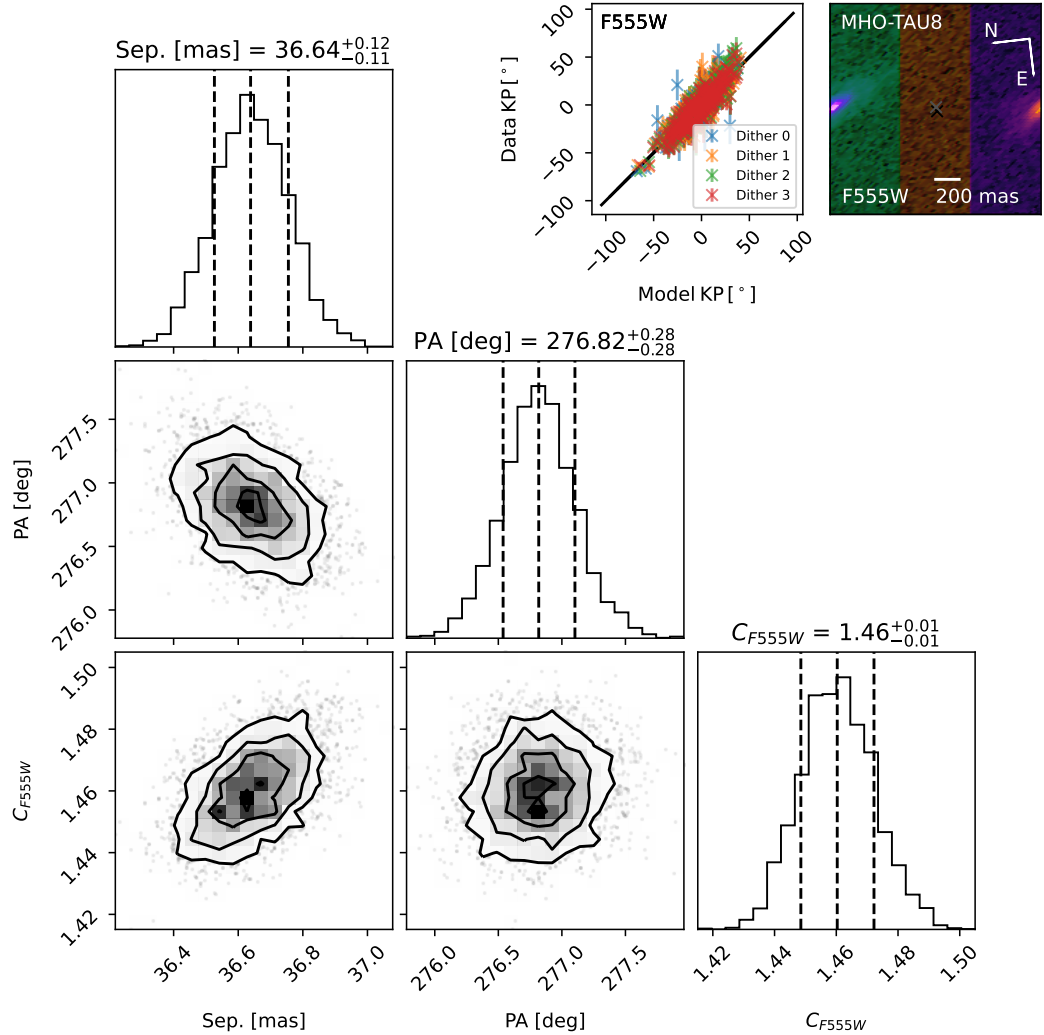


Figure K.13: Results of fitting a double point source to observations of MHO-Tau-8 in F555W (example image shown in the upper right corner with X's showing the position and contrast ratio of the two sources). Lower Left: Corner plot showing the posterior distributions of the binary fit. Dashed lines indicate the median and $\pm 1\sigma$ values. (16th, 50th, and 86th percentiles). Top Center: Data kernel phases plotted against the best-fit model kernel phases indicating a good fit.

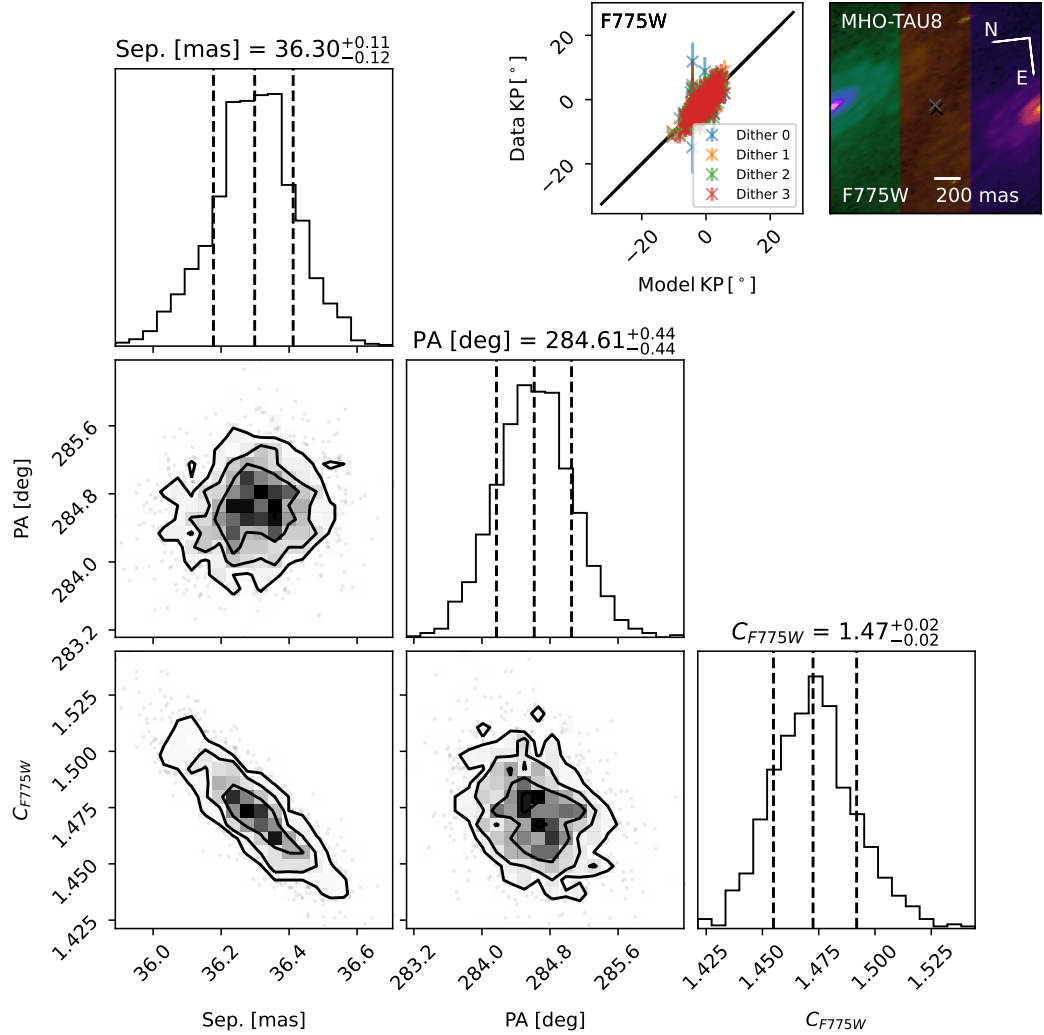


Figure K.14: Results of fitting a double point source to observations of MHO-Tau-8 in F775W (example image shown in the upper right corner with X's showing the position and contrast ratio of the two sources). Lower Left: Corner plot showing the posterior distributions of the binary fit. Dashed lines indicate the median and $\pm 1\sigma$ values. (16th, 50th, and 86th percentiles). Top Center: Data kernel phases plotted against the best-fit model kernel phases indicating a good fit.

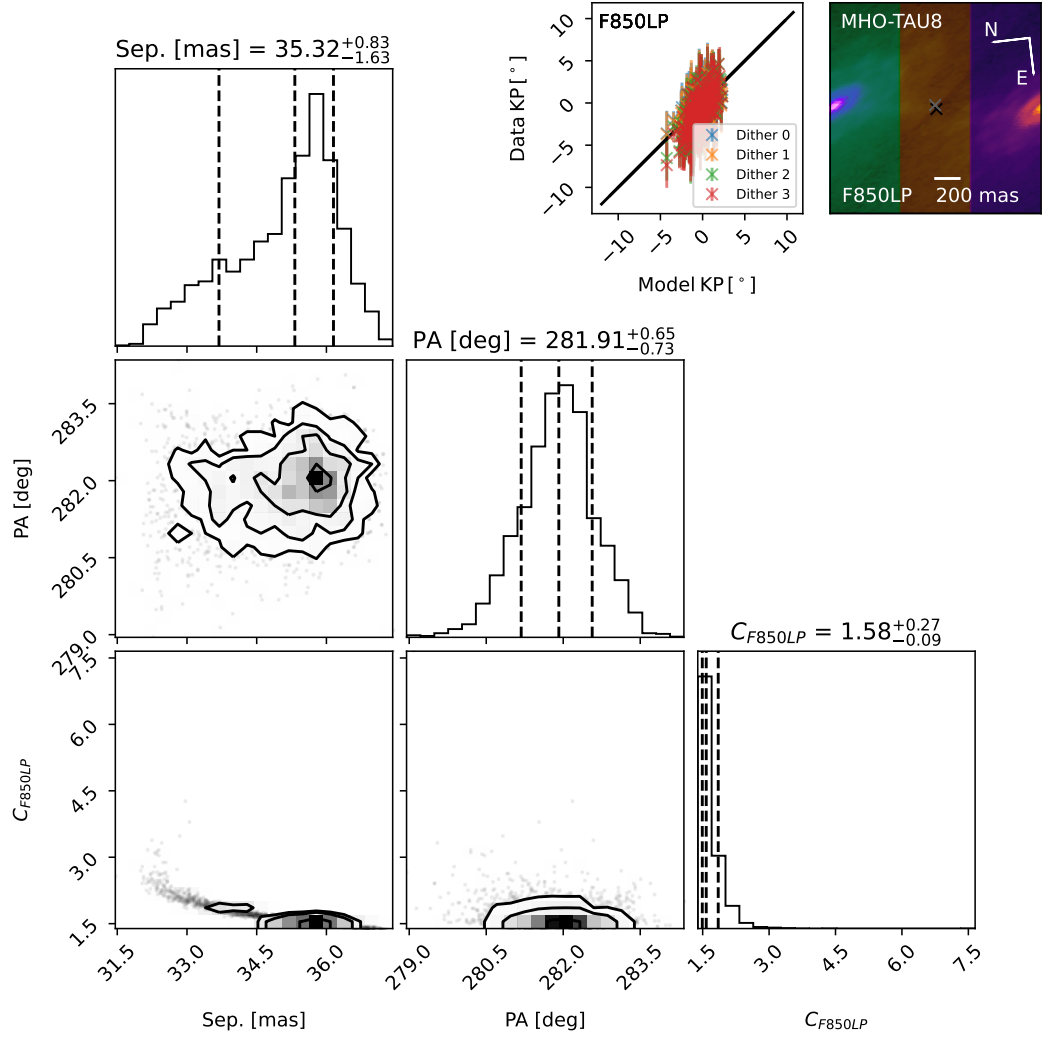


Figure K.15: Results of fitting a double point source to observations of MHO-Tau-8 in F850LP (example image shown in the upper right corner with X's showing the position and contrast ratio of the two sources). Lower Left: Corner plot showing the posterior distributions of the binary fit. Dashed lines indicate the median and $\pm 1\sigma$ values. (16th, 50th, and 86th percentiles). Top Center: Data kernel phases plotted against the best-fit model kernel phases indicating a good fit.

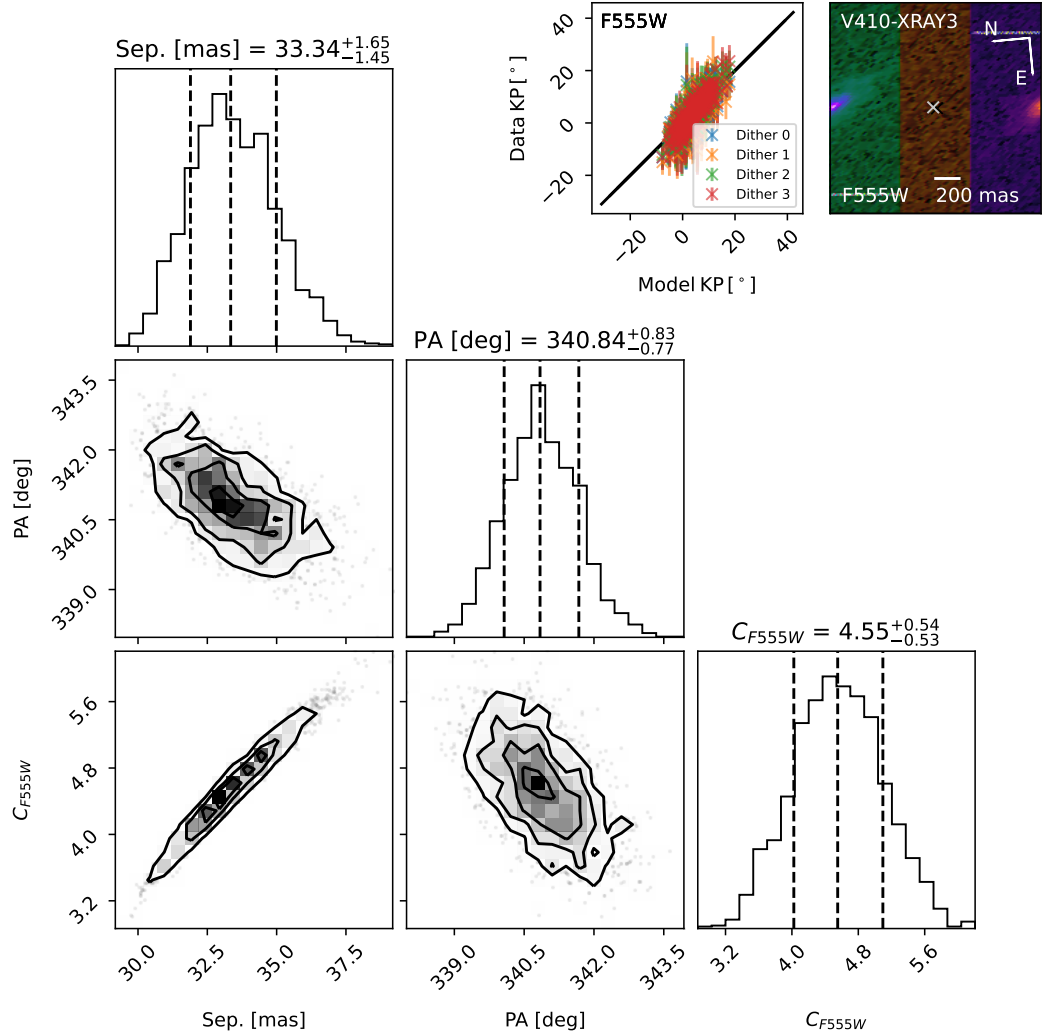


Figure K.16: Results of fitting a double point source to observations of V410 Xray-3 in F555W (example image shown in the upper right corner with X's showing the position and contrast ratio of the two sources). Lower Left: Corner plot showing the posterior distributions of the binary fit. Dashed lines indicate the median and $\pm 1\sigma$ values. (16th, 50th, and 86th percentiles). Top Center: Data kernel phases plotted against the best-fit model kernel phases indicating a good fit.

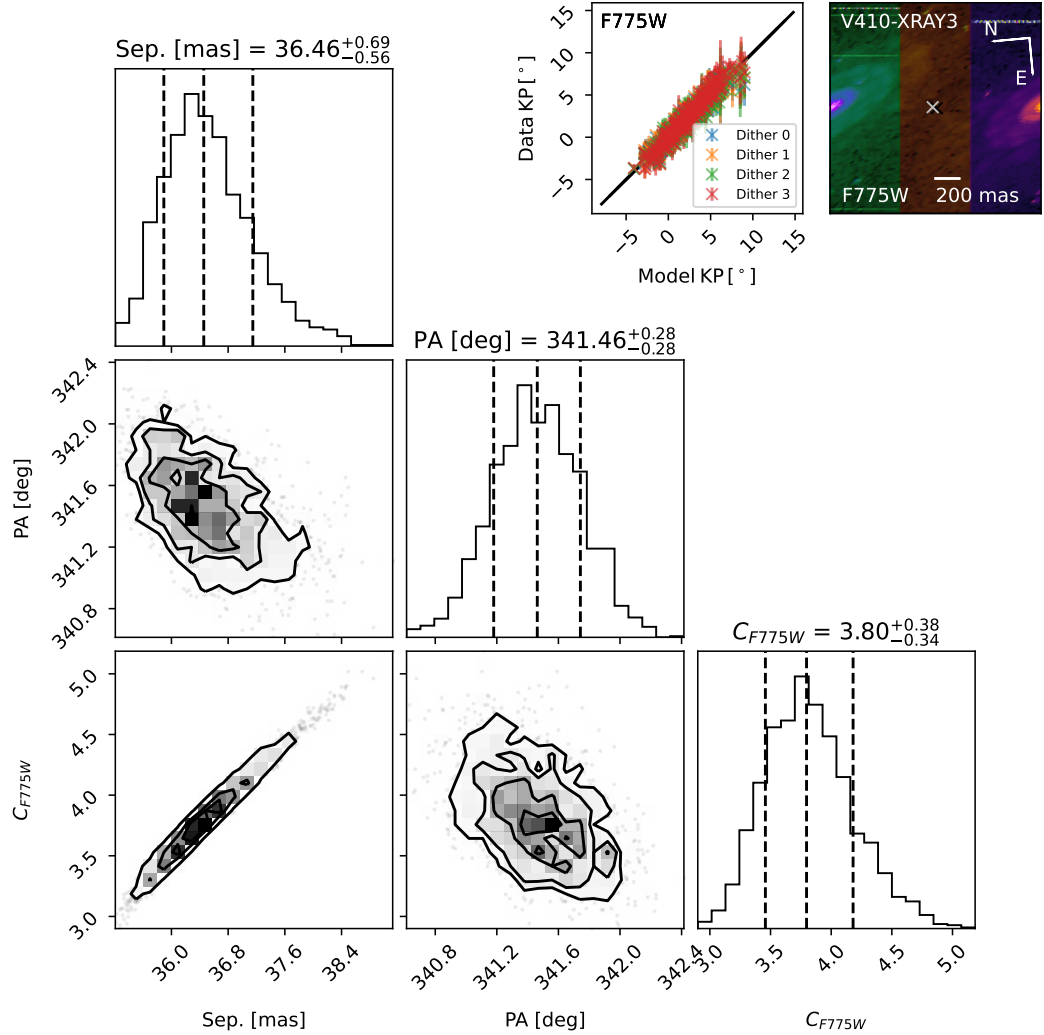


Figure K.17: Results of fitting a double point source to observations of V410 Xray-3 in F775W (example image shown in the upper right corner with X's showing the position and contrast ratio of the two sources). Lower Left: Corner plot showing the posterior distributions of the binary fit. Dashed lines indicate the median and $\pm 1\sigma$ values. (16th, 50th, and 86th percentiles). Top Center: Data kernel phases plotted against the best-fit model kernel phases indicating a good fit.

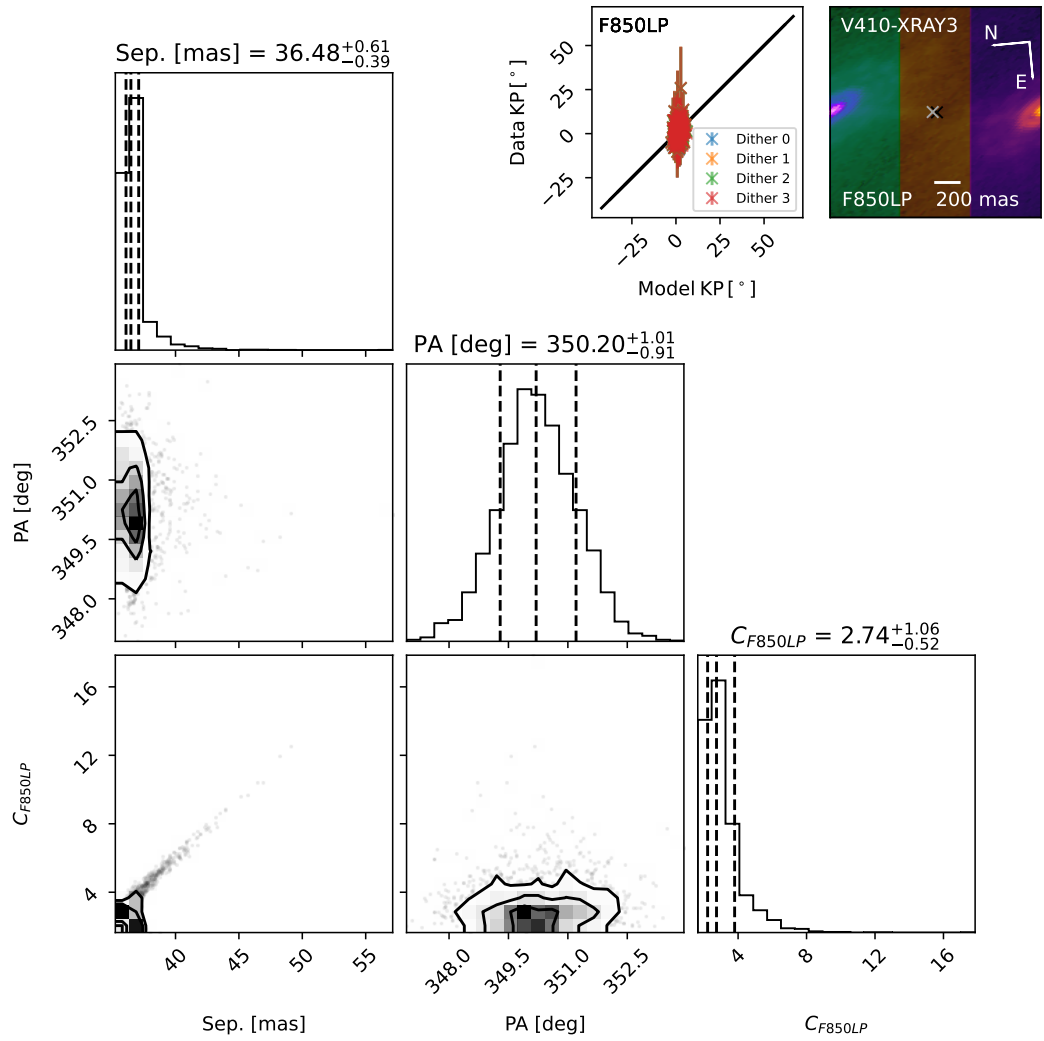


Figure K.18: Results of fitting a double point source to observations of V410 Xray-3 in F850LP (example image shown in the upper right corner with X's showing the position and contrast ratio of the two sources). Lower Left: Corner plot showing the posterior distributions of the binary fit. Dashed lines indicate the median and $\pm 1\sigma$ values. (16th, 50th, and 86th percentiles). Top Center: Data kernel phases plotted against the best-fit model kernel phases indicating a good fit.

Appendix L

**Figure Set corresponding to Figure 4.3:
Detection Limits for Significant Detections**

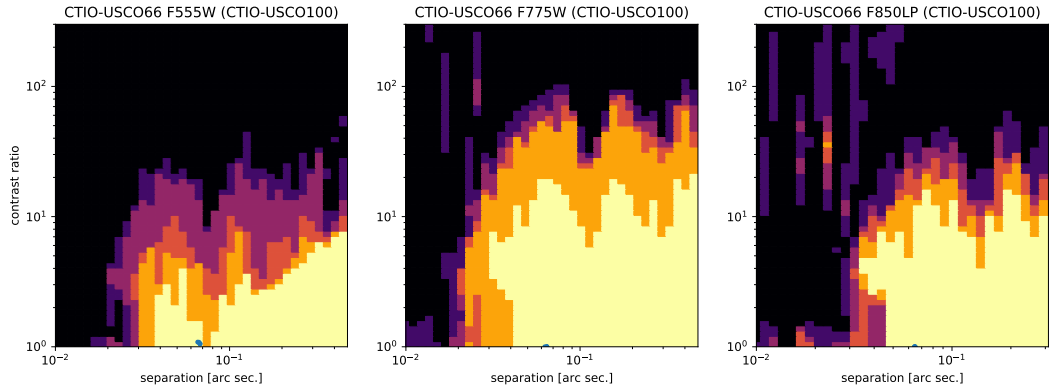


Figure L.1: Detection limits for CTIO-USCo-66 with a significant detection. The science target is indicated in the title of each panel along with the detection limit grid in parentheses. The color scale is the number of calibrators (0 to 5 and black to yellow) which would significantly ($> 5\sigma$) detect a companion as a function of separation and contrast ratio in the three filters (three columns). Best fit companion parameters are plotted (with error bars) for the 5 calibrators in blue, if significantly detected, and in orange, if not significantly detected. The source was determined to be a detection if at least 4 fits were significant and consistent with each other.

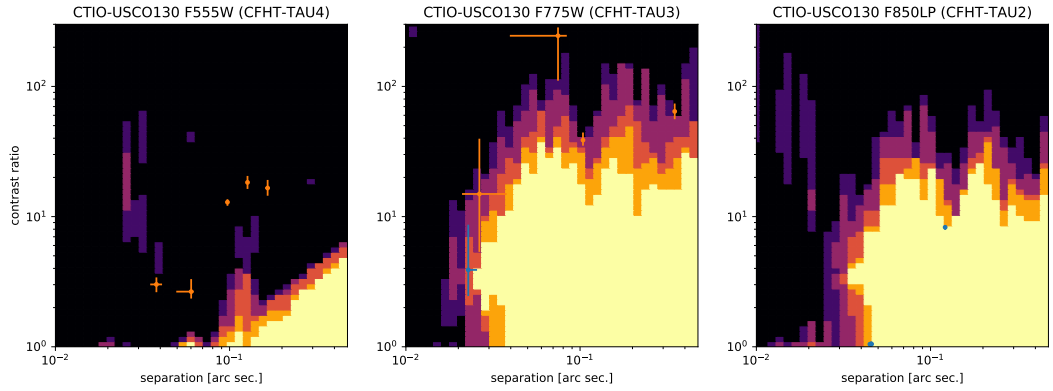


Figure L.2: Detection limits for CTIO-USCo-130 with a significant detection. The science target is indicated in the title of each panel along with the detection limit grid in parentheses. The color scale is the number of calibrators (0 to 5 and black to yellow) which would significantly ($> 5\sigma$) detect a companion as a function of separation and contrast ratio in the three filters (three columns). Best fit companion parameters are plotted (with error bars) for the 5 calibrators in blue, if significantly detected, and in orange, if not significantly detected. The source was determined to be a detection if at least 4 fits were significant and consistent with each other.

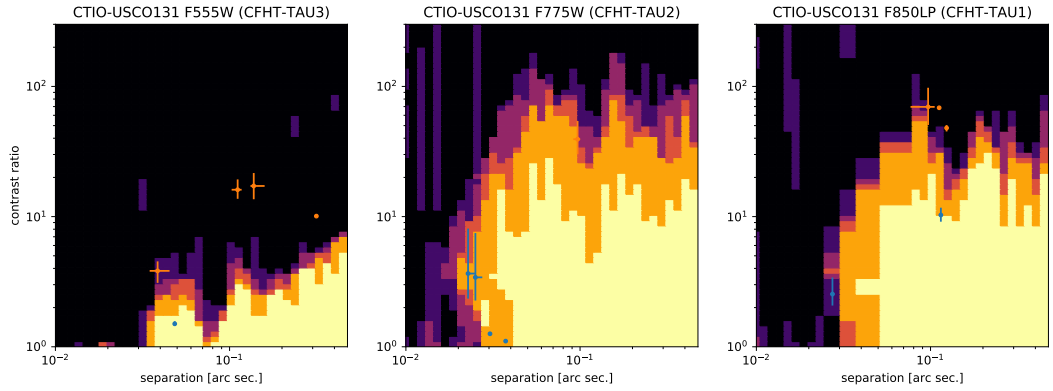


Figure L.3: Detection limits for CTIO-USCo-131 with a significant detection. The science target is indicated in the title of each panel along with the detection limit grid in parentheses. The color scale is the number of calibrators (0 to 5 and black to yellow) which would significantly ($> 5\sigma$) detect a companion as a function of separation and contrast ratio in the three filters (three columns). Best fit companion parameters are plotted (with error bars) for the 5 calibrators in blue, if significantly detected, and in orange, if not significantly detected. The source was determined to be a detection if at least 4 fits were significant and consistent with each other.

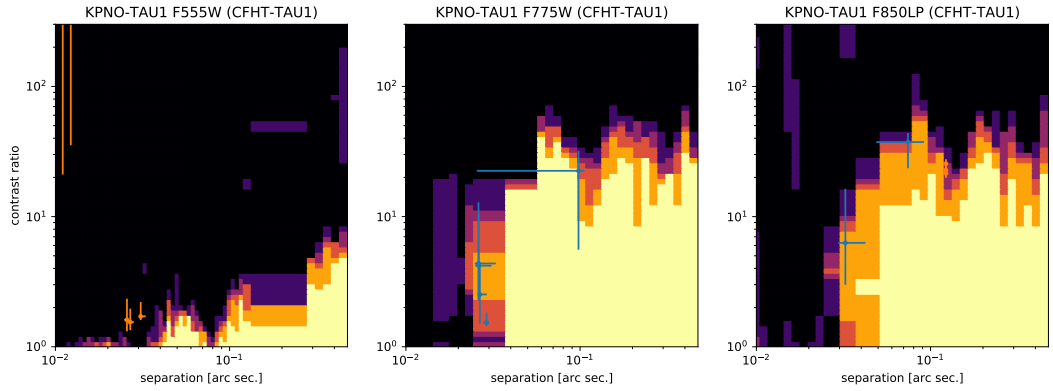


Figure L.4: Detection limits for KPNO-Tau-1 with a significant detection. The science target is indicated in the title of each panel along with the detection limit grid in parentheses. The color scale is the number of calibrators (0 to 5 and black to yellow) which would significantly ($> 5\sigma$) detect a companion as a function of separation and contrast ratio in the three filters (three columns). Best fit companion parameters are plotted (with error bars) for the 5 calibrators in blue, if significantly detected, and in orange, if not significantly detected. The source was determined to be a detection if at least 4 fits were significant and consistent with each other.

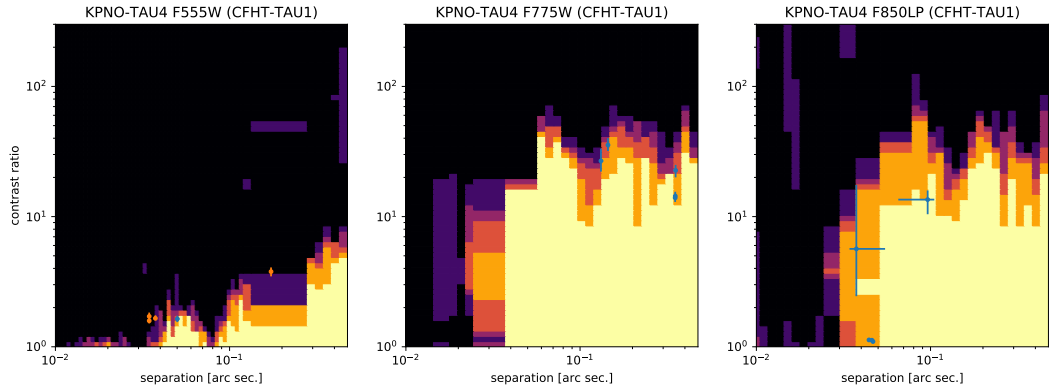


Figure L.5: Detection limits KPNO-Tau-4 with a significant detection. The science target is indicated in the title of each panel along with the detection limit grid in parentheses. The color scale is the number of calibrators (0 to 5 and black to yellow) which would significantly ($> 5\sigma$) detect a companion as a function of separation and contrast ratio in the three filters (three columns). Best fit companion parameters are plotted (with error bars) for the 5 calibrators in blue, if significantly detected, and in orange, if not significantly detected. The source was determined to be a detection if at least 4 fits were significant and consistent with each other.

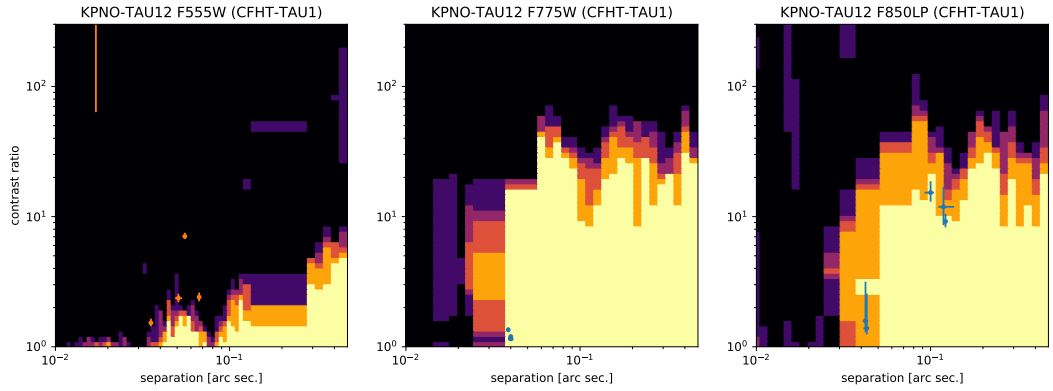


Figure L.6: Detection limits for KPNO-Tau-12 with a significant detection. The science target is indicated in the title of each panel along with the detection limit grid in parentheses. The color scale is the number of calibrators (0 to 5 and black to yellow) which would significantly ($> 5\sigma$) detect a companion as a function of separation and contrast ratio in the three filters (three columns). Best fit companion parameters are plotted (with error bars) for the 5 calibrators in blue, if significantly detected, and in orange, if not significantly detected. The source was determined to be a detection if at least 4 fits were significant and consistent with each other.

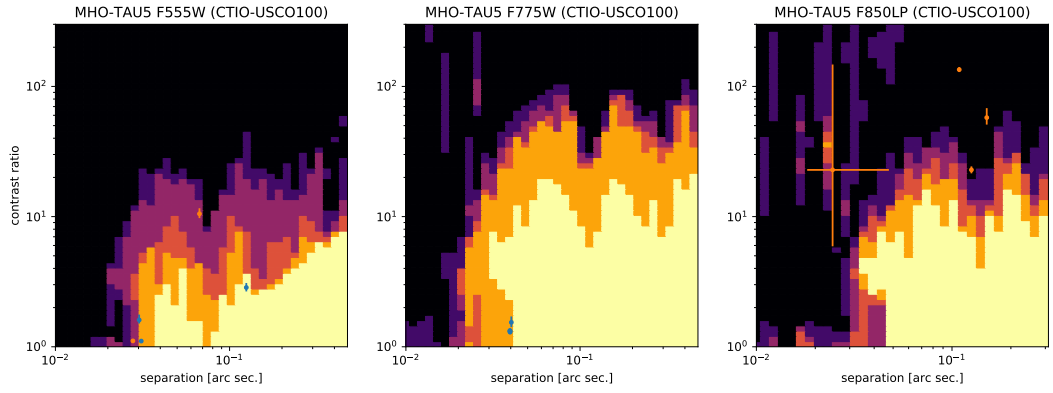


Figure L.7: Detection limits for MHO-Tau-5 with a significant detection. The science target is indicated in the title of each panel along with the detection limit grid in parentheses. The color scale is the number of calibrators (0 to 5 and black to yellow) which would significantly ($> 5\sigma$) detect a companion as a function of separation and contrast ratio in the three filters (three columns). Best fit companion parameters are plotted (with error bars) for the 5 calibrators in blue, if significantly detected, and in orange, if not significantly detected. The source was determined to be a detection if at least 4 fits were significant and consistent with each other.

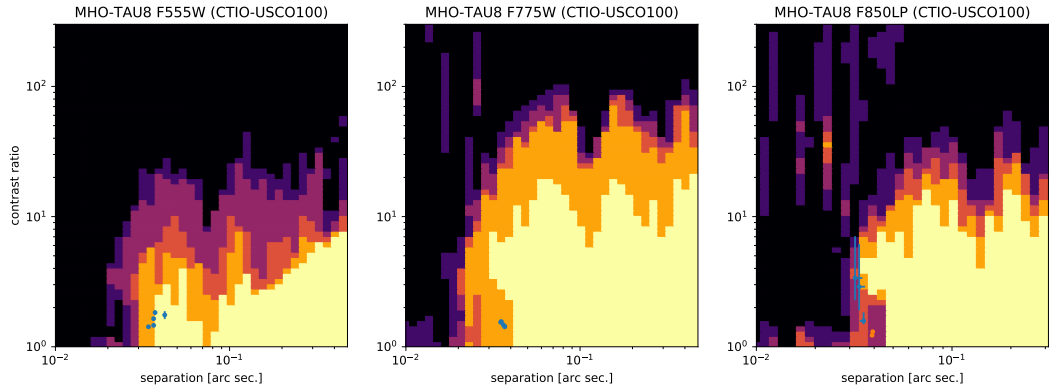


Figure L.8: Detection limits for MHO-Tau-8 with a significant detection. The science target is indicated in the title of each panel along with the detection limit grid in parentheses. The color scale is the number of calibrators (0 to 5 and black to yellow) which would significantly ($> 5\sigma$) detect a companion as a function of separation and contrast ratio in the three filters (three columns). Best fit companion parameters are plotted (with error bars) for the 5 calibrators in blue, if significantly detected, and in orange, if not significantly detected. The source was determined to be a detection if at least 4 fits were significant and consistent with each other.

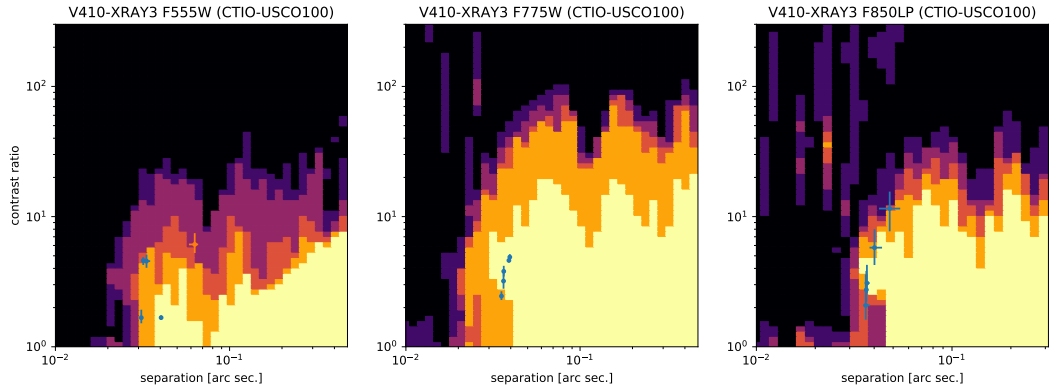


Figure L.9: Detection limits for V410-Xray-3 with a significant detection. The science target is indicated in the title of each panel along with the detection limit grid in parentheses. The color scale is the number of calibrators (0 to 5 and black to yellow) which would significantly ($> 5\sigma$) detect a companion as a function of separation and contrast ratio in the three filters (three columns). Best fit companion parameters are plotted (with error bars) for the 5 calibrators in blue, if significantly detected, and in orange, if not significantly detected. The source was determined to be a detection if at least 4 fits were significant and consistent with each other.

Appendix M

**Figure Set corresponding to Figure 4.4:
Detection Limits for Single Sources**

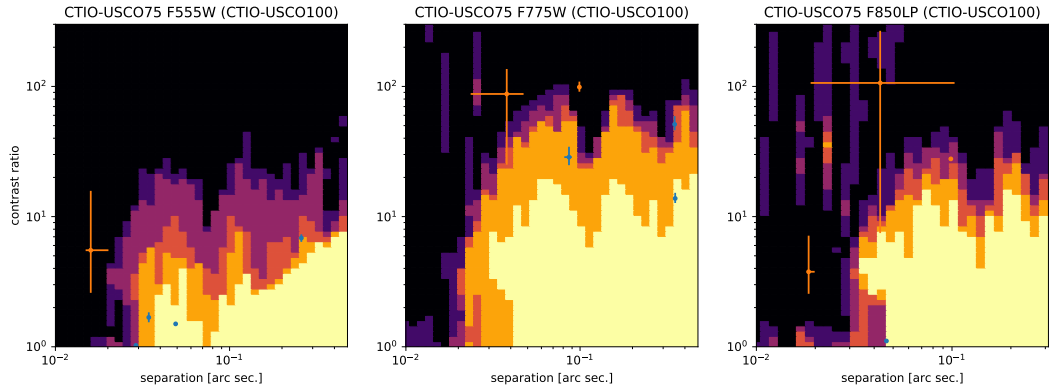


Figure M.1: Detection limits for CTIO-USCo-75 with no significant detection. The science target is indicated in the title of each panel along with the detection limit grid in parentheses. The color scale is the number of calibrators (0 to 5 and black to yellow) which would significantly ($> 5\sigma$) detect a companion as a function of separation and contrast ratio in the three filters (three columns). Best fit companion parameters are plotted (with error bars) for the 5 calibrators in blue, if significantly detected, and in orange, if not significantly detected. The source was not determined to be a detection since less than 4 fits were significant and consistent with each other.

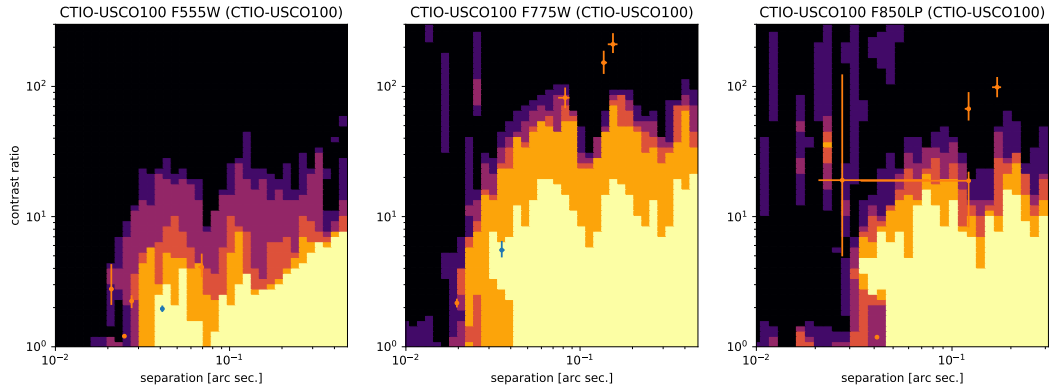


Figure M.2: Detection limits for CTIO-USCo-100 with no significant detection. The science target is indicated in the title of each panel along with the detection limit grid in parentheses. The color scale is the number of calibrators (0 to 5 and black to yellow) which would significantly ($> 5\sigma$) detect a companion as a function of separation and contrast ratio in the three filters (three columns). Best fit companion parameters are plotted (with error bars) for the 5 calibrators in blue, if significantly detected, and in orange, if not significantly detected. The source was not determined to be a detection since less than 4 fits were significant and consistent with each other.

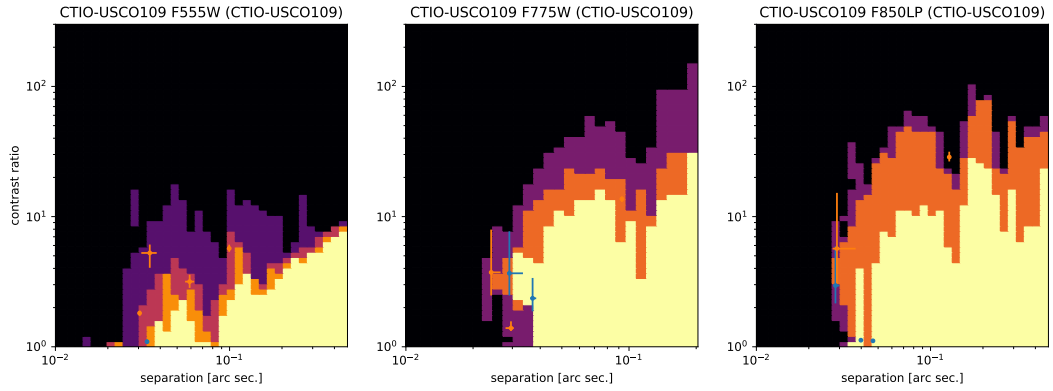


Figure M.3: Detection limits for CTIO-USCo-109 with no significant detection. The science target is indicated in the title of each panel along with the detection limit grid in parentheses. The color scale is the number of calibrators (0 to 5 and black to yellow) which would significantly ($> 5\sigma$) detect a companion as a function of separation and contrast ratio in the three filters (three columns). Best fit companion parameters are plotted (with error bars) for the 5 calibrators in blue, if significantly detected, and in orange, if not significantly detected. The source was not determined to be a detection since less than 4 fits were significant and consistent with each other.

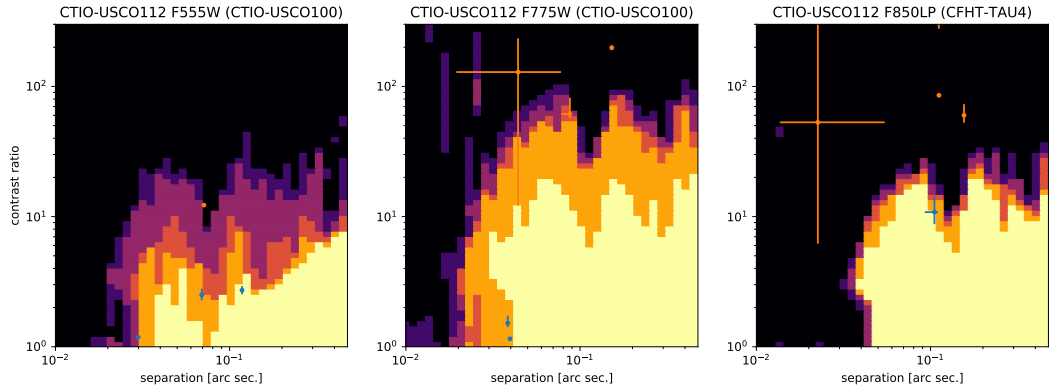


Figure M.4: Detection limits for CTIO-USco-112 with no significant detection. The science target is indicated in the title of each panel along with the detection limit grid in parentheses. The color scale is the number of calibrators (0 to 5 and black to yellow) which would significantly ($> 5\sigma$) detect a companion as a function of separation and contrast ratio in the three filters (three columns). Best fit companion parameters are plotted (with error bars) for the 5 calibrators in blue, if significantly detected, and in orange, if not significantly detected. The source was not determined to be a detection since less than 4 fits were significant and consistent with each other.

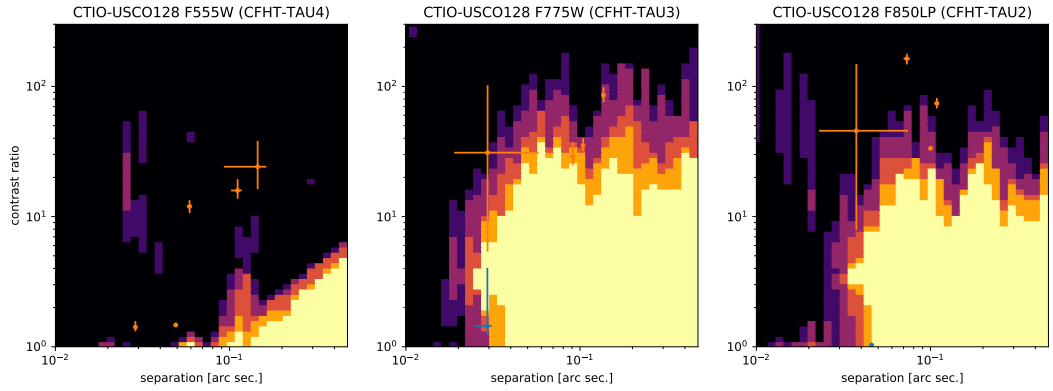


Figure M.5: Detection limits for CTIO-USCo-128 with no significant detection. The science target is indicated in the title of each panel along with the detection limit grid in parentheses. The color scale is the number of calibrators (0 to 5 and black to yellow) which would significantly ($> 5\sigma$) detect a companion as a function of separation and contrast ratio in the three filters (three columns). Best fit companion parameters are plotted (with error bars) for the 5 calibrators in blue, if significantly detected, and in orange, if not significantly detected. The source was not determined to be a detection since less than 4 fits were significant and consistent with each other.

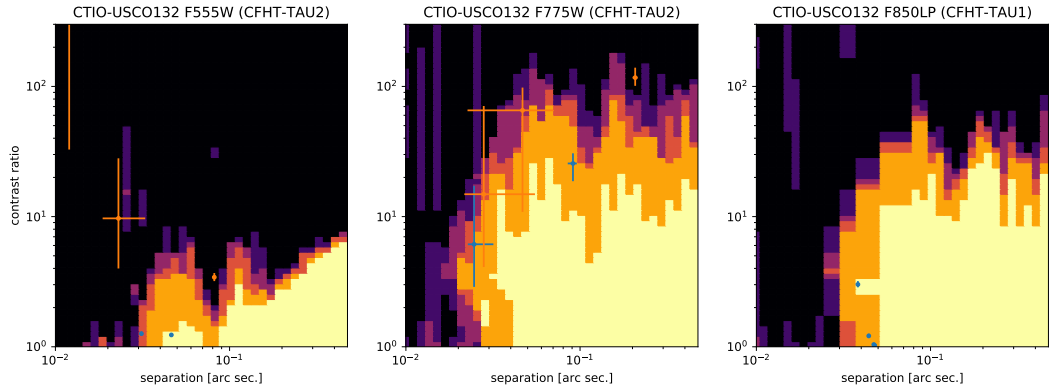


Figure M.6: Detection limits for CTIO-USco-132 with no significant detection. The science target is indicated in the title of each panel along with the detection limit grid in parentheses. The color scale is the number of calibrators (0 to 5 and black to yellow) which would significantly ($> 5\sigma$) detect a companion as a function of separation and contrast ratio in the three filters (three columns). Best fit companion parameters are plotted (with error bars) for the 5 calibrators in blue, if significantly detected, and in orange, if not significantly detected. The source was not determined to be a detection since less than 4 fits were significant and consistent with each other.

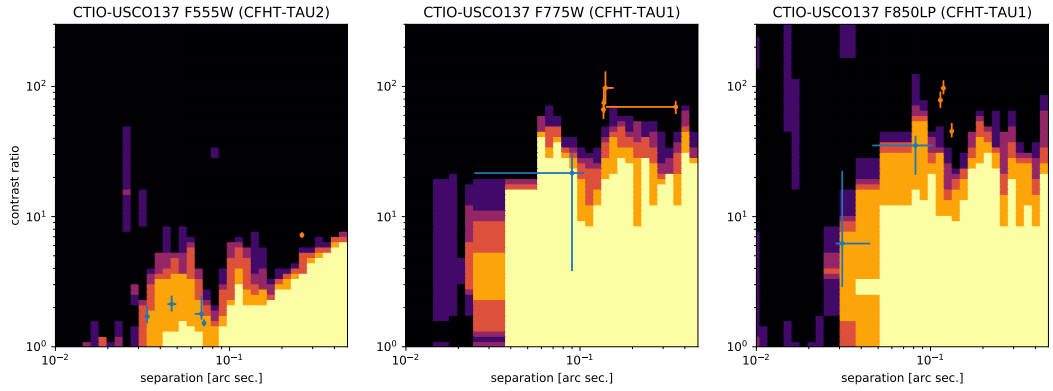


Figure M.7: Detection limits for CTIO-USco-137 with no significant detection. The science target is indicated in the title of each panel along with the detection limit grid in parentheses. The color scale is the number of calibrators (0 to 5 and black to yellow) which would significantly ($> 5\sigma$) detect a companion as a function of separation and contrast ratio in the three filters (three columns). Best fit companion parameters are plotted (with error bars) for the 5 calibrators in blue, if significantly detected, and in orange, if not significantly detected. The source was not determined to be a detection since less than 4 fits were significant and consistent with each other.

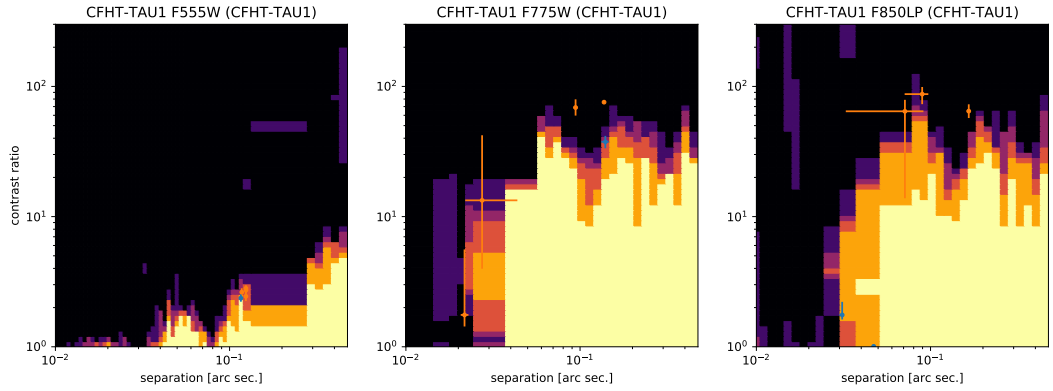


Figure M.8: Detection limits for CFHT-Tau-1 with no significant detection. The science target is indicated in the title of each panel along with the detection limit grid in parentheses. The color scale is the number of calibrators (0 to 5 and black to yellow) which would significantly ($> 5\sigma$) detect a companion as a function of separation and contrast ratio in the three filters (three columns). Best fit companion parameters are plotted (with error bars) for the 5 calibrators in blue, if significantly detected, and in orange, if not significantly detected. The source was not determined to be a detection since less than 4 fits were significant and consistent with each other.

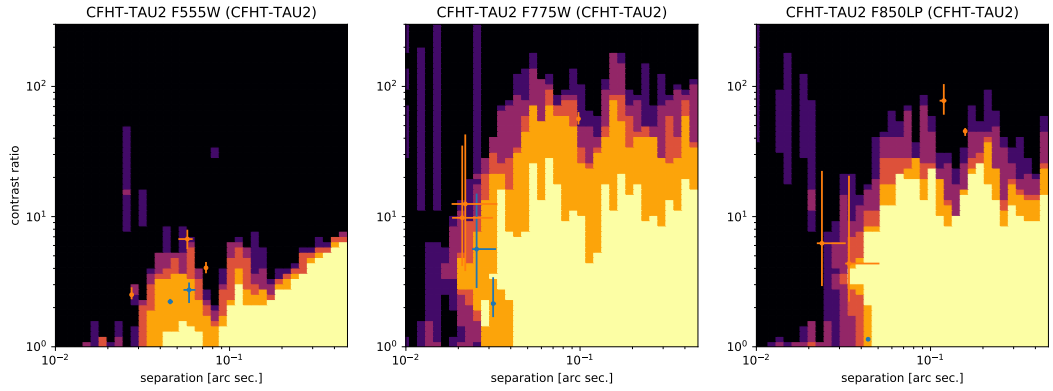


Figure M.9: Detection limits for CFHT-Tau-2 with no significant detection. The science target is indicated in the title of each panel along with the detection limit grid in parentheses. The color scale is the number of calibrators (0 to 5 and black to yellow) which would significantly ($> 5\sigma$) detect a companion as a function of separation and contrast ratio in the three filters (three columns). Best fit companion parameters are plotted (with error bars) for the 5 calibrators in blue, if significantly detected, and in orange, if not significantly detected. The source was not determined to be a detection since less than 4 fits were significant and consistent with each other.

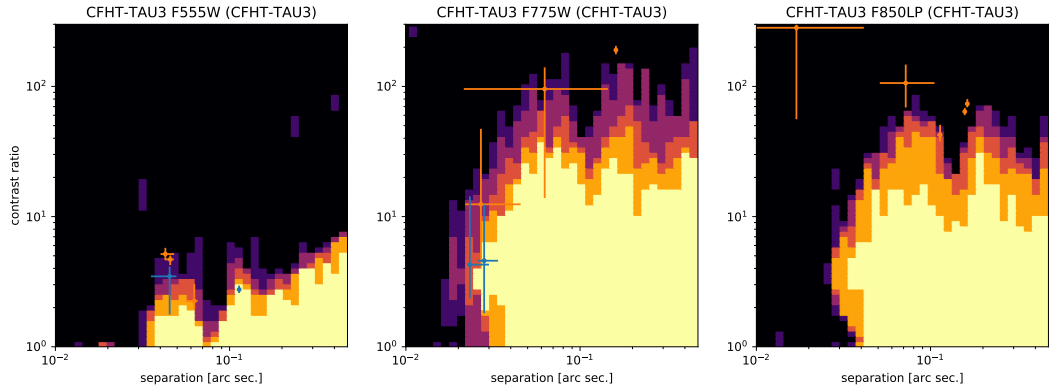


Figure M.10: Detection limits for CFHT-Tau-3 with no significant detection. The science target is indicated in the title of each panel along with the detection limit grid in parentheses. The color scale is the number of calibrators (0 to 5 and black to yellow) which would significantly ($> 5\sigma$) detect a companion as a function of separation and contrast ratio in the three filters (three columns). Best fit companion parameters are plotted (with error bars) for the 5 calibrators in blue, if significantly detected, and in orange, if not significantly detected. The source was not determined to be a detection since less than 4 fits were significant and consistent with each other.

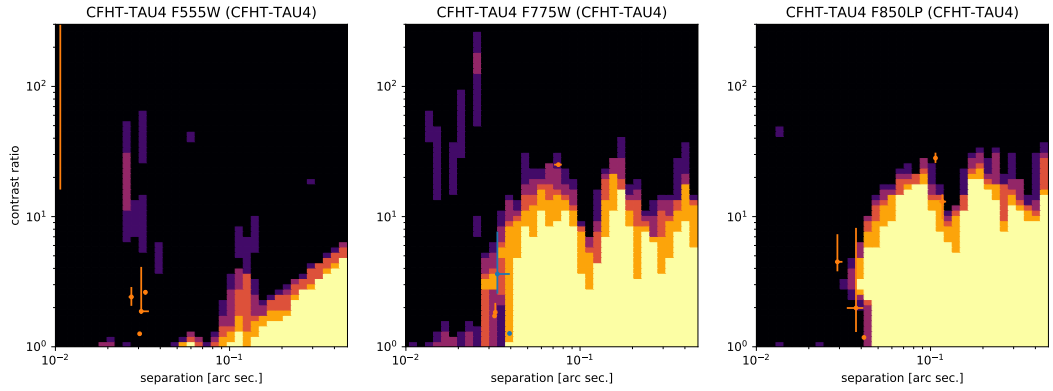


Figure M.11: Detection limits for CFHT-Tau-4 with no significant detection. The science target is indicated in the title of each panel along with the detection limit grid in parentheses. The color scale is the number of calibrators (0 to 5 and black to yellow) which would significantly ($> 5\sigma$) detect a companion as a function of separation and contrast ratio in the three filters (three columns). Best fit companion parameters are plotted (with error bars) for the 5 calibrators in blue, if significantly detected, and in orange, if not significantly detected. The source was not determined to be a detection since less than 4 fits were significant and consistent with each other.

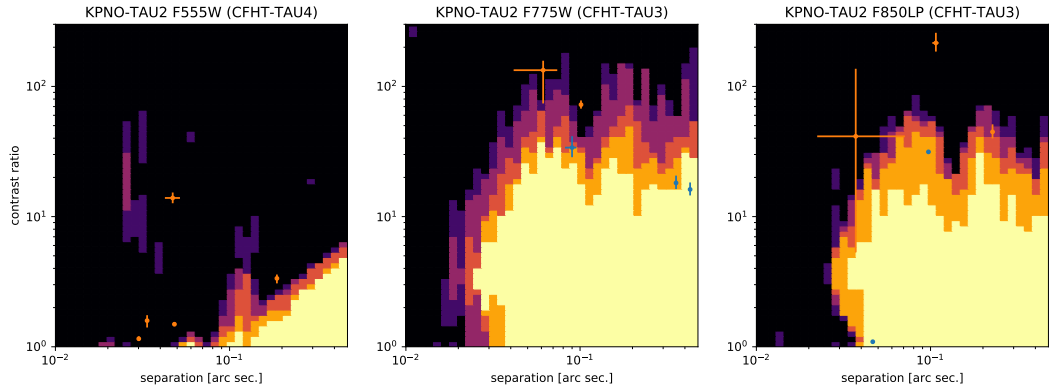


Figure M.12: Detection limits for KPNO-Tau-2 with no significant detection. The science target is indicated in the title of each panel along with the detection limit grid in parentheses. The color scale is the number of calibrators (0 to 5 and black to yellow) which would significantly ($> 5\sigma$) detect a companion as a function of separation and contrast ratio in the three filters (three columns). Best fit companion parameters are plotted (with error bars) for the 5 calibrators in blue, if significantly detected, and in orange, if not significantly detected. The source was not determined to be a detection since less than 4 fits were significant and consistent with each other.

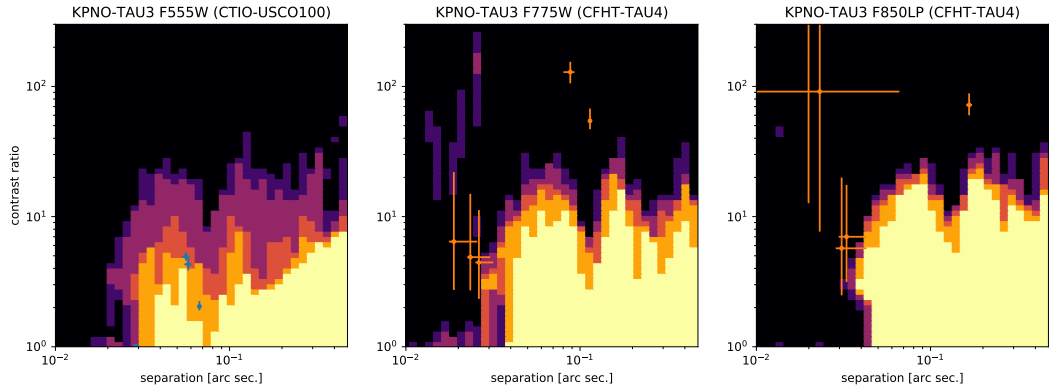


Figure M.13: Detection limits for KPNO-Tau-3 with no significant detection. The science target is indicated in the title of each panel along with the detection limit grid in parentheses. The color scale is the number of calibrators (0 to 5 and black to yellow) which would significantly ($> 5\sigma$) detect a companion as a function of separation and contrast ratio in the three filters (three columns). Best fit companion parameters are plotted (with error bars) for the 5 calibrators in blue, if significantly detected, and in orange, if not significantly detected. The source was not determined to be a detection since less than 4 fits were significant and consistent with each other.

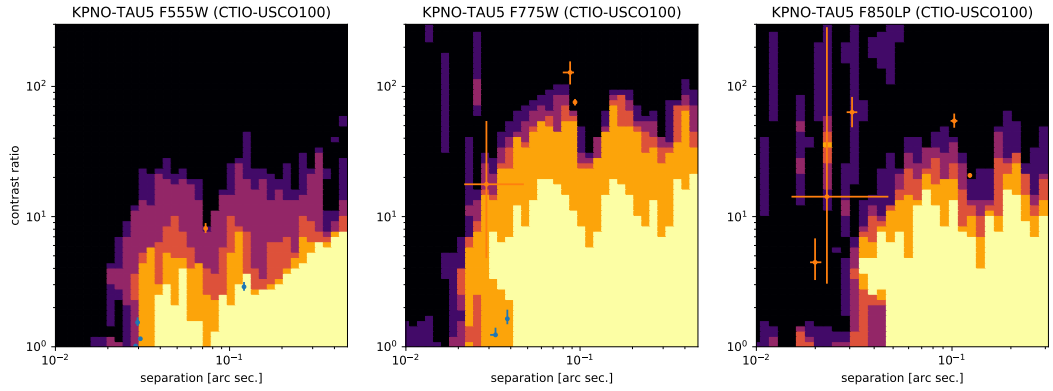


Figure M.14: Detection limits for KPNO-Tau-5 with no significant detection. The science target is indicated in the title of each panel along with the detection limit grid in parentheses. The color scale is the number of calibrators (0 to 5 and black to yellow) which would significantly ($> 5\sigma$) detect a companion as a function of separation and contrast ratio in the three filters (three columns). Best fit companion parameters are plotted (with error bars) for the 5 calibrators in blue, if significantly detected, and in orange, if not significantly detected. The source was not determined to be a detection since less than 4 fits were significant and consistent with each other.

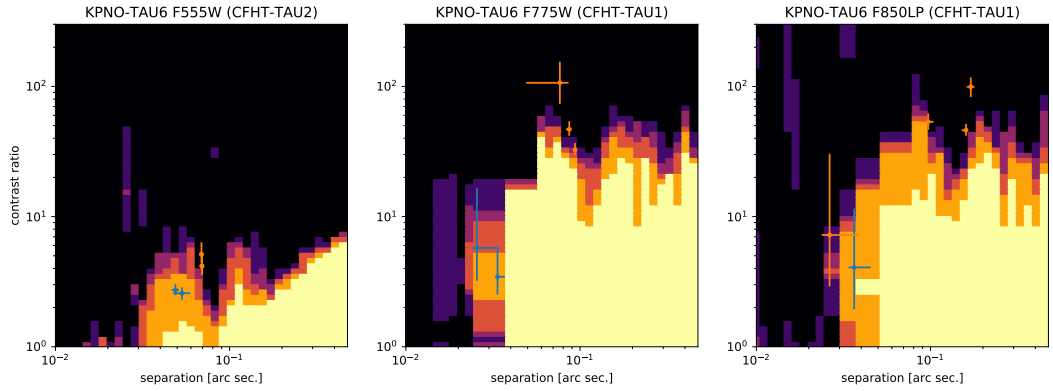


Figure M.15: Detection limits for KPNO-Tau-6 with no significant detection. The science target is indicated in the title of each panel along with the detection limit grid in parentheses. The color scale is the number of calibrators (0 to 5 and black to yellow) which would significantly ($> 5\sigma$) detect a companion as a function of separation and contrast ratio in the three filters (three columns). Best fit companion parameters are plotted (with error bars) for the 5 calibrators in blue, if significantly detected, and in orange, if not significantly detected. The source was not determined to be a detection since less than 4 fits were significant and consistent with each other.

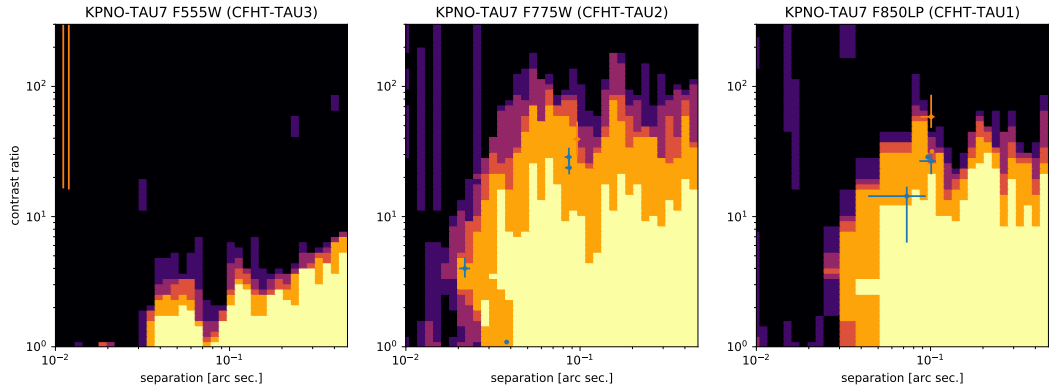


Figure M.16: Detection limits for KPNO-Tau-7 with no significant detection. The science target is indicated in the title of each panel along with the detection limit grid in parentheses. The color scale is the number of calibrators (0 to 5 and black to yellow) which would significantly ($> 5\sigma$) detect a companion as a function of separation and contrast ratio in the three filters (three columns). Best fit companion parameters are plotted (with error bars) for the 5 calibrators in blue, if significantly detected, and in orange, if not significantly detected. The source was not determined to be a detection since less than 4 fits were significant and consistent with each other.

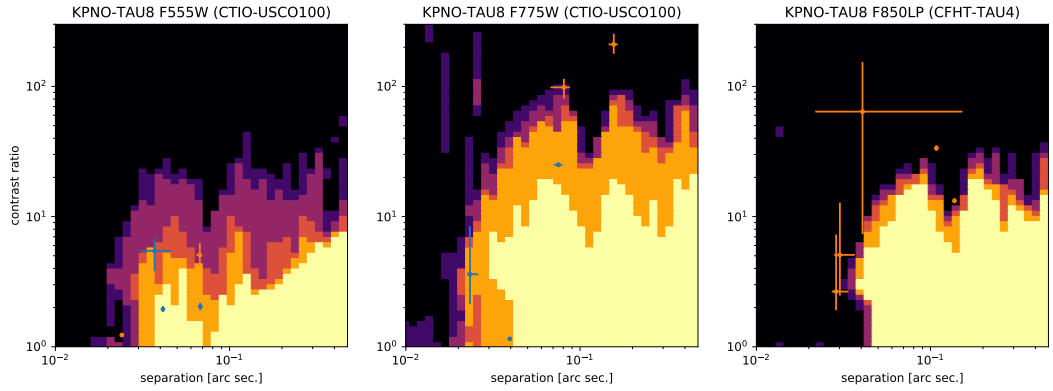


Figure M.17: Detection limits for KPNO-Tau-8 with no significant detection. The science target is indicated in the title of each panel along with the detection limit grid in parentheses. The color scale is the number of calibrators (0 to 5 and black to yellow) which would significantly ($> 5\sigma$) detect a companion as a function of separation and contrast ratio in the three filters (three columns). Best fit companion parameters are plotted (with error bars) for the 5 calibrators in blue, if significantly detected, and in orange, if not significantly detected. The source was not determined to be a detection since less than 4 fits were significant and consistent with each other.

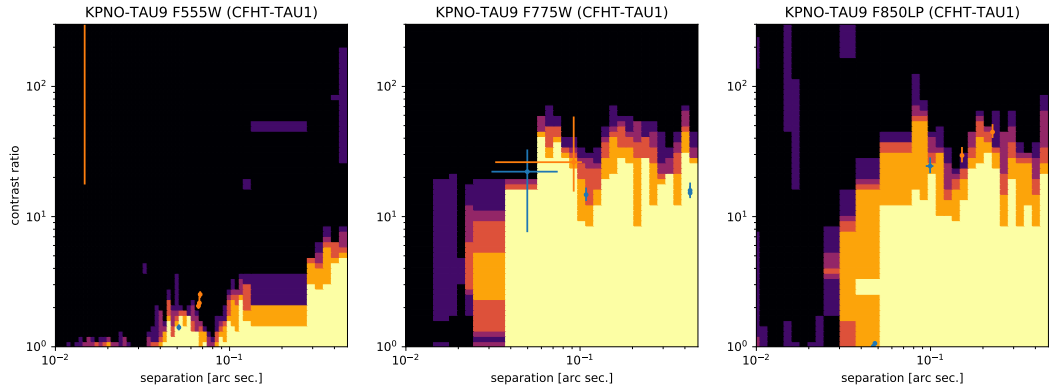


Figure M.18: Detection limits for KPNO-Tau-9 with no significant detection. The science target is indicated in the title of each panel along with the detection limit grid in parentheses. The color scale is the number of calibrators (0 to 5 and black to yellow) which would significantly ($> 5\sigma$) detect a companion as a function of separation and contrast ratio in the three filters (three columns). Best fit companion parameters are plotted (with error bars) for the 5 calibrators in blue, if significantly detected, and in orange, if not significantly detected. The source was not determined to be a detection since less than 4 fits were significant and consistent with each other.

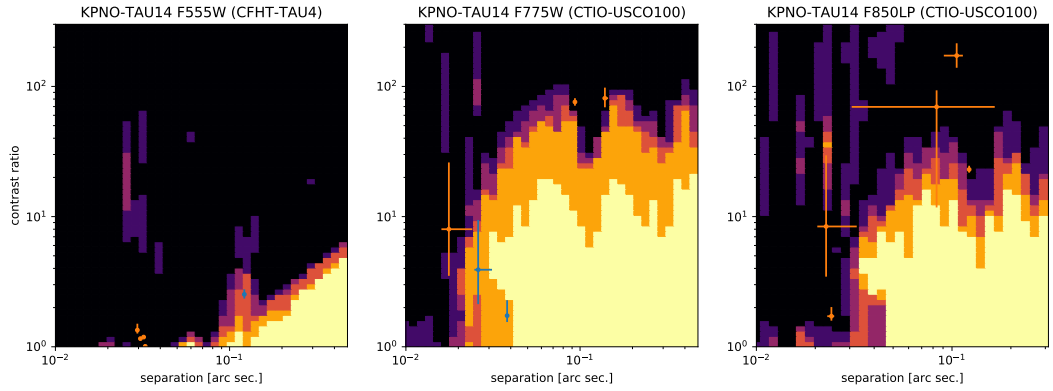


Figure M.19: Detection limits for KPNO-Tau-14 with no significant detection. The science target is indicated in the title of each panel along with the detection limit grid in parentheses. The color scale is the number of calibrators (0 to 5 and black to yellow) which would significantly ($> 5\sigma$) detect a companion as a function of separation and contrast ratio in the three filters (three columns). Best fit companion parameters are plotted (with error bars) for the 5 calibrators in blue, if significantly detected, and in orange, if not significantly detected. The source was not determined to be a detection since less than 4 fits were significant and consistent with each other.

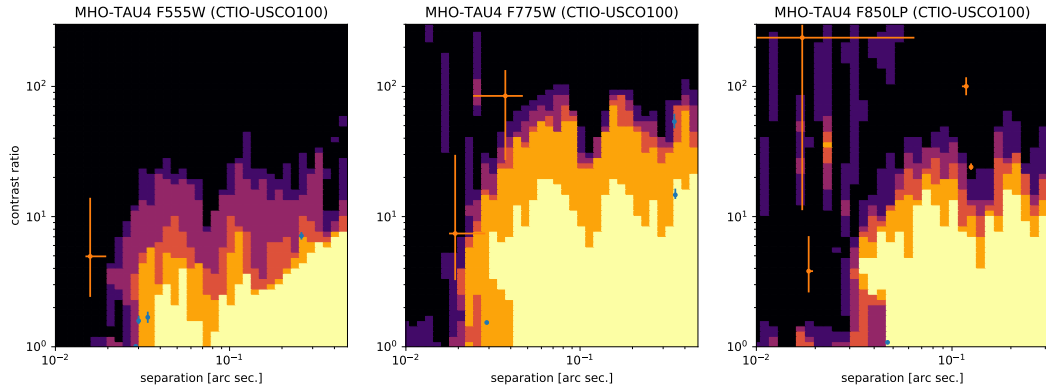


Figure M.20: Detection limits for MHO-Tau-4 with no significant detection. The science target is indicated in the title of each panel along with the detection limit grid in parentheses. The color scale is the number of calibrators (0 to 5 and black to yellow) which would significantly ($> 5\sigma$) detect a companion as a function of separation and contrast ratio in the three filters (three columns). Best fit companion parameters are plotted (with error bars) for the 5 calibrators in blue, if significantly detected, and in orange, if not significantly detected. The source was not determined to be a detection since less than 4 fits were significant and consistent with each other.

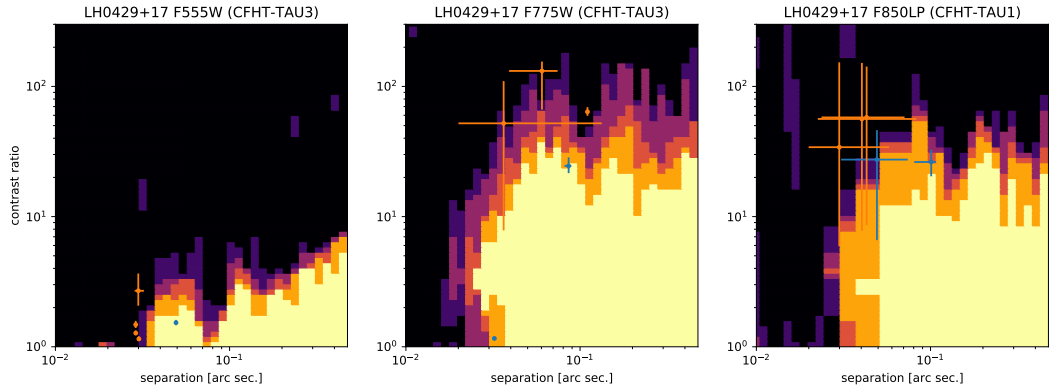


Figure M.21: Detection limits for LH0419+15 with no significant detection. The science target is indicated in the title of each panel along with the detection limit grid in parentheses. The color scale is the number of calibrators (0 to 5 and black to yellow) which would significantly ($> 5\sigma$) detect a companion as a function of separation and contrast ratio in the three filters (three columns). Best fit companion parameters are plotted (with error bars) for the 5 calibrators in blue, if significantly detected, and in orange, if not significantly detected. The source was not determined to be a detection since less than 4 fits were significant and consistent with each other.

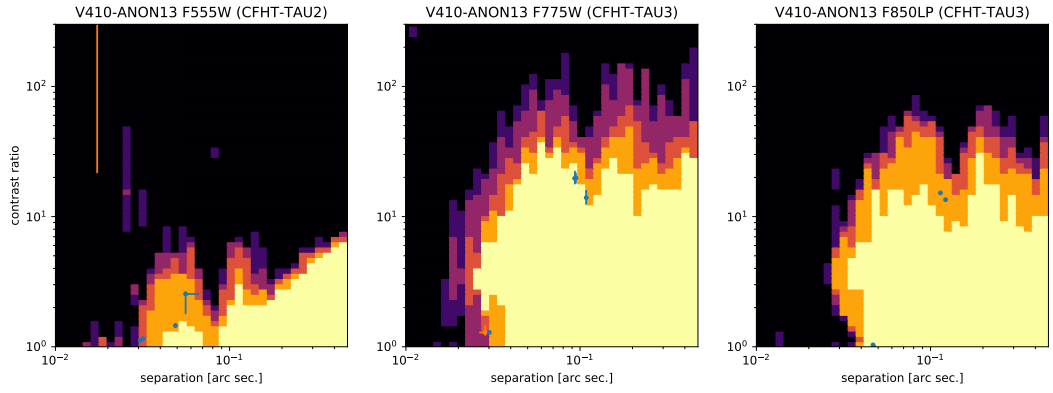


Figure M.22: Detection limits for V410-Anon-13 with no significant detection. The science target is indicated in the title of each panel along with the detection limit grid in parentheses. The color scale is the number of calibrators (0 to 5 and black to yellow) which would significantly ($> 5\sigma$) detect a companion as a function of separation and contrast ratio in the three filters (three columns). Best fit companion parameters are plotted (with error bars) for the 5 calibrators in blue, if significantly detected, and in orange, if not significantly detected. The source was not determined to be a detection since less than 4 fits were significant and consistent with each other.

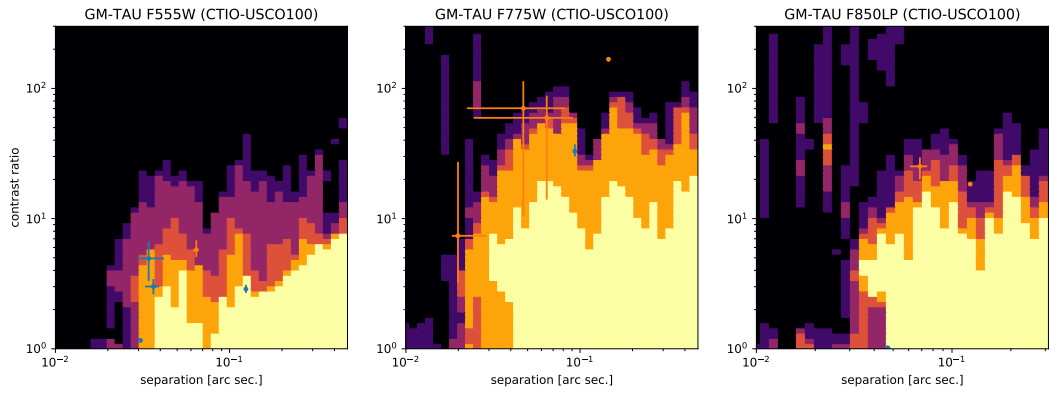


Figure M.23: Detection limits for GM-Tau with no significant detection. The science target is indicated in the title of each panel along with the detection limit grid in parentheses. The color scale is the number of calibrators (0 to 5 and black to yellow) which would significantly ($> 5\sigma$) detect a companion as a function of separation and contrast ratio in the three filters (three columns). Best fit companion parameters are plotted (with error bars) for the 5 calibrators in blue, if significantly detected, and in orange, if not significantly detected. The source was not determined to be a detection since less than 4 fits were significant and consistent with each other.

Bibliography

Aberasturi, M., Burgasser, A. J., Mora, A., et al. 2014, AJ, 148, 129, doi: 10.1088/0004-6256/148/6/129

Aganze, C., Burgasser, A. J., Malkan, M., et al. 2022, ApJ, 934, 73, doi: 10.3847/1538-4357/ac7053

Airy, G. B. 1835, Transactions of the Cambridge Philosophical Society, 5, 283.
<https://ui.adsabs.harvard.edu/abs/1835TCaPS...5..283A>

Alibert, Y., Mordasini, C., Benz, W., & Winisdoerffer, C. 2005, A&A, 434, 343, doi: 10.1051/0004-6361:20042032

Allen, P. R. 2007, ApJ, 668, 492, doi: 10.1086/521207

Aller, K. M., Liu, M. C., Magnier, E. A., et al. 2016, ApJ, 821, 120, doi: 10.3847/0004-637X/821/2/120

Anderson, J., & King, I. R. 2004, Multi-filter PSFs and Distortion Corrections for the HRC, Instrument Science Report ACS 2004-15, 51 pages. <https://ui.adsabs.harvard.edu/abs/2004acs..rept...15A>

Andrews, S. M., Huang, J., Pérez, L. M., et al. 2018, ApJ, 869, L41, doi: 10.3847/2041-8213/aaf741

Ardila, D., Martín, E., & Basri, G. 2000, AJ, 120, 479, doi: 10.1086/301443

- Bailer-Jones, C. A. L., Rybizki, J., Fouesneau, M., Demleitner, M., & Andrae, R. 2021, AJ, 161, 147, doi: 10.3847/1538-3881/abd806
- Baraffe, I., Chabrier, G., Allard, F., & Hauschildt, P. 2003, in Brown Dwarfs, ed. E. Martín, Vol. 211, 41. <https://ui.adsabs.harvard.edu/abs/2003IAUS..211...41B>
- Baraffe, I., Chabrier, G., Allard, F., & Hauschildt, P. H. 2002, A&A, 382, 563, doi: 10.1051/0004-6361:20011638
- Bardalez Gagliuffi, D. C., Gelino, C. R., & Burgasser, A. J. 2015, AJ, 150, 163, doi: 10.1088/0004-6256/150/5/163
- Basri, G., & Reiners, A. 2006, AJ, 132, 663, doi: 10.1086/505198
- Basu, S. 2012, Science, 337, 43, doi: 10.1126/science.1224342
- Bate, M. R. 2009, MNRAS, 392, 590, doi: 10.1111/j.1365-2966.2008.14106.x
- . 2012, MNRAS, 419, 3115, doi: 10.1111/j.1365-2966.2011.19955.x
- . 2014, MNRAS, 442, 285, doi: 10.1093/mnras/stu795
- Bate, M. R., Bonnell, I. A., & Bromm, V. 2002, MNRAS, 332, L65, doi: 10.1046/j.1365-8711.2002.05539.x
- . 2003, MNRAS, 339, 577, doi: 10.1046/j.1365-8711.2003.06210.x

Beckers, J. M. 1993, ARA&A, 31, 13, doi: 10.1146/annurev.aa.31.090193.
000305

Béjar, V. J. S., Zapatero Osorio, M. R., Pérez-Garrido, A., et al. 2008, ApJ,
673, L185, doi: 10.1086/527557

Belokurov, V., Penoyre, Z., Oh, S., et al. 2020, MNRAS, 496, 1922, doi: 10.
1093/mnras/staa1522

Bender, N., Factor, S., Bodyfelt, J. D., et al. 2013, Phys. Rev. Lett., 110,
234101, doi: 10.1103/PhysRevLett.110.234101

Bernat, D., Bouchez, A. H., Ireland, M., et al. 2010, ApJ, 715, 724, doi: 10.
1088/0004-637X/715/2/724

Best, W. M. J., Dupuy, T. J., Liu, M. C., Siverd, R. J., & Zhang, Z. 2020a, The
UltracoolSheet: Photometry, Astrometry, Spectroscopy, and Multiplicity for
3000+ Ultracool Dwarfs and Imaged Exoplanets, 1.0.0, Zenodo, doi: 10.
5281/zenodo.4169085

Best, W. M. J., Liu, M. C., Dupuy, T. J., & Magnier, E. A. 2017, ApJ, 843,
L4, doi: 10.3847/2041-8213/aa76df

Best, W. M. J., Liu, M. C., Magnier, E. A., & Dupuy, T. J. 2020b, AJ, 159,
257, doi: 10.3847/1538-3881/ab84f4

—. 2021, AJ, 161, 42, doi: 10.3847/1538-3881/abc893

Best, W. M. J., Magnier, E. A., Liu, M. C., et al. 2018, ApJS, 234, 1, doi: 10.3847/1538-4365/aa9982

Biller, B., Allers, K., Liu, M., Close, L. M., & Dupuy, T. 2011, ApJ, 730, 39, doi: 10.1088/0004-637X/730/1/39

Blake, C. H., Charbonneau, D., & White, R. J. 2010, ApJ, 723, 684, doi: 10.1088/0004-637X/723/1/684

Bohlin, R. C. 2016, AJ, 152, 60, doi: 10.3847/0004-6256/152/3/60

Bonnell, I. A., Clark, P., & Bate, M. R. 2008, MNRAS, 389, 1556, doi: 10.1111/j.1365-2966.2008.13679.x

Boss, A. P. 1988, ApJ, 331, 370, doi: 10.1086/166563

Bouy, H., Brandner, W., Martín, E. L., et al. 2003, AJ, 126, 1526, doi: 10.1086/377343

Bouy, H., Martín, E. L., Brandner, W., & Bouvier, J. 2005, AJ, 129, 511, doi: 10.1086/426559

Bowler, B. P. 2016, PASP, 128, 102001, doi: 10.1088/1538-3873/128/968/102001

Briceño, C., Hartmann, L., Stauffer, J., & Martín, E. 1998, AJ, 115, 2074, doi: 10.1086/300338

Briceño, C., Luhman, K. L., Hartmann, L., Stauffer, J. R., & Kirkpatrick, J. D. 2002, ApJ, 580, 317, doi: 10.1086/343127

Buchner, J., Georgakakis, A., Nandra, K., et al. 2014, A&A, 564, A125,
doi: 10.1051/0004-6361/201322971

Burgasser, A. 2003, T Dwarf Companions: Searching for the Coldest Brown
Dwarfs, HST Proposal. <https://ui.adsabs.harvard.edu/abs/2003hst.prop.9833B>

Burgasser, A. J., Bardalez-Gagliuffi, D. C., & Gizis, J. E. 2011, AJ, 141, 70,
doi: 10.1088/0004-6256/141/3/70

Burgasser, A. J., Cruz, K. L., Cushing, M., et al. 2010, ApJ, 710, 1142, doi: 10.
1088/0004-637X/710/2/1142

Burgasser, A. J., Geballe, T. R., Leggett, S. K., Kirkpatrick, J. D., &
Golimowski, D. A. 2006a, ApJ, 637, 1067, doi: 10.1086/498563

Burgasser, A. J., Kirkpatrick, J. D., Cruz, K. L., et al. 2006b, ApJS, 166, 585,
doi: 10.1086/506327

Burgasser, A. J., Kirkpatrick, J. D., Liebert, J., & Burrows, A. 2003a, ApJ,
594, 510, doi: 10.1086/376756

Burgasser, A. J., Kirkpatrick, J. D., & Lowrance, P. J. 2005, AJ, 129, 2849,
doi: 10.1086/430218

Burgasser, A. J., Kirkpatrick, J. D., McElwain, M. W., et al. 2003b, AJ, 125,
850, doi: 10.1086/345975

Burgasser, A. J., Kirkpatrick, J. D., Reid, I. N., et al. 2003c, ApJ, 586, 512,
doi: 10.1086/346263

Burgasser, A. J., Reid, I. N., Siegler, N., et al. 2007, in Protostars and Planets
V, ed. B. Reipurth, D. Jewitt, & K. Keil, 427. [https://arxiv.org/abs/
astro-ph/0602122](https://arxiv.org/abs/astro-ph/0602122)

Burgasser, A. J., Kirkpatrick, J. D., Cutri, R. M., et al. 2000, ApJ, 531, L57,
doi: 10.1086/312522

Burgasser, A. J., Kirkpatrick, J. D., Brown, M. E., et al. 2002, ApJ, 564, 421,
doi: 10.1086/324033

Burrows, A., Hubbard, W. B., Lunine, J. I., & Liebert, J. 2001, Reviews of
Modern Physics, 73, 719, doi: 10.1103/RevModPhys.73.719

Burrows, A., Marley, M., Hubbard, W. B., et al. 1997, ApJ, 491, 856, doi: 10.
1086/305002

Cardoso, C. V., Burningham, B., Smart, R. L., et al. 2015, MNRAS, 450,
2486, doi: 10.1093/mnras/stv380

Ceau, A., Mary, D., Greenbaum, A., et al. 2019, A&A, 630, A120, doi: 10.
1051/0004-6361/201935247

Chabrier, G., Baraffe, I., Allard, F., & Hauschildt, P. 2000, ApJ, 542, 464,
doi: 10.1086/309513

Chaushev, A., Sallum, S., Lozi, J., et al. 2023, arXiv e-prints, arXiv:2305.17065, doi: 10.48550/arXiv.2305.17065

Chauvin, G., Lagrange, A. M., Dumas, C., et al. 2004, A&A, 425, L29, doi: 10.1051/0004-6361:200400056

Chitsazi, M., Factor, S., Schindler, J., et al. 2014, Phys. Rev. A, 89, 043842, doi: 10.1103/PhysRevA.89.043842

Chiu, K., Fan, X., Leggett, S. K., et al. 2006, AJ, 131, 2722, doi: 10.1086/501431

Chomez, A., Squicciarini, V., Lagrange, A. M., et al. 2023, arXiv e-prints, arXiv:2307.01195, doi: 10.48550/arXiv.2307.01195

Close, L. M., Siegler, N., Freed, M., & Biller, B. 2003, ApJ, 587, 407, doi: 10.1086/368177

Close, L. M., Siegler, N., Potter, D., Brandner, W., & Liebert, J. 2002, ApJ, 567, L53, doi: 10.1086/339795

Close, L. M., Zuckerman, B., Song, I., et al. 2007, ApJ, 660, 1492, doi: 10.1086/513417

Colavita, M. M., Wizinowich, P. L., & Akeson, R. L. 2004, in Society of Photo-Optical Instrumentation Engineers (SPIE) Conference Series, Vol. 5491, New Frontiers in Stellar Interferometry, ed. W. A. Traub, 454, doi: 10.1117/12.552149

Cruz, K. 2004, Resolving a Binary System that Straddles the L/T Transition, HST Proposal. <https://ui.adsabs.harvard.edu/abs/2004hst.prop10247C>

Cruz, K. L., Burgasser, A. J., Reid, I. N., & Liebert, J. 2004, ApJ, 604, L61, doi: 10.1086/383415

Cruz, K. L., Reid, I. N., Liebert, J., Kirkpatrick, J. D., & Lowrance, P. J. 2003, AJ, 126, 2421, doi: 10.1086/378607

Cutri, R. M., Skrutskie, M. F., van Dyk, S., et al. 2003, VizieR Online Data Catalog, 2246. <https://ui.adsabs.harvard.edu/abs/2003yCat.2246...0C>

Dahn, C. C., Harris, H. C., Subasavage, J. P., et al. 2017, AJ, 154, 147, doi: 10.3847/1538-3881/aa880b

De Furio, M., Liu, C., Meyer, M. R., et al. 2022a, ApJ, 941, 161, doi: 10.3847/1538-4357/aca285

De Furio, M., Meyer, M. R., Reiter, M., et al. 2022b, ApJ, 925, 112, doi: 10.3847/1538-4357/ac36d4

De Furio, M., Reiter, M., Meyer, M. R., et al. 2019, ApJ, 886, 95, doi: 10.3847/1538-4357/ab4ae3

De Rosa, R. J., Patience, J., Wilson, P. A., et al. 2014, MNRAS, 437, 1216, doi: 10.1093/mnras/stt1932

- Deshpande, R., Martín, E. L., Montgomery, M. M., et al. 2012, AJ, 144, 99, doi: 10.1088/0004-6256/144/4/99
- Dodson-Robinson, S. E., Bodenheimer, P., Laughlin, G., et al. 2008, ApJ, 688, L99, doi: 10.1086/595616
- Duchêne, G. 2008, New Astron. Rev., 52, 117, doi: 10.1016/j.newar.2008.04.007
- Duchêne, G., & Kraus, A. 2013, ARA&A, 51, 269, doi: 10.1146/annurev-astro-081710-102602
- Dupuy, T. J., & Kraus, A. L. 2013, Science, 341, 1492, doi: 10.1126/science.1241917
- Dupuy, T. J., & Liu, M. C. 2011, ApJ, 733, 122, doi: 10.1088/0004-637X/733/2/122
- . 2012, ApJS, 201, 19, doi: 10.1088/0067-0049/201/2/19
- Dupuy, T. J., & Liu, M. C. 2017, ApJS, 231, 15, doi: 10.3847/1538-4365/aa5e4c
- Dupuy, T. J., Liu, M. C., Bowler, B. P., et al. 2010, ApJ, 721, 1725, doi: 10.1088/0004-637X/721/2/1725
- Duquennoy, A., & Mayor, M. 1991, A&A, 248, 485. <https://ui.adsabs.harvard.edu/abs/1991A&A...248..485D>

- Event Horizon Telescope Collaboration, Akiyama, K., Alberdi, A., et al. 2019,
ApJ, 875, L1, doi: 10.3847/2041-8213/ab0ec7
- Factor, S. M. 2022, smfactor/Argus: Version 1.0 for publication in AJ, 1.0,
Zenodo, doi: 10.5281/zenodo.6842148
- Factor, S. M., & Kraus, A. L. 2016, Kernel-Phase Interferometry for Super-
Resolution Detection of Faint Companions, HST Proposal. Cycle 24, ID.
#14561. <https://ui.adsabs.harvard.edu/abs/2016hst..prop14561F>
- . 2021a, Discovery of Young Planetary Systems with Kernel-Phase Inter-
ferometry, HST Proposal. Cycle 29, ID. #16612. <https://ui.adsabs.harvard.edu/abs/2021hst..prop16612F>
- . 2021b, Kernel-Phase Detection Limits for Planet Discovery with JWST,
JWST Proposal. Cycle 1, ID. #2509. <https://ui.adsabs.harvard.edu/abs/2021jwst.prop.2509F>
- . 2022a, AJ, 164, 244, doi: 10.3847/1538-3881/ac88d3
- . 2022b, Figure Sets and Data Associated with AJ Publication: “NICMOS
Kernel-Phase Interferometry I: Catalogue of Brown Dwarfs Observed in
F110W and F170M”, Zenodo, doi: 10.5281/zenodo.6986242
- . 2022c, Figure Sets Associated with AJ Publication: “NICMOS Kernel-
Phase Interferometry II: Demographis of Nearby Brown Dwarfs”, Zenodo,
doi: 10.5281/zenodo.7370349

- . 2022d, MCMC chains for demographic fits presented in “NICMOS Kernel-Phase Interferometry II: Demographics of Nearby Brown Dwarfs”, Zenodo, doi: [10.5281/zenodo.7065651](https://doi.org/10.5281/zenodo.7065651)
- . 2023, AJ, 165, 130, doi: [10.3847/1538-3881/aca475](https://doi.org/10.3847/1538-3881/aca475)
- Factor, S. M., Hughes, A. M., Flaherty, K. M., et al. 2017, AJ, 153, 233, doi: [10.3847/1538-3881/aa6c2c](https://doi.org/10.3847/1538-3881/aa6c2c)
- Faherty, J. K., Burgasser, A. J., Cruz, K. L., et al. 2009, AJ, 137, 1, doi: [10.1088/0004-6256/137/1/1](https://doi.org/10.1088/0004-6256/137/1/1)
- Faherty, J. K., Burgasser, A. J., Walter, F. M., et al. 2012, ApJ, 752, 56, doi: [10.1088/0004-637X/752/1/56](https://doi.org/10.1088/0004-637X/752/1/56)
- Faherty, J. K., Riedel, A. R., Cruz, K. L., et al. 2016, ApJS, 225, 10, doi: [10.3847/0067-0049/225/1/10](https://doi.org/10.3847/0067-0049/225/1/10)
- Faherty, J. K., Goodman, S., Caselden, D., et al. 2020, ApJ, 889, 176, doi: [10.3847/1538-4357/ab5303](https://doi.org/10.3847/1538-4357/ab5303)
- Feroz, F., & Hobson, M. P. 2008, MNRAS, 384, 449, doi: [10.1111/j.1365-2966.2007.12353.x](https://doi.org/10.1111/j.1365-2966.2007.12353.x)
- Feroz, F., Hobson, M. P., & Bridges, M. 2009, MNRAS, 398, 1601, doi: [10.1111/j.1365-2966.2009.14548.x](https://doi.org/10.1111/j.1365-2966.2009.14548.x)
- Feroz, F., Hobson, M. P., Cameron, E., & Pettitt, A. N. 2019, The Open Journal of Astrophysics, 2, 10, doi: [10.21105/astro.1306.2144](https://doi.org/10.21105/astro.1306.2144)

Filippazzo, J. C., Giorla Godfrey, P., Cruz, K. L., et al. 2016, The BDNYC Database, 1.0, Zenodo, doi: [10.5281/zenodo.45169](https://doi.org/10.5281/zenodo.45169)

Filippazzo, J. C., Rice, E. L., Faherty, J., et al. 2015, ApJ, 810, 158, doi: [10.1088/0004-637X/810/2/158](https://doi.org/10.1088/0004-637X/810/2/158)

Fisher, R. T. 2004, ApJ, 600, 769, doi: [10.1086/380111](https://doi.org/10.1086/380111)

Fitton, S., Tofflemire, B. M., & Kraus, A. L. 2022, Research Notes of the American Astronomical Society, 6, 18, doi: [10.3847/2515-5172/ac4bb7](https://doi.org/10.3847/2515-5172/ac4bb7)

Fontanive, C., Biller, B., Bonavita, M., & Allers, K. 2018, MNRAS, 479, 2702, doi: [10.1093/mnras/sty1682](https://doi.org/10.1093/mnras/sty1682)

Fontanive, C., Allers, K. N., Pantoja, B., et al. 2020, ApJ, 905, L14, doi: [10.3847/2041-8213/abcaf8](https://doi.org/10.3847/2041-8213/abcaf8)

Foreman-Mackey, D., Hogg, D. W., Lang, D., & Goodman, J. 2013, PASP, 125, 306, doi: [10.1086/670067](https://doi.org/10.1086/670067)

Gagné, J., Faherty, J. K., Cruz, K. L., et al. 2015, ApJS, 219, 33, doi: [10.1088/0067-0049/219/2/33](https://doi.org/10.1088/0067-0049/219/2/33)

Gaia Collaboration. 2020, VizieR Online Data Catalog, I/350. <https://ui.adsabs.harvard.edu/abs/2020yCat.1350....0G>

Gaia Collaboration, Brown, A. G. A., Vallenari, A., et al. 2018, A&A, 616, A1, doi: [10.1051/0004-6361/201833051](https://doi.org/10.1051/0004-6361/201833051)

- . 2021, A&A, 649, A1, doi: 10.1051/0004-6361/202039657
- Gelino, C. R., Smart, R. L., Marocco, F., et al. 2014, AJ, 148, 6, doi: 10.1088/0004-6256/148/1/6
- Gilliland, R. L., & Riess, A. 2003, in HST Calibration Workshop : Hubble after the Installation of the ACS and the NICMOS Cooling System, 61. <https://ui.adsabs.harvard.edu/abs/2003hstc.conf..61G>
- Gizis, J. 2003, NICMOS Observations of Cool Brown Dwarf Doubles, HST Proposal. <https://ui.adsabs.harvard.edu/abs/2003hst..prop.9843G>
- Gizis, J. E., Reid, I. N., Knapp, G. R., et al. 2003, AJ, 125, 3302, doi: 10.1086/374991
- Glindemann, A., Abuter, R., Carbognani, F., et al. 2000, in Society of Photo-Optical Instrumentation Engineers (SPIE) Conference Series, Vol. 4006, Interferometry in Optical Astronomy, ed. P. Léna & A. Quirrenbach, 2–12, doi: 10.1117/12.390163
- Goodman, J., & Weare, J. 2010, Communications in Applied Mathematics and Computational Science, 5, 65, doi: 10.2140/camcos.2010.5.65
- GRAVITY Collaboration, Nowak, M., Lacour, S., et al. 2020, A&A, 633, A110, doi: 10.1051/0004-6361/201936898
- Grudić, M. Y., Guszejnov, D., Offner, S. S. R., et al. 2022, MNRAS, 512, 216, doi: 10.1093/mnras/stac526

- Guszejnov, D., Hopkins, P. F., & Krumholz, M. R. 2017, MNRAS, 468, 4093, doi: 10.1093/mnras/stx725
- Guyon, O., Pluzhnik, E. A., Kuchner, M. J., Collins, B., & Ridgway, S. T. 2006, ApJS, 167, 81, doi: 10.1086/507630
- Haniff, C. A., Scholz, M., & Tuthill, P. G. 1995, MNRAS, 276, 640, doi: 10.1093/mnras/276.2.640
- Hardy, J. W. 1998, Adaptive optics for astronomical telescopes, Vol. 16 (Oxford Optical and Imaging Sci)
- Hathi, N. P., Lucas, R. A., & Ryon, J. E. 2023, in ACS Data Handbook v. 12.0, Vol. 12, 12. <https://ui.adsabs.harvard.edu/abs/2023acsd.book..12H>
- Herczeg, G. J., & Hillenbrand, L. A. 2014, ApJ, 786, 97, doi: 10.1088/0004-637X/786/2/97
- Ho, P. T. P., Moran, J. M., & Lo, K. Y. 2004, ApJ, 616, L1, doi: 10.1086/423245
- Högbom, J. A. 1974, A&AS, 15, 417. <https://ui.adsabs.harvard.edu/abs/1974A&AS...15..417H>
- Hsu, C.-C., Burgasser, A. J., Theissen, C. A., et al. 2021, ApJS, 257, 45, doi: 10.3847/1538-4365/ac1c7d
- Ireland, M. J. 2013, MNRAS, 433, 1718, doi: 10.1093/mnras/stt859

Ireland, M. J., Kraus, A., Martinache, F., Lloyd, J. P., & Tuthill, P. G. 2008,
ApJ, 678, 463, doi: 10.1086/529578

Jeans, J. H. 1902, Philosophical Transactions of the Royal Society of London
Series A, 199, 1, doi: 10.1098/rsta.1902.0012

Jeffreys, H. 1961, The Theory of Probability, Oxford Classic Texts in the
Physical Sciences (OUP Oxford). <https://books.google.com/books?id=vh9Act9rtzQC>

Jennison, R. C. 1958, MNRAS, 118, 276, doi: 10.1093/mnras/118.3.276

Joergens, V. 2008, A&A, 492, 545, doi: 10.1051/0004-6361:200810413

Kammerer, J., Ireland, M. J., Martinache, F., & Girard, J. H. 2019, MNRAS,
486, 639, doi: 10.1093/mnras/stz882

Kammerer, J., Kasper, M., Ireland, M. J., et al. 2021, A&A, 646, A36, doi: 10.
1051/0004-6361/202039366

Kammerer, J., Cooper, R. A., Vandal, T., et al. 2023, PASP, 135, 014502,
doi: 10.1088/1538-3873/ac9a74

Kirkpatrick, J. D., Henry, T. J., & McCarthy, Donald W., J. 1991, ApJS, 77,
417, doi: 10.1086/191611

Kirkpatrick, J. D., Reid, I. N., Liebert, J., et al. 2000, AJ, 120, 447, doi: 10.
1086/301427

Kirkpatrick, J. D., Kellogg, K., Schneider, A. C., et al. 2016, ApJS, 224, 36,
doi: 10.3847/0067-0049/224/2/36

Kirkpatrick, J. D., Martin, E. C., Smart, R. L., et al. 2019, ApJS, 240, 19,
doi: 10.3847/1538-4365/aaf6af

Kolmogorov, A. 1941a, Akademiia Nauk SSSR Doklady, 30, 301. <https://ui.adsabs.harvard.edu/abs/1941DoSSR..30..301K>

Kolmogorov, A. N. 1941b, Akademiia Nauk SSSR Doklady, 32, 16. <https://ui.adsabs.harvard.edu/abs/1941DoSSR..32..16K>

Konopacky, Q. M., Ghez, A. M., Barman, T. S., et al. 2010, ApJ, 711, 1087,
doi: 10.1088/0004-637X/711/2/1087

Konopacky, Q. M., Ghez, A. M., Rice, E. L., & Duchêne, G. 2007, ApJ, 663,
394, doi: 10.1086/518360

Kraus, A. L., Herczeg, G. J., Rizzuto, A. C., et al. 2017, ApJ, 838, 150,
doi: 10.3847/1538-4357/aa62a0

Kraus, A. L., & Hillenbrand, L. A. 2012, ApJ, 757, 141, doi: 10.1088/0004-637X/757/2/141

Kraus, A. L., & Ireland, M. J. 2012, ApJ, 745, 5, doi: 10.1088/0004-637X/745/1/5

Kraus, A. L., Ireland, M. J., Martinache, F., & Hillenbrand, L. A. 2011, ApJ, 731, 8, doi: 10.1088/0004-637X/731/1/8

Kraus, A. L., Ireland, M. J., Martinache, F., & Lloyd, J. P. 2008, ApJ, 679, 762, doi: 10.1086/587435

Kraus, A. L., White, R. J., & Hillenbrand, L. A. 2005, ApJ, 633, 452, doi: 10.1086/449303

Kraus, A. L., White, R. J., & Hillenbrand, L. A. 2006, ApJ, 649, 306, doi: 10.1086/503665

Krist, J. E., & Hook, R. N. 1997, in The 1997 HST Calibration Workshop with a New Generation of Instruments, ed. S. Casertano, R. Jedrzejewski, T. Keyes, & M. Stevens, 192. <https://ui.adsabs.harvard.edu/abs/1997hstc.work..192K>

Krist, J. E., Hook, R. N., & Stoehr, F. 2011, in Society of Photo-Optical Instrumentation Engineers (SPIE) Conference Series, Vol. 8127, Optical Modeling and Performance Predictions V, ed. M. A. Kahan, 81270J, doi: 10.1117/12.892762

Krolikowski, D. M., Kraus, A. L., & Rizzuto, A. C. 2021, AJ, 162, 110, doi: 10.3847/1538-3881/ac0632

Kroupa, P., Aarseth, S., & Hurley, J. 2001, MNRAS, 321, 699, doi: 10.1046/j.1365-8711.2001.04050.x

Kroupa, P., Bouvier, J., Duchêne, G., & Moraux, E. 2003, MNRAS, 346, 354, doi: 10.1046/j.1365-2966.2003.06994.x

- Kroupa, P., & Burkert, A. 2001, ApJ, 555, 945, doi: 10.1086/321515
- Lada, C. J., & Lada, E. A. 2003, ARA&A, 41, 57, doi: 10.1146/annurev.astro.41.011802.094844
- Lafrenière, D., Marois, C., Doyon, R., & Barman, T. 2009, ApJ, 694, L148, doi: 10.1088/0004-637X/694/2/L148
- Lafrenière, D., Marois, C., Doyon, R., Nadeau, D., & Artigau, É. 2007, ApJ, 660, 770, doi: 10.1086/513180
- Lambrechts, M., & Johansen, A. 2012, A&A, 544, A32, doi: 10.1051/0004-6361/201219127
- Larson, R. B. 1969, MNRAS, 145, 271, doi: 10.1093/mnras/145.3.271
- Larson, R. B. 1999, in Star Formation 1999, ed. T. Nakamoto, 336–340, doi: 10.48550/arXiv.astro-ph/9908189
- Laugier, R., Martinache, F., Ceau, A., et al. 2019, A&A, 623, A164, doi: 10.1051/0004-6361/201834387
- Laugier, R., Martinache, F., Cvetojevic, N., et al. 2020, A&A, 636, A21, doi: 10.1051/0004-6361/201937121
- Law, N. M., Dhital, S., Kraus, A., Stassun, K. G., & West, A. A. 2010, ApJ, 720, 1727, doi: 10.1088/0004-637X/720/2/1727
- Lee, J. M., Factor, S., Lin, Z., et al. 2014, Phys. Rev. Lett., 112, 253902, doi: 10.1103/PhysRevLett.112.253902

Leggett, S. K., Allard, F., Geballe, T. R., Hauschildt, P. H., & Schweitzer, A. 2001, ApJ, 548, 908, doi: 10.1086/319020

Leggett, S. K., Golimowski, D. A., Fan, X., et al. 2002, ApJ, 564, 452, doi: 10.1086/324037

Lindgren, L., Hernández, J., Bombrun, A., et al. 2018, A&A, 616, A2, doi: 10.1051/0004-6361/201832727

Lindgren, L., Klioner, S. A., Hernández, J., et al. 2021, A&A, 649, A2, doi: 10.1051/0004-6361/202039709

Liu, M. 2007, Resolving Ultracool Astrophysics with Brown Dwarf Binaries, HST Proposal. <https://ui.adsabs.harvard.edu/abs/2007hst.prop11136L>

Liu, M. C., Dupuy, T. J., & Allers, K. N. 2016, ApJ, 833, 96, doi: 10.3847/1538-4357/833/1/96

Liu, M. C., Leggett, S. K., Golimowski, D. A., et al. 2006, ApJ, 647, 1393, doi: 10.1086/505561

Lloyd, J. P., Martinache, F., Ireland, M. J., et al. 2006, ApJ, 650, L131, doi: 10.1086/508771

Lodie, N., Scholz, R. D., McCaughrean, M. J., et al. 2005, A&A, 440, 1061, doi: 10.1051/0004-6361:20042456

Luhman, K. L. 2004, ApJ, 614, 398, doi: 10.1086/423666

- . 2012, *ARA&A*, 50, 65, doi: 10.1146/annurev-astro-081811-125528
- . 2022, *AJ*, 163, 24, doi: 10.3847/1538-3881/ac35e2
- . 2023, *AJ*, 165, 37, doi: 10.3847/1538-3881/ac9da3
- Luhman, K. L., Briceño, C., Rieke, G. H., & Hartmann, L. 1998, *ApJ*, 493, 909, doi: 10.1086/305171
- Luhman, K. L., Briceño, C., Stauffer, J. R., et al. 2003, *ApJ*, 590, 348, doi: 10.1086/374983
- Luhman, K. L., Herrmann, K. A., Mamajek, E. E., Esplin, T. L., & Pecaut, M. J. 2018, *AJ*, 156, 76, doi: 10.3847/1538-3881/aacc6d
- Luhman, K. L., Mamajek, E. E., Allen, P. R., Muench, A. A., & Finkbeiner, D. P. 2009, *ApJ*, 691, 1265, doi: 10.1088/0004-637X/691/2/1265
- Luhman, K. L., Mamajek, E. E., Shukla, S. J., & Loutrel, N. P. 2017, *AJ*, 153, 46, doi: 10.3847/1538-3881/153/1/46
- Lyot, B. 1939, *MNRAS*, 99, 580, doi: 10.1093/mnras/99.8.580
- Malmquist, K. G. 1922, *Meddelanden fran Lunds Astronomiska Observatorium Serie I*, 100, 1. <https://ui.adsabs.harvard.edu/abs/1922MeLuF.100....1M>
- Mamajek, E. E. 2009, in American Institute of Physics Conference Series, Vol. 1158, *Exoplanets and Disks: Their Formation and Diversity*, ed. T. Usuda, M. Tamura, & M. Ishii, 3–10, doi: 10.1063/1.3215910

- Manjavacas, E., Goldman, B., Reffert, S., & Henning, T. 2013, A&A, 560, A52, doi: 10.1051/0004-6361/201321720
- Marocco, F., Andrei, A. H., Smart, R. L., et al. 2013, AJ, 146, 161, doi: 10.1088/0004-6256/146/6/161
- Marocco, F., Jones, H. R. A., Day-Jones, A. C., et al. 2015, MNRAS, 449, 3651, doi: 10.1093/mnras/stv530
- Marois, C., Lafrenière, D., Doyon, R., Macintosh, B., & Nadeau, D. 2006, ApJ, 641, 556, doi: 10.1086/500401
- Martín, E. L., Dougados, C., Magnier, E., et al. 2001, ApJ, 561, L195, doi: 10.1086/324754
- Martinache, F. 2010, ApJ, 724, 464, doi: 10.1088/0004-637X/724/1/464
- Martinache, F. 2013a, in Proceedings of the Third AO4ELT Conference, ed. S. Esposito & L. Fini, 6, doi: 10.12839/AO4ELT3.12659
- . 2013b, PASP, 125, 422, doi: 10.1086/670670
- Martinache, F., Ceau, A., Laugier, R., et al. 2020, A&A, 636, A72, doi: 10.1051/0004-6361/201936981
- Martinez, R. A., & Kraus, A. L. 2019, AJ, 158, 134, doi: 10.3847/1538-3881/ab32e6
- Metchev, S. A., Kirkpatrick, J. D., Berriman, G. B., & Looper, D. 2008, ApJ, 676, 1281, doi: 10.1086/524721

- Michelson, A. A. 1891, *Nature*, 45, 160, doi: 10.1038/045160a0
- Michelson, A. A., & Pease, F. G. 1921, *ApJ*, 53, 249, doi: 10.1086/142603
- Monnier, J. D., Tuthill, P. G., Ireland, M., et al. 2009, *ApJ*, 700, 491, doi: 10.1088/0004-637X/700/1/491
- Muzerolle, J., Hillenbrand, L., Calvet, N., Briceño, C., & Hartmann, L. 2003, *ApJ*, 592, 266, doi: 10.1086/375704
- Napier, P. J. 1995, in *Astronomical Society of the Pacific Conference Series*, Vol. 82, Very Long Baseline Interferometry and the VLBA, ed. J. A. Zensus, P. J. Diamond, & P. J. Napier, 59. <https://ui.adsabs.harvard.edu/abs/1995ASPC...82...59N>
- Öberg, K. I., Murray-Clay, R., & Bergin, E. A. 2011, *ApJ*, 743, L16, doi: 10.1088/2041-8205/743/1/L16
- O'Brien, D. P., & Greenberg, R. 2005, *Icarus*, 178, 179, doi: 10.1016/j.icarus.2005.04.001
- Offner, S. S. R., Dunham, M. M., Lee, K. I., Arce, H. G., & Fielding, D. B. 2016, *ApJ*, 827, L11, doi: 10.3847/2041-8205/827/1/L11
- Offner, S. S. R., Klein, R. I., McKee, C. F., & Krumholz, M. R. 2009, *ApJ*, 703, 131, doi: 10.1088/0004-637X/703/1/131
- Offner, S. S. R., Kratter, K. M., Matzner, C. D., Krumholz, M. R., & Klein, R. I. 2010, *ApJ*, 725, 1485, doi: 10.1088/0004-637X/725/2/1485

Offner, S. S. R., Moe, M., Kratter, K. M., et al. 2023, in Astronomical Society of the Pacific Conference Series, Vol. 534, Astronomical Society of the Pacific Conference Series, ed. S. Inutsuka, Y. Aikawa, T. Muto, K. Tomida, & M. Tamura, 275. <https://ui.adsabs.harvard.edu/abs/2023ASPC..534..275O>

Oppenheimer, B. R., & Hinkley, S. 2009, *ARA&A*, 47, 253, doi: [10.1146/annurev-astro-082708-101717](https://doi.org/10.1146/annurev-astro-082708-101717)

Parker, R. J., & Goodwin, S. P. 2011, *MNRAS*, 411, 891, doi: [10.1111/j.1365-2966.2010.17722.x](https://doi.org/10.1111/j.1365-2966.2010.17722.x)

Patience, J., Ghez, A. M., Reid, I. N., & Matthews, K. 2002, *AJ*, 123, 1570, doi: [10.1086/338431](https://doi.org/10.1086/338431)

Perryman, M. A. C., Lindegren, L., Kovalevsky, J., et al. 1997, *A&A*, 323, L49. <https://ui.adsabs.harvard.edu/abs/1997A&A...323L..49P>

Phillips, M. W., Tremblin, P., Baraffe, I., et al. 2020, *A&A*, 637, A38, doi: [10.1051/0004-6361/201937381](https://doi.org/10.1051/0004-6361/201937381)

Pope, B., Martinache, F., & Tuthill, P. 2013, *ApJ*, 767, 110, doi: [10.1088/0004-637X/767/2/110](https://doi.org/10.1088/0004-637X/767/2/110)

Pope, B., Tuthill, P., Hinkley, S., et al. 2016, *MNRAS*, 455, 1647, doi: [10.1093/mnras/stv2442](https://doi.org/10.1093/mnras/stv2442)

Pope, B. J. S. 2016, *MNRAS*, 463, 3573, doi: [10.1093/mnras/stw2215](https://doi.org/10.1093/mnras/stw2215)

Pope, B. J. S., Pueyo, L., Xin, Y., & Tuthill, P. G. 2021, ApJ, 907, 40,
doi: 10.3847/1538-4357/abcb00

Press, W. H., Teukolsky, S. A., Vetterling, W. T., & Flannery, B. P. 2002,
Numerical recipes in C++ : the art of scientific computing (Cambridge Uni-
versity Press). <https://ui.adsabs.harvard.edu/abs/2002nrca.book...>
. . P

Radigan, J., Lafrenière, D., Jayawardhana, R., & Doyon, R. 2009, ApJ, 698,
405, doi: 10.1088/0004-637X/698/1/405

Raghavan, D., McAlister, H. A., Henry, T. J., et al. 2010, ApJS, 190, 1,
doi: 10.1088/0067-0049/190/1/1

Reggiani, M., & Meyer, M. R. 2013, A&A, 553, A124, doi: 10.1051/
0004-6361/201321631

Reid, I. 2004, Ultracool companions to the nearest L dwarfs, HST Proposal.
<https://ui.adsabs.harvard.edu/abs/2004hst..prop10143R>

—. 2006, A search for planetary-mass companions to the nearest L dwarfs -
completing the survey, HST Proposal. <https://ui.adsabs.harvard.edu/abs/2006hst..prop10879R>

Reid, I. N., Cruz, K. L., Burgasser, A. J., & Liu, M. C. 2008a, AJ, 135, 580,
doi: 10.1088/0004-6256/135/2/580

Reid, I. N., Cruz, K. L., Kirkpatrick, J. D., et al. 2008b, AJ, 136, 1290,
doi: 10.1088/0004-6256/136/3/1290

Reid, I. N., Gizis, J. E., Kirkpatrick, J. D., & Koerner, D. W. 2001, AJ, 121,
489, doi: 10.1086/318023

Reid, I. N., Kirkpatrick, J. D., Gizis, J. E., et al. 2000, AJ, 119, 369, doi: 10.
1086/301177

Reid, I. N., Lewitus, E., Allen, P. R., Cruz, K. L., & Burgasser, A. J. 2006,
AJ, 132, 891, doi: 10.1086/505626

Reipurth, B., & Clarke, C. 2001, AJ, 122, 432, doi: 10.1086/321121

Reipurth, B., & Mikkola, S. 2015, AJ, 149, 145, doi: 10.1088/0004-6256/
149/4/145

Reylé, C., Delorme, P., Willott, C. J., et al. 2010, A&A, 522, A112, doi: 10.
1051/0004-6361/200913234

Rizzuto, A. C., Ireland, M. J., Dupuy, T. J., & Kraus, A. L. 2016, ApJ, 817,
164, doi: 10.3847/0004-637X/817/2/164

Roberts, Lewis C., J., & Neyman, C. R. 2002, PASP, 114, 1260, doi: 10.1086/
343221

Rodriguez, D. R. 2016, AstrodBWeb, v1.0, Zenodo, doi: 10.5281/zenodo.
47866

Roye, E., Krist, J., Schultz, A. B., & Wiklind, T. 2003, Measuring the Cold Mask Offset, Tech. rep. <https://ui.adsabs.harvard.edu/abs/2003nicm.rept....4R>

Safronov, V. S. 1972, Evolution of the Protoplanetary Cloud and Formation of the Earth and the Planets (Israel Program for Scientific Translations)

Sallum, S., & Skemer, A. 2019, Journal of Astronomical Telescopes, Instruments, and Systems, 5, 018001, doi: [10.1117/1.JATIS.5.1.018001](https://doi.org/10.1117/1.JATIS.5.1.018001)

Sallum, S., Follette, K. B., Eisner, J. A., et al. 2015, Nature, 527, 342, doi: [10.1038/nature15761](https://doi.org/10.1038/nature15761)

Schmidt, S. J., Cruz, K. L., Bongiorno, B. J., Liebert, J., & Reid, I. N. 2007, AJ, 133, 2258, doi: [10.1086/512158](https://doi.org/10.1086/512158)

Schneider, A. C., Cushing, M. C., Kirkpatrick, J. D., et al. 2014, AJ, 147, 34, doi: [10.1088/0004-6256/147/2/34](https://doi.org/10.1088/0004-6256/147/2/34)

Schultz, A. 2002, NICMOS Deep PSF for Determining Cold Mask Offsets, HST Proposal. <https://ui.adsabs.harvard.edu/abs/2002hst..prop.9704S>

Shannon, C. 1949, Proceedings of the IRE, 37, 10, doi: [10.1109/JRPROC.1949.232969](https://doi.org/10.1109/JRPROC.1949.232969)

Shu, F. H. 1977, ApJ, 214, 488, doi: [10.1086/155274](https://doi.org/10.1086/155274)

Shu, F. H., Adams, F. C., & Lizano, S. 1987, ARA&A, 25, 23, doi: [10.1146/annurev.aa.25.090187.000323](https://doi.org/10.1146/annurev.aa.25.090187.000323)

Sirianni, M., Jee, M. J., Benítez, N., et al. 2005, PASP, 117, 1049, doi: 10.1086/444553

Sivaramakrishnan, A., Koresko, C. D., Makidon, R. B., Berkefeld, T., & Kuchner, M. J. 2001, ApJ, 552, 397, doi: 10.1086/320444

Skrzypek, N., Warren, S. J., & Faherty, J. K. 2016, A&A, 589, A49, doi: 10.1051/0004-6361/201527359

Smart, R. L., Tinney, C. G., Bucciarelli, B., et al. 2013, MNRAS, 433, 2054, doi: 10.1093/mnras/stt876

Smart, R. L., Bucciarelli, B., Jones, H. R. A., et al. 2018, MNRAS, 481, 3548, doi: 10.1093/mnras/sty2520

Soummer, R. 2005, ApJ, 618, L161, doi: 10.1086/427923

Soummer, R., Aime, C., & Falloon, P. E. 2003, A&A, 397, 1161, doi: 10.1051/0004-6361:20021573

Stamatellos, D., & Whitworth, A. P. 2009, MNRAS, 392, 413, doi: 10.1111/j.1365-2966.2008.14069.x

Strom, K. M., & Strom, S. E. 1994, ApJ, 424, 237, doi: 10.1086/173886

STScI Development Team. 2013, pysynphot: Synthetic photometry software package. <http://ascl.net/1303.023>

Sullivan, K., & Kraus, A. L. 2021, ApJ, 912, 137, doi: 10.3847/1538-4357/abf044

Susemiehl, N., & Meyer, M. R. 2022, A&A, 657, A48, doi: 10.1051/0004-6361/202038582

ten Brummelaar, T. A., McAlister, H. A., Ridgway, S. T., et al. 2005, ApJ, 628, 453, doi: 10.1086/430729

Thompson, A. R., Moran, J. M., & Swenson, G. W. 2017, Van Cittert–Zernike Theorem, Spatial Coherence, and Scattering (Cham: Springer International Publishing), 767–786, doi: 10.1007/978-3-319-44431-4_15

Tinney, C. G., Faherty, J. K., Kirkpatrick, J. D., et al. 2014, ApJ, 796, 39, doi: 10.1088/0004-637X/796/1/39

Tobin, J. J., Kratter, K. M., Persson, M. V., et al. 2016, Nature, 538, 483, doi: 10.1038/nature20094

Todorov, K., Luhman, K. L., & McLeod, K. K. 2010, ApJ, 714, L84, doi: 10.1088/2041-8205/714/1/L84

Todorov, K. O., Luhman, K. L., Konopacky, Q. M., et al. 2014, ApJ, 788, 40, doi: 10.1088/0004-637X/788/1/40

Tokovinin, A., & Briceño, C. 2020, AJ, 159, 15, doi: 10.3847/1538-3881/ab5525

Toomre, A. 1964, ApJ, 139, 1217, doi: 10.1086/147861

Tuthill, P., Lloyd, J., Ireland, M., et al. 2006, in Society of Photo-Optical Instrumentation Engineers (SPIE) Conference Series, Vol. 6272, Society

of Photo-Optical Instrumentation Engineers (SPIE) Conference Series, ed. B. L. Ellerbroek & D. Bonaccini Calia, 62723A, doi: [10.1117/12.672342](https://doi.org/10.1117/12.672342)

Tuthill, P. G. 2012, in Society of Photo-Optical Instrumentation Engineers (SPIE) Conference Series, Vol. 8445, Optical and Infrared Interferometry III, ed. F. Delplancke, J. K. Rajagopal, & F. Malbet, 844502, doi: [10.1117/12.925794](https://doi.org/10.1117/12.925794)

Tuthill, P. G., Monnier, J. D., Danchi, W. C., Wishnow, E. H., & Haniff, C. A. 2000, PASP, 112, 555, doi: [10.1086/316550](https://doi.org/10.1086/316550)

Tyson, R. K. 2000, Introduction to adaptive optics, Vol. 41 (SPIE press)

Umbreit, S., Burkert, A., Henning, T., Mikkola, S., & Spurzem, R. 2005, ApJ, 623, 940, doi: [10.1086/428602](https://doi.org/10.1086/428602)

van Cittert, P. H. 1934, Physica, 1, 201, doi: [10.1016/S0031-8914\(34\)90026-4](https://doi.org/10.1016/S0031-8914(34)90026-4)

Virtanen, P., Gommers, R., Oliphant, T. E., et al. 2020, Nature Methods, 17, 261, doi: [10.1038/s41592-019-0686-2](https://doi.org/10.1038/s41592-019-0686-2)

von Braun, K., Boyajian, T. S., ten Brummelaar, T. A., et al. 2011, ApJ, 740, 49, doi: [10.1088/0004-637X/740/1/49](https://doi.org/10.1088/0004-637X/740/1/49)

Wallace, A. L., Kammerer, J., Ireland, M. J., et al. 2020, MNRAS, 498, 1382, doi: [10.1093/mnras/staa2434](https://doi.org/10.1093/mnras/staa2434)

Weinberg, M. D., Shapiro, S. L., & Wasserman, I. 1987, ApJ, 312, 367, doi: 10.1086/164883

West, A. A., Hawley, S. L., Bochanski, J. J., et al. 2008, AJ, 135, 785, doi: 10.1088/0004-6256/135/3/785

White, R. 2003, A Search for Young Binary Brown Dwarfs: Constraining Formation Scenarios and Masses Through Multiplicity, HST Proposal ID 9853. Cycle 12. <https://ui.adsabs.harvard.edu/abs/2003hst..prop.9853W>

White, R. J., & Basri, G. 2003, ApJ, 582, 1109, doi: 10.1086/344673

Williams, J. P., & Cieza, L. A. 2011, ARA&A, 49, 67, doi: 10.1146/annurev-astro-081710-102548

Winters, J. G., Henry, T. J., Jao, W.-C., et al. 2019, AJ, 157, 216, doi: 10.3847/1538-3881/ab05dc

Wood, M. L., Mann, A. W., & Kraus, A. L. 2021, AJ, 162, 128, doi: 10.3847/1538-3881/ac0ae9

Young, T. 1804, Philosophical Transactions of the Royal Society of London Series I, 94, 1. <https://ui.adsabs.harvard.edu/abs/1804RSPT...94...1Y>